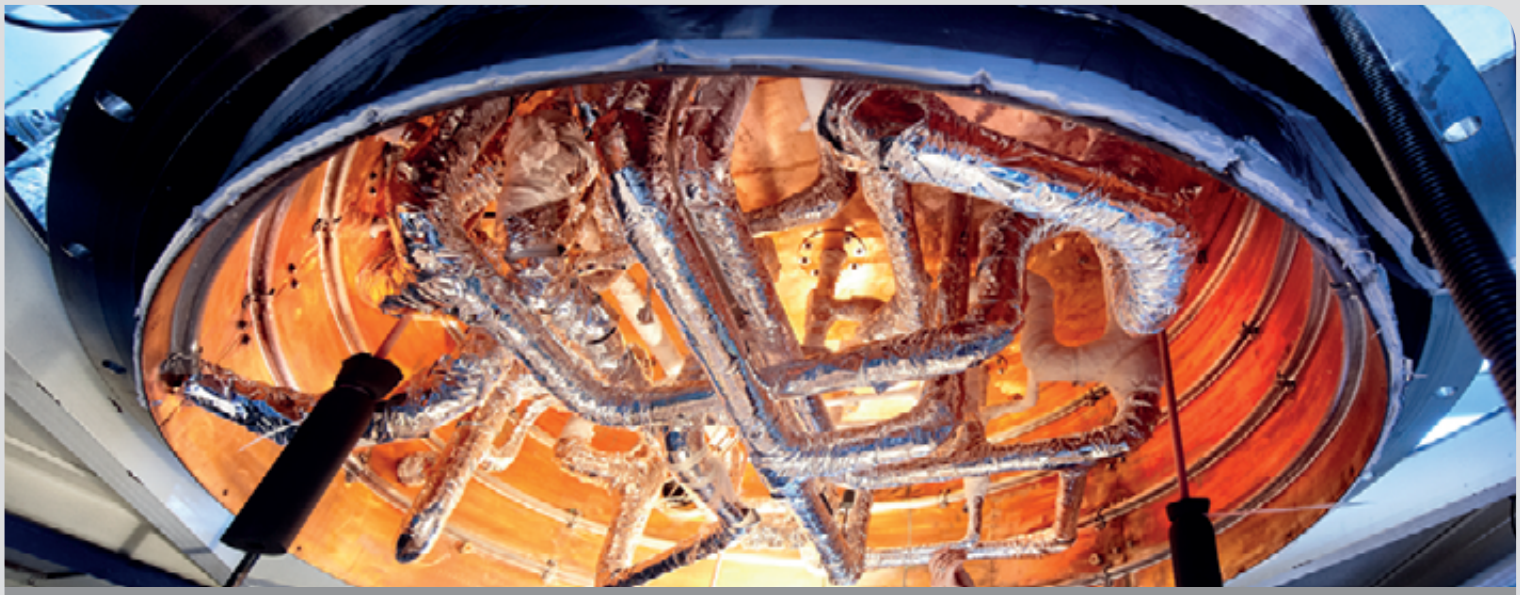

KIT SCIENTIFIC REPORTS 7647

Nuclear Fusion Programme

Annual Report of the Association Karlsruhe Institute of Technology/EURATOM

January 2012 – December 2012

KIT Scientific Publishing

I. Pleli (ed.)

Nuclear Fusion Programme

Annual Report of the Association Karlsruhe Institute of Technology/EURATOM

January 2012 – December 2012

Karlsruhe Institute of Technology
KIT SCIENTIFIC REPORTS 7647

Nuclear Fusion Programme

Annual Report of the Association
Karlsruhe Institute of Technology/EURATOM

January 2012 – December 2012

I. Pleli (ed.)

KIT Scientific Publishing

Report-Nr. KIT-SR 7647

Impressum

Scientific Publishing

Karlsruher Institut für Technologie (KIT)
KIT Scientific Publishing
Straße am Forum 2
D-76131 Karlsruhe

www.ksp.kit.edu

Print on Demand 2013

ISSN 1869-9669

Overview

Preface

Year 2012 has brought significant changes within the European Fusion Programme. The most noticeable one is the new focus and specific program target defined in the document “Fusion Electricity – A roadmap to the realization of fusion energy”. This development has been largely anticipated, and welcomed, by the KIT Fusion Programme, which has always aimed at providing the technologies necessary for fusion power, with ITER being the most important milestone and scientific experiment. It is also aligned with the goals of the German DEMO Working Group, which was created in 2010, for the purpose of integrating the power plant oriented work in the three German fusion centres.

Within the Accompanying Programme, the Power Plant Physics & Technology activity under EFDA now has gained momentum and is driving the necessary developments in parallel to ITER. KIT is committed to this approach, taking the most active role therein, with a total of 72 individual tasks in the areas of Design Assessment Studies, Design Tools & Methodologies, Materials, Power Exhaust Physics Integration Studies and System Design Integration. Another focus of our dedication to the Accompanying Programme is the Training of young researchers and engineers. Five new Goal Oriented Training Networks with KIT participation were started in 2012, in addition to the eight others already running. KIT coordinates seven of these networks, with 15 trainees employed at KIT in 2012.

Nevertheless, ITER is the most important field of our research. Taking active part in ten consortia with other EURATOM Associates for providing the European contributions to ITER via F4E, KIT has set up a considerable share of them, and coordinates in four of these partnerships. As the coordinator of the Test Blanket Module consortium, KIT has signed two Framework Partnership Agreements with F4E in 2012. All in all, at the end of 2012, KIT had signed a total of 55 contracts (grants, procurements and services) with F4E and ITER, most of them in consortia with our European partners.

Cooperation with industry is increasingly important in fusion – for constructing ITER, for transferring technologies developed in fusion into the market, and for preparing the industrial involvement in the DEMO conception and design. KIT is playing an active role here, too. Examples are the long-stand collaboration with TED for the development and production of high-power gyrotrons for ITER and Wendelstein 7-X, the joint development of new refractory materials and materials combinations with Plansee, or the development of Be products and technology with Goraieb Versuchstechnik and Materion. In the area of fusion magnets, quite a number of companies from all over the world have been used KIT capabilities for testing and qualification of materials at cryogenic temperatures.

The KIT Fusion Programme is taking benefit from the process of integration among the former University of Karlsruhe and Karlsruhe Research Centre, now together constituting KIT. In 2012, 6 PhD candidates, who had started their work in fusion before the integration, have successfully completed their work. Furthermore, the level of PhD involvement in the programme has almost doubled, with 33 additional PhD students now working within the programme . Simultaneously, the number of fusion-related lectures at the university has increased significantly. Furthermore, the programme has available now additional competences from the university side, e.g., in the area of remote maintenance and logistics.

At the end of 2012, KIT Fusion Programme underwent a mid-term evaluation, according to the funding cycle of the national programme and conducted by a high-level European panel. This evaluation confirmed the quality and relevance of the KIT work in fusion technology, as well as our strategic orientation and focusing. Thus, KIT is well prepared to take on the tasks ahead on the way to fusion energy.

Klaus Hesch, July 2013

Plasma Wall Interaction

The transient events such as disruptions and edge localized modes (ELMs) are anticipated in the future tokamaks ITER and DEMO to be the most serious threat to surfaces of plasma-facing components (PFCs), because of melt motion, vaporization and brittle destruction (BD) erosion of tungsten (W) divertor and beryllium (Be) or W first wall (FW) under the high heat loads by plasma and runaway electrons (RE). In order to predict the tolerable impacts and disruption mitigation by means of massive gas injection (MGI) of noble gas, computer codes have been developed at KIT: MEMOS for melting/vaporization caused by heating, ENDEP for RE stopping in W and Be, PEGASUS for BD after the following thermostress, and TOKES for MGI thermal quench (TQ). The codes were earlier validated against experiments performed in JET and DIII-D tokamaks as well as the electron beam facility JUDITH and plasma guns MK-200UG and QSPA.

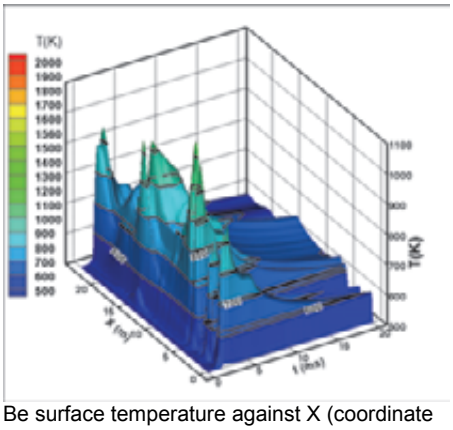

Be surface temperature against X (coordinate along poloidal surface contour) and t (time); $J_m = 1.3\times10^{26}$/s.

In MGI a heavy puff of impurity (neon) is injected rapidly into confined plasma to dissipate the heat through the radiation. ITER foresees three toroidally separated upper port injectors. TOKES code models them as one gap in FW which is uniformly distributed on toroidal angle. The simulation includes the gas dynamics in the injector, ionization of injected atoms in the plasma, the passage of a cooling radiative wave through the plasma and an anomalous thermal transport. Poloidal asymmetries in the radiation density distribution can increase local Be FW temperature above the melting point 1560 K. The MGI scenarios are examined by varying the gas inflow J_m in the injector gas plenum, which results in TQ time from 3 ms to 12 ms. The simulations showed that the wall starts melting when J_m exceeds the value of 1.3×10^{26} atom/s, which corresponds to 20 g of injected neon and complete plasma cooling on a timescale of 5.7 ms.

During MGI mitigated disruptions at JET, RE beams were observed as in earlier experiments with the carbon fibre composite (CFC) FW as (since 2011) with the new Be covered ITER-like wall (ILW) in which a local melting of poloidal limiter by RE occurred. To numerically assess current and planned JET experiments with melting of typical Be tiles caused by RE, the codes ENDEP and MEMOS are applied, aiming at melting threshold W_{melt} for energy deposition density W_{RE} and the melt motion and surface vaporization as RE after effects. RE caused melt layer can move due to the J×B force of halo-, eddy-, and thermo-currents and the gradients of surface tension and impacting plasma pressure. For viscous melt motion an upgraded and validated against TEXTOR experiments 3D version of MEMOS is now available. Detailed surface temperature evolution and spatial distributions as well as melting and evaporation erosion are simulated for single Be tile installed at the upper dump plate in JET accounting for geometrical peculiarities of it. At first, the energy deposition function was calculated with the code ENDEP and then with MEMOS the wall temperature for RE impacts ranged from 1 to 4 ms for the current densities up to 0.6 MA/m^2 and wall loads of few MW/cm2. Approximately 40% of energy is passing through the tile and escapes as primary and secondary electrons. Significant melt motion of the melt layer of ~ 10^2 μm develops at rather small secondary electron current above 2 kA/m^2.

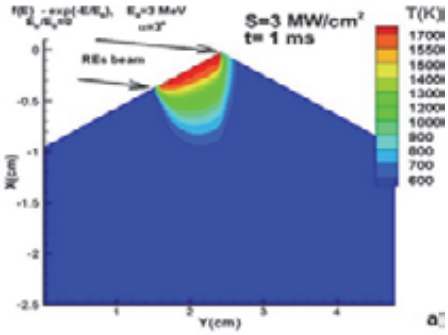

Typical temperature field inside Be tile of JET ILW for RE load 3 MW/cm^2

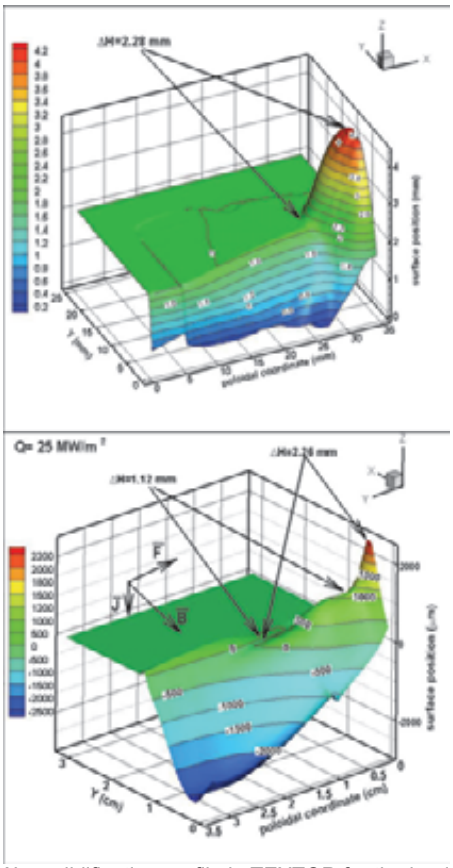

W resolidification profile in TEXTOR for the load 25 MW/m^2. Top panel: TEXTOR experiment, Bottom panel: the corresponding MEMOS results.

The MEMOS calculations to support TEXTOR experiments and validate the code were continued. The simulations were done for 3.5×3.2×0.3 cm flat W targets assuming the Child-Langmuir model of the thermoemission current due to which the melt motion develops in the magnetic field of 2.25 T. Several scenarios of pulse duration 6 s with the plasma loads from 21 to 27 MW/m^2 are calculated. In the 25 MW/m^2 case the resolidification profile is in a good agreement with the TEXTOR measurements. The ENDEP and MEMOS codes were also validated against TEXTOR experiments on interaction of RE electrons with graphite limiter. In the experiment the mean RE energy is about 4 MeV, the RE energy absorbed in the graphite limiter 3 kJ and the RE pulse duration of 10 ms. Maximum surface temperature reached 3.5×10^3 K both in the experiment and the simulation.

Next numerical investigations for wall surface erosion at the conditions expected in DEMO using ENDEP and MEMOS have been undertaken. In steady-state operation, as long as melting and ignition of arcing not involved, the important erosion process for the FW and divertor baffles is physical sputtering. Dependencies of sputtering yield on the incidence angle of bombarding ions accelerated by a pre-surface potential of 3.5T/e were obtained. An important process of the sputtering is charge-exchanges at the surface. The most intensive W release is expected from the baffles. Due to rather low level of W sputtering rates even for high plasma boundary temperatures and expected particle fluxes of lost deuterium, tritium and helium (5%), the resulting W impurity concentrations in plasma centre remains below ~5×10^{-5}. For continuous DEMO operation W erosion rate remains below 5 mm/year.

For off-normal DEMO processes MEMOS calculations for W/EUROFER armour show that a plasma vertical displacement event (VDE) inevitably causes surface melting and evaporation of W PFCs. The runaway electrons of 50-80 MeV expected during the event deposit their energy so much deep that RE thermal conduction heat penetrates through W into the EUROFER substrate. The required minimum armour thickness to prevent thermal destruction of EUROFER by melting and creeping is at least ≥1.4cm. Calculations for the W/EUROFER bound show that it might be compatible with high neutron fluencies, so that the loss of creep strength at relatively low temperature represents the main drawback of EUROFER as a structural material.

As a contribution to DEMO conceptual analysis by EFDA the snow flake (SF) alternative divertor magnetic configuration with respect to coupling of ballooning instability with thermal (MARFE) instability was examined aiming at the pedestal plasma density limit for symmetric equilibrium with two SF X-points. Ballooning instability near the X-points was also addressed. As it follows from the carried out analytical consideration, the ballooning perturbation inside the configuration is much weaker than outside, which is due to the stabilising effect of convex magnetic curvature in the inner side. The upper attainable density exhibits almost linear dependence on the plasma current similarly to the Greenwald limit. However it differs from the Greenwald value: at boundary plasma temperatures smaller than 100 eV the density limit for SF is higher than that of usual X-point. A weak dependence of maximum density on impurity fraction was obtained. However an unfavourable influence of impurities can emerge through the resistive electromagnetic modes, which in turn can trigger the ideal modes and finally destroy the MHD equilibrium. Further principal research of SF configuration is required.

Physics: Heating and Current Drive - ECRH

Electron Cyclotron Heating & Current Drive (ECRH & CD) will play a major role in forthcoming long pulse or continuous fusion devices like ITER, W7-X and DEMO. Due to its excellent coupling to the plasma and well localized power deposition in the plasma, microwaves in the range of 100 – 200 GHz are already applied in existing fusion machines to heat and stabilize the plasma and to drive a toroidal current, which would be of particular importance for a continuous tokamak. Since many years, KIT has been developing high power gyrotrons as microwave sources, diamond window units, and launchers to inject the power into the fusion plasma.

Together with several European institutions and with a commercial partner, KIT developed the gyrotrons for the W7-X ECRH heating system. Continuous progress is being reported on the tests of the series gyrotrons and the assembling of the complete ECRH system at IPP Greifswald.

The development of a European 170 GHz gyrotron for ITER has been pursued within the EU Gyrotron Consortium (EGYC), acting as a single scientific partner for F4E. The goal of this development is the supply of sources for 170 GHz ECH & CD to ITER, providing 8 MW CW power.

In another European consortium, the ITER ECRH Upper Launcher is being developed together with ultra-low loss diamond torus windows. The main purpose of these launchers is plasma stabilization, an additional equatorial launcher will provide central plasma heating.

For DEMO as the next step on the fusion step ladder towards power generation, new concepts of ECRH heating like frequency tuneable systems are under development, including ECRH RF sources, launcher components and broadband windows.

Microwave Heating for Wendelstein 7-X

The ECRH system for W7-X (10 MW, 140 GHz, CW) will be provided under the responsibility of KIT together with national and European partners. Most of the components of the transmission system, HV-systems and in-vessel-systems have been installed at IPP Greifswald, and have been already used for testing new concepts and components for ECRH. Progress has been made w.r.t. performance improvements of the series gyrotrons.

ECRH-plug-in launcher with adjustable copper mirrors (left) supporting 3 beams.

In 2012 long pulse conditioning and testing of the gyrotron SN6 was continued. SN6 is the first series gyrotron equipped with all improvements developed so far. The final acceptance tests of SN6 were finished successfully at IPP Greifswald, showing more than 900 kW RF output power and reliable operation at 30 min pulse length.

Within the site acceptance tests of gyrotron SN6, the "long load” (a 23 m long absorbing stainless steel tube with a water jacket) could be tested successfully with 910 kW output power at the gyrotron window for 30 min.

The four ECRH-plug-in launchers have been equipped with water manifolds and flow sensors and are ready for operation.

Development of the European 170 GHz Gyrotron for ITER

The development of the European 170 GHz gyrotron for ITER is pursued within the European Gyrotron Consortium (EGYC, consisting of CRPP, Switzerland; KIT, Germany; HELLAS, Greece; CNR; Italy). EGYC acts as the scientific partner for Fusion for Energy (F4E). In 2012, F4E decided to focus on the 1 MW conventional cavity gyrotron development which was initiated in 2007 as a risk mitigation action during the development of the 2 MW coaxial cavity gyrotron. Within this development, important results of the emitter design of the electron gun and on tolerances were achieved.

Work on the development of a 2 MW coaxial cavity gyrotron has been progressed in order to achieve more stable operation in terms of suppression of instabilities and avoidance of the effects of trapped particles in the electron optical system. In this configuration the coaxial gyrotron has been operated with up to 1.9 MW. For the first time, the pre-prototype has been operated with a single stage depressed collector.

Other Developments on Gyrotrons

Besides the major scientific topics described above, several accompanying activities were ongoing:

- For the first time a step tuneable high power gyrotron has been operated with a CVD diamond Brewster angle window. This configuration provides operation of the gyrotron in the frequency range from 124 to 162 GHz without spurious reflections, and has long pulse capabilities due to the excellent material properties of diamond.
- Triggered by parasitic oscillations in the gyrotron, the field of spectral measurement techniques for gyrotrons has gained interest. A prototype of a new measurement system capable of analyzing the gyrotron's output spectrum for transient effects with a high bandwidth and dynamic range was developed throughout the year 2012.

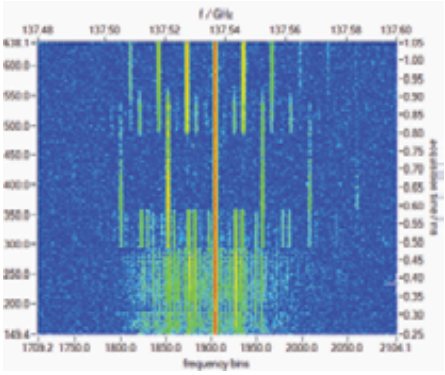

Spectrogramm of transient modulation during operation with TE27,8.

- The design of a 10kW/28GHz gyrotron with a segmented emitter based on controlled-porosity reservoir cathodes (CPR) has been continued. The outstanding features of CPR emitters, which are supposed to allow for a considerably higher emission current density and a much longer life time compared to conventional emitter materials, are particularly attractive for high power applications and increased reliability.
- The application of simulation codes on wave beam interaction has been broadened by including (dynamic) after-cavity interaction (ACI) and non-uniform magnetic fields. Effects of misalignment of the electron beam and the magnetic field were studied. To overcome the simplifications of models using the slow variables approach Position Independent Code (PIC) or PIC-like codes have been studied.

ITER ECRH Upper Launchers

The key challenge for the four ECRH upper launchers in ITER is to provide a system capable of focusing millimeter waves, through eight beam lines, on specific positions in the plasma. The success of the suppression of neoclassical tearing modes depends on the instability detection, a fast steering to the magnetic island and a focused injection of the beam power providing local current drive. Based on the preliminary design, the development of the upper launchers has been continued by the European ECH Upper Launcher Consortium (ECHULCA, consisting of CNR/Italy, CRPP/Switzerland, DIFFER/Netherlands, IPP/Germany and the leading party KIT/Germany in collaboration with F4E). New input from regular operation,

such as plasma profiles, has been included, as well as updated load cases for the plasma facing launchers. Significant progress could be made in establishing stabilization criteria and the optical design, as well as for the structural design and the optimization of the system for maintenance operations. In the current design phase, the launcher design is progressing as a whole system with an emphasis on finalizing the design of the First Confinement System (FCS) consisting of diamond windows, waveguides, mitre bends and the port plug closure plate design. The design development is accompanied by the preparation of a prototyping and testing program (planned for 2013-2014) for demonstration of the maturity of the design in the first upper launcher final design review at ITER related to the FCS part of the system.

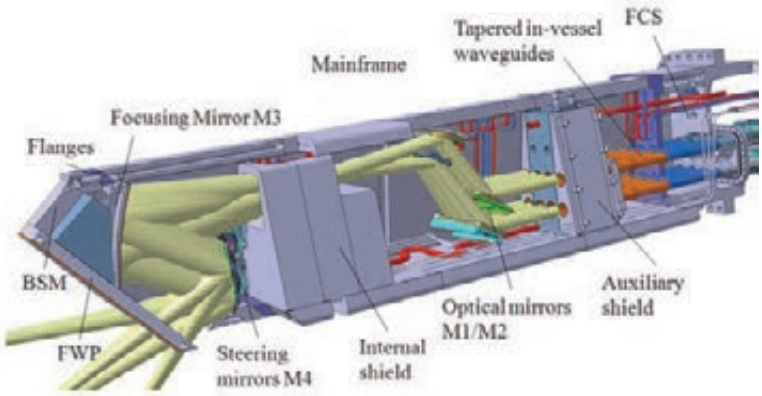

Magnets and Affiliated Components

Cryomechanical Tests in the TOSKA-MTL CryoMaK (Cryogenic Material Testing Karlsruhe)

Cryogenic material performance is crucial for fusion reactors due to the high level of mechanical stresses at low temperature. The TOSKA-Magnet Technology Lab CryoMaK is dedicated for mechanical testing at temperatures from 4 K to room temperature. For ITER and other fusion related facilities material characterization and microscopic inspection are needed in order to guarantee the soundness of design, material and production quality.

As an example, a Helium-Inlet that transports the 4 K cold He to the ITER toroidal field coils was tested in CryoMaK. Following statistics and FEM analysis for fatigue qualification 261,000 cycles are required with applied strain of (10.2 ± 2.3) x 10-4 ε to qualify the component. However, two prototypes were tested even up to 600,000 cycles, attesting a robust design. The figure shows the inlet mounted in the ATLAS test facility of CryoMaK.

Current Leads for Wendelstein 7-X and JT-60SA

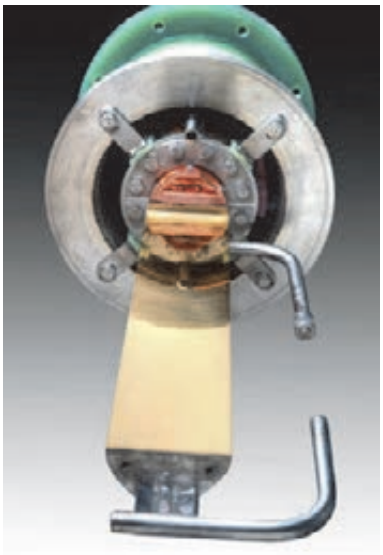

In Greifswald the stellarator W7-X is presently under construction. The current of maximum 18.2 kA for the 50 non-planar and 20 planar superconducting coils is fed to the low temperature level by 14 current leads, designed, constructed and tested by KIT.

In early 2013 the last two of 14 plus 2 spare High-Temperature Superconductor (HTS) current leads were successfully tested at KIT. The current leads have been delivered to Greifswald for the installation in the torus.

In the frame of a BMBF project (no POF activity) KIT designs, constructs and tests 26 HTS current leads for the satellite tokamak JT-60SA. The maximum current is 26 kA for 6 current leads and 20 kA for the other 20.

Quench Detection System for Fusion Magnets (HGF)

If superconductivity in a powered magnet is lost, the conductor of the magnet starts to heat up fast. If such a quench occurs it has to be detected as fast as possible by the emerging voltage to allow an early discharge of the magnet. KIT has developed the All-In-One quench detection system "UNIQD". The dedicated software QVision has served as the central operating and diagnostics tool for “UNIQD” and includes now an automatic balancing menu for all detectors connected to the embedded host IPC in a cabinet (max. 128 detectors). Adjusting the detector to the lowest quench detection thresholds allows save but fast quench detection.

High Temperature Superconductors for Fusion Magnets

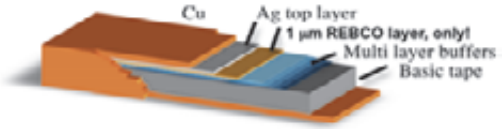

High-temperature superconductors (HTS) show superior current carrying capability at high magnetic fields. With a peak field at the magnet around 12 Tesla, the classical superconductor Nb3Sn used for ITER has only a small temperature margin left. With HTS, even magnetic fields in the range of 14-15 Tesla are possible. The draw-back of the most prominent HTS candidate REBCO: this material is available only in form of thin tapes. The challenge is to form a high current conductor which can be used for fusion.

Several Euratom associations have formed an initiative under EFDA, which is coordinated by KIT, to develop such a high current cable concept.

KIT proposed a Rutherford cable concept using Roebel cables as strands. This fully transposed cable would be ideal with respect to ac losses. The concept shown in the figure should provide 20 kA transport current at 12 T when fully equipped with superconductor.

For testing the real behaviour of Roebel strands in a Rutherford configuration, 3 Roebel strands were applied on the Rutherford former. The experiment showed a slight degradation of 5 – 10%, which correlates to bending experiments. This led to the idea of using a round Roebel former, which is actually under test.

The Roebel approach, which can be used for the Rutherford cable is quite promising with respect to ac losses. The potential is shown from measurements made at CERN where a KIT sample made of ten 12 mm wide REBCO strands showed a critical current of 14 kA at 10 Tesla and 4 K.

With the FBI facility, force F, magnetic field B and transport current I can be applied to superconducting sub-cable samples which was used to test several cable concepts. In the upgraded version with an integrated heater it is now possible to perform measurements at enhanced temperatures up to 77 K (schematic figure and view to the FBI facility shown here).

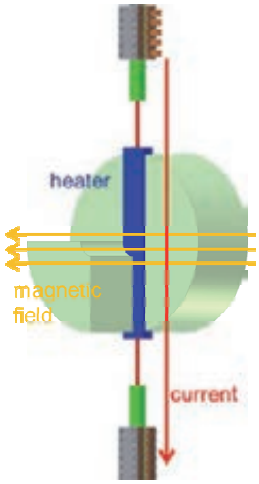

This FBI facility was used to test other high current cable designs with the HTS material REBCO.

Test results from

- Conductor on Round Core cable (CORC cable from "Advanced Conductor Technologies" company)
- and from Twisted stacked cable samples provided by MIT

gave promising results, too.

Breeding Blanket

The development of breeding blankets, their integration in the fusion reactor and their testing are central elements of KIT´s long term programme towards a fusion power reactor. In particular KIT is developing Helium cooled concepts for these systems, namely the Helium Cooled Pebble Bed (HCPB) blanket. Several activities are also in support of liquid breeder blankets like the Helium Cooled Lithium Lead (HCLL) blanket concept developed by CEA and the Dual Coolant Lithium Lead concept (KIT-US). In addition tasks have been performed for the improvement (in fabrication, characterization and modelling) of functional materials like Li-orthosilicate, Beryllium and Beryllium alloys.

The Design for the helium-cooled blanket concepts (WP12-DAS02-T01/T04/T09) has been continued in 2012 in the frame of the PPP&T studies. The activities of KIT have been focused in the adaptation of the box architecture developed in the EU TBM to the new con-

cept of PPP&T DEMO. The new design has been verified with several mechanical analyses in order to dimension the different sub-components like the First Wall (FW), the manifold and the supporting structure. The CAD developed in these tasks will be used in 2013 for dedicated neutronic calculations (e.g. power distribution, tritium production). Furthermore, a first version of the DDD for the HCPB Blanket systems has been produced summarising the new Design and proposing a R&D development plan.

Further Studies regarding the Use of Liquid Metal as Blanket Coolant (WP12-DAS02-T14) have been done. Liquid metals like PbLi are promising candidates for coolants and breeder materials in thermonuclear power reactors, but are strongly constraint through magneto-hydrodynamic (MHD) phenomena. The DCLL blanket considered in a recent design study represents a very attractive design option for a liquid metal blanket and could yield high thermal efficiency. An electrical insulation (flow channel inserts; FCI) between the liquid metal and the duct walls interrupts the electric current path from the fluid into wall. As a result, electric currents induced by the interaction of the moving liquid metal with the strong plasma-confining magnetic field are reduced to a minimum and the MHD induced pressure drop, resulting from electromagnetic Lorentz forces, becomes acceptable. The study presents the impact of gaps in electrical insulation at the junction of different FCI pieces.

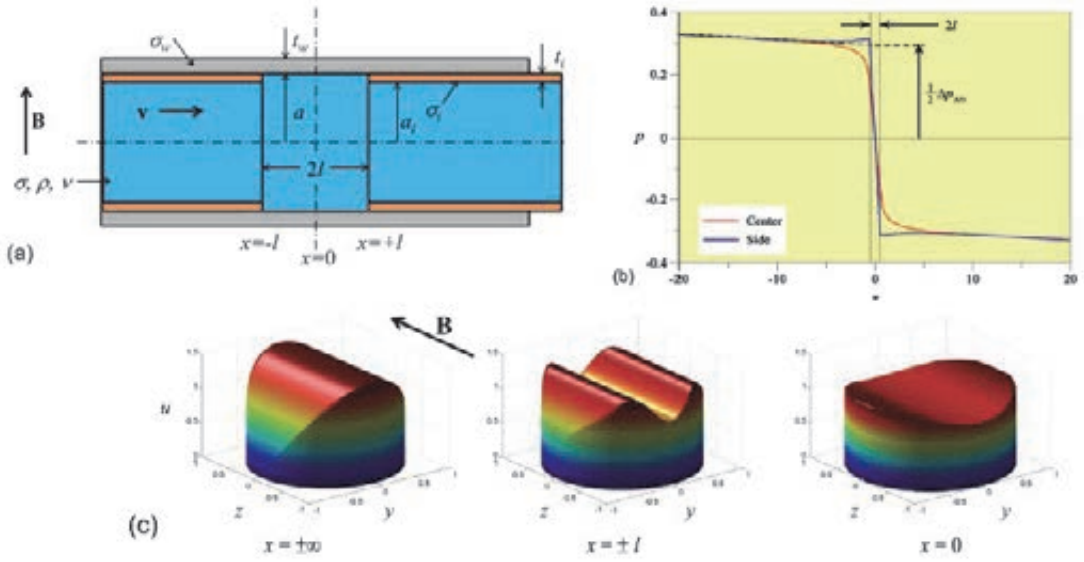

Gap between two FCIs (a) geometry; (b) dimensionless pressure distribution along the pipe axis y=0 and along the side wall y=±1; (c) typical velocity profiles in fully developed regions (x→±∞), at the beginning and end of the gap (x=±l) and in the middle of the gap (x=0).

TBM manufacturing (national funding): A further task is the development and qualification of manufacturing technologies for the HCPB TBM. A typical TBM box is done by plates that contain channels for the cooling of the structures; these channels have to withstand Helium at high pressure (10 MP), at structure temperatures up to 550°C and heat flux of 500 kW/m^2 as First Wall. In 2012 non-destructive ultrasonic immersion testing have been used for the quality assurance and defect quantification with higher accuracy of the uniaxial diffusion-welded cooling plate of a stiffening grid (U-DW-Ar-welded cooling plate) and material for Mock Up (MU)-components. Ultrasonic immersion testing data was used as input for 3D visualization software programmed by I-Deal Technologies. Using 3D visualization software, all detected flaws can be visualized clearly.

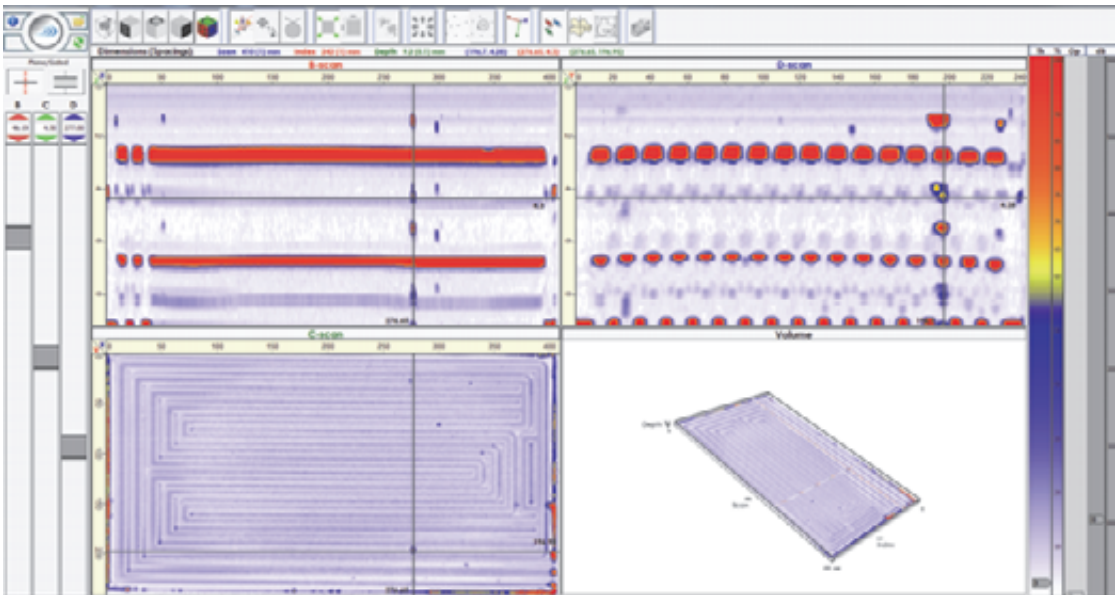

Screen-shot of 3D visualization of the U-DW-Ar-welded cooling plate of a stiffening grid.

Production of Advanced Breeder Pebbles (national funding): As part of the BA DEMO activities, the KALOS facility (KArlsruhe Lithium OrthoSilicate) was assembled to investigate a modified fabrication process for lithium orthosilicate pebbles. Recently, a larger platinum crucible, able to process a three times larger amount of melt, was procured and the two standard crucibles were restored. Lithium orthosilicate pebbles with a lithium metatitanate content of up to 40 mol% have been fabricated. The fabrication of this material is studied is a promising alternative to the reference material because of its higher mechanical rigidity.

Development of Beryllium Alloy Pebble Beds with Improved Tritium Release Characteristics (national funding): Be12Ti is considered to be one of the candidate materials for neutron multiplier of Breeding Blankets in future fusion power plants. In comparison with pure Be, it shows lower chemical activity in contact with steam and better T release characteristics.

Cylinder-shaped Be12Ti samples (diameter of 3 mm) fabricated at the beryllium laboratory by an arc-melting of cold-pressed Be-Ti tablet were irradiated in the frame of HIDOBE-01 campaign in High Flux Reactor in Petten, Netherlands.

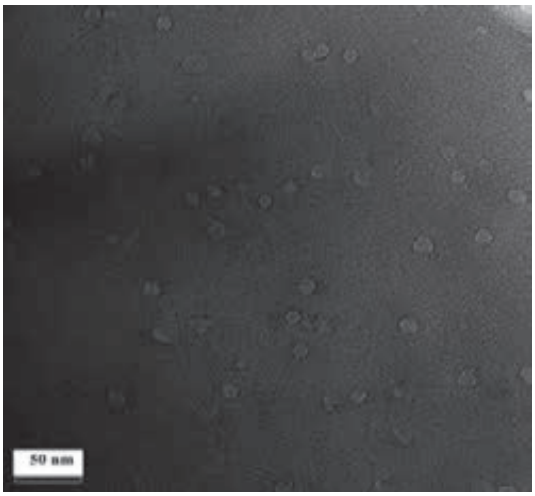

High-resolution TEM image of titanium beryllide irradiated at 873 K.

The sizes and shapes of radiation-induced gas bubbles as well as swelling of samples were evaluated by means of TEM. Also, the mechanical behavior of titanium beryllide specimens in initial and irradiated states was investigated using compression tests under constant loading. The figure shows radiation-induced gas bubbles with the sizes of 15-20 nm after neutron irradiation at 873 K.

Identification of DEMO Failure Modes (WP12-DTM-03-T02-01): The activities within this task aim for the identification of failure modes of candidate structural materials in a helium cooled blanket and of divertor components of a DEMO. **Identification of Equivalent Failure Modes in ITER and Gen-IV** (WP12-DTM-03-T03-01): The activity aims the identification of equivalent failure modes in DEMO and GEN IV of fission power plants by reviewing documents on structural analyses and failure modes in components of GEN IV fission power plants and comparing them with those identified in WP12-DTM-03-T02 for blanket and di-

vertor components of DEMO. Thereby similarities in selected structural materials and expected failure modes will be concluded; mainly the GEN-IV high temperature reactor concepts are considered, in particular the Sodium Fast Reactor (SFR), the Very High Temperature Reactor (VHTR) and the Gas Fast Reactor (GFR**). Identification of Gaps in Existing Design Criteria** (WP12-DTM-03-T04-01): The objective of this activity is to perform a gap analysis on existing standards in context of DEMO. The gap analysis is focused on the divertor (water and helium cooled systems) and the blanket module (helium cooled system). In particular the KIT activity within this task is focused on the rules of the ASME Boiler Pressure Vessel Code (ASME-BPVC).

The EUROBREED network (WP08-GOT-EUROBREED) that integrates almost the all the important aspects of the breeder blanket programme (development of breeder materials, characterization and modelling of properties, test of these materials in out-of-pile experiments, integration in ITER) has been successfully concluded in 2012. **In the GOT Programme "Power Supply Engineering" (WP08-GOT-PSE)**, the major part of the work in 2012 was committed to the extension of the HELOKA facility and the preparations for the high heat flux experiments. This encompassed the upgrade of the mains power supply, the investigations about the feasibility and performances of a surface heating concept for the first wall with simulations in ANSYS and Matlab/Simulink and the procurement of the electron beam gun for the future extension of HELOKA-HP.

Manufacturing and Testing of Mock-ups for Investigation of Coolant Flow in the Manifold System of HCPB TBM (GRICAMAN Experiments) (TW5-TTBB-003 D 1): This Task dealt with investigations of flow distribution in the coolant system of Helium-Cooled-Pebble-Bed Test Blanket Module (HCPB TBM). The facility has been constructed keeping real geometry of manifold 2 and manifold 3 and replacing complicated grid and cap cooling channels with simple pipes having the same flow resistance as the real channels. The facility has been experimentally tested by measuring flow rate distribution through equivalent channels and pressure distribution within manifold boxes. The draft version of the Final report for this Task has been submitted in December 2012.

Divertor

In the framework of EFDA PPPT design assessment studies (DAS) 2012 two divertor studies were performed focusing at modular integration of small tungsten cooling fingers to an entire target plate (WP12-DAS-02-T05) (Figure) and a possible alternative design (WP12-DAS-02-T06) using tantalum-based material rather than tungsten alloy for thimble material. The latter provides a way to mitigate risk, since tungsten is inherently brittle and the expected increase of its brittleness under neutron irradiation is unknown. The results of the integration studies (DAS-02-T05) indicate that the integration of the multiple array of finger modules to a target plate including the necessary shading of the edges of the plate to avoid the sputtering is feasible. While the results of the DAS-02-T06 study show that the use of a tantalum alloy containing 8-10% W is suitable at a decreased helium temperature range of 350 °C. This solution beneficially allows for the use of the Eurofer steel in its basic composition and makes the use of its complex oxide dispersion strengthening (ODS) form dispensable.

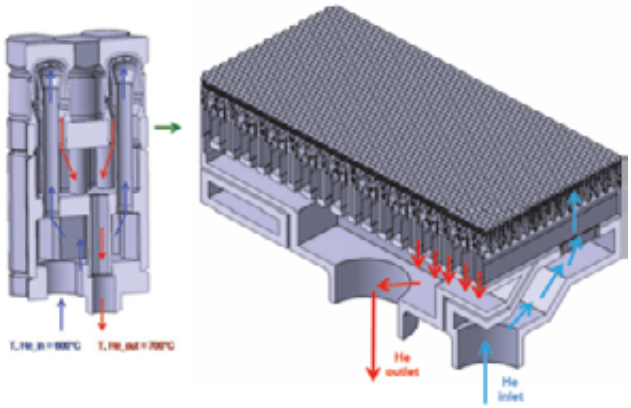

Integration of 9-finger modules (left) to a target plate (right) (PPPT-WP12-DAS-02-T05).

Another task (WP12-MAT-01-HHFM-05) deals with the fabrication of the 9-finger mock-ups for the HHF tests and non-destructive tests (NDT) of the manufactured mock-ups as a pre-check. Under cooperation with CEA, Cadarche, first NDT experiments with 9-finger modules were successfully performed at the SATIR facility. The results show that the SATIR method is applicable for NDT testing the He-cooled modules.

Structural Materials - Steels

Reduced Activation Ferritic/Martensitic (RAFM) steels are reference structural materials for in-vessel components of a Fusion Power Plant because of their better irradiation resistance and improved radiological properties compared to commercial martensitic steels. EUROFER is the European development foreseen as material for structural parts of ITER-TBM and DEMO blanket and divertor. One of the most crucial items for the application of EUROFER is its performance under fusion-relevant intense neutron irradiation. Consequently, H/He embrittlement effects, their simulation by boron doping, and tritium release were in the focus of the 2012 activities of KIT.

Electron energy loss spectroscopy (EELS) was used to detect and study the spatial distribution of He and Li on the nanoscale in boron-alloyed steel after neutron irradiation. Li and He are the products of the 10B(n, α)7Li nuclear reaction and knowledge of their distribution is important to understand their influence on mechanical properties. The spatial distribution of Li inside the Fe matrix was detected and investigated by means of EELS plasmon spectra. The new method appears to be more reliable and informative than the usual analysis of the Li-K edge. Using linear background subtraction, spatial distribution of Li inside He-filled bubbles may be imaged and clearly distinguished. Some bubbles are half filled with Li and half with He. The fine structure of the Li plasmon peak suggests the presence of Li in the different chemical compounds.

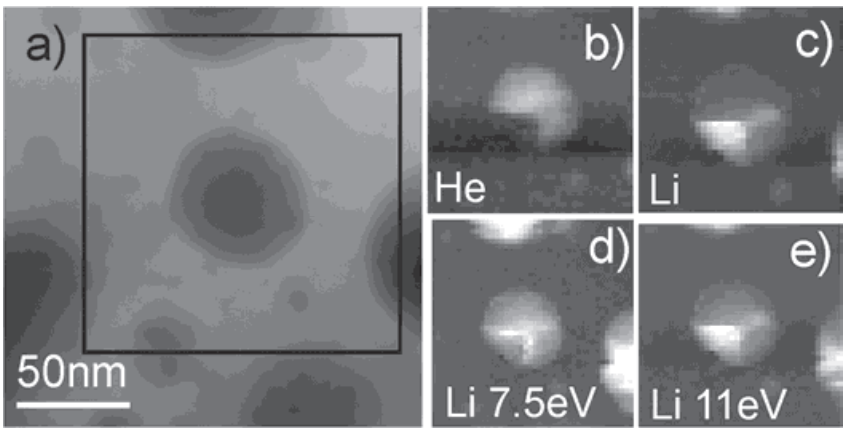

Analytical TEM investigation of an individual bubble. The HAADF image of the investigated area is shown in (a), He and Li maps are shown in parts b and c. The Li map obtained by a 2.3eV energy window at 7.7eV and 10.7eV are shown in parts d and e respectively.

A comprehensive post-irradiation program was performed which included tensile, impact and LCF tests. The irradiation of EUROFER97 specimens was performed in a central position in the HFR Petten at 250, 300, 350, 400, and 450 °C. The neutron irradiation was carried out up to a nominal dose of about 15 dpa. The figure shows the tensile properties of irradiated and non-irradiated specimens.

As expected, a significant irradiation-induced strength increase, $\Delta\sigma_{irr}$, has been observed at the lowest irradiation temperatures, 250 and 300 °C, while above about 400 °C even a minor softening appears. This temperature behavior is expected and is a general feature of ferritic-martensitic steels, and is due to smaller dislocation loops and nanoscaled precipitates that are stable only below about 400 °C. As they are not formed above about 400-420 °C, at least in a helium-free bcc matrix, uniform and total elongation are nearly the same at 450 °C for irradiated and unirradiated specimens.

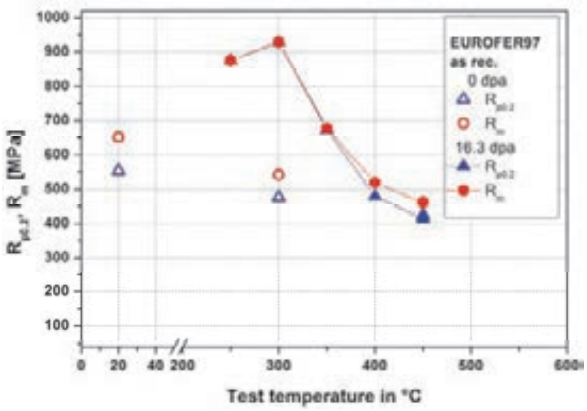

Yield strength Rp0.2 and tensile strength Rm.

A new quadrupole mass spectrometer, able to identify the tritium release and retention of fusion-relevant materials, was used for quantitative analysis of a high number of tritium release experiments (Be of HIDOBE I).

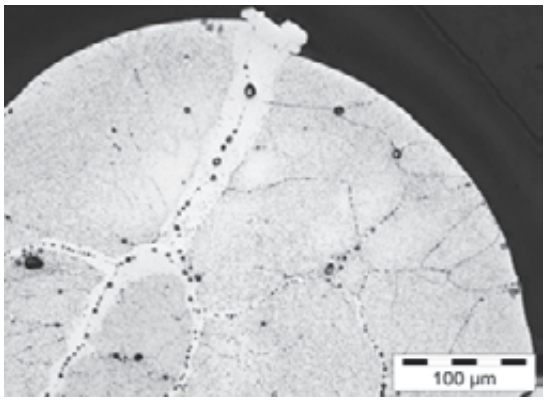

Open porosity (He) network in irradiated Beryllium pebble (microstructure after special preparation in metallographic Hot Cell).

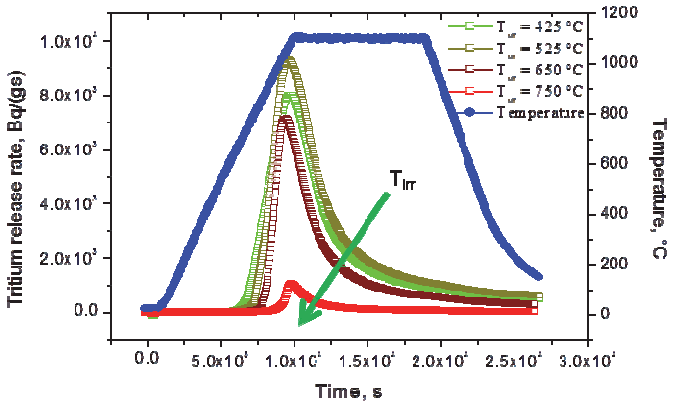

Tritium release tests on Beryllium for different irradiation temperatures.

Structural Materials – Refractory Alloys

The development of a divertor for DEMO or a power plant is very challenging since heat loads of up to 10-15 MW/m² have to be removed. KIT is pursuing a concept based on helium cooling and a modular arrangement of cooling fingers, which use refractory alloys as tile at the plasma facing side and as structural material forming the cap of the cooling fingers. Tungsten and tungsten alloys are presently considered for both applications mainly because of their high temperature strength, good thermal conductivity, and low sputter rates. For armour materials, high crack resistance under extreme thermal operation condition is required, while for structural materials, sufficient ductility within the operation temperature range is mandatory. Moreover, an alternative design for helium cooled divertors is based on the development of tungsten composite pipes.

For the required mass fabrication, powder injection moulding (PIM) is an ideal near net shape fabrication process with tight tolerances and good surface finishes. This process enables the mass production at low costs for high performance parts with complex geometries. Materials with high melting points such as tungsten or tungsten alloys can be effectively fabricated with this process. At KIT, the PIM process was successfully modified for rapid production of tungsten alloys as well as for the fabrication of parts, which consist of two different tungsten materials.

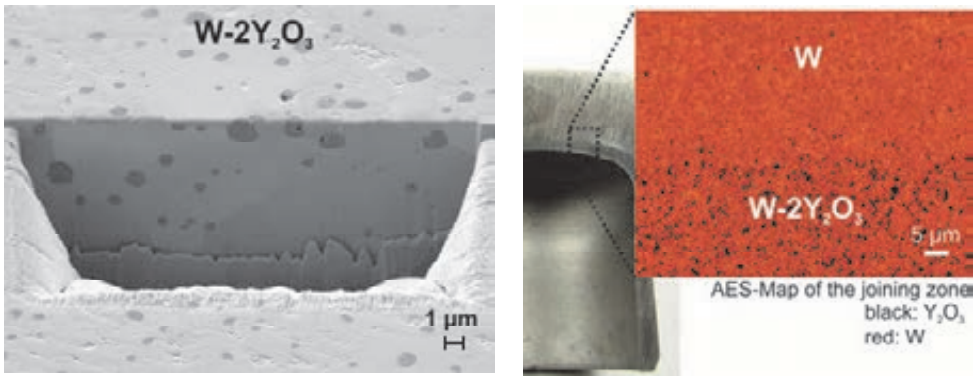

Left: For the development of tungsten materials the PIM process is an ideal rapid production tool. The resulting isotropic microstructure with fine and homogeneously distributed yttria particles is shown for the case of W-2wt.%Y_2O_3.
Right: It is possible to fabricate and/or join parts of two different tungsten alloys within one PIM process. The image shows a cross-section of a direct joint between W and W-2wt.%Y_2O_3. Despite the curved surface, the joining zone is free of defects.

Tungsten foil is ductile and can be bent plastically even at room temperature. This beneficial behavior can be transferred to bulk materials by assembling and joining several layers of tungsten foil. The resulting tungsten laminate can be used (I) as a cooling structure, especially in the shape of a tungsten laminate pipe, or (II) as transition layer between steel (or Cu-CrZr) pipes and the tungsten armor, in order to deal with the different thermal expansion coefficients.

A fabrication and performance study was accomplished for the latter application. To investigate a real worst case scenario, the ITER divertor concept was altered by using austenitic steel 316 for the pipe and half tungsten monoblocks (saddle type) as armor. The CTE (coefficient of thermal expansion) of 316 steel is about three-times higher compared to tungsten, that is, there is a significant mismatch. Therefore, a 1mm thick W-Cu laminate was chosen as compliance layer between the 316 steel pipe and the armor. After fabrication and vacuum brazing of the mock-up parts, quality assurance was done by ultra-sonic non-destructive tests. High heat flux tests were performed in the GLADIS facility at IPP, Garching. Here, the mockup was exposed to a pulsed He beam (20 s on, 40 s off) with a mean heat load of 6 MW/m2. Until now the mockup was tested for 100 cycles and showed no damage at all. Later on, the test will be continued until failure.

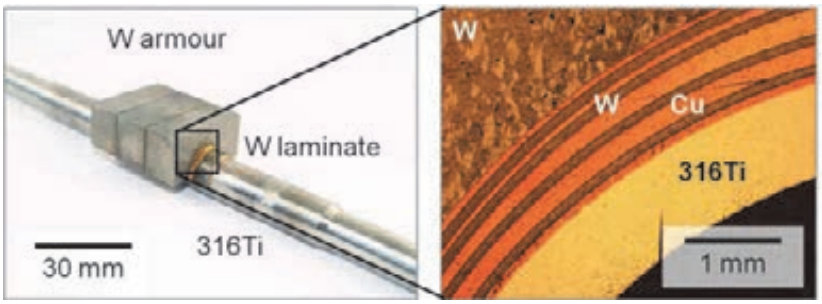

A water-cooled divertor mock-up for high heat flux tests. The mock-up consists of a steel pipe (austenitic steel, 316Ti) with an attached tungsten armor block. Between the steel pipe and the tungsten block, a tungsten-copper laminate compensates the different thermal expansion coefficients.

Nuclear Data

Theoretical and experimental activities have been conducted in the frame of F4E grants and contracts with ITER, EDFA-PPPT and EFDA-JET to provide nuclear data developments, measuring techniques, and nuclear analyses for ITER and DEMO. The KIT contribution to the theoretical activities for nuclear data is on the evaluation of general purpose nuclear cross section data, the qualification of new and updated data evaluations and the development of advanced computational schemes for sensitivity calculations. The experimental ac-

tivities aim at providing the experimental data base for validation analyses and the development of experimental techniques for the nuclear TBM (Test Blanket Module) test programme in ITER. The focus of the KIT contribution is on measurements of nuclear responses in TBM mock-up experiments and on advanced measurement techniques both for ITER-TBM and for future experiments at JET. KIT's fusion neutronics group has also provided dedicated contributions to ITER and DEMO design by specific nuclear analyses comprising neutron- gamma transport simulations as well as shut-down dose rate calculations using the Rigorous-2-Step method (R2S).

Experiments

For measurement of neutrons below 2 MeV a **proton-recoil proportional counter tube** has been calibrated with thermalized neutrons from the DT neutron generator of TU Dresden operated in pulsed mode using 650 keV protons from the $^{14}N(n,p)$ reaction and the respective response matrix function has been calculated. These results were used for the unfolding procedure to obtain experimental data below 2 MeV complementary to earlier performed measurements with a NE-213 scintillator spectroscope. The response matrix was calculated with MCNPX, and, together with the pulse height spectra measured at two positions in the mock-up, used as input for the unfolding procedure with the MAXED code. The results of the neutron spectrum measurements were then compared to MCNP calculation of the neutron spectrum using JEFF-3.1.1 and FENDL-2.1 nuclear data.

Self-powered neutron detectors (SPND) were studied to see whether this type of detector can be proposed for neutron flux monitoring in an ITER-TBM. Originally designed for the operation in a thermal nuclear reactor, SPNDs have a number of interesting properties such as small dimensions, capability to operate in harsh environments, absence of external bias, simplicity etc.; therefore they are attractive neutron monitors for TBM in ITER. Several state-of-the-art SPND were tested in fast neutron irradiations including different emitters such as V, Co, and Rh. The results clearly indicate that in fast neutron spectra, the response of SPNDs is much lower than in thermal neutron flux. Activation calculations were performed to search for SPND materials which are suitable for operation in the TBM.

The suitability of a combination of **lithium glass scintillators, optical fibers and photodiodes** as candidates for TBM diagnostics was also investigated. The detector used in the test irradiations was a ^{6}Li-enriched lithium glass from Nuclear Enterprises. Pulse height spectra were recorded under neutron irradiation with and without Cd cover. The scintillation signal in such a lithium glass is generated from gamma interactions and the tritium-breeding reaction of low-energy neutrons on ^{6}Li. Gamma-rays lead to low pulses which can be separated from the distinctive peak caused by the tritium breeding reaction in the pulse height spectrum. When using optical fibers to transmit the signals between the lithium glass and the photodiode, the peak due to the tritium breeding reaction cannot be seen clearly. Thus, further development work is required to optimize the design for such a detector arrangement.

Shut-down dose rate measurements on JET were performed with an OD-02 dose rate meter which is based on a calibrated open ionization chamber. This allows measuring the ambient dose equivalent alone and together with the directional dose equivalent. The dose rate meter is suitable for dose rate levels above 1 µSv/h. The measurements performed on JET agree well with values measured with the other dose rate meters.

Nuclear Data and Tools Development

The development of nuclear data and tools is performed within the Framework Partnership Agreement F4E-FPA-168 on "Development of Nuclear Data Files" between F4E and the "Consortium on Nuclear Data Development and Analysis". The Consortium, consisting of the research institutions of KIT (Germany), CCFE (UK), NRG (The Netherlands), JSI (Slovenia), TUW (Austria), CIEMAT (Spain) and IFIN-HH (Romania), combines available European expertise to provide the services requested by F4E to meet their objectives in the field of nucle-

ar data development. These services include nuclear data evaluations relevant to the various fusion applications encompassing neutron, proton and deuteron induced reactions, the generation of associated co-variance data for uncertainty assessments, the development of advanced nuclear models and codes, the processing and benchmarking of the evaluated data against integral experiments, as well as the development of suitable software tools for sensitivity and uncertainty analyses of fusion systems.

KIT is leading the Consortium and is co-ordinator of the FPA-168 and the associated grants. It contributes to the first specific grant, FPA-168.01, with the following tasks: (i) evaluation of general purpose nuclear data files for n + ^{63,65}Cu including covariance data up to 200 MeV, (ii) benchmark analyses of Pb neutron cross-section data to assess their quality for design analyses of the HCLL breeder blanket concept, (iii) upgrading of the MCSEN sensitivity software to comply with the current standard of the MCNP-5 Monte Carlo code, and (iv) evaluation of advanced damage energy and displacement cross-sections for the major EUROFER constituents based on an atomistic modelling approach. FPA-168.01 was started in April 2012 and will run over a period of two years.

The figures below show, as an example, results of neutron cross-section and co-variance data obtained with KIT's evaluation methodology for copper up to 200 MeV neutron energy. It is recalled that Cu is an important heat sink material for fusion power reactors, which is also used for diagnostics, microwave waveguides and mirrors in ITER.

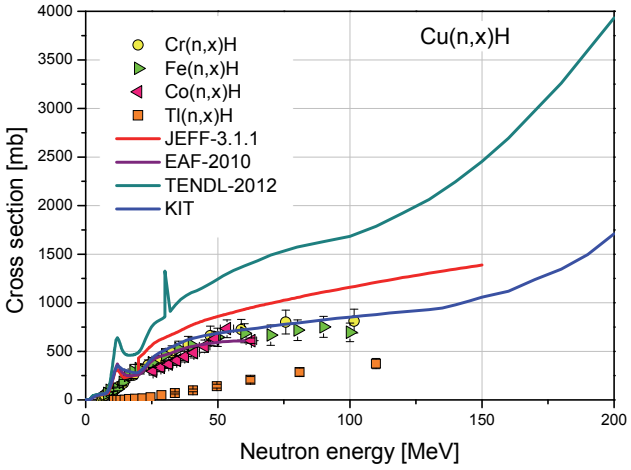

Evaluated total hydrogen production cross section

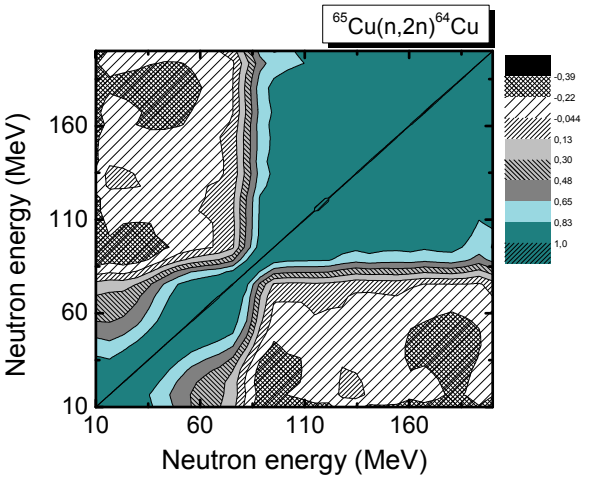

Evaluated covariance matrix for ^{65}Cu(n,2n)^{64}Cu reaction cross section

PPPT – DTM-04: Design Tools and Methodologies - Neutronic Studies

The DTM-04 programme aimed at performing first neutronic scoping studies to assess the nuclear performance of DEMO and provide important nuclear responses which are required for the engineering design and its verification. A dedicated part of the programme was devoted to the evaluation and further development of neutronic tools which are required for applications to DEMO nuclear analyses.

The nuclear analyses strand of activities comprised the development of a provisional MCNP model of DEMO, shielding analyses for the definition of the radial build, the assessment of the Tritium breeding capability and of radiation loads to the TF coil taking into account neutron streaming effects, the calculation of the nuclear heating, radiation induced damage and gas production in the steel structure at different locations in the DEMO plant, as well as calculations of the activation inventory and the afterheat production.

The activities in the tools development strand focussed on the evaluation of available tools with the main objective to identify further development needs towards mature, robust and flexible European software tools for DEMO nuclear analyses. These included, first of all,

suitable Monte Carlo codes for particle transport simulations in DEMO, second, coupling schemes of radiation transport and activation codes with the capability to provide shut-down dose radiation maps, and, finally, geometry conversion tools which enable the import of CAD data in the Monte Carlo codes.

The Task DTM-04 activities were conducted in a joint effort by CCFE (UK), CEA (France), CIEMAT (Spain), ENEA (Italy), HAS (Hungary), IPPLM (Poland), JSI (Slovenia), and KIT (Germany). KIT co-ordinated the DTM-04 activities, conducted tasks on the “Development of a provisional DEMO model”, on the “Shielding analyses in response to system code studies“, and contributed to tasks on “Tools for CAD geometry import in Monte Carlo codes” and “Tools for coupled radiation transport and activation calculations”, respectively.

The shielding analyses, performed by KIT with the provisional DEMO model and a radial build in agreement with the DEMO parameters provided by the PROCESS code analyses of CCFE, showed that the shielding efficiency is to satisfy the radiation design limits as specified for DEMO. This also applies for the peak power density in the TF-coils which is well below the recommended limit of 50 W/m^3. The radial thickness assumed for the inboard midplane amounts to 80 cm, for the blanket and the manifold region, and 65 cm, for the shield and the vacuum vessel (VV), summing up to a total thickness of 145 cm for the entire inboard blanket/shield/VV system.

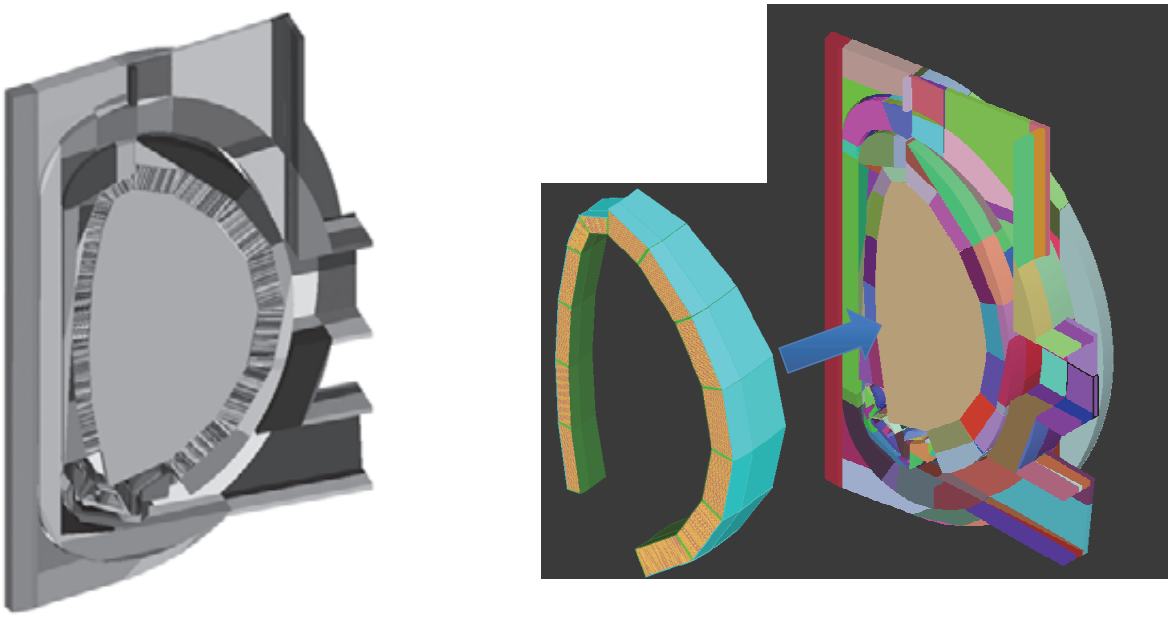

CAD neutronics model of DEMO with integrated HCLL blanket modules (left); right side: Simple generic model with blanket boxes and blanket internal geometry separated.

The McCad approach for the CAD geometry import in MCNP was evaluated within DTM-04 with the primary aim to check McCad’s capabilities for the DEMO model conversion by independent users and thereby identify further development needs. The conversion was shown to best proceed in two processing steps. A simple generic model is first set up with empty blanket boxes. This model can be easily converted and completed by void cells as required for the neutronic calculations. Second, the detailed internal blanket geometry of a complete sector with all blanket modules is devised. This model can be converted, again easily, and subsequently filled in the empty blanket boxes of the already available generic model. Following such an approach, a suitable MCNP model was generated that can be used in application analyses. As part of this activity, McCad’s capabilities were significantly improved including the conversion and the void filling algorithms.

Nuclear Analyses for ITER Diagnostics Ports

Nuclear analyses were performed in the frame of a service contract with the ITER Diagnostics Division with the objective to guide and assist the design developers with optimal shielding solutions for the Diagnostic Generic Equatorial Port Plug (EPP). The crucial issue in this regard is the shutdown dose radiation level in the interspace behind the port. Systematic neutronics analyses were conducted to improve the radiation shielding performance, to reduce the neutron streaming through the lateral gaps and, thus, to minimize the activation and the resulting shut-down dose rate levels behind the EPP.

A series of different shield and gap configurations were investigated including e.g., labyrinth-type gap configurations and horizontal rails on the drawers of the EPP. The analyses included neutron transport calculations (MCNP) for the assessment of the neutron flux distribution and coupled transport/activation calculations for the estimation of the shut-down dose rate levels. The latter calculations were performed with the cell based R2S system, supplemented and verified by the extended R2Smesh approach for providing both the decay gamma source and the shut-down dose rate distribution on a super imposed mesh. As essential outcome of the parametric analyses, an EPP design with a double-labyrinth gap configuration has been recommended. The optimized EPP model was integrated into the recent B-lite MCNP model of ITER.

The figure below shows a typical shut-down dose rate distribution obtained with KIT's R2Smesh approach for the EPP with the ITER B-lite model. It is noted that the distribution is overlaid on the CAD geometry of B-lite. The enlarged 3D dose rate map, visualised with the ParaView software, provides a detailed view of the distribution showing also the streaming paths inside the EPP.

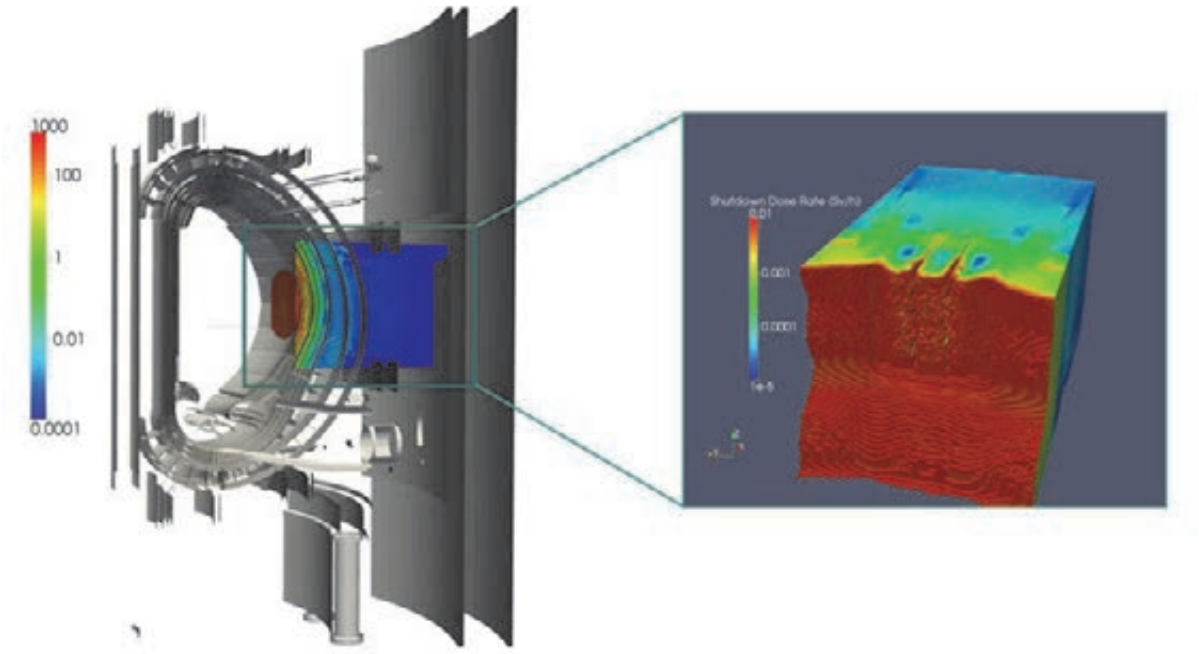

Shut-down dose rate distribution calculated with KIT's R2Smesh approach for the EPP in ITER. Left side: Distribution overlaid on the CAD geometry of the ITER B-lite model, right side: Isometric view of the 3D distribution visualized with the ParaView software.

International Fusion Materials Irradiation Facility (IFMIF)

Broader-Approach Activity: IFMIF Test Cell and High Flux Test Module

In the Engineering Validation and Engineering Design Activities (EVEDA) for the International Fusion Material Irradiation Facility IFMIF, which is an element of the Broader Approach activities launched jointly by several European countries and Japan, the German contribution includes engineering tasks for the IFMIF Test cell and the IFMIF irradiation experiments. This report covers tasks performed at the KIT attributed to the following procurement arrangements (PAs):

- PA TF-1 EU : Engineering design and Validation of the IFMIF High Flux Test Module
- PA TF-2: Irradiation in fission reactor (Responsible SCK-CEN, contribution by KIT)
- PA TF-4: Other irradiation modules (Responsible CIEMAT, contribution by KIT)
- PA ED-04: Test Cell, Access Cell, Test Module Handling Cell and Technology Rooms

According to the planning for EVEDA, these tasks will be performed in the timeframe up to 12/2013. In this report, the progress for the year 2012 is described.

The IFMIF facility is dedicated to fusion-relevant irradiation of structural and functional material specimens, with the objective to create an experimentally validated material properties database suitable for design and licensing of future fusion power plants. The facility is composed of several subsystems, namely the 40MeV 250mA deuteron accelerator facility (AF), the lithium target facility (LF) and the test facilities (TF). The target- and test cell (TTC) is part of the test facilities, containing the lithium target neutron source and the test modules. It has the primary function to shield the environment against the intense radiation generated by the target, and to safely contain all hazardous materials. Inside the TTC, the target and test modules are arranged, as shown the figure.

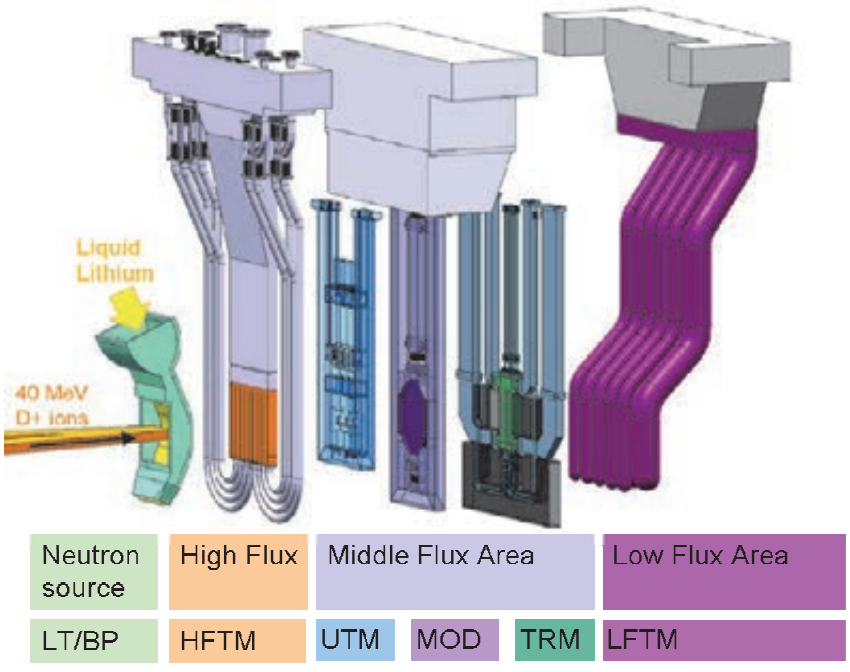

Overview on the irradiation experiments inside the IFMIF Target- and Test Cell (TTC).

Engineering Design of the Target- and Test Cell

The TC design followed the previously decided rectangular concept. Details in the routing of media and signal lines have been engineered. The overall sealing concept was detailed. In the final stage, the integration into the IFMIF building was arranged.

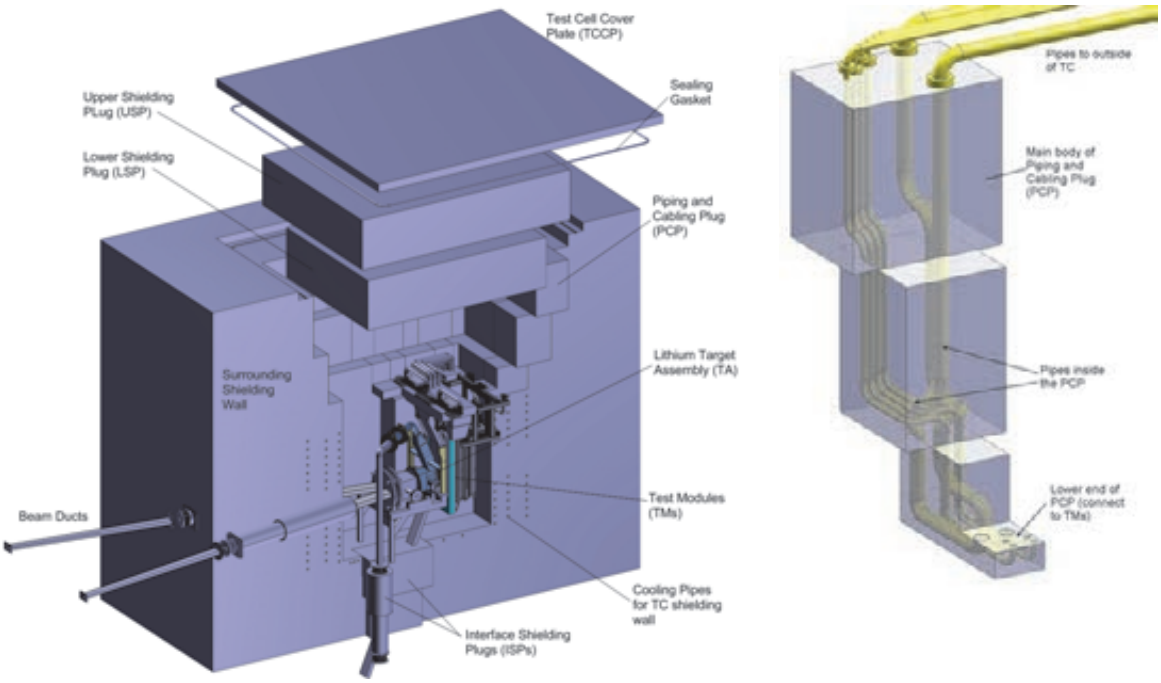

Design of the IFMIF Test Cell, on the right a detail of the removable Piping and Cabling Plug with bent pipes to reduce the neutron streaming.

Based on process descriptions, functional models of several key maintenance processes have been implemented. Simulations on the needed process times were performed for several scenarios.

Engineering Design of the Tritium Release Test Module

The design of the Tritium Release Test Module (TRM) was matured, and 3D CAD models, as well as manufacturing drawings were produced. Engineering analyses were performed for thermal and mechanical issues. Neutronic and tritium transport calculations were done to assess safety issues. From the engineering CAD model, a 3D model was derived suitable as input for more detailed Neutronic (MCNP) analyses, to assess the local heat release and tritium production. 3D CFD simulations are in preparation. For the future tritium transport simulation, a MATLAB code based on FUS-TCP has been customized to the TRTM topology.

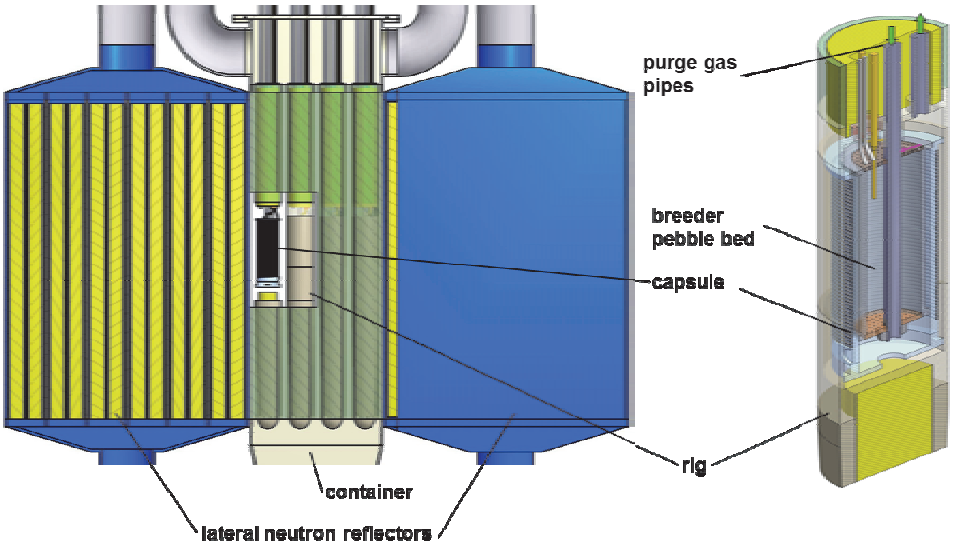

Overview of the TRTM module and detail from capsule CAD model.

Fuel Cycle – Vacuum Pumping

For more than two decades, KIT has been developing vacuum pumping systems for fusion reactors.

The concept of cryogenic pumping based on cryosorption at activated charcoal has been successfully demonstrated at KIT, and is now the common technology used for all primary vacuum pumping systems at ITER. As these cryopumps are part of the European procurement package for ITER, KIT is charged with the elaboration of the complete build-to-print package of the torus and cryostat cryopumps and the neutral beam injection (NBI) cryopumps.

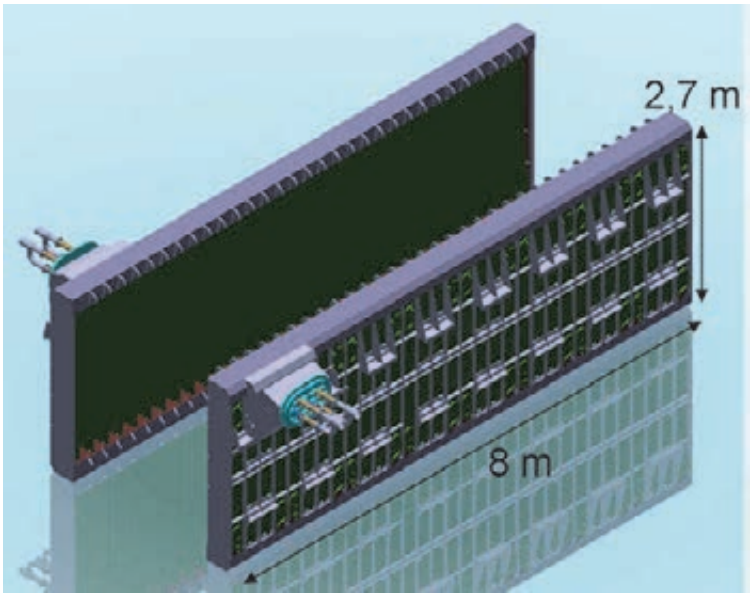

The neutral beam cryopump build-to-print design has been accomplished.

As an outstanding engineering highlight in 2012, the **detailed design of the NBI cryopump** was delivered to F4E / ITER. This pump is unique in size and will provide world record pumping speed for hydrogen. For the design finalization, many open design details have been solved and optimized, in all cases supported by an impressive number of thermo-mechanical FEM analyses and the development of all needed documentation to demonstrate compliance with the relevant standards, especially EN13445. Furthermore, a complete set of 2D manufacturing drawings was derived from the 3D CAD model. Caused by the great complexity of the pump with ~ 20,000 individual parts and approximately 6,000 m of welding seams, these steps required an enormous effort and concluded a long-term development programme that started more than 8 years ago. The NBI cryopump, in a slightly adapted design, will be manufactured and installed in the NBI test bed, currently being built on site of Consorzio RFX, Padova, Italy.

The engineering work on the ITER cryopumps was complemented by an ITER physics activity to describe in a more systematic way the whole ITER inner fuel cycle. For this purpose, particular attention was paid to establish a physically sound description of the interfaces between fuel cycle and plasma. New understanding has been gained in the area of pellet core fuelling and the related fuelling rate requirements as well as in the area of **divertor neutral gas flow simulation beyond the current state-of-the art**, aiming to include a proper and physically self-consistent Monte Carlo modelling approach, which removes the limits of the mostly used EIRENE code. This 2-year programme will be continued in 2013.

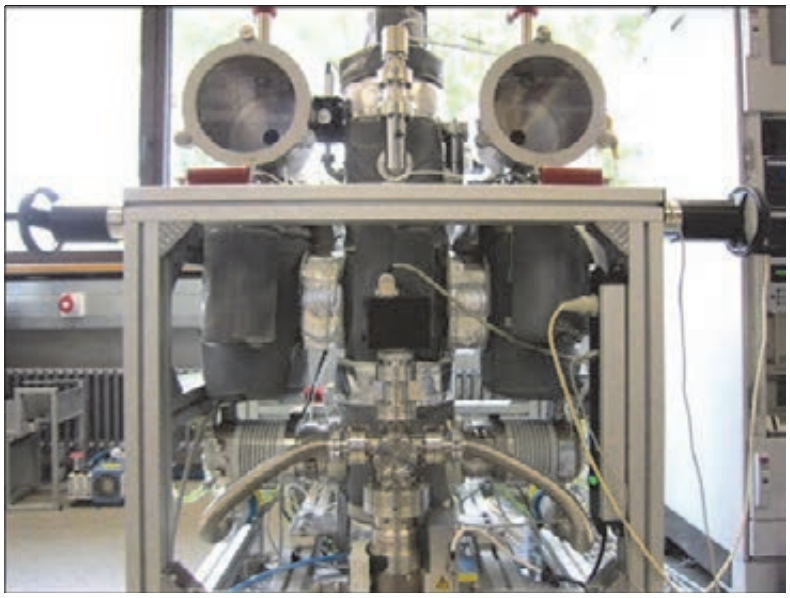

The new outgassing measurement apparatus (OMA).

Also, a new test facility for **high-resolution measurements of outgassing rates** of materials under vacuum has been developed, installed and commissioned. This facility will be employed to characterize outgassing rates of steels and other ITER relevant materials that are directly facing the torus chamber, such as polyimides or elastomer gaskets routinely used in diagnostics.

In 2012, a new momentum has been given to support the DEMO-related activities coordinated from the Power Plant Physics and Technology Department at EFDA. In this context, the Direct Internal Recycling (DIR) concept to improve the fusion fuel cycle was developed further on. This included the start of a mid-term programme to elaborate a **fuel cycle simulator**. The quantification of inventories and flows in the different sub-systems of this improved fuel cycle became possible even using the preliminary version of the simulator, developed in 2012. The simulation tool was successfully benchmarked against the ITER fuel cycle. It was found that, if the DIR solution works as expected, DEMO could be operated with a tritium inventory similar to the ITER inventory.

As technical solution to implement the DIR concept, a **novel DEMO pumping system** was suggested, comprising a liquid metal diffusion pump as primary pump, and a liquid metal ring pump as backing pump. In this new concept, the necessary hydrogen separation and compression will be provided by a metal foil pump. In 2012, a mercury diffusion pump was investigated experimentally with big success and proof-of-principle test set-ups for the metal foil pump and the liquid ring pump were prepared for testing next year. Moreover, modelling activities have started to simulate all three pumping systems. A special computational effort, thereby exploiting the resources at the Supercomputer HPC-FF in Jülich and Helios in Rokkasho, Japan was needed to develop a simulation code to support the design of a diffusion pump. For the near-term validation of the DIR concept in technical scale and under hydrogen operation, the dedicated test facility THESEUS is under construction.

Fuel Cycle – Tritium Processing

The work performed by TLK on tritium and fuel cycle covered a large variety of activities tackling major tritium related issues for ITER and DEMO.

Intervention in CAPER C to install new equipment for R&D on highly tritiated water.

A new project covering **R&D on highly tritiated water handling and processing** for ITER was launched in 2012. In this ambit, the first part of the study was dedicated to material screening tests to identify the most promising material candidate to be used for the Capture & Exchange method proposed by ITER. In parallel, the preparation for the experimental campaign with tritium was a huge and important work. Due to the very high radio-toxicity of highly tritiated water, a meticulous and comprehensive safety analysis accompanied the necessary and significant CAPER upgrades. The main concerns were on the safe operation of an especially dedicated new micro-channel catalytic reactor that burns tritiated hydrogen using oxygen to produce tritiated water up to very high specific activities. The integration of all the new equipment (lines, instruments, reactors, cubicles, command and control system) was completed. Small scale experiments with tritium as well as full scale tests with deuterium will follow.

Tritium related studies for DEMO were re-launched by EFDA, focusing at first on the major and well known issue of tritium migration from the breeding blanket to the coolant, and the consecutive tritium losses into the environment. TLK with strong support from INR carried out a **tritium permeation study in DEMO breeding blanket** to identify issues and effective mitigation strategies, taking into account and balancing the size / efficiency of tritium extraction systems, and the feasibility / efficiency of anti-permeation barriers (thin coatings or chemically assisted oxide layers). The work covered a comprehensive literature review on the state of the art for tritium processes and anti-permeation barriers, along with a review of the material database to be considered for the numerical approach. The so-called FUS-TPC simulation software has been widely improved and adapted to three breeding blanket candidates (HCPB, HCLL and WCLL) for DEMO, considering the latest blanket designs. This work will be continued with a more detailed numerical approach and a more substantiated tritium process assessment study.

In 2012, TLK took over part of the coordination and management work in the frame of the TBM Consortium of Associates. Two Framework Partnership Agreements were established with F4E for future experiments to be performed over the next 4 years in different European facilities in support to the **EU TBMs ancillary systems** design process. Major contributions from KIT are expected along experimental campaigns to be carried out in HELOKA, MEKKA and TLK facilities.

Fusion Programme Management Staff

Head of the Research Unit	Dr. K. Hesch	ext. 25460 e-mail: klaus.hesch@kit.edu
Secretariat:	Mrs. M. Spies	ext. 25461 e-mail: michelle.spies@kit.edu
Program Budget, Administration, Reports, EU-Affairs	BW. M. Henn	ext. 25547 e-mail: michael.henn@kit.edu
	Mrs. I. Pleli	ext. 28292 e-mail: ingrid.pleli@kit.edu
Blanket and Divertor Development, HELOKA, IFMIF, Structural Materials, CAD-Office ,Public Relations	Dr. D. Radloff	ext. 28750 e-mail: dirk.radloff@kit.edu
Fuel Cycle, Superconducting Magnets	Dr. M. Ionescu-Bujor	ext. 28325 e-mail: mihaela.ionescu-bujor@kit.edu
Plasma Heating Technology, Safety Studies, Neutronics, Physics	Dr. K. Hesch	ext. 25460 e-mail: klaus.hesch@kit.edu
Quality Management, Resource Loaded Planning, Document Management	Dr. J. Gafert	ext. 22923 e-mail: juergen.gafert@kit.edu
	Dr. I. Ignatiadis	ext. 85465 e-mail: Ioannis.ignatiadis@kit.edu
	Mrs. DI. Ch. Schweier	ext. 28325 e-mail: christine.schweier@kit.edu

Address: **Karlsruhe Institute of Technology**
Nuclear Fusion Programme Management

Post Office Box 3640, D - 76021 Karlsruhe / Germany

Telephone No: **0721-608-Extensions .....**

Telefax No: **0721-608-25467**

world wide web: **http://www.fusion.kit.edu/**

Contents Page

Page

Page

Page

Plasma Wall Interaction

Simulation of ITER First Wall Energy Loading during Mitigated Disruptions and Runaway Electrons (F4E-GRT-315 (PMS-PE)

Introduction

The disruptions in ITER are the most serious threat to plasma-facing component (PFC) integrity. Stored energies during burning plasma operation will be much higher than anything which can be achieved in today's devices and ITER will face the prospect of very serious damage to first wall (FW) and divertor armour by the plasma and runaway electrons. The objective of this task is to predict the possible wall damage in the ITER tokamak.

So far the first part of the project has been finished, namely the wall loading by photon radiation during the thermal quench (TQ) of mitigated disruption. The most commonly used mitigation technique, which has been successfully tested on current devices (e.g. JET and DIII-D) and is foreseen for ITER, is the massive gas injection (MGI) of the noble gas neon, in which a heavy puff of impurity species is introduced rapidly into the plasma chamber to dissipate the energy through the radiation. The MGI process includes the ionization of injected atoms in the plasma, the passage of a cooling wave through the plasma and an anomalous thermal transport. The process is very time dependent, leading to poloidal asymmetries in the radiation density distribution on the beryllium FW.

The main results [1] have been obtained by using as input the simulations of neon MGI in ITER obtained earlier with the two-dimensional code TOKES [2]. The beryllium wall surface temperature has been obtained with the melt motion code MEMOS [3]. The calculations are performed for the baseline Q = 10 ITER burning plasma magnetic equilibrium configuration, assuming toroidal symmetry and the thermal stored energy ~400 MJ. In current calculations deuterium and neon are assumed for the plasma species. The output of TOKES simulations is used by MEMOS to assess the resulting maximum surface temperature and any possible melting on the FW surface (without assessing melt motion).

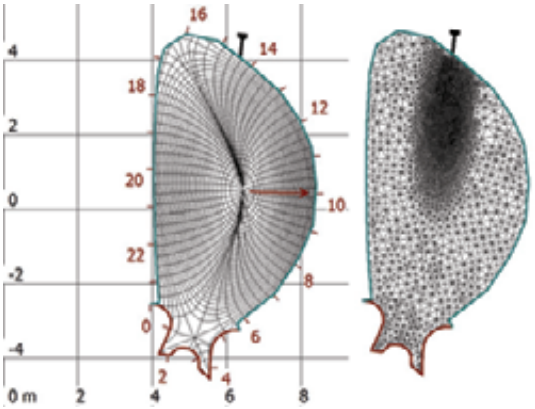

Fig. 1: **Left panel:** plasma cells and the injector location are shown.
Right panel: refined triangular meshes in front of gas injector (Δ_{min} = 5 cm).

The radiation energy deposition over ITER vessel surface

Fig. 1 demonstrates the ITER configuration implemented in TOKES. The code generates orthogonal magnetic flux coordinates which cover the whole vacuum volume of the vessel. Directly in front of the injector orifice (at the poloidal location X ~14.5 m in Fig. 1), very small triangular meshes are used in the simulation. This is important for appropriate modelling of neutral propagation.

The spatial-temporal dependencies of impacting radiation flux on ITER first wall surface for different neon amounts aiming at reaching an optimal disruption MGI mitigation effect have been calculated with TOKES. At present, ITER foresees three, toroidally separated upper port MGI locations, with a fourth system injecting from an outboard mid-plane port. Being a 2D code, the TOKES code cannot simulate such toroidally discrete gas injection. Instead, a single injection orifice is modelled as a gap in the FW contour, uniformly distributed toroidally such that the gas injection is toroidally symmetric in the code (the fourth injector location is not yet simulated).

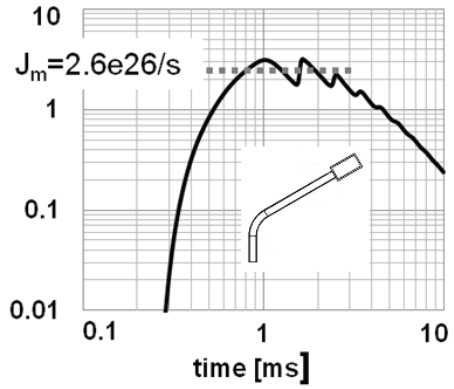

Fig. 2: The inflow of neon into the vessel as a function of time is shown. The median inflow J_m characterizes the magnitude. A sketch of the assumed injector geometry is also shown.

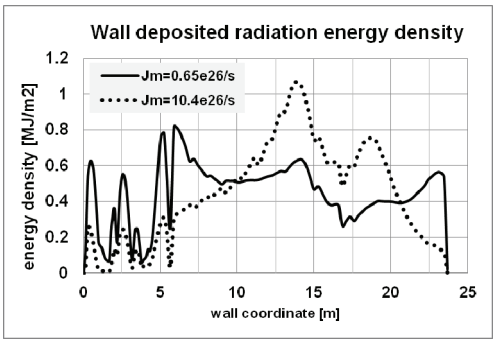

Fig. 3: Comparison of radiation load for intense and moderate injection scenarios. In both cases the last moment of TQ phase is shown (τ_c=3.44 ms for $J_m = 10.4\times10^{26}$/s and 7.8 ms for $J_m = 0.65\times10^{26}$/s).

It is further assumed that the gas is stored at the room temperature (309 K) and that the injection valves open instantly at time t = 0. A simple geometric form is assumed for injector itself, incorporating a small bend to account for the need to direct the gas towards the plasma centre (see inset in Fig. 2). The necessity to outpace the dump of disruptive plasma energy limits the acceptable cooling time, τ_c to a few ms (and thus the TQ stage duration; τ_c is the whole cooling time from t=0). The heat penetration depth δ into the wall bulk is small: $\delta \sim (\tau_c k/C)^{1/2} \sim 300$ μm on the timescale of the mitigated disruption heat pulse.

The MGI scenarios are examined by varying the initial pressure in the injector gas plenum from 500 bar down to 8 bar. The calculations consiered several scenarios, which cover the range of thermal quench time (TQ time) from 3 ms up to 12 ms. The physical parameter chosen below for the injection intensity is the median gas inflow J_m, which was varied in the range $(0.33 - 21)\times10^{26}$ atom/s in the performed simulations. Fig. 2 demonstrates the moderately oscillating dynamics of the incoming gas calculated for the case of Ne MGI and for the simple injector geometry assumed for ITER in these simulations.

Figure 3 shows the results for 2 scenarios: the first one, where the Ne inflow is $J_m < J_{m0} = 2.6\times10^{26}$/s and the second one, where $J_m \geq J_{m0}$. In the case of the highest Ne inflow $J_m = 10.4\times10^{26}$/s, the cooling time is very rapid (3.4 ms) and the maximum radiation load appears throughout in front of the injector - the ionized Ne has insufficient time to leave the injector location. In the low inflow case ($J_m = 0.65\times10^{26/}$s) the cooling time is longer (7.8 ms) giving the ionized gas more time to expand along the magnetic field lines. This decreases the load in front of injector. At $J_m = 10.4\times10^{26}$/s the maximum radiation flux reaches about 1.5 GW/m^2 in front of injector and about 1.2 GW/m^2 in the inner mid-plane. As to the case of $J_m = 0.65\times10^{26}$/s, typical radiation flux is about 0.5 MJ/m^2.

The surface temperature distributions

For preliminary assessing the wall surface temperatures the TOKES code has a simplified algorithm, in which the material properties are described by means of two physical constants only: the thermal conductivity taken for Be equal to k=70 W/m/K and the heat capacity C=5.54 MJ/m^3/K. The improved temperature distributions obtained with MEMOS which take into account the surface evaporation, melt and evaporation enthalpies, and the thermophysical parameters of the material in their dependence on temperature is shown for comparison. The elaborated simulations allowed assessment of possible evaporation wear layer and melt pool depth over the beryllium surface.

The radiation coming at the wall surface is transferred into the heat and the heat transported into the wall bulk by the thermal conduction mechanism. The results obtained are presented for the ITER wall surface initial temperature $T_0 \sim 500$ K. This is an upper limit for the expected quasi-uniform steady state wall temperature under burning plasma operation. At $J_m < J_{m0} = 2.6\times10^{26}$/s (moderate injection), T_{wmax} is below the Be melting point $T_{melt} = 1564$ K and otherwise (intense injection) $T_{wmax} > T_{melt}$. The simulations demonstrated complete plasma cooling during 5.7 ms as a minimum TQ phase duration without the melting of Be wall surface. The corresponding MEMOS simulations confirmed this result despite of the fact that the wall surface temperatures obtained with MEMOS are substantially lower than that obtained with TOKES (see Fig. 4).

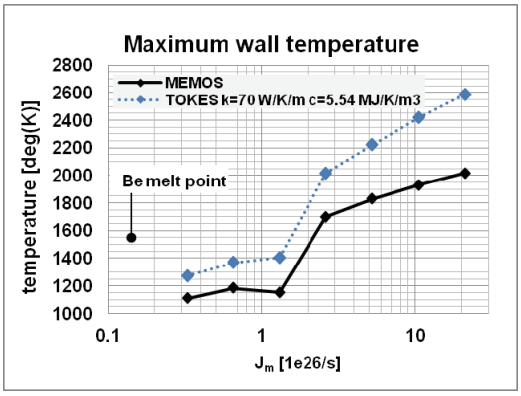

Fig. 4: Maximum wall surface temperatures achieved in the MGI scenarios. The maximum temperature was achieved at different positions on the surface: at X ≈ 5.9 m for Jm ≤ 1.3×10^{26}/s otherwise at X ≈ 13.8 m.

Fig. 5 shows the distributions of wall surface temperature over the wall surface coordinate X and in time t. One can see a fast increase of surface temperature which makes $T_{w,max}$ higher for about 100 deg(K). This is due to the radiation flash after switching on an anomalous transport mechanism, which is triggered when the cooling wave crosses the resonance surface of safety factor q = 2. At that moment the electron thermal transport to the cooling front causes a significant increase of radiation power.

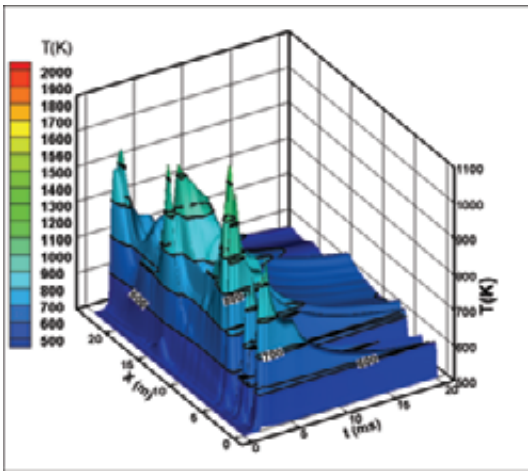

Fig. 5: Distributions of Be wall surface temperature vs X and t; $J_m = 1.3\times10^{26}$/s.

The code MEMOS calculated also the Be melt pool depth for the intense injection cases. The images of the melt pool are shown in Fig. 6. The melted area occupies on the first wall a rather wide stripe of the width 1-2 m in the vicinity of injector. Typical melt pool depth does not exceed 30 μm. The evaporation of Be is also estimated, however, the evaporation wear layer is so small (maximum ~0.02 μm) that it cannot be a concern with respect to the MGI events.

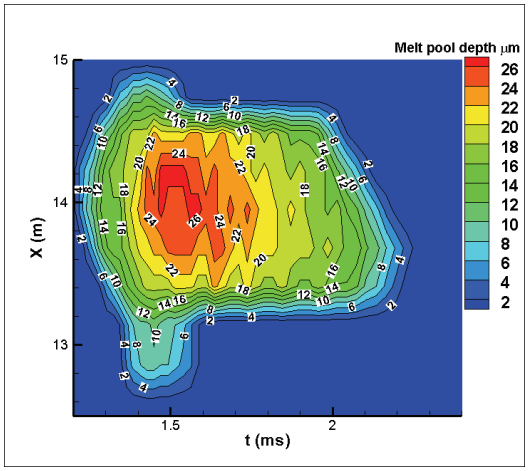

Fig. 6: Distributions of Be melt pool depth vs X and t. $J_m = 21\times10^{26}$/s.

Conclusions

Simulations using the codes TOKES and MEMOS have been performed to study numerically the massive gas injection of neon for disruption mitigation in ITER burning plasmas and the heating for the beryllium first wall as a result of the intense photon flash accompanying the injection. A preliminary analysis has been completed, in which the quantity of injected Ne is varied, finding, for example, that for an initial gas plenum pressure of 30 bar and gas inflow rate of 1.3×10^{26} atom/s (corresponding to 20 g of injected Ne), complete plasma cooling occurs on a timescale of 5.7 ms with a maximum wall surface temperature at the thermal quench of ~1400 K and avoiding Be melting at any point on the first wall. For more intense

injection (with cooling time < 5 ms), the photon radiation load is highest in front of the injector location, resulting in surface temperatures exceeding Be melting.

In moderate injection cases, the cooling time is long enough to provide effective expansion of ionized neon along magnetic field lines, allowing ionized Ne to radiate energy more broadly along the poloidal coordinate, spreading energy more efficiently and decreasing wall loads significantly. Therefore, the ions reradiate energy rather broadly along the poloidal coordinate, which substantially decreases the load in front of injector. Estimated assimilation factors and stored energy radiation fractions for the injected gas are consistent with values measured during MGI experiments in current devices.

One important shortcoming of these simulations is the two-dimensional nature of TOKES, which cannot reproduce the toroidally discrete nature of the injection in the real situation. Therefore, the conclusions related to the margin with respect to melting must be treated with caution, since in reality the same amount of gas would be injected into a smaller effective area. However, this 3D effect may be much less pronounced than might be thought owing to the rapid longitudinal expansion of plasma along field lines. The velocity of gas jet propagation across magnetic surfaces is much smaller than this parallel transport and the thermal energy density in the peripheral plasma much lower than that in the core. Further studies are planned to examine this possibility more closely.

Staff:

B. Bazylev,
I. Landman
S. Pestchanyi

Literarture:

[1] I. Landman et al., “Radiation loads on the ITER first wall during massive gas injection”, presented at the SOFT-27 conference, Liege, 23-28 Sep. 2012.

[2] I. Landman et al Fusion Eng. Des. 86 (2011) 1616-1619.

[3] B. Bazylev et al., Phys. Scr. T145 (2011) 014054

Acknowledgement

This work was supported by Fusion for Energy under the grant contract No. F4E-GRT-315 (PMS-PE). The views and opinions expressed herein reflect only the author’s views. Fusion for Energy is not liable for any use that may be made of the information contained therein.

Analysis and Computer Simulation of Disruption Mitigation Schemes of Massive Gas Injection (WP12-IPH-A07-1-1-02)

Introduction

In the future tokamak ITER the disruptions can locally damage the wall surface. For protecting plasma facing components (PFC) a massive gas injection (MGI) of a noble gas into the confined plasma at the disruption onset is under investigation. During MGI the plasma thermal energy (~ 0.5 GJ) transforms into photonic load scattered over the surface. The MGI thermal quench phase (TQ) must outpace the disruption, which limits the acceptable MGI cooling time τ_c to a few ms.

From MGI experiments it can be concluded that an effective ionization of injected atoms in the plasma and a radiating cooling wave into plasma bulk occur. Some moderate anomalous heat cross-transport develops in the bulk until the cooling wave reaches the magnetic surface of safety factor $q = 2$ ('resonance surface'); then, the transport significantly rises, which rapidly decreases the bulk electron temperature T_e.

Our purpose is the numerical assessments of MGI in JET and ITER. The modelling is performed with the two-dimensional tokamak code TOKES. Multi-species plasma and the neutrals are implemented in the entire tokamak vessel assuming toroidal symmetry. The code calculates the motion of the plasma across and along the magnetic field lines in each of numerical magnetic layers. The motions of neutrals (injected gas and atoms after full recombination) and the gas motion in the injector are calculated, too. Calculations for heat transport into the material bulk are also performed. The MGI process is divided into the pre-TQ, TQ itself and the current quench (CQ) phases.

Validations of TOKES results against the tokamak JET experimental results done earlier are now continued aiming at the heat transport during TQ and magnetic energy evolution at CQ onset. It is to mention that JET diagnostics are most suitable for measurements of quasi-stationary plasma parameters. The measurements during the disruptions (few ms) are very incomplete, which makes their interpretation rather controversial. But the issue is so critical that a combination of available experimental facts and theoretical estimations for getting better insight into the mitigated disruptions is undertaken.

Another TOKES MGI modelling concerns maximal possible temperatures of the ITER wall (beryllium or tungsten) and a gas amount (argon) sufficient for plasma cooling with $\tau_c < 5$ ms. For the fastest cooling several compact horizontal gas injectors located at the mid-plane as close as possible to the plasma centre at different toroidal positions are chosen, with equal cross-sections of gas store and the delivery tube.

Energy transport during MGI: JET experiments and TOKES simulations

Pre-TQ: After the injected gas (G-gas, below argon) arrived at the separatrix, initially only the confined periphery plasma is cooled (Fig. 1). The T_e falls in a thin layer where G-gas is ionized and G-ions irradiate plasma thermal energy. In the core T_e remains unchanged until the cooling front comes, which proves that the heat cross transport was negligible. The measured duration of the pre-TQ phase in JET (4-8 ms) is mainly determined by the long delivery tube (4 m). As it is seen in Fig. 2 (the insert) the total plasma current I_{tot} is almost constant, which can indicate that the poloidal magnetic field B_θ does not evolve. The pre-TQ phase ends when T_e abruptly falls everywhere in the core as it is seen in Fig. 1 (the pulses 76320 and 76314).

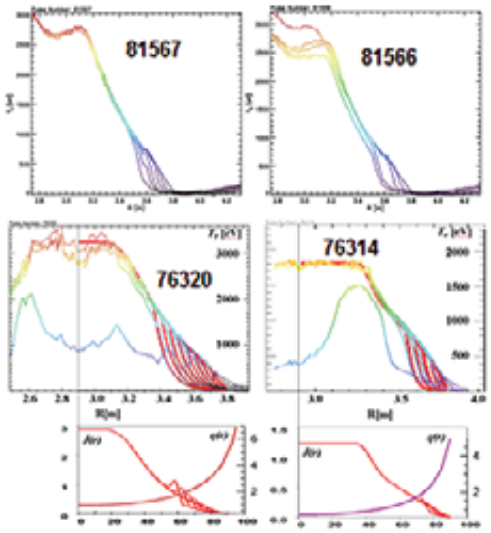

Fig. 1: Te profiles during the pre-TQ phase measured in JET and simulated with time step 0.2 ms. Shown are 4 pulses: JPN81567, JPN81566 with ITER-like wall (ILW) and JPN 76320, JPN76314 with CFC wall. For the last two pulses the simulated Te, current density and q-profiles (lower panels) are plotted.

TQ itself: Fast drop of measured T_e indicates upon some fast anomalous cross transport. We suppose that it happens due to microscopic tearing mode instability. Helical magnetic field fluctuations at the non-linear phase of the tearing instability can effectively enhance plasma transport across the magnetic field. An evidence for the enhanced thermal conductivity can be a sharp increase of oscillations of poloidal magnetic field B_θ during the TQ, which Fig. 2 illustrates. Those oscillations are typical of TQ under consideration. They can result in some ergodic behaviour of magnetic field (magnetic braiding). This anomalous transport mechanism is implied in TOKES simulations for fitting the calculations to the experiments in order to justify an increase by three orders of value of thermal cross conductivity. Such anomalous thermal cross conductivity (both of electrons and ions) is proportional to the classical longitudinal one. As the ions classical thermal conductivity is small as the square root of mass ratio m_e/m_i, the whole thermal transport can be provided by electrons only. It is also to note that the magnetic configuration cannot be reformed quickly (large inductance and small resistance of hot plasma) and thus a convective transport is not expected. Substantial convective transport at the TQ phase would imply the hot core plasma to cross the separatrix, which is not the case: the total heat flux to the divertor of only a few percent of the confined energy was measured.

However, the measured time dependence of plasma diamagnetic energy W_{dia} (see Fig. 2) indicates that the ion cooling time is nevertheless of the same order as that of electrons. The electron-ion thermal energy exchange time seems too long to explain ions cooling by means of electron thermal conductivity. Therefore, for providing fast cooling of ions we can also take into account a macroscopic convection, which involves already cooled regions of plasma with high resistivity. The convection can redistribute the plasma by interchanging the magnetic flux tubes with hot plasma and those with the cold plasma richly contaminated by the G-ions. For the fast MGI mixing a macroscopic ideal MHD instability can be responsible, which in the non-linear phase causes the ‘bubbles’, i.e. a convective transport by swapping helical flux tubes containing cold periphery plasma and the centre plasma. It is to note also that the diagnostics for L-mode pulses shows that W_{dia} drops at first to approximately half of the initial value after the TQ start. This is indirect evidence that T_e fast drops to zero but T_i changes slowly.

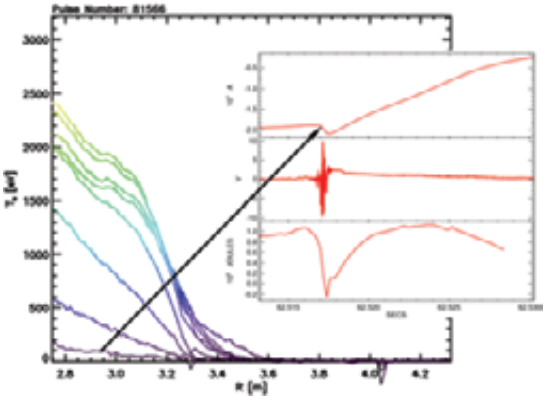

Fig. 2: Measured T_e profiles with time step 0.2 ms during TQ. In the insert the time dependences for I_{tot}, B_θ and W_{dia} (plasma energy) are shown. The current spike corresponds to T_e < 100 eV.

At the end of TQ phase the total plasma current I_{tot} reaches its minimum, which can indicate that the shrinking of current channel in the narrowed hot plasma column stops (see Fig. 3). The conservation of poloidal magnetic flux Φ between the magnetic axis and the metallic wall holds until considerable cooling of the plasma centre. Before the complete cooling of plasma the current I_{tot} decreases and as the flux $\Phi = I_{tot}L$ is constant the internal inductance L increases, which is natural for the contracting discharge. The magnetic energy $E_{mag} = \Phi^2/2L$ decreases as well because of the Joule heating at the cooling front. At the end of TQ the magnetic flux conservation fails, because the whole electron fluid gets cold and thus the resistivity increased also on the magnetic axis. Indeed, T_e drop coincides with the minimum of I_{tot}. Then the convective mixing starts and effectively redistributes the current thus making a flat current profile, which produces the current spike. To increase I_{tot}, a rapid decrease of L and some moderate decrease of Φ are needed.

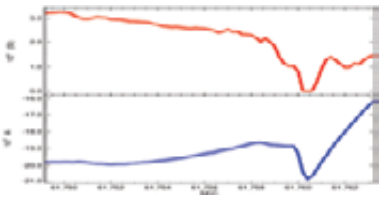

Fig. 3: Time dependences for W_{dia} and I_{tot}.

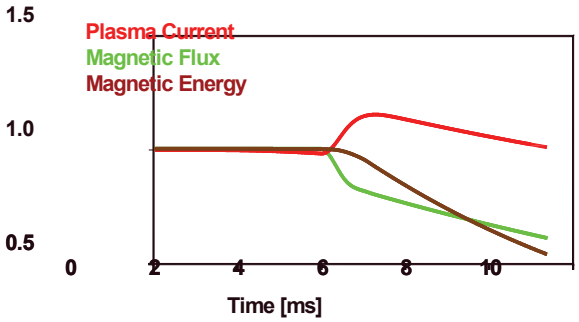

Fig. 4: The results of simplified model.

So far we developed a simplified numerical model to prove that such behaviour of the discharge is possible. In the model we used energy conservation, the boundary conditions B_θ(wall) = 0 and the flux conservation at the wall. Evolution of B_θ is due to the measured T_e during MGI, which drives the magnetic diffusivity. The results are shown in Fig. 4. The energy and the flux decrease monotonically, but the plasma current shows spike like that of the experiment.

Modelling of massive gas injection for ITER disruption mitigation

Fig. 5 shows the ITER wall surface and injector inflow in the MGI simulation with TOKES. The gas is stored at 300 deg(K), the valves open instantly at time $t = 0$. In the figures below the calculated longitudinal variations are omitted and only variables integrated over the magnetic layers are shown. They are functions of the radial coordinate ρ and comprise the whole complexity of plasma longitudinal motion. Fig. 5 includes also a test for argon jet in an empty vessel: the jet shows the expected velocity of ~0.5 km/s but the propagation is slightly distorted because of a numerical diffusion.

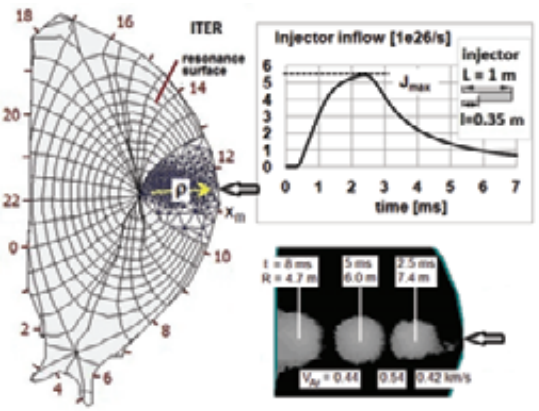

Fig. 5: Magnetic flux coordinates, wall surface coordinate *X* and minor radius coordinate ρ. A fragment of underground triangular meshes is seen Below an argon propagation test is shown.

The electron heat cross-transport due to the magnetic braiding is assumed as it is mentioned above. One can estimate the magnetic braiding effect in terms of electron thermal cross-conductivity $k_{\perp b} = D_b n_e \upsilon_e$; υ_e is the electron thermal velocity and braiding parameter D_b can be determined from experiments. The thermal conductivity is estimated as $k_{\perp e} \sim k_{\perp be}(\upsilon_e \tau_e / l) \sim (D_b/a)^2 k_{\|e}$, where $k_{\|e} = 3.2 T_e n_e \tau_e / m_e$ is the electron classical thermal longitudinal conductivity depending mainly on T_e: $k_{\|e} \propto T_e^{5/2}$.

The best fitting was achieved by splitting TQ into two phases during which $k_{\perp e}$ was differently fixed in the confining region.

Before the cooling front reached the resonance surface $k_{\perp e} = 6.5\times10^{20}$ m^{-1}s^{-1} was set and afterwards $k_{\perp e} = 260\times10^{20}$. A centre initial electron temperature $T_{ce} \approx 2.5$ keV was measured; however, in ITER $T_{ce} \approx 15$ keV is required. Therefore, as the dependence of $k_{\perp e}(T_e)$ is determined by that of $k_{\|e}$, $k_{\perp e}$ is also assumed proportional to $T_e^{5/2}$.

From TOKES validations by JET we concluded that the estimation $k_{\perp e} \approx 3\times10^{-8} k_{\|e}$ fits the TQ phase heat transport, which is about 3 times larger than that of earlier done DIII-D validation. Below we assume that the difference is due to the size: plasma minor radius $a_{\mathrm{JET}} \approx 1$ m and $a_{\mathrm{DIII\text{-}D}} \approx 0.5$ m; thus we assume $k_{\perp e} \propto a^{3/2}$.

We assume that the position of the cooling front $x = x_c(t)$ drives D_b in the whole confining region, where x is a magnetic flux coordinate. The ratio $\eta = (x_c - x_s)/(x_r - x_s)$ is chosen as the driving parameter ($0 \le \eta \le 1$), where x_s is the separatrix and x_r the resonance surface positions. For the calculations the fitting formula is applied:

$$k_{\perp e} = f\times10^{20}\left(\frac{T_e(t,x,y)}{2.5\ \mathrm{keV}}\right)^{\frac{5}{2}}\begin{cases}13\eta, & \eta < 1\\ 260, & \eta > 1\end{cases} \quad (1)$$

Here the factor $f = (a[\mathrm{m}]/0.5)^{3/2}$; for ITER ($a_{\mathrm{ITER}} \approx 2$ m) $f \approx 8$ follows. At $\eta = 1$ the cooling front crosses the resonance surface and $k_{\perp e}$ increases by a factor of 20.

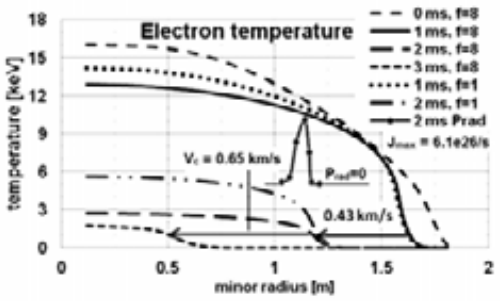

Fig. 6: Radial profiles of T_e. The factor f characterizes the cross-transport. The maximum radiation power density P_{rad} is ~10 GW/m^2 at $t = 2$ ms.

The calculations are performed with 59 layers of equal poloidal magnetic fluxes inside the separatrix. In Eq.(1) mainly the factor $f = 8$ is used (as assumed for ITER) but for checking the sensitivity of results with respect to an uncertainty of $k_{\perp e}$ some calculations are done with $f = 1$. The maximum inflow $J_{\max}$ (see Fig. 5) determines the MGI process.

Fig. 6 shows the initial T_e and radiation power distribution in the cooling wave. The initial thermal energy and wall temperature are high (420 MJ and 500 K, respectively), which gives an upper estimation of the wall temperature after TQ. The TQ starts after reaching the resonance surface at $t \approx 1.1$ ms. Then T_e decreases very differently for $f = 1$ and $f = 8$ (by a factor of 2 at $t = 2$ ms). The cooling front $x = x_c(t)$ increases its speed V_c with t.

Fig. 7 demonstrates the evolutions of the radiation power and the rising surface temperature $T_{w\max}$ at its maximum. There are three phases: 1) pre-TQ with rather small power, 2) powerful photon flash during which T_e in the core significantly drops, 3) long TQ tail corresponding to the travel of cooling front through the confining region. Decreasing $k_{\perp e}$ (i.e. $f = 8$ down to 1) results in substantial redistribution of the load in time. However, only some moderate changes of $T_{w\max}(t)$ happen, and at the end of TQ $T_{w\max}$ gets almost the same for both values of f.

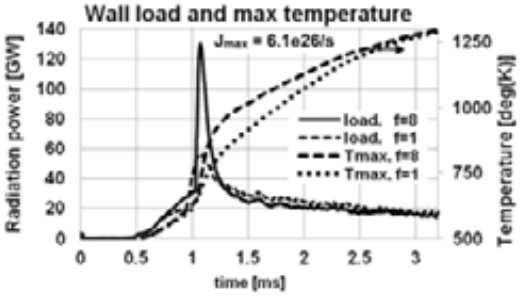

Fig. 7: Total radiation power and maximum wall surface temperature.

Conclusions

The analysis of available JET data with the described simulations allowed a qualitative description of energy and particles transport processes in the course of MGI.

The MGI scenario includes (i) the pre-TQ phase in which the thermal cross transport is rather small, (ii) the TQ itself, with the development of magnetic braiding, and (iii) final convective mixing of cold plasma with still hot plasma, which manifest the start of CQ. The Pre-TQ occurs at the plasma edge, with ionization of injected atoms and radiation as the main contributors to plasma cooling. During TQ the plasma current is contracted by the cooling front. The convective mixing can contribute as to the fast cooling of ions as to the current flattening and the current spike. Sufficient understanding of physics of these processes would allow proper extrapolations of the JET results upon ITER.

The maximal possible temperature $T_{w\max}$ of an ITER Be or W wall after Ar massive gas injection is numerically simulated with TOKES using short (flight length 35 cm) horizontal mid-plane injectors. The injected mass M_{Ar} was varied by one order of magnitude ($17 < M_{\mathrm{Ar}} < 160$ g). With increasing M_{Ar} the cooling time τ_c decreases from 5 ms down to 2.8 ms.

For a W wall, MGI with the mid-plane injectors is always melt-free. For a Be wall this cannot be expected because $T_{w\max}$ is obtained near the Be melting point. Therefore, W is preferable at the most loaded position (wall coordinate $X \approx 11$ m in Fig. 5). Due to the assumption of toroidal symmetry, the simulations give the lowest possible maximum of wall temperature and thus the minimal possible cooling time. In this way we could prove that by using a large number of injectors in one poloidal plane a melt-free MGI in ITER can be achieved in a few ms. .

Staff:

I.S. Landman
S.E. Pestchanyi

Literature:

[1] I.S. Landman et al. ‘Modelling of massive gas injection for ITER disruption mitigation’, Paper presented at the PSI-20 conference, recommended for publication.

[2] S. Pestchanyi et al. ‘Analysis of energy cross-transport during MGI: JET experiments and TOKES simulations’, Paper presented at SOFT-27, recommended for publication.

Acknowledgement

This work, supported by the European Communities under the contract of Association between EURATOM and Karlsruhe Institute of Technology, was carried out within the framework of the European Fusion Development Agreement. The views and opinions expressed herein do not necessarily reflect those of the European Commission.

Modelling of Tungsten PFCs Damage in Support of TEXTOR and JET Experiments and under ITER Relevant Conditions (WP12-IPH-A11-1-02)

Introduction

A major concern for ITER operation in the H-mode with high fusion gain is the occurrence of disruptions which can damage plasma facing components (PFCs) and therefore decrease their durability. It is expected that during several milliseconds of the disruption half of plasma energy can be dumped onto the first wall (FW) during the thermal quench (TQ). Moreover, relativistic runaway electrons (RE) can be generated in the decaying plasma and produce additional damage to FW.

In earlier JET experiments with the carbon fibre composite (CFC) first wall the RE beams were also observed during the disruptions mitigated by means of massive gas injection (MGI) of argon. Since 2011 JET operates with the new ITER-like wall (ILW) covered with beryllium. In one ILW experiment with low density plasma a local melting of poloidal limiter due to RE impact was observed.

To numerically assess the melting of typical Be tiles caused by RE in next JET experiments and ITER the codes ENDEP and MEMOS are applied. An upgraded 3D version of MEMOS is now available for motion dynamics of viscous melt. In tokamaks the melt fluid acceleration can be due to surface tension, applied plasma pressure and the **J**×**B** force of halo-, eddy-, and thermo-currents. The 3D version has been validated against TEXTOR experiments for long timescale (of several seconds) melt motion displacements and for RE impact on TEXTOR graphite limiter. Simulations of after effects of RE impact on the JET Be FW are performed including also the surface vaporization and determination of melting threshold W_{melt} for RE energy density W_{RE}.

Simulations of RE impact on single Be tile of JET ILW

Detailed temperature evolution and spatial distributions as well as melting and evaporation erosion are simulated for single beryllium tile installed at the upper dump plate in JET (Fig. 1) accounting for geometrical peculiarities of it. It is assumed that the impacting relativistic electrons have exponentially decaying distribution on electron energy E: the energy density distribution function $f(E) \sim \exp(-E/E_0)$ with the parameter E_0 below 10 MeV. A small ratio E_{tr}/E_e of transversal electron energy E_{tr} to the longitudinal energy E_e in the magnetic field B is assumed. In JET $B \approx 3$ T can be assumed. The impact duration τ ranged from 1 to 4 ms.

The simulations are divided into two steps. At first the volumetric energy deposition function is calculated with the Monte Carlo code ENDEP.

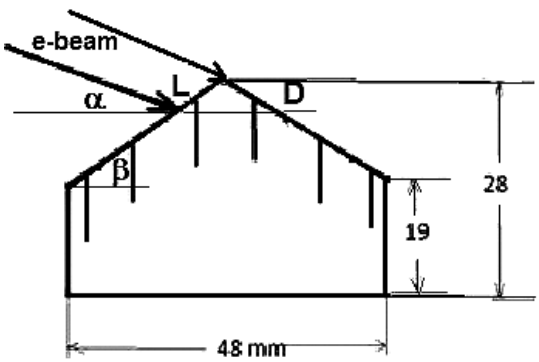

Fig. 1: Sketch of Be tile of JET ILW.

At the second the code MEMOS is applied for the calculations of temperature distribution in the material bulk. Temperature-dependent thermo-physical properties of beryllium are used in MEMOS.

We assumed that the RE beam parameters used in the simulations are equal to those from the JET experiments with CFC FW: typical RE current up to 0.5 MA and RE beam radius of 0.5 m, so that the current density up to 0.6 MA/m^2. The total wetted area of the impact is expected to be of 0.6 m^2.

The incident electrons move along the magnetic force lines and gyrate about. The value of E_{tr} determines the gyro-radius ρ. The incidence angle at the crossing of target surface depends on E_{tr}/E_e and the inclination angle $\alpha \sim 20°$ between the target surface and the field line (see Fig. 1). The simulations are carried out for $E_{tr}/E_e=0$ (electrons move strictly along field lines) and $E_{tr}/E_e=0.02$; $E_0=3$, 5 and 8 MeV (the range of RE energies expected in JET is 1-10 MeV). Two scenarios with different width of wetted area along the tile surface: L=1 cm (i.e. D=3.4 mm) and L=0.5 cm (D=1.7 mm) have been considered. In both scenarios the rectangular profile in time and the pulse durations τ=1, 2, 3, and 4 ms are assumed. The load varied as W_{RE} = 5 to 60 GW/m^2.

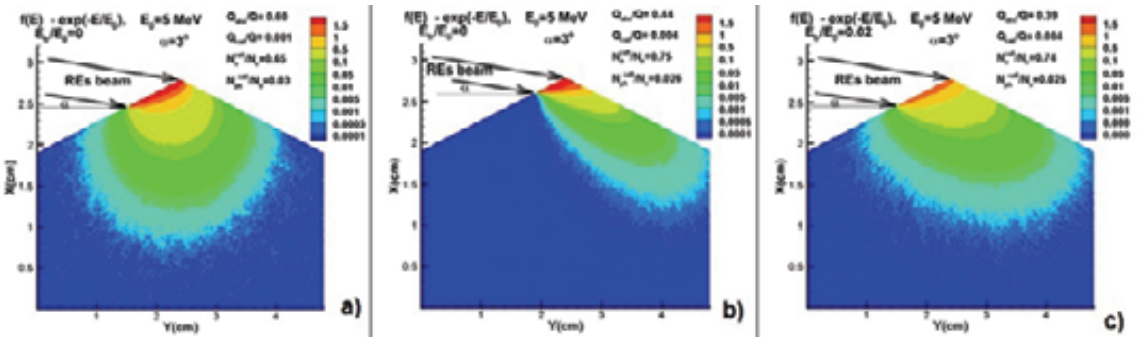

Fig. 2: Normalized function of absorbed energy inside the Be tile:

a) L=1 cm, $E_{tr}/E=0$ b) L=0.5 cm, $E_{tr}/E=0$ c) L=1 cm, $E_{tr}/E=0.02$.

The normalized distributions of deposited RE energy are used as input data in the MEMOS simulations. Typical temperature distributions inside the tile at the end of the RE impact are demonstrated in Fig. 3 for both scenarios.

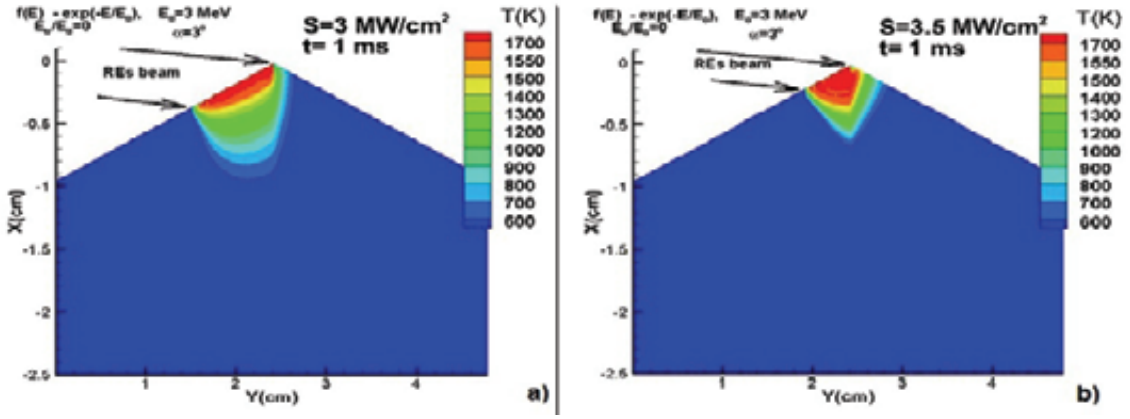

Fig. 3: Typical temperature field inside the Be tile for RE load scenarios with $E_{tr}/E=0$. Time moment 1 ms corresponds to the end of pulse. a) L=1 cm; b) L=0.5 cm.

In case of $E_{tr}/E_e=0$ and L=1 cm the impact energy is deposited rather uniformly inside the tile (see Fig. 2). Approximately 40% of energy is passing through the tile and escapes as primary and secondary electrons. RE current density J_{RE} drops by 35%. Increasing E_{tr}/E_e results in smaller absorption so that in case of $E_{tr}/E_e=0.02$ the J_{RE} drops less than for 26%. Decreasing the wetted area (L=0.5 cm) leads to a decrease of absorbed energy and an increase of number of RE passing through the tile. Dependences of the maximum surface temperature against heat load density W_{RE} and the current density J_{RE} are shown in Fig. 4 for different scenarios. These curves determine the threshold W_{melt} (or J_{melt}) which depends on the pulse duration as 1/τ.

The calculated values of J_{melt} (ranged in the carried out calculations from 2 to 12 kA/m^2) are much less than the J_{RE} up to 500 kA/m^2 as expected in JET. A small increase of J_{RE} above J_{melt} by 10-20% results in the Be melting pool deepness up to several hundred microns; the

calculated solidification time is rather long: ~20 ms. With the expected wetted area of 0.6 m^2 the RE current of 10 kA can produce the melt layer of 0.5 mm thickness at the JET Be tiles.

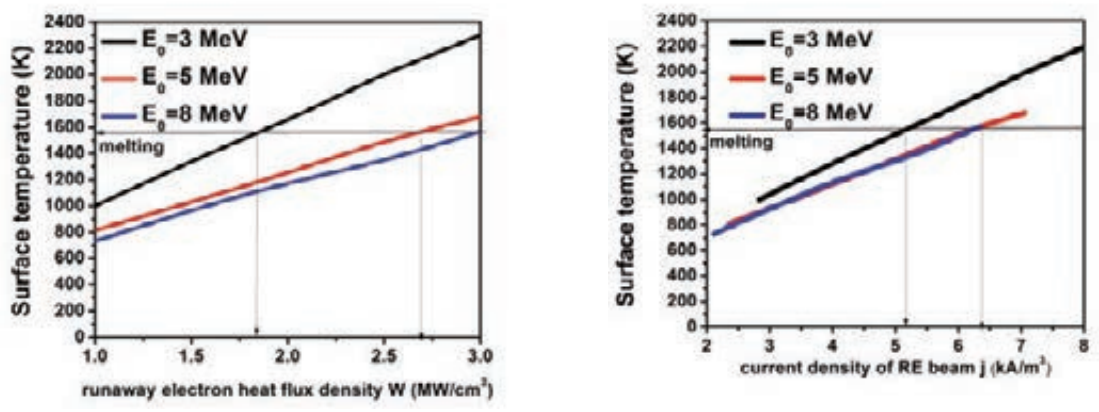

Fig. 4: Dependencies of maximum Be surface temperature on W_{RE} and J_{RE}.

Simulations of TEXTOR experiments on JxB melt motion and RE interaction with graphite limiter

The TEXTOR simulations were carried out in the magnetic field B = 2.25 T for not castellated targets with the sizes 3.5×3.2×0.3 cm. The heat flux W along the poloidal direction is assumed to be constant (smoothed experimental flux). Along the toroidal direction an exponential function of flux decay was assumed. The Child-Langmuir model is used for calculation of the thermo-emission current.

Several scenarios of the duration 6 s with different maximum of W ranged from 21 to 27 MW/m^2 are calculated. For example, in case of W_{max} = 25 MW/m^2 the simulated final erosion profile on the target surface after the melt motion driven by the **J×B** force of thermo-currents is in a good agreement with the TEXTOR measurements (Fig. 5).

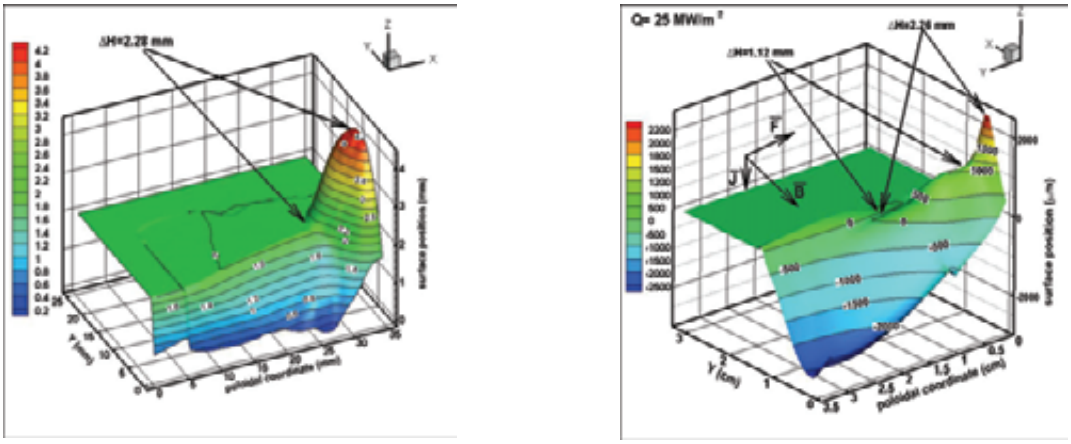

Fig. 5: Final surface profile of W target after plasma heat loads in TEXTOR experiments with Q=25 MW/m^2.
Left: TEXTOR experiment, Right: corresponding MEMOS results.

It is worth noting that additional 3D simulations carried out with MEMOS for reproducing melt motion on JET Be tiles have also demonstrated the importance of the **J×B** force (in JET due to the halo currents of VDE events). That simulation results are also in a qualitative agreement with experimentally observed Be tile damage.

Furthermore, interactions of the RE electrons with TEXTOR graphite limiter have been investigated and then simulated with MEMOS. In the experiment the mean RE energy is about 4

MeV, the RE energy absorbed in the graphite limiter 3 kJ and the RE pulse duration of 10 ms was measured. The ENDEP and MEMOS codes validated against these TEXTOR experiments have reached at reasonable quantitative agreement of simulations with the experiment (Fig. 6).

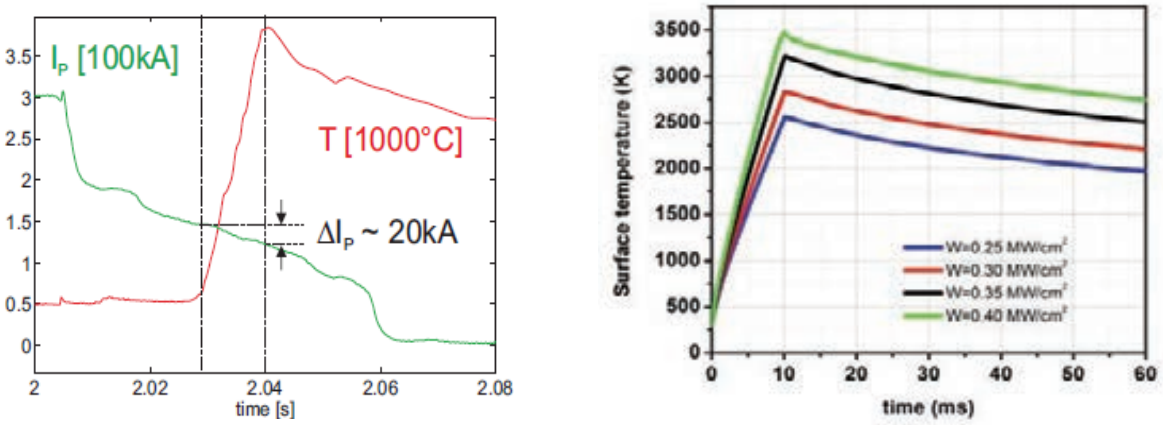

Fig. 6: Experimental (left) and calculated (right) dependences of maximum surface temperature of TEXTOR graphite limiter under RE loads on time.

Staff:

B.N. Bazylev

Literature:

[1] B. Bazylev et al. 'Modelling of the impact of runaway electrons on the ILW in JET' Paper presented at PSI-12 O-21. (May 2012) Aachen, Germany. Recommended for publication.

[2] B. Bazylev, J.W. Coenen, R.A. Pitts, V. Philipps, "Modeling of Tungsten Armour Damage under ITER-like Transient Heat Loads", 15th International Symposium on Flow Visualization. (June 2012) Minsk, Belarus.

[3] B. Bazylev et al. Modelling of material damage and High Energy Impact on Tokamak PFCs during Transient Loads. Paper presented at International Conference & School on Plasma Physics and Controlled Fusion I-01. (September 2012) Alushta, Ukraine. Recommended for publication.

[4] B. Bazylev et al. Modelling of material damage and High Energy Impact on Tokamak PFCs during Transient Loads. Pater presented at 24th IAAE FEC P1-39. October 2012 San Diego USA.

Acknowledgement

This work, supported by the European Communities under the contract of Association between EURATOM and Karlsruhe Institute of Technology, was carried out within the framework of the European Fusion Development Agreement. The views and opinions expressed herein do not necessarily reflect those of the European Commission.

Prepare Tools for Erosion Estimates (WP12-PEX-01-T03-01)

Introduction

In this task we perform erosion simulation under a range of conditions as might be expected in DEMO. For that reason we are employing codes MEMOS and ENDEP developed in KIT [1]. The codes were primarily benchmarked with JET experimental results.

The advanced MEMOS and ENDEP codes

The Fluid Melt Motion on Surface code MEMOS has been developed for estimation of surface erosion (melting and the melt-layer dynamics) of the plasma facing components (PFC) at specified power input. It simulates a surface melting and evaporation, heat transport across the fluid and solid structures, a melt front propagation due to pressure of incident particles and electromagnetic forces and arcing formation.

The ENDEP code calculates the power deposition in the bulk material of PFC. It aims to evaluate distribution of power in bulk PFC due to run-away electron and plasma particle flux deposition. The code includes various atomic processes: the electron-electron and electron-nuclear scattering for RE, bremsstrahlung radiation losses, Compton scattering, Auger processes, photo-ionisation and recombination, electron-positron interactions and electron and photon avalanche. The results of the ENDEP code are required for MEMOS code as an input data. The ENDEP was updated by including 1) the effect of the target's material polarization on energy deposition depth of the incident RE and 2) the conversion of the magnetic energy of the RE beams into heat in the bulk of materials [2]. The code has been benchmarked with experimental results from JET and other tokamaks. Both codes were substantially updated for the proper erosion calculation under DEMO conditions. Some preliminary results are presented below.

Sputtering erosion in a steady state DEMO operation

The important erosion process for the FW and baffles under steady-state DEMO operation is expected to be physical sputtering, since the W surface temperature remains below the melting point and ignition of arcing is insufficient for life-time limitation under normal (without ELMs) operation [3]. In our calculation we have emphasised two new important effects, which previously were ignored or approximately accounted for [5]. This is the dependence of sputtering yield on the angle of incidence and, particularly, the sheath potential effect on deviation of the distribution function of incident ions from Maxwellian one. The thickness, *d* of plasma facing elements (e.g. the FW blanket armour, limiter, etc.) sputtered away during Δt operation time by incident particle fluxes Γ_j of different species j, can be expressed as [6]

$$d(t) = \Delta t \cdot \frac{A_t \cdot m_p}{\rho_t} \cdot \sum_j \left\langle Y_j \Gamma_j \right\rangle \qquad (1)$$

where A_t is the target atomic mass (in amu), ρ_t is the target material density, $Yj(E,\theta)$ is the sputtering yield of particle j with energy E and angle of incidence θ and Γ_j is the flux of particles j. The brackets in (1) represent an average over the angular and energy distribution of incident particles. Thus, the precise determination of the erosion rate needs the correct form of the energy distribution function of the incident particles and the sputtering yield $Y_j(E,\theta)$. Here we present the results of erosion rate calculations taking into account deviation from Maxwellian distribution function at the divertor plates due to the sheath acceleration and the angular dependence of the sputtering yield.

Following [6] the twice averaged sputtering yield, defined as the yield averaged over the distribution of energy and angle of incidence of the projectiles, is given by

$$\overline{Y_j}\left(\frac{atom}{ion}\right) = S_0 \int_0^1 \int_{\varepsilon^*}^{\infty} \exp\left(-\frac{\varepsilon}{\beta}\left(1-t^2\right)\right) \times \exp\left[-\left(\sqrt{\frac{\varepsilon}{\beta}t^2 - \delta} - M_0\right)^2\right] \cdot tS(\varepsilon,t) \cdot \varepsilon d\varepsilon \qquad (2)$$

Where $S_0 = \frac{2E_{Th}^2}{T_i^2 F(M_0)}$, $t \equiv \cos\theta$, $\varepsilon = E/E_{Th}$ $\varepsilon^* = \max(1,\delta)$; $\beta = T_i/E_{Th}$, $\delta = Z_j e\varphi_0/T_i$

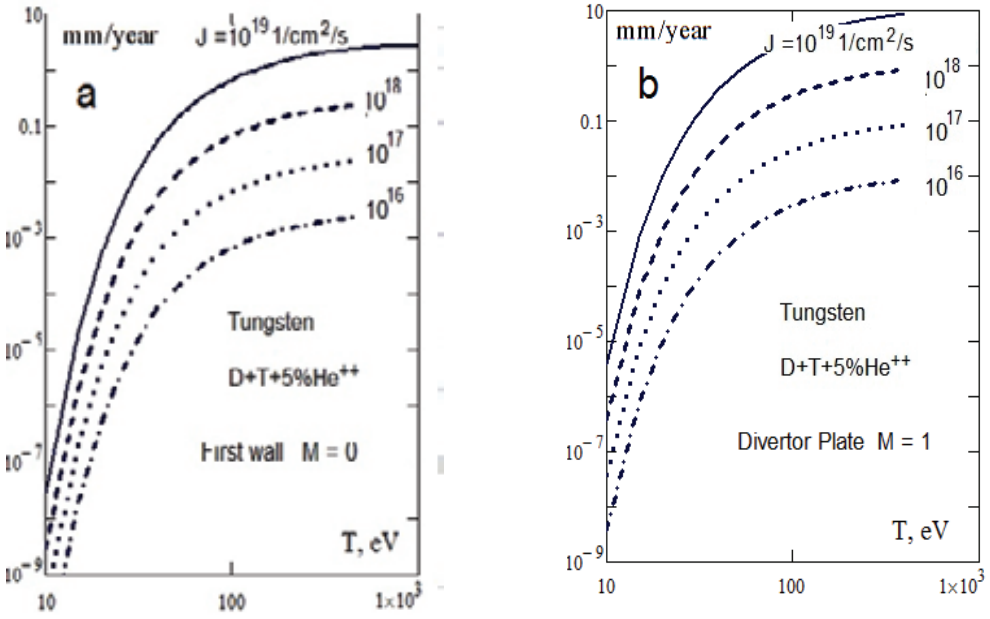

Fig. 1: The thickness of W armour (a) and divertor plate (b) sputtered during one year of continues operation by various particle fluxes of D/T/5%He of incident ions J($cm^{-1}sec^{-1}$).

Here M_0 is a Mach number of incoming particle flux (which must be taken to one at the divertor plate according to Bohm condition and to zero at the FW), $S(\varepsilon, t)$ represents, the sputtering yield for a certain energy and angle of incidence of the particles. This dependence can be described by the revised Bohdansky formula [7] for the energy dependence and the Yamamura formula [8] for the angular dependence.

Using these formulas, the erosion rate of W armour sputtered during one year of continues operation by various particle fluxes of D+T+5%He+ incident ions is shown in Fig.1a for the FW and in Fig. 1b for divertor plates. Here we are taking into account that the 'fatal' concentration of He is about 5% from the average DT plasma density [see e.g. in ITER Concept Definition vol.2, IAEA, Viena1989 ITER Documentation Series 3].

Stronger erosion of divertor plates compare with the FW erosion is due to the acceleration of incoming ions in the sheath potential and deviation of energy distribution function from Maxwellian. It is seen that at temperatures ≤ 100eV sputtering of W material falls off rapidly and for ≤ 30eV is negligible. However, for neutrals, undergoing the charge-exchange collisions in the pedestal region, strong erosion can be expected for particle fluxes several orders of magnitude exceeding DT particle flux expected for

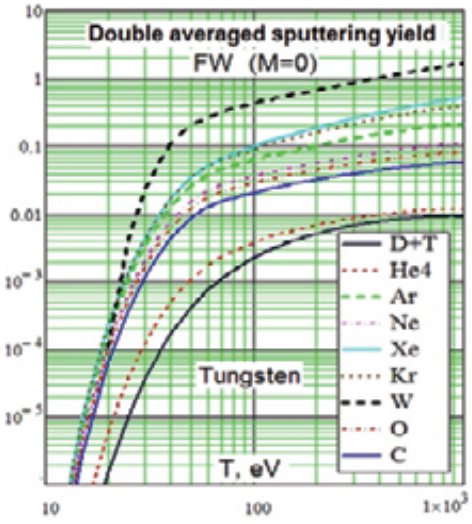

Fig. 2: The double averaged values of tungsten sputtering yields vs. temperature for various incident impurity ions.in the most representative ionization charge state at given temperatures.

DEMO (10^{14}-10^{15}/cm^2/s). The most intensive W ions release due to charge-exchange collisions is expected from baffles. However, under steady-state operation and normal conditions due to rather low level of W sputtering rates even for higher pedestal temperatures and expected particle fluxes of hydrogen isotopes and 5% of helium the W impurity concentrations will remain below the fatal values~0.005%. The sputtering erosion with external impurity ions could pose a problem and must be simulate numerically by transport code. The double averaged values of W sputtering yields for various incident impurity ions taken in the most representative charge state at given temperature are also evaluated based on Eq. (2) and data from [7,8, 12] (see Fig. 2).In these calculations the case of Maxwellian distribution of incident impurity ions on the FW is assumed.

The FW erosion during a long period steady-state DEMO operation

Here we consider steady state DEMO operation under normal conditions, when the sandwich type blanket first wall module is considered (see Fig.3). Heating of a W-clad EUROFER PFC by radiation and neutral flux as well as by transients like ELM is discussed. We have analysed the cases, when heat fluxes into coolant (water) remain under critical heat flux (CHF) value. We assume the heat transfer into rectangular tube of 10mm x 18mm cross-section with a water temperature of 150°C and in that case the tube wall temperature stays below 300°C.

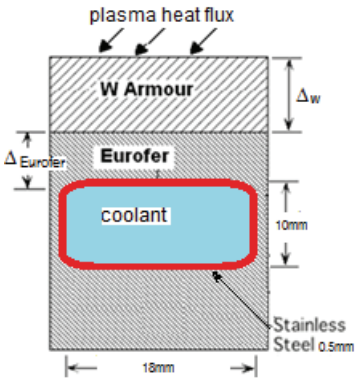

Fig. 3: Sandwich type blanket first wall module used for the Monte Carlo MEMOS computation of the plasma impact.

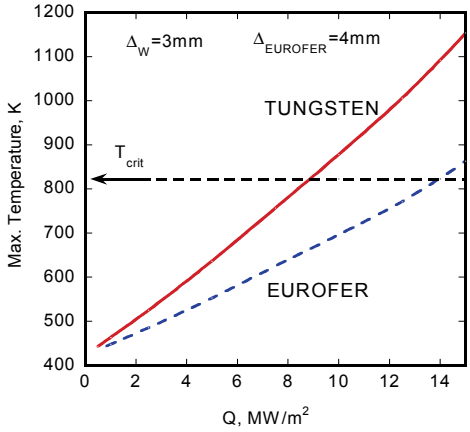

Fig. 4: W surface temperature and maximum EUROFER temperature vs net incoming heat flux Q under steady-state operation.

During normal operation the erosion of the FW and baffle surface could mainly occur due to collisions with hot neutral atoms. Undergoing charge–exchange collisions with the hot ions at the separatrix or in pedestal region, energetic neutrals will deliver the plasma energy to the armour surface, thus producing a strong sputtering. Fig. 4 shows the armour surface temperature and the maximum EUROFER temperature (interlayer temperature) for different incoming heat flux values Q. When Q reaches~14 MW/m^2 the interlayer temperature exceeds the critical value $T_{crit.}$~ 550ºC and EUROFER can experience irremediable thermal distraction [4]. Such values of Q one can expect in DEMO due to transient events like ELMs or convective radial plasma losses, associated with unstable convective cells in the SOL region during steady-state operation. Calculations show that for expected incoming fluxes the W surface temperature remains below the melting point and evaporation is negligible. Calculations where performed for armour thickness Δ_w=3mm and for EUROFER thickness $\Delta_{EUROFER}$ = 4mm. Fig. 5 shows the maximum W temperature under design heat load (13.5 MW/m^2 for the limiter, and 0.5 MW/m^2 for the FW) as a function of the W armour thickness. It is shown that under steady-state operation for heat flux value~13.5MW/m^2 the surface armour temperature increases with increasing the armour thickness, whereas the W/EUROFER interlayer temperature remains as expected almost unchanged for fixed coolant temperature. For low power load of~0.5MW/m^2 a weak dependence of the armour surface temperature and the interlayer temperature on armour thickness is shown. Under expected steady-state operation

heat loads and the thickness of W armour, surface temperature remains well below the vaporization and melting points and, as calculations also show, coolant heat flux remains below CHF thus avoiding severe degradation of the heat removal capability.

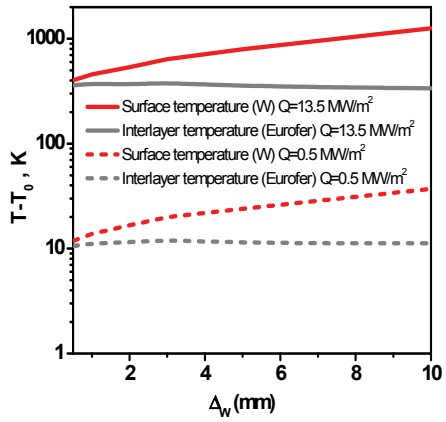

Fig. 5: Maximum armour surface temperature and maximum EUROFER temperature vs armour thickness ΔW for two cases of incoming heat fluxes Q=13.5MW/m^2 and 0.5MW/m^2; SS water cooled rectangular channel; Δ_{EROFER}= 4mm, Δ_{SS} =0.4mm, Tcoolant=150 ºC. The temperature is calculated from the initial value T_0 = $T_{coolant}$

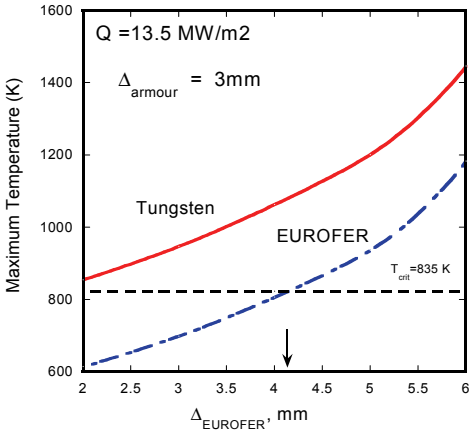

Fig. 6: Maximum temperature of W and EUROFER vs EUROFER thickness. For $\Delta_{EUROFER}$ < 4.3 mm max EUROFER temperature remains below the critical value.

For incoming heat flux ≥10MW/m^2 W temperature approaches a soft limit of~900-1050K based on degradation of the structural properties and on possible crack growth through the W could also affect the EUROFER eventually. To keep the W surface temperature below 1000°K, the armour thickness should be taken ≤ 3-4 mm (see Fig. 6). As it will be show further this thickness could be sacrificed during about three years of continuous operation by taking into account only the sputtering erosion. Unlike graphitic carbon the sputtering erosion of W is independent on surface temperature.

Variation of the surface armour temperature and interlayer temperature with EUROFER thickness is shown in Fig. 7 for given ΔW =3mm and Q=13.5MW/m^2. Under these conditions and ΔEUROFER ≤ 4.5mm there will be no thermal degradation of the structural material properties. Fig. 7 shows heat loads and corresponding thickness of EUROFER when operation causes no thermal degradations (region below the curve). Arrow indicates the thickness value for the same case as in Fig.6.

Calculations show that the volumetric heating associated with the neutrons is not particularly demanding for the first walls blanket design, whereas the surface heating is important in term of allowable temperatures and stresses.

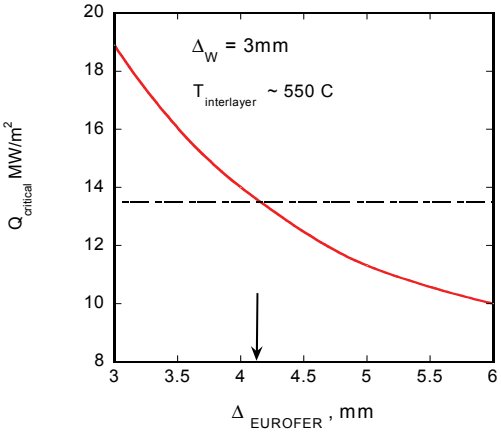

Fig. 7: Critical incident heat flux Q_{crit} vs EUROFER thickness when interlayer EUROFER temperature exceeds the critical value~550ºC above which creep-fatigue is likely to be a problem; W armour thickness Δ_w=3mm.

Effect of off-normal events on the FW erosion in DEMO

The various types of off-normal conditions can occur during the DEMO operation, which represent a potential threat to the integrity and availability of a fusion reactor. Here we consider a consequence of two types of off-normal events: a loss-of control “hot” and following a disruption “cold” VDEs and RE generation that can occur during the current quench following a

disruption or as a consequence of disruption mitigation by means of massive gas injection. Both VDE and RE energy deposition would affect mostly the first wall [10]. Although VDE and RE events are taken place within a short time and limited number of events in DEMO life time, the damage induced by ˜thermal stresses can accumulate. The exact energy density on the first wall depends on the plasma parameters and assumed deposition area. The characteristics of VDE in DEMO can be assessed by extrapolate calculations made for ITER and using the scaling arguments [10,11]. The input parameters for calculation are given in Table 1:

events	**Energy density, MJm^{-2}/ deposition time, sec**	**Deposited area, m^2**	**Max. EUROFER temperature, ^oK**
hot VDE	~50-100/1	24	~1610
cold VDE	~30-50/0.3-1	24	~1260
RE	100/0.05-0.3	0.8	~1500

The off-normal events will affect mostly the FW structure causing both the excessive erosion of armour and stresses in structural material. For calculation of RE impact, we have considered mono-energetic RE beams (50 and 80 MeV) and RE beams with a Gaussian energy distribution and an average incident energy E_0. The RE current in DEMO can be estimated as I_{re} ~10-15MA, which is about ≤70% (this ratio is similar in ITER assessments) of the total plasma current. The average RE energy can be assessed as $E_0 \approx 18{,}5$MeV (for details see Ref.10). For comparison, in JET the RE current is measured about 1-2MA and the average RE kinetic energy about 5-8MeV [13]

Calculations show that in the case of VDE almost all plasma energy is converted into heat causing melting, evaporation and radiation from the W surface. In the case of RE the percentage of absorbed energy in W armour reaches ~60%, while the percentage of energy emitted as photons is ~11-15%. The RE beam generates a considerable amount of radiation (mainly the X-ray radiation) upon impacting the W surface. The emissive power for temperatures ≥ 3600°K (emissivity $\varepsilon \sim 0.2$) is about several hundreds of kW/m^2. Although, the emissive power cools the W surface, its ratio in energy balance is small. The rest of the kinetic energy of incident RE is reflected off by back-scattered electrons (~16-34%).

The fraction of RE passing to the structural material is negligible and therefore the heat transfer from armour to EUROFER occurs though the tungsten thermal conductivity. There is no major difference between the RE and hot VDE cases in terms of EUROFER temperature, melt layer thickness and heat flux to the coolant since for W armour the heat deposition occurs very close to the surface. For the RE case, a somewhat larger part of the heat generation occurs deeper in the material in particular for the mono-energetic RE beams. Consequently, the RE energy deposition results in thicker melt layer, higher maximum EUROFER temperature and higher evaporated thicknesses than VDE energy deposition. The latter occurs because of the vapour screening effect, which is less pronounced for the RE case. The total molten and evaporated thickness is~2 mm for W, which, depending on the VDE and RE frequencies, would seriously restrict the armour lifetime.

It is shown, that in the case of a VDE and ≥10mm of armour thickness the surface temperature will exceeds the W melting temperature, for deposition times ≥1s. The RE beams with $100MJ/m^2/0.3s$ will melt the W surface at any thicknesses. For an energy deposition of $100MJ/m^2$ and relatively long exposition periods ~1s, melting could be avoided for smaller armour thicknesses <1cm.For the RE with $30MW/m^2$ and t=0.1s the temperature remains below the melting point and is independent on armour thickness. In general, the larger the incident energy, the higher the surface temperature and it becomes independent on the W thickness for deposition periods shorter than the thermal conductivity time in tungsten.

The maximum of EUROFER temperature and maximum W melt layer as a function of W armour thickness is show in Fig. 8. The EUROFER creep point limits the minimum W thickness (indicated by vertical arrows for 30MJ/m^2/0.1s and 50MJ/m^2/0.05s cases). For instance, for the RE case with moderate energy deposition density and exposure time (50MJ/m^2 and 0.05s, respectively), the W armour thickness must be ≥ 1.4cm in order to reduce the EUROFER temperature below the creep point. However, at that thickness the W armour will melt. Only in the case of 30MJ/m^2/0.1s for thickness ≤ 0.8cm the W surface doesn't melt and it is possible to avoid the potential thermal stresses. In the cases of 100MJ/m^2 the critical point is always exceeded and, moreover, EUROFER will melt for armour thickness ≤ 0.8cm. It is also shown on the right ordinate the depth of the W molten layer as a function of armour thickness. It is shown that the higher incident energy and the smaller the exposure time, the larger the molten layer thickness. This is consistent with the fact that the W heat conductivity drops with increasing temperature and that the conductivity time increases with armour thickness.

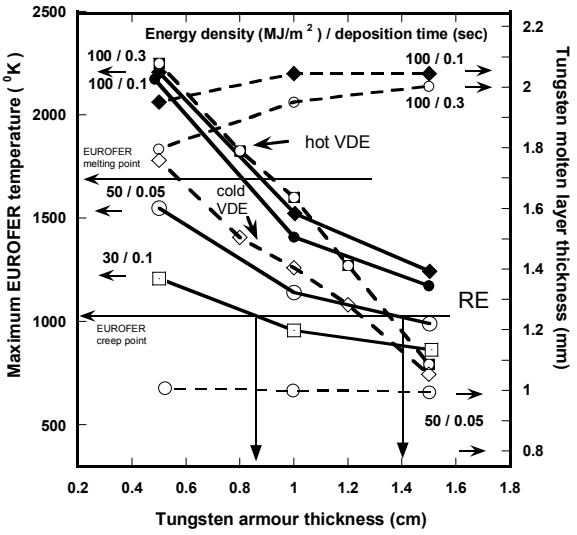

Fig. 8: The maximum EUROFER temperature and the maximum W melt layer as a function of W armour thickness in the cases of mono-energetic RE beams and VDEs. The EUROFER critical temperature (1023 K^o) limits the minimum W thickness (indicated by vertical arrows for 30 and 50MJ/m2, τ=0.1s); the higher incident energy and the smaller the exposure time, the larger the molten layer thickness.

Heat generation in W armour occurs very close to the surface and there is no major difference between the RE and VDE cases in terms of EUROFER temperature melt layer thickness and heat flux to the coolant.

The evaporated thickness is smaller owing to the vapour screening effect. The total melted and evaporated thickness is~2 mm for W, which, depending on the VDE and RE frequencies, would seriously affect the armour life-time.

Conclusions

As expected, under steady state operation the armour surface temperature increases with the armour thickness increase and for the reference case of~3mm remains well below the tungsten melting point and the W front surface temperature remains high enough to mitigate the consequences of neutron irradiation.

Both temperatures of the W surface and the EUROFER interlayer are increasing with an increase of incoming heat flux. For reference conditions (Δw~3mm, $\Delta_{EUROFER}$~4mm) the maximum heat flux which does not causes intolerable thermal stresses in structural material is about~13.5MW/m^2. Calculations show that for envisaged in DEMO conditions [9] (particle fluxes and boundary temperatures) the total sputtering erosion of W armour by the charge-exchange neutrals could reach~1mm during one year of steady-state operation.

In the case of off-normal events calculations show that in the 'hot' VDE case the energy deposition into the W armour is very shallow (~nm) and causes surface melting and evaporation. The accommodation of slow VDE power requires thicker W armour to maintain the maximum heat flux and temperature in the material structure to acceptable level. It is shown that the presence of a vaporized layer and a macroscopic molten layer is unavoidable for expected exposure times and power loads. The RE deposit their energy deeper into armour and for energies ≥ 50MJ/m2 and deposition times ≤ 0.1s, the minimum armour thickness required to

prevent EUROFER from thermal destruction is ≥1.4cm.However, this size of layers doesn't prevent the W surface from melting. At higher RE energy deposition rates (≥100MJ/m2 in 0.1s), the required armour thickness to prevent creeping destruction is even larger so that the bulk of the armour layer will melt and evaporate

Although the W/EUROFER bound might be made compatible with high neutron fluencies, the loss of creep strength at relatively low temperature represents the main drawback of EUROFER as a structural material. Our estimations of erosion of the FW by charge-exchange neutrals and the divertor plates by incoming ions show the importance of angular dependence of sputtering yield and, particularly, the sheath potential effect.

We have shown that the sputtering yield increases if the sheath potential is taken into account and that the usual estimation of the sputtering yield at energy 3.5Te is too low. It is found that it is essential to account for the angular distribution of incident light ions at low and high temperatures in order to calculate correctly the sputtering yield averaged over the distribution function of the incident particles

Staff:

Yu. L. Igitkhanov
B. Bazylev

Literature:

[1] B. BAZYLEV et.al, Journal of Nuclear Materials 307-311 (2002) 69

[2] Yu. Igitkhanov et al., PFMC-13 Rosenheim (in press)

[3] Yu. Igitkhanov, B. Bazylev, Journal of Modern Physics, 2011, 2, 131-135; R. Raffray, G. Federici, Journal of Nuclear Materials 244 (1997) 85-100

[4] R Linday, A Möslang, Fusion Engineering and Design 75-79, (2005) 989

[5] R. Raffray, G. Federici, Journal of Nuclear Materials 244 (1997) 85-100; G. Federici et al., Journal of Nuclear Materials, 290-293 (2001) 260-265; R. Behrisch, G. Federici, A. Kukushkin, D. Reiter Journal of Nuclear Materials, ; 313–316 (2003) 388–392; G.F. Matthews, Journal of Nuclear Materials, 337–339 (2005) 1–9

[6] V. Abramov, Yu. Igitkhanov, V. Pistunovich and V. Pozharov, J. Nucl. Mater. 162-164 (1989) 462.

[7] W. Eckstein, C. Garcia-Rosales, J. Roth and W. Ottenberger, Max-Planck-Institut für Plasmaphysik Report, IPP 9/82 (1993).

[8] Y. Yamamura, Y. Itikawa and N. Itoh, Nagoya University Report, 1PPJ-AM-26 (1983)

[9] D Word and W Han., DEMO. Results of Systems Studies for DEMO, TW6-TRP-002, DEMO/UKAEA/PROCESS5 July 2007

[10] Yu. Igitkhanov, B. Bazylev Fusion Science and Technology, Volume 60, Number 1, July 2011, Pages 349-353;

[11] Yu Igitkhanov, B Bazylev and Landman I.,Journal of Nucl. Mat. 415 (2011) S845–S848)

[12] D. E. Post, R. V. Jensen, C. B. Tarter, W. H. Grasberger, W. A. Lokke, Atomic Data and Nuclear Data Tables 20, 397-439 (1977).

[13] G. Aenoux, et al., Heat load measurements on the JET first wall during disruption, Journal of Nuclear Materials 415, (2011), S817

Acknowledgement

This work, supported by the European Communities under the contract of Association between EURATOM and Karlsruhe Institute of Technology, was carried out within the framework of the European Fusion Development Agreement. The views and opinions expressed herein do not necessarily reflect those of the European Commission.

Interim Report on Assessment of Physics Basis (WP12-PEX-02-T03-01)

Introduction

Here we analyse a snow flake (SF) alternative divertor magnetic configuration with respect to coupling of ballooning instability with thermal (MARFE) instability under DEMO conditions [1]. We also consider of ballooning instability in specific snow-flake topology of magnetic field in the vicinity to X-point.

The separatrix and x-point region is immediate affected by boundary plasma and as a result could trigger MHD instability. However the features of MHD perturbation near the expanded SF region is not well known .Ballooning modes appear to be the most unstable in this region due to increase of potential magnetic well.

The MHD stability near the separatrix and SF area

The ballooning equation for the marginal stability reads as:

$$\left(\vec{B}\nabla\right)\left[\frac{k_\perp^2}{B^2}\left(\vec{B}\nabla\right)\xi\right]+2(1-\gamma)\left(\left[\vec{B}\times\vec{k}_\perp\right]\nabla p\right)\left(\frac{\left[\vec{B}\times\vec{k}_\perp\right]\vec{k}}{B^4}\right)\xi=0 \qquad (1)$$

Metrics for SF geometry is simplified and is taken as magnetic topology of the straight current strings combine with the toroidal angle ϕ (see Fig.1).

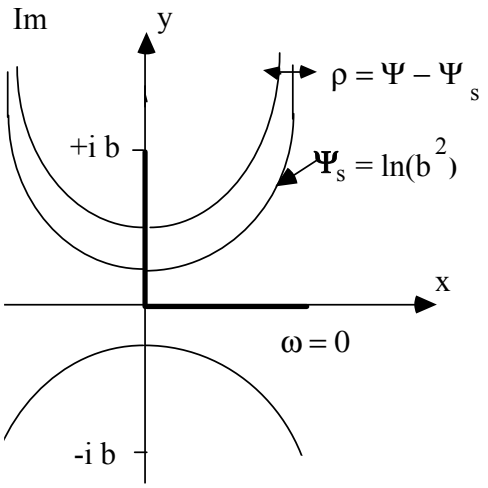

Fig. 1: Magnetic topology of the straight current strings.

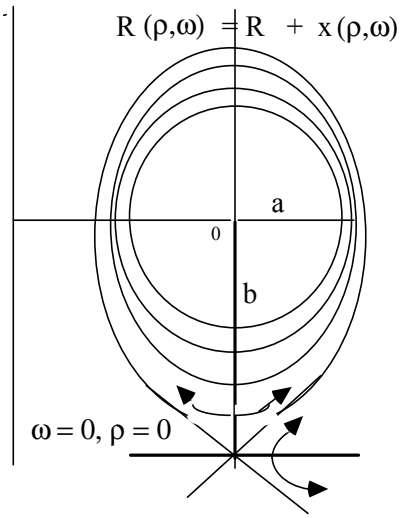

Fig. 2: Magnetic topology of SF used for ballooning stability analysis.

$$ds^2 = h_\rho^2 d\rho^2 + h_\omega^2 d\omega^2 + R^2 d\phi^2$$

And near the SF region, were ρ,ω <<1

$$h \equiv h_\rho = h_\omega = \frac{b}{2\sqrt{1-\cos\omega+\rho^2/2}}$$

The flux expansion at the SF-region:

$$\Delta_{X-point} \approx \sqrt{\Delta_{mid-pl.} b}$$

Criterion of ballooning stability near the separatrix and SF area

Using the magnetic topology shown in Fig: 2 the criterion for ballooning stability can be written as [2]:

$$\left.\frac{dP}{d\rho}\right|_{X-point} < Const. \frac{B^2 R}{q^2} \frac{b}{\sqrt{\rho}}, \qquad (2)$$

or as:

$$\frac{4\pi q_\pi^{\,2} R}{B^2}\left(\frac{dP}{dr}\right)\Big|_{mid-plane} > \sqrt{\frac{b}{\Delta}} \quad or \quad \left(\frac{dP}{dr}\right)\Big|_{mid-plane} > \frac{b}{P_0}\left(\frac{B^2}{4\pi q^2 R}\right)^2 \qquad 3)$$

Where

$$\alpha \equiv \frac{4\pi q_\pi^{\,2} R}{B^2}\left(\frac{dP}{dr}\right)\Big|_{mid-plane} > \frac{b}{P_0}\left(\frac{B^2}{4\pi q^2 R}\right)$$

Here the safety factor q was taken as: $q_\pi(\rho) \equiv q_\pi(0.1) = q_{95} / 3$

Neglecting the dependence on shear and assuming that P0 is the pedestal pressure, one can find that:

$$\left.\frac{\partial P}{\partial r}\right|_{x-point} \approx \frac{P}{\sqrt{\Delta_{mid.-pl.} b}} < Const. \frac{B^2}{4\pi R q_s^2} s(q, k, \varepsilon, \delta), \quad where \;\; q_s = q_{95} \frac{\pi}{6} \ln(4\pi / \rho),$$

The difference in magnetic potential well for the SF case and normal X-point configurations are shown in Fig. 3.

One can conclude that due to different magnetic well inside and outside in the case of SF configuration the critical pressure gradient inside is less than outside.

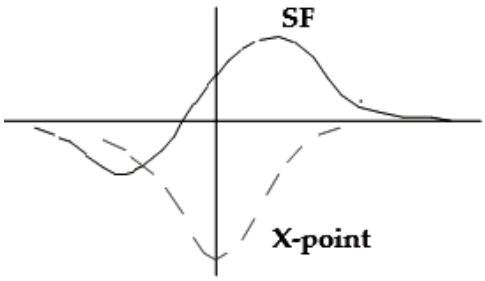

Fig. 3: Magnetic well in case of SF and normal X-point configurations (dashed line).

Edge density limitations

From Ballooning MHD mode stability ($\Delta_{mid.-plane} \sim \lambda\, \rho_\theta$) it follows that the density

$$n_{[10^{20} m^{-3}]} < 1,15 \left(\frac{I_{MA}}{\pi a^2}\right)^{3/2} \left(\frac{1}{T_{100}^{3/4}}\right)\left(\frac{R}{a}\right)^{3/4} \frac{A^{1/4}\sqrt{k}}{(1+k^2)^{3/4}} \lambda a \; s(k, \delta, \varepsilon q)$$

From the other side, the requirements to avoid thermal (MARFE) stability

$$\chi_{//}^{0} T^{5/2} / Z_{eff} R^2 q^2 \quad > \quad n^2 C_Z \overline{L_Z}, \qquad \text{where } \overline{L_Z} = (2L - TdL/dT)$$

The electron density at the separatrix mid-plane has to be

$$n_{[10^{20} m^{-3}]} = \frac{45 \left(T_{100}\right)^{7/4}}{qR} \frac{1}{\sqrt{\overline{L_Z} C_Z Zeff}}$$

Thermal - Ballooning stability diagram

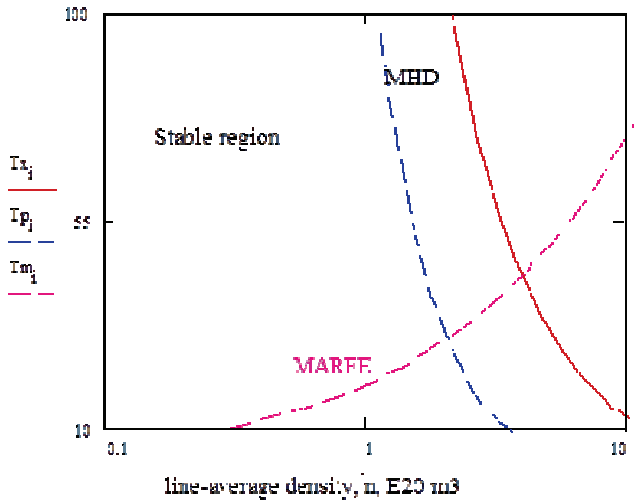

Fig. 4: Stability diagram for DEMO. For expecting densities at the edge (>10^{20} m^{-3}) and temperatures above several keV the SF divertor will be unstable against the coupled ballooning-thermal modes.

Thermal instability (MARFE) is suppressed for higher temperature range, whereas the ballooning modes are unstable for higher pressure. Critical density can for perturbation in inner region (see Fig. 4) reads:

$$n_{[10^{20} m^{-3}]} = 1.15 \left(\frac{I}{\pi a_m^2}\right) \frac{a_m^{0.175} R^{-0.3}}{\left(\sqrt{Z_{eff} \alpha \overline{L_{33}} C_Z q_{95}^2}\right)^{3/10}} \left(\frac{A^{1/4} \left(s\sqrt{k\lambda}\right)}{(1+k^2)^{3/4}}\right)^{7/10}$$

and for outer region

$$n_{[10^{20} m^{-3}]} = 0.67 \left(\frac{I}{\pi a_m^2}\right)^{7/9} \frac{1}{\left(Z_{eff} \alpha \overline{L_{33}} C_Z q_{95}^2\right)^{1/9}} \left(\frac{A(s\lambda)^2}{\sqrt{\frac{R}{a}}(1+k^2)}\right)^{7/18}$$

Conclusions

The analysis of a density limit in tokamaks for DEMO configuration is done for up-down symmetric equilibrium of SF configuration

The ideal ballooning mode significantly change their feature

The ballooning perturbation inside the configuration is much weaker, than outside, due to the stabilising effect of a favourable magnetic curvature in inner side.

The upper attainable density exhibits almost linear dependence on the plasma current similar to the Greenwald limit. However it differs from the Greenwald value: at low temperatures (<100eV) this limit is less restrictive.

A weak dependence on impurity content was obtained. However the influence of impurities can emerge through the resistive modes, which in turn can trigger the ideal modes.

Staff:

Yu. L. Igitkhanov

Literature:

[1] H. Zohm: On the minimum size of DEMO, Fusion Science and Technology 58

[2] [O. Pogutse et al., EPS, 1995

Acknowledgement

This work, supported by the European Communities under the contract of Association between EURATOM and Karlsruhe Institute of Technology, was carried out within the framework of the European Fusion Development Agreement. The views and opinions expressed herein do not necessarily reflect those of the European Commission.

Physics: Heating and Current Drive – ECRH

Microwave Heating for Wendelstein 7-X (CoA)

Introduction

Electron cyclotron resonance heating (ECRH) and current drive (ECCD) are the standard methods for localized heating and current drive in future fusion experiments. Thus, ECRH will be the basic day-one heating system for the stellarator W7-X which is currently under final construction at IPP Greifswald. It is expected that the ECRH system for W7-X will be finalized in 2014. In its first stage W7-X will be equipped with a 10 MW ECRH system operating at 140 GHz in continuous wave (CW).

The complete ECRH system is coordinated by the project “Projekt Mikrowellenheizung für W7-X (PMW)”. PMW has been established by KIT together with IPP and several EU partners in 1998. The responsibility of PMW covers the design, development, construction, installation and system tests of all components required for stationary plasma heating on site at IPP Greifswald. PMW coordinates the contribution from Institut für Plasmaforschung (IPF) of the University of Stuttgart too. IPF is responsible for the microwave transmission system and part of the power supply (HV-system). IPP Greifswald is responsible for the in-vessel components and for the in-house auxiliary systems. PMW benefits from the collaboration with Centre de Recherche de Physique des Plasmas (CRPP) Lausanne, Commissariat à l´Energie Atomique (CEA), Cadarache and Thales Electron Devices (TED), Vélizy.

A contract between CRPP Lausanne, KIT and TED, Vélizy, had been settled to develop and build the series gyrotrons. First step in this collaboration was the development of a prototype gyrotron for W7-X with an output power of 1 MW CW at 140 GHz.

Seven series gyrotrons have been ordered from industrial partner Thales Electron Devices (TED), Vélizy. First operation and long pulse conditioning of these gyrotrons is being performed at the test stand at KIT. Pulses up to 180 s duration at full power are possible (factory acceptance test, FAT) whereas 30 minutes shots at full power are possible at IPP (necessary for site acceptance test, SAT). Including the pre-prototype tube, the prototype tube and the 140 GHz CPI-tube, in total 10 gyrotrons will be available for W7-X in final state. To operate these gyrotrons, in addition to the Oxford Instruments and Accel magnets, eight superconducting magnet systems have been manufactured at Cryomagnetics Inc., Oak Ridge, USA.

Most of the components of the transmission system, HV-systems and in-vessel-components have been ordered, manufactured, delivered and are ready for operation at IPP Greifswald. A part of the existing ECRH system has been already used to test new concepts and components for ECRH. A significant delay arose in the project due to unexpected difficulties in the production of the series gyrotrons.

Series Gyrotrons

In 2005, the first TED series gyrotron SN1 had been tested successfully at KIT and IPP (920 kW/1800 s). It met all specifications during the acceptance test, no specific limitations were observed. In order to keep the warranty SN1 has been sealed, one prototype gyrotron is routinely used for experiments.

Series gyrotrons following SN1 did show a more or less different behaviour with respect to parasitic oscillations excited in the beam tunnel region. These oscillations resulted in an excessive heating of the beam tunnel components, in particular of the absorbing ceramic rings. The gyrotrons re-opened after operation showed significant damages due to overheating at the ceramic rings and the brazing of the rings. A possible solution was proposed and successfully tested by KIT. As the main difference to the usual beam tunnel this design features corrugations in the copper rings which handicap the excitation of parasitic modes.

The thermal loading of the collector depends very much on the efficiency of the interaction and on the pulse length. For CW high power operation this loading is close to what is feasible in terms cooling and lifetime of the collector. For the series tubes a sweeping procedure has been introduced which combines a vertical and radial displacement of the electron beam at the collector. This results in an almost constant power deposition at the inner wall along the axis and removes the particularly dangerous temperature peaks at the lower and upper reversal points of the electron beam. In 2012 the complete sweeping systems for the series gyrotrons have been procured.

Modifications have been realized and already tested in order to reduce the internal absorption of stray RF power by covering stainless steel components with copper.

A possible corrosion in the water cooling circuit of the diamond window at the brazing structure is prevented by replacing the water by inert Silicon oil.

In 2012 long pulse conditioning and testing of the gyrotron SN6 was continued. SN6 is the first series gyrotron equipped with all improvements developed. The final acceptance tests of SN6 were finished successfully at IPP Greifswald showing above 900 kW RF output power and reliable operation at 30 min pulse length.

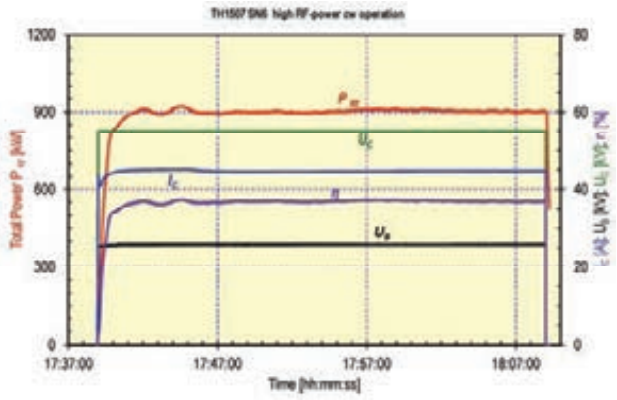

Fig. 1: Output power P_{rf}, beam current I_c, efficiency and operating voltages U_c, U_B of series gyrotron SN6, measured at IPP Greifswald during long pulse operation (30 min.).

The next series gyrotron, SN7, was delivered to KIT in autumn 2012. During installation at KIT test stand a vacuum leak was detected in the copper of an internal cooling pipe. The tube has been repaired at Thales already, acceptance tests at KIT are starting at January 2013.

Transmission Line System

The transmission of the RF output power to the plasma happens via a quasi-optical system. IT consists of different single-beam and multi-beam waveguide (MBWG) elements, which adds up in total more than 150 reflectors. For each gyrotron, a beam correcting assembly of four mirrors is used. It matches the RF power at the gyrotron output to a fundamental gaussian beam with the correct beam parameters, and it sets the appropriate polarization needed for optimum absorption in the plasma. A fifth mirror directs the beam to the beam combining optics, which is situated at the input plane of a multi-beam waveguide. This MBWG is designed to transmit up to seven beams (5x 140 GHz beams, 1x 70 GHz beam, and 1x channel connected to the N-port launchers via a switch) from the gyrotrons (entrance plane) to the stellarator hall (exit plane). To transmit the power of all gyrotrons, two symmetrically arranged MBWGs are used. At the output planes of the MBWGs, two mirror arrays separate the beams again and distribute them via two other mirrors and CVD-diamond vacuum barrier windows to individually movable antennas (launchers) in the torus.

The manufacturing and installation of the components of the basic transmission system has been completed. Cooling tube manifolds to supply the mirrors and stray radiation absorbers mounted in the towers in front of the stellarator were installed.

For beam diagnostics and power measurement of the gyrotron beams, linearization amplifiers for the detectors have been developed. The receivers attributed to the directional couplers on the mirrors M14 have been mostly built; present work concentrates on the design of the conical scan mechanics and electronics for the alignment control.

For gyrotron SN6 installed at IPP Greifswald, beam characterization and the subsequent design and manufacturing of the surfaces of the matching mirrors have been performed.

Within the site acceptance tests of gyrotron SN6, the "long load" (a 23 m long absorbing stainless steel tube with a water jacket) could be tested in more detail. Successful shots of 910 kW output power at the gyrotron window for 30 min pulses were performed using this load. As the long load operates as a pre-attenuator (attenuation typ. 77 %), the residual power at the output was dumped in one of the calorimetric loads, which originally had been designed for short pulses (400 ms) at 1 MW. Nevertheless, CW operation was possible for an RF power of 210 kW, qualifying the design principle of the short-pulse load also for high-power CW loads.

In the past years, the ECRH system at IPP-Greifswald was used as a test bed for novel components, e. g. for the test of high-power diplexers. These devices are developed for use as a combiner for the RF output power of two gyrotrons as well as a fast directional switch (FADIS) between two RF output signals, and therefore are of potential interest for ITER. In 2012, the diplexer MC IIa was operated in the corrugated waveguide system at ASDEX Upgrade, and switching and in-line ECE experiments were performed successfully. An evacuated version (MQ IV) compatible with the ITER system has been designed, and mirrors are being manufactured. Provided that the funding for the fabrication for the evacuated casing is available, high-power tests on the ITER test system at JAEA, Naka are foreseen.

For two of the N-ports of W7-X, "remote-steering" (RS) launchers are foreseen (RSL1 and RSL5). This is due to the fact, that front steering launchers as used in the A and E ports will not fit into these narrow ports. The remote-steering properties are based on multi-mode interference in a square waveguide leading to imaging effects: For a proper length of the waveguide, a microwave beam at the input of the waveguide (with a defined direction set by a mirror system outside of the plasma vacuum) will exit the waveguide (near the plasma) in the same direction.

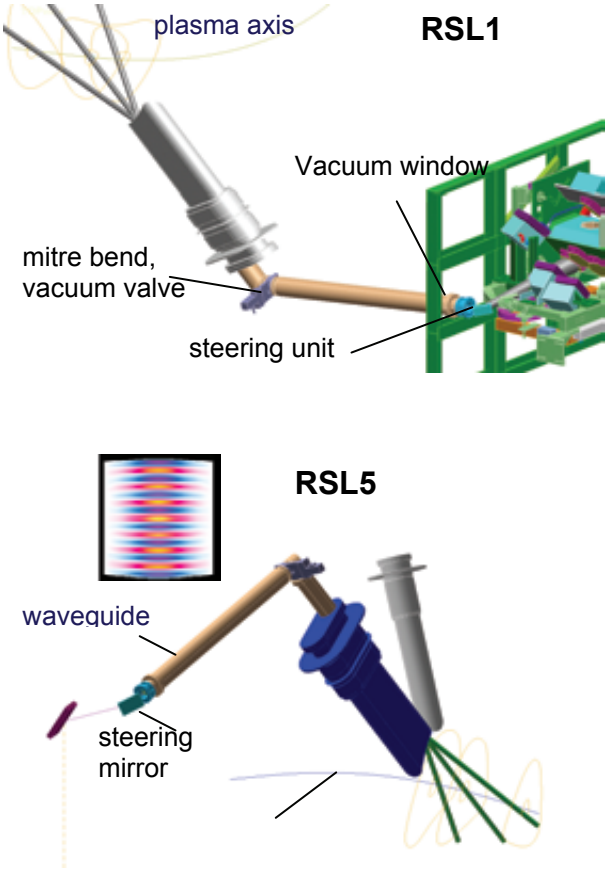

Fig. 2: Conceptual design of the remote steering launchers RSL1 (top) and RSL5 (bottom), designed for the narrow N-ports of W7-X. The insert bottom, left shows the transverse field structure of an m= 15 mode in the slightly bulged waveguide cross-section of RSL5.

In autumn of 2012, the engineering design and manufacturing of the RS launchers was started within the frame of a "BMBF Verbundprojekt" with special funding by the German Bundesministerium für Bildung und Forschung (BMBF). The leading institution of the project is IPP with its branches at Greifswald and Garching. Partners of the project are the IPF Stuttgart together with two industrial partners, Neue Technologien GmbH, Gelnhausen (NTG), and Galvano-T electroforming-electroplating GmbH, Windeck (GT).

Within this Project FORMIK3 (Fortgeschrittene Mikrowellen-Heizsysteme für die kontrollierte Kernfusion"), the detailed design of the launchers as well as the preparation for manufacturing was started at IPP. Both launcher waveguides will consist of two straight corrugated square waveguides (total length typically 5 m), which will be connected via mitre

bends to fit the antenna into the available space at W7-X, as seen in the figure below. The waveguide parts will be manufactured by electroforming techniques from copper. This method had been identified before as best suited for long, vacuum compatible corrugated waveguides, which need relatively strong water cooling. Within the FORMIK3 project, NTG will care for the manufacture of the mandrels and the final machining of the waveguides, while GT will provide the electroforming works. A drawing of the RSL1 waveguide part to be situated in the vacuum vessel is shown in Fig. 3.

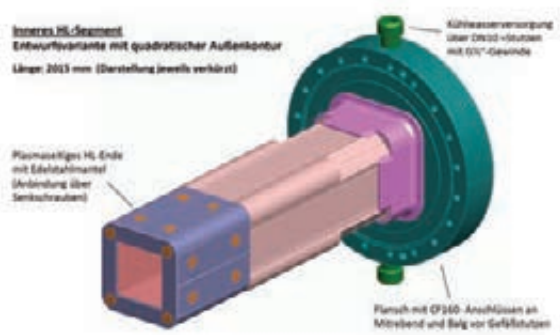

Fig. 3: Design of the inner waveguide segment of RSL1 showing the port vacuum flange with connections for the water cooling of the waveguide, the outer machining and the plasma facing side with protection from stainless steel. Note the shortened view in the drawing, the real waveguide length is 2015 mm.

The RS launchers will be fed from the main transmission via one (RSL1) and two reflectors (RSL5), respectively. The optical beam path and the mirror parameters have been defined. The design of the reflectors, which will be similar to the reflectors of the main transmission system, has been started. In the construction phase, which is planned for the next year (2013), NTG will fabricate the mirror stainless steel blanks, the reflector mounts and the final mirror surfaces, and GT will provide the copper mirror surfaces with the cooling system embedded.

Prior to the start of the Verbundprojekt, basic research on the optimization of remote-steering antennas was continued at IPF Stuttgart. As the imaging characteristics of square waveguides diminish at steering angles > 12°, a prototype antenna waveguide with an optimized cross-section (square with outward bulges) with respect to the steering range was manufactured and tested. Antenna patterns recorded at a variety of steering angles show that an increase of the useful steering range up to 16° was reached, however, at the expense of a reduction of the quality of the antenna beam. A detailed analysis of the radiation patterns showed, that the dispersion relation for the deformed waveguide was optimal for the $HE_{1,n}$ modes, however, $HE_{3,n}$ modes, which also contribute to the antenna beam, did not obey the prescribed ideal dispersion. The results were confirmed by a resonator technique, for which the spectrum of the transverse resonances of the waveguide was measured and analysed.

A new simulation code was set up, which allows the simultaneous calculation of all propagation constants in the deformed waveguide; and calculations have started to find the best performing RS waveguide cross-section. Its application is foreseen for the RSL5 launcher; in contrast, RLS1 will be designed as square waveguide.

In-vessel components

The four ECRH-plug-in launchers have been equipped with water manifolds and flow sensors. One of the launcher was used to test the assembly within similar cramped geometrical conditions as they are expected for W7-X operation. Together with the assembly department at IPP-Greifswald a successful assembly procedure was elaborated which insures a reliable vacuum closure with a HelicoFlex- sealing.

The electron cyclotron absorption (ECA) diagnostics was developed and fabricated at IPP-Greifswald. It measures the transmitted ECRH power, the beam position and polarization. The waveguide vacuum interfaces had been slightly modified. A detailed leakage measurement showed that the entire helium penetration rate through the o-ring sealing of all 33 vacuum interfaces of one B-port plug-in would violate the W7-X vacuum restriction. Alternative sealing methods had been investigated consequently. Finally, CF-type copper sealing with a glued mica window was chosen. It showed a sufficiently small helium penetration rate and a high mechanical reliability. The modified B-port insert passed the official W7-X vacuum leak

test procedure successfully. Outside the vacuum vessel the microwave interfaces will be equipped by filigree components and detectors, which must be protected from mechanical damage. Therefore a protection bonnet had been designed, which also provides electrical connections and mechanical access. Finally the ECA-diagnostic had been officially committed to the assembly department for installation at the W7-X vacuum vessel.

Measurement system development for investigation of undesired transient spectral effects in gyrotrons

The field of spectral measurement techniques for gyrotrons has gained interest in the scientific gyrotron community and has also undergone substantial developments throughout the last years. Main focus are parasitic oscillations, but with increasing possibilities other effects like modulation phenomena and mode switching also get into focus.

In last year's report, an early prototype of a new measurement system capable of analyzing the gyrotron's output spectrum for transient effects with a high bandwidth and dynamic range was presented. Throughout the year 2012, the system was continuously developed further and in parallel allowed for the documentation and investigation of highly interesting phenomena.

As depicted in fig. 4, the new system is utilizing a fast digital oscilloscope, receiving a down-mixed time domain signal with bandwidths exceeding 3 GHz. This permits the calculation of instantaneous spectra, and with a special dual-receiver technique, undesired mixing signals can be safely excluded while actually increasing the usable bandwidth. This is done through a signal post-processing chain, in which the IF spectrograms S1 and S2 are used to reconstruct the original RF data RLSI, RHSI. Through this, the system gains the almost unique feature of unambiguous RF frequency measurement despite receiving in a harmonic-mixer heterodyne setup.

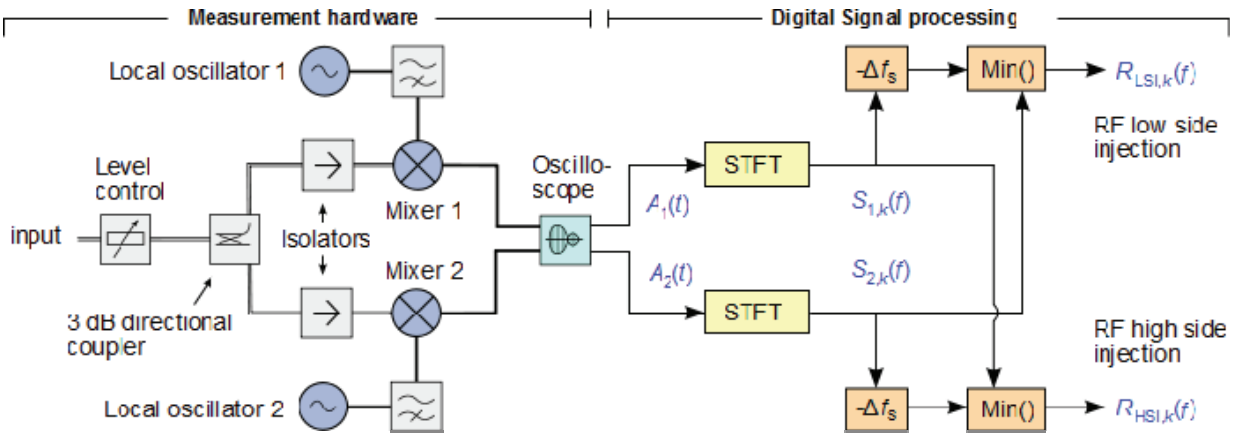

Fig. 4: Hardware setup and data flow in new measurement system. From each of the detected time signals $A_i(t)$, through short-time Fourier transform (STFT), an independent IF spectrogram $S_{i,k}(f)$ is created. Through the utilization of the dual-channel arrangement, the unambiguous RF spectrograms $R_{LSI,k}(f)$ and $R_{HSI,k}(f)$ can be obtained.

Figure 5 shows the direct observation of a mode jump, which occurred during the operation of a W7-X gyrotron close to the edge of the stability area of nominal mode $TE_{28,8}$.

The aforementioned modulation effects can be observed in figure 6, where alternating modulation patterns in the multiple-MHz range are clearly present.

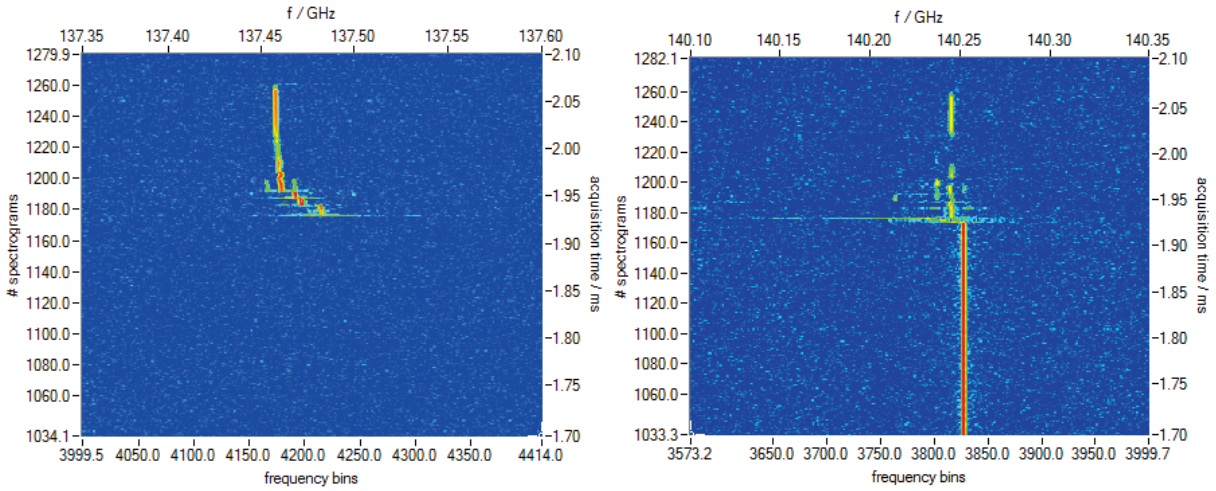

Fig. 5: Measurement example of spectrum versus time. It can be seen in the waterfall plot that, after a stable operation with $TE_{28,8}$ at 140.25 GHz, a destabilization and diminution of the nominal mode occurs, which is accompanied by the start of the azimuthal neighbour mode $TE_{27,8}$ around 137.45 GHz. The example is zoomed for presentation, while the total frequency span of the measurement covers ~7GHz.

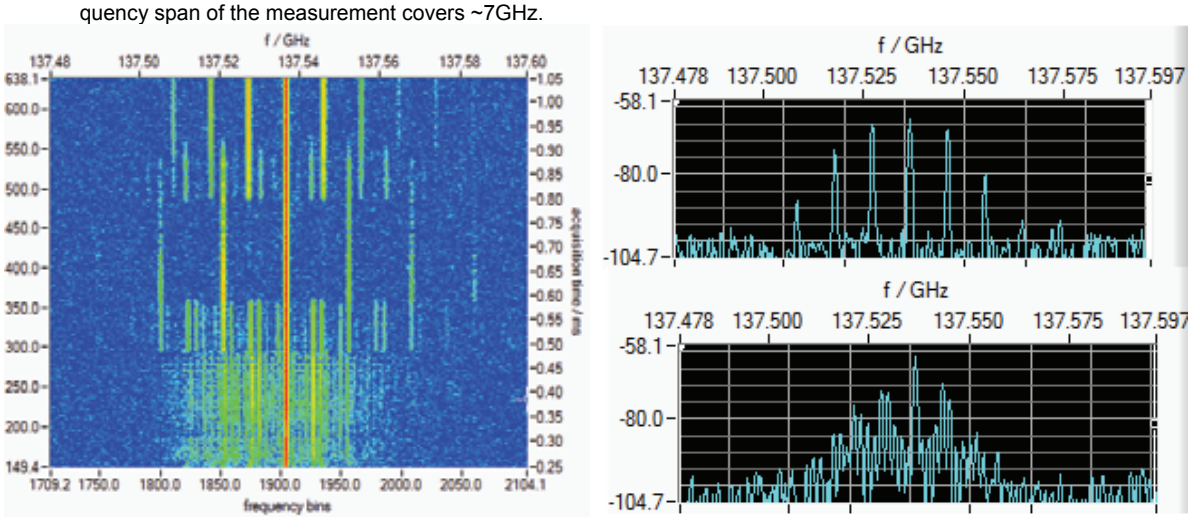

Fig. 6: Measurement example of transient modulation during operation with TE27,8. In the spectrogram (left), the highly transient nature of the modulation effect is clearly visible. Instantaneous spectra at two different time positions (A, B) illustrate the strong changes in modulation pattern.

Staff:

IHM / KIT
K. Baumann
K. Boschert
G. Dammertz
G. Gantenbein
H. Hunger
S. Illy
J. Jelonnek
S. Kern
R. Lang
W. Leonhardt
M. Losert
D. Mellein
S. Miksch
A. Papenfuß
B. Piosczyk
A. Samartsev
M. Schmid
W. Spiess
D. Strauss
J. Szczesny
M. Thumm
J. Weggen

IPF (University of Stuttgart)
H. Höhnle
W. Kasparek
H. Kumric
C. Lechte
R. Munk
F. Müller
B. Plaum
P. Salzmann
K.H. Schlüter
U. Stroth
S. Wolf
A. Zeitler

(Diploma/Master students)
Z. Popovic
P. Rohmann
D. Tretiak

IPP (Greifswald/Garching)
B. Berndt
H. Braune
V. Erckmann (PMW)
F. Hollmann
L. Jonitz
H. Laqua
G. Michel
F. Noke
F. Purps
T. Schulz
P. Uhren
M. Weißgerber

Humboldt Universität Berlin:
G. Fußmann, R. Brose

Eindhoven University of Technology:
J.W. Oosterbeek, S. Paquay

Design and Development of the European Gyrotron (F4E-2009-GRT-049-01, F4E-GRT-432)

Introduction

The development of a 2 MW, CW, 170 GHz coaxial cavity gyrotron for ITER is pursued within the European Gyrotron Consortium (EGYC, consisting of CRPP, Switzerland; KIT, Germany; HELLAS, Greece; CNR; Italy). EGYC acts as the scientific partner for Fusion for Energy (F4E). Within this consortium, KIT acts as the cooperation partner of ISSP, Latvia. The EU part to ITER is the delivery of RF sources (gyrotrons) to provide in total 8 MW of RF input power. In contrast to the other parties (Russia, Japan) delivering 1 MW, CW conventional cavity gyrotrons to ITER, the EGYC consortium planned to provide 2 MW, CW RF power units to reduce total costs and to limit the space requirements. Additionally, it would have offered to double the system power for ECH&CD.

While the industrial gyrotron prototype, built by Thales Electron Devices (TED, France), is tested at CRPP, KIT does the main part in the research and the development of the physical designs of the gyrotron components. It does low power tests of the different components and does high power tests at short-pulses. The latter are done using KIT's 2 MW modular pre-prototype gyrotron. KIT is responsible for the cavity, the uptaper and the mode converter system. It is simulating the beam generation, the interaction between the electrons and the RF field and the electron-optical system up to the collector.

In 2011, the 2 MW industrial prototype gyrotron was successfully upstarting in short pulse operation with RF output powers up to 2 MW (@1 ms). However, after a fatal event in December 2012, at which a water leak destroyed the tube, F4E and EGYC decided together to move to the 1 MW fallback solution for the initial gyrotron installation of ITER. The corresponding physical design did start in 2007 already. Nevertheless, the 2 MW coaxial cavity design is continued towards a suitable design for an update of ITER and for future fusion devices.

In this chapter results of the coaxial cavity gyrotron development as well as the activities towards a conventional cavity gyrotron at 170 GHz for ITER will be described.

Recent modifications on the KIT Test Facility

The following modifications and improvements on the gyrotron test setup have been done in 2012:

1. A normal conducting (NC) coil with improved cooling has been installed inside the bore hole of the KIT Oxford Instruments super-conducting (SC)-magnet. After that installation, the magnetic field of the SC magnet can be increased to the required value of 6.87 T in continuous-wave (CW) operation.
2. The diode-type magnetron injection electron gun (MIG) has been redesigned to be identical to the corresponding components of the industrial CW gyrotron. Furthermore, the new construction of the electron gun allows a simple replacement of the emitter nose. In addition, an anode aperture (halo-shield) (see Fig.) has been introduced in order to avoid electrons trapped between the cathode region and the magnetic mirror.
3. The improved isolation between the gyrotron body and the top plate of the cryostat enables an operation of the gyrotron with single-stage depressed collector (SDC).
4. A new design of the waveguide antenna (launcher) of the quasi-optical system has been installed. The launcher got a significant smoother inner surface. Simulations predict a significant reduction of the stray radiation.

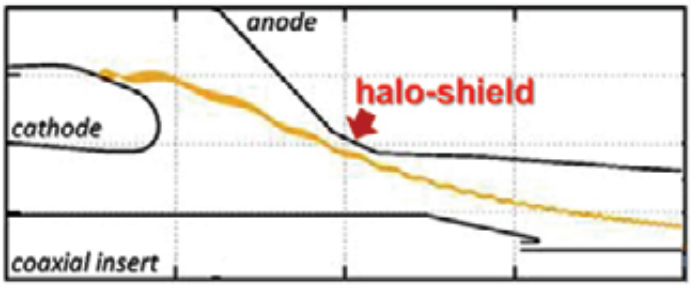

Fig. 1: The profile of the gyrotron anode used in the experiment (halo-shield has been indicated).

Experimental results

In experiments the current flow to the newly introduced halo-shield (see Fig. 1) has been found. Further investigations have shown that at the position of the halo-shield the clearance between the electron beam and the wall is only about $\delta R_{beam\text{-}halo}$ =~0.2 mm in contrast to about 2.3 mm obtained from numerical calculations.

It is assumed that the observed significant increase of the beam width is caused by electrons trapped between the cathode and the magnetic mirror. Mentioned effects have been accompanied by a rise of I_{body} and of the pressure inside the tube as well as the occurrence of parasitic low frequency oscillations. These parasitic oscillations could be responsible for the observed instabilities in the electron beam and further chaotic behaviour of the gyrotron. The root cause of the instabilities is still under study.

Due to above mentioned instabilities the experiments could be continued with reduced pulse lengths only. Finally an RF output power of 1.9 MW and an electronics efficiency of 28 % (without depressed collector, pulse length ~0.5 ms) has been obtained in single $TE_{34,19}$-mode operation at 170 GHz. Achieved results are shown in the Fig. 2 below (left). In addition, at high power the profile of the RF beam has been measured outside the gyrotron window with an IR camera. The analysis of the data confirmed the results of the low power measurements. The tube provides an excellent quality of the generated RF beam.

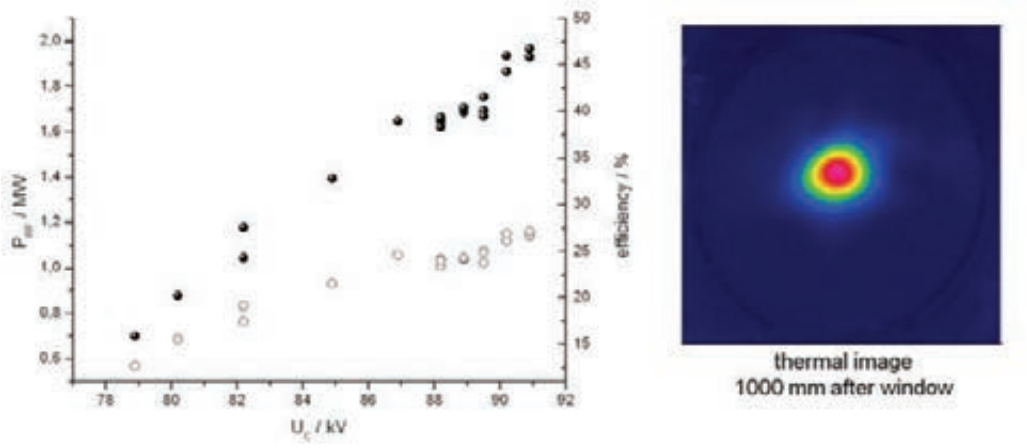

Fig. 2: RF output power and gyrotron efficiency vs. cathode voltage measured at nominal magnetic field (left) and profile of the RF output beam measured 1000 mm after the gyrotron window (right).

For the first time, the KIT 2 MW pre-prototype has been operated with a single stage depressed collector. Reduced operation parameters has been used with respect to the technical limitations of the body power supply and due to the above mentioned instabilities observed in a certain voltage range and accompanied by a sudden rise of the body current, I_{body}, . Final operating parameters have been an accelerating voltage $\leq$ 80 kV and a beam current <~70 A. Within the parameter limits a very stable operation of the tube has been demonstrated up to a depression voltage of 35 kV. With depression gyrotron efficiency increased from ~19 % up to 37 %. The RF output power at those conditions was measured to be about 1.2 MW.

First studies on an alternative method for the verification of the alignment of the electron beam with respect to the axis of the gyrotron cavity have been performed. The idea is based on the radial displacement of the electron beam inside the cavity by applying dipole coils and on the influence of the displacement on the excitation of a cavity mode. The figure 3 shows the oscillation region of the TE34,19 mode as obtained for two different beam currents in dependence of the dipole currents IX and IY. The center of the measured values (IX/IY=6.5A/3.2A) corresponds to a displacement of the beam inside the cavity. Out of this values a displacement of the electron beam with respect to the cavity axis by ~0.25 mm is obtained (IXY = 1 A corresponds to a shift of 0.035 mm). This number is in agreement with measurements of the beam position relative to a capacitive probe in front of the cavity.

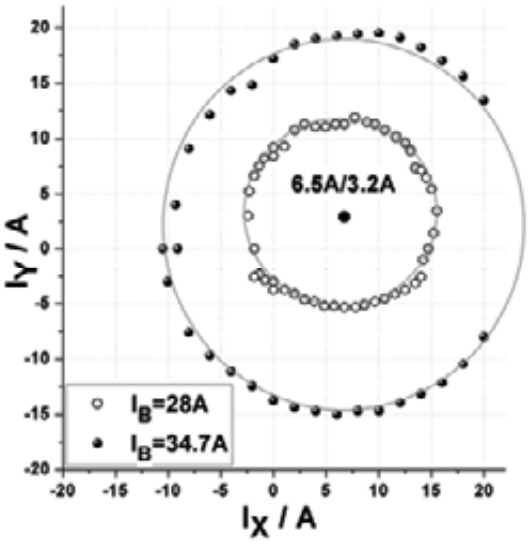

Fig. 3: The oscillating area of the $TE_{34,19}$ mode in dependence of the transverse displacement due to the dipole field.

Studies on the electron gun

The attempt to employ the gun design of the industrial prototype in the KIT pre-prototype as far as possible did not lead to the desired performance. While the industrial prototype gun demonstrated all the desired improvements, with no trace of LF oscillations or voltage standoff problems, the refurbished KIT gun suffered from strong LF oscillations. The difference is obviously caused by the remaining design deviations. This observation may have some relation to halo electrons and to body currents.

The industrial prototype showed an unexpectedly high, but still acceptable body current. For the pre-prototype gyrotron with refurbished gun and halo shield, the body current was too high at nominal parameters. In the first experiment in this configuration, the magnetic field shape had to be changed to be able to operate. For this reason, the halo shield was removed in a second phase.

In frame of the 1 MW gyrotron development for ITER, important results on details of the emitter design where achieved. The thermal gaps around the emitter cause a high sensitivity to tolerances, which may be the reason for halo currents and low efficiencies which had not be understood before.

Experimental and theoretical investigations on RF parasitic oscillations

The suppression of parasitic oscillations is crucial for the performance of any gyrotron. Parasitic oscillations may occur in either the beam tunnel or in the after cavity region (ACI). A realistic simulation to understand these effects is still open.

Other parasitic oscillations may be generated in the uptaper as dynamic ACI as well as in the electron gun as LF parasitic oscillation. This later subject is strongly related to the studies on the electron gun and numerical simulations. In 2012 the aim has been to gain a better understanding on ACI.

In detail, the activities have been:

- Experimental studies of beam tunnel oscillations: in total, three experimental phases at KIT were performed, the first using the old 165 GHz electron gun at KIT combined with a beam tunnel with stacked corrugated copper and ceramic rings, the second one with the

same beam tunnel, but the refurbished 170 GHz electron gun of KIT and the third employed a SiC beam tunnel instead. In all of these tests, no indication of any parasitic beam tunnel oscillation was found. In particular for the tests at KIT, it can be said that the RF spectrum was checked carefully and with high dynamic without any indication of spurious RF. This is a very robust validation of both beam tunnel concepts at the chosen operating parameters.

- Low frequency (LF) oscillations (around 80 MHz and 452 MHz) have been observed in recent experiments. The origin of the generation is still under study.
- Extensive measurements on dynamic ACI: the experiments with coaxial gyrotrons found no spurious RF signal at all. This is a particularly strong statement for the KIT experiments, where the measurement system described next was applied. This is a very good result for coaxial cavity devices, and is in agreement with simulations.
- For all these experimental studies, it was necessary to apply a suitable spectral diagnostic system (developed independently within a doctoral thesis) in parallel. This system permits unambiguous spectral measurements over a wide bandwidth and with high dynamic range, and was extended to also capture measurements of LF oscillations.

The main conclusions from the work in 2012 are:

- The chosen stacked beam tunnel concept appears successful and suitable, as well as the SiC beam tunnel which was checked in parallel. This is well proven by a wide band spectral measurement system with high dynamic range. On the other hand, it is still not possible to reliably simulate such beam ducts, so the determination of the limits of the chosen concepts still need essentially more background work.
- Other parasitic RF signals like ACI were not observed at all in the coaxial gyrotron, in strong contrast to any conventional gyrotron under investigation. While this is a very positive finding for coaxial cavity devices, the permanent appearance of spurious signals in conventional gyrotron operation has to be kept under observation and justifies extended work towards a full understanding of such spurious.
- Finally, LF oscillations are still not under control and need more investigation as well.

Improving the simulation codes for wave-beam interactions

This work was executed in coordinated efforts at KIT, CRPP, HELLAS and ISSP. This diversity is desired for cross-validation of results for which no experimental data are available.

In 2012 the following topics were investigated:

- Dynamic ACI: The generation of spectral lines indicating spuriouses caused by undesired gyrotron interaction in the cavity uptaper was assumed as a hypothesis. Same has been valid for their possible influence on the final gyrotron operation. Evidence has been gained that such spuriouses exist in reality and are not caused by artefacts in numerical simulations. Additionally, to measurements, such spectral lines appeared in the simulations using different numerical tools. However, work is still ongoing to verify the different simulations, and how far the results are depending on shortcomings of the employed simulation models. For this reason, it remains still unclear how far dynamic ACI influences gyrotron operation, and how far this can be predicted reliably. Additional efforts are necessary to improve the understanding of dynamic ACI.
- Non-uniform magnetic fields: In the uptaper the axial magnetic field starts to get non-uniform. Therefore, in the simulation this non-uniform magnetic field must be considered. That is particularly true for dynamic ACI, which is assumed to be to a high extend related to gyrotron interaction in regions of lower magnetic fields. The simulation code SELFT at KIT has been improved to consider non-uniform magnetic fields. The validation of the final code and numeric simulations are still ongoing.

- Particle-in-Cell simulation (PIC approach): Self-consistent simulation is typically using a slow-variables approach for the electron trajectories. Additionally, the field amplitudes are taken as constant during the transit time of an electron through the cavity. This approach is becoming critical if changes in the slow variable fields take place during electron transit time. This is for example the case when a spurious frequency, generated by dynamic ACI, turns up in addition to the dominating cavity oscillation. To overcome the simplifications and to investigate their actual influence, it is necessary to drop the trajectory approach and to replace it by a PIC or PIC-like code. This was done for the EURIDICE code, while other PIC-code versions for SELFT and TWANG are still in work. It may be mentioned here that a simulation done using the full wave PIC code “HALO” of University of Stuttgart has already shown some dynamic ACI.
- Misalignment of the electron beam versus magnetic field axis: Effort has been spent on studies on the influence of electron beam misalignment. This effort was directly triggered by the observations made during the industrial prototype experiment at Lausanne, but it has a general importance beyond that. First results are that the influence of the electron beam misalignment on the beam parameters can be simulated with sufficient accuracy. It showed that misalignment is increasing mode competition and causes operation of counter-rotating modes.

Summary:

- Dynamic ACI has been essentially substantiated by simulation and measurements. Still, most important influence factors e. g. boundary conditions and even correct modelling of the non-uniform magnetic fields need further investigation. It is quite natural that those discussions are arising at a point at which the existing cavity interaction codes are extended for usage in wider ranges of the gyrotron. First attempts on answering above questions were done by improving the simulation models regarding implementation of non-uniform magnetic fields, using particle-in-cell codes and by investigation of the implementation of boundary conditions for the cavity ports.

  The investigation on electron beam misalignment serves purpose to ensure reliable series production and operation of gyrotrons at proper levels of output power and plug-in efficiency. First results already indicate the strong influence of beam misalignment on gyrotron performance.

Design of highly efficient quasi-optical mode converters

The synthesis method for the waveguide antennas (launchers) of the quasi-optical system has been significantly improved. Namely, in the optimization, the wall surface is smoothed in terms of the spectrum reconstruction method.

On the base of the improved method, a new so-called smoothed launcher has been designed for the coaxial-cavity, $TE_{34,19}$-mode gyrotron.

The smoothed launcher as well as a new mirror system for the original launcher, featuring phase-correcting mirrors, were tested in a low power setup (see figure 4). The new launcher was also installed into the pre-prototype gyrotron and tested in high power experiments as well. In preceding cold tests and another high power experiment, using the KIT 165 GHz electron gun, the launcher provided by IAP was measured for comparison as well. The complete quasi-optical system of the industrial prototype was also measured in low power, yielding a slightly reduced Gaussian mode content of 94.2 % and the following results:

- The Gaussian mode contents for all tested systems remained high (~96 %) as before.

  The stray radiation of the system featuring the smoothed launcher (4%) was reduced by nearly to its half, compared to the unsmoothed design (7%). This is a major step for reliability due to reduced heat loads in the mirror box. For comparison, the IAP launcher featured a stray radiation value of 5.5%.

In parallel, a new method for fast simulation of tapered launchers was developed and applied to the launchers of the coaxial gyrotron. This method permits fast simulations of tapered launchers, which could until now only be simulated with slow methods (SURF3D).

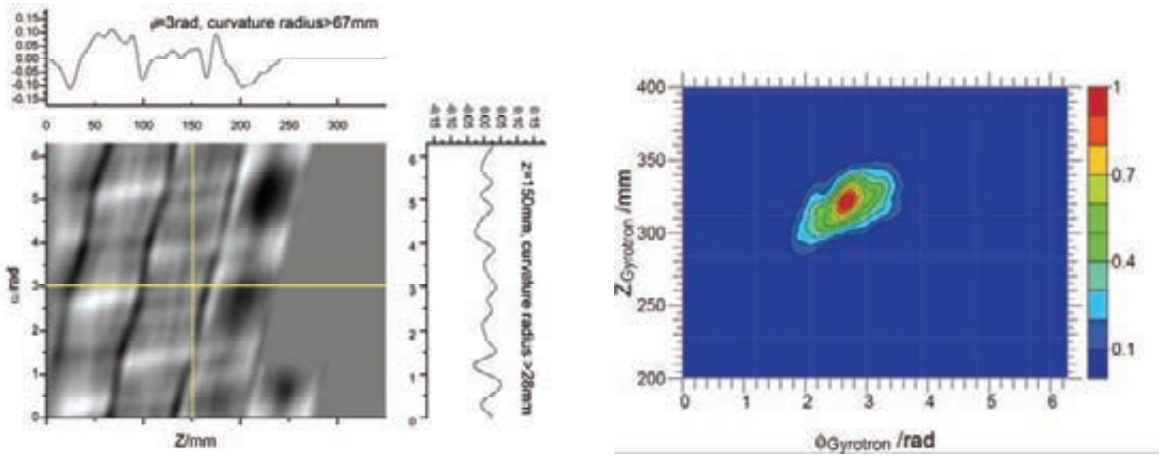

Fig. 4: New smoothed launcher: Perturbation profile (left) with -0.166mm<δr<0.183mm, R_z>678mm and R_Φ>28mm; Radiated field (SURF 3D calculation) (right).

There are major discrepancies between the measured stray radiation and the simulated values. The reasons for these discrepancies are under investigation. Furthermore, there is no method to determine stray radiation in low power tests. In consequence, the stray radiation of a system is only known after high power tests, which is the last step of the development.

The development of the improved launcher synthesis method and its application in a new launcher design represents a major step towards reliable gyrotron operation. The alternative method of applying phase correcting mirrors is another approach of interest which may in future be combined with smoothed launchers as well.

For future work, it is highly recommendable to finalize the stray radiation measurements of the phase correcting mirror system and to refine the methods for Gaussian mode content calculation. It is furthermore highly desirable to determine the reasons for discrepancies between calculations and measurements of the stray radiation, with the goal of predicting realistic values for the stray radiation in the simulations.

Staff:

K. Baumann	D. Mellein
D. D'Andrea	I. Pagonakis
J. Flamm	B. Piosczyk
G. Gantenbein	T. Rzesnicki
H. Hunger	A. Samartsev
S. Illy	A. Schlaich
J. Jelonnek	M. Schmid
J. Jin	R. Schneider
S. Kern	W. Spieß
R. Lang	J. Szczesny
W. Leonhardt	M. Thumm
M. Losert	J. Weggen

Acknowledgement

This work was supported by Fusion for Energy under the grant contracts No. F4E-2009-GRT-049-01 and F4E-GRT-432 with collaboration by EPFL, Switzerland; HELLAS, Greece; and CNR, Italy. The views and opinions expressed herein reflect only the author's views. Fusion for Energy is not liable for any use that may be made of the information contained therein.

Assessment of the HCD Systems for DEMO (WP12-DAS-HCD)

Numerical Tool Development for Gyrotron Design and Simulation (WP12-DAS-HCD-EC-04-01)

Introduction

There are several numerical codes which allow the design and optimization of components of high power gyrotrons available at KIT. These codes have been verified continuously and benchmarked with ongoing experiments. This task is considered as a first step towards the preparation and extension of the codes in order to provide fully consistent design tools applicable at RF frequency up to around 350 GHz. It is a continuation of former activities, aiming at the following capabilities: (i) design of the Magnetron Injection Gun (MIG) and electron optics, (ii) design of advanced collectors (single and multiply depressed collector structures), (iii) simulation of the interaction of the electron beam in the cavity and the prediction and avoidance of pre- and post-cavity wave particle interaction, (iv) optimization of the quasi-optical mode converter and mirror system in the gyrotron, (v) design of a frequency tunable gyrotron.

Numerical Codes at KIT

In the following tables the different codes, a short description and the required activities towards the prospected DEMO requirements are listed.

MIG and Collector Design

Name	Purpose / Short Description	Required activities
ESRAY	Self-consistent electrostatic beam optics code for electron gun and collector design. Based on a fast 2D multi-grid finite-difference field solver and PIC methods for electron treatment. Can handle secondary emission effects (mandatory for multi-stage collector simulation). Implemented in C++, Parallelized (OpenMP).	The increase of frequency has only minor influence on the beam optics codes (finer meshes are required, which will result in a still acceptable increase of CPU time). For a reliable simulation of secondary emission effects, the secondary emission models have to be optimized and adapted to the requested impact energy ranges and materials.
ARIADNE2D	Self-consistent electro-static trajectory code based on the finite element method for the 2D design and optimization of electron guns and collectors. Implemented in C++, Parallelized (MPI)	No actions required.
ARIADNE3D	3D version of ARIADNE2D for the study of non-azimuthal phenomena in gyrotron operation and the 3D design of gun and collector (with some limitations). Implemented in C, Parallelized (MPI)	Extend to full 3D geometries (without limitations) in order to design 3D multi-stage depressed collectors to increase the overall efficiency of the gyrotron
COLLSIM3D	3D electrostatic electron beam ray tracing code for the design and optimization of single-stage depressed collectors with transverse sweeping system. Implemented in C++, Parallelized (OpenMP)	No activities required.

Simulation of Interaction of Electron Beam and RF Field

Name	Purpose / Short Description	Required activities
SELFT	SELFT is the most important component of the code package CAVITY used for design and optimization of conventional and coaxial Gyrotron cavities. Based on time-dependent multi-mode simulation of the gyrotron interaction. A preliminary modified version can handle tapered magnetic field profiles and targets the investigation of pre and post cavity wave particle interaction. Additional modules of CAVITY package include the stationary single-mode code SELFC, a scattering matrix mode conversion code and the design support tool and power estimator MAXPO. All implemented in FORTRAN, not parallelized.	Due to the higher operation frequency, one has to switch to higher order modes with a much denser mode spectrum. As a consequence, an increased number of critical modes have to be taken into account in the SELFT simulation which will slow down the calculation speed significantly. To compensate this, a parallelization of the code is required. In addition, the work on tapered B-field profiles has to be continued to allow simulation of more realistic scenarios.
HALO	3D Particle-in-Cell code based on the discontinuous Galerkin method. Can be applied to the Maxwell-Vlasov system and has successfully demonstrated the simulation of high-order Gyrotron resonators and quasi-optical launchers. Ideal verification tool for conventional codes like SELFT, but very high demand on computational time and resources. Parallelized (MPI)	Continuation of the collaboration with Univ. Stuttgart (Prof. C.-D. Munz). Further optimizations are required to reduce the demand on CPU time. In addition, better pre and post processing tools have to be implemented to make it easier to use the code for Gyrotron related problems.

Optimization of Quasi-Optical Converter and Mirror System

Name	Purpose / Short Description	Required activities
TWLDO	Analysis and design of quasi-optical launchers. Based on the scalar diffraction theory of electromagnetic waves and the gradient descent method. Can handle analysis and synthesis of launchers with arbitrary wall deformations. Implemented in C++, not parallelized	Shorter wavelength will result in an increase of the required CPU time (memory demand is not an issue). It will be very helpful to implement a parallelized and/or GPU based version of the code to speed up the launcher design
ASP	Analysis and synthesis of phase-correcting mirrors. Based on the scalar diffraction theory of electromagnetic waves and enhanced Katsenelenbaum-Semenov algorithm. Can handle the correction of astigmatism and ellipticity of astigmatic Gaussian wave beams with quadratic mirrors. Implemented in C++, not parallelized	See TWLDO
SURF3D	Commercial code: vector analysis of the RF field scattered from an arbitrary metal surface. Based on the vector diffraction theory of electromagnetic waves and fast multipole method. Can handle field simulation and diffraction loss calculation. Not parallelized.	The requested shorter wavelength will result in a significant increase of CPU time and memory usage. A parallelized code would be very helpful.

Future developments and recommendations

Parallelization of codes: A subset of the simulation tools (e.g. SELFT, TWLDO) does not take advantage of multiprocessor systems. To speed up the design and verification process for the gyrotron components under consideration, a parallelization of these codes with OpenMP, MPI or CUDA will be very helpful.

Work towards a full 3D electron beam optics code: This will allow the simulation of complex structures with broken rotational symmetry like enhanced multistage depressed collectors.

Implementation of realistic emission models in ESRAY: The surface roughness of the emitter introduces an initial velocity spread to the electron beam that also increases the velocity spread at the cavity. In addition, it may lead to unwanted effects like trapped electrons in the electron gun region. Investigations on implementing different, enhanced emission models should help to understand these phenomena. A further modification of ESRAY will allow the simulation of low frequency space charge oscillations caused by the trapped particles.

Verification of SELFT and/or EURIDICE with PIC codes: Ongoing investigations show that 3D particle-in-cell codes like HALO are very useful tools to verify the existing gyrotron interaction codes. Additional development work is required to enhance the calculation speed and the usability of HALO. As an alternative, one may also take into account commercial codes like CST Particle Studio or VORPAL.

Staff:

G. Gantenbein
S. Illy

Acknowledgement

This work, supported by the European Communities under the contract of Association between EURATOM and Karlsruhe Institute of Technology, was carried out within the framework of the European Fusion Development Agreement. The views and opinions expressed herein do not necessarily reflect those of the European Commission.

300 - 350GHz Gyrotrons and Ancillary Equipment (WP12-DAS-HCD-EC-05-01)

Introduction

A possible DEMO reactor may call for an EC system with a frequency exceeding 300 GHz. Actually power sources in the MW range do not exist for this task. Gyrotrons are able to work at very high frequency, in the range of several hundred GHz up to the THz regime. Proof of principle experiments have been demonstrated THz oscillation by second or third harmonic operation. Several groups have designed and realized gyrotrons at several hundred GHz used for Dynamic Nuclear Polarization (DNP). However, since mode competition and thermal loading in the cavity becomes more and more critical with increasing frequency the achievable output power is strongly reduced.

In this task we will refer to a recent presentation of a group from IAP, Nizhny Novgorod, Russia which discussed a preliminary design of a conventional 300 GHz gyrotron for fusion research [1].

Gyrotron Design

One of the main restrictions in the design of gyrotrons is the maximum specific heating of the cavity wall which must not exceed a certain value in order to ensure a proper cooling of component. This results in a minimum radius of the cavity for a given frequency and output power. On the other hand, mode density and mode competition become more severe with increasing inner radius of the cavity, thus limiting the order of the design mode.

In figure 1 the dependence of the calculated output power and the maximum Ohmic losses on the beam current for different cavity designs are shown for the $TE_{22,8}$ mode. Taking a realistic value of 2 kW/cm^2 as the technical limit of a cooling system shows that an output power of only 200 kW at 300 GHz can be achieved in a conventional gyrotron.

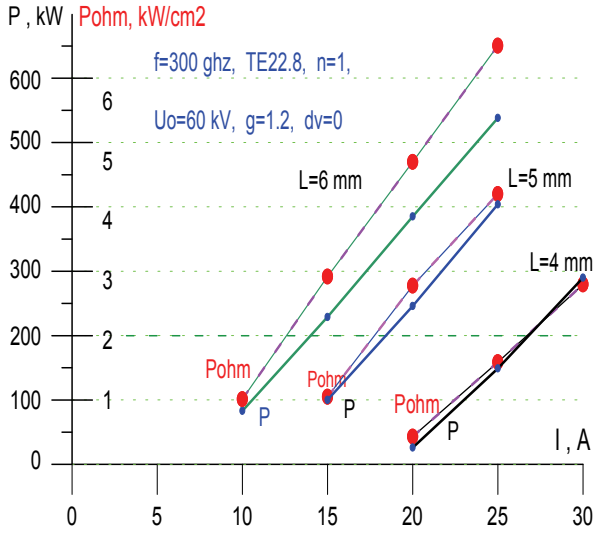

Fig. 1: Output power and specific Ohmic losses in the cavity vs. beam current for different length L at 300 GHz ($TE_{22,8}$).

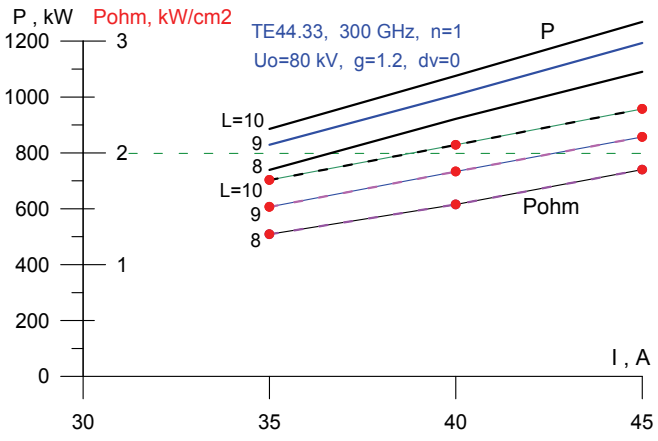

Fig. 2: Output power and specific Ohmic losses in the cavity vs. beam current for different length L at 300 GHz ($TE_{44,33}$).

These investigations have been extended in order to achieve a higher output power and to limit the specific Ohmic losses to about 2 kW/cm^2 by taking into account very high order modes. The example in figure 2 shows results with the mode $TE_{44,33}$ for cavities with a different length L. These simulations demonstrate that the specific Ohmic losses can be reduced to a reasonable value, even at 1 MW output power. However, it should be mentioned that the mode $TE_{44,33}$ is of much higher order than $TE_{34,19}$ which is the highest order mode applied so far in a high power

coaxial cavity gyrotron. Simulations on detailed mode competition and stability analysis are necessary to verify these results.

It should be noted that results of a conventional gyrotron will be reported, only. The use of coaxial cavity technology will improve the performance considerably.

Superconducting Magnet

Due to the high frequency the magnetic system has to support a field strength of at least 12 T. Currently, the superconducting wire for standard gyrotron magnets is made with NbTi. However, it is not clear if a 12 T magnet can be manufactured with this technology. An alternative would be using the Nb3Sn technology which is of course much more challenging.

Summary and Conclusions

In 2012 preliminary studies of an EC system at 300 GHz or above for DEMO have been performed. They show that

- the performance, e.g. in terms of achievable output, will be clearly reduced with increasing frequency
- coaxial cavity technology show a clear advantage versus conventional technology.

If the frequency range 300 – 350 GHz is a serious option for DEMO a more intense exploration of this area should be launched in order to gain more profound knowledge.

Staff:

G. Gantenbein

Literature:

[1] Zapevalov, V.E., et al, “Preliminary design of 300GHz/200kW/cw gyrotrons for fusion research”, 23rd Joint Russian-German Workshop on ECRH and Gyrotrons (STC-Meeting), May 23 – May 28, 2011, Karlsruhe - Stuttgart – Garching and Zapevalov, V.E., et al., “Numerical simulations of processes at the cavities of powerful 300GHz gyrotrons”, 24th Joint Russian-German Meeting on ECRH and Gyrotrons, June 11-15, 2012, IAP RAS, Nizhny Novgorod

Acknowledgement

This work, supported by the European Communities under the contract of Association between EURATOM and Karlsruhe Institute of Technology, was carried out within the framework of the European Fusion Development Agreement. The views and opinions expressed herein do not necessarily reflect those of the European Commission.

EC Ports Requirement, Launcher, Transmission Lines and Gyrotron Investigation (WP12-DAS-HCD-EC-06-01)

Introduction

One of the major challenges for future gyrotron development is the enhancement of the efficiency from an up-to-date value of 50-55% up to about 70 %. Such a development will require a serious attempt over several years in order to increase the understanding of the mechanisms of beam formation in a magnetron injection gun (MIG) and to improve existing technologies and introduce new and innovative technologies. In the frame of this work concepts for efficiency enhancement by improvement of the quality of the helical electron beam will be provided. A proposal of a new emitter concept will be presented which suggests a lifetime which is 10 times higher compared to conventional emitters. First considerations for a concept of a high frequency gyrotron (e.g. ~240 GHz in the 1 – 2 MW range) will be described.

EC ports requirement, launcher, transmission lines

Port requirements

Different plant architectures for a DEMO reactor have been investigated during the recent years. Among these the Multi-Module Segment (MMS) concept, in which large blanket modules are foreseen to be exchanged through the vertical port, is generally accepted as the most promising in terms of lowering the machine downtime.

Preliminary port definition has been based on rescaling by a factor 1.2 the ITER ports. Below in Fig. 1 (NOT IN SCALE) the scaled dimensions of the port plugs are shown.

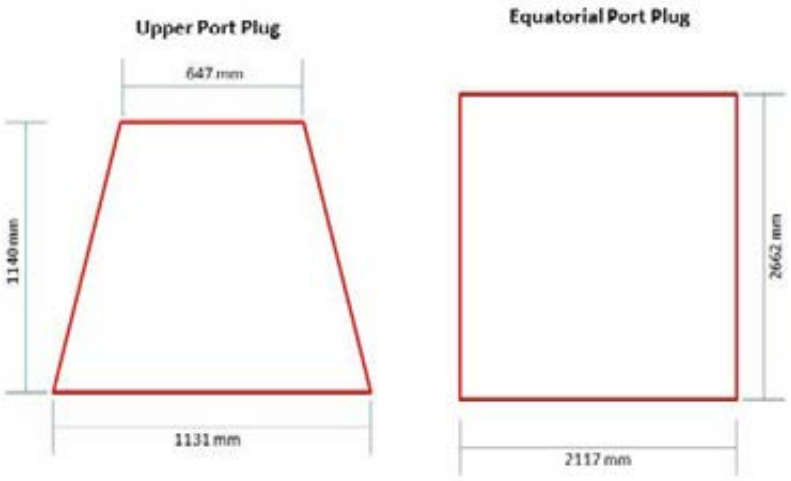

Fig. 1: Port sizes as scaled from ITER to DEMO.

Particularly delicate are the requirements on the Upper Port Plug, that must allow the replacement of 48 Outboard and 32 Inboard MMS.

ECH Launcher concepts and integrated transmission lines

In a DEMO reactor an ECH system can be used to inject high power microwave beams within a highly localized volume of plasma, in order to provide heating and/or to perform mitigation of instabilities (e.g. MHD activity), which might represent a potential threat for plasma operations and for the machine itself.

The ITER ECRH launcher design is based on front steering mirrors providing a fast scan of the plasma column on specific toroidal and poloidal positions where the fixed frequency, the

steered incident angle and the local magnetic field match for maximum energy deposition to the electron cyclotron resonance. Due to the high neutron and radiation fluxes, movable parts close to the plasma, e.g. a steerable mirror used in a FS launcher, are best to be avoided. Moreover, such systems require a relatively large volume occupation in the blanket and would therefore reduce the critical potential tritium breeding volume. There are two possible alternatives: one presented in the next section is the remote steering approach, which has been the former reference design of the ITER ECRH upper launchers. The other one, briefly covered in the section 2.4, is the frequency tuneable ECRH. Here in principle the millimeter wave frequency can be adjusted instead of the incident angle to achieve electron cyclotron resonance. A major challenge of this system is the development of broadband diamond windows, as the established designs are limited to fixed frequencies in order to avoid arcing/reflections back towards the gyrotrons.

In this and the past design assessment studies an equatorial launcher was investigated. For the coming WP13 an assessment of the possible need for an upper launcher for MHD stabilization is proposed.

Remote steering

A solution, which might maximize the system reliability, can be provided by a corrugated squared waveguide of proper length, in a way such the Talbot Law is satisfied:

$$L = 4a^2/\lambda$$

Injecting the beam with a certain angle at one end of the waveguide, results in a reflected beam at the other end (see figure 2), having the same angle. Placing a movable mirror that allows to inject the beam into the waveguide at different angles, allows than to obtain the so-called RS concept antenna [1]

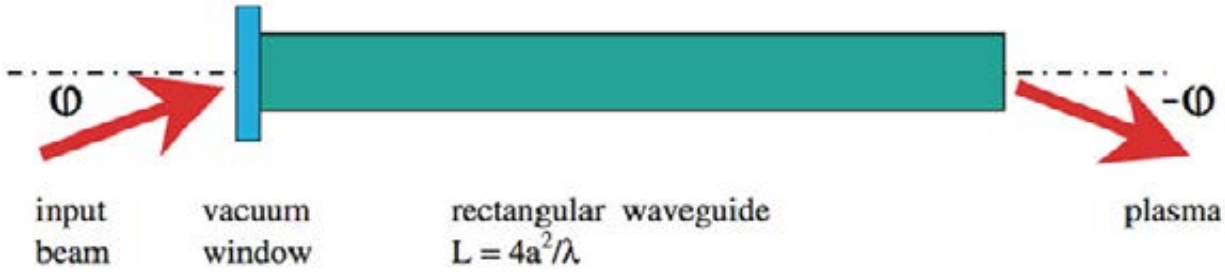

Fig. 2: Sketch of a RS Concept antenna [2].

In table 1 is presented a trade-off on the RS concept highlighting advantages and disadvantages of such configuration.

Table 1: Trade-off on the RS configuration for an ECH system on DEMO.

Advantages	Disadvantages
No moveable mirrors (parts) close to the plasma (simplified scheme with respect to FS)	Steering range ~ 10°
Reduced remote handling activity needed in case of launcher removal and repair	Focusing ability might be limited due to the restricted space for the launcher in the port plug
The corresponding NTM stabilization efficiency could be sufficient if the wave guide size is large so that the beam divergence is kept small (depending on the launching geometry and distance to the resonance)	Larger deposition profile in the plasma compared with FS
Elliptical polarization (necessary for ECCD) can be transmitted without depolarization with steering angles up to 20	
Low power measurements carried on for ITER similar concept shown that mitre bends can be integrated into the waveguide	

RS launchers with Pre-Focused beams and linear tapers

The limitation associated to the coupling between the steering and focusing capabilities of a RS concept can be partially overcome by introducing modification in the launched beam (through the waveguide) and in the waveguide itself.

In figure 3 is shown a pre-focused beam injected into a straight rectangular waveguide.

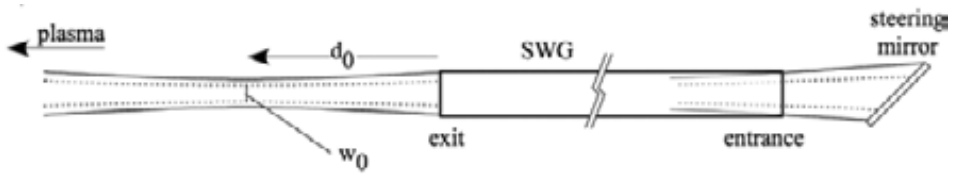

Fig. 3: Sketch of a pre-focused beam injected into a RS Concept antenna [3].

The advantage of such configuration is the possibility to adjust the projected beam waist w_0 at a distance d, with the consequence to maximize the power density[1] on the instability that shall be mitigated.

To further increase the injection angle, instead of a straight corrugated waveguide, a taper (down), can be used. In figure 4 are represented the cases of a downtaper (figure 4 top) and an uptaper (figure 4 bottom).

In the former an increased steering angles (> 15°) can be obtained, at the cost of a larger beam waist. In the latter, a decrease beam divergence can be achieved and the deposition width can be minimized if distance between WG and deposition location is large.

[1] Minimizing the spot size at the deposition location

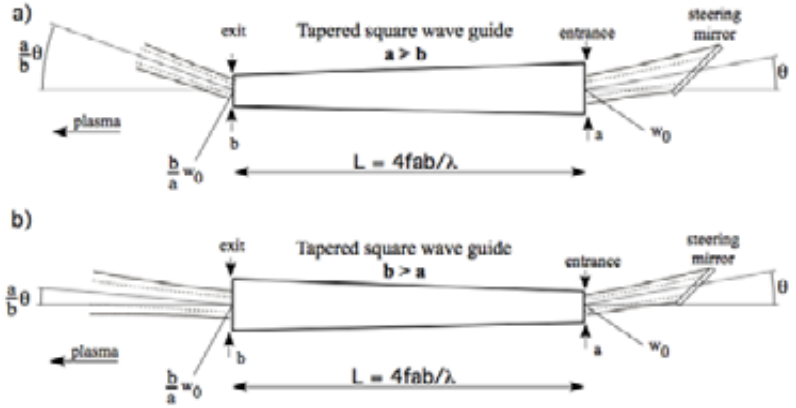

Fig. 4: Sketch of down- and uptapers for a RS Concept antenna [3].

It is then worth to report that, as shown by Kasparek et al. [2] (see figure 5), inserting mitre bends into the corrugated waveguide has the benefit to compact the design without altering the properties of the injected beam.

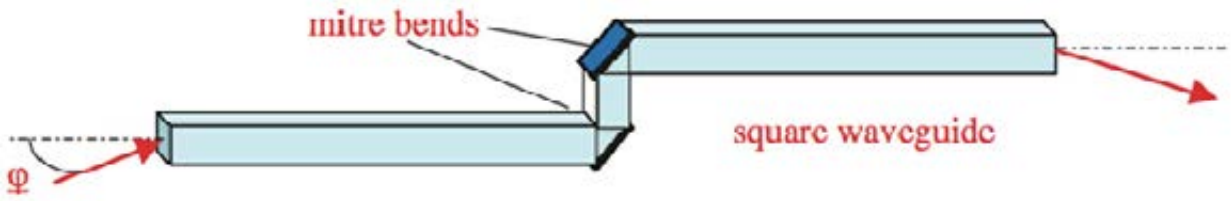

Fig. 5: Sketch of a RS Concept antenna with a mitre bend inserted in order to compact the design [2].

From these preliminary considerations appear that a downtaper might be the favourable solution, assuming a RS concept, for an ECH launcher. However, this pre-conceptual study need to be further developed in order to achieve a sufficient level of details.

Frequency tuneable systems: broadband windows

The key challenge to develop a frequency tuneable ECRH is, apart from the gyrotrons, the design of broadband diamond torus- and gyrotron window. In the following a short introduction to one possible design – a diamond disk brazed in the “reflection free” Brewster angle – is sketched. For following WP13-DAS-HCD-EC an assessment including also other concepts such as tuneable double disk systems, surface modified “anti reflection” diamond is proposed.

The Brewster window is a broadband window solution for heating and current drive (H&CD) applications. It consists of a cylindrical waveguide with an elliptical diamond disk brazed in the Brewster angle. The thermal expansion mismatch between copper and diamond is greater than 15 which results in a very challenging brazing process. The stresses and the resulting leak tightness of the brazing depend strongly on geometric optimization which is reported here as a result of FEM structural analyses.

Introduction and background

Chemical vapour deposition (CVD) diamond windows are used as confinement barriers in the transmission of high power mm-wave beams such as, for instance, in the ITER electron cyclotron H&CD system. The thickness of the diamond disc must match the desired beam wavelength in order to minimize the amount of reflected power, as it is a fixed frequency system moveable mirrors are necessary to deploy the beam at different positions in the plasma in order to achieve electron cyclotron resonance. However, looking at DEMO, the higher heat

loads and neutron fluxes doesn't permit the ITER type front steering launcher with moveable mirrors close to the plasma.

A promising alternative might be the use of gyrotrons able to tune the beam frequency to the desired resonance, but this concept requires transmission windows that work in a given frequency range (e.g. 105-140 GHz), such as the Brewster window. It consists of a CVD diamond disc brazed to two oxygen-free high conductivity (OFHC) copper cuffs at the Brewster angle (67.22°). The brazing process is carried out at about 800°C and then the temperature is decreased down to room temperature. Diamond and copper have very different thermal expansion coefficients (ratio of 1 to 16 at 20°C, respectively), therefore high stresses build up during the cool down phase that might lead to failure of disc or brazing. This brazing process of different geometrical configurations of the Brewster window was simulated and is summarized in the following.

Requirements for MHD mitigation

In order to guarantee safe tokamak operation, proper control systems must be implemented. Among these, ECH can be used to mitigate MHD activity that represent a potential threat to tokamak operations, and that might cause huge damage to the machine itself.

Studies on plasma scenarios shows that the efficiency in driving current injected from an Upper port Plug, increase dramatically. Therefore, the requirement for an Upper Port Plug in DEMO dedicated to ECCD for plasma stabilization.

Current Drive realized by using ECH systems, called therefore Electron Cyclotron Current Drive (ECCD), is generally considered **technologically mature, but not very attractive** because of comparatively low CD efficiency (driven current per injected power). However some advantages compared to other CD methods (i.e. NB), rises the interest in this kind of approach (for instance, **smaller openings** in the blanket are required for ECCD as compared to NB).

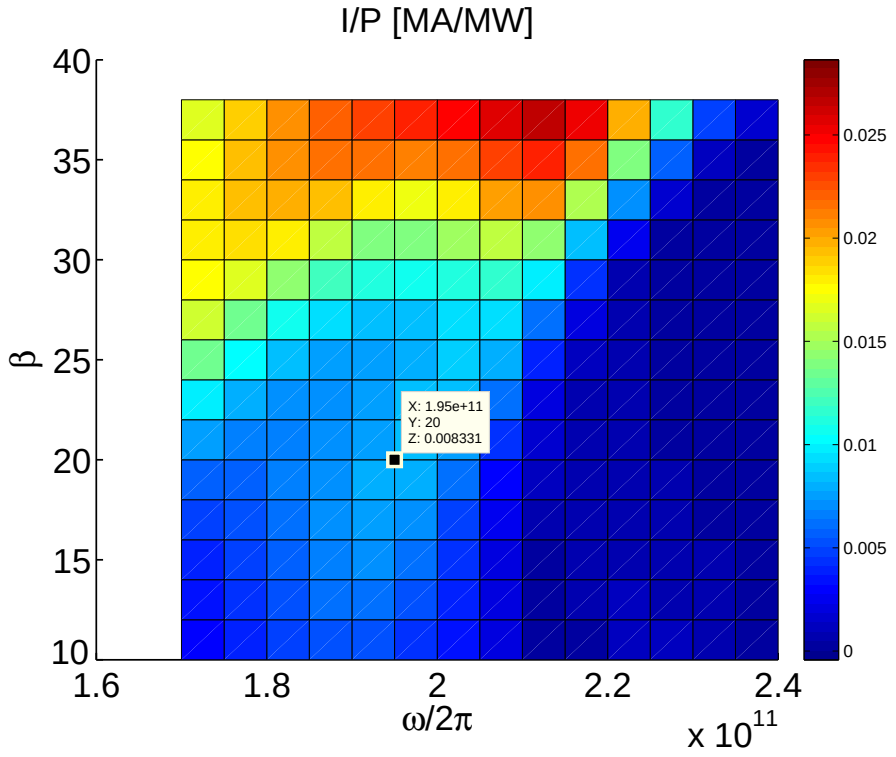

Fig. 6: Current Drive Efficiency as function of the injected frequency and the toroidal angle with respect to the radial direction [4].

Scans over the injected frequency ω/2π and toroidal angle β (setting the poloidal angle = 0) show that (figure 6) current drive efficiency first rises as the deposition is pushed towards the plasma centre, then decreases because of too large parasitic absorption. These preliminary studies estimate the optimum injection angle around **β = 38° @ ω/2π = 215 GHz.**

This value has been used to define the axial direction of the openings into the MMS for the integration of possible ECH launchers.

Efficiency enhancement of the gyrotron

According to simulations the optimum interaction efficiency of a gyrotron is achieved assuming a thin annular electron beam with a minimum spread of beam radii and velocity distribution of the electrons. In some cases the electron beam is very sensitive to geometrical tolerances and small modifications of the ideal design. However, in a real high power gyrotron there are only limited possibilities to monitor the beam parameters and to control these parameters. The goal of this work is to identify the most important parameters and to design and built test devices for MIG.

A novel approach to a MIG which offers the possibility to control the azimuthal current density and a considerably increased lifetime is presented.

<u>Numerical investigations on emitter ring tolerances on the beam quality</u>

Here we present first preliminary studies on the radial deviation of the emitter ring on the beam quality. This example is taken from studies on a 1 MW 170 GHz tube.

The emitter ring region is shown in Fig. 7. The black lines represent the ideal geometry of the emitter ring, while the red and the blue lines represent an outward (100 μm) and an inward (-100 μm) radial deviation of the emitter ring. In this study, the electron beam parameters at the cavity have been estimated for several values of radial deviation between 200 and 100 μm.

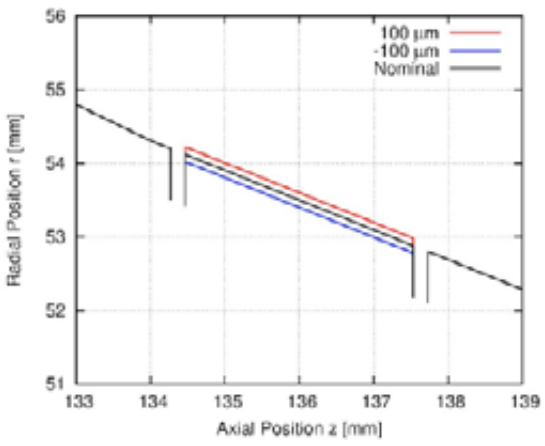

Fig. 7: The outward and inward radial deviation of the emitter ring for 100 μm.

The variation of the average pitch angle and the transverse velocity spread versus the deviation of the emitter ring radius are presented in Fig. 8 for the start-up and the neutralized case. In both case, a strong variation of the average pitch angle is observed. As it is shown in the figure, an inward radial deviation of 100 μm causes a significant decrease of the pitch angle, from 1.5 (nominal value) to 1.2 for the start-up while from 1.32 (nominal value) to 1.1 for the neutralized case. On the other hand, an outward deviation of 100 μm causes an increasing of the alpha value, from 1.5 to a value more than 2 for the start-up and from 1.32 to 1.6 for the neutralized case.

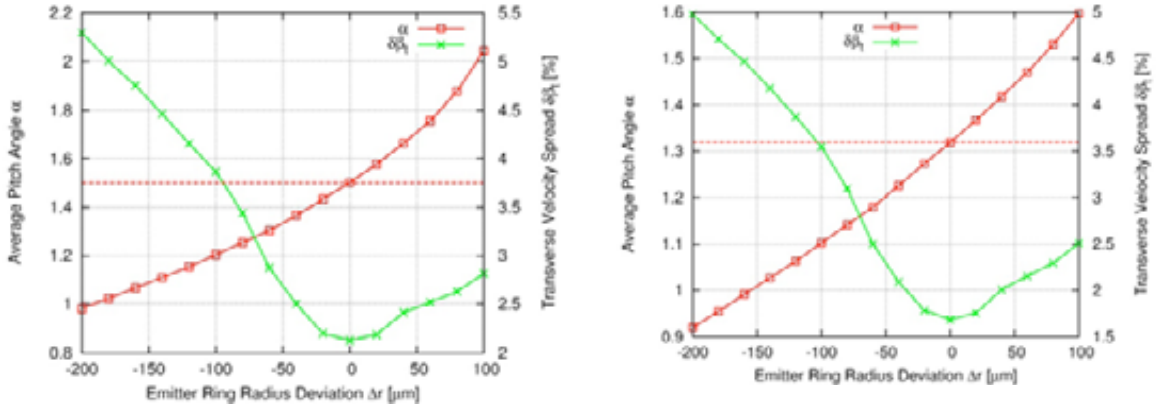

Fig. 8: The average alpha and the velocity spread of the electron beam versus the emitter ring radial deviation for the start-up (left) and the neutralized beam (right).

In addition the emitter ring radius deviation has a significant effect also on the velocity spread. The nominal velocity spread is around 2.2 % for the start-up case and ~1.6 % for the neutralized case. These values are significantly affected in both case from the inward and the outward radial deviation of the emitter ring. For the inward deviation of 100 μm the spread is increasing to ~3.9 % for the start-up and to ~3.5 % for the neutralized case. For the outward deviation of 100 μm, the spread is affected less than the inward deviation and it is ~2.8 % and ~2.5 % for the start-up and the neutralized case respectively. Very interesting conclusions are extracted by the pitch angle distributions for several cases of radial deviation. For the outward radial deviation a harmful long tail in high alpha values is formed, which could have an important impact on the gyrotron operation.

It should be pointed out that this long tail appears also for small values of radial deviation. For only 20 μm the tail approaches the value 2 and for 100 μm the tail approaches the value 5. On the other hand, for the inward radial deviation even if the average pitch angle and the velocity spread are significantly affected, no any harmful tail in high alpha side is formed. The simulations show that the electrons which are responsible for the long tails in the cases of the outward radial deviations are emitted by the rear part of the emitter ring. This sensitivity is related to the local variation of the electric field due to the thermal isolation gaps and the radial positions of the two edges of the neighbouring parts of the cathode structure.

More comprehensive work is required in order to fully understand the reasons of this sensitivity which is observed in the numerical simulations.

Gun testing device

As a first step towards an experimental device consists in verifying the parameters of a MIG a gun testing system has been designed and manufactures. One goal of this system is to allow a measurement of the (radial) dimensions of the cold and hot emitter ring with a contact-free method. Therefore, a capacitive probe, installed in the vacuum, measures the distance to the emitter surface which is rotated around the axis of the MIG. A HV can be applied to the device and the emitter can be heated up to the operating temperature, thus extracting a current to the anode. Several small cups are integrated into the anode in order to monitor the current density emitted at different locations. A schematic picture of the device and a test MIG are shown in Fig. 9. First experimental results are expected during 2013.

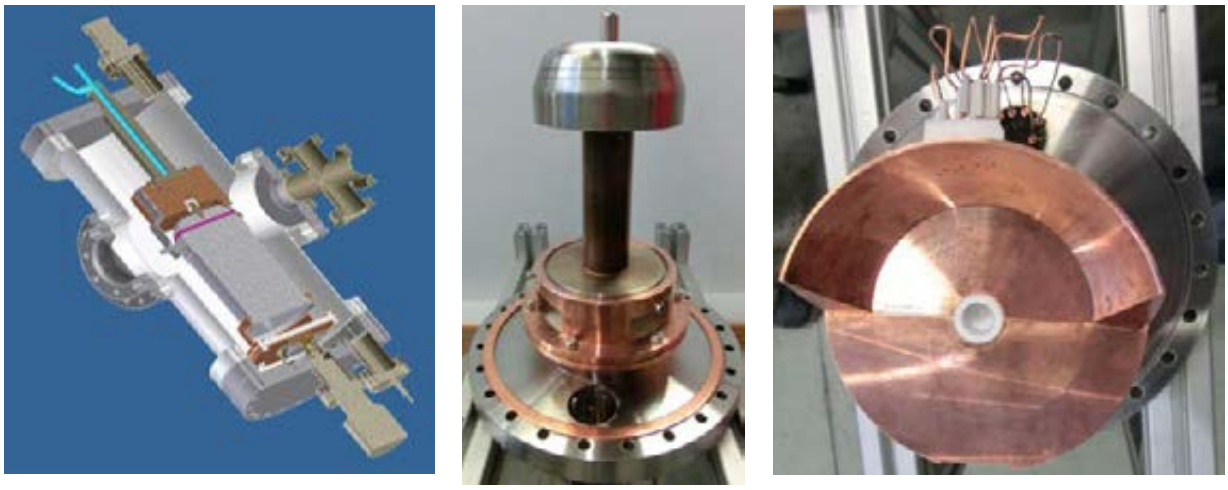

Fig. 9: Gun test device to measure homogeneity of emission current in azimuthal direction.

Advanced beam test set-up

The quality of the electron beam plays an important role in the gyrotron operation. In particular, the average pitch factor and the velocity spread are key parameters for the electronic and the overall efficiency of any gyrotron. For the generation of the electron beam in gyrotrons, MIGs are used, which are designed using electrostatic, self-consistent numerical codes, such as EGUN, ESRAY and Ariadne. In the computer modelling of the gun geometry, many factors which could significantly affect the quality of the electron beam, such as, roughness of the emitter ring, mechanical tolerances, non-uniformities in the heating of the emitter ring, etc., are not taken into account. This fact has as a result always to have some doubts about the quality of the electron beam during the experiments. In order to experimentally evaluate the operation of a MIG, the conceptual design of a new diagnostic tool has been initiated.

The goal of this device is to measure the pitch angle distribution for many azimuthal positions in the nominal (or if it is not possible in a scale-down) operational parameters, such as, the magnetic field, the voltage and the current. The main difficulty of such a device is how to distinguish the trajectories of the electrons with different pitch angles. We work on two different approaches. The first based on the application of a decelerating potential. This idea has been already used in the past for the built of a similar gun diagnostic tool, as it is presented in [5] The second approach based on the separation of the electron trajectories with different pitch angles using the drift velocity. This concept has been proposed in the past for the design of gyrotron multistage collectors [6].

Currently, we have concentrated our effort only in the first approach. A controlled rotated diaphragm is placed at the position of the cavity entrance with a small hole on an azimuthal angle permitted only a small portion of the electron beam to pass through. On the other side of the diaphragm is placed a probe in a negative decelerating potential. An axial electric field is generated between the diaphragm and the probe which acts only on the axial velocity of the electrons. The current measured on the probe indicates the number of the electrons which reach the probe, overcoming the decelerating electric field. On the other hand, electrons with low axial velocity (high pitch angle) are not overcome the decelerated electric field and they are collected by the diaphragm. The pitch angle distribution for the electrons which pass through the hole of the diaphragm could be extracted by the measured current on the probe for many value of the decelerating voltage. A preliminary conceptual design has been modelled using the 3D CST Particle Studio in order to evaluate the concept. The operation of such a diagnostic tool is limited to the low energy electron beam since the most part of it, is collected by a small surface on the diaphragm.

In the near future, a more realistic design of the diagnostic tool based on the decelerated potential will be implemented, while in parallel the investigation of a conceptual design based on the second approach will be started.

Design of a 10kW/28GHz Gyrotron with a Segmented Emitter Based on Controlled-Porosity Reservoir Cathodes

See pages 65 and 66 in Chapter “Advanced Gyrotron Development – Studies on Electron Beam Diagnostic Systems”

Concept of high frequency gyrotron

Basically there are two possible concepts of a high frequency gyrotron: coaxial cavity gyrotron and conventional gyrotron. According to simulations the coaxial cavity gyrotron shows the possibility of higher output power at a higher beam current compared to the conventional gyrotron. However the coaxial technology is more complex and less mature than the conventional gyrotron.

Due to its improved potential at higher frequency and output power a detailed work on a coaxial cavity has been started end of 2012. Preliminary results are expected during 2013.

As a first step in this field a study of a conventional cavity gyrotron at 238 GHz has been performed. Five candidate modes have been selected and their suitability for delivering 1.0 – 1.3 MW RF operation has been investigated. Preliminary simulations using single-mode self-consistent and time dependent multi-mode calculations showed that three of them ($TE_{43,15}$, $TE_{44,15}$, $TE_{46,15}$) did not gave a stable numerical result. The simulations with the modes $TE_{49,17}$ and $TE_{50,17}$ suggests that operation at 238 GHz could be possible with the following parameters: beam voltage up to 90 kV, beam current up to 60 A, magnetic field up to 9.8 T. However, since all the modes examined so far are of very high order, mode competition has to be studied more carefully verified by additional simulations. No design work on the electron gun and beam optics has been performed up to know.

Future developments and recommendations

In the field of gyrotron development towards DEMO the following developments and recommendations are strongly suggested:

- Intensify numerical studies on MIGs.
- Exploration of new gun technologies to improve beam performance and reliability.
- Development and construction of measurement system to analyse the performance of MIGs.
- Continuation on studies on coaxial or conventional high frequency gyrotrons (~ 240 GHz) including step-tunability.

Staff:

G. Gantenbein
D. Strauss

Literature:

[1] R. Prater et al., A design study forthe ECH launcher for ITER Proc. 10th Joint Workshop on ECE and ECRH (Ameland, The Netherlands) ed T. Donne and A.G.A. Verhoeven (Singapore: World Scientific) ISBN 981-02-3219-5, pp 531–40

[2] W. Kasparek et al., Performance of a remote steering antenna for ECRH/ECCD applications in ITER using a four-wall corrugated square waveguide Nucl. Fusion 43 (2003) 1505–1512

[3] M.A. Henderson et al., Possible enhancement of remote steering, Workshop on Physics and technology of RF heating of fusion plasmas, 2006, Nara, Japan

[4] E. Poli et al., Electron-Cyclotron-Current-Drive Efficiency in DEMO Plasmas, Nuclear Fusion 53, 013011 (2013)

[5] B. Piosczyk, “Experimental Beam Parameters on Different Gyrotron Electron Guns”, Proceedings of the International Workshop on Strong Microwaves in Plasmas, Nizhny Novgorod, 1994.

[6] I. Gr. Pagonakis, “A new concept for the collection of an electron beam configured by an externally applied axial magnetic field”, IEEE Transaction on Plasma Science, vol. 36, pp 469-480, 2008.

Acknowledgement

This work, supported by the European Communities under the contract of Association between EURATOM and Karlsruhe Institute of Technology, was carried out within the framework of the European Fusion Development Agreement. The views and opinions expressed herein do not necessarily reflect those of the European Commission.

DEMO: Broadband Window (WP12-DAS-HCD-EC-06-01)

The Brewster window is a broadband window solution for heating and current drive (H&CD) applications. It consists of a cylindrical waveguide with an elliptical diamond disk brazed in the Brewster angle. The thermal expansion mismatch of roughly 20 between copper and diamond brazing results in a very challenging brazing process. The stresses and the resulting leak tightness of the brazing depend strongly on geometric optimization which is reported here as a result of FEM structural analyses.

Introduction and background

Chemical vapour deposition (CVD) diamond windows are used as confinement barriers in the transmission of high power mm-wave beams such as, for instance, in the ITER electron cyclotron H&CD system [1]. The thickness of the diamond disc must match the desired beam wavelength in order to minimize the amount of reflected power, as it is a fixed frequency system moveable mirrors are necessary to deploy the beam at different positions in the plasma in order to achieve electron cyclotron resonance. However, looking at DEMO, the higher heat loads and neutron fluxes doesn't permit the ITER type front steering launcher with moveable mirrors close to the plasma.

A promising alternative might be the use of gyrotrons able to tune the beam frequency to the desired resonance, but this concept requires transmission windows that work in a given frequency range (e.g. 105-140 GHz) [2], such as the Brewster window [3]. It consists of a CVD diamond disc brazed to two oxygen-free high conductivity (OFHC) copper cuffs at the Brewster angle (67.22°). The brazing process is carried out at about 800°C and then the temperature is decreased down to room temperature. Diamond and copper have very different thermal expansion coefficients (ratio of 1 to 16 at 20°C, respectively), therefore high stresses build up during the cool down phase that might lead to failure of disc or brazing. This brazing process of different geometrical configurations of the Brewster window was simulated and is summarized in the following.

Methods

A FEM model of the Brewster window was set up as reference case and it is shown in Figure 1. The diamond disc has an elliptical shape with major axis of 160 mm, minor axis of 80 mm and thickness of 1.9 mm. The cuffs are cylindrical with inner diameter of 50 mm, thickness of 1 mm and total length of 200 mm. Symmetry was assumed along the major axis of the disc allowing the analysis of half structure. Constant, temperature dependent and non linear material properties were used [4, 5, 6]. A fixed support was applied to the two ends of the cuffs as boundary condition. Stresses and deformations were first calculated in a structural analysis by decreasing the temperature from 800°C to 20°C.

A parameters impact analysis was subsequently carried out by varying the thickness of the cuffs and the disc and the aspect ratio of the disc. The thickness varies from 0.8 to 2 mm for the cuffs and from 1 to 2.5 mm for the disc. The disc has an aspect ratio of 2 with major axis of 160 mm which is maybe too big for a real manufacturing of the disc. Other two aspect ratios, 1.4 and 2.33, were so considered with major axis of 140 mm and minor axis respectively of 100 mm and 60 mm. Other two constraint configurations were also investigated with respect to the reference case. One configuration (named configuration 1) has one end free to move along only the axis of the cuffs while the other configuration (named configuration 2) has one end without constraints.

Results

For the analysis of stresses in the brittle diamond the first principal stress was used while for the ductile copper the averaging von Mises stress was checked. The first principal stress in the reference case, shown in Figure 1, is generally in the range 30-75 MPa along the contact region between the disc and the cuffs and has a maximum of 137.4 MPa, located at the tip of the disc in the contact region with the longer side of the cuffs. The cuffs experience plastic behaviour, in fact the equivalent stress, varies between 50 and 75 MPa (yield strength of OFHC copper is 45 MPa at 20°C [6]) in the most part of the cuffs and has maxima values in the range 103.1-110.6 MPa, located close to the area of maximum principal stress and to the support. However, the maximum first principal stress is below the permissible stress of diamond which is 150 MPa (ultimate strength is 450-500 MPa [7]) and the maximum equivalent stress is below the ultimate strength of OFHC copper (250 MPa at 20°C [6]).

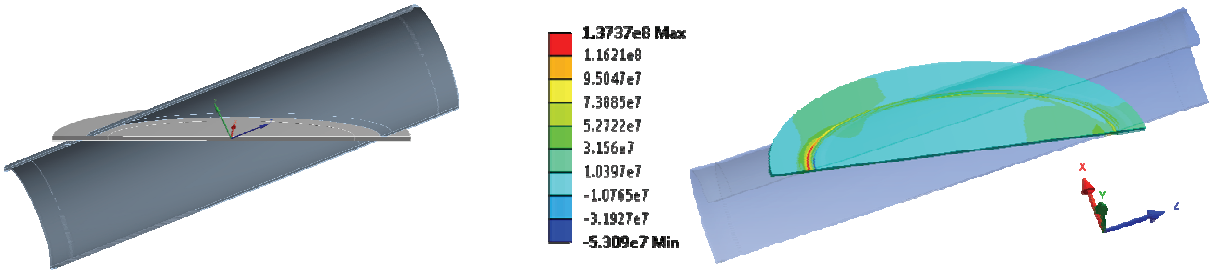

Fig. 1: Reference configuration of the Brewster window (left) and first principal stress distribution on the top side of the diamond disc in the reference case (right). Values are in Pa.

Figure 2 shows the maximum stresses in the disk (first principal stress) and the brazing/cuff (equivalent or von Mises stress) as functions of the thickness of the cuffs and the disc. Values of cuff thickness above 1.2 mm and of disc thickness below 1.7 mm are not recommended. Then, the aspect ratio of the disc affects the first principal stress profile by less than 3%.

Finally, the constraint configurations 1 and 2 lead to a maximum stress in the disc of 181 MPa, greater than that obtained in the reference case. This might be explained considering for instance the configuration 1. Because of the boundary condition, here the plastic deformation occurs only in the part of the cuffs near the disc but the deformation is big (maximum is 2.83 mm) and the deformation mechanism would lead to severe stresses in the disc. In contrast, in the reference case due to the fixed support, the deformation is more limited (maximum is 1.23 mm), occurring in the plane perpendicular to the axis, but the cuffs are wholly plastically deformed. This would result in a more relaxed stress profile in the diamond disc of the reference case. The considerations done for the configuration 1 are also valid for the configuration 2, but here the maximum deformation amounts to 3.32 mm.

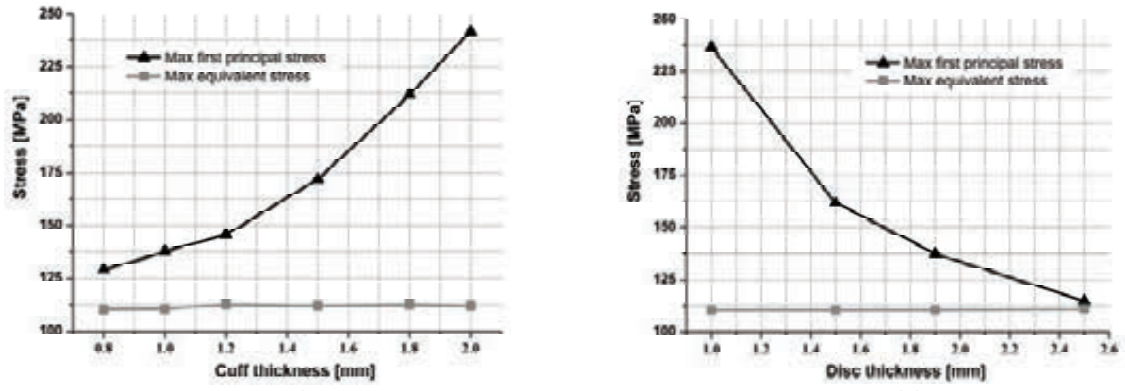

Fig. 2: Maxima first principal stress and von-Mises stress as functions of cuff thickness (a) and disc thickness (b).

Conclusion

FEM structural analyses showed that the CVD diamond Brewster window is a feasible solution to achieve resonance in a plasma with a radially decaying magnetic field by frequency tuning. Values of the cuff thickness greater than 1.2 mm and of the disc thickness less than 1.7 mm are not recommended.

Literature:

[1] T. Scherer et al., proc. 36th IRMMW-THz conf., Houston, USA, 2011.

[2] R. Heidinger et al., proc. 32nd IRMMW-THz conf., Cardiff, GB, 2007.

[3] X. Yang et al., Int. J. Infrared Milli Waves 24, 5 (2003).

[4] D.C. Harris, Infrared Window and Dome Materials, SPIE, 1992.

[5] Y.S. Touloukian et al., Thermophysical Properties of Matter - Vol. 5.

[6] M. Merola et al., ITER plasma facing component materials database in ANSYS format, ITER Doc. G17 MD 71 96-11-19 W 0.1, 1997.

[7] M. Thumm, State of the Art of High Power Gyro-Devices and Free Electron Masers, KIT Scientific Reports 7575, Update 2010.

Staff:

G. Aiello
A. Meier
T. Scherer
D. Strauss
A. Vaccaro

Acknowledgement

This work, supported by the European Communities under the contract of Association between EURATOM and Karlsruhe Institute of Technology, was carried out within the framework of the European Fusion Development Agreement. The views and opinions expressed herein do not necessarily reflect those of the European Commission.

EC Efficiency (WP12-DAS-HCD-EC-08-01)

Introduction

An estimate of overall EC system efficiency (wall plug efficiency) based on the DEMO ECCD physics analysis and best estimates of future gyrotron efficiency will be provided. This estimate will include power supply efficiency, gyrotron efficiency, transmission line efficiency, launcher efficiency and current drive efficiency.

Overall EC System Efficiency

These considerations are split into two parts which focus on the technical efficiency including HV power supply, gyrotron (details are given in WP12-DAS-HCD-EC-06-01-KIT) and transmission line. It is supposed that the current drive efficiency taking into account the coupling to the plasma and current drive efficiency at optimized frequency is given in detail in WP12-DAS-HCD-EC-03-01/IPP.

Technical Efficiency

HV Power Supply: Modern devices, built with PSM technology () are a commercial standard product and have a typical efficiency of >= 95%.

State-of-the-art **gyrotrons** of the 1 MW class show an efficiency of 50 – 55 % at 170 GHz. With improved MIG technologies and progress in energy recovery by applying multi-staged collectors an efficiency of >= 70 % seems possible.

Following drivers are responsible for the efficiency of the **transmission line:** length, type (waveguide/quasi-optical), diameter of waveguide, evacuated, non-evacuated operation. The table gives an overview on typical existing machines as well as planned devices (as far as available).

¤	LHD¤	ASDEX-U¤	DIII-D¤	TCV¤	W7-X¤	ITER¤	JT60-SA¤
Frequency·(GHz)¤	77/82.7/84/168¤	140¤	110¤	82.7/118¤	140¤	170¤	110¤
Power per unit (MW)¤	1/0.5/0.8/0.4¤	0.5/1.0¤	0.7–0.85¤	0.5¤	1¤	1·(2)¤	1¤
Units¤	3/1/2/1¤	4/4¤	6¤	6/3¤	10¤	16·+·4¤	9¤
Total Power/injected (MW)¤	2.3/0.4/1.0/0.3¤	4·/·4.9¤	4.5/3.5¤	2.7/1.3¤	10/8¤	24/20¤	9·/·7¤
Pulse·length·(s)¤	5/2/3/1¤	2/10¤	5¤	2¤	1800¤	1000·¤	100¤
Transmission¤	HE_{11} evacuated waveguide (88.9·mm)¤	Quasi-optical / HE11 waveguide (87°mm)¤	HE_{11} evacuated waveguide (31.75·mm)¤	HE_{11} evacuated waveguide (63.5·mm)¤	Open mirror transmission system¤	HE_{11} evacuated waveguide (63.5·mm)¤	¤
Efficiency (%)(Transmission system)¤	77/80/75/75¤	93¤	70 – 80, average, 100 m¤	93¤	>·85·(60·m)¤	85·¤	75¤

Not included in these considerations are: pumps, heating and cooling systems, ventilation, control and DA. The efficiency of the auxiliary system is estimated to be approximately 98%.

These assumptions summarize to the total technical efficiency:

$\eta_{tech} = \eta_{HV} * \eta_{Gyrotron} * \eta_{TL} * \eta_{Aux} = 0{,}96 * 0{,}70 * 0{,}93 * 0{,}98 = 0{,}61$

Physics efficiency: see WP12-DAS-HCD-EC-03-01/IPP

Coupling to plasma
Optimised frequency
Top Launch

Staff:

G. Gantenbein

Acknowledgement

This work, supported by the European Communities under the contract of Association between EURATOM and Karlsruhe Institute of Technology, was carried out within the framework of the European Fusion Development Agreement. The views and opinions expressed herein do not necessarily reflect those of the European Commission.

Advanced Gyrotron Development
Studies on Electron Beam Diagnostic Systems (CoA)

One of the big unknowns in experimental gyrotron diagnostic is still the electron energy distribution at the absorption in the collector. Even though the distribution can be simulated with many tools today, a measurement in full operation is impossible yet. On the other hand, the energy distribution is one of electron beam features that determines the possible energy recovery, on the other hand measuring them after interaction would give valuable insight into the interaction mechanisms, as well as a good tool for code validation.

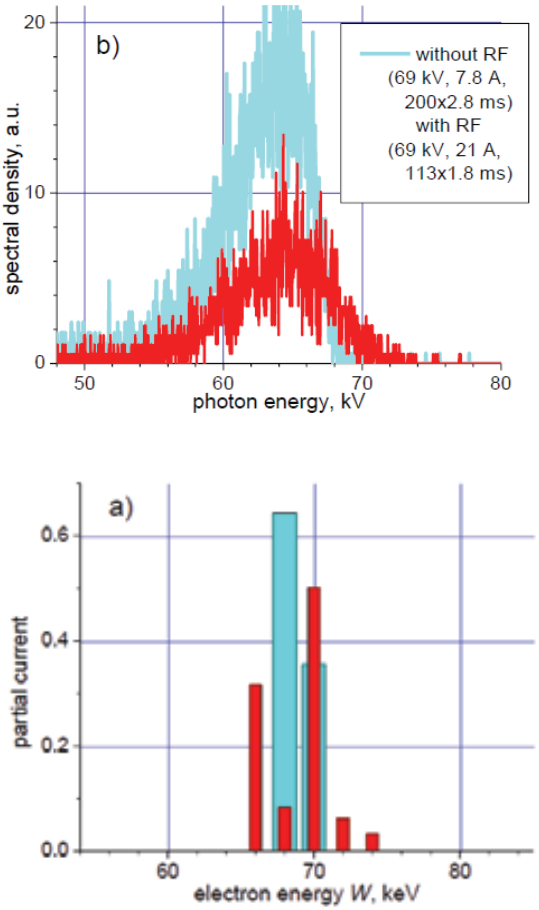

Fig. 1: Electron energy distributions (bottom) reconstructed from x-ray spectra (top) for gyrotron regimes with (red curves) and without (blue) rf output via inverse integral transformation.

One possibility for creating a diagnostic tool for energy distribution is to measure the X-ray spectra that are emitted as bremsstrahlung at the collector. One of the problems is to find a solution to reconstruct the electron's energy distribution through de-convolution. Other problems are sensitivity and possible error sources through shielding. With such a diagnostic in hand, an important tool would be available for further optimisation of gyrotron efficiencies and simulation codes.

In 2012 the following steps were performed:

1. Performance of test experiments: Measurement of X-ray spectra at the conditions of quasi-monoenergetic HEBs with different energies of electrons and subsequent analysis of the experimental data with an estimation of their suitability for reconstruction of electron energy spectra, development of necessary corrections of apparatus and algorithms.
2. Definition of conditions for practical realization of X-ray diagnostics for HEBs with electron energies up to approximately 100 keV, and with currents of tens of amperes.
3. Performance of experiments at the KIT facility working in its typical regimes.

These objectives were achieved during two experimental sessions that took place at the IHM gyrotron facility in April and October 2012 and in the following periods of data processing.

Figure 1 shows an experimental result which confirms that the application of the developed technique for diagnostics of gyrotron electron beam is principally possible. The X-ray flux produced by the investigated gyrotron has been sufficiently intense. The shapes of the spectral distributions agree with expectations. The spectral characteristics of the x-rays (high-energy cut-off, spectrum width) correlate with the gyrotron gun voltage and rf output power. Electromagnetic pick-up signals have little or no effect on the spectrometer performance. However, a magnetic field above a certain threshold makes the spectrometer inoperative, but doesn't visibly affect its performance below the threshold.

Design of a low power gyrotron for the test of a new emitter concept

A 10kW/28GHz gyrotron has been designed to evaluate the use of CPR emitters for gyrotron applications. CPR cathodes allow operation with higher current density (up to 50 A/cm^2) and provide much longer life time (~100000 h) compared to conventional emitter materials (LaB6, conventional dispenser cathodes etc.). In addition, the azimuthally segmented emitter ring provides the possibility to generate controlled non-uniform electron beams in order to study the effect of the non-uniform emission on the gyrotron output power and efficiency.

The design of all parts of the gyrotron has been finalized. The drawing of the 10kW/28GHz gyrotron is shown in the figure 2. A triode type magnetron injection gun (MIG) was preferred in order to increase the range of operating parameters. The cavity and the collector are water cooled to allow CW operation. The tube is also equipped with flanges instead of welded connections for easy exchange of components of the tube. The design of the test stand is nearly finished including water, interlock and power supply systems.

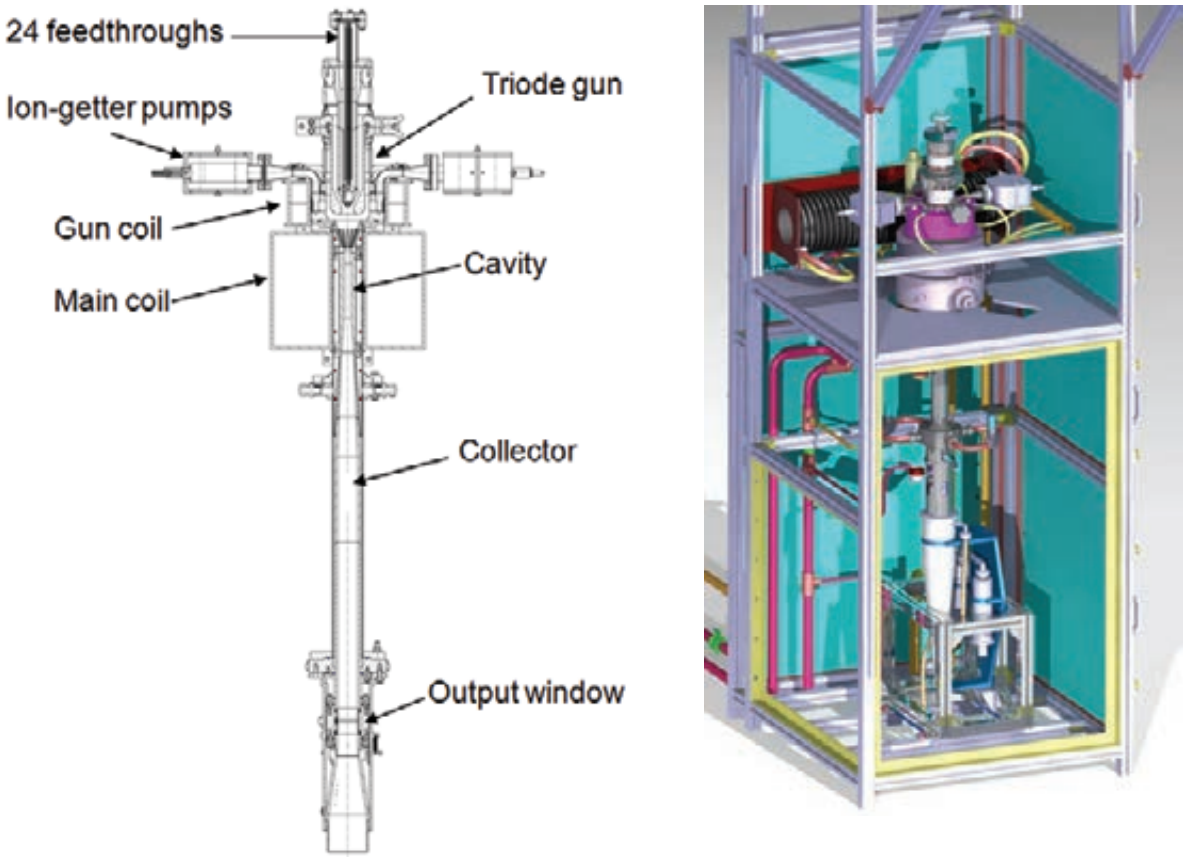

Fig. 2: Design drawing of the 10kW/28GHz gyrotron (left), and layout of the test stand (right).

For the cavity design we selected two modes at the second harmonic of the cyclotron frequency: $TE_{1,2}$ with the cavity radius 9.08 mm and beam radius 3.13 mm and $TE_{3,1}$ with the cavity radius 7.16 mm and the same beam radius as for the $TE_{1,2}$ mode. The optimization of the cavity profile was done by a self-consistent single mode code and the start-up investigations by the non-stationary multi-mode code EURIDICE. In simulations it was shown that for the cavity with $TE_{3,1}$ operating mode it is not possible to avoid the generation of the parasitic mode $TE_{1,1}$ on the first harmonic of the cyclotron frequency. For the cavity with the $TE_{1,2}$ main mode, simulations showed that from optimization of the cavity and magnetic field design it is possible to suppress the mode $TE_{1,1}$, and reach stable operation on the second harmonic $TE_{1,2}$, which can be seen from the figure 3, where the start-up scenario of the gyrotron is shown.

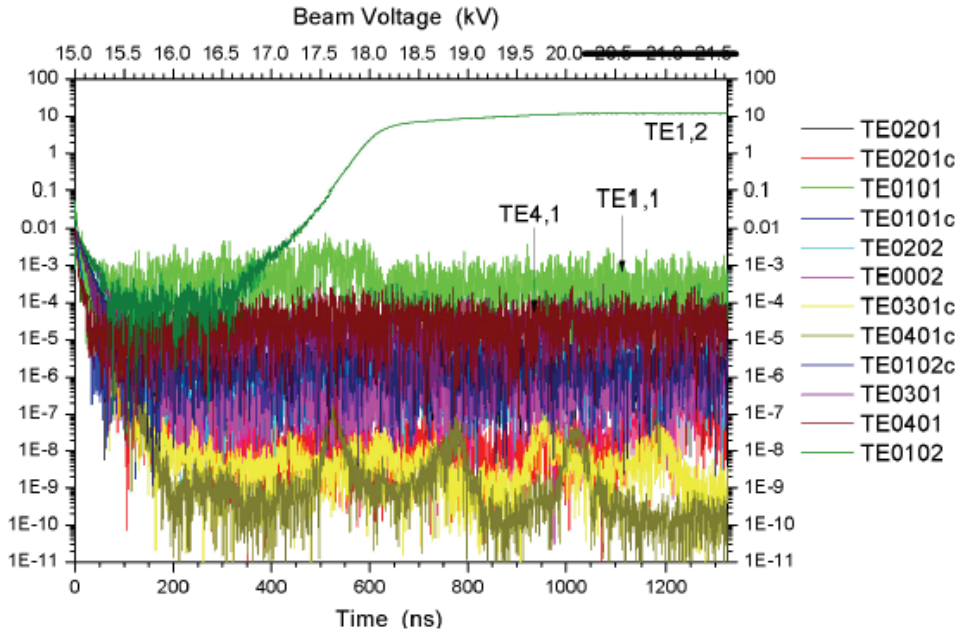

Fig. 3: Start-up scenario for the 10kW/28GHz gyrotron (excitation of the mode $TE_{1,2}$).

Experiments will be performed with two types of emitters, a conventional M-type emitter (with continuous emitter ring) for evaluation of the parameters of the gyrotron and with a controlled porosity reservoir segmented emitter. The manufacturing of the conventional M-type emitter has been finished. For the segmented cathode 8 segments have been built. The assembly of the segmented cathode and preliminary tests are planned in near future. The construction of the segmented cathode and an individual segment are given in figure 4.

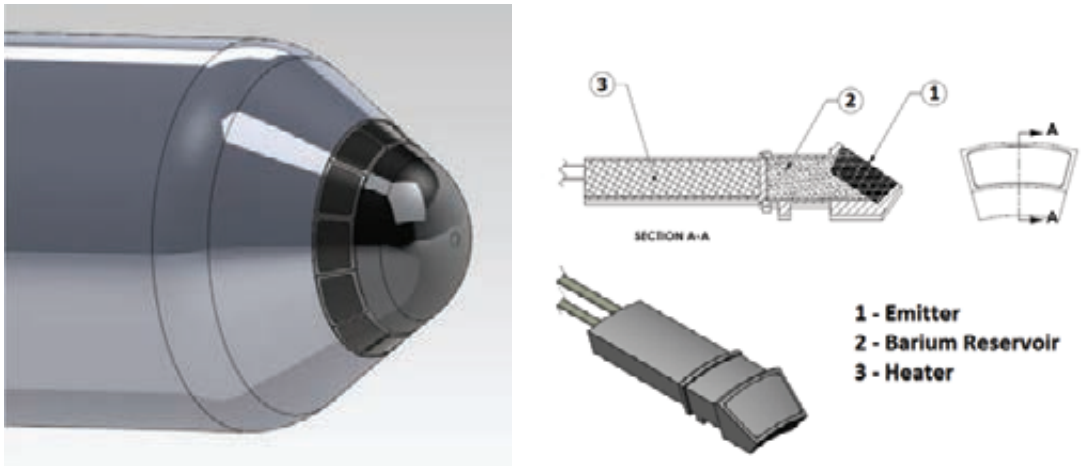

Fig. 4: Cathode with the segmented emitter ring (left) and design of an individual segment (right).

Staff:

D. D'Andrea
G. Gantenbein
S. Illy
S. Kern
R. Lang
A. Malygin
I. Pagonakis
B. Piosczyk
A. Samartsev
W. Spiess
J. Szczesny
J. Weggen

Advanced Gyrotron Development
Step-Tunable Gyrotron Development (CoA)

Introduction

In recent years electron cyclotron resonance heating and current drive (ECRH and ECCD) has been established as a successful instrument in magnetically confined fusion plasmas. Gyrotrons are the unique devices which meet the extraordinary requirements of those applications: output power in the MW range, 100 – 200 GHz output frequency, and pulse length of several seconds up to continuous wave (CW). Due to its excellent coupling to the plasma and the very good localization of the absorbed RF power, ECRH is applied in present day machines and is also foreseen in large forthcoming fusion projects: it will be the main heating system for the stellarator W7-X which is currently under construction and it will play a major role in the ITER tokamak. In particular, advanced tokamaks are and will be operated in plasma regimes where MHD instabilities are probably limiting the performance. To a large extent the stability in a tokamak is influenced by the distribution of the internal plasma currents which can be manipulated by the injection of RF waves. The location of the absorption of RF waves with the angular frequency ω is dependent on the resonance condition $\tilde{\omega}-k_z v_z=\omega_c$ (k_z: axial(z)-component of the wave number, v_z: electron velocity along z-axis). Thus, by changing the wave frequency ω the absorption can be moved to any radial position where the local cyclotron frequency of the electrons ω_c holds for the expression above.

Today, fusion gyrotrons in the relevant frequency range (between 100 GHz up to 300 GHz (for future devices)) with an output power of minimum 1 MW are designed for fixed frequency operation. Future frequency tunability will require additional optimization of all the major gyrotron components, the electron beam forming optics, the interaction cavity, the quasi-optical mode converter, the RF output window and, finally, the collector.

For experiments on plasma stabilization at ASDEX Upgrade (IPP Garching) with advanced ECRH and ECCD, step-frequency tunable (105 – 143 GHz) 1 MW gyrotrons operating at continuous-wave are strongly requested.

In 2012, major progress has been made in the Brewster angle window technology and in the performance of the gyrotron operation at KIT.

CVD diamond Brewster window development

For 2012 it was planned to introduce the already brazed CVD diamond window into the housing and to perform an experimental study with a new window using the step tunable gyrotron.

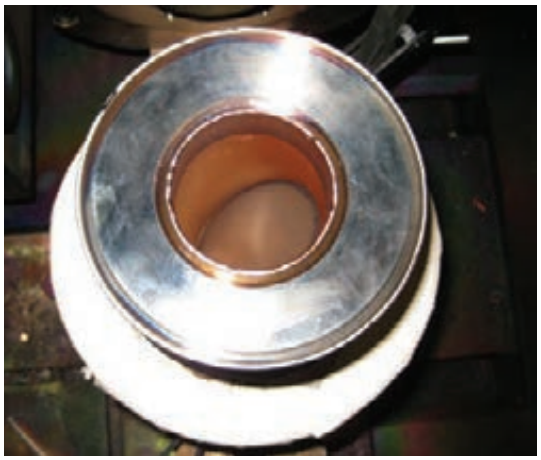

Fig. 1: CVD diamond Brewster window after welding into the housing .

The housing for the new window was designed and produced, however, vacuum tests of the window have shown vacuum tightness only on one side of the brazing. Therefore, that vacuum tight side was used as the inner one.

The copper cuffs of the diamond window were welded using electron beam welding technology to the housing. After successful UHV tests the window was prepared for the installation into the gyrotron (see Fig. 1).

Low power measurements with new CVD diamond Brewster window

Before installation into the gyrotron, “cold” tests with the full set of quasi-optical system were done, using a vector network analyzer.

Earlier tests using a quartz Brewster window did show, that the spatial distribution of the power in the output beam has multiple maxima, and, as a consequence, a low Fundamental Gaussian Mode Content (FGMC). Related measurements of the multiple maxima had been done using a thermo-imaging camera. As the reason for this beam deterioration the quartz Brewster window itself was suspected. Careful inspection of the surface of the window revealed traces of damages, probably due to overheating. It has been concluded that the inhomogeneity of the window surface disturbs the phase front of the beam and introduces higher order Hermite–Gaussian modes in the field distribution. To compare these results with the results using the diamond window, comparative measurements of the quasi-optical system equipped with the quartz Brewster window, the new CVD diamond Brewster window and without window have been performed. In Fig. 2 the power distributions measured with the two types of Brewster windows (quartz and CVD-diamond) and without window are shown. As can be seen, the distribution of the RF power measured after the quartz Brewster window shows multiple maxima. It strongly deviates from the expected Gaussian distribution. This is in agreement with experimental measurements performed earlier using the step tunable gyrotron. In contrary to these results, the RF power distributions measured using the CVD-diamond window, as well as without window, show the expected single peak distribution.

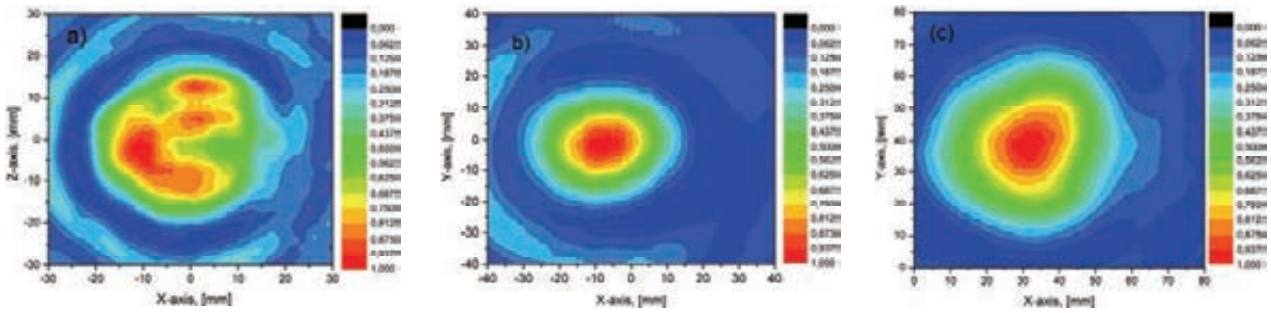

Fig. 2: Power distribution measured from: a) quartz Brewster window, b) CVD-diamond Brewster window, c) without window.

Measurements of the gyrotron performance with installed CVD-diamond Brewster window

After low power measurements the CVD-diamond Brewster window was installed in the step tunable gyrotron. Measurements with 1 MW RF output power were prepared. The basic configuration of the step tunable gyrotron was kept constant, only the quartz window was replaced. Thus, it was possible to compare the final performance of the gyrotron using those two different types of windows.

Table 1: Measured and predicted FGMC

Mode	Frequency, [GHz]	Measured FGMC, %	Projected FGMC, %
$TE_{20,7}$	124.1	92.5	93.4
$TE_{22,8}$	140.1	93.9	93.3
$TE_{23,8}$	143.3	96.0	91.7
$TE_{24,9}$	155.92	86.3	--
$TE_{25,9}$	159.2	89.3	--
$TE_{26,9}$	162.5	87.3	--

The measurements using the CVD-diamond Brewster window demonstrated a significant improvement in the Fundamental Gaussian Mode Content (FGMC). A first analysis showed that the values of FGMC are in accordance with the original designed values, which had been verified by numerical simulations using the “Surf3d” code package.

The FGMC measured for the modes $TE_{20,7}$ and $TE_{22,8}$ are in excellent agreement with the predicted values, while for $TE_{23,8}$ the FGMC is even bit better. The quasi-optical system was not projected for $TE_{24,9}$, $TE_{25,9}$ and $TE_{26,9}$, therefore, it has been expected that the beam properties and the final FGMC values are lower in comparison with the operating modes $TE_{20,7}$, $TE_{22,8}$ $TE_{23,8}$. For these modes the QOS had been optimized. The measured intensity of the spatial distributions of the RF power measured with a thermo-imaging camera is shown in Fig. 3. The profiles from non-optimized modes show larger contribution from side lobes.

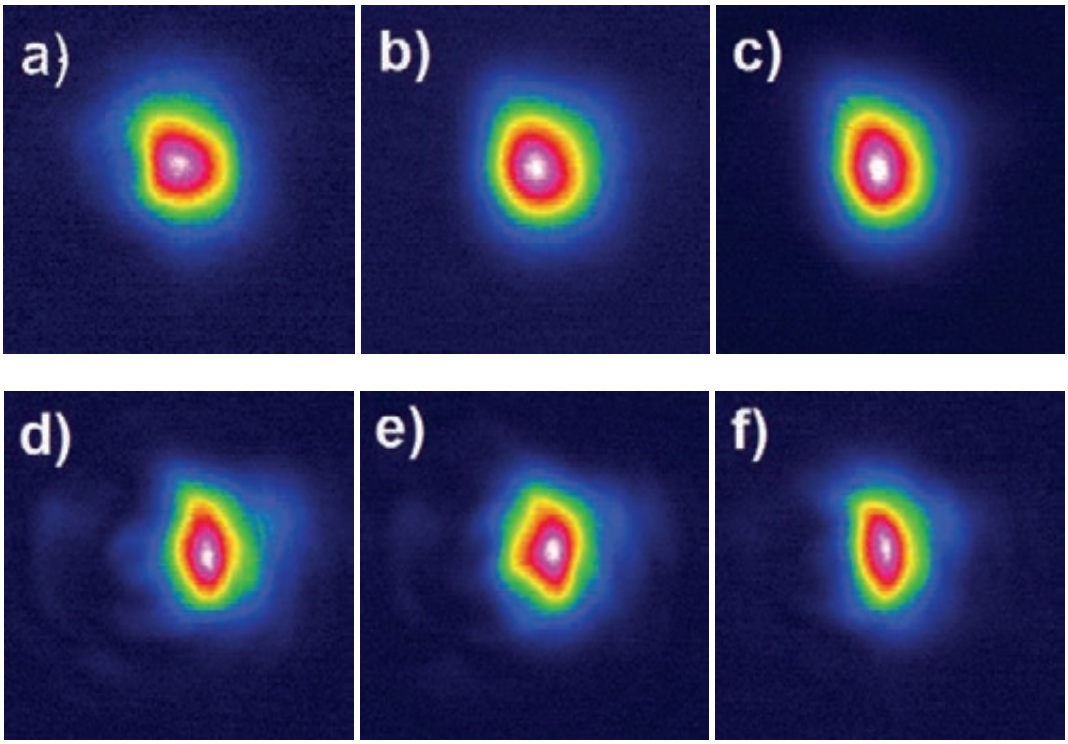

Fig. 3: Intensity spatial profile measured by termocamera for : a) TE20,7 mode, b) TE22,8 mode, c) TE23,8 mode, d) TE24,9 mode, e) TE25,9 mode, f) TE26,9 mode.

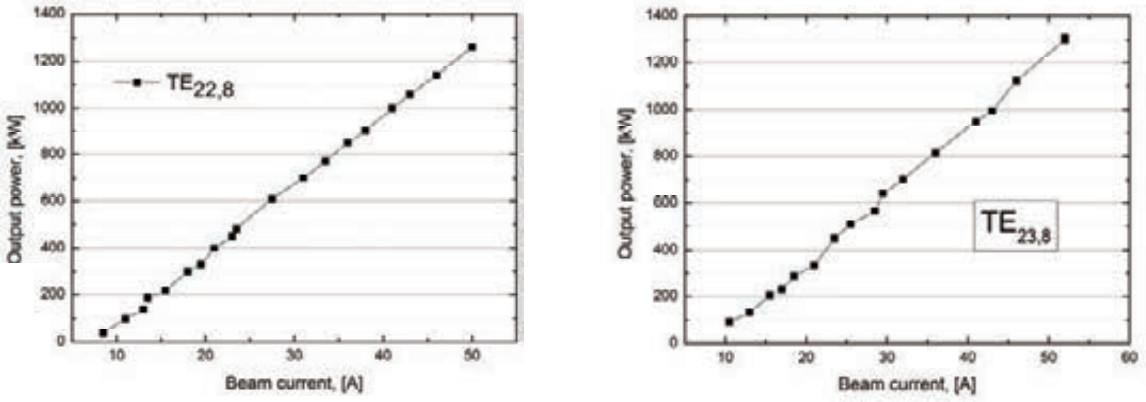

Fig. 4: Power dependency on beam current for TE22,8 and TE23,8 modes.

The RF power measurements showed that the gyrotron is capable of producing up to 1.3 MW RF output power in short-pulses. Measurements with beam currents above 50 A were not performed because of the limitation of the power supply used for heating. The transmission of the RF output power through the window was possible without any problem. As an example, fig. 4 shows the dependencies of the RF output power on the beam current for $TE_{22,8}$ and $TE_{23,8}$ modes.

Table 2: The power and efficiency for a number of experimentally studied modes

Mode	Frequency, [GHz]	U_{cath}, [kV]	I_{beam}, [A]	Power, [kW]	Efficiency, %
$TE_{20,7}$	124.1	91.7	42	900	23.4
$TE_{21,7}$	127.4	90	42	920	23.8
$TE_{22,8}$	140.1	91	40	1000	27.5
$TE_{22,8}$	140.1	91	50	1250	26.5
$TE_{23,8}$	143.3	90.3	40.5	1020	27.7
$TE_{23,8}$	143.3	92.9	52	1300	27
$TE_{25,9}$	159.2	92.3	40	974	26.2
$TE_{26,9}$	162.5	92.3	41	950	25.7

Table 2 shows the dependencies of the RF power and the gyrotron efficiency for a number of experimentally studied modes from the beam current.

The total RF output power and gyrotron efficiency are at comparable values as it was observed in the previous studies in 2011 using the quartz-Brewster window. Therefore, the improvement of the gyrotron performance results mainly from the quality of the RF power distribution at the window. Important to note, the operation of the gyrotron with a new CVD diamond Brewster window showed that previously observed parasitic oscillations at lower frequencies (at 5 – 6 GHz lower than the frequency of the working mode) with BWO-like dependence on the cathode voltage and magnetic field did not appear for any measured mode.

The operation of the gyrotron was accompanied by the appearance of parasitic low frequency (LF) oscillations in the region 105 MHz, which was already observed in the earlier set-up. It is assumed, that those parasitics occur due to the oscillation of space charges in the electron beam. In order to get rid of these oscillations, the optimization of electron optics magnetron injection gun would be required.

Investigation of the dependence of the electron beam on the performance of the step tunable gyrotron

An experimental study on the influence of the lateral misalignment between the axis of the annular electron beam and the cavity is performed. The dependence of the output power by the oscillation of $TE_{22,8}$ mode are shown in Fig. 5. The output power has maximum at optimal alignment of electron beam to the caustic of the mode and gradually reduced with a lateral shifting of the beam away from a maximal coupling. The power of the working mode scales linearly with the cathode voltage also in the case of off-axis beam. In addition, the measurements show that at large beam misalignment the excitation of concurrent counter rotation mode is possible. The data is interpreted qualitatively in the frame of theory. The results of the study will be published in IEEE Transactions on Plasma Science.

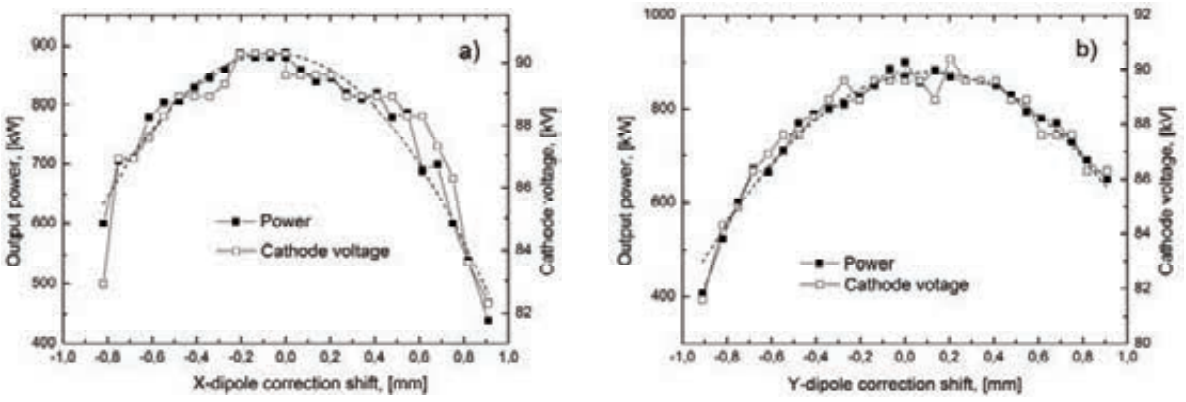

Fig. 5: Output power and cathode voltage as a function of applied beam steering: a) – steering in X-direction, b) –steering in Y-direction.

The measured data have a practical application for the development of gyrotrons, because from this data one can obtain an acceptable range of tolerances of the production. This study suggests that the setup of gyrotron in cryostat have to be equipped with X-Y table for an adjustment in the lateral direction perpendicularly to the gyrotron axis.

Development of a new code for numerical simulation of gyrotron performance

A self-consistent time-dependent multimode code with particles has been developed to simulate the interaction in a gyrotron (GyroDyne). The motion of particles is calculated from first principles; therefore the inhomogeneity of the static magnetic field in the resonator region and various beam imperfections can be easily taken into account. The code is based on a model in which the transverse dependence of the radiation field is expanded in a set of waveguide modes. In contrast to standard models based on a such approach, like SELFT, the numbers of assumption to speed up of calculations are removed from the treatment. The code is already used in the design of a technological second harmonic 28 GHz gyrotron.

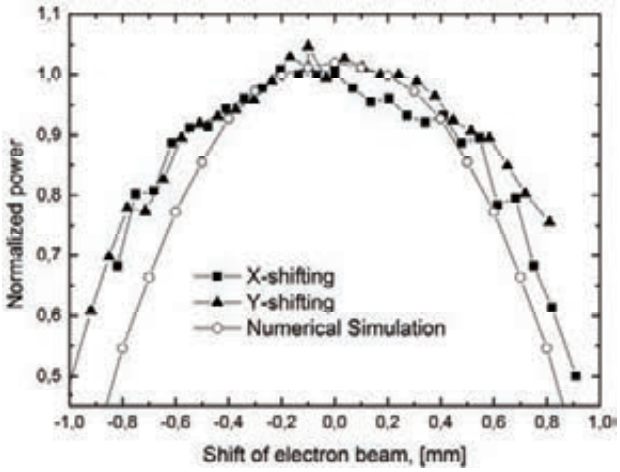

Fig. 6: Output power measured experimentally and from simulation by GyroDyne.

The code is applied to simulate the power output for various beam shifts. In total 8 modes were taken into account in simulation: $TE_{22,8}$+-, $TE_{21,8}$+-, $TE_{23,8}$+-, $TE_{19,9}$+-, because the frequencies corresponding to oscillations at these cavity modes with such indices were observed in the experiment.

The beam parameters used in simulation are the following: pitch factor 1.3, beam current 40A, no spread of velocity and energy is used.

As one can see from Fig. 6, numerical simulation shows more steep decay of the power with beam shift in contrast to the experiment. This can be explained by the fact that in the numerical simulation idealized particle beam was used.

New numerical simulation are under way where the spread of the guiding center of particles is introduced in addition to the expected spread of velocity and energy, or in other words, to use thicker, more realistic, annular beam.

Further improvements of the code are under way.

Staff:

D. D'Andrea
G. Dammertz
J. Flamm
G. Gantenbein
S. Illy
S. Kern
W. Leonhardt
M. Losert
J. Jelonnek
J. Jin
D. Mellein
A. Papenfuss
T. Rzesnicki
A. Samartsev
T. Scherer
A. Schlaich
M. Schmid
R. Schneider
W. Spieß
D. Strauss
J. Szczesny

Fusion Researcher Fellowship (WP11-FRF-KIT/D'Andrea)

Simulations on Start-up and Parasitic Modes Analysis in a TE_{12} Cavity Resonator

In order to evaluate a new type of controlled-porosity reservoir emitter, a 10kW/28GHz gyrotron has been designed. Initially, a self-consistent single-mode code was used to optimize the cavity. Two modes were selected at the second harmonic of the cyclotron frequency: $TE_{1,2}$ with the cavity radius 9.08 mm and beam radius 3.13 mm and $TE_{3,1}$ with the cavity radius 7.16 mm and the same beam radius as for the $TE_{1,2}$ mode. The main competing mode is the $TE_{1,1}$ mode on the first harmonic of the cyclotron frequency. In order to suppress the excitation of this mode, a proper profile of the magnetic field had to be chosen. As a first assumption we took a constant magnetic field along the cavity profile. The fig. 1 shows the efficiency versus magnetic field calculated with the self-consistent single-mode code for the $TE_{1,1}$ (first harmonic) and $TE_{1,2}$ (second harmonic) modes. One can see that from B=0.424 T there is a transition from $TE_{1,1}$ forward wave, to the backward wave. In addition, one can see that at the region of the $TE_{1,2}$ generation there is also the presence of a $TE_{1,1}$ backward wave. The introduction of the non-uniform magnetic field restricts the excitation zone of the mode $TE_{1,1}$ and the mode $TE_{1,1}$ is not exited at magnetic fields for which the the $TE_{1,2}$ mode is excited. In contrast to the $TE_{1,2}$ interaction simulations, calculations of the $TE_{3,1}$ cavity showed that the non-uniform magnetic field does not help to suppress the $TE_{1,1}$ mode.

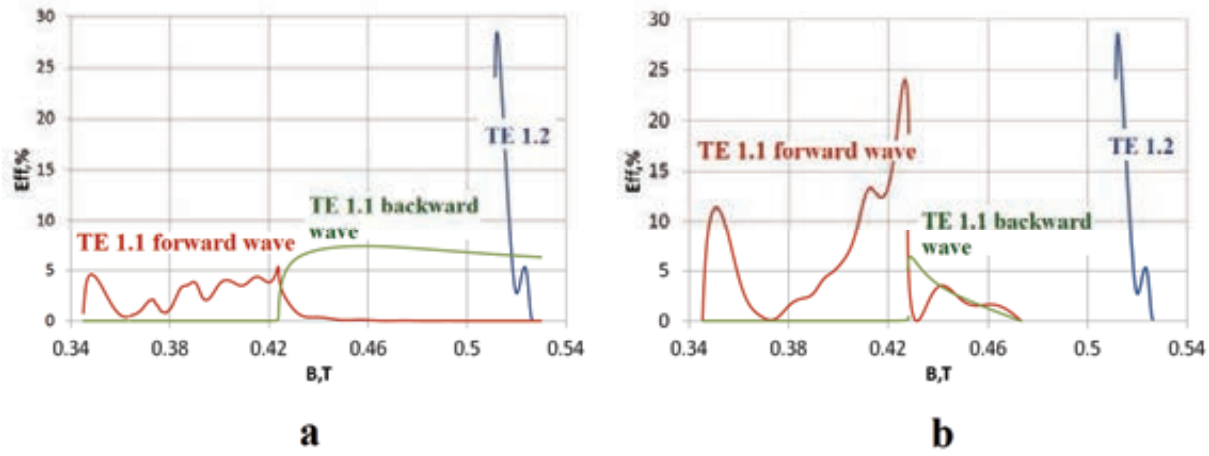

Fig. 1: Dependence of the efficiency for the modes $TE_{1,1}$ and $TE_{1,2}$ vs. maximum value of the magnetic field, in the case of (a) constant magnetic field; (b) non-uniform magnetic field.

For multi-mode non-stationary start-up calculations of the gyrotron resonator, the highly flexible, high-order HALO-PIC code was used. This work and its results represent a new frontier in the exploitation of HALO-PIC potential. Using the HALO-PIC code the $TE_{1,2}$ cavity was discretized by splitting in ~32000 tetrahedrons, the field and particle solvers are set to an 4th order of approximation and the calculations were performed on 128 processors. The results presented in the last figure show the B_z pattern at 150 ns, corresponding to a beam energy of 20 keV. In these simulations it was shown that for the cavity with $TE_{3,1}$ operating mode it is not possible to avoid the generation of the parasitic mode $TE_{1,1}$ on the first harmonic of the cyclotron frequency. For the cavity with the $TE_{1,2}$ main mode, simulations with uniform magnetic field showed the excitation of the parasitic mode $TE_{1,1}$. Simulations for non-uniform magnetic field are in progress.

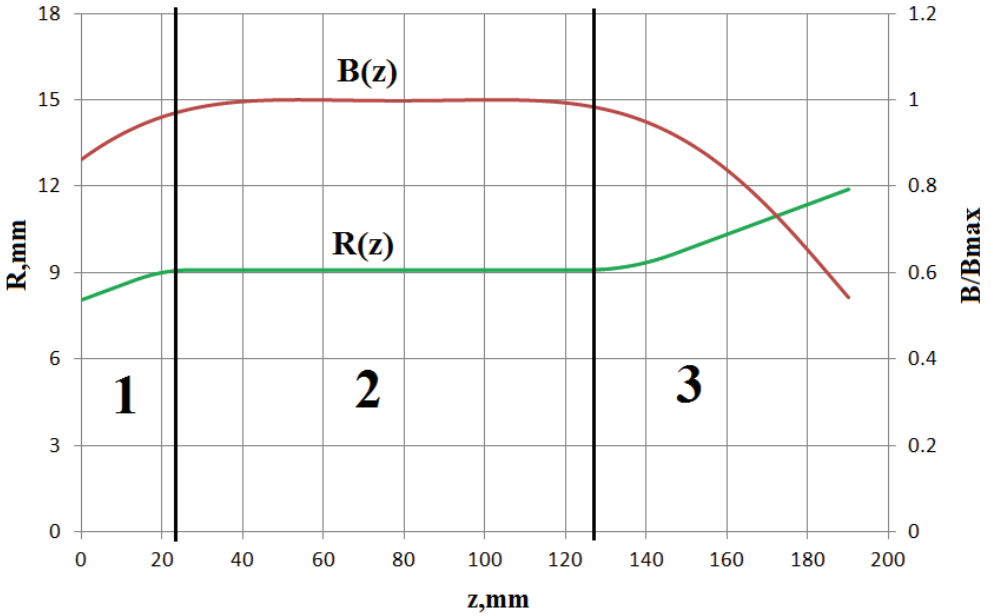

Fig. 2: Green line: cavity profile ((1) - down-taper, (2) - constant part, (3) - up-taper); red line non-uniform magnetic field profile.

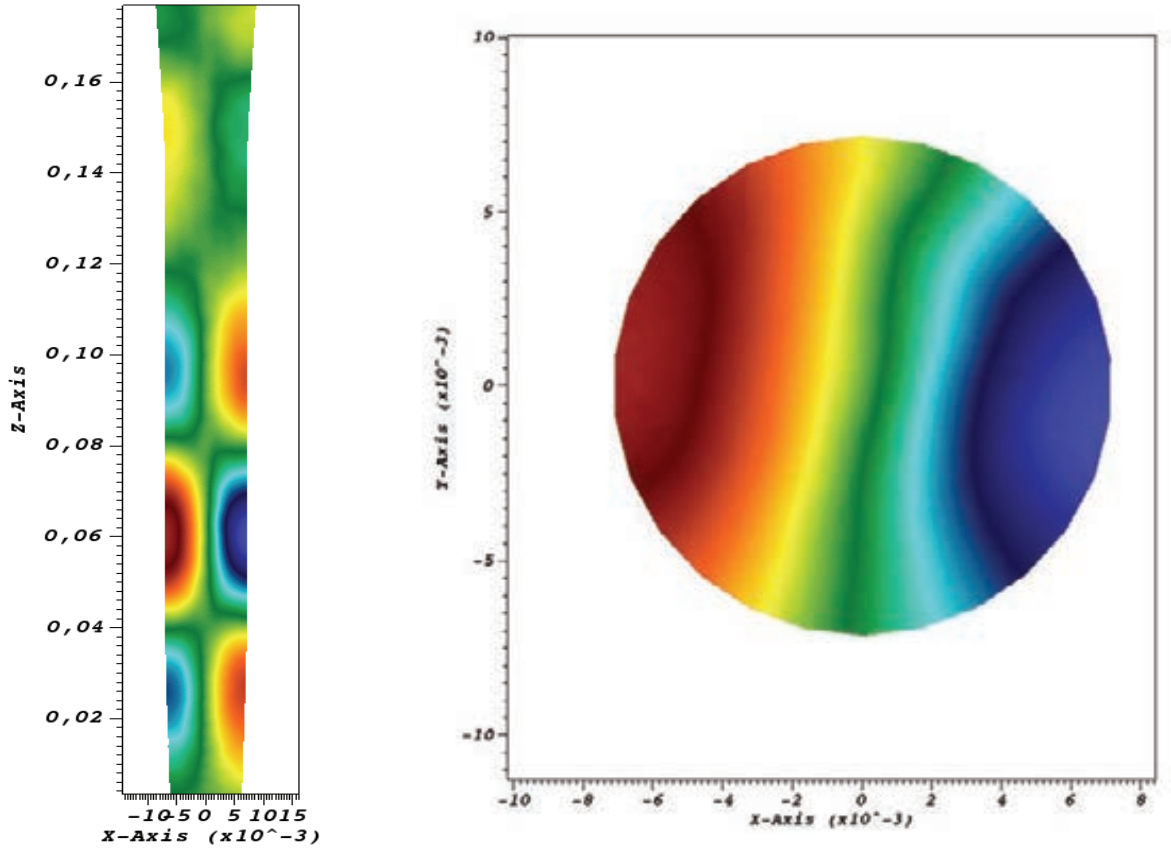

Fig. 3: B_z RF field profile in the XZ (left) and XY (right) cross section of the $TE_{1,2}$ resonator showing $TE_{1,1}$ mode

Staff:

D. D'Andrea
S. Illy

Acknowledgement

This work, supported by the European Communities under the contract of Association between EURATOM and Karlsruhe Institute of Technology, was carried out within the framework of the European Fusion Development Agreement. The views and opinions expressed herein do not necessarily reflect those of the European Commission.

Design, Analysis and Documentation to Produce the ITER EC H&CD Upper Launcher Final Design – Part 1 (F4E-GRT-161-01)

Part A

In the framework of the contract F4E-2010-GRT-161, several analyses have to be carried out for the ITER ECH&CD Upper Launcher (UL) and all its associated components. A seismic analysis of the UL was performed using the *response spectrum* (RS) method in the case of the seismic event SL-2 [1] and stresses and displacements were calculated. An important UL component is the chemical vapor deposition (CVD) diamond window unit which acts as confinement barrier allowing transmission of mm-wave beams between 1 and 2 MW at the same time. The unit was simulated by CFD, thermal and structural analysis to calculate the thermal stresses due to the mm-wave beam power absorption in the disc. ANSYS Workbench and ANSYS CFX were used for such analyses and the results are here reported.

Seismic analysis of the UL

The RS approach works in the frequency domain. It is based on the modal analysis of the structure and the input is the floor response spectrum (FRS) which is a plot of maximum acceleration versus frequency. This approach gives positive results only as information about phase angle among the modes is lost and appropriate modes combination methods must be used to provide the final results.

FRS to be used in the analysis were provided by [2] for the radial, toroidal and vertical directions. The analysis was performed for two geometric configurations: "UL" by applying the FRS at the UL support flange and "UL plus upper port" by applying the FRS at the connection point between the vacuum vessel and the upper port. Fig. 1 shows the two geometric configurations. Three point masses were used to take account for the inertial effects of the internal shield back, mirror box and internal shield front. SS 316L(N)-IG is used as material, but equivalent densities are applied to the double wall section since this is modelled as a single wall.

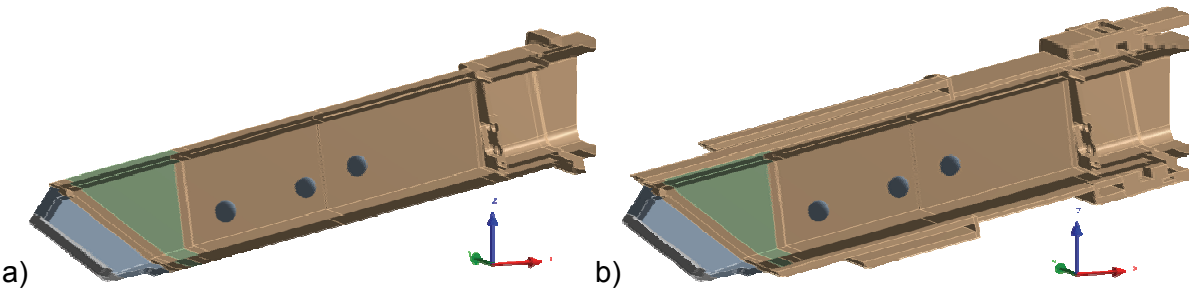

Fig. 1: Cross-section view of the UL (a) and UL plus upper port (b) geometric configurations used for the seismic analysis of the UL. Internal components are considered using the point masses and the different colours indicate the different used materials.

Three RS analyses were performed for each geometric configuration in correspondence to the three directions of seismic excitation (radial, toroidal and vertical directions). For each RS analysis, the results of all considered vibration modes were obtained using the combination method SRSS (Square Root of Sum of Squares). Then, the displacements calculated by the three RS analyses for each geometric configuration were combined together by Newmark's rule in order to obtain the maximum total displacement of the UL. Newmark's rule cannot be applied to the stresses and, since the vertical seismic excitation is very much higher than the other two excitations, the maximum equivalent stress of the UL was taken from the RS analysis in the vertical direction.

For the "UL" geometric configuration, the maximum total displacement of the UL amounts to 0.64 mm. It is located at the UL front and most of this displacement is in the vertical direction.

The maximum equivalent stress of the UL is 19 MPa and it is located at the upper corners of the UL closure plate.

For the "UL plus upper port" geometric configuration, the maximum total displacement of the UL is 1.57 mm and the maximum equivalent stress of the UL is 26 MPa.

CFD, thermal and structural analysis of the window unit

The design of the diamond window unit was updated and Fig. 2 shows the new geometric configuration. It is symmetric with respect to the *xy* plane and also to the middle plane of the diamond disc. There are two inlet pipes and two outlet pipes. The disc is brazed to the copper cuff which forms a single component with the copper cooling channel. The channel is then welded to the SS waveguide through the nickel spacer ring and welded to the SS middle ring through the nickel upper ring. It should be noted that the disc is not in contact with the SS waveguide, there is a gap of 0.1 mm in between them.

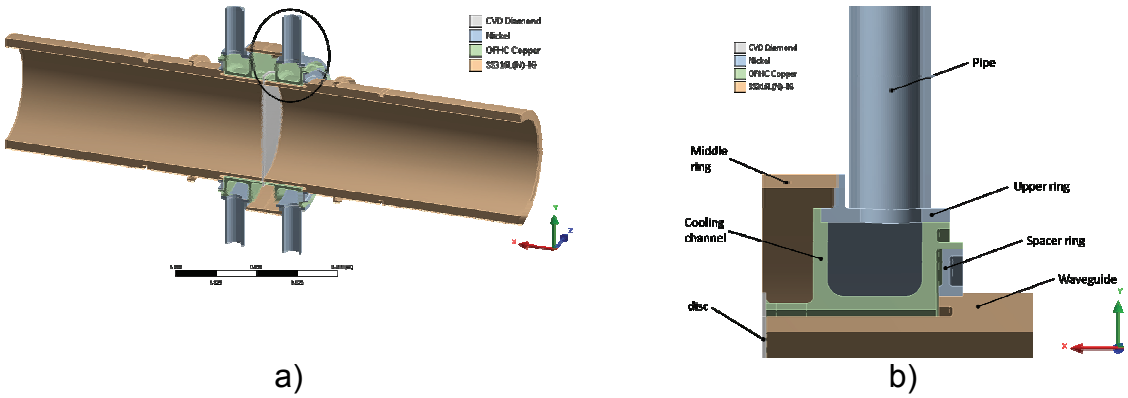

Fig. 2: View of the new geometric configuration of the diamond window unit (a). Materials of the window unit are shown. The portion of the configuration marked by a black circle is shown in detail in (b).

First, a CFD analysis of the window unit was carried out in order to calculate the pressure drop and the heat exchange coefficient profile along the cooling path. Fig. 3-a shows the CFD model which consists of the water domain only. The mass flow rate considered for the complete window unit was 20 l/min (0.333 kg/s). A reference pressure of 0 Pa was applied to the outlet. The inlet water has a reference temperature of 20°C, which can be considered constant along the cooling path. Water properties defined in the CFX library were used. The analysis has led to a pressure drop of 0.056 bar along the cooling path and to a mean value of the heat exchange coefficient along the cooling interface of 65341 W m^{-2} K^{-1}.

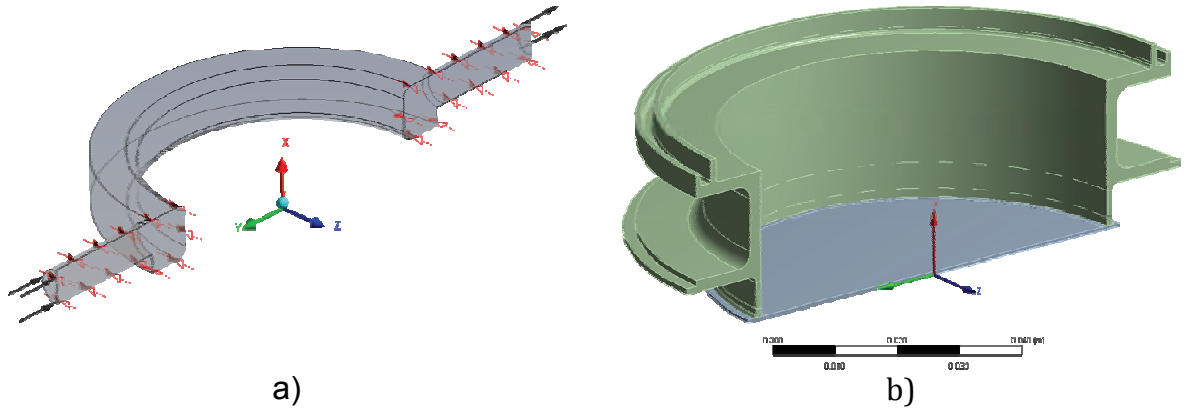

Fig. 3: The CFD model (a) and the geometry of the diamond window unit used for the thermal analysis (b) correspond, due to symmetry reasons, respectively to a quarter of the complete cooling circuit and to a quarter of the complete geometric configuration of the unit.

The thermal analysis of the window unit was then performed to calculate the temperature distribution in the unit due to the mm-wave beam power absorption in the disc. The heat exchange coefficient profile calculated by the CFD analysis was interpolated at the surfaces in contact with the water. HE_{11} mode beam was considered and the heat generation load was applied to the disc in terms of volumetric power density distribution according to this beam pattern. Fig. 3-b reports the geometry of the window unit used for the analysis. It consists of the diamond disc and the copper cooling circuit only since the other parts do not give any contribution to the cooling. Constant, temperature dependent and non linear material properties were used in the analysis [3, 4, 5]. The analysis was carried out for thickness values of the disc 1.111, 1.481 and 1.851 mm and values of the beam power 1 and 2 MW. Fig. 4 reports the temperature profiles along the disc diameter for the several considered cases of disc thickness and beam power. As expected, the maximum temperature is located at the centre of the disc.

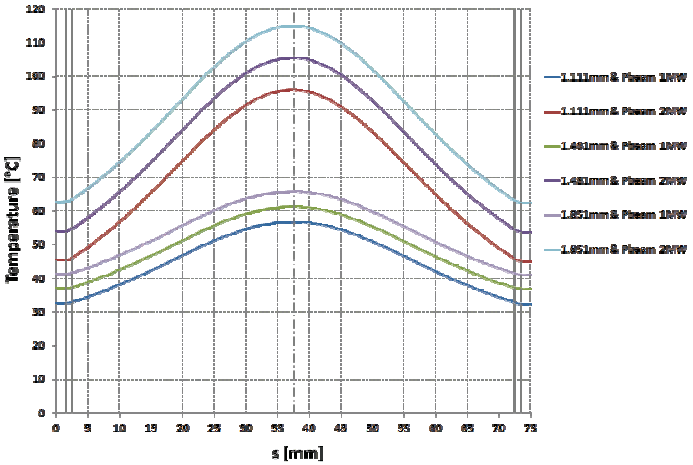

Fig. 4: Temperature profiles along the disc diameter for the three values of disc thickness and two values of beam power. The position of the axis of symmetry and the copper cuffs is also shown.

Finally, the temperature distribution calculated by the thermal analysis was applied in a structural analysis of the diamond window unit in order to calculate the thermal stresses. Looking at the Fig. 3-b, symmetry conditions were applied to the *xy* plane and to the middle plane of the disc and a fixed support was applied to the interface with the nickel spacer ring. In the brittle diamond the first principal stress was used as result while for the ductile copper the von Mises or equivalent stress was checked. Table 1 shows the maximum stresses which are located at the contact region between the diamond and the copper. Looking at the principal stresses, it can be noted that the values are very far from the 150 MPa permissible stress of CVD diamond (ultimate strength is 450-500 MPa [6]). However, looking at the equivalent stresses, it can be observed that a very small plastic behaviour of the copper starts occurring when the beam power is 2 MW (yield strength of OFHC copper is 45 MPa at 20°C [5]).

Table 1: The maximum first principal stress in the disc (a) and the maximum equivalent stress in the copper cooling circuit (b) are reported for the values of disc thickness and beam power. Units are in MPa.

	P_{beam} = 1 MW	P_{beam} = 2 MW
1.111mm	15.6	35.4
1.481mm	22.3	43.9
1.851mm	29	47.9

a) First principal stress

	P_{beam} = 1 MW	P_{beam} = 2 MW
1.111mm	22.3	46.8
1.481mm	31	45.8
1.851mm	39.4	46.6

b) Equivalent stress

Staff:

G. Aiello
A. Meier
T. Scherer
S. Schreck
P. Spaeh
D. Strauss
A. Vaccaro

Literature:

[1] Load Specifications, ITER_D_222QGL v6.0.

[2] Global Tokamak Seismic Analysis Report, ITER_D_33W3P4 v2.1.

[3] D.C. Harris, Infrared Window and Dome Materials, SPIE, 1992.

[4] Y.S. Touloukian et al., Thermophysical Properties of Matter - Vol. 5.

[5] M. Merola et al., ITER plasma facing component materials database in ANSYS format, ITER Doc. G17 MD 71 96-11-19 W 0.1, 1997.

[6] M. Thumm, State of the Art of High Power Gyro-Devices and Free Electron Masers, KIT Scientific Reports 7575, Update 2010.

Part B

Overview

In the frame of the new grant started in November 2011 between Fusion for Energy (F4E) and the ECHUL-CA consortium, the development process of the Electron Cyclotron Heating and Current Drive (EC H&CD) Upper Launcher (UL) in ITER has moved a step towards the final design phase. A new assessment of the EM loads (Lorentz forces due to the interaction between the static magnetic field and the eddy currents generated during plasma disruptions) is required. The loads acting on the new configuration of the UL, based on the 2009 preliminary design review design, have been calculated for six different disruption scenarios: upward linear (36 ms) and exponential (36 ms) vertical displacement events (VDE), upward linear (36 ms) and exponential (16 ms) major disruptions (MD), category II upward slow and slow-fast VDEs.

The loads obtained by the EM analyses have been applied to a structural model of the UL, the results enabling further design of its structural components.

Electromagnetic model

The EM 20-degree sector model (see 5) features the vacuum vessel's shells, blanket modules with Be-Cu first walls, the equatorial port and plug, plus a more detailed geometry of the upper port and plug and the TF coils. This model is used for analysis of the upper segment of ITER, thus the divertor has a minor influence and is not included.

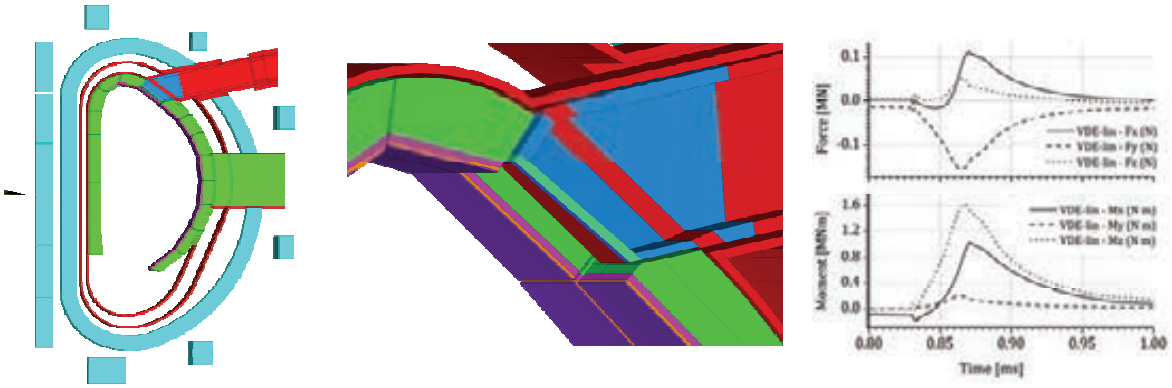

Fig. 5: Snapshots and results of the GRT161 EM 20-degree sector model: conductive material and coils (left); section of the upper port and plug (front part and neighbouring components, middle); EM loads due to an upward linear VDE 36 ms (worst case scenario, right).

The analyses have confirmed the upward vertical displacement event (VDE) linear 36 ms as the worst case scenario. The radial and vertical moments are the most significant loads and are the main responsible of the displacement and the stresses induced on the UL structure.

Structural model

The structural analyses of the UL have been performed on two different configurations: in the first, the UL is modelled alone and fixed at the rear flange; in the second configuration the UL is integrated in the upper port and the fixation is provided at the attachment of the port to the vacuum vessel.

In a first approach, the same simplified geometry of the EM model is used and the loads are directly transferred, node by node, to the mesh. In a second approach, both the UL and the port are subdivided in several partitions (Fig. 6) and partial sets of loads are applied to each segment.

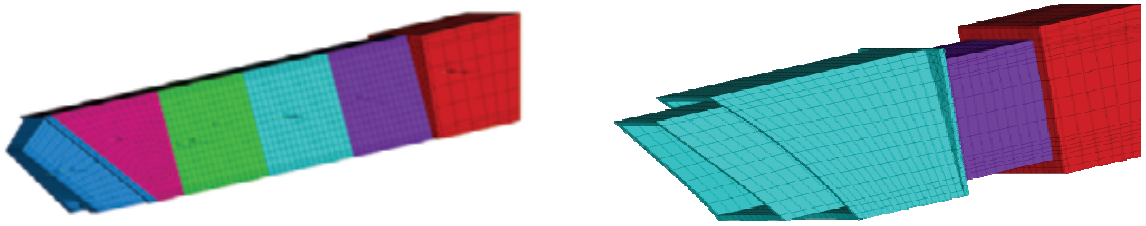

Fig. 6: Mesh and volumes segmentation of the UL (left) and the upper port (right).

Although the two approaches do not return exactly the same results, they both confirm the capability of the mainframe to withstand the very high loads due to the most severe plasma disruption.

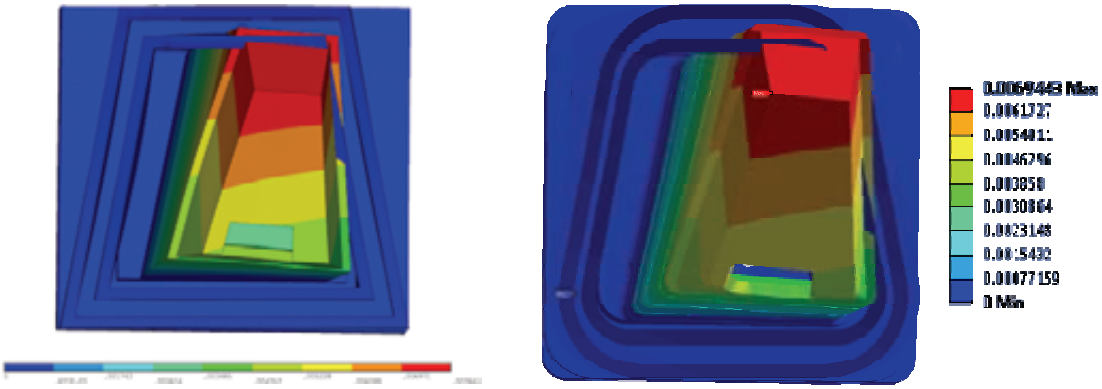

Fig. 7: Total displacement of the UL integrated in the upper port. When the loads are directly transferred to the mesh (left), the maximum displacement is 7.8 mm; when the loads applied to different partitions (right), the maximum displacement is 6.9 mm.

Staff:

D. Strauß
T. Scherer
G. Aiello
R. Geßner
A. Meier
S. Schreck
P. Spaeh
A. Vaccaro

Literature:

[7] Y. Kitazawa and K. Sugiyama, J. Plasma Fusion Res 16, 40 (2001).

[8] D. Strauss, et al., FEM analyses and prototype tests of the UPP structure for the ECRH in ITER, Fusion Eng. Des. 84 (2009) 1799–1802

[9] A. Vaccaro, D. Strauss, et al., Mechanical analysis of the EC upper launcher with respect to electromagnetic loads, Fusion Eng. Des. 84 (2009) 1896–1900.

[10] M. Roccella, Summary of EM Analyses on the Plug Limiter of the Upper Port (draft of results), ITER_D_22LZ98, ITER Org. Int. Document.

[11] A. Vaccaro, et al., The ITER EC H&CD Upper Launcher: Transient mechanical analysis, Fusion Eng. Des. 86 (2011) 851-854.

[12] C. S. Pitcher, Upper Port Plug Exposure to Disruptions in ITER, ITER_D_23HSK3, ITER Org. Int. Document.

[13] R. Gessner, et al., The ITER EC H&CD upper launcher: Design, analysis and testing of a bolted joint for the Blanket Shield Module, Proc. 27th SOFT Conference, Liege, 2012.

[14] Duck-Hoi Kim, et al., Eddy current induced electromagnetic loads on shield blankets during plasma disruptions in ITER: A benchmark exercise, Fusion Eng. Des. 85 (2010) 1747-1758

Teil C

Introduction

The ITER ECH&CD (Electron Cyclotron Heating & Current Drive) system features four upper launchers to inject up to 20 MW of mm-wave-power into the plasma. They will be installed into four upper ports in order to counteract plasma instabilities.

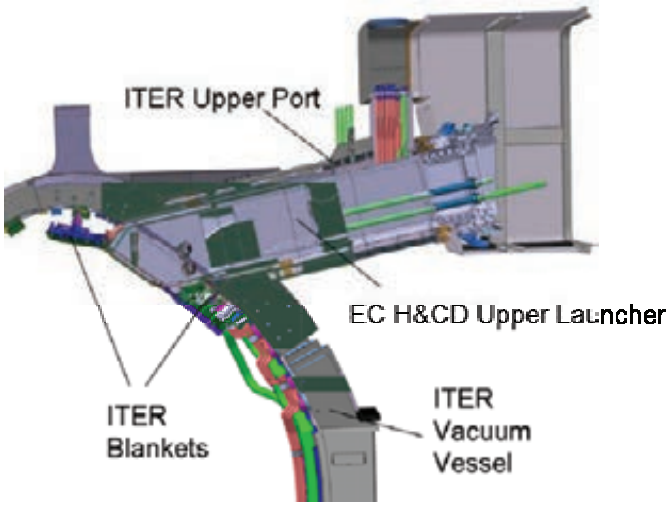

Fig. 8: Outline of the ECRH Upper launcher.

An upper launcher in principle consists of the launcher port plug and the mm-wave system. The port plug forms the casing of the launcher. It accommodates the launcher mm-wave system, which is composed of individual waveguides and a set of mirrors to inject the microwaves precisely to the targeted plasma instabilities. In combination with dedicated shielding elements, the port plug provides protective and accurate installation of the mm-wave components. Figure 8 shows the launcher, mounted in one of the upper ports of the ITER Tokamak.

Preliminary design of the EC H&CD launcher

The preliminary design [15] of the EC H&CD upper launcher, which was finalized and approved at the end of 2009 represented the basic layout of the structural system of the launcher. It includes all individual components, forming the casing of the launcher (typically called “port plug”) and the main internal shielding blocks. Additional features like fasteners, feed-throughs, piping supports were just sketched without specific details. The preliminary design was made according to generic engineering calculations and basic computational

simulations for mechanical strength [16] and for the heat balance. This means, that for instance the maximum deflection of the structural system and the maximum equivalent stresses were concerned as well as e.g. the total heat to be removed referring to the overall flow rate of the cooling system. The structural system consists mainly of two components: The BSM (Blanket Shield Module) and the Launcher Mainframe, which are connected by a bolted joint, capable to be loosened by RH (Remote Handling) procedures [17].

The BSM houses dedicated shielding and also the mirrors M3 and M4 of the mm-wave-system. The BSM is exposed to substantial volumetric heat load of up to 5 W/cm³ plus radiation heat on the FWP (First Wall Panel) of up to 500 W/cm². Thus a proper cooling system is mandatory. The mainframe houses some major shielding blocks and also the mirrors M1 and M2. Its front-part is an actively cooled double-wall, while the middle part is un-cooled and therefore designed as a single wall element, providing sufficient space for internals. The rear part (also called the back-end) consists of the closure plate, forming the main Tritium and vacuum barrier, the socket (a double wall section with water channels in order to support the baking process) and the support flange, which provides cantilevered fastening of the plug inside the port.

After approval of the preliminary design of the ITER EC H&CD Upper Launcher, ECHUL-CA, a consortium of several European research institutes, was founded to pool resources for approaching the final design. At the end of 2011 the consortium has signed a 2-years-contract with F4E to go ahead with the work on the launcher.

The contract deals with design work on both the port plug, forming the structural system, and the mm-wave-system as well. Within the period of this contract all components being part of the Tritium confinement, of which the closure plate, the support flange, the diamond windows and the waveguide feed-throughs are the most outstanding ones, will get the status of the final design.

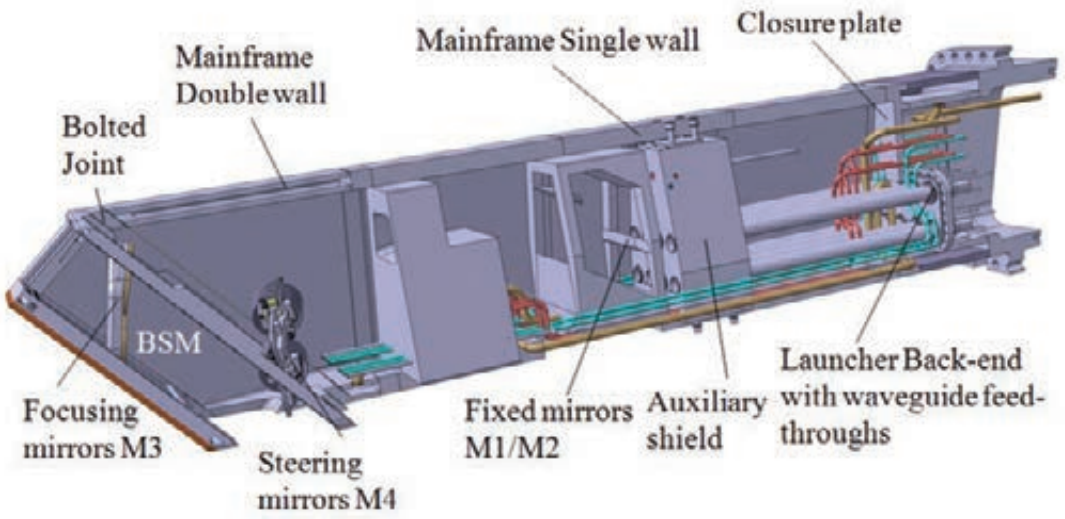

Fig. 9: Cutaway of the EC H&CD launcher (partially updated towards final design).

For the final design it is necessary to complete the structural system by developing all design details and to verify this design by making up all required analyses according to applicable codes and standards and the ITER baseline documentation and also in accordance with the available RH procedures [18]. Important steps that were done for the structural system in 2012 were the optimization of the mechanical behaviour of the launcher, leading to minimum deflections of the port plug during plasma disruptions and optimum seismic resistance. To reduce the effect of halo currents it was decided to recess the first wall of 100 mm compared to the regular blanket tangent. This recess required substantial changes of the cooling sys-

tem and the thermo-hydraulic design of the launcher. Also the layout of the shielding arrangement and the integration of the mm-wave system needed significant revision. Moreover manufacturing aspects and enhanced remote handling capability were taken into account. For the final design also quality aspects are considered; thus the design is elaborated with respect to applicable codes and standards, material specifications, risk analyses and the RAMI (reliability, availability, maintainability and inspectability) analysis to guarantee maximum performance of the device. Figure 9 gives an outline of the present status of the main components and their sub-structures.

Detailing of components

Being important parts of the FCS and influencing the design of RH-devices and the mm-wave system as well, the designs of the waveguide feed-throughs and the auxiliary shield must be preferably investigated in detail. Further design improvement must be performed during this design phase for the joint between BSM and the mainframe and for the cooling channel arrangement of the cooled components, particularly related to manufacturing aspects. The geometry of the BSM needs revision, according to a recess of the First Wall panel of 100 mm and with respect to adjacent components.

Design of the Waveguide feed-throughs

The EC H&CD Upper Launcher features eight waveguide beam lines in order to inject microwave power of up to 2 MW each into the plasma.

The microwaves are guided from the Gyrotrons far outside the Tokamak hall into the plasma by transmission lines and must penetrate the closure plate. The waveguides end inside the launcher shielding area (from where the mm-waves propagate as quasi-optical beams via several mirrors into the plasma). These internal parts are supposed to be cooled (at least their tapered end section) and should be replaceable in case of damage. Guiding the waveguides through the closure plate, which is part of the vacuum- and Tritium confinement) requires a sophisticated design of feed-throughs. The preferred design option is shown in figure 10 and described below.

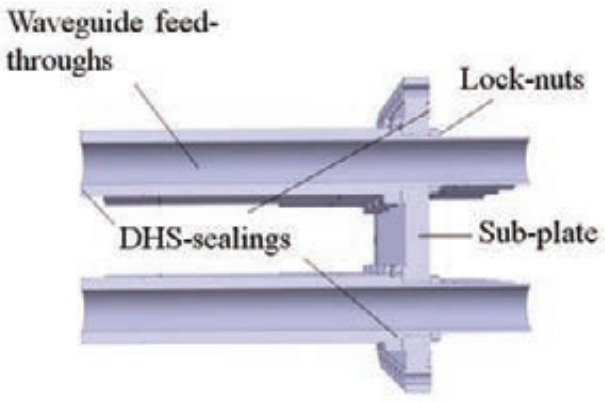

Fig.10: Cutaway of waveguide feed-throughs in sub-plate arrangement (closure plate not shown)

The feed-through design features an assembly with a sub-plate and eight individual waveguide stubs. The sub-plate is bolted to the closure plate and sealed off by a DHS (Double HELICOFLEX® Seal).

The compact design of the assembly allows DHS for the seals between the waveguides and the sub-plate as well. The individual feed-throughs are fixed in the sub-plate as plug-in units with a DHS and held in place by additional ring-nuts at the inside of the sub-plate. They are of different length to allow the use of standard waveguide clamps for DHS-waveguides. These clamps have a diameter of 140 mm. Assuming 134 mm toroidal waveguide-distance, only such a staggered arrangement will be feasible.

The lock-nuts are standard parts in principle, however availability of these items made from SS 316 L(N) must be proven. Individual manufacturing of such lock-nuts might be required. For alignment reasons and maintainability the circular joint fit for the stubs and the sub-plate shall be of H7/h6 or similar quality. Perpendicular alignment of flange surface and beam-line

axis must be guaranteed. The stubs can be manufactured from standard stainless steel rods by turning. Deep drilling of up to 720 mm bores requires special tooling but is seen as feasible.

Design of the Auxiliary shield

The waveguides end inside the launcher in the auxiliary shield. It provides support and alignment of the waveguides. The design update of the auxiliary shield deals with its generic layout, local cooling requirements, handling and fixation and interaction with the waveguides. Since every design step is intimately related to the rest of the launcher in terms of remote handling, cooling concept, thermal and structural aspects etc., a set of design rules is postulated as follows:

- The mean thickness of the auxiliary shield is set at 40 cm according to former results from neutronic analysis [19]. The thickness could be easily increased towards the back end if needed. The distance between the closure plate and the shield block´s rear side is 800 mm.
- The auxiliary shield is classified to be RH-class 3, which would require RH-maintenance in case of failure, why particular features must be implemented into the design. As the present design is very robust and since no access is required to the area behind the auxiliary shield, a revision of the RH-class might be considered for cost reduction (an assessment including failure mode- and risk analysis is ongoing). Ideally the design could be simplified by the shield block being aligned and bolted to the launcher main structure during workshop assembly without the option for RH-maintenance.
- The auxiliary shield serves as support structure for the internal parts of the WGs. It also provides WG alignment and guidance during WG insertion. The waveguide supports must be manufactured with a required tolerance of about 30 µm relative to the ideal waveguide axis.
- Stray radiation heating from mm-waves exposed to the auxiliary shield has to be assessed. The waveguide tapers must be cooled by heat conduction on the loose bearing of the waveguides. These assumptions require active cooling of the shield block.

These main design requirements led to a first design update, shown in figure 11.

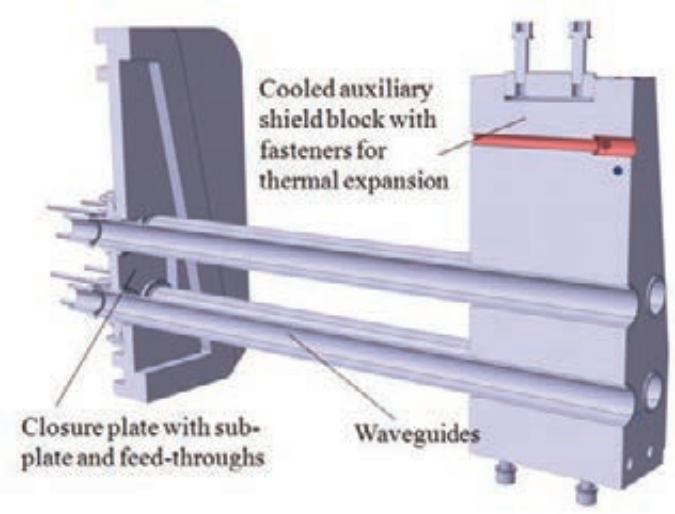

The shield block is fastened to the mainframe by bolts. It features also a sliding element to allow thermal expansion. Additional shear keys in the bottom area are foreseen in order to minimize stresses in the bolts. The shield block will be connected to the PHTS-cooling circuit to ensure proper heat removal from stray radiation and waveguide tapers. Re-shaping of the blocks profile in the bottom area allows guidance of pipes towards the front mirrors.

Fig.11: Cutaway of auxiliary shield block (showing also waveguides and closure plate).

Design update of the BSM

The recess of the First Wall Panel about 100 mm and the replacement of the Be-layer by a stainless steel plate raised the need for an update of the BSM design. The recess was realized by shortening the BSM shell. Manufacturing tests have shown cost reduction about factor of two for machined manufacturing route compared to HIP or welding route. Therefore the former rectangular cooling channels were replaced by machined circular channels. To ensure uniform coolant flow, CFD analysis must be performed and specific chokes must be placed inside the channels [20]. Non-destructive inspection of all welds is considered. The flange design was revised with respect to RH capability. Figure 12 shows the revised BSM from two perspectives.

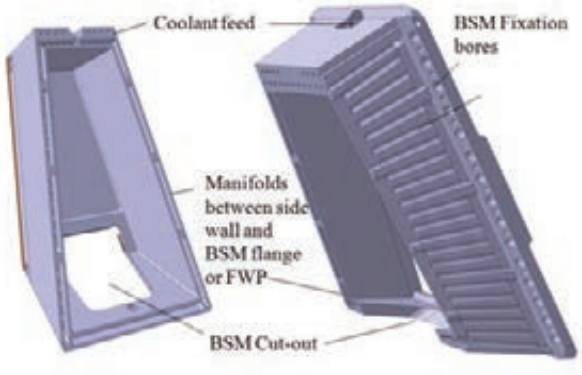

Fig. 12: Partial cutaways of the BSM (FWP not shown here).

Staff:

G. Aiello
R. Gessner
G. Grossetti
A. Meier
T. Scherer
S. Schreck
A. Serikov
P. Späh
D. Strauss
A. Vaccaro
B. Weinhorst

Literature:

[15] D. Strauss et al., Preliminary Design of the ITER ECH Upper Launcher; proceedings of the 27th SOFT conference, Liége, Belgium, 2012

[16] A. Vaccaro et al., The ITER EC H&CD upper launcher: Transient mechanical analysis, Proceedings of the 26th SOFT conference, Porto, Portugal, 2010

[17] R. Gessner et al., The ITER EC H&CD Upper Launcher: Design, Analysis and Testing of a bolted joint for the Blanket Shield Module; proceedings of the 27th SOFT conference, Liége, Belgium, 2012

[18] D. Ronden et al., The ITER EC H&CD Upper Launcher: Maintenance concepts; proceedings of the 27th SOFT conference, Liége, Belgium, 2012

[19] A. Serikov et al., Nuclear-Safety-Related and Shielding Analyses of the ITER Quasi-Optical ECH Launcher, IEEE Transactions on Plasma Science, V. 38, Issue 3, 224 (2010)

[20] P. Spaeh et al., Manufacturing Studies of Double Wall components for the ITER EC H&CD Upper Launcher. Proceedings of the 10th ISFNT conference, Portland, US, 2011

Acknowledgement

This work was supported by Fusion for Energy under the grant contract No. F4E-GRT-161-01 (part of ITA C52TD39FE between IO and F4E in support of the final design of the launcher) with collaboration by CRPP Switzerland, DIFFER Netherlands, CNR Italy and IPP Germany. The views and opinions expressed herein reflect only the author's views. Fusion for Energy is not liable for any use that may be made of the information contained therein.

Manufacturing of ITER ECH Upper Port Plug Structural Systems Prototypes (BMBF-Reference No. 03FUS0010)

Prototyping and Testing

Introduction

The structural system of the port plug consists basically of two main components: -the plasma-facing Blanket Shield Module (BSM) and the Main frame (MF). The structural components have to resist very high Electro-Magnetic loads from disruptions, while they experience substantial thermal cycling during operation. Therefore, a rigid structure to comply with the maximum allowable limits of deflection of the plug is required. The welding of such strong parts usually causes shrinkage and distortion of the welded structure, while the installation of precisely performing mm-wave-systems requires high accuracy. Moreover, dedicated components must be capable to be maintained by Remote Handling (RH) tools. In order to evaluate the performance of such demanding designs, prototyping and testing are essential.

Prototyping and testing of the BSM Joint

The BSM is attached to the Launcher Main Frame by a bolted joint in order to perform Remote Handling maintenance on internal components in the Hot Cell Facility, once the BSM itself has been removed. To fulfill a major aspect of the RH requirements, the joint features captive bolts in order to avoid their accidental loss.

The BSM is mounted to the MF by a bolted joint using two sets of 15 bolts (M22x2), placed along the sides. The flanges are equipped with shear keys of 30 mm depth at all four sides. They serve for release of radial moments and for alignment of the BSM as well. The keys are shaped as to allow removal of the BSM along the launcher axis by RH tools.

The radial thickness of the flanges (normal to the interface) is 100 mm. The lateral or vertical width matches the adjacent double-walls thickness. The flange is made of 316L(N)-IG SS. In order to fix or loosen the bolts, additional pin holes are located in the front flange to take up the torque applied from the bolt runner, which must be decoupled from the arm of the RH device. Side pin holes will be used by a grabber to hold the BSM structure during its removal. Two different views of the flange connection are shown in figure 1.

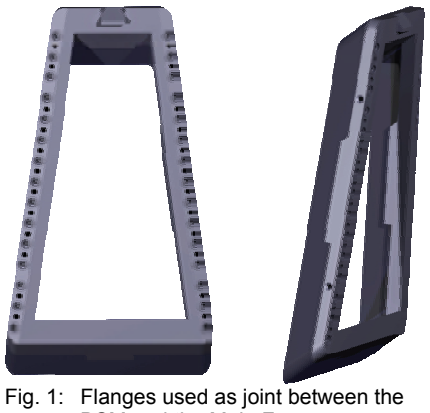

Fig. 1: Flanges used as joint between the BSM and the Main Frame.

In order to meet RH requirements, a captive bolt design was investigated. It is based on a bolt with two threads to secure it in a form-locking stop. In contrast to standard bolts it is pre-stressed by a spiral spring so that loosening is possible by a manipulator. The first thread within the front flange prevents the bolt from falling out accidentally when loosened. The side-mounted cylinder bores are used to hold the tightening torque of the volt-runner, since most manipulators can accommodate only small forces. Because of the minimal available space, the bolts are inclined by about 10 degrees relative to the flange surface and made of the high-temperature resistant material Inconel 718. To keep the shear forces in the threads and also the seating stresses at an acceptable level, inserts will be used in order to increase contact surfaces between the bolt and the flanges. Figure 2 shows the concept of these joints.

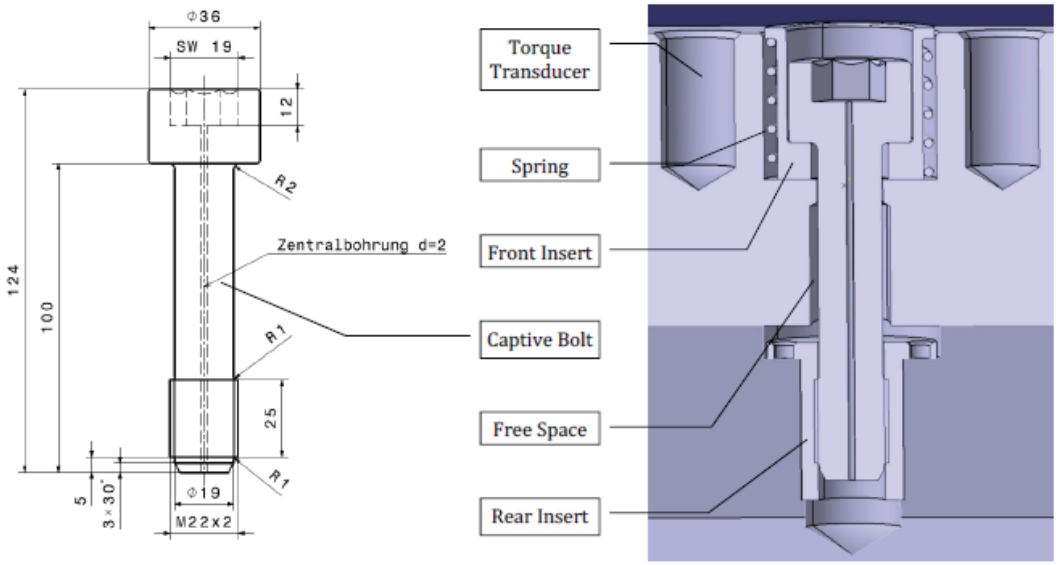

Fig. 2: Captive bolt design as assembly and draft.

For reasons of cost and development risk it was decided to manufacture only the part of the BSM flange connection relevant for the test to be carried out. Therefore, the middle region of the flanges seemed to be an appropriate section, representing all parts of the bolting setup with the rear and front flange, seven captive bolts with associated springs and inserts and the shear keys as well (cf. figure 3).

After successful manufacturing of the flange joint prototype, the mechanical strength and fracture behavior of the captive bolts was tested. Figure 4 shows the experimental setup. All tests were carried out at “Campus Süd” at KIT.

Fig. 3: BSM flange connection prototype.

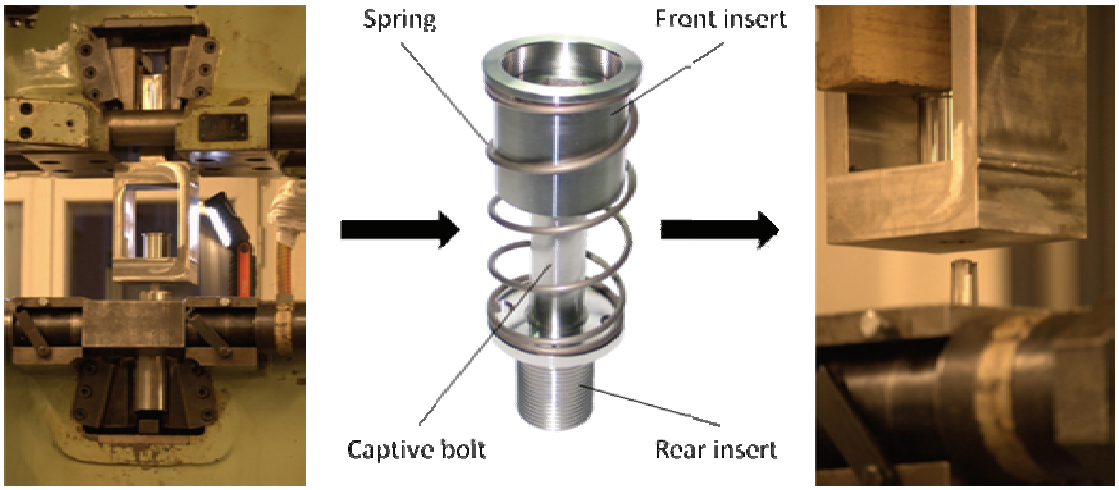

Fig. 4: Tensile test setup.

From the technical point of view the most interesting result of these tests are the force-elongation-diagrams, shown in figure 5. For all test runs the bolts broke in middle of the un-

threaded shank (cf. figure 6). The maximum ultimate strengths and test speeds are shown in table 1. Based on these tests the following results were obtained:

- The bolts made from Inconel 718 have nearly the same elastic/plastic behavior like standard specimen from this material
- The test speed has almost no influence on the force/elongation behavior
- The bolts break as previously calculated in the unthreaded shank
- The theoretically calculated force per bolt of 393 kN was exceeded
- This results in a tensile strength of 1464 MPa

Table 1: Maximum force F_{max} over test speed v.

Test	Max. force F_{max} [kN]	Test speed v [mm/min]
V1	411.5	1
V2	408.6	50
V3	410	125

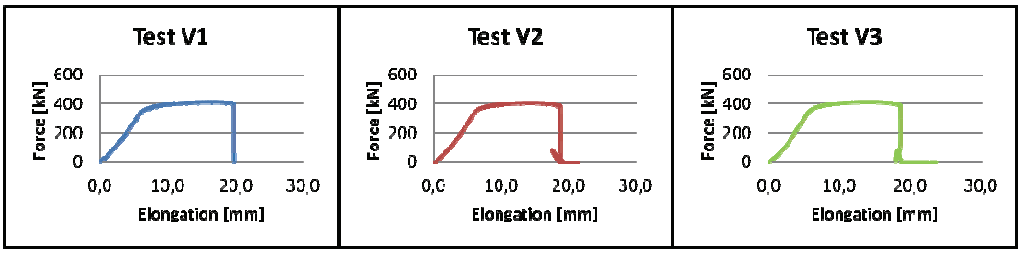

Fig. 5: Force-elongation-diagrams.

Fig. 6: Brocken captive bolts V1-V2-V3.

Additional tests of the prototype in terms of RH compatibility and manufacturing accuracy will be performed. These tests will be part of the 2013 campaign.

Manufacturing of prototypic Double Wall structures

In order to verify the preliminary design of the ITER EC H&CD upper launcher and to identify optimum manufacturing procedures of rigid port plug structures, prototyping of dedicated segments of the launcher structure is mandatory. To identify the preferable design and the optimum manufacturing route, two pre-prototypes were sketched and manufactured in 2011. Based on the results of these test pieces, full-size prototypes for the BSM and the Main Frame double wall section were designed. Both prototypes are under construction yet, why the latest status of 2012 is outlined here.

BSM Prototype

Due to results of the pre-prototyping, which showed better flow characteristics, higher manufacturing accuracy, simplified welding procedures and cost reduction, the BSM full-size prototype was finally designed in accordance with the deep-drilling manufacturing route. Therefore the cooling layout of the BSM shell was revised completely. It features now circular channels of 24 mm diameter, of which three each of them are merged together in manifolds at the front and the rear side respectively. The arrangement of the channels results in a steel/water ratio of about 80/20, which is preferable for optimum shielding capability. The cut-out was adapted to the latest layout of the mm-wave system. Figure 7 shows a front view of the new design with First Wall Panel (FWP) removed.

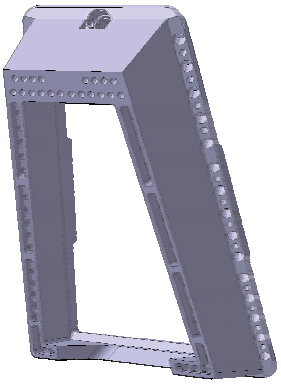

Fig. 7: Front view of the latest BSM prototype design (w/o FWP).

The body of the BSM consists of four stainless steel sheets, which will be jointed together by means of EB-welding. The parameters for the welding procedure have been determined and welding tests have been performed (cf. figure 8).

Fig. 8: EB test welds for the BSM prototype.

The FWP has undergone design revisions as well. The former Be-layer of 10 mm thickness has been removed now and will be replaced by a 3 mm stainless steel layer. This design change will be considered for the prototype as well. The joints between the BSM shell and the FWP and Flange respectively will be made by TIG-welding. The flange will be equipped with captive bolts, requested for RH tests.

The prototype assembly is envisaged for mid of 2013. Comprehensive test campaigns in terms of thermo-hydraulic and thermo-mechanical behavior will follow up.

Double Wall Main Frame (DWMF) Prototype

As for the BSM the DWMF prototype designed was revised in 2012. The rectangular cooling channels were replaced by several sets of circular channels of 30 mm diameter. The cooling layout features meandering flow from bottom to top as it was already sketched for the preliminary design. The DWMF prototype will be assembled from four wall elements, which will be welded by means of EB-weld to create the trapezoidal profile. Two TIG-welded cover plates, on face and rear side, will enclose the body. Figure 9 shows the CAD-model of the prototype. EB- and TIG-weld parameters were

Fig. 9: Cutaway of the latest DWMF prototype design.

determined and a series of test welds has been performed.

The prototype assembly is envisaged for spring of 2013. Comprehensive test campaigns in terms of thermo-hydraulic and thermo-mechanical behavior will follow up.

Industry cooperation

MAN Diesel & Turbo, D-94452 Deggendorf, Germany

Staff:

R. Geßner
G. Grossetti
A. Meier
T. Scherer
P. Späh

Acknowledgement

This work was financially supported by the Ministry of Research and Education (BMBF) under the grant No. 03FUS0010. The views and opinions expressed herein do not reflect necessarily those of the BMBF or the European Commission.

Heating and Current Drive System Integration with Outboard (MMS) Blanket System Task Requirements (WP12-DAS-06-T05-01)

The development of remote maintenance concepts for DEMO is of particular importance within the PPPT work programme, since ITER maintenance scheme for in-vessel components is not power plant-relevant. Therefore, within 2012 work programme, a design integration study of the ECRH and NB heating systems with the outboard multi-module blanket (OB-MMS), has been carried out. Scope of the task has been to provide a requirements analysis, concept generation and evaluation of the remote maintenance for a DEMO fusion power plant.

This study has been carried out considering the following inputs: each OB-MMS to be kept as single unit and toroidal launching angles defined to maximize CD efficiency [1]. Moreover, as details of the internal structure of the blanket modules were not provided, an average value for density has been used, the materials composition of the blanket being provided in [2]. The work has been then divided into three phases:

4. Conceptual study for ECRH and NB launchers configurations to define the openings required. For the former, a Remote Steering concept (see Fig. 1 left)) has been initially considered, and the system has been assumed to operate within small variation from a specific angular set up. For NB, the ITER NB system has been scaled to define the opening sizes and to extrapolate the tangential radius.

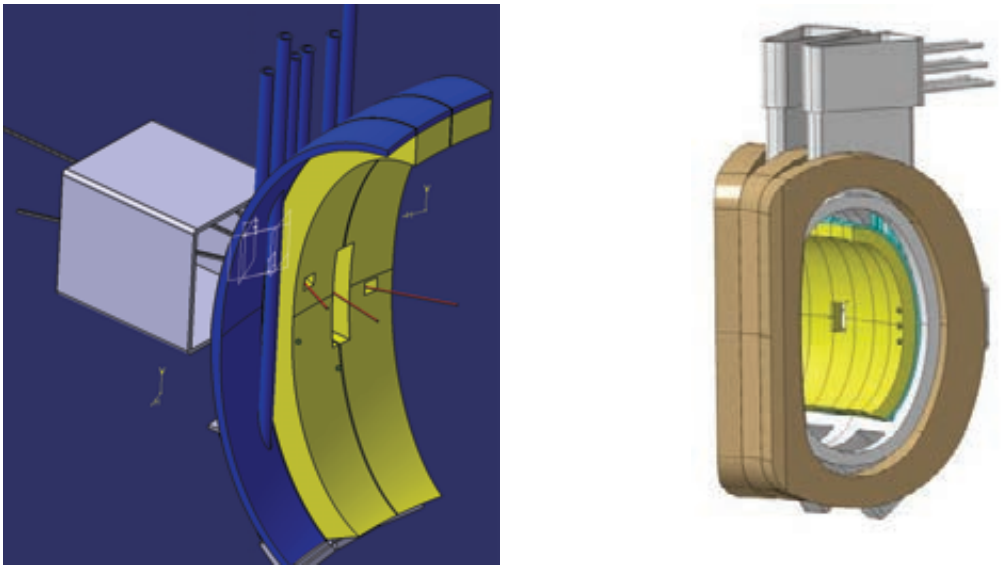

Fig. 1: Left) Sketch of a Remote Steering concept launcher for ECRH and NB in DEMO , Right) Integration of port openings into the MMS Blanket for NB and ECRH systems

5. The CAD model (see Fig. 1 right)) has been modified introducing the port openings an0d coarse port plugs. For ECRH, 3 openings have been inserted into the OB_MMS in a way to maximize Current Drive efficiency. The openings size has been established assuming a high safety factor to be applied to the beam waist at the position of the blanket. For NB, the extrapolation from ITER NB concept leaded, due to the new tangential radius to a port inclination of 28 deg w.r.t. the radial direction.
6. Preliminary structural and electro-magnetic analysis has been carried out. In both cases, two set of analyses have been performed to consider the different densities of the breeding zone in the Helium Cooled Lithium Lead (HCLL) and Helium Cooled Pebble Bed (HCPB) concepts. The results here presented are preliminary, in the sense that a more detailed model (with blanket segmentation and attachments to the manifold) would provide a much more realistic picture of the system and its behaviour.

a) The structural analysis consisted in applying gravity to each single outboard modified MMS. In the CATIA model, the modules are given as a single body (no poloidal segmentation) attached to the related manifold section. The analysis consists of calculating the stresses in the blanket segment that are weakened by the port openings. The preliminary results have shown that, although the structure is obviously weakened by the openings, the stress concentration is not yet significant and in any case not a concern for the structural integrity.

b) The EM analysis has been done considering the modified blankets for reserving access to the ECRH system. Preliminary results shows that the loads on the MMS whether modified or not appear to be similar.

Staff:

G. Aiello
G. Grossetti
D. Strauß
A. Vaccaro

Literature:

[1] E. Poli et al., Assessment of Electron-Cyclotron-Current-Drive-Assisted Operation in DEMO, Proc. Conf. EC-17, 7-10 May 2012, Deurne (The Netherlands)

[2] M. Mittwollen et al., EFDA_D_2LJUTE, 2012

Acknowledgement

This work, supported by the European Communities under the contract of Association between EURATOM and Karlsruhe Institute of Technology, was carried out within the framework of the European Fusion Development Agreement. The views and opinions expressed herein do not necessarily reflect those of the European Commission.

Goal Oriented Training Network on Remote Handling (WP10-GOT-GOTRH (FU07-CT-2010-00065))

Overview / Introduction

The EFDA European Goal Oriented Training programme on Remote Handling (RH) “GOT RH “ aim is to train engineers for activities to support the ITER project and the long-term fusion programme in European Associations, associates, Fusion for Energy, the ITER organization, Industry and activities beyond ITER (DEMO). The GOT RH serves as practical level project for increasing the coherence within RH context of collaborative training between 5 participating European Associations: TEKES - Finland; coordination, CEA - France, CIEMAT - Spain, DIFFER - Netherland, KIT - Germany. The official start of the program that will last for 3 - 4 years (depending on the recruitment time for trainees) has been set to October 1st 2010. The KIT Trainee started on 01.09.2011.

The major objective is to implement a structured remote handling system design and development oriented training task that is carried out in a multidisciplinary Systems Engineering (SE) framework by using ITER/F4E task and QA processes and available documents, and ITER-relevant software products. The approach is top-down engineering with multidisciplinary design requirements considerations on reliability, availability, maintainability and inspectability (cf. RAMI).

The training program is divided into 3 Work Packages. WP1 is implemented by using ITER relevant RH system design and development case studies that possibly extend the ITER catalogue of existing RH procedures and tools. The System Engineering framework, in which the project is implemented, requires writing of a case study project Quality Plan (QP), System Requirements Documents (SRD) and Design Description Documents (DDD) following F4E and ITER baseline documents, catalogue of existing concepts and other documents like ITER RH Code of Practice. WP1 is divided in several Work Programs. The trainee at KIT is involved in WP1.1. The aim of the WP1.1 is the Identification of main requirements and elaboration of RH procedures for providing a high availability of the ECH Upper Port Plug system.

Status of the activity

During 2012 the GOTRH training program at KIT has concentrated on different aspects related with two main projects:

- Design and analyses for the ITER EC H&CD Upper Launcher Final Design.
- Development of remote maintenance concepts for DEMO.

1. Design and analyses for the ITER EC H&CD Upper Launcher Final Design

On ITER, due to the high neutron fluxes generated during plasma operations, material activation of the in-vessel components occur. Therefore, maintenance can only be performed by robust RH operations. These have to be developed through a RAMI analysis that consists of an association of methods and integrative concepts based on the results obtained for the control of technical risks.

The maintenance development of the ECH&CD Upper Launcher (shown in Fig. 1), which is *presently going towards Final Design Review*[1], is a process strongly related to the structural and the mm-wave components designs.

[1] Components are still subjected to changes and variation to meet the requirements of the structural components, the mm-wave system and the Remote Handling.

The work for 2012 concentrated mainly to three specific section of the launcher:

- The Blanket Shield Module, the plasma facing component of the launcher (BSM)
- The Mid-Optics
- The Waveguide Assembly

However, the fairly immature level of the Upper Launcher baseline CAD model (e.g. piping routing not yet confirmed, supports for the quasi optical system not yet defined) represented a limitation for the development of a fully compliant RH strategy.

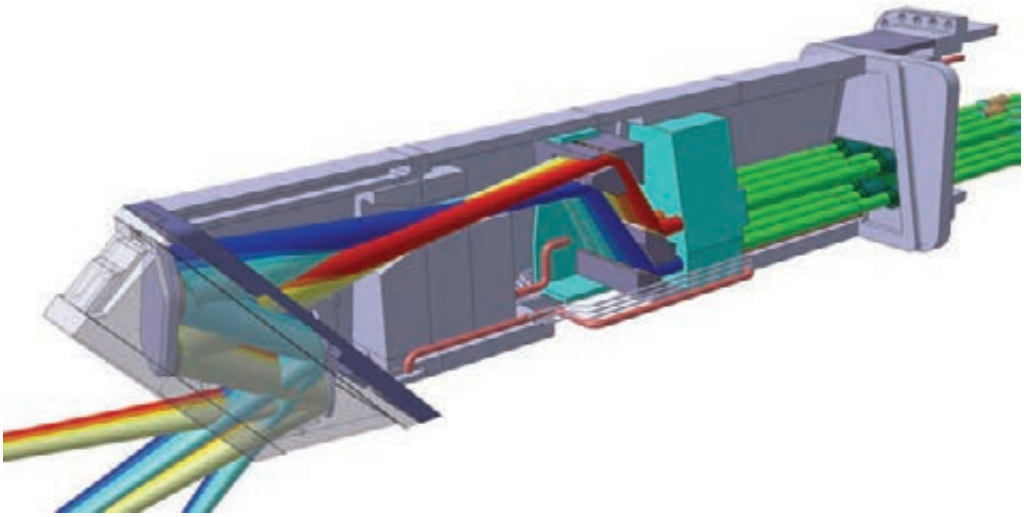

Fig. 1: Sketch of the ITER ECH&CD Upper Launcher (Baseline). The BSM (left side of the launcher), the mid-optics (central grey blocks) and the waveguide assembly (the green section on the right side of the launcher, are represented.

To overcome these difficulties while meeting the requirements of the structural and mm-wave component designs and of RH, a System Engineering approach (SE) has been implemented in order to deal with the design and application of the whole system (Upper Launcher) as distinct from its parts (structural, optics and maintenance related through RH). The process is iterative and structured with a top-down synthesis, development and operation that aim to satisfy, in a near optimal manner, the full range of System Requirements. The core of the process consisted in the formalization of:

- A set of assumption to be applied on the Baseline CAD model (structural and mm-wave component designs).
- Development of Trade-Off documents that aim to compare different possible designs meeting different requirements.

The results have been collected in a “living” document (Technical Report). This document will be constantly updated as the project moves on towards the Final Design Review.

2. Development of remote maintenance concepts for DEMO

The development of remote maintenance concepts for DEMO and future fusion power plants is driven by the following key requirements:

- Feasibility and reliability of the plant maintenance system.
- High overall plant availability, and therefore, minimization of plant down time for the foreseen maintenance operations

The ITER maintenance scheme for in-vessel components is not optimized on availability; therefore novel maintenance concepts must be developed and validated for use in DEMO. A design integration study of the ECRH and NBI heating systems with the outboard Multi-Module Segment blanket (MMS) system of DEMO has been started. Through this study, it has been assessed if the structural integrity of a single outboard MMS, when subjected to maximum electromagnetic loading conditions, can be achieved if the necessary port openings for the NBI and ECRH systems are made through the MMS. A preliminary port opening definition has been implemented starting from ITER ECH and NBI system parameters.

For ECH&CD launched from the Equatorial port, 3 openings allowing multiple beams were located at one single MMS and properly inclined (toroidal and poloidal) in order to focus at VV center, assuming an optimized toroidal launching angle.

Preliminary structural and EM analysis showed that the MMS with respect to the port openings can withstand the stresses and therefore such openings might be implemented into the machine. Further refined analysis will be performed in future.

Staff:

G. Grossetti (trainee)
S. Schreck

Literature:

[1] G. Grossetti et al., The ITER EC H&CD Upper Launcher: Analysis of Vertical Remote Handling applied to the BSM maintenance, 27th Symposium Of Fusion Technology, 24th – 28th September 2012, Liege (Belgium). Submitted to Fus. Eng. and Des. in 2013.

Acknowledgement

This work, supported by the European Communities under the contract of Association between EURATOM and Karlsruhe Institute of Technology, was carried out within the framework of the European Fusion Development Agreement. The views and opinions expressed herein do not necessarily reflect those of the European Commission.

Goal Oriented Training Programme “ITER Port Plug Engineering” (WP08-GOT-ITER-PPE (FU07-CT-2008-00047))

A concept for instrumentation of the cylindrical attachment system for the ITER EU-HCPB-TB

The Test Blanket Module (TBM) is one important component that will be tested in ITER. It has the task to breed tritium, contribute to the shielding and to remove heat from the plasma. The TBM is located next to another TBM inside an equatorial port plug and connected to the shield. This connection is established by the attachment system.

The first wall of the TBM is a plasma-facing component and therefore a highly cooled component. This leads to a high thermal gradient in radial direction of the TBM at plasma operation, as the first wall is at temperature of about 550 °C and the rear side, the back plate, at about 300 °C. The attachment system has to compensate the differential expansion between back plate and shield, which is cooled to 120 °C. Another operating state with a high temperature difference between the TBM and the shield is tritium outgassing at 500 °C which is required to remove the tritium from the breeder units.

On the other side, high mechanical loads act on the TBM. The mechanical loads that are considered the most demanding for the attachment system are caused by electro-magnetic effects during different operating states and plasma scenarios as well as by the dead weight. These loads have to be transferred to the shield by the attachment system.

Different concepts have been developed to address these two contradicting requirements over the past years. The latest development of a concept based on a cylindrical central connection element for the EU-HCPB-TBM has been evaluated based on analyses of a fast vertical displacement event type II and the operating state tritium outgassing. The results have shown that the design fulfills the requirements given by the relevant design codes.

The connecting cylinder is welded to the TBM box. In order to avoid welding of dissimilar materials the connection to the shield is established by a splined shaft and additional screws to prevent an axial movement.

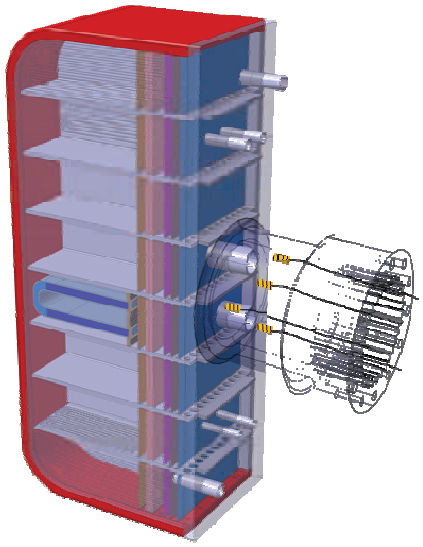

Fig. 1: TBM box and cylindrical attachment system equipped with strain sensors.

In order to be able to measure the loads that act on the TBM during operation a concept for instrumentation of the cylindrical attachment system is developed. One promising solution under investigation is the placement of strain sensors on the surface of the attachment system. An exemplary placement of the sensors on the cylinder is shown in figure 1.

A suitable strain sensor system for application in ITER has to be able to cope with harsh conditions consisting of high temperatures, electromagnetic fields and radiation. Therefore, strain sensors based on optical fibers could be a possible solution.

Staff:

H. Neuberger
C. Zeile

Acknowledgement

This work, supported by the European Communities under the contract of Association between EURATOM and Karlsruhe Institute of Technology, was carried out within the framework of the European Fusion Development Agreement. The views and opinions expressed herein do not necessarily reflect those of the European Commission.

Magnets and Affiliated Components

Conductor Jacket Mechanical Testing Reference Laboratory (ITER/IO/10/4300000292)

Background and objectives

The He inlet of the TF coil was tested under fatigue in 2005 following ASME criteria for fatigue qualification which indicates one among two options: 1) service life at x2 calculated strains or 2) calculated strains at x2 service life. FE analysis performed in CEA resulted in tests conditions of 11 x 10^{-4} static strain +/-3 x 10^{-4} cyclic strains. Though the cyclic loads are transversal to the He inlet axis, the tests were performed axially since the stresses developed are mostly in this direction and the approach was conservative. Tests carried out at 4K broke at 80% of the 20 x 30000 = 600000 cycles; however the breaking region seems to indicate that an annealing of the HAZ took place during the welding process weakening the metal possibly due to a poorly controlled weld.

The design has evolved since 2005 based on two reasons:

1. Jacket of conductor was increased to 2 mm to reduce the void fraction,
2. Geometry of He inlet changed following feedback from industry.

The objective of this work is to qualify the new design that implements different alternatives aiming to extend the fatigue life beyond the qualifying threshold cycles. The tests will be performed until rupture at 4.5K with a static strain of 10.2 x 10^{-4} ε +/- 2.3 x 10^{-4} $\tilde{\varepsilon}$ The cycles shall present a maximum frequency of 4 Hz.

At present, KIT is capable of providing this test at helium cryogenic temperature.

Scope of work

Under the framework agreement of this service contract, a steering committee consisting of one Responsible Officer (RO) from both ITER and KIT shall define Tasks to be completed under the agreement, including scope, deliverables, due dates, and cost. The scope of the task shall include:

Preparative works

1. Establishment of the test plan
2. Review on documents and drawing submitted by DA and EU Consortium
3. Clamping system validation and finalization of instrumentation (one sample)

Qualification test

4. He inlet qualification (six samples)

Clamping system validation and finalization of instrumentation

Process steps in this sub-task are as follows:

- Reception of a clamping system validation sample by KIT
- Installation and instrumentation
- Fatigue test
  - Applied strain: (10.2 +/- 2.3) x 10^{-4} ε
  - End of the test: 600,000 cycles
- Validation criteria: No obvious slippage observed.
- Preliminary test report

A sketch of the He-inlet samples to be measured in a second step is shown in Fig. 1. The mounted sample is shown in Fig. 2. The main extensometer signal was the 270 mm length

measurement. After cool down four load lines were measured to verify that the system reacts reproducible and now slipping occurs. In Fig. 3 the load versus time is shown. Fig. 4 gives the corresponding load versus strain of the 270 mm extensometer system. A slight deformation is visible. Nevertheless, the system reacts reproducible. Additionally in Fig. 5 the displacement measured directly on the jacket using the 270 mm extensometer system and the overall machine displacement is shown. Again a good agreement and reproducibility is given.

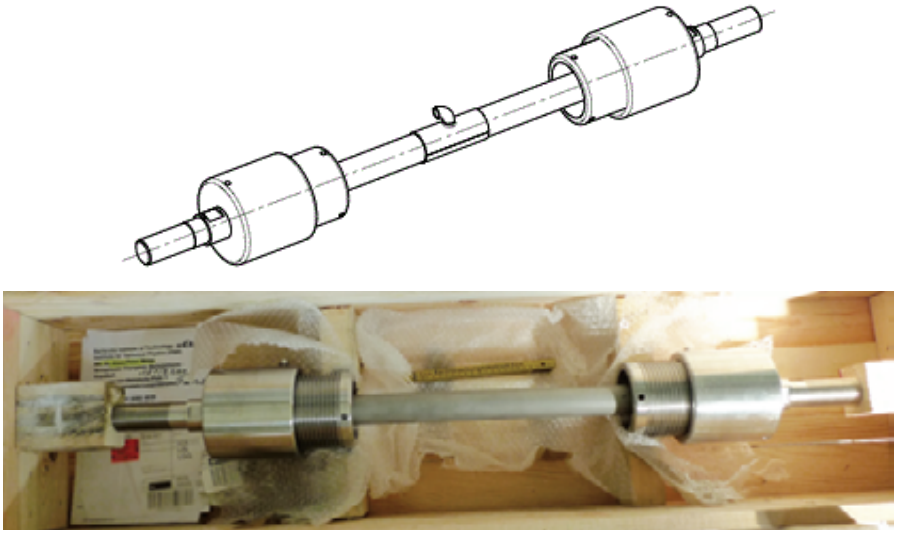

Fig. 1: Sketch of the TF He-inlet prototype equipped with mounting fixture provided by ITER, below the first dummy tested in first sub-task up to 500,218 cycles.

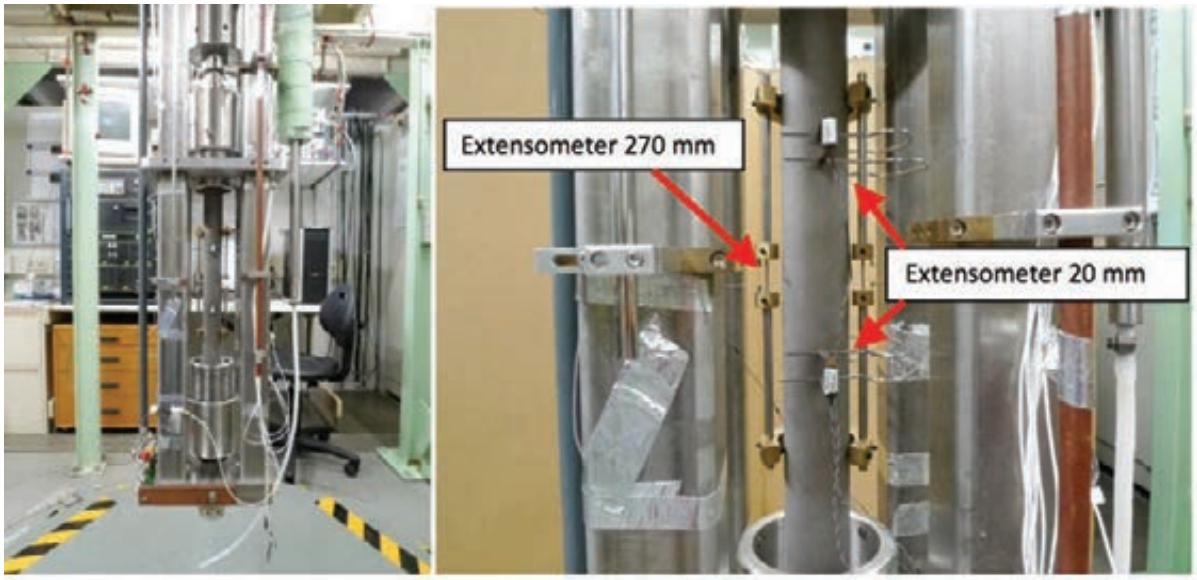

Fig. 2: Pre prototype of He-inlet mounted in ATLAS (left). The three double extensometer systems of 270 mm and 20 mm (right).

After successful loading, fatigue testing according to above given conditions was started (triangular shaped). The maximum frequency is approximately 2 Hz, limited by the boundary conditions of the ATLAS facility. In Fig. 6 (about 250,000 cycles) and Fig. 7 (about 500,000 cycles) the displacement of the 270 mm extensometer system is shown versus relative testing time. After successful testing till 400,000 cycles, it was decided to stop the fatigue test of this first prototype at 500,000 cycles. The overall test time were 2 days preparation and 10 working days cycling, stopped at 500,218 cycles.

The test was concluded successful without apparent damage. The mounting clamp showed very good performance during testing as no slipping was visible.

After finalizing this part, several He-inlet prototypes with welded nozzle, needs to be tested under fatigue load.

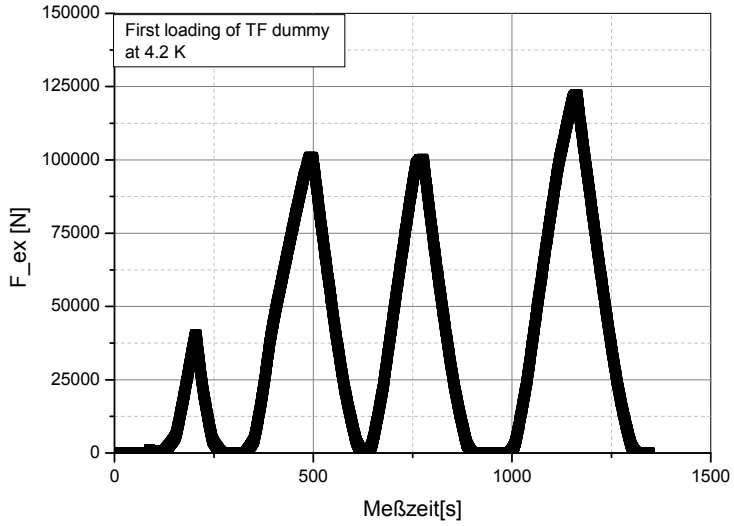

Fig. 3: Overview of first loading cycles up to maximum strain and load at 42K.

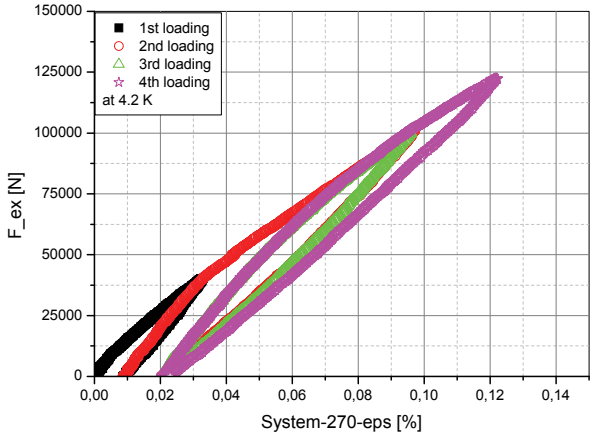

Fig. 4: Load versus strain (270 mm system) at 4 K.

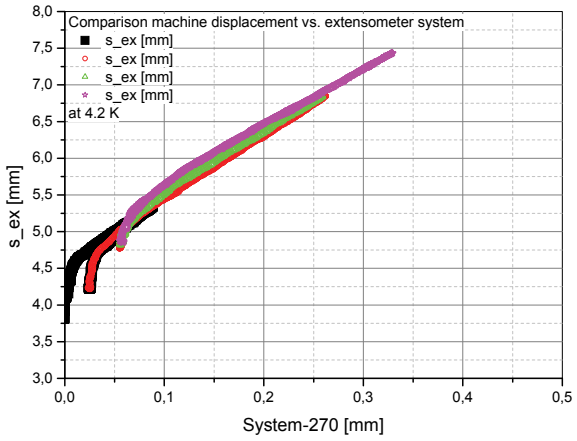

Fig. 5: Machine displacement versus strain (270 mm system) at 4.2 K.

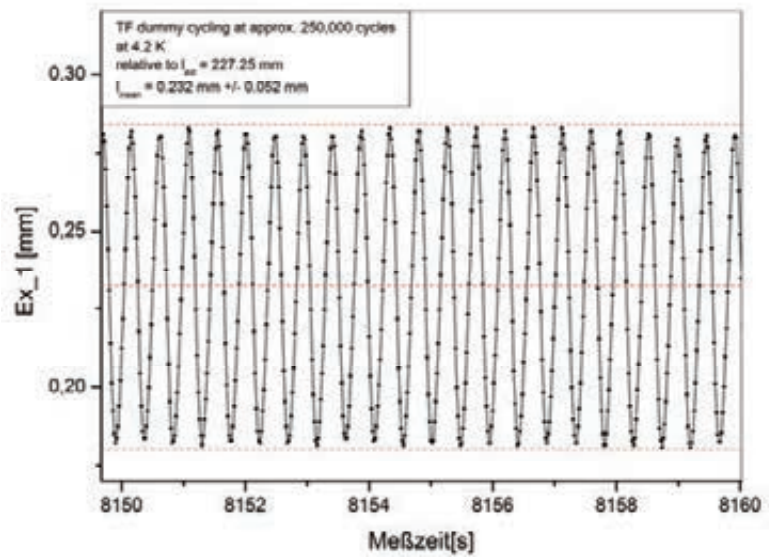

Fig. 6: Displacement (270 mm system) versus relative testing time around 250,000 cycles at 4.2 K.

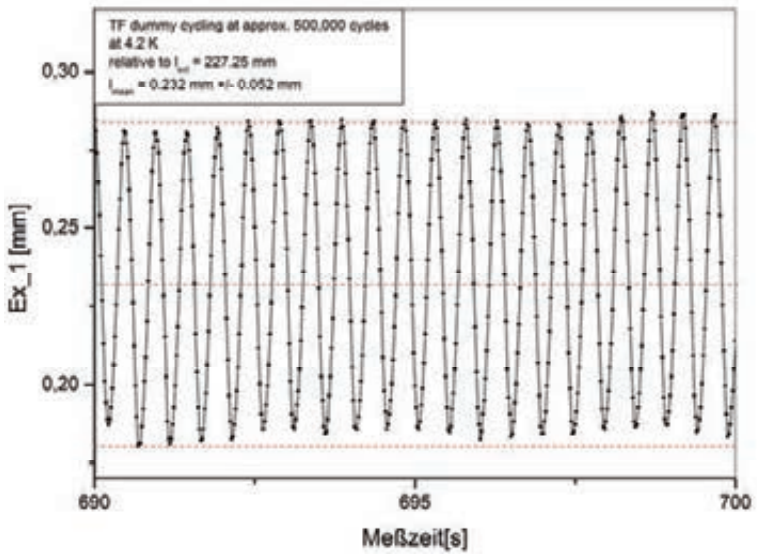

Fig. 7: Displacement (270 mm system) versus relative testing time around 500,000 cycles at 4.2 K.

He inlet qualification

Process steps in this sub-task are as follows:

- Reception of six He inlet qualification samples by KIT.
- Clamping systems are delivered together.
- Installation and instrumentation.
- Fatigue test Criteria
  - Applied strain: (10.2 +/- 2.3) x 10^{-4} ε, 67,000 cycles
  - End of the test: 600,000 cycles
- Preliminary test report.

Cooperation:

Joint work within conductor production. Mechanical analysis of stainless steel 316LN/316L material.

ICAS, Italy
POSCO, R. of Korea
ASIPP, China
CERN, Switzerland

Staff:

N. Bagrets
B. Purr
V. Tschan
E. Urbach
K.-P. Weiss
S. Westenfelder

Acknowledgement

This work was supported by ITER Organization under the service contract No. ITER/IO/10/4300000292. The views and opinions expressed herein reflect only the author's views. The ITER Organization is not liable for any use that may be made of the information contained therein.

Mechanical and Physical Characterization of Materials at Cryogenic Temperatures (F4E-OPE-084 (ES-MF))

Background and Objectives

The performance of materials is crucial for the operation of fusion reactors, so their quality needs to be assured with high certitude. Material characterizations and microscopic inspections are needed in order to support the construction and development of components and materials for ITER and other fusion related facilities under the responsibility of F4E. The LOT 1 of this technical specification concerns materials at cryogenic temperatures, which are present in particular in the ITER reactor's magnet system operating at 4 K.

Scope of Work

The Suppliers of this specific LOT shall be able to provide the following material characterization activities.

Mechanical testing (at 4 K – 77 K typical):

1. Tensile tests to determine material's tensile strength, yield strength, elongation, reduction of area, pull strength of joints, etc.
2. Shear tests.
3. Interlaminar shear strength of electrical insulation materials.
4. Fatigue tests to determine material's fatigue strength, develop Wöhler-curves, fatigue crack growth rates (FCGR, da/dN).
   I. Number of cycles range for Wöhler-curves up to 10^6.
   II. Required R ratio is R = 0.1.
5. Fracture toughness (Critical stress intensity factor K_{1C}).
6. Charpy-V impact test (standard size or mini-Charpy-V).

Physical properties measurements (at 4 K – 77 K typical):

1. Electrical conductivity.
2. Thermal conductivity.
3. Magnetic properties (magnetic permeability, susceptibility).
4. Thermal contraction from RT to 4K.

Specimens sizes and types shall follow relevant EN, ISO, ASTM or equivalent standards. Materials that the Supplier shall be able to characterize are:

1. Structural metals: stainless steels, steels, copper alloys, aluminium alloys, titanium base alloys, nickel base alloys.
2. Glass/resin composites and other electrical insulation materials.
3. Weld-, braze etc. joints and other kind of combinations of the above mentioned materials.

Within Task Order 2, four sub-tasks were defined:

Sub-task 1: ITER TF-Conductor's Jacket weld qualification tests

Sub-task 2: ITER TF-Conductor's Jacket qualification

Sub-task 3: JT-60SA TF-Conductor's Jacket material Fatigue tests at 4 K

Sub-task4: JT-60SA TF-Coil Case material tests

Material was provided by F4E and specimens were prepared by KIT. Details of performed tests can be found below.

Sub-task 1: ITER TF-Conductor's Jacket weld qualification tests

The scope of this sub task was changed to measure TF jacket material after special cleaning process at CERN, in order to investigate the possibility of chemical diffusion process due to contamination of the surface during production. The steps taken were as follows:

1. Two compacted jacket section samples coming from two different heats (or at least section lots) will be sent to KIT by ICAS. These samples should be 2 m long.
2. KIT will cut 1.5 m from the two samples and stretch them by 2.5 %.
3. After removing 15 cm at both edges, KIT will cut each tube to 4 sections of 30 cm (A, B, C, D).
4. If numbering the sections from one edge sequentially, the two central sections (i.e. sections B and C) of the two tubes will be sent to CERN, whereas section A of each tube will be prepared and tested at KIT following your proposal and sections D should be used by the Koreans for their tests.
5. The 4 jacket sections (2x2), 30 cm long each, will be sent to CERN for cleaning and heat treatment (see long heat treatment 1 in Sub-Task 2).
6. The sections will be returned to KIT for testing.

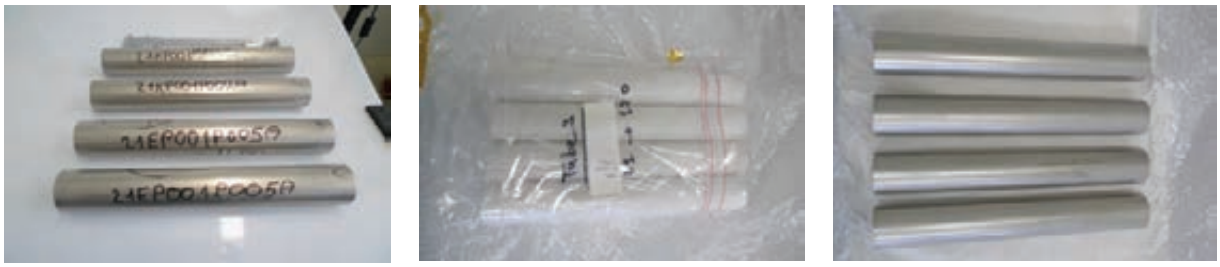

Fig. 1: On the left jacket sections after 2.5% stretching at room temperature and sectioned to be send to CERN. In the middle, the received jackets after cleaning and heat treatment at CERN and after unwrapping.

Below the results 6 tested specimens taken of the two jacket samples are shown:

Table 1: Results of tensile test POSCO TF jacket.

File-name	Temperature	Young's Modulus	Yield Strength	Ultimate Tensile Strength	Uniform Elongation	Total Elongation
-	K	GPa	MPa	MPa	%	%
21KP001P002A (section B and C)						
T2A-B1	4.2	209.8	1301	1592	19.8	20.9
T2A-B3	4.2	216.7	1298	1601	20.9	21.0
T2A-C1	4.2	212.8	1279	1591	19.0	22.1
T2A-C2	4.2	204.8	1280	1573	13.6	21.9
T2A-C3	4.2	211.1	1240	1554	13.9	20.0
T2A-C4	4.2	205.1	1293	1566	15.2	18.6
21EP001P005A (section B and C)						
T5A-B1	4.2	204.8	1229	1499	16.6	18.1
T5A-B2	4.2	217.0	1228	1511	15.9	19.2
T5A-B3	4.2	207.0	1239	1510	15.1	19.0
T5A-B4	4.2	207.5	1245	1498	14.4	16.8
T5A-C2	4.2	205.3	1248	1557	12.2	15.0
T5A-C4	4.2	208.8	1301	1593	16.6	15.6

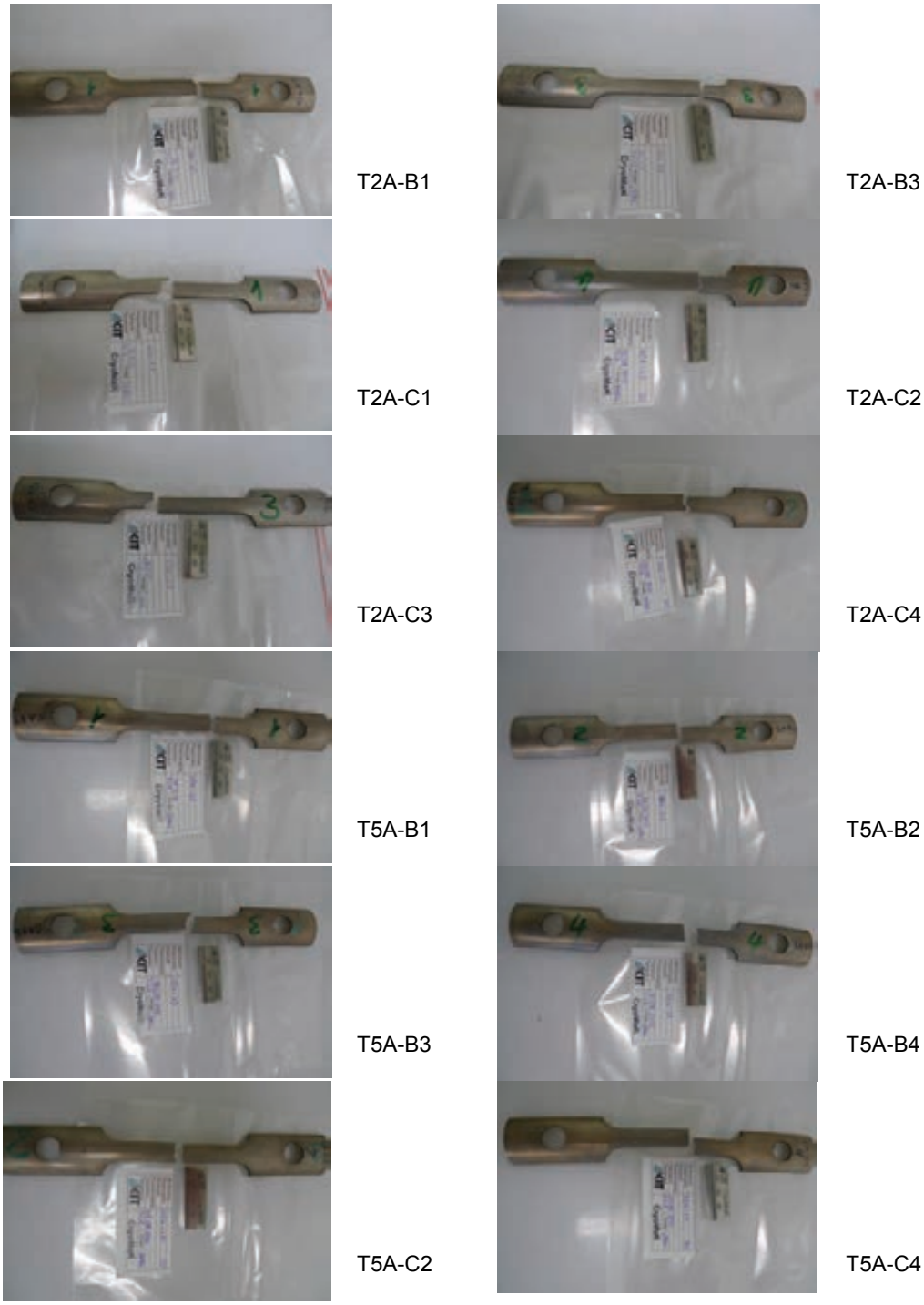

Fig. 2: Fracture appearance of TF jacket material according to Table 1.

Sub-task 2: ITER TF-Conductor's Jacket qualification

TF jacket characterization (SMST/POSCO 21EP001P003A).

TF jacket material was tested in different stages of process:

- as received (A1-A2)
- heat treated according to ht1 specification (B1-B4)
- heat treated according to ht2 specification (C1-C4)

Results can be found in Table 2 and 3. The tested specimen can be seen in Figure 4 and 5.

The SMST and POSCO jacket material were heat treated together in the same furnace to get a direct comparison of the performance.

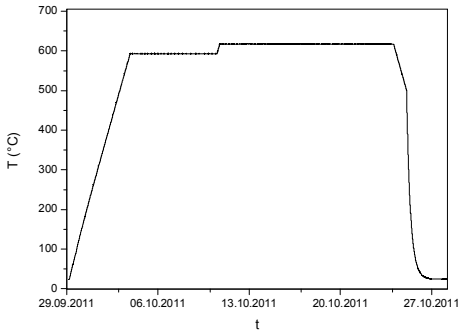

heat treatment 1

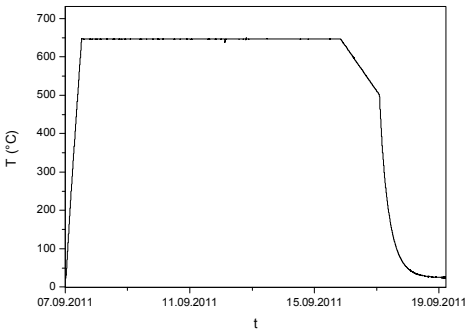

heat treatment 2

Fig. 3: SMST (top) surface is not that dark as POSCO (bottom) surface after heat treatment 2.

Table 2: Results of tensile test SMST TF jacket.

-	K	GPa	MPa	MPa	%	%
TF jacket material as received						
SA1	4.2	200.5	1049	1528	33.3	33.3
SA3	4.2	216.4	1040	1528	35.5	39.7
TF jacket compacted, stretched 2.5 % at RT and heat treatment 1						
SB1	4.2	220.3	1201	1644	31.5	33.8
SB2	4.2	223.6	1219	1644	28.7	29.1
SB3	4.2	215.2	1186	1626	30.6	34.9
SB4	4.2	216.4	1213	1657	29.9	31.6
TF jacket compacted, stretched 2.5 % at RT and heat treatment 2						
SC1	4.2	194.1	1161	1586	34.6	34.6
SC2	4.2	216.0	1160	1611	30.5	30.5
SC3	4.2	197.7	1162	1589	37.2	37.2
SC4	4.2	210.4	1212	1646	37.3	37.3

Fig. 4: Tested SMST TF jacket specimen according to Table 1.

Table 3: Results of tensile test POSCO TF jacket.

Filename	Temperature	Young's Modulus	Yield Strength	Ultimate Tensile Strength	Uniform Elongation	Total Elongation
-	K	GPa	MPa	MPa	%	%
TF jacket material as received						
PA1	4.2	201.8	1181	1561	31.9	31.9
PA3	4.2	219.5	1165	1521	25.2	25.2
TF jacket compacted, stretched 2.5 % at RT and heat treatment 1						
PB1*	4.2	222.1	1351	(1585)	(7.6)	-
PB2*	4.2	215.6	1359	(1649)	(14.5)	-
PB3	4.2	226.8	1348	1666	18.9	22.5
PB4	4.2	209.8	1347	1625	12.0	12.0
TF jacket compacted, stretched 2.5 % at RT and heat treatment 2						
PC1	4.2	194.2	1281	1600	19.8	19.8
PC2	4.2	204.8	1280	1614	19.5	19.5
PC3	4.2	210.6	1283	1608	17.3	17.3
PC4	4.2	212.9	1294	1601	17.8	17.8

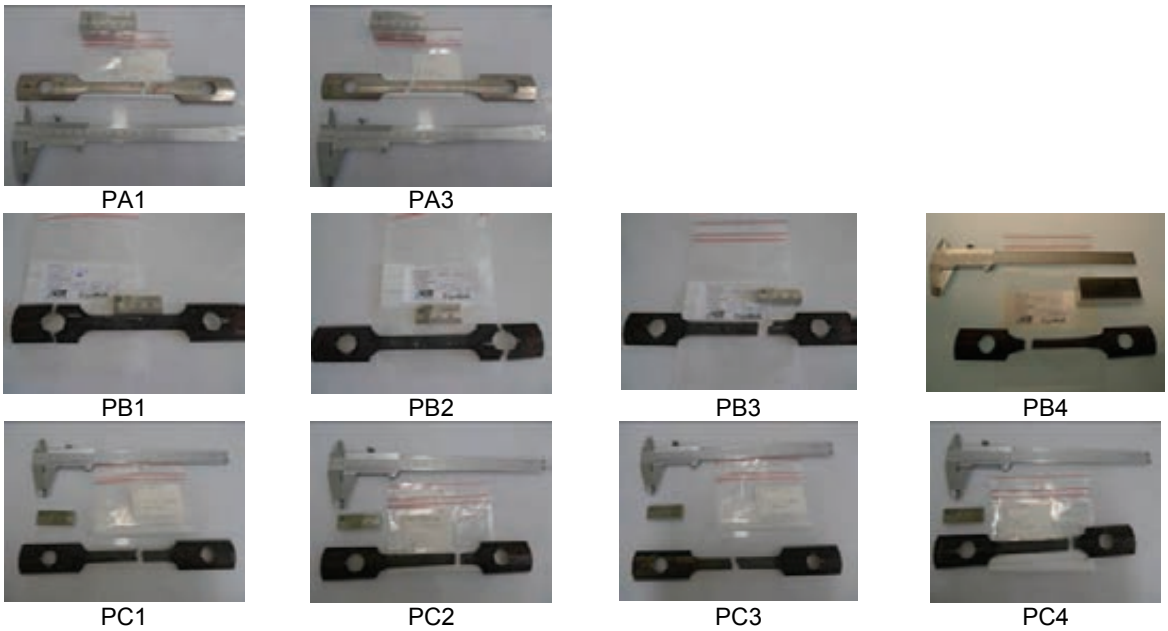

Fig. 5: Tested POSCO TF jacket specimens according to Table 2.

Sub-task 3: JT-60SA TF-Conductor's Jacket material Fatigue tests at 4 K
Sub-task4: JT-60SA TF-Coil Case material tests

These tasks are currently running and will be finalized beginning of next year 2013.

Cooperation:

Joint work within conductor production. Mechanical analysis of stainless steel 316LN/316L material.
ICAS, Italy
POSCO, R. of Korea
ASIPP, China
CERN, Switzerland

Staff:

N. Bagrets
B. Purr
V. Tschan
E. Urbach
K.-P. Weiss
S. Westenfelder

Acknowledgement

This work was supported by Fusion for Energy under the service contract No. F4E-OPE-084 (ES-MF) The views and opinions expressed herein reflect only the author's views. Fusion for Energy is not liable for any use that may be made of the information contained therein.

Current Leads for Wendelstein 7-X and JT-60SA (CoA; BMBF Reference No. 03FUS0013)

Current Leads for Wendelstein 7-X

The stellarator W7-X presently under construction at the Greifswald branch of the Max-Planck-Institute for Plasma Physics consists of 50 non-planar and 20 planar coils with a maximum conductor current of 17.6 kA. Karlsruhe Institute of Technology delivers the current leads for the magnet system. In total 14 current leads are required (maximum design current I_{max} = 18.2 kA, nominal current I_{nom} = 14 kA).

Series current lead manufacturing (Status of Nov 12, 2012)

Due to the tight schedule it was decided to manufacture and assemble the series current leads for W7-X in KIT. All 14 series current leads have been fabricated and 12 of them successfully tested. Series current leads 13 and 14 are assembled and prepared for the test. Two series current leads were prepared due to a failure after test they will be tested beginning of 2013. The delay of about two months is due to an additional test requested and finalized by IPP Greifswald for qualification of the joint box design of the current lead busbar connection in W7-X. Then the project “Current Leads for Wendelstein 7-X” is finished.

Current Leads for JT-60SA

In the frame of the Broader Approach Agreement between Japan and the EU and concomitantly to the ITER project, a satellite tokamak project called JT-60SA has been agreed. The magnet system of JT-60SA consists of 18 toroidal field coils (25.7 kA), 4 central solenoid modules (20 kA) and 7 poloidal field coils (20 kA). Following the commitment of the German Government to the EU, KIT shall design, construct and test the current leads. In total 6 leads for a maximum current of 26 kA and 20 leads with a maximum current of 20 kA, mounted in vertical, upright position are required.

Status

The status is as follows:

- Small adaptations in the design of the HTS current leads has been made and approved by the project team.
- The detailed design of the heat exchangers was approved by TÜV. All materials and half pieces needed to start the series production of the current leads are ordered or already delivered.
- KIT has asked BMBF for funding of the manufacturing and test of the HTS current leads for JT-60SA. Presently the request is under negotiations.
- As part of an industrial contract JAEA is presently working on the manufacturing of the short circuit bus bar (so called “jumper”) needed for the series test of the current leads in CuLTKa. Large discussions were done for the design of the joint box of the jumper where no final agreement was achieved. JAEA will manufacture and deliver the jumper in March 2013 but if the jumper will not work properly the series tests of the current leads could not be performed and KIT will deliver those leads untested.
- The test facility CuLTKA is under construction. All cryostat boxes are manufactured in house. The LN2-shields ordered in industry were delayed by about six months due to improper quality. The transfer lines as well as the interface line between the main transfer line from the 2 kW refrigerator and CuLTKa are ordered in industry and presently under manufacturing.

- Due to delays in the procurement and due to lack of personal resources the assembly of CuLTKa is delayed. In addition the connection between the main transfer line from the 2 kW refrigerator and CuLTKa can be performed only after the completion of the series current lead tests for W7-X in TOSKA because during this work the whole cryogenic system will not be operational.
- The commissioning of CuLTKa is now planned for late summer and autumn of 2013 to be ready for the test of the current leads for JT-60SA end of 2013 or beginning of 2014.

Staff:

W7-X CL:

M.S. Darweschsad
G. Dittrich
S. Eckerle
W.H. Fietz
S. Fink
U. Fuhrmann
M. Gehrlein
F. Gröner
R. Heger
M. Heiduk
R. Heller
S. Heuser
M. Hollik
A. Kienzler
C. Lange
R. Lietzow
I. Meyer
C. Molnar
R. Müller
T. Richter
R. Rotondo
E. Specht
E. Urbach
T. Vogel
P. Wagner-Nagy
V. Zwecker

JT-60SA:

W.H. Fietz
B. Ganninger,
M. Gehrlein
R. Heger
R. Heller
M. Hollik
A. Kienzler
C. Lange
A. Opitz
R. Rotondo
U. Saller
E. Urbach
T. Vogel

CuLTKa:

M.S. Darweschsad
G. Dittrich
W.H. Fietz
U. Fuhrmann
M. Gehrlein
F. Gröner
R. Heger
M. Heiduk
R. Heller
M. Hollik
C. Lange
O. Langhans
R. Lietzow
I. Meyer
R. Müller
T. Richter
R. Rotondo
E. Specht

Literature:

[1] T. Rummel, K. Risse, G. Ehrke, K. Rummel, A. John, T. Mönnich, K.-P. Buscher, W. H. Fietz, R. Heller, O. Neubauer, A. Panin, The Superconducting Magnet System of the Stellarator Wendelstein 7-X, IEEE Transactions on Plasma Science 40(3) (2012) 769-775

[2] S. Drotziger, W.H. Ffietz, M. Heiduk, R. Heller, C. Lange, R. Lietzow, T. Möhring, Investigation of HTS current leads under pulsed operation for JT-60SA, IEEE Transactions on Applied Superconductivity, VOL. 22, NO. 3, JUNE 2012, 4801704

[3] K. Yoshida, K. Kizu, K. Tsuchiya, H. Murakami, K. Kamiya, M. Peyrot, L. Zani, M. Wanner, P. Barabaschi, R. Heller, F. Michel, The Manufacturing of the Superconducting Magnet System for the JT-60SA, IEEE Transactions on Applied Superconductivity, VOL. 22, NO. 3, JUNE 2012, 4200304

[4] E. Rizzo, R. Heller, L. Savoldi Richard, R. Zanino, CtFD-based correlations for the thermal-hydraulics of an HTS current lead meander-flow heat exchanger in turbulent flow, presented at CHATS-AS 2011, Geneva, Switzerland, Oct 12-14, 2011, accepted for publication to CRYOGENICS, available online, http://dx.doi.org/10.1016/j.cryogenics.2012.06.001

[5] S. Drotziger, W. H. Fietz, M. Heiduk, R. Heller, M. Hollik, C. Lange, R. Lietzow, T. Richter, K.-P. Buscher, T. Moennich, T. Rrummel, Overview of results from Wendelstein 7-X HTS current lead testing, presented at 27th Symposium on Fusion Technology, Liège, Belgium, September 24-28, 2012, submitted for publication in Fusion Engineering And Design

[6] R. Heller, S. Drotziger, W. H. Fietz, A. Kienzler, R. Lietzow, T. Richter, E. Weiss, K.-P. Buscher, T. Moennich, T. Rummel, Status of series production and test of the HTS current leads for Wendelstein 7-X, presented at 27th Symposium on Fusion Technology, Liège, Belgium, September 24-28, 2012, submitted for publication in Fusion Engineering And Design

[7] M. Hollik, W. F. Fietz, S. Fink, M. Gehrlein, R. Heller, C. Lange, T. Möhring, Design of electronic measurement and quench detection equipment for the Current Lead Test facility Karlsruhe (CuLTKa), presented at 27th Symposium on Fusion Technology, Liège, Belgium, September 24-28, 2012, submitted for publication in Fusion Engineering And Design

[8] E. Rizzo, R. Heller, L. SavoldiI-Richard, R. Zanino, Computational thermal-Fluid Dynamics analysis of the laminar regime in the meander flow geometry characterizing the heat exchanger used in the High Temperature Superconducting current leads, submitted for publication to Fusion Engineering and Design

Acknowledgement

This work was financially supported by the Ministry of Research and Education (BMBF) under the grant No. 03FUS0013 and is done in the Project JT-60SA under the Broader Approach Agreement between Europe and Japan. The views and opinions expressed herein do not reflect necessarily those of the BMBF or the European Commission.

Quench Detection System for Fusion Magnets (HGF)

Software QVision Version 3.1 features automatic coil balancing

Since several years the All-In-One software *QVision* has served as the central operating and diagnostics tool for the KIT-Quench detection System “UNIQD”. After a major expansion in the year 2011 (e.g. multi lingual edition) at the end of 2012 the software now includes an automatic balancing menu not only for a single detector, but for all detectors connected to the embedded host IPC in a cabinet (max. 128 detectors).

Correct balancing of the differential input of the KIT-Quench detector UNIQD (Type 3410/20) is an important task before adjusting the detector to the lowest quench detection thresholds, which should allow save but fast quench detection.

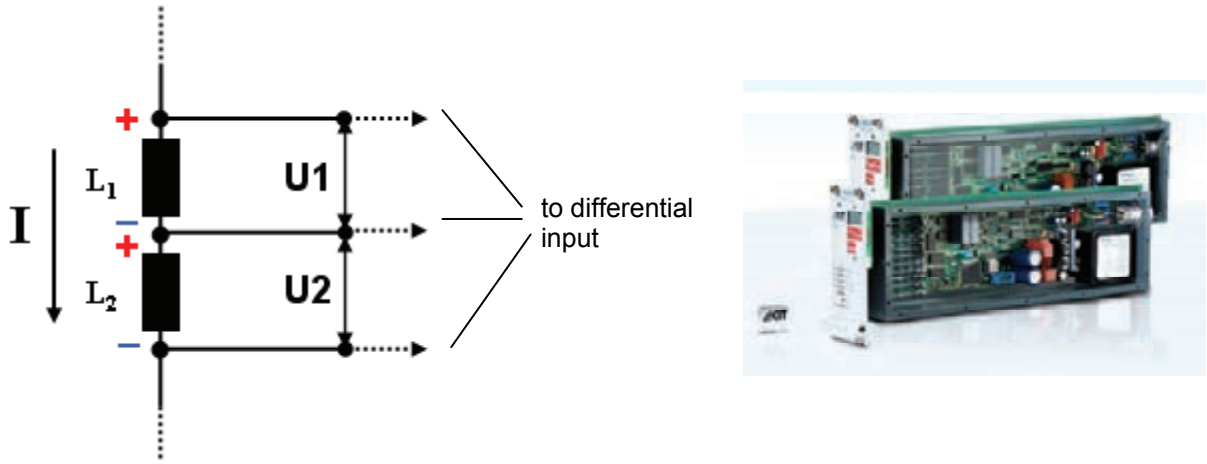

Fig. 1: Typical symmetrical connection of coils to the differential input of the detector.

During ramp-up of current (providing constant di/dt) the ratio of U_1/U_2 directly corresponds to the ratio of L_1/L_2. An unbalanced mismatch of L_1 to L_2 creates an undesirable offset voltage, which has to be added to the lowest threshold and therefore generates an additional delay to the quench detection.

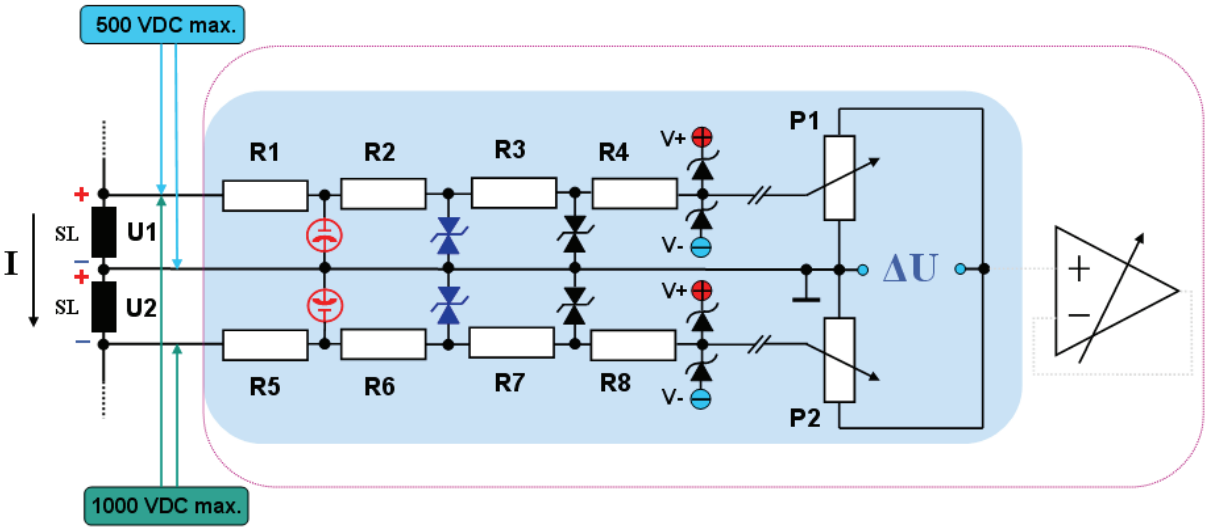

Fig. 2: Limiting and balancing input network of KIT-Quench detector.

The special design of the input limiting and balancing network of the KIT-Quench detector UNIQD allows fast measurement of the single voltages U_1 and U_2 in addition to the standard acquisition of the differential voltage (ΔU).

This measurement of the single voltages U_1 and U_2 is the key feature to make a precalculation of the desired balancing settings of the detector. The QVision software release 3.1 now includes this fast precalculation procedure completed by an additional closed loop controller to eliminate small linearity errors to perform best balancing settings.

The operator, who had to observe the differential voltage during setting of the balancing slider normally was not able, to make a complete balancing procedure for all detectors connected during the ramp-up time. Therefore in the past several ramp-up cycles were necessary for balancing settings resulting in additional stress applied to the magnets.

The new QVision software replaces (perhaps improper) manual balancing (the time required is in the range of seconds / per detector) by a fast and precise automatic procedure in the range of ms / detector.

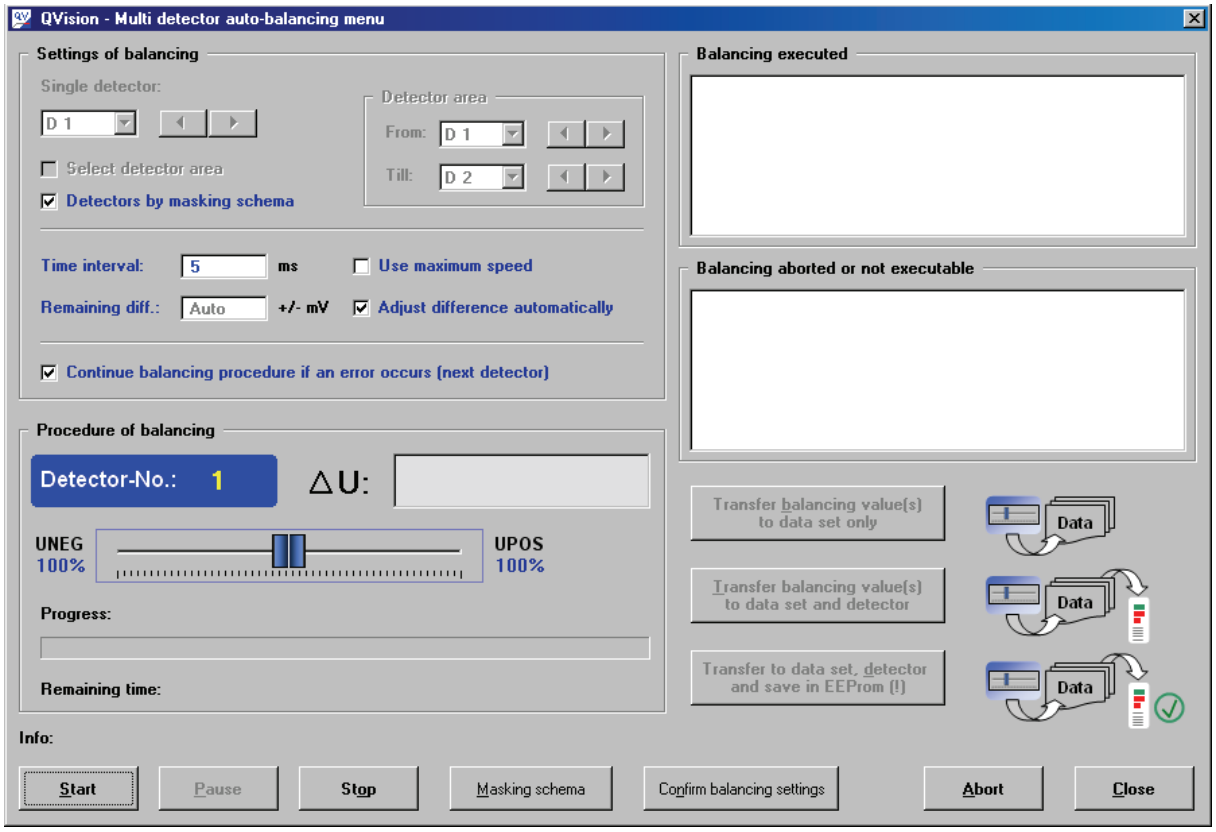

Fig. 3: Multi detector autobalancing menu in QVision 3.1.

The new software is able to balance the coils operated with constant ratio of di/dt automatically. For extended applications with not constant di/dt (e.g. operation of coils with pulsed currents) an automatic balancing presently is not possible.

Staff:

A. Ebersoldt
K. Petry
D. Tcherniakhovski

Testing of Insulating Breaks in Room Temperature Helium Gas (ITER/CT/12/4300000646)

Objectives

Experimental study conducted in KIT test lab on two of the three prototype insulating breaks produced by BNG in the framework of ITER/CT/09/4300000115. The tests are to be performed with warm gaseous helium at room temperature and after discussion of the results from the first testing day possibly at different flow rates and pressures.

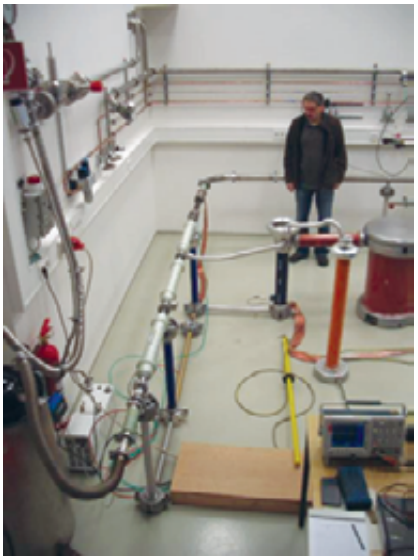

Status

- A special high flow He setup was installed at KIT which allows controlled mass flows up to 10 g/s warm helium gas and recirculates the helium to the purifier system of ITEP.
- He gas purity was monitored with respect to water and nitrogen content.
- Three warm breaks fabricated by BNG plus a fourth break fabricated by KIT were mounted to allow dedicated testing of single breaks.
- From the results it can be concluded that with a flow of 4.5 g/s pure He-gas, the AC testing shows good results for 35 kV_{peak}. However, for stagnant pure helium the breaks show flashovers during DC testing below 50 kV and for AC testing below 24.7 kVrms.

Staff:

W.H. Fietz
S. Fink
E. Weiß
V. Zwecker

Acknowledgement

This work was supported by ITER Organization under the service contract No. ITER/CT/12/4300000646. The views and opinions expressed herein reflect only the author's views. The ITER Organization is not liable for any use that may be made of the information contained therein.

Superconducting Magnet (WP12-DAS-01)
HTS Activity Coordination (WP12-DAS-01-T05)

The WP12-DAS01 Superconducting Magnet task was organized in subtasks with contributions from the associations for each subtask as indicated below in brackets:

WP12-T05 (KIT)	HTS Activity Coordination
WP12-T06 (KIT)	Construction and test of DEMO-relevant HTS cables
WP12-T07 (ATI)	Characterisation of HTS tape test samples following neutron irradiation
WP12-T08 (CRPP)	Study of the performance of HTS twisted stacked cable
WP12-T09 (CRPP)	Study on the effect of transverse loads on RE-123 Roebel cables
WP12-T10 (ENEA)	Design, manufacturing and testing of HTS cable joining techniques
WP12-T11 (CIEMAT)	Mechanical tests of single YBCO tape joints under magnetic field condition
WP12-T13 (FOM)	Ic (B,T,e) characterization in relevant window for HTS tape configurations and exploring transverse load sensitivity

Coordination Work

3 Meetings have been held in 2012:

Kick off Meeting
The Kick-off Meeting was held on June 19th, 2012 in Garching.

Interim Review Meeting
An Interim Review Meeting was held on October, 16th, 2011 using video connection and EFDATV.

Final Review Meeting
A summary meeting was held on on December, 14th 2012 in Garching. At this meeting the draft final reports of the associations were discussed.

In early 2013 the reports of the different subtasks have to be reviewed together with EFDA.

Staff:

W.H. Fietz

Acknowledgement

This work, supported by the European Communities under the contract of Association between EURATOM and Karlsruhe Institute of Technology, was carried out within the framework of the European Fusion Development Agreement. The views and opinions expressed herein do not necessarily reflect those of the European Commission.

Construction and Test of DEMO Relevant Cables (WP12-DAS-01-T06)

Investigation of HTS cable samples in the FBI facility

Upgrade of the FBI facility

For the measurement of HTS cable samples the FBI facility was adapted to allow higher sample temperatures. For this purpose a temperature variable insert has been designed to heat the sample in the 4.2 K environment. With the constructed insert, sample temperatures from 4.2 K to 80 K are possible. It consists of heating foils wrapped around the sample and a thermal shielding through a helium gas chamber which is surrounded by G10.

With the temperature variable insert the FBI facility is upgraded for HTS cables. A schematic of the improved test facility is shown in Fig. 1.

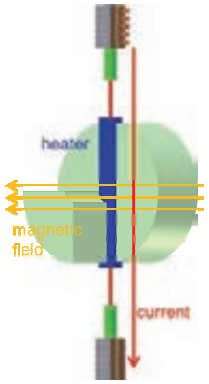

Fig. 1: Schematic drawing of the FBI test facility for the characterization of superconductor cables at temperatures from 4.2 K up to 80 K. The current carrying capabilities can been determined in dependence of magnetic background fields and sample temperature. This setup is used for the characterization of HTS cables. The additional possibility in FBI to apply tension is not used during the experiments described here.

Test of a Conductor on Round Core (CORC) cable

The CORC cable was provided by the company "Advanced Conductor Technologies" (D. van der Laan). The cable is 1160 mm long and consists of 15 4 mm wide copper stabilized SuperPower tapes arranged in 5 layers. The twist pitch is17 mm. The CORC cable as well as parts of the temperature variable insert are shown in Fig. 2.

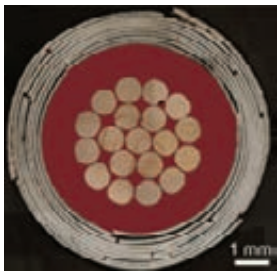

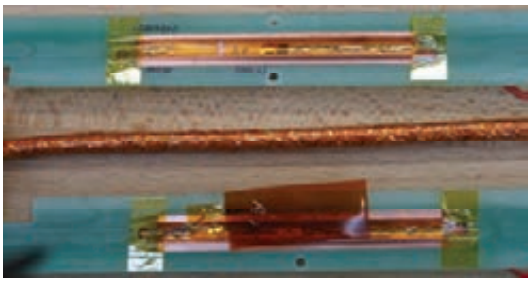

Fig. 2: Left: Cross-section of CORC cable. Right: CORC cable and inner parts of the temperature variable insert.

The CORC cable was characterized at 77 K in magnetic self-field, measured in a liquid nitrogen bath. This results in a critical current I_c(self-field, 77 K, 1µV/cm at contacts) of 1638 A.

Using the FBI facility, tests were performed in a field range up to 12 T and temperature range of 4.2 K – 80 K. Due to the cable layout with a twist pitch of 17 mm, approx. 4 transposition lengths of the cable are in the homogeneous field region.

The transitions from superconducting to normal conducting state are steep. The shape of the transition has only a minor influence by temperature and magnetic field. In addition, there are only small differences in the current at which the transitions occur for the different voltage taps (tapes and contacts). The corresponding n-values are >30, which is in the range of the single tapes. The dependence of the current carrying capabilities on magnetic field and surface temperature is shown in Fig. 3.

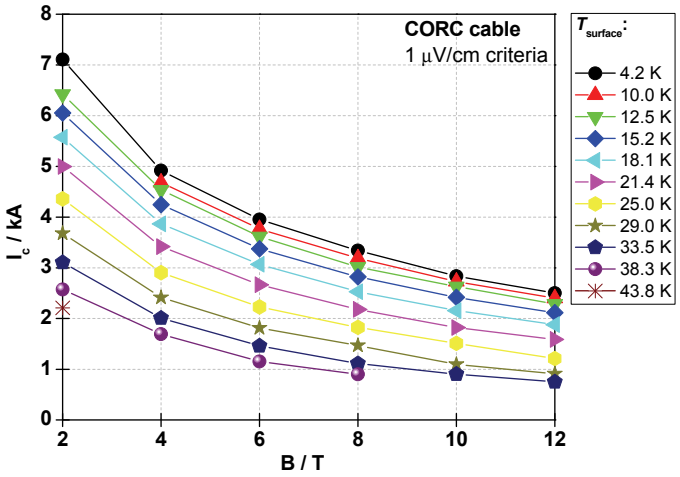

Fig. 3: Critical currents of a 15 tape CORC cable as a function of the magnetic background field for different surface temperatures.

Test of a Roebel Assembled Coated Conductor (RACC) cable

This cable was made by KIT and consists of 10 tapes which are punched from 12 mm wide copper stabilized SuperPower tapes, has a length of 1160 mm long, and has a twist pitch of 125 mm. At both terminations all tapes were contacted individually, resulting in identical contact areas and pressures during soldering. The RACC cable from KIT as well as the clamped mechanical support are shown in Figure 4.

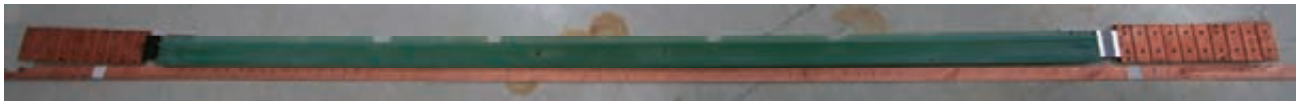

Fig. 4: RACC cable from KIT including terminations and G10 mechanical support (clamped).

The cable was characterized in 77 K and magnetic self-field as shown in Fig. 5, left side. The transitions from superconducting to normal conducting state happen at nearly identical currents for all the tapes as well as the contacts. This indicates a homogeneous contact resistance for all the tapes. The overall contact resistance was also determined to be 48 nΩ. On the right side of Fig. 5, n-values are shown in a double logarithmic plot of electric field vs. current. With n-values of 20.1 to 23.5 for all tapes, these values are close to the n-values published by the manufacturer for as-received tapes (n-values of 21-37). This implies that there is no degradation of the performance of the tapes due to punching or contacting.

The 77 K self-field performance of the cable is very good. The method of contacting has been shown to be excellent.

Additionally tests were performed for a magnetic field range up to 12 T and in a temperature range from 4.2 K to 80 K. In these test the cable is tested in “worst case” field orientation. The magnetic field is oriented perpendicular to the cable surface. This means that the Lorentz forces are acting on the thin side of the cable. To stabilize mechanically the RACC cable, it was clamped in a support structure of glass-fiber reinforced plastic (G10).

Due to the limited space in the gap of the split coil magnet of the FBI test facility, the support has to be quite thin. Therefore the clamping forces are limited.

During the in-field test, it became clear that this type of mechanical stabilization is not sufficient. The performance of the cable degrades as the magnetic field is increased. In Fig electric field vs. current is shown for low fields (2 T: on the left side) as well as high magnetic background fields (12 T: on the right side). At low field the cable still works as expected. At high field it is almost completely degraded. This degradation is neither a problem of RACC cables nor the chosen field orientation. Instead, the mechanical stabilization was insufficient to handle the Lorentz forces. Tapes in the RACC cable moved under applied Lorentz forces and were pressed together which led to damage of the tapes at the crossing sections of the meander structure present in RACC cables.

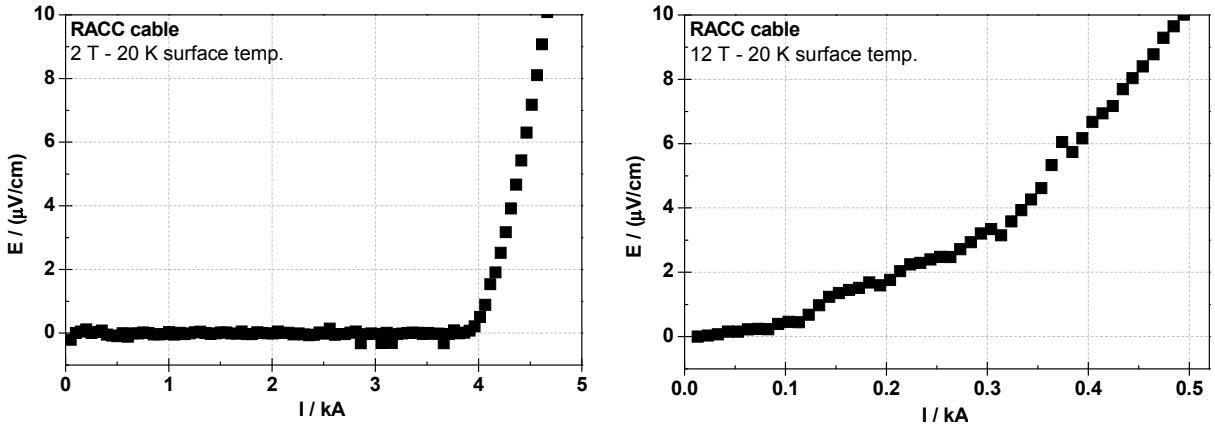

Fig. 5: Electric field vs. current curves of RACC cable in worst field orientation with insufficient mechanical stabilization. At 2 T (left side) the performance is still good. At 12 T the cable is almost completely degraded (right side). There is not superconducting transition visible.

Test results on ROEBEL cables from CERN

Experiments performed by CERN on a ROEBEL cables fabricated by KIT showed that mechanical forces are not a principal problem of this cable type, but can be handled.

Two Roebel samples with standard features (10 strands of 12 mm width with a typical critical current around 1 kA at 77 K in self field) were ordered by CERN as a possible candidate for bus bar and magnets. These Roebel samples were mounted in FRESCA and characterized at 4.2 K and in both field orientations. The observed critical current is close to 14 kA at 4.2 K in self field which is more than 10 times higher than at 77 K. For the field perpendicular to c-axis of REBCO, a critical current > 2kA was found at 10 Tesla and in the parallel direction the critical current was well above 10 kA.

This demonstrates that the Lorentz forces can be handled and that the critical current of the CC Roebel cable scales like a simple CC in external magnetic field. Second, the artificial pinning centres obviously support the high field performance, in particular at low temperatures, leading to a very high current enhancement ration upon cooling. The temperature dependent behaviour of the transport current (not measured at CERN) may have a sample specific slope and shape, which is correlated to the applied pinning technology. Unfortunately the currents in the less favourable field orientation also show the strong (expected) degradation as a function of magnetic field which is known from single tapes behaviour. These results enable magnet designers to extrapolate roughly the low temperature in-field properties in windings from 77 K data.

Optimisation of ROEBEL cables

As actual R&D work focus on lengths of a few meters, the technique of hand-made cables was optimized. A cable with 4.5 m length was fabricated as shown in Figure 6. Very important for this sample was the test of the punching accuracy along a conductor length of 50 m. For non-sufficient constancy of the transposition length, the preparation of a cable will fail. It could be

Fig. 6: Roebel cable with 4.5 m length and 12 mm width, consisting of 10 strands.

demonstrated that the accuracy of the punching machine is excellent, i.e., no change of the transposition length was found. This qualifies the tool for industrial lengths!

Bending behaviour of CC tapes and Roebel strands

A completely unknown parameter was the bending ability of a Roebel strand around an edge. CC's and CC's punched to Roebel strands have partly a cut-off of the Cu stabilization at the conductor edge, which usually surrounds the CC edge completely and provides stabilization of the composite. The behaviour of such an open edge upon bending is so far unknown. Systematic investigations are therefore necessary to establish reliable data for bending strains. For this purpose a KIT unique edge bending device was developed to test the bending ability of single coated conductors and 4 mm wide Roebel cables consisting of 10 strands (see Figure 7).

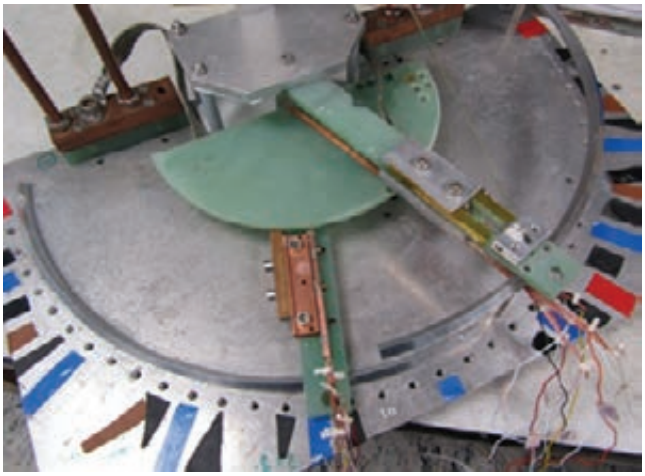

Fig. 7: Edge bending device for conductors and cables with varied angle and former thickness for 77 K investigations.

The bending type is pure bending along a direction inclined by an angle to the tape direction, which corresponds to the transposition length. The bending results obtained on single CC's were very well compatible with the geometry of the Rutherford cable, since degradations occurred at significantly smaller transposition lengths. The same experiments on Roebel strands were quite different however shown in Figure 8.. Applying Roebel strands e.g. in a Rutherford cable structure one has also the option of both orientations. The results also reported in Fig propose to orient the SC layers of the strands towards the central former. This is also favourable if joining is considered. The results show however that the bending ability of the strands is already at the limit for this demonstrator.

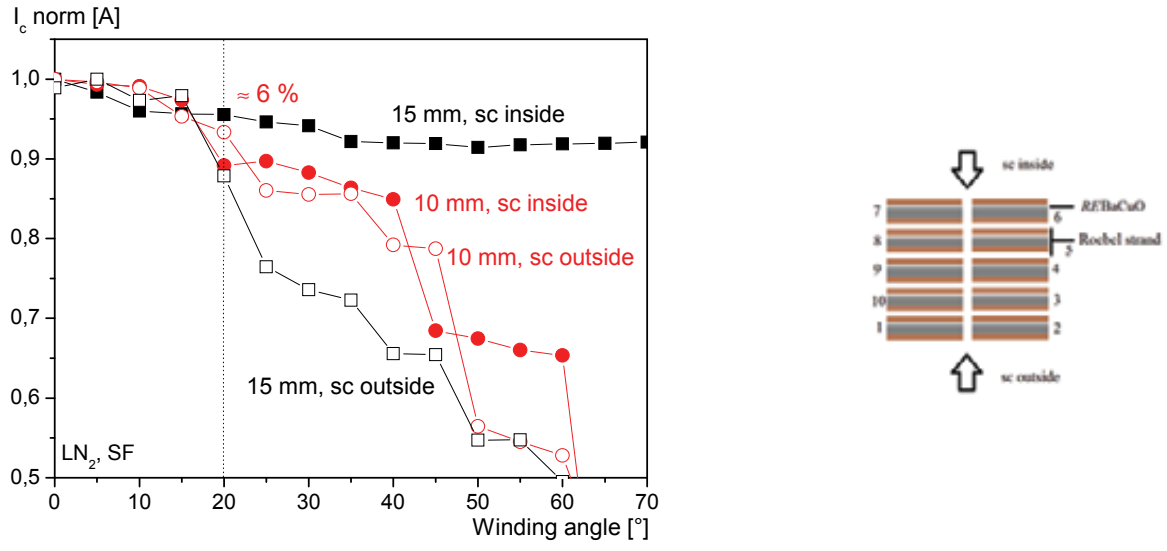

Fig. 8: Continuous edge bending strain measurements for Roebel strands from SuperPower coated conductors and edge radius of 10 and 15 mm. The numbers indicate the radius of the bending edge and sc inside and sc outside means the orientation of the superconducting layer inside or outside the bending shape.

Coated Conductor Rutherford Cable (CCRC) with HTS Roebel strands

Concept

The Rutherford cable concept using Roebel cables was identified to be able providing a 20 kA transport current at 12 T and 50 K operation temperature. The feasibility of the concept however has to be proven by systematic investigations. A first sample of about 0.5 m length (free middle part) should demonstrate the potential of the idea and should deliver first results.

CCRC demonstrator results

To test the real behaviour of Roebel strands in a Rutherford configuration, three Roebel strands were applied on the Rutherford former (see

Fig 9) and tested with transport current (Table 1). Reference values were measured on the straight samples before. The current carrying behaviour of the strands in the central section of the cable showed a slight degradation of 5 – 10%, which correlates with the bending experiments.

Fig. 9: CCRC demonstrator cable with 3 ROEBEL strands

Close to the soldered ends stronger degradations of the currents occurred since in the case of Roebel strand 1 and 3 solder penetrated too close to the bended zone before bending was applied. However, this can be avoided by adapted working instructions.

To optimize the application of Roebel strands on Rutherford structure, the bending angle should be reduced which will lead to longer transposition length in case the former dimensions are unchanged.

Table 1: Results of the critical current measurements of the Roebel strands in the Rutherford structure

I_c self-field	Roebel 1	468.8
I_c self-field in Rutherford	Roebel 1 – Rutherford	152
	Roebel 2	464.2
	Roebel 2 – Rutherford	423.2
	Roebel 3	463.2
	Roebel 3 – Rutherford	58

Transport AC losses of single Roebel strands and Roebel-strands in CCRC geometry

Transport AC-losses at 18, 36 and 72 Hz for different current amplitudes were measured for single Roebel strands and for single Roebel strand wound on the stainless steel former as well (see Fig 10). The results are compared to model calculations which use a strip and an ellipse model.

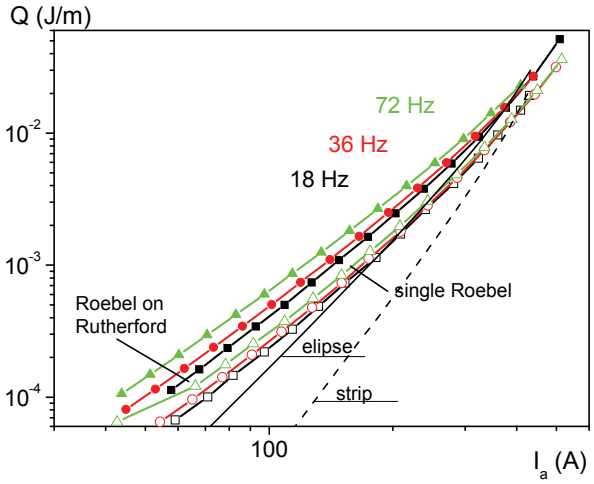

Fig. 10: Transport AC loss measurements of single Roebel strands and mounted on Rutherford structure

An important outcome of these very preliminary investigations was the identification of the former material as a significant source of eddy currents: although the former has been manufactured of two half pieces which are electrically insulated the Roebel strands acted as a connecting “bridge”. As a consequence the design of the former should be optimized; this can be used in parallel to adopt the transposition length.

Summary

In WP12-DAS-01-T06 "Construction and test of DEMO relevant cables" the existing FBI facility has been upgraded to allow a measurement of cable samples not only at 4.2 K, but at elevated temperatures, too.

Measurement on a Round Core Cable (CORC) showed e.g. an Ic = 2.6 kA at 12 Tesla and 4.2 K that decreased to 1.8 kA at 12 Tesla and 21.4 K. A measurement on Twisted stacked-tape cable (out of the scope of the contract) showed an Ic = 4.1 kA at 12 Tesla and 21.6 K.

The measurement of a Roebel cable showed e.g. an Ic = 4.1 kA at 2 Tesla and 20 K, but with increasing field the degradation increased. This shows the necessity of mechanical support against Lorentz forces in particular in azimuthally direction. That such a protection is principally possible was demonstrated by a measurement performed by CERN on a KIT Roebel sample with 12 kA at 6 Tesla and 4.2 K (parallel direction of the magnetic field).

In extended experiments the Ic degradation of Roebel cables caused by bending combined with torsion was investigated. If Roebel cables are used as strands in a Rutherford cable structure, a minimum former thickness of 10 to 15 mm is necessary with not too large winding angles to avoid degradation by crack formation.

The feasibility of a Rutherford cable with 4 mm wide Roebel cables as strands was demonstrated with a typical Ic degradation below 10% compared to the initial Ic of the Roebel cables.

Staff:

C. Barth
W.H. Fietz
W. Goldacker
R. Heller
A. Kario
A. Kling
B. Ringsdorf
S. Schlachter
M. Vojenciak
K.P. Weiss

Literature:

[1] N. Bagrets, W. Goldacker, A. Jung, and K.-P. Weiss, “Thermal properties of REBCO copper stabilized superconducting tapes,” in Applied Superconductivity Conference, 2012.

[2] N. Bagrets, W. Goldacker, S. I. Schlachter, C. Barth, and K.-P. Weiss, “Thermal properties of materials for Coated Conductor Rutherford Cables (CCRC),” submitted for publication, 2012.

[3] C. Barth, D. C. van der Laan, M. Takayasu, K.-P. Weiss, and W. Goldacker, “Measurements of HTS cables in a temperature range of 4.2 K to 80 K and background fields up to 12 T,” in Applied Physics Letters, 2012.

[4] Barth, K.P. Weiss, M. Vojenčiak, and S. Schlachter, “Electro-mechanical analysis of Roebel cables with different geometries”, Supercond. Sci Technol. 25 (2012) 025007.

[5] Kario et al. Investigation of the Coated Conductors Rutherford-cable using ROEBEL-cables as strands, presented at Applied Superconductivity Conference Portland, to be published in SuST.

[6] Stenvall, F. Grilli, and M. Vojenčiak, “On the role of a tape's aspect ratio in the hysteresis losses of round superconducting cables”, Supercond. Sci Technol. 24 (2011) 085016.

Acknowledgement

This work, supported by the European Communities under the contract of Association between EURATOM and Karlsruhe Institute of Technology, was carried out within the framework of the European Fusion Development Agreement. The views and opinions expressed herein do not necessarily reflect those of the European Commission.

Cryogenic Infrastructure (CoA)

Introduction

The cryogenic infrastructure of the ITEP supplies different experiments within the ITEP and other KIT institutes, which are working for the Fusion Programme, with refrigeration power or liquid helium. Such experiments in the ITEP are tests of superconductive components in the TOSKA facility, experiments for the ITER-cryopump in TIMO, and mechanical material tests in different cryostats equipped with traction engines.

For these experiments the cryogenic infrastructure comprises among other things:

- A 2 kW-refrigerator at 4.4 K with a liquefaction rate of 21 g/s (equivalent to 600 litres/h).
- A 300 W-refrigerator at 1.8 K with a liquefaction rate of 5 g/s (equivalent to 145 litres/h).
- A high pressure helium purifier working at 200 bar with a continuous purification mass flow of 14 g/s and a discontinuous purification mass flow of 28 g/s. The residual impurity content is lower than 1 ppm.
- Three recovery compressors with a pressure increase from one to 200 bar and a maximum mass flow of 26 g/s or 527 standard cubic meter respectively.
- A Helium storage system consisting of:
  - stationary liquid helium vessels with a capacity of 15,000 litres or 1,875 kg respectively
  - storage tanks for impure helium with a capacity of 1,075 kg
  - storage tanks for pure helium with a capacity of 1,275 kg
  - The whole storage system has consequently a capacity of 4,225 kg or 23,985 standard cubic meter respectively, see Fig. 3.
- A liquid nitrogen storage vessel with a capacity of 32,650 litres for the supply of all experiments and a filling station to distribute liquid nitrogen in transport vessels.

Fig. 1: He-purifier with a continuous purification rate of 14 g/s at 200 bar.

Fig. 2: Cold box and valve box of the 2 kW-He-refrigerator.

The cryogenic infrastructure is controlled by a state-of-the-art control system based on PCS7 and WinCC. The operation of the components can be done in two control rooms or via clients installed directly at the experiments.

A team of five operators, three engineers and one academic staff member is responsible for maintenance, repair, upgrading and extension of the cryogenic infrastructure for new or changed experiments.

Additional tasks are the supervision of peripheral installations such as

- energy distribution system
- re-cooling water unit
- compressed-air distribution system.

Also, maintenance, repair, upgrading and extension of the

- vacuum systems
- different safety devices like oxygen monitors are tasks of this group.

Beyond these regularly routine works this report is focused on selected extension projects, as well as giving an overview of the cryogenic supply activities for fusion projects.

Fig. 3: Revision of the screw compressors of the 2 kW-He-refrigerator.

Selected maintenance and extension works

2 kW (4.4 K) refrigerator

The following selected maintenance and extension works at the 2 kW-refrigerator were done in 2012:

- new design and reconstruction of the ventilation system of the noise cancelling box
- revision of the screw compressors V2 and V3 of the 2 kW-He-refrigerator
- change or installation respectively of new valve actuators.

Fig. 4: New design and reconstruction of the ventilation system of the noise cancelling box.

300 W (1.8K) refrigerator

The following selected maintenance and extension works at the 300 W-refrigerator were done in 2012:

- remanufacturing of the water cooling cycle.

He-recovery and purification system

The following selected maintenance and extension works at the He-recovery and purification system were done in 2012:

- extension of the warm Helium gas supply system to the calibration laboratory
- reconstruction and modernisation of the filling station for pressurized He gas.

Miscellaneous

- preliminary work for the implementation of the CuLTKa control system in the cryogenic infrastructure.

Cryogenic supply for the Fusion Programme

The different experiments for the Fusion programme in ITEP are supplied with circa 36,747 litres liquid helium. In addition the refrigerators ran nearly 1,550 hours in 2012 for the supply of refrigeration power.

For comparison, the average consumption for such experiments in the period between 2002 and 2011 is about 25,539 litres liquid Helium and 1,679 hours of refrigeration power. So in 2012 we had a higher liquefaction rate and a lower refrigeration power than the mean values of the years before.

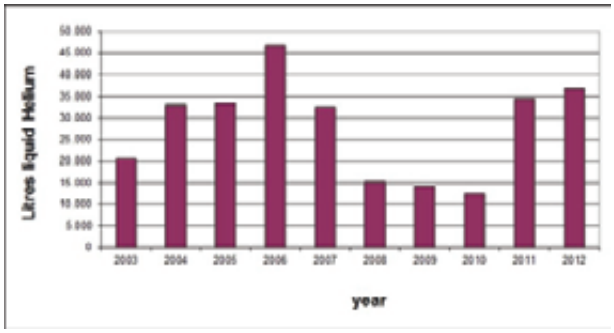

Fig. 5: Liquid Helium supply between 2003 and 2012.

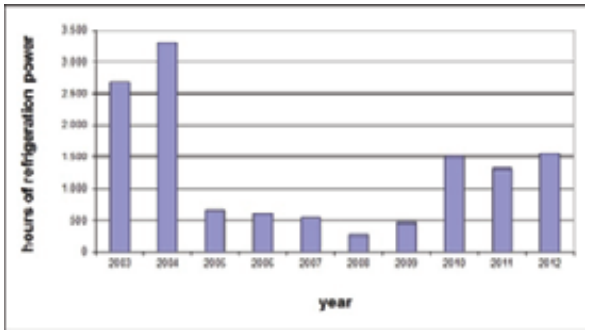

Fig. 6: Hours of refrigeration power between 2003 und 2012

Staff:

A. Baumgärtner
S. Bobien
M. Duelli
U. Fuhrmann
H. Neumann
S. Holzmann
B. König
K. Metzger
D. Wetzel
H. Zimmermann

Fusion Researcher Fellowships (WP11-FRF-KIT/Vojenciak)

Objectives

The project's goal is building, testing and routinely using comprehensive experimental facility to fully characterize HTS conductors for power applications, both in dc and ac.

The goals of this project for the year 2012 are current-voltage characterization of Roebel cables, numerical modeling of Roebel cables and building system for measuring transport losses in liquid helium environment.

Magnetization loss in twisted MgB_2 wires

For reduction of the AC loss in practical superconductor one should reduce diameter of a superconducting filament. Wires with filaments' diameter as small as ~ 50 μm were produced. However, the coupling loss takes a place in multifilamentary wires. To reduce the coupling loss a wire should be twisted. The length of the twist pitch should be optimized to effectively reduce the coupling loss, but don't reduce the critical current too much. We measured samples of MgB_2 wires with the Ti barrier, the Cu stabilization and the stainless steel reinforcement. Samples with various twist pitch were prepared from the same parent wire. Experimental results are shown in figure 1.

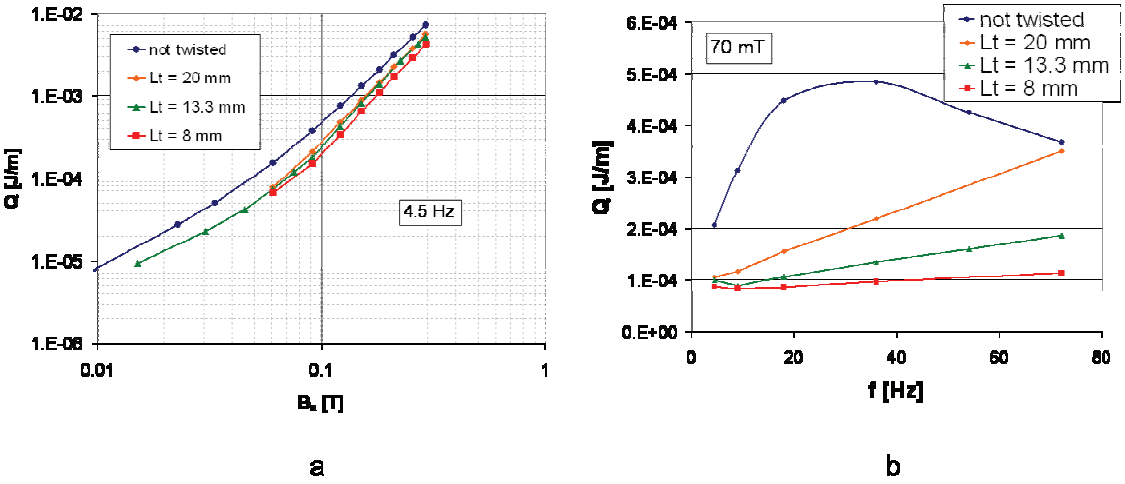

Fig. 1: The magnetization AC loss measured on the twisted MgB_2 wires at 4.2 K. a – dependence of the loss on applied magnetic field (f = 4.5 Hz), b – frequency dependence of the loss at constant field amplitude.

Results show that the not twisted sample was already saturated by the coupling current even with a length of the sample only 80 mm – see peak in the frequency dependence. With shorter and shorter twist pitch the coupling loss decreases. The sample with twist pitch of 8 mm has only very week frequency dependence. It means that such a twist pitch is sufficiently short. The reduction of the critical current caused by twisting was only ~10 %.

The results were presented at International Conference on Superconductivity and Magnetism (ICSM 2012, Istanbul)

Experimental and numerical analysis of coils made from Roebel cable

Roebel cables are one of the options to prepare low inductance, low AC loss coils from a *RE*BCO material. We prepared several coil demonstrators and we investigated influence of the turns spacing on the critical current and the AC loss. Photo of one of the prepared coils is shown in figure 2a.

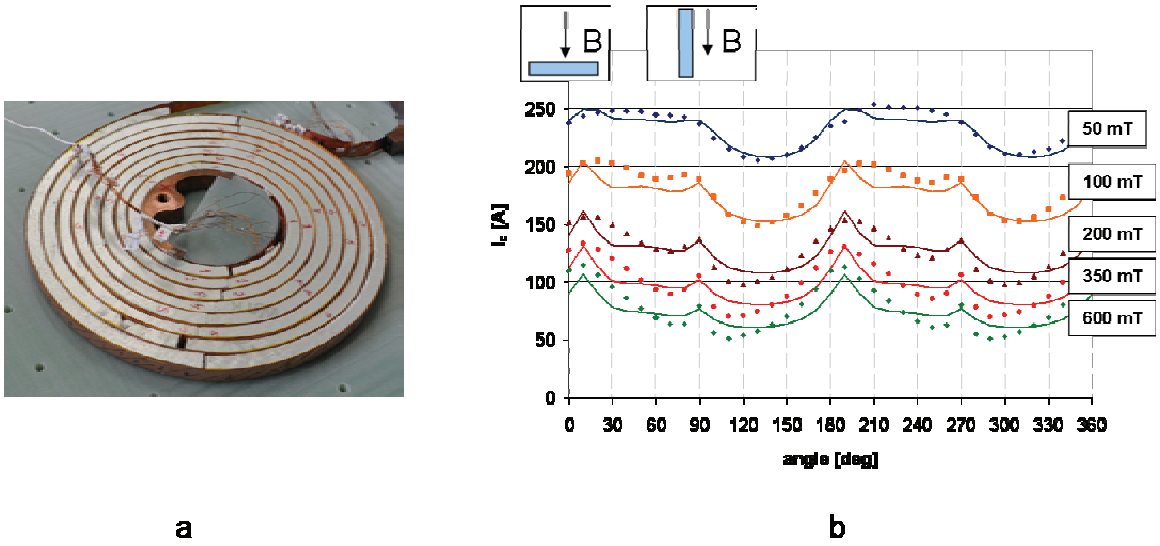

Fig. 2: a – photo of demonstrator coil (spacer 10 mm),
b – dependence of the critical current on the magnetic field and its orientation (original tape, 77 K); points represent experimental data, lines numerical calculation.

A *RE*BCO material exhibits the strong anisotropy; therefore calculation of the critical current is not straightforward. We measured the dependence of the critical current on the magnetic field and its orientation at 77 K for the superconducting tape from which the Roebel cable and consequently the coils were made. Measured characteristics (points) are shown in figure 2b together with results of FEM calculations.

In next step we performed FEM calculations of magnetic field and current density distribution in coils – figure 3.

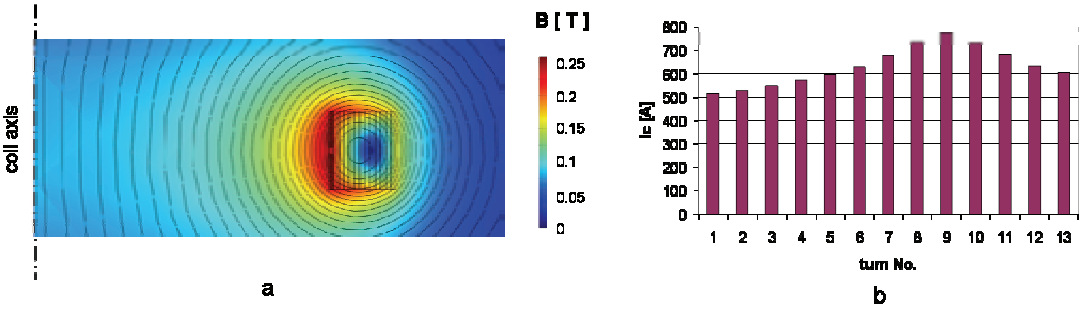

Fig. 3: a – distribution of the magnetic flux density in the coil interior and ambient,
b – calculated critical current in individual turns of the coil.

With help of the numerical calculations we were able to predict not only global I-V characteristic of the coil, but also local distribution of the current density and the critical current of individual turns – as it is shown in figure 3b.

After the measurement of the critical current (figure 4a) we performed measurement of a transport AC loss. The AC loss strongly depends on the spacer thickness; experimental results are shown in figure 4b.

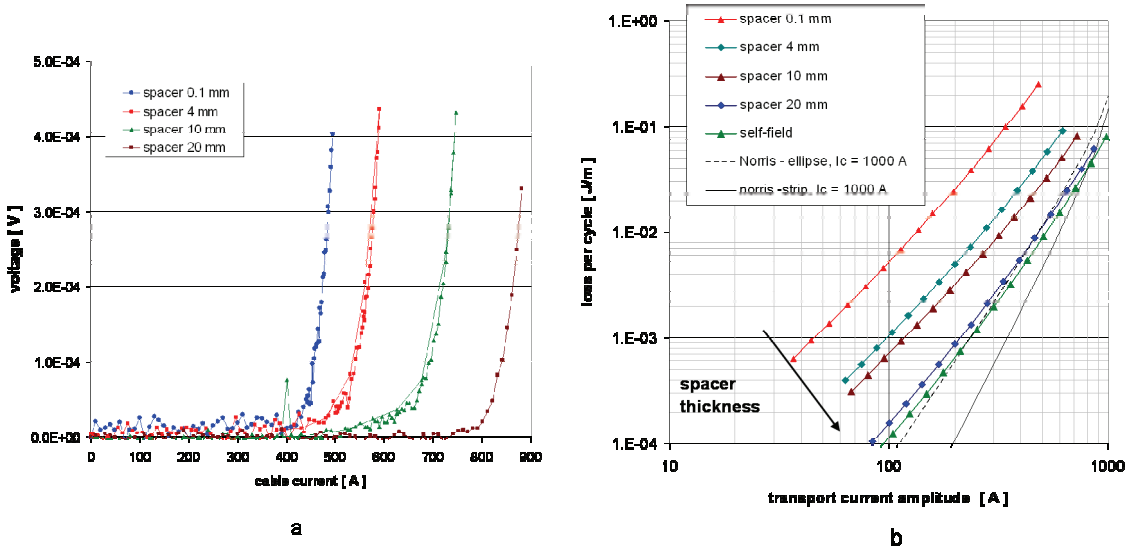

Fig. 4: I-V curves (figure a) and AC loss (figure b) measured on coils with various spacer thickness.

These characteristics show that in some cases it can be beneficial to increase the spacing between individual turns to reduce the AC loss – difference between loss in the coil with the thickest and loss in the coil in the thinnest spacer is 30-fold.

The results were presented at Applied Superconductivity Conference (ASC 2012, Portland).

Magnetization loss in striated *RE*BCO tapes

Practical *RE*BCO superconductors are made in form of coated conductors with high aspect ratio. This has consequence in a relatively high hysteretic loss caused by a component of the magnetic field perpendicular to the wide face of a conductor. Effective way to reduce the AC loss caused by this component of the magnetic field is striation of the superconducting layer to filaments. We measured the AC loss of the samples prepared by laser scribing technique. Samples with various numbers of filaments (up to 120) were prepared. The lowest width of the filament was less than 100 μm. The magnetization losses measured by the recently developed calibration free setup are shown in figure 5.

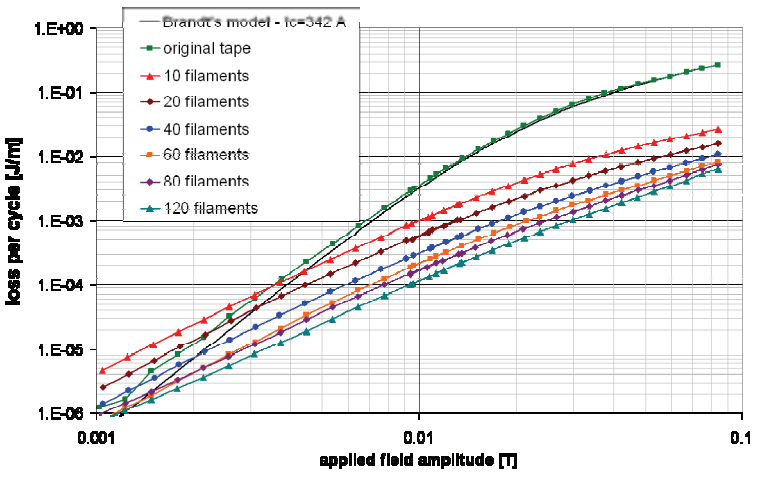

Fig. 5: Magnetization AC loss measured on samples with various number of filaments.

The results show that striations effectively reduce the magnetization loss at high fields. However, there is probably certain level of the electric coupling between filaments, because the measured AC loss reduction is not directly proportional to the number of the filaments as it is theoretically predicted.

The results were presented at workshop Coated Conductors for Applications (CCA 2012, Heidelberg).

Transport AC loss in *RE*BCO tape in LHe environment

Measurement of the transport AC loss in the liquid helium environment is challenging because the critical current of practical conductors in self-field conditions is usually high. The main technical problems are following: current leads for high currents, heating by resistive current leads, stability of a conductor and a quench protection. A new apparatus simplifying some of these problems was designed, constructed and tested. We use a toroidal transformer to supply AC current to the sample – see figure 6.

The transformer is designed to provide high secondary current, while primary current is several hundred times lower. Therefore current leads from room temperature can be made of conductors with small cross-section. We performed measurements on the 4 mm wide *RE*BCO sample in metal cryostat at temperatures of 77 K and 65 K in liquid nitrogen and of 4.2 K in liquid helium. Results of measurements at frequency of 72 Hz are summarized in Figure 7a. A secondary circuit has very small impedance and therefore quench of the sample does not lead to its damage. Particular sample quenched several times during the measurements. Measured resistance during the quench test is shown in figure 7b.

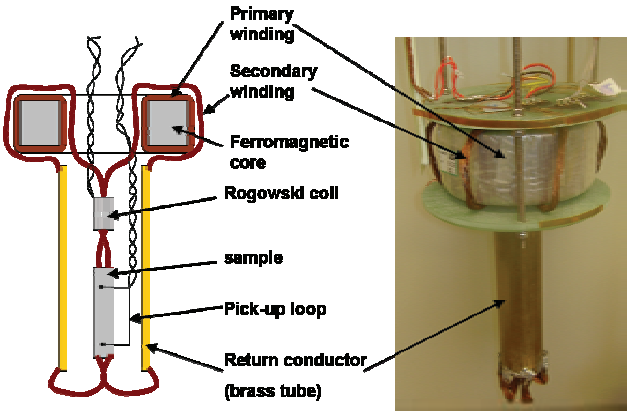

Fig. 6: Coaxial arrangement of the setup for transport AC loss measurement.

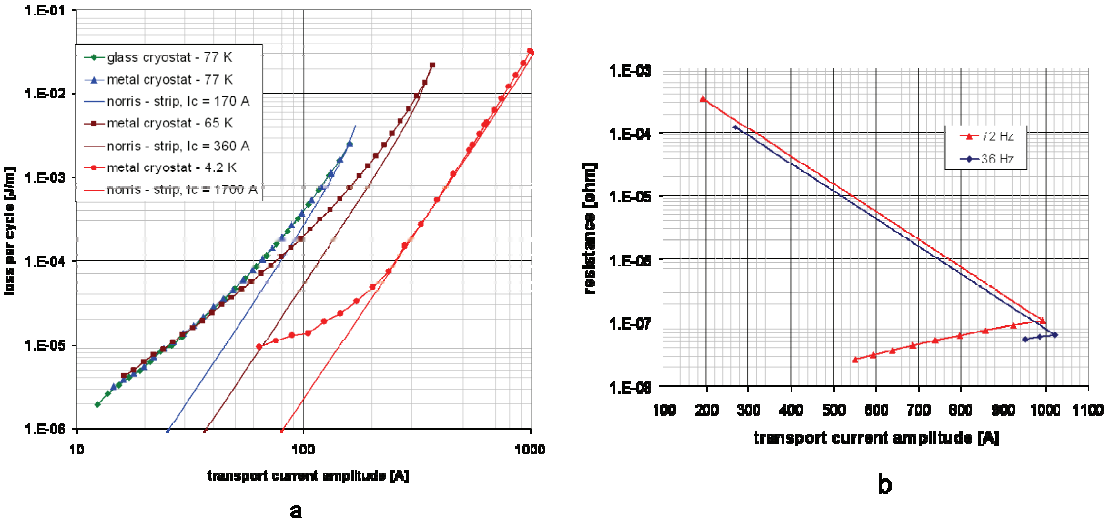

Fig. 7: a – Transport AC loss measured on the same sample at 3 temperatures.
b – change of the sample resistance during quench test

The results were presented at workshop Coated Conductors for Applications (CCA 2012, Heidelberg).

Staff:

M. Vojenciak

Acknowledgement

This work, supported by the European Communities under the contract of Association between EURATOM and Karlsruhe Institute of Technology, was carried out within the framework of the European Fusion Development Agreement. The views and opinions expressed herein do not necessarily reflect those of the European Commission.

Goal Oriented Training Programme" Cryogenic Training Programme for Fusion" (WP10-GOT-GIRO (FU07-CT-201000065))

Objectives

In the frame of a structured training program, it is intended to train early-stage engineers during 3 years. This program will take place within a collaborative group to provide the technical know-how and the skills which are necessary for the engineering of components for ITER or fusion program and for the management of ITER relevant projects. The aim of the training is to reinforce the knowledge of the trainees thanks to their involvement in an engineering team constituted of experts in various domains.

Status

End of February/Begin of 2012 the "Large Refrigeration School" was held at CEA Grenoble to teach all trainees in the field of refrigeration. At this occasion an acting board and an advisory board meeting was held at CEA Grenoble and the trainees gave presentations about their work. From February to April B. Kuffner participated at the 400 W test campaign in CEA Grenoble. In September 2012 the "Cryogenic School" was held at KIT in connection to the VDI course " cryogenics - basics and working methods, development status, applications, development". In addition the trainees gave presentations over their work and an acting board meeting was held at KIT.

Staff:

W.H. Fietz
B. Kuffner
R. Lietzow
M. Schrank
M. Süßer

Literature:

[1] Schrank M., *Süßer M.:“Compilation of an uncertainty budget for cryogenic temperature measurements”, to be published in the proceedings of the International Crogenic Engineering Conference (ICEC-24),Fukuoka Japan, May 14th - 18th, 2012, volume 24

[2] Müller R., *Schrank M., Süßer M.: Optimizing the geometry of Venturi tube flow meters“, to be published in the proceedings of the International Crogenic Engineering Conference (ICEC-24),Fukuoka Japan, May 14th - 18th, 2012, volume 24

[3] Schrank M., Süßer M.: “Gasdurchflussmessung in der Kryotechnik“, to be published in the proceedings of the Meeting of the "Deutscher Kälte- und Klimatechnischer Verein" (DKV), Würzburg, Nov. 21st – 23rd, 2012, volume 39

Acknowledgement

This work, supported by the European Communities under the contract of Association between EURATOM and Karlsruhe Institute of Technology, was carried out within the framework of the European Fusion Development Agreement. The views and opinions expressed herein do not necessarily reflect those of the European Commission.

Breeding Blanket

Design Tools and Methodologies – Evaluation / Tests of CAD-based Computational Tools for Engineering Analysis (WP12-DTM-01)

Assessment of ANSYS Workbench Hybrid Platform (WP12-DTM-01-T03)

During the past few years there has been a dramatic increase in simulation efforts relevant to fusion technology. Commercial software vendors have expanded the breadth of their offerings to include rapid physical modeling, smooth integration with CAD packages and convenient coupling across physical disciplines. Traditional neutronics modeling via MCNP has been extended to arbitrary geometries by providing CAD interfaces. Broadly multi-physical modeling efforts in the area of fusion plasma and structures under radiation have been initiated. These developments are very important as they have the potential to vastly improve and accelerate the design analysis process.

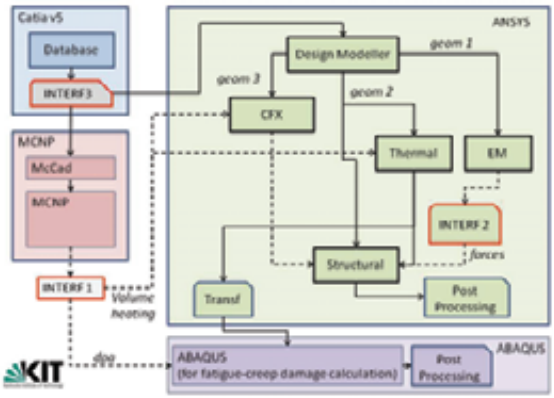

Fig. 1: The KIT ANSYS Hybrid Platform.

The activity performed in the framework of this EFDA task aims to develop a computational platform for supporting the integrated design of Fusion reactor components and systems. KIT is participating to this activity presenting a system that is currently used for design activities in Blanket Systems and that is under further development to improve its interfacing tools for a rapid and almost automatic exchange of data among the main design tools. This platform (see Figure 1) is based on CAD (Catia), Neutronic (MCNP), ANSYS for thermo-hydraulic, mechanic and electromagnetic analysis, and ABAQUS for special programme for inelastic fatigue-creep assessment or pebble bed thermo-mechanics (see Figure 1). The interface tools of the ANSYS platform constitutes the main tools for the exchange of data (from this the name of “ANSYS Hybrid platform”); the transfer of data with other platform is integrated with interfaces able to transfer CAD files from the CAD System (interface 1) or to transfer results of the neutronic analyses (e.g. power distribution) to the thermo-hydraulic section in ANSYS (interface 1). Special procedures are also integrated in the ANSYS platform to transfer data from EM analysis and structural models (interface 2).

The first step of the work was the identification of the design work-flow for the blanket system. This work started from the experience of the teams involved in the design and analysis of the systems. The output is a flow chart in which the different necessary calculations (and related software) are identified and the relationships among them at different stages are defined. The blanket is a highly complex system requiring to develop an appropriate combination of materials, manufacturing and cooling technologies and a design integrating these with neutronics, thermo-mechanical, electro-mechanical, thermo-hydraulic, fluid-dynamical, magneto-hydrodynamic, radiation and safety aspects. The scheme presented in Figure 2 shows the whole integrated process used in a conceptual phase of the design: in this extended process description Tritium analyses and manufacturing feasibility are included, as well. The core of the process is based on iterations among CAD engineering, neutronics, fluid-dynamic, EM and structural analysis. This part has been fully implemented in the KIT Design Platform.

On the basis of the identified workflow the interfaces among all the software tools as part of the codes included in the system should be identified. For each of these interfaces the specifications for the data transfer have been defined, existing tolls listed, gaps identified and solutions proposed.

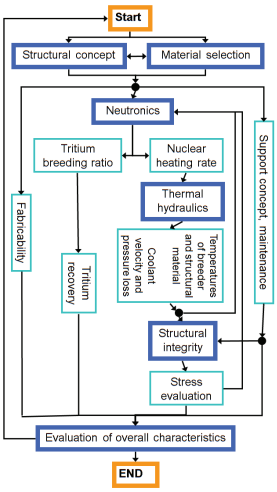

Fig. 2: Blanket Design work-flow.

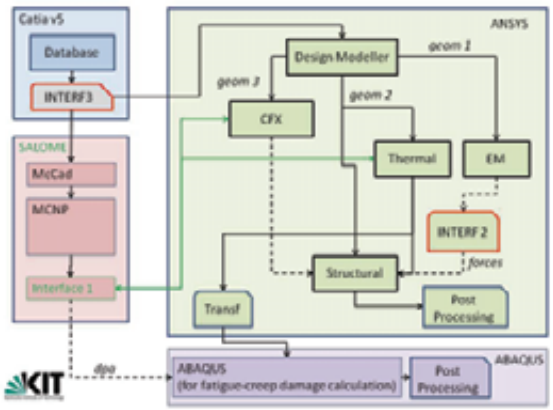

Fig. 3: Improved (green arrows) data transfer at the ANSYS hybrid platform.

During 2012 the development of the KIT ANSYS Hybrid platform has continued in parallel to this EFDA task. The main improvements have been achieved in the development of the MCNP transfer data capability and CAD file management. The different modules of the neutronic software tools (i.e. McCad, MCNP) have been integrated in a SALOME platform and a new 3-D neutronic tool has been developed to prepare data for the ANSYS calculations. A test to transfer data to CFX tools has been successfully performed.

Preparation of Test Cases (WP12-DTM-01-T02)

The main scope and objective of this task is to provide a suitable modeling and computational platform as an environment for the design of DEMO in-vessel-components (blanket test case).

For the testing of that computational platforms (Ansys Workbench and Salome) the below introduced test case was defined according to the conceptual engineering design of the Helium Cooled Pebble Bed Test Blanket Module (HCPB TBM). The main dimensions and geometrical layout of the test case model were determined from an advanced blanket design. The blanket test case has been assembled that way to give an acceptable complexity for different physical disciplines from the point of view of the numerical modeling.

The test model (blanket test case) contains all the relevant geometrical features, which characterize a blanket machine and seem important from a FE modeling point of view. As these components are actively cooled, the presence of the internal cooling channels was mandatory - especially from the thermo hydraulic point of view. As a matter of course the design of such a component requires an iterative design procedure and since the performed engineering simulations are multi-physics, the appropriate data transfer has to be tested and evaluated between the different physical disciplines on each computational platform with a simplified blanket model.

All physical fields (thermo-hydraulic, structural, electro-magnetic, and neutronic) might introduce some sort of further modifications in the investigated geometries and require different elaborated enclosure (environment). The scope of the test model is to integrate these simplifications and try to take into account all the requirements from the different physical fields.

The test model has the following poloidal-toroidal-radial dimensions: 655*484*711mm.

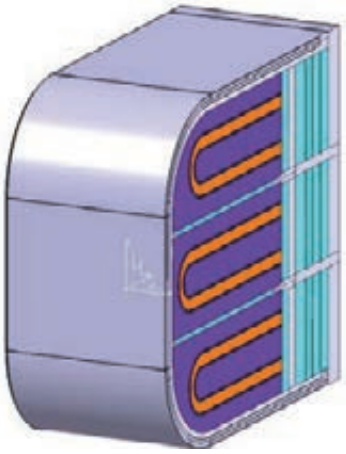

Fig. 4: Blanket test case assemblycross section in breeding zone.

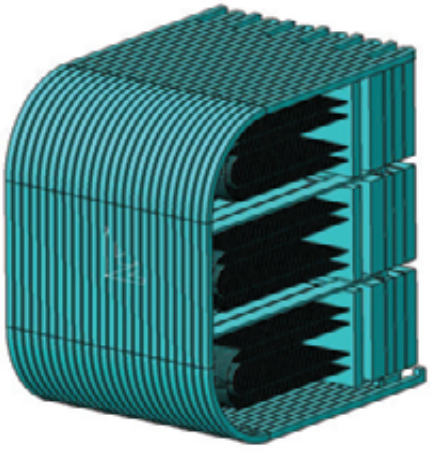

Fig. 5: Helium circuit (filled voids) Component in test case CAD file FLUID_X.

The investigations were mainly focused on the data transfer between MCNP output and ANSYS (CFX and Thermal) (Interface1 in Figure 3) and on the required CATIA input of MCNP computations (Interface 3) to facilitate the usage of McCad conversion tool.

The previously listed numerical calculations might have to be carried out by different experts and each field requires different mesh resolutions. Therefore an appropriate (typically mesh data) transfer has been implemented between these different physical fields. A mesh translation module has been developed, tested and integrated into the computational platform SALOME, performing the translation of neutronic results into an appropriate format and providing 3D input for thermo mechanical calculation (nuclear heating).

Staff:

L. V. Boccaccini
Sz. Kecskés
I.A. Maione
Y. Qiu

Acknowledgement

This work, supported by the European Communities under the contract of Association between EURATOM and Karlsruhe Institute of Technology, was carried out within the framework of the European Fusion Development Agreement. The views and opinions expressed herein do not necessarily reflect those of the European Commission.

Identification of DEMO Failure Modes (WP12-DTM-03-T02-01)

Objectives

The activities within this task aim for the identification of failure modes of candidate structural materials in a helium cooled blanket and of divertor components of a DEMO. Therefore the reference designs of these components are reviewed considering the results of structural analyses performed on them. The impact of loadings and loading conditions on damage and failure of structural materials at the different loading levels is evaluated.

Failure Modes in Helium Cooled Blanket of DEMO

Design and structural materials

To determine the failure modes in helium cooled blanket concepts the European Helium Cooled Pebble Bed (HCPB) Blanket is considered as reference. The HCPB blanket developed at KIT [1, 2] consists of a U shaped first wall, cyan coloured part in Figure 1, surrounded by a grid of cooling plates, brown coloured part in Figure 1. The first wall and the grid cooling plates as well as the grid cooling plates to each other's will be attached by welds. To lead the coolant, here helium, to the cooling channels inside the first wall and the grid cooling plates different manifold plates are foreseen which also will be welded to the grid plates and the first wall. The so resulting blanket box will be closed by the cap plates at the bottom and at the top (in Figure 1 the top cap plate is withdrawn). The cap plates have also proper channels for cooling and will be attached to the box by welds. The grid inside the box hosts the breeder units (BU) each of them is a box filled with the breeder and neutron multiplier pebble beds.

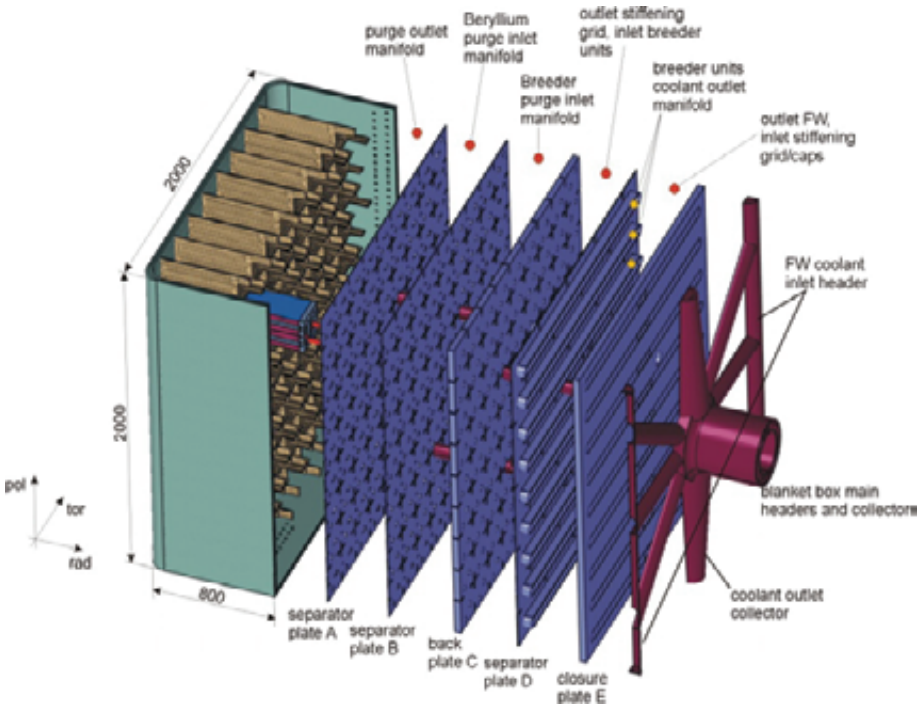

Fig. 1: Schematic layout the European Helium Cooled Pebble Bed (HCPB) Blanket [1].

The main functions of the blanket are:

- Collecting fusion power carried out by fusion neutrons and radiation and transferring it as heat to the coolant
- breeding tritium by nuclear transmutation of lithium

A secondary function of the blanket is shielding and hence protecting the vacuum vessel. As structural material for the different components of the blanket the ferritic martensitic steel EUROFER has been selected. Diffusion bonded, tungsten inert gas (TIG) bonded, electron beam (EB) bonded, and laser bonded EUROFER welds shall be used for joining. Under operation the nominal temperature in the EUROFER structures of the HCPB blanket varies between 350 and 550°C, which are the specified limits of the operational temperature windows for EUROFER under fusion reactor conditions. The nominal coolant pressure is selected in the range 80 to 100 bar (8 to 10 MPa).

Loadings and failure modes

The coolant pressure results in primary stresses in all cooled components of the HCPB blanket. Due to the nonhomogeneous temperature fields secondary stresses are induced. In addition further secondary as well as peak stresses appear at geometrical discontinuities [3]. Under pulsed mode, and even under steady state operation of DEMO the temperature fields in the different components and hence the secondary and peak stresses are cycled resulting in cyclic thermo-mechanical loading superimposed to the primary loading [3]. In addition and in view to possible plasma disruptions other electromagnetic loadings (halo and eddy current loadings) yield stresses of primary type [4].

The loadings identified above determine the failure modes against which the components shall be designed considering their relevance for and the loadings of the different loading levels:

- Immediate inelastic collapse and instability
- Progressive inelastic deformation (Ratcheting)
- Creep (steady state operation)
- Fatigue
- Creep-fatigue
- Fast fracture (welds)

Immediate inelastic collapse and instability is usually caused by too high primary stresses and can be prevented by limiting them. Progressive inelastic deformation is the increase in inelastic strain under cyclic loading due to primary and secondary stresses. Its evaluation aims either preventing ratcheting or keeping inelastic strains under the allowable strain limits. Creep is relevant for the high temperature region of the blanket where the temperature rises higher than that determining the regime of negligible creep. It is of main importance for steady state and long pulsed operation and lifetime limiting in combination with fatigue where failure is accelerated by the mutual interaction between creep and fatigue. In the blanket regions where the temperature remains in the negligible creep regime of EUROFER fatigue as an important failure mechanisms needs to be considered, particularly at notches, discontinuities, etc. where high peak stresses appear [3].

Fast fracture is failure caused by defects, which might be unavoidable particularly in the numerous welds foreseen for the fabrication of the blanket. All these failure modes are affected by in-service environmental conditions, in particular neutron irradiation, impurities in the coolant and high temperatures which yield changes in the material properties relevant for the different failure modes. Here the environmental effects are subdivided in primary and secondary environmental effects. While the primary environmental effects are well known and need anyhow to be considered, the secondary environmental effects are uncertain in their appearance and importance for the structural integrity which are strongly dependent on service time and external conditions, e.g. quality of the coolant:

- Primary environmental effects
  - Irradiation induced hardening and embrittlement

- Secondary environmental effects
  - Impure helium on fatigue & creep-fatigue
  - Irradiation induced swelling
  - Thermal aging

Irradiation induced hardening and embrittlement are identified as primary effects because of the very high irradiation dose expected within the service time. Hardening and embrittlement are particularly significant for the regions where the temperature goes below the nominal lower operation temperature of EUROFER (350°C). For the other regions embrittlement, which is mainly caused by the generation of transmutation helium, is important and need to be considered. While hardening increases the material limits determined by strength like those for immediate plastic collapse embrittlement yields loss of ductility and toughness and hence decrease in the material limits for the other failure modes, particularly for progressive inelastic deformation (strain limits) and fast fracture (DBTT, toughness limits). Irradiation induced swelling is considered as a secondary environmental effect because EUROFER, as a ferritic martensitic steel has high resistance against swelling as it is observed in irradiation experiments in fission reactors. Nevertheless under irradiation with fusion neutrons higher helium generation rates are expected leading to more swelling [5] which, dependent on swelling non-homogeneity, component geometry and boundary conditions, might be significant for failure.

Further secondary environmental effect is that of impure helium which is found to affect fatigue and creep-fatigue behaviour of structural materials of helium cooled high temperature fission reactor (HTGR) [6]. However the effect of impure helium on EUROFER is unknown and need to investigated and verified. Thermal aging is another effect which needs to be considered for the hot regions of the blanket with regard to a long service time. Also here further investigations are necessary to quantify the effect of thermal aging on particular failure modes taking into account possible role of irradiation.

Failure Modes in Helium Cooled Divertor of DEMO

Design and structural materials

For determining the failure modes of helium cooled (HC) divertor of DEMO the HC divertor developed at KIT [7, 8] is considered as reference. This divertor has a modular design where several units of the so-called 9-finger-module are assembled to build the divertor target plate. The 9-finger-module itself consist of 9 finger modules with a common manifold (s. Figure 2). Due to the differences in functionality and operating temperature range different materials are selected for the parts of the finger module. For the tile, which is particularly the interacting part with the plasma having an armour function, tungsten is selected because of its low sputtering yield and its very high melting point. The expected temperatures when cooling this part are in the range 1200-2000°C. Cooling is realized by attaching the tile to a thimble shaped part which is cooled at the inner surface by helium and therefore pressurized acting as a structural component. Because of the very high temperatures expected in the thimble WL10, tungsten with 1% La_2O_3 is selected and for the first time as structural material. The operational temperatures in the thimble vary between 1200°C at the tile side down to 650°C at the opposite side. The lower temperature is determined considering the brittleness of tungsten in the low temperature regime and possible shift of its ductile-to-brittle transition towards higher temperatures. Consequently a joint of the thimble to another part built from a more ductile structural material is required. This part can be a EUROFER-ODS or a ferritic-ODS ring which is joint to the housing built from EUROFER.

In summary, for realizing the hybrid material concept required for the HC divertor considered here the following structural materials and joints are foreseen:

- Structural materials and operational temperature ranges:

- EUROFER97, 350 – 550°C
- EUROFER-ODS / Ferritic ODS, 450 – 650°C
- WL10, 650°C – 1200°C

- Welds and joints
  - EUROFER97 welds (diffusion bonding, TIG, EB, laser)
  - Brazed tungsten-tungsten joints
  - Dissimilar tungsten-steel joints

The main functions of the divertor are removing the fusion reaction products, in particular α-particles from the plasma and to transfer their energy to heat carried out by the coolant. Thereby very high heat flux is expected. The HC divertor considered here is designed for a heat flux of 10 MW/m^2 what requires jet impingement cooling [7]. This is realized using a steel cartridge carrying jet holes and placed concentrically inside the thimble [7-10] (see Figure 2). The maximum helium velocity achieved by the jet cooling is around 240 m/s whereas the pressure drop amounts approximately 0.12 MPa for a nominal helium pressure of 10 MPa [9-10]. The inlet/outlet temperatures of helium are specified equal 600°C/700°C [7].

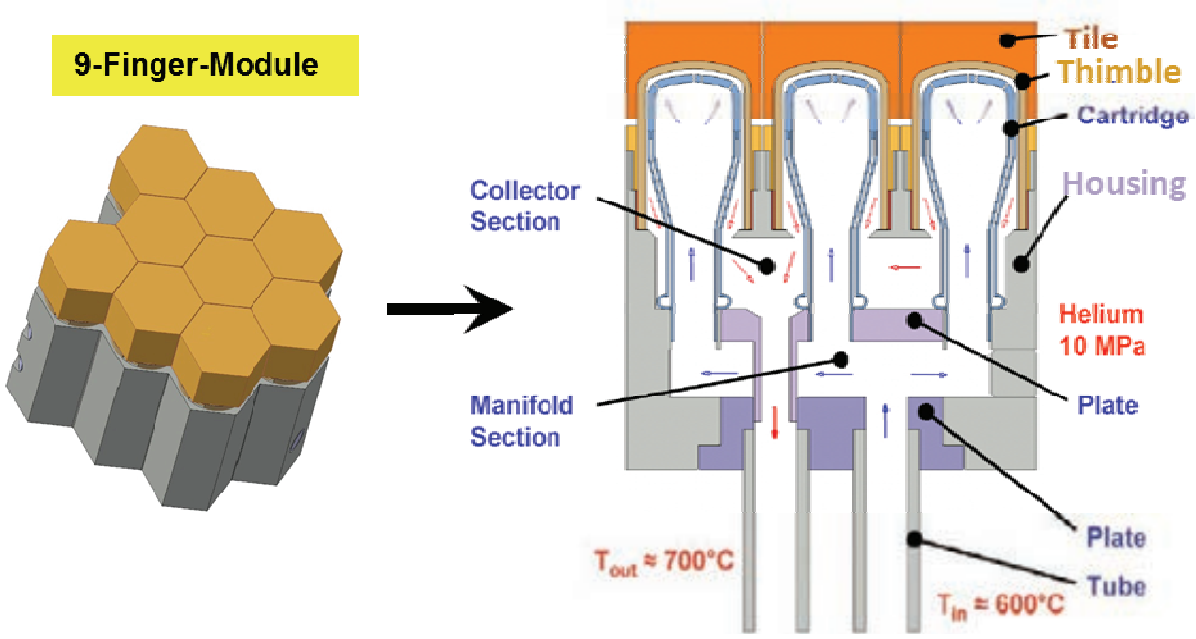

Fig. 2: Schematic cross sectional view of the helium cooled divertor design considered [8].

Loadings and failure modes

Considering the loadings in the structural parts, WL10 thimble, EUROFER-ODS ring and EUROFER housing, primary stresses are expected mainly due to the coolant pressure. The non-homogeneous temperature fields and the thermal mismatch between the different structural materials selected induce secondary stresses in addition [10]. Peak stresses are also expected particularly at geometrical as well as material discontinuities. Due to the thermal mismatch between the different structural materials fractions of secondary and peak stresses are already induced during fabrication particularly at the joints and need also to be considered.

These loadings determine the failure modes against which the components shall be designed considering their relevance for and the loadings of the different loading levels:

- Immediate inelastic collapse and instability
- Progressive inelastic deformation (Ratcheting)
- Creep

- Fatigue
- Creep-fatigue
- Fast fracture (tungsten / tungsten joints, welds)

Immediate inelastic collapse and instability is usually caused by too high primary stresses and can be prevented by limiting them [10]. Progressive inelastic deformation is the increase in inelastic strain under cyclic loading due to primary and secondary stresses. Its evaluation aims either preventing ratcheting or keeping inelastic strains under the allowable strain limits. Creep is relevant for the high temperature region of the divertor parts where the temperature rises higher than that determining the regime of negligible creep of the structural material. It not only affects the ratcheting behaviour but also limits the lifetime due to creep damage. In addition creep yields in combination with fatigue creep accelerated failure due to mutual interaction between creep and fatigue damage. In the divertor regions where the temperature remains in the negligible creep regime of WL10 (thimble) and EUROFER (housing) fatigue is an important failure mechanism and needs to be considered, particularly at discontinuities where peak stresses are particularly high.

Fast fracture is significant for the thimble and the joint between the thimble and the EUROFER-ODS ring particularly when cooling down to temperatures below the ductile to brittle transition temperature (DBTT). It can be also caused by defects, which might be unavoidable in the numerous welds foreseen for the fabrication of the steel parts of the divertor.

All these failure modes are affected by in-service environmental conditions, in particular neutron irradiation, impurities in the coolant and high temperatures which yield changes in the material properties relevant for the different failure modes. Here the environmental effects are subdivided in primary and secondary environmental effects. While the primary environmental effects are well known and need anyhow to be considered, the secondary environmental effects are uncertain in their appearance and importance for the structural integrity which are strongly dependent on service time and external conditions, e.g. quality of the coolant:

- Primary environmental effects
- Irradiation induced hardening and embrittlement
- Secondary environmental effects
- Impure helium on fatigue & creep-fatigue
- Thermal aging
- Erosion due to high helium flow rates

Even the irradiation dose expected during the design lifetime of the divertor is much lower than that of the blanket it is high enough for inducing hardening and embrittlement particularly of WL10 in the low temperature region of the thimble. In EUROFER-ODS and even EUROFER parts low hardening and embrittlement are expected due to the high operational temperatures and relatively low irradiation dose. While hardening increases the material limits determined by strength like those for immediate plastic collapse the accompanying embrittlement yields loss of ductility and toughness and hence decrease in the material limits for the other failure modes, particularly for progressive inelastic deformation (strain limits) and fast fracture (DBTT, toughness limits). Irradiation induced swelling is not considered as an environmental effect because the irradiation dose does not induce significant swelling in the selected structural materials. However, irradiation induced swelling shall be considered and evaluated for brazed joints, where other less swelling resistant materials might be used, e.g. Cu based brazing.

Further secondary environmental effect is that of impure helium which might affect fatigue and creep-fatigue behaviour of the structural materials selected. However the effect of impure helium on WL10, EUROFER-ODS and EUROFER is unknown and need to investigated and verified. Thermal aging is another effect which needs to be considered for the hot re-

gions of the divertor with regard to a long service time. Also here further investigations are necessary to quantify the effect of thermal aging on particular failure modes taking into account possible role of irradiation.

The last failure mode listed here is related to the high flow rate of helium required for the jet impingement cooling, which might cause erosion at the inner surface of the thimble. This erosion might be significant with regard to the thin wall of the thimble and cannot yet be excluded due to the lack of proper information and data.

Finally it is worth to note that even the tile is not a structural part, its failure and the failure of the joint between the tile and the thimble would have a strong impact on the temperatures occurring in the thimble and might hence accelerates its failure. Dependent of their probability failure of the tile and the joint between the tile and the thimble have to be considered in the design assessment of the thimble, e.g. by evaluating the resulting loadings as accidental loading scenarios in proper loading level.

Staff:

J. Aktaa

Literature:

[1] L.V. Boccaccini et al., J. Nucl. Mat. 329-333(2004)148-155.

[2] F. Cismondi et al., Fus. Eng. Design 84 (2009) 607-612.

[3] J. Aktaa, S. Kecskés, F. Cismondi, Fus. Eng. Design 87 (2012) 1085-1090.

[4] L.V. Boccaccini, P. Norajitra, P. Ruatto, F. Scaffidi-Argentina, Fus. Eng. Design 39-40 (1998) 843-849.

[5] R.L. Klueh, Current Opinion in Solid State and Materials Science 8 (2004) 239-250.

[6] V. N. Shah, S. Majumdar, K. Natesan, C.A. Greene, Review and Assessment of Codes and Procedures for HTGR, Technical Report, Argonne National Laboratory, ANL-02/36, 2003.

[7] P. Norajitra et al., Fus. Eng. Design 82 (2007) 2740-2744.

[8] P. Norajitra et al., Fus. Eng. Design 84 (2009) 1429-1433.

[9] R. Krüssmann, T. Ihli, P. Norajitra, Jahrestagung der Kerntechnischen Gesellschaft Deutschland, Aachen, 2006.

[10] P. Norajitra, Divertor Development for a Future Fusion Power Plant, PhD thesis, Karlsruhe Institute of Technology, 2011.

Acknowledgement

This work, supported by the European Communities under the contract of Association between EURATOM and Karlsruhe Institute of Technology, was carried out within the framework of the European Fusion Development Agreement. The views and opinions expressed herein do not necessarily reflect those of the European Commission.

Identification of Equivalent Failure Modes in ITER and Gen-IV (WP12-DTM-03-T03-01)

Objectives

The activity aims the identification of equivalent failure modes in DEMO and GEN IV of fission power plants by reviewing documents on structural analyses and failure modes in components of GEN IV fission power plants and comparing them with those identified in WP12-DTM-03-T02 for blanket and divertor components of DEMO. Thereby similarities in selected structural materials and expected failure modes will be concluded.

As at KIT the work within WP12-DTM-03-T02 is concentrated on the identification of failure modes of helium cooled blanket and divertor, mainly the GEN-IV high temperature reactor concepts are considered, in particular the Sodium Fast Reactor (SFR), the Very High Temperature Reactor (VHTR) and the Gas Fast Reactor (GFR).

GEN-IV High Temperature Reactor Concepts in Comparison to Fusion DEMO

Structural Materials

Reviewing the Technology Roadmap for Generation IV Nuclear Energy Systems [1] a list of main selected structural materials can be summarized in Table 1. In two of the concepts considered here (SFR and GFR) ferritic-martensitic as well as their ODS variants are chosen as primary candidate. For the third concept (VHTR) Ni-base alloys beside graphite and ceramics are the first choice. The main reason for selecting ferritic-martensitic (F/M) as well as their ODS variants is actually the same than selecting them for DEMO, namely their high resistance to irradiation induced swelling. In comparison to austenitic steels they withstand very high irradiation doses (> 150 dpa) with nearly no swelling [2]. The ductile to brittle transition of this type of steels is a drawback which however depends on the composition, in particular the Cr content [3]. Irradiation at high temperatures (> 400°C) shows nearly no embrittlement and shift in the ductile to brittle transition temperature for 9Cr F/M steels and even a shift to lower temperatures for the more brittle 12% and 17% Cr steels [3]. These properties make this type of steels very useful for applications under high temperature and high irradiation dose conditions and therefore they are selected for the components operating under these conditions in GEN-IV fission as well as in future fusion power plants. In addition the F/M steels have in comparison to the austenitic steels lower thermal expansion coefficient what makes them good option for constrained high-temperature components, e. g. the pipes of heat exchanger (see Table 2). Never the less austenitic steels are also selected as structural materials for the high temperature hot gas components of the GFR and the vessel of the SFR.

Table 1: Selected structural materials for the different GEN-IV fission reactor concepts (P = primary option, S = secondary option) [1].

System	F-M Steels	Austenitic S. S.	ODS Steel	Ni-base Alloys	Graphite	Refractory Alloys	Ceramics
GFR	P	P	P	P	-	P	P
LFR	P	P	S	-	-	S	S
MSR	-	-	-	P	P	S	S
SFR	P	P	P	-	-	-	-
SCWR	P	P	S	S	-	-	-
VHTR	S	-	-	P	P	S	P

The commonalities in the selected structural materials have also to do with the similarities in the aimed maximum irradiation dose, which is for the GFR and SFR in the same range than that of fusion DEMO (see Table 2) [4]. The two orders of magnitude lower He generation

rates expected in structural materials of considered GEN-IV than that of fusion DEMO makes the He generation and the resulting embrittlement fusion specific problems which probably can only be solved by fusion R&D activities.

Table 2: Candidate structural materials of the GEN-IV fission reactor concepts considered and their specified operational conditions (data from [1], [4-5], [9]).

Reactor concept	Coolant temp. T_{in}/T_{out} in °C	Coolant pressure in MPa	Max. irradiation damage in dpa	He generation rate in appm/dpa	Candidate structural materials
VHTR	650 / 1000	7	10	0.1	• 9Cr or 12Cr steel for pressure vessel • Graphite for core structures • Nickel-base alloys for very-high-temperature hot-gas components
GFR	490 / 850	7	80	0.1	• 9Cr to 12 Cr martensitic steel or 2 1/4Cr-1Mo steel for pressure vessel • Nickel-base alloys, AISI 316 SS, or 9Cr-ODS for very-high-temperature hot-gas components
SFR	350 / 550	0.1	200	0.1	• AISI 316 SS or its modifications for vessel • 9Cr steel, F/M-ODS or SiC/SiC for core structures • 9Cr-1Mo for heat exchangers

Failure modes

In the Gen-IV reactor concepts considered the following failure modes have to be taken into account [5-8]:

- Inelastic collapse
- Progressive inelastic deformation (Ratcheting)
- Aging (VHTR)
- Creep
- Fatigue
- Creep-fatigue
- Environmental effects
  - Irradiation induced swelling, creep, hardening and embrittlment
  - Coolant and its impurities on fatigue & creep-fatigue (e. g. helium in GFR)

Most failure modes identified for 9Cr steels in GEN-IV are similar to those identified for EUROFER97 in DEMO, particularly for its application as structural material for helium cooled in-vessel components (blanket and divertor) [10].

Conclusions

Similarities between GEN-IV high temperature reactor concepts and fusion DEMO could be identified in the selected structural materials and their failure modes. The main commonality is the selection of F/M steels and their ODS variants as structural materials. Consequently, the R&D work in fusion can for sure take profit of that done and foreseen for GEN-IV fission

reactor. However, the high He generation rate in fusion structural materials due to the 14 MeV neutron spectrum is and remains a fusion specific problem.

Staff:

J. Aktaa

Literature:

[1] A Technology Roadmap for Generation IV Nuclear Energy Systems, Issued by the U.S. DOE Nuclear Energy Research Advisory Committee and the Generation IV International Forum 2002.

[2] J.-L. Seran, IAEA Technical Committee Meeting, 2006.

[3] J.-L. Seran et al., J. Nucl. Mater. 212-215 (1994) 588-593.

[4] P. Yvon, F. Carré, J. Nucl. Mater. 385 (2009) 217–222.

[5] J. M. Corum, T. E. McGreevy, R&D Plan for Development of High Temperature Structural Design Technology for Generation IV Reactor Systems, ORNL, 2004.

[6] Generation IV Nuclear Energy Systems Ten-Year-Program, Appendix 9.0: Materials, DOE Office of Nuclear Energy, 2007.

[7] S. Mohanty, S. Majumdar, M. Srinivasan, HTGR Graphite Core Component Stress Analysis Research Program – Task 1, Technical Letter Report, Argonne National Laboratory, 2011.

[8] R. K. Nanstad, D. A. McClintock, D. T. Hoelzer, L. Tan, T. R. Allen, J. Nucl. Mater. 392 (2009) 331–340.

[9] L.K Mansur, A.F Rowcliffe, R.K Nanstad, S.J Zinkle, W.R Corwin, R.E Stoller, J. Nucl. Mater. 329–333 (2004) 166–172.

[10] J. Aktaa et al., Final report of WP12-DTM-03-T02, 2012.

Acknowledgement

This work, supported by the European Communities under the contract of Association between EURATOM and Karlsruhe Institute of Technology, was carried out within the framework of the European Fusion Development Agreement. The views and opinions expressed herein do not necessarily reflect those of the European Commission.

Identification of Gaps in Existing Design Criteria (WP12-DTM-03-T04-01)

Objectives

The objective of this report is to perform a gap analysis on existing standards in context of DEMO. The gap analysis is focused on the divertor (water and helium cooled systems) and the blanket module (helium cooled system).

The KIT activity within this task is focused on the rules of the ASME Boiler Pressure Vessel Code (ASME-BPVC [1]) whereas the other partners considered the rules of the RCC-MRx and the SDC-IC.

ASME-BPVC Gap Analysis

Reviewing the ASME-BPVC shows that most failure modes identified for the structural materials of helium cooled blanket and divertor as well as of water cooled divertor are covered by the rules of ASME-BPVC as far as environmental effects like high dose neutron irradiation are out of consideration. Analyzing the rules in their capability in ensuring safe designs concerns rise related to the specific behavior of certain structural materials under fusion loading and environmental conditions, in particular

- cyclic softening and its impact on ratcheting
- creep-fatigue
- influence of high dose irradiation (embrittlement, hardening and swelling)
- stress corrosion cracking (water cooled divertor).

Ratcheting rules and their consideration of cyclic softening

For design against progressive inelastic deformation due to cyclic loadings (ratcheting) the $3S_m$-rule is considered by the ASME-BPVC. For materials showing neither hardening nor softening this rule does not provide a safety margin in addition to that included in the S_m value. Hence, the safety margin of the $3S_m$ rule increases for materials exhibiting cyclic hardening and decreases for those showing cyclic softening like RAFM-steels (EUROFER). Consequently it is important to verify that the $3S_m$ rule is sufficiently conservative for RAFM-steels despite their cyclic softening. Nevertheless the consideration of cyclic softening by the ratcheting rules of the ASME-BPVC can be used only for induced ratcheting by thermal stresses In these rules and for accounting cyclic softening the endurance limit determined at 10^6 cycles fatigue lifetime shall be used instead of the yield stress when determining the primary and secondary stress parameters (Section III, Division 1, Appendix XIV-1400).

Creep-fatigue rules

Creep-fatigue is a complex failure mode which is considered by the ASME-BPVC within Section III, Subsection NH. Accordingly the creep-fatigue rules provided in the Non-mandatory Appendix T can be used. “Non-mandatory” means that alternative criteria may be applied by the manufacturer which shall be subjected to approval by the owner. In Appendix T a creep fatigue accumulation rule is proposed. For its application beside design fatigue curves and stress-to-rupture curves, the allowable total creep-fatigue damage envelope is required. These are material design data which are available in Appendix T for 304 and 316 stainless steels, 21/4Cr-1Mo, Ni-Fe-Cr Alloy 800H and 9Cr-1Mo-V steel (grade 91) only. In comparison a too conservative allowable total creep-fatigue damage envelope has to be used for 9Cr-1Mo-V steel (see Figure 1) what has its origin in the cycling softening of this material [2]. Applying the creep-fatigue rules of ASME-BPVC to the structural materials of the blanket and divertor requires for all of them the proper material design data. In case of RAFM-steels investigations are even necessary to justify an allowable total creep-fatigue damage envelope

less conservative and, hence, more applicable than that included in the code for the 9Cr-1Mo-V steel. Alternatively and according to the ASME-BPVC other creep-fatigue criteria can be developed and used after sufficient verification. This is particularly desirable for avoiding unnecessary conservatism the accumulation rule might have.

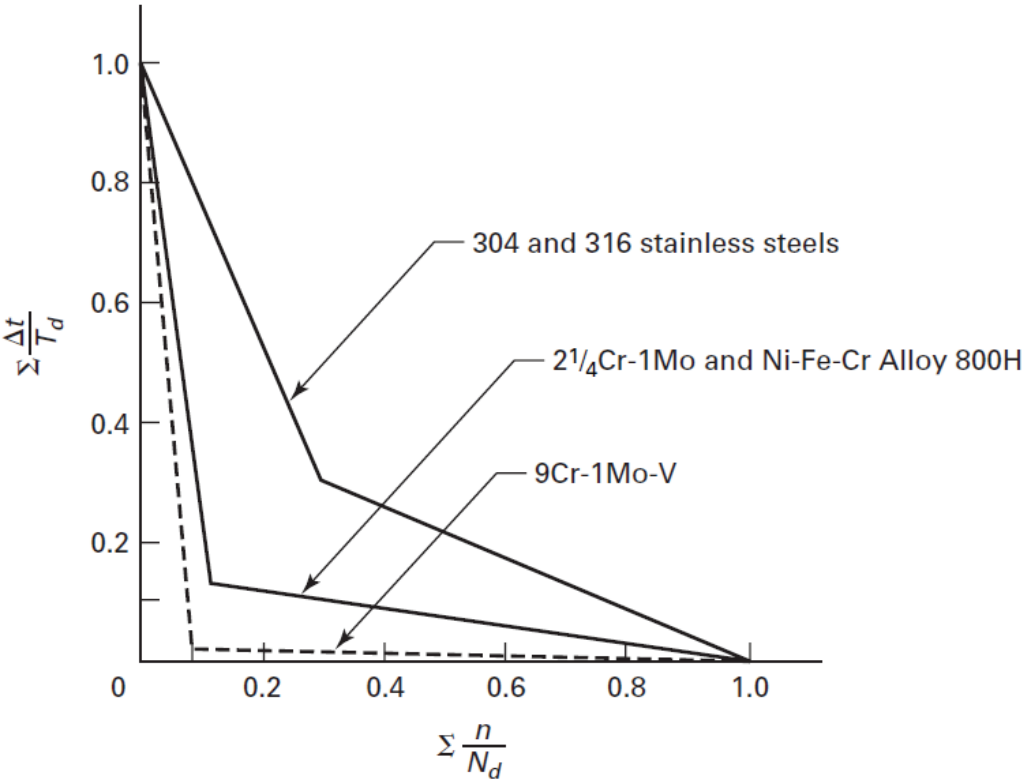

Fig. 1: Creep-fatigue damage envelopes implemented in the ASME-BPVC.

Influence of high dose irradiation

In general irradiation effects are not included in the ASME-BPVC. However the necessity of considering irradiation is mentioned in the rules for the protection against non-ductile failure (Section III, Division 1, Appendix G) particularly for taking into account irradiation induced embrittlement and the resulting shift in the reference nil ductility temperature. In addition irradiation effects are also mentioned in considering stress corrosion cracking (Section III, Division 1, Appendix W).

Stress corrosion cracking (SCC)

In ASME-BPVC recommendations rather than rules for design against stress corrosion cracking (SCC) are given (Section III, Division 1, Non-mandatory Appendix W). They are mainly deduced from the fact that SCC is affected by the three factors: Material composition, tensile stress and corrosive environment (see Figure 2). In addition irradiation assisted stress corrosion cracking (IASCC) due to neutron enhanced diffusion of elements (Cr) and impurities (S, Si, P) preferentially to the grain boundaries in oxidizing high temperature water environments is indicated as an important damage mechanism. Stress from service loads or fabrication processes is a contributing factor to IASCC.

The main recommendations for preventing SCC are:

- Careful selection of materials aimed at preventing the use of materials susceptible to SCC in the service environment,

- Employing design features and processing techniques aimed at tensile stress reduction, and
- Eliminating or reducing the severity of the corrosive environment through proper in-service chemistry control.
- Reducing exposure to neutron irradiation by e.g. including water gaps between the neutron source and structural elements (a threshold irradiation of 5×10^{20} n/cm^2, >1 MeV is generally accepted as the minimum fluence necessary for susceptibility to IASCC).

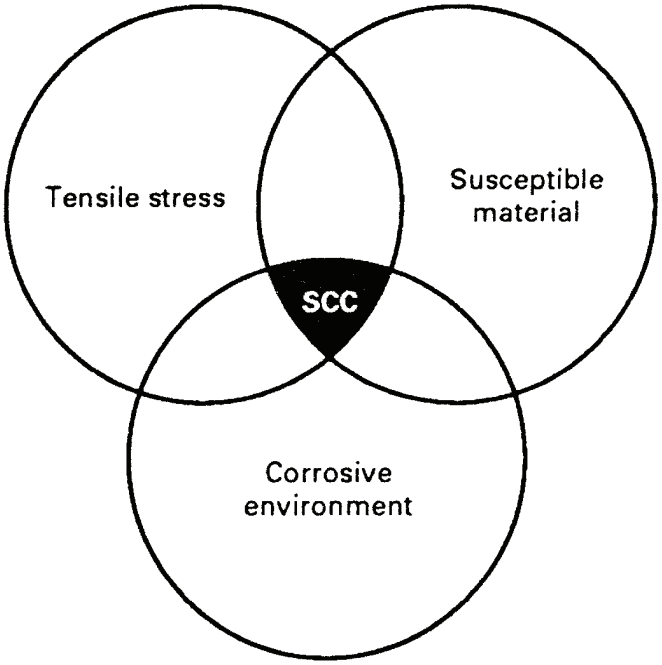

Fig. 2: Conditions required for stress corrosion cracking (SCC) [5].

Staff:

J. Aktaa

Literature:

[1] ASME BOILER AND PRESSURE VESSEL CODE, Edition 2010

[2] Tai Asayama and Yukio Tachibana, JAEA, Technical Report, 2007

Acknowledgement

This work, supported by the European Communities under the contract of Association between EURATOM and Karlsruhe Institute of Technology, was carried out within the framework of the European Fusion Development Agreement. The views and opinions expressed herein do not necessarily reflect those of the European Commission.

Radiation Hardness Assessment of Remote Handling Equipment (WP12-DAS-06-T02)

Executive Summary

In fusion reactors, nuclear power stations, and high-energy accelerators the ionizing radiation (this report is exclusively concentrated on the damages created by high energetic gamma rays) is a factor that influences or accelerates the malfunctioning of Remote Handling Equipment (RHE).

Thus to assess the influence of the radiation, an excel table, given by CCFE, containing all types of parts and components to be used in RHE was taken by KIT and filled with – amongst others - information about the total integrated doses that every component can withstand before failure (see an example below). The presented values should be considered as tentative values, due the difficulty to define an exact level of failure.

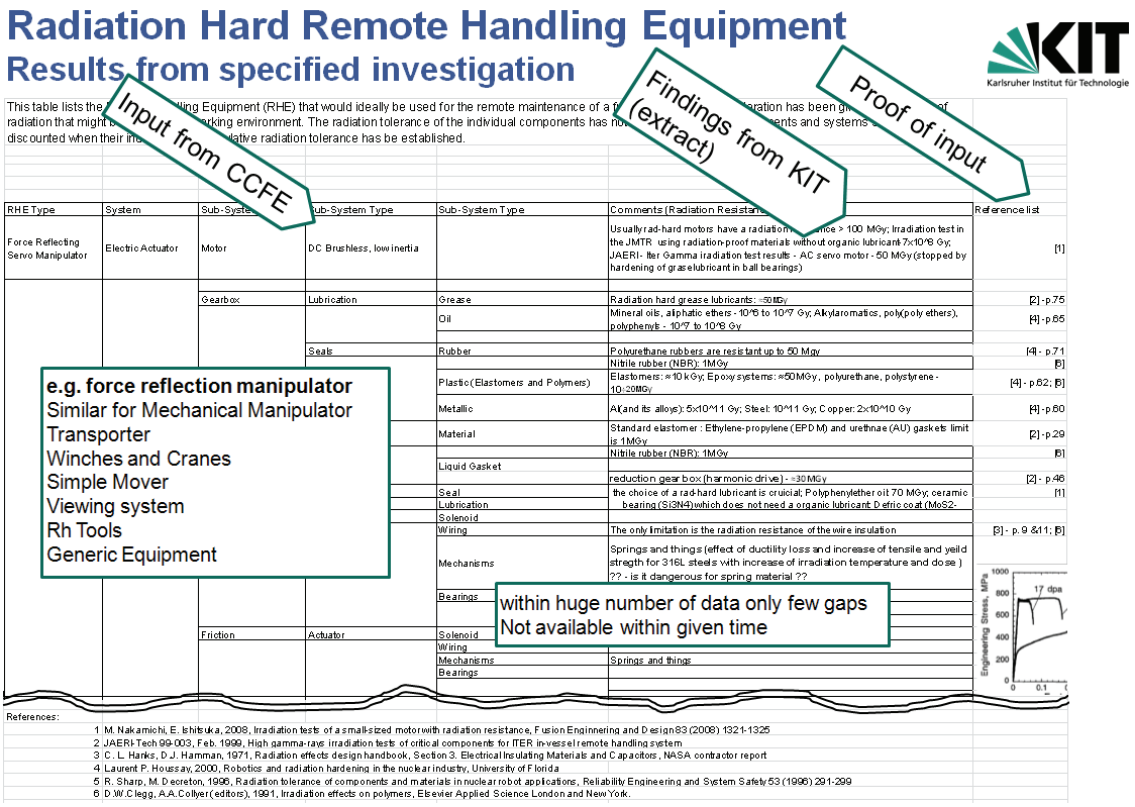

Generally the components used in the RHE can be classified in a few major categories:

- drive mechanisms (actuators, gear boxes, bearings),
- viewing systems and sensors (cameras, positioning sensors etc.) and
- Semi-conductors (electronic devices).

For each of these components the specific problems were described which occur due to the irradiation, and possible solutions were suggested to avoid the radiation effects. It was assessed that gamma radiation can have a serious impact on the reliability of the electronic components (the most critical part of the RH equipment), the organic compounds (part of the motor insulation, lubricants etc.), camera lens (part of the viewing systems) and not at least an intensive gamma radiation can even reduce the ductility of steel (radiation embrittlement is not only caused by neutrons, but in some cases by gamma radiation).

Staff:

V. Madzharov
M. Mittwollen

Acknowledgement

This work, supported by the European Communities under the contract of Association between EURATOM and Karlsruhe Institute of Technology, was carried out within the framework of the European Fusion Development Agreement. The views and opinions expressed herein do not necessarily reflect those of the European Commission.

Development of Vertical MMS Maintenance Concepts Including Ex-vessel Operations and Design Integration at Plant Level (WP12-DAS-06-T04)

Ex-vessel Operations Concept, i.e. Remote Handling Equipment for Opening and Closing Port Covers, Cask and Cask Transfer System

Executive Summary

In DEMO due to the neutron activation, the repair, inspection and/or maintenance of the in-vessel components must be carried out using Remote Handling Equipment (RHE).

1) A concept for opening and closing of the access ports (upper ports) is introduced based on the vertical maintenance system. A (small) robot is foreseen to prepare opening/closing by untightening/tightening the bolts / cutting/welding the welding seams – after removal of the bioshield. Contamination may be avoided following the ITER double-door-principle.
2) A cask concept is introduced, using vertical casks to fulfill the remote-handling operations to replace blanket segments and pipes, etc. The casks may be equipped with RHE.
3) A cask transfer system is introduced based on an overhead conveyor system and a polar crane above the vessel.
4) (Final CAD work is done presently for all of the mentioned components).

System activities sequence preliminary defined for opening (closing vice versa)

1. Removing the bio-shield plug
2. Robot inserted, running on rails on top of port cover for unbolting / cutting
3. Removing the robot
4. RHE cask brought by polar crane settles down, opens port (using double door system)
5. RHE unfixes and extracts pipes and stores them in cask.
6. RHE cask closes port with cover, brought to hot cell by cask transportation system
7. “MMS” cask settles down, opens port,
8. MMS-cask takes in first MMS, using telescopic ladder and RHE
9. MMS-cask is equipped with transportation cooling => see next summary

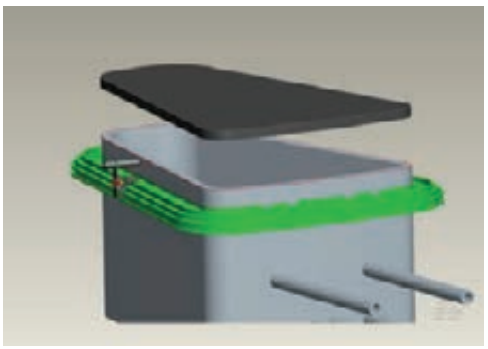

Autonomous Robot preparing opening / closing of port cover

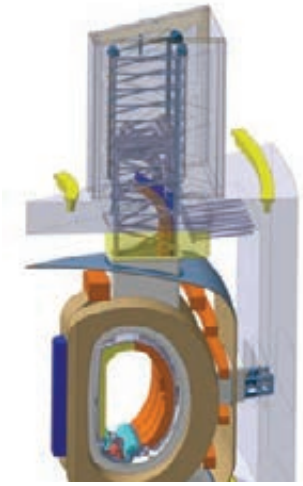

Vertical transportation cask settled on upper port extracting one OB-MMS

Polar crane and overhead conveyor concept for fast cask transport

Staff:

M. Kubaschewski
V. Madzharov
M. Mittwollen

Ex-vessel Simulation and Evaluation

Executive Summary

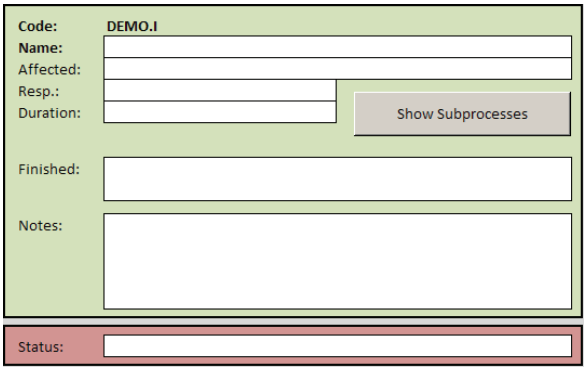

The progress on the simulation of processes depends strongly on changes and the current status of the DEMO design. Therefore the analysis of the processes which are necessary for the exchange of blankets and all other maintenance tasks can only be done on a very rough level of detail. Information on the current design is collected and aggregated into a process map. Therefore an Excel-based template was developed, which is used for gathering all information. This consists of single process cards like shown in the figure. This short description names all relevant information of the process, e.g. the responsibility, the duration of the process or the level of detailing. The information will be collected on several levels of detail, depending on the progress of the design. On lower levels this description will focus on organizational aspects that concern the whole maintenance process (like interfaces), on higher levels (more detailing), information on the technical procedure of a process becomes more important.

Big advantages for this approach are the forced accuracy in describing processes, the possibility to change / delete / add processes as you like, to give details later and etc.

In a second step all information are transferred to a software tool called iGrafx®. Following, an analysis of the total maintenance time, the reliability of several maintenance tasks and the possibility for optimizing the processes is performed. Beside the already mentioned information gained from the simulation like process duration and failure rates, the modeling of processes has also some more useful benefits.

This could be amongst others:

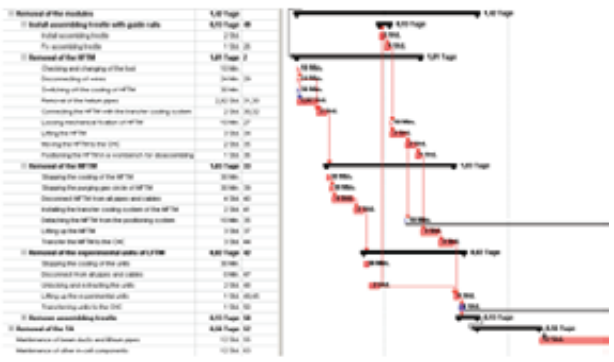

- Detection of problems arising of interactions between different design groups on a technical level. The modeling of the processes describes also the flow of information and determines requirements regarding the technical design.
- Definition of responsibilities
- It can be estimated which resources are required to fulfill the given tasks. With the time calculations and the costs for operating IFMIF and buying additional equipment, the optimal amount of resources can be calculated (e.g. number of manipulators)

- A consequent documentation in the process overview can identify fields where technical solutions are still missing and that need attention during the engineering phase.
- The sequence of the processes can then be visualized in a Gantt-chart which gives an easy overview on the sequence and duration of all tasks.

Staff:

M. Kubaschewski
M. Mittwollen

Assess Cooling Requirements during Transport

Executive Summary

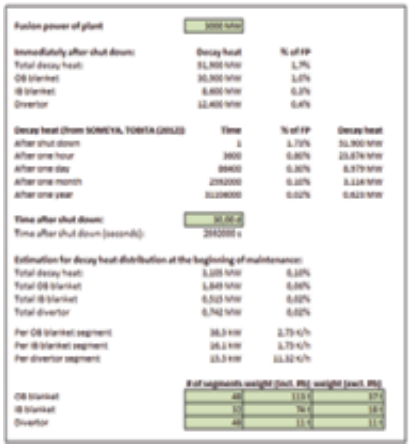

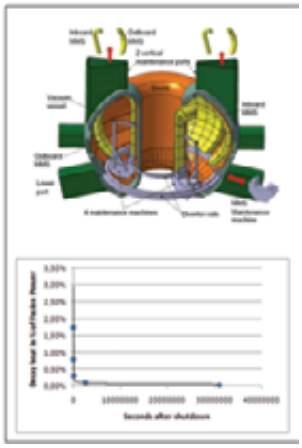

During the operation of DEMO, the material surrounding the plasma will be activated and releases a certain amount of decay heat even after the shutdown of the reactor. After the shut down this decay heat initially decreases quickly and later on slowly. For the design of an appropriate cooling device it is at first necessary to determine approximately the heat flow of the single elements.

The Basis for this estimation was a publication by Someya and Tobita [1]. Although the design (for example number of in-board/outboard blankets) was different, it was assumed that the level of activation and the reduction of the decay heat after shutdown will be comparable. Directly after shutdown, the total decay heat will be roughly 1.7% of the fusion power of DEMO.

With that, a decay heat calculation tool was introduced, that allows changing numbers like fusion power, time after shut down, number and weight of segments. As output one will get the according decay heat power of the component and an estimation of the temperature increase under adiabatic boundaries.

Currently, it is assumed that approximately 30 days will pass, before the maintenance begins. Under this assumption, the decay heat has already reduced to about 6% of the initial decay heat, respectively 0.1% of the fusion power of DEMO. Assuming a fusion power of 3GW, the segments of the outboard blanket will have the highest heat flux with about 38kW. A segment of the divertor has with 15kW the lowest heat flux. Although the divertor has the lowest heat flux, it has with about 11K/h the highest temperature increase in uncooled and adiabatic conditions. The reason is the lower mass of the divertor segments, which have a much higher activation level than the blanket. The temperature increase for the inboard and outboard segment will be in the range of two to three Kelvin per hour.

Staff:

M. Kubaschewski
M. Mittwollen

Initiate Remote Maintenance Requirements

Executive Summary

Remote Handling Equipment (RHE) developers are provided with comprehensive available information about their working area mainly ex-vessel, with some interface to in-vessel work.

A very preliminary classification about items to be removed versus items to remain in the vessel was undertaken. Simple load cases were investigated – one very important result was that the weight of the IB and OB segments is much lower than expected due to the required draining of all media (gas & liquids).

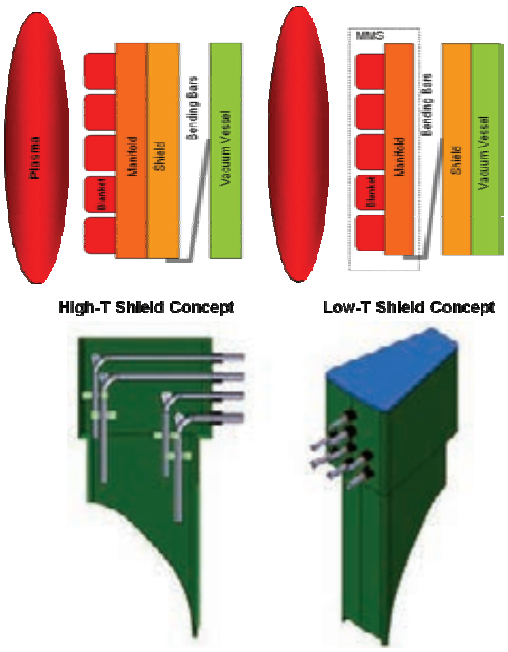

Structure and fixation and weight of the segments have strong interlocking to temperature shield concept (HTS / LTS) which is not decided yet and left to future development. HTS and LTS have big differences e.g. in fixation and clamping design.

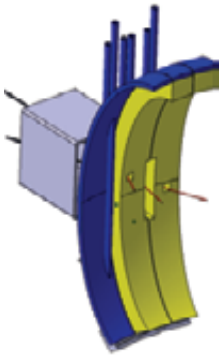

It was pointed out that cooling / purge pipes have to be further designed to avoid neutron streaming. Together with the future decision about type of pipe connections that has a big impact on RH.

H & CD systems type is not decided yet, but the result will also have impact on RH (big/small opening; penetration of blanket segments; heater type)

The existing preliminary concept for IVT system and mainly its support structure was defined requirements of loads to bear.

Summarizing table of crucial requirements and assumptions:

	Requirement	Comment
1	Media drained from MMS	Weight, avoid plugging (with PbLi)
2	Shear keys to be declamped/clamped	LTS-case: between MMS and vv HTS-case: between MMS and shielding
3	HTS-case: shielding to be opened/closed	1 homogeneous shielding shell
	Assumption	Comment
1	Items to be removed/remaining	Classification to be done in future
2	Weight of MMS max. 40t	Based on Initial CAD model – (max. with HCPB)
3	Weight of divertor cassette ca. 11t	Based on Initial CAD model - Scaled from ITER by VTT
4	Weight of pipes max. 1,5t	Based on Initial CAD model
5	Weight of port cover ca. 21t	Based on Initial CAD model
6	Fixing locations, type and loads	Based on Initial CAD model – HTS / LTS not decided yet
7	Pipe connections	Further piping design necessary
8	Port plugs ending outside MMS	Current statement from T05

Staff:

V. Madzharov
M. Mittwollen

Literature:

[1] SOMEYA, Youji and TOBITA, Kenji (2012): Estimation of Decay Heat in Fusion DEMO Reactor

Acknowledgement

This work, supported by the European Communities under the contract of Association between EURATOM and Karlsruhe Institute of Technology, was carried out within the framework of the European Fusion Development Agreement. The views and opinions expressed herein do not necessarily reflect those of the European Commission.

Study and Recommendations of Alternative Pipe Connection and Non-destructive Testing Technologies for DEMO (WP12-DAS-06-T06)

Mechanical pipe connections

Executive Summary

Mechanical pipe connections are one alternative amongst others. Finding a feasible solution would provide a quick and easy to handle concept for disassembling and assembling the cooling pipes and purge pipes. Some of the needed connections are located in the upper part of the vessel. The present operation scenario foresees a replacement of the blanket segments every 5 Years. For the according maintenance operations all pipe connections have to be disconnected and newly connected after insertion of the new segments.

The mechanical connection system is made up of two separate sub-systems. The first one is the mechanical mean for bringing two pipe ends together tight, the second one is the sealing compound which ensures tightness.

Investigation on disruption loads on the pipe connections brought out, that there are no loads expected due to closed force-circles throughout the blanket ring. The whole system then has to meet several requirements as shown in Fig. 1.

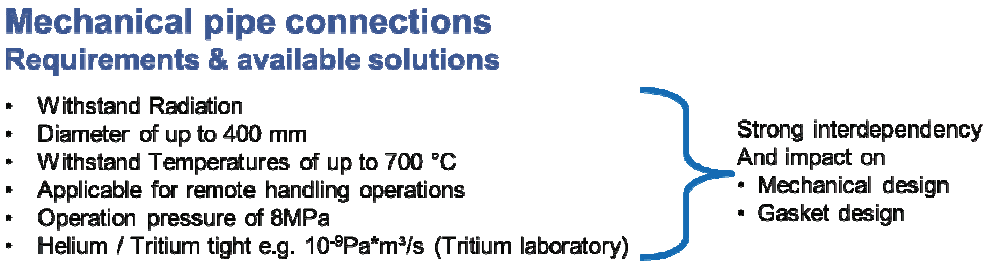

Fig. 1

Searching available systems brought out, that there are solutions for each single requirement but nothing that meets all requirements simultaneously. Nevertheless, there are solutions capable for empowering them for use in DEMO. This could not be done by simple up scaling thus it should be given some attention within WP13.

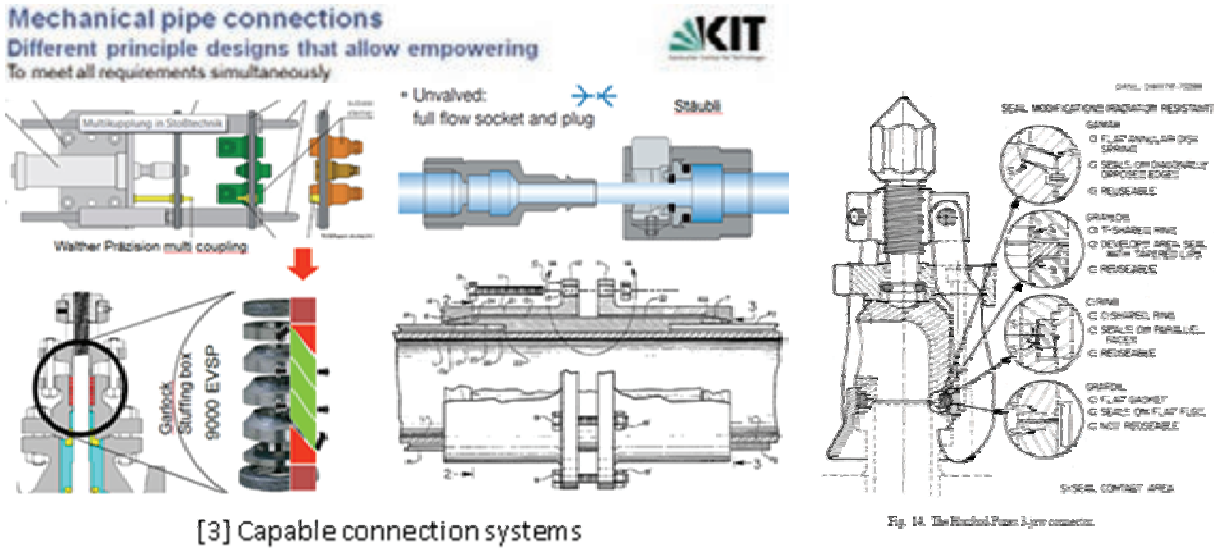

Fig. 2

Staff:

D. Eilert
M. Mittwollen

Acknowledgement

This work, supported by the European Communities under the contract of Association between EURATOM and Karlsruhe Institute of Technology, was carried out within the framework of the European Fusion Development Agreement. The views and opinions expressed herein do not necessarily reflect those of the European Commission.

Goal Oriented Training Programme “Power Supply Engineering” (WP08-GOT-PSE (FU07-CT-2009-00084))

The Power Supply Engineering plays an important role in the design, operation and exploitation of the fusion experimental devices and relevant test facilities. The role of the power supply engineers in this sense is a key role, as the power supplies are active devices which can be designed, optimized and upgraded to satisfy the requirement. These are the power supply engineers needed for ITER and to form them in this sense is the main objective of this training program.

The training activities are divided into two main areas:

- General engineering training and experience including personal development.
- Training and experience in specific technical areas to conclude with involvement in and/or management of one or more significant technical projects.

The general training consists mainly of a collaborative training program in coorporation with the participating associations, based on comprehensive set courses and shadowing activities on the operation of the facilities present in each laboratory. In 2012 the trainee attended to two courses: one at ENEA, Frascati and the other at CCFE, Culham. The task at CCFE was to create a reply to the recently issued tender document for the MAST toroidal field coil power supply together with the other trainees. This required us to apply everything learned so far in the different courses of the training programme. The results have been presented to the MAST power supply engineering division staff, who gave very positive feedback.

The specific training consists of practical work experience at the HELOKA-HP experimental facility (HELOKA-HP stands for “Helium Loop Karlsruhe – High Pressure”). The object of HELOKA is to test the HCPB-blanket concept and to gain experience in operating such kind of helium facilities. In this sense it also acts as a prototype for the ITER TBM helium cooling system.

In 2012 work on the Data Acquisition and Control System of the HELOKA facility continued with the integration of the second turbo circulator being a major milestone. This time the commissioning could be followed very closely giving support where possible.

The major part of the work in 2012 was committed to the extension of the HELOKA facility and the preparations for the high heat flux experiments. On the one hand this encompassed the upgrade of the mains power supply: with the procurement and installation of several power distribution cubicles a total of 4 MVA at 400 V have been made available to the HELOKA facility to make available the power for all the future extensions. On the other hand the investigations about the surface heating concept for the first wall were continued. With a substantial amount of simulations in ANSYS and Matlab/Simulink the feasibility and conceptual design of an induction heating system able to supply 150 kW of heating power as homogeneous as possible to a rectangular metal surface have been studied in depth. The results of these studies have been presented at the Symposium on Fusion Technology 2012 in Liège.

As a last point the involvement in the procurement of the electron beam gun for the future extension of HELOKA-HP shall be mentioned. The activities were mostly related to the factory acceptance test, delivery of equipment and procurement of the power grid connection. The device will be commissioned next year.

Fig. 1: nstallation of a new 2 MVA Transformer for the HELOKA power supply upgrade.

Cooperation with industry

ATE/ATEKO/VUES, Czech Republic, contractor:
- installation and commissioning of the second turbo circulator

EPROS Elektrotechnik GmbH Mannheim, Germany, contractor:
- construction, installation and commissioning of power supply cubicles

SIEMENS AG Karlsruhe, Germany, contractor:
- installation of instrumentation
- implementation of hard- and software into control system

VON ARDENNE Anlagentechnik GmbH, Germany, contractor:
- supply of a 800 kW electron beam gun

Staff

A. Kunze
M.Schmid

Acknowledgement

This work, supported by the European Communities under the contract of Association between EURATOM and Karlsruhe Institute of Technology, was carried out within the framework of the European Fusion Development Agreement. The views and opinions expressed herein do not necessarily reflect those of the European Commission.

Goal Oriented Training Programme “Breeding Blanket Developments for Fusion Reactors” (WP08-GOT-EUROBREED (FU07-CT-2008-00047))

Introduction

EUROBREED has been a network in the frame of the EFDA Goal Oriented Training Programme in the EFDA Work Programme 2008. It officially started on 1st September 2008 after the proposal of a group of associations under the coordination of KIT (former FZK), which was selected by EFDA for the financing. The duration of the activities was 4 years (until September 2012).

The overall objective of EUROBREED was helping to provide the necessary broad expert basis to successfully conduct the European breeding blanket development programme along with ITER and the developments beyond ITER (testing of the breeding blanket in the TBM Programme, for DEMO or the future Fusion Power Plan (FPP), development of the optimum breeder and neutron multiplier materials and design of specific breeder blanket components). The training programme enhanced already existing projects in the framework of the European Breeder Blanket Programme and the supporting activities in the associations. Existing experimental facilities like Helium loops, irradiation facilities and laboratories were used in the training programme and as well new projects related to the other relevant topics.

The proposed network integrated almost the complete breeder blanket development programme, including development of breeder materials, characterisation and modelling of properties (e.g. thermo-mechanics and tritium release), test of these materials in out-of-pile and in-pile experiments, integration of them in ITER, and also some aspects for the integration in the future DEMO reactor. Thus, the broad range of competences required in the European breeder development in the future were addressed, and the proposed program provided a significant and necessary improvement in the expert basis required.

The EUROBREED programme consisted of eight work packages (WP). Each of the WPs represented a training programme unit for a trainee that is employed in the association leading the WP. Each association supported the trainee with a supervisor, which was responsible of the organisation for the WP in front of the networks. Two associations (ENEA and UKAE) are not leader of a WP, but supported the network hosting trainees offering the possibility to work with members of the local group.

The basis trainee’s programme consisted of educational units (about 1/3 of the time), in which the trainee attended courses in fusion technology and on the particular research field. These courses were organised by the employing associations or in common sections with the participation of all the trainees (e.g. the “International Summer School on Fusion Technologies” in Karlsruhe, on 31 August- 9 September 2009). The remaining time was dedicated to the participation in technical work. The trainees had to demonstrate their capability to manage and execute their own project, planning the activities and at the end reporting them with the presentation of the results in conferences and journals. A research mobility of at least 2 months in another association was obligatory for each trainee.

Central elements of the network activity were the Progress Meetings that were held every six months. In these meetings the trainees had to present the work performed in the monitoring period in front of the supervisors and mentors. The presentations were evaluated taking into account the quality of the technical work, the capacity of the trainees to manage the technical and educational programme, and the quality of the presentation. Feedback was given to the trainees at the end of the meeting with suggestions for improving the programme and the presentation. The Progress Meeting was held in each laboratory of the WP Leading Association; this gave the possibility to the hosting Association to present its activity done to the trainees (including a visit to laboratories). The Progress Meetings took place in: Petten (May

26-27, 2009), Saclay (November 17-18, 2009), Riga (May 18-19, 2010), Budapest (Nov 25-26, 2010), Madrid (May 23-24, 2011) and the final one in Karlsruhe (Nov 15-16, 2011).

Table 1: Work Packages (WP) in EUROBREED Network.

WP Id	Leader Org.	WP Description
WP1	KIT	Design, procurement and test of solid breeder units
WP2	KIT	Pebble bed development and testing for the EU solid breeder blanket
WP3	CEA	Neutronics and radiation protection shielding design of the HCLL reactor
WP4	CEA	TBM integration in Port Plug with engineering design and interfaces management
WP5	HAS	Measurement techniques development for breeder blankets
WP6	NRG	Pebble bed nuclear performance testing
WP7	CIEMAT	Tritium transport predictive modelling tool for Breeding Blanket design analyses and system modelling
WP8	AEUL	

In work package No. 1, the revised technical programme of the trainee consisted in four parts: (1) the design and analyses of a TBM Breeder Unit (BU), (2) fabrication, procurement and assembly of a BU mock-up, (3) preparation of an experimental plan including selection of parameters, selection and installation of dedicated diagnostic systems and experimental devices and (4) Involvement of the trainee in the design and commissioning of the KATHELO Helium loop. The three years long training period started on the 24th of August 2009.

The task (1) was completed in 2011 with the release of the final BU design, which has been taken as the reference design for the manufacturing of the BU mock-ups. The task (2) about fabrication and procurement of BU components is on-going. The major challenge for this activity is the qualification of the fabrication procedures of the BU cooling plates (CP). During 2011, CP on a length of 300mm and real scale width (i.e. 30 cooling channels) has been successfully produced. During 2012 it was decided to build a short BU mock-up, namely SHOBU (Fig. 1-top), which shares all the parts of the real scale BU mock-up, with exception of the CP, which are the 300mm. While the qualification of the full-scale CP is running, relevant pressure and leak tightness tests will be performed in SHOBU, which will serve already as a first qualification of the welding assembly for the full scale BU mock-up. In Fig. 1-bottom several components of SHOBU are shown.

In parallel to the manufacturing and procurement tasks, the activity (3) related to the preparation of a relevant experimental plan for the BU has started on 2012. The first and major task during the design of a relevant BU experiment has been to reproduce the neutronic heating in the pebble beds in a non-nuclear environment: this must be done by means of, e.g. electric heaters. The updated geometry of the BU includes the so called “ceramic bridge”, which makes the new BU to have the particular U-shape of the CP, in contrast with the previous BU versions with parallel CP and meandering cooling channels. This curved geometry makes it difficult to place conventional plate heaters like in past experiments that involved the old model of the BU. More motivations to look for an alternative heating system other than plate heaters have been to minimize the impact of the heaters in the pebble bed mechanics and to reproduce more accurately the exponential decay of the volumetric heating in the radial direction from the first wall.

Position	Part name	Amount
1	Cooling plate outer	1
2	Cooling plate inner	1
3	Side plate	2
4	Manifold frontplate	1
5	Manifold backplate	1
6	BU backplate	1
7	Purge gas pipe	2
8	Manifold filter plate	2
9	Filter plate short	18
10	Filter plate long	9
11	Inlet pipe	2
12	Outlet pipe	1
13	Manifold plate 1	1
14	Manifold plate 2	1
15	Frame plate	1

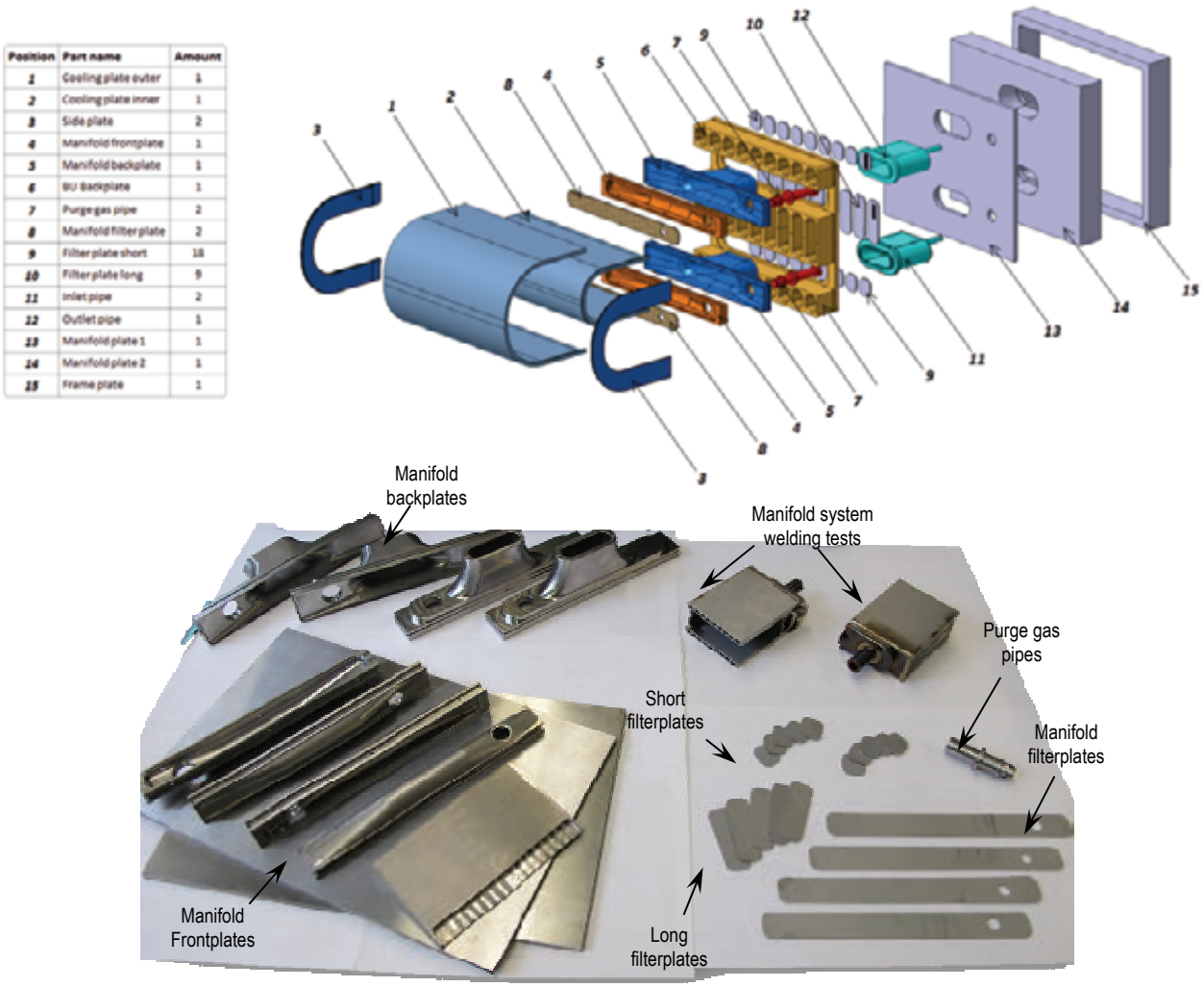

Fig. 1: Explosion view (top) and picture of different manufactured components (bottom) of SHOBU.

All these features have led to create a new heating system, which consists in several hexagonal matrixes of wire heaters grouped in blocks with same power. Fig. 2-top shows the temperature distribution in the Li4SiO4 with ITER nuclear conditions while Fig. 2-bottom shows the temperature distribution with the new wire heater matrix. As it can be seen, the temperature relevancy in the bulk of the pebble bed with this heater system is high.

As there is no previous experience with this heating system and its manufacturing is complex, a PRE-test Mock-Up eXperiment (PREMUX) has been designed and it is under construction to check the feasibility and performance of this heating system before implementing it in a full-scale BU test.

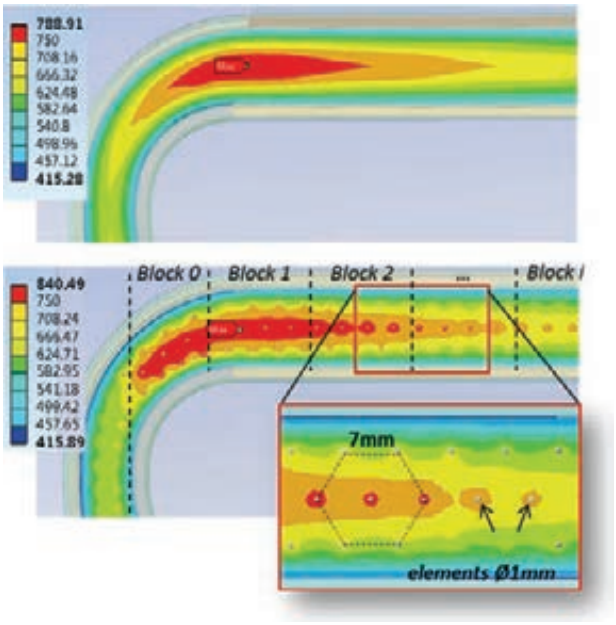

Fig. 2: Temperature profile (in °C) of a BU mock-up with neutronic heating (top) and a matrix of wire heaters (bottom).

A slice of the real scale BU (block 1 and block 2 in Fig. 2-bottom) is going to be tested under relevant power conditions. Other important issues than the feasibility of this new heater system are to be tested in PREMUX, like the thermal conductivity of the Li4SiO4 pebble bed and a benchmarking of different FE codes (ANSYS and ABAQUS) used during the design process of the BU, in order to validate them.

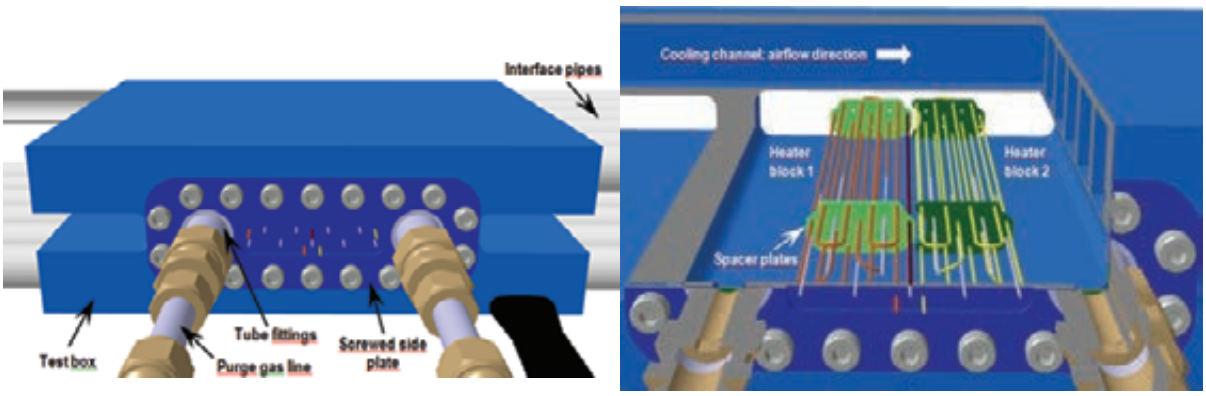

Fig. 3: PREMUX test section (top) and 3D cut (bottom).

The PREMUX test section is shown in Fig. 3-left. The heater system reproducing 2 blocks of the real scale BU can be observed in the 3D section cut of Fig. 3-right. The heater blocks have their own thermocouple layout in order to take temperature measurements along a vertical line in the pebble bed (Fig. 6). The PREMUX containment box has relevant dimensions to the Li4SiO4 pebble bed in the BU. For the cooling, pressurized air has been chosen as media, as it is not necessary to keep coolant medium relevancy.

The air supply will be given by the air loop L-STAR/LL available in the KIT-INR building. The integration of the PREMUX test section with L-STAR can be seen in Fig. 4. The work for the construction of PREMUX has already started and will be concluded during the first quarter of 2013. First experimental results are expected to be obtained in summer 2013. Once the adequacy of this heater system has been proven, the BU relevancy of PREMUX will allow implementing directly the heater system into a future full scale BU experimental set-up in KATHELO.

In work package No. 2, the technical programme of the trainee consisted of three parts: the fabrication and characterization (1) of lithium orthosilicate pebbles as ceramic breeder and (2) of beryllium/beryllium alloy pebbles as neutron multiplier, and (3) the experimental testing of TBM Breeder Unit (BU) mock-ups in collaboration with WP 1.

Part 1 and 2 of the programme were completed in 2010 and 2011 respectively. Within part 3 the trainee for WP 2 was responsible for selected tasks of the setup of breeder unit test experiment which aims to qualify the thermal performance of the HCPB concept of the EU for ITER. With the breeder unit design being complete, it has to be tested under relevant conditions in order to verify the validity of the previously performed simulations. Therefore a full-scale mock-up will be fabricated and it will be tested in a non-nuclear environment at KIT. The aim is to achieve highly relevant conditions with regard to the expected thermal environment in the breeder unit during operation in ITER and to extract as much experimental data as possible.

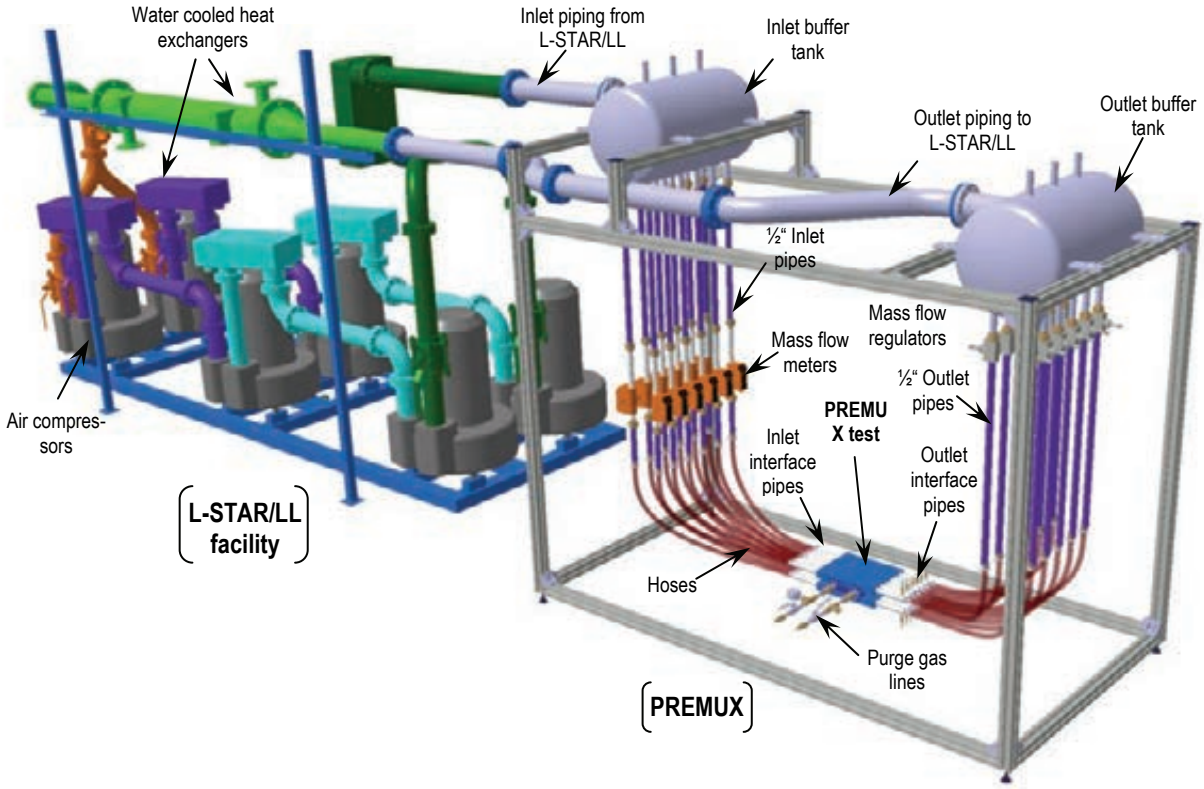

Fig. 4: PREMUX integration in L-STAR.

As already mentioned in the WP1, the most important experimental point of these tests is to mimic the neutronic heating of the two pebble beds with a non-nuclear heating system. WP1 and WP2 developed several designs of possible heating systems. The most promising design (candidate design) is going to be tested in the so-called Pre-Test Mock-Up Experiment (PREMUX), as up to now, there is no experience in KIT with the planned heater arrangement. The to-be-tested candidate design features a single, long, bended heater wire for a heater block as detailed in figure 5 in a scaled drawing of the PREMUX design. The full scale breeder unit mock-up is going to use numerous of these individual blocks to deposit the heating power in the pebble beds. For the PREMUX tests, the heaters will be operated within a lithium orthosilicate pebble bed.

Two heater blocks are going to be tested at once, since the control of several heater blocks in the final breeder unit mock-up will be critical. One aim is to reach the maximum temperatures that are expected in the breeder unit mock-up and to achieve high accordance between the theoretical predictions and the experiment.

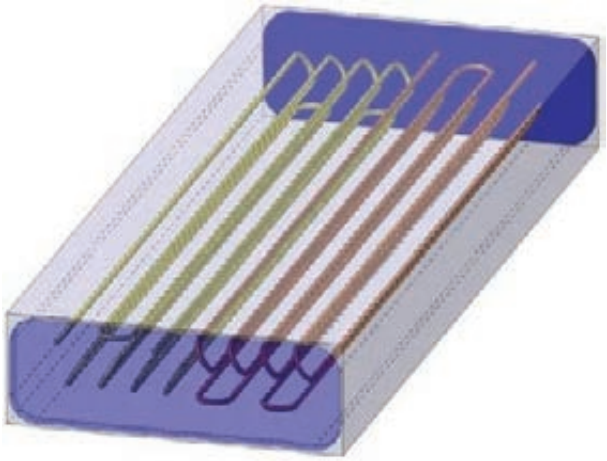

Fig. 5: Scaled drawing of two heater blocks of the most promising candidate concept installed in the so-called pre-test mock-up, PREMUX.

The packing factor of pebble beds has significant influence on their mechanical and thermal behaviour. The experimentally determined thermo-mechanical behaviour of the pebble beds is only valid for high packing factors, thus it has to be ensured that the pebble beds reach satisfyingly high values. Since the packing factor is maximized when the pebble bed is virtually undisturbed, the use of many, although small,

heaters and thermocouples may reduce the packing of the pebbles.

If that is the case, the presented heating system would not be applicable. To evaluate this issue before building the mock-up or the pre-test mock-up, a series of tests was performed with dummy heaters made out of steel wire.

Preliminary FEM simulations of the breeder unit mock-up assumed a distance of 7 mm between the centres of the individual heaters and a diameter of the heaters of 1 mm to achieve good accordance with the expected neutronic heating. These values were taken as input values for the design of the dummy heaters. In order to test the impact of the heater spacing on the packing factor, also distances of 9 mm and 11 mm between the heater centres were evaluated. For the tests a jolting volumeter, equipped with a glass cylinder of 35 mm diameter was used. To keep the distance between the cylinder wall and the dummy heaters as large as possible, only segments of the full heater blocks were used. For the 7 mm dummy heaters, a larger segment of the heater block (half size) was also fabricated and tested.

For the tests, each dummy heater had to be stiffened by two cardboard spacers, which were attached to the heaters with adhesive tape, as the steel wire was too flexible to keep its desired shape. The half heater block was stiffened by six cardboard spacers. This experience also led to a revision of the candidate concept, which now also includes stiffening structures.

Lithium orthosilicate pebbles with a diameter between 250 µm and 630 µm of a recent batch of reference material were used as test material. The geometrical density of this material had been measured by mercury porosimetry (2.26 g/cm³). In order to achieve high packing factors, the pebbles were pre-compacted by 2000 jolts and then compacted further using a vibrator.

The packing factor is defined as the percentage of the observed density from the maximum density. For the calculation of the packing factor the volume of the heaters and the cardboard spacers was neglected as it had little influence on the results. The results of the packing factor experiments are listed in table 2.

Table 2: Determined pebble bed packing factors with the four dummy heater configurations submerged in the lithium orthosilicate pebble bed (geometrical density of 2.26 g/cm³).

Heater configuration	Pebble bed mass	Pebble bed volume	Packing factor
11 mm	332.73 g	224 ml	65.7 %
9 mm	349.72 g	236 ml	65.6 %
7 mm	354.51 g	238 ml	65.9 %
7 mm (half block)	368.52 g	248 ml	65.8 %
7 mm (half block + TC)	371.46 g	250 ml	65.7 %

The results clearly show that there is very little influence of the heater configuration on the packing factor. Also, the finite element simulations consider a packing factor of 64 % for the pebble beds and the observed values lie significantly above this value, which means that there is no perturbing reduction of the packing factor by the introduction of the heaters. More importantly, the packing factor lies in a range for which the thermo-mechanical behaviour is well described.

In the presented design (fig. 5) thermocouples (TC) in the pebble beds are not incorporated, however they are a crucial part of the instrumentation, and have to be implemented in PREMUX and full scale mock-up.

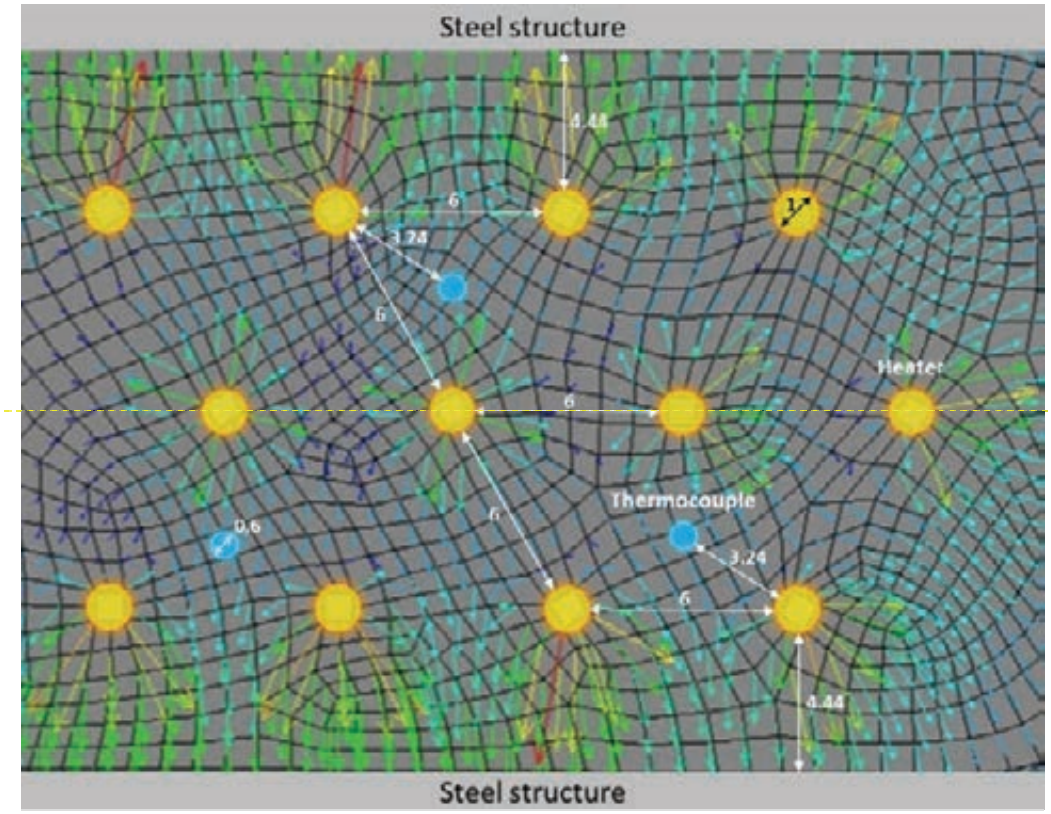

Fig. 6: 2D simulation of the thermal flux from the heaters in the tritium breeder pebble bed. The positions of the heaters and thermocouples are given as well as important distances in millimetres.

Currently, thermocouples in the two pebble beds are considered as the only disturbing elements of the instrumentation within the pebble beds. A sufficient amount of thermocouples is necessary to verify that a temperature field, similar to that expected in the ITER TBM, is achieved by the heaters. It is currently planned to place not more than one thermocouple per three projected heater wires in the pebble bed (see figure 6). In regions where only slight temperature variations are expected, less thermocouples are going to be implemented.

The smallest commercially available thermocouples have an outer diameter of 0.25 mm. To protect them against mechanical forces and to place them in the desired location, tubes of alumina or titanium with an outer diameter of 0.6 mm are going to cover the thermocouples and provide enough rigidity for the application in the pebble beds. Because the outer diameter of these tubes lies within the range of the lithium orthosilicate pebble diameter, there is presumably low disturbance of the pebble bed. One alumina tube with these dimensions was also tested in the packing factor experiments. It was attached to the cardboard spacers of the half 7 mm block, which means that the distance between heater and alumina tube was roughly 2.7 mm, which is a rather extreme case when considering the current design (see figure 6). Still the determined packing factor lies in the range of all other determined values (see table 2, 7 mm (half block + TC)).

It is, however, difficult to manufacture alumina-steel joints for the given application as the thermal expansion coefficients of Eurofer and alumina differ significantly. A spacer of a certain Ni-Fe-alloy is principally applicable to compensate these differences, but it would raise the manufacturing complexity and the manufacturing costs dramatically. Therefore thermocouples with Inconel sheath are chosen instead, which have a diameter of 1 mm. To compensate for the larger diameter, the heaters on the middle plane (dotted yellow line in figure 6) are slightly displaced to achieve an equal spacing of roughly 4.4 mm, which is larger than that for the tested 7 mm half block + TC.

The presented results clearly indicate that the candidate heating system can be operated without disturbing the pebble bed too much, also considering the necessary thermocouples. Consequently this heating system, with slight modifications, is being procured to test it in PREMUX.

Staff:

L.V. Boccaccini (EUROBREED coordinator)
M. Henn (Financial responsible)
F.A. Hernández González (trainee, WP 1)
R. Knitter (Supervisor WP2)
M. Kolb (trainee, WP 2)
D. Radloff (EUROBREED Secretary)

Acknowledgement

This work, supported by the European Communities under the contract of Association between EURATOM and Karlsruhe Institute of Technology, was carried out within the framework of the European Fusion Development Agreement. The views and opinions expressed herein do not necessarily reflect those of the European Commission.

Manufacturing and Testing of Mock-ups for Investigation of Coolant Flow in the Manifold System of HCPB TBM (GRICAMAN Experiments) (TW5-TTBB-003 D 1)

Introduction

This Task deals with investigations of flow distribution in the coolant system of Helium-Cooled-Pebble-Bed Test Blanket Module (HCPB TBM). The coolant system HCPB TBM consists of 4 large manifolds containing numerous internal obstacles and 66 long narrow channels meandering in the first wall, cap, stiffening grids and cooling plates of breeding units. Since there is no possibility for an external regulation of helium distribution, the designed mass flow rate for each of these internal channels should be achieved only by proper definition of their hydraulic resistance. Taking into account the complexity of the HCPB TBM flow domain it was of ultimate importance to examine whether the designed flow distribution can take place. For that purpose an experimental facility named GRICAMAN has been designed, manufactured and tested at the Institute for Neutron Physics and Reactor Technique. As basis for the development of the GRICAMAN facility the design Version 2.1-W of the HCBP TBM has been used.

A detailed consideration of the designed flow scheme in HCPB TBM has shown that most critical is the flow distribution among cooling channels in caps, vertical and horizontal stiffening grids which takes place in manifold 2 and the flow distribution among breeding unit channels which takes place in manifold 3. In relation to this, GRICAMAN facility involves the upper poloidal half of HCPB TBM bounded at the outlets of first wall channels, at the outlet of by-pass pipe and at the inlets of cooling channels in the breeding units as relevant flow domain. Using relations for flow similarity HCPB TBM coolant (helium at 80bar and 370^0C) has been replaced by air pressurized at 3bar and at ambient temperature.

Before starting the design of the GRICAMAN facility 3D CFD computations of the cooling channels as designed in HCPB TBM V2.1-W for vertical/horizontal grids and caps have been performed in order to get data on their hydraulic resistance. The results of these computations performed for nominal values of mass flow rate gave pressure losses of 8900(Pa) for a vertical grid channel, of 6860(Pa) for horizontal grid channels and of 2460(Pa) for cap channels. Using these data a simplified hydraulic analysis of the parallel connection of grid/cap channels has been done in which constant values of pressure in both manifolds have been adopted. The flow rate distribution obtained in this way has shown drastic discrepancies from those prescribed by the design. For that reason, the original design of grid/cap channels had been redefined in the following way. For vertical grid channels the cross section of inlet/outlet legs has been increased from 20x6mm to 29x6mm (shorter sides in the form of half circles). For cap channels the original cross section of 10x10mm (with radius of 3mm in corners) has been decreased to 10x6mm (with shorter sides in the form of half circles) and a single inlet leg with cross section 29x6mm (with shorter sides in form of half circles) has been foreseen as connection to manifold 2 instead of originally planned three independent channel chunks. For horizontal grid channels, no changes have been introduced.

Construction of GRICAMAN experimental facility

Using the aforementioned redefined design of grid/cap channels the GRICAMAN facility has been constructed as presented in Figure 1. The main body of the facility which includes mock-ups for manifold 2, manifold 3 and all connecting channels has been developed in the following way. Manifold chambers with all channel attachments are presented exactly as designed in HCPB TBM V2.1-W. Coolant channels in stiffening grids, caps and breeding unit channels are simulated by so called equivalent channels, which involve an inlet leg, an outlet leg and an equivalent pipe. In order to provide realistic conditions at channel inlets/outlets, the geometry of inlet/outlet legs is the same as in real HCPB TBM cooling channels, while the intermediate part named equivalent pipe can be presented by a simple pipe equipped with flow meters for determination of flow rate and a series of three slide valves for adjust-

ment of desired hydraulic resistances. It is noted that the construction of manifold assembles is based on screw connections in order to provide the possibility for investigation of different HCPB TBM design layouts.

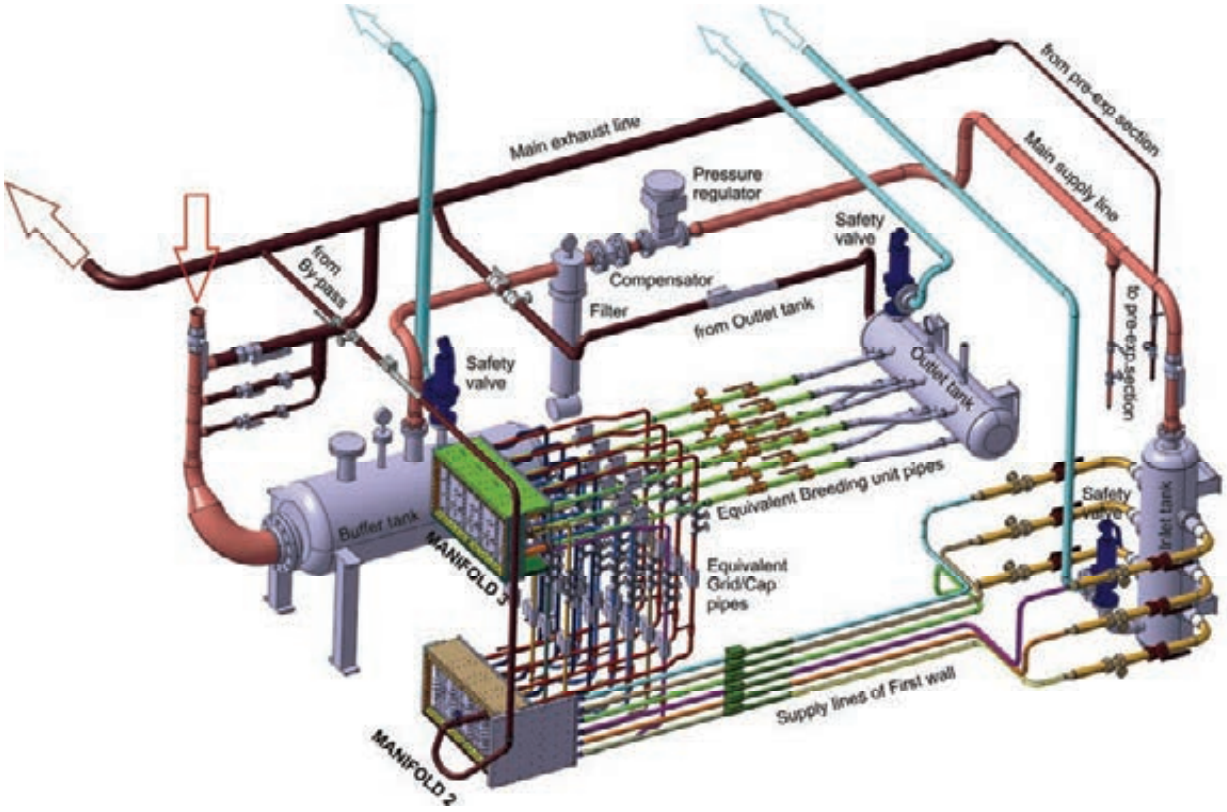

Fig. 1: Main components of GRICAMAN experimental facility.

The facility operates with compressed air taken from the network of compressed air at KIT. To condition air at mock-up boundaries, a number of auxiliary components had to be involved in the GRICAMAN facility (like buffer tank, inlet tank, outlet tank, filter, pressure regulator, safety valves as well as different pipelines presented in Figure 1).

In order to determine precisely flow conditions in fluid domains of both manifolds and in numerous parallel flow paths of equivalent channels, detailed measurements are foreseen – the experimental setup involves 36 flow meters and more than 250 pressure measurement points. The data acquisition and control of the facility is performed by a PC with data acquisition hardware running LabView.

Experimental investigations performed in the framework of GRICAMAN experiments

The main experimental campaign involves three measuring series which have been performed for nominal values of total air flow rate of 0.364(kg/s) with total flow rate between manifold mock-ups of 0.224(kg/s) and flow rate through by-pass outlet of 0.140(kg/s).

Manifold 2 has been tested for two measuring series in which the By-pass outlet was attached to the manifold chamber 1 which lies next to the first wall (series BPCh1BUFrM) or to the chamber 3 which is in central part of manifold space (series BPCh3BUFrM). Experimental results for flow rate distribution have shown that for channels attached to the chamber 1 (vertical grid channel v1 and cap channels c1 and c5) flow rates are significantly lower than nominal (see Figure 2). Stronger discrepancies of flow rate through cap channels have been found in measuring series BPCh1BUFrM (~12.5% for channel c1 and ~6.8% for channel c5) than in series BPCh3BUFrM (~9% for channel c1 and ~4.4% for channel c5). However, in the case of vertical grid channel the situation is opposite: the discrepancy of measured flow

rate from the nominal value is higher in series BPCh3BUFrM (~10%) than in series BPCh1BUFrM (~8.1%).

Measured flow rates for channels attached to the central part of manifold 2 (chambers 2-4) are much closer to their nominal values. This is especially true for vertical grid channels v2-v4 whose discrepancies are in the range of experimental error for both measuring series. For cap channels attached to chambers 2-4 something higher flow rates are measured (but with discrepancy from nominal value below 5%). Finally, although flow rates in horizontal grid channels located in chambers closer to the first wall (chamber 1 and chamber 2) are lower than in channels attached to the central part of manifold 2, no dramatic differences from the nominal values have been recorded in both measuring series.

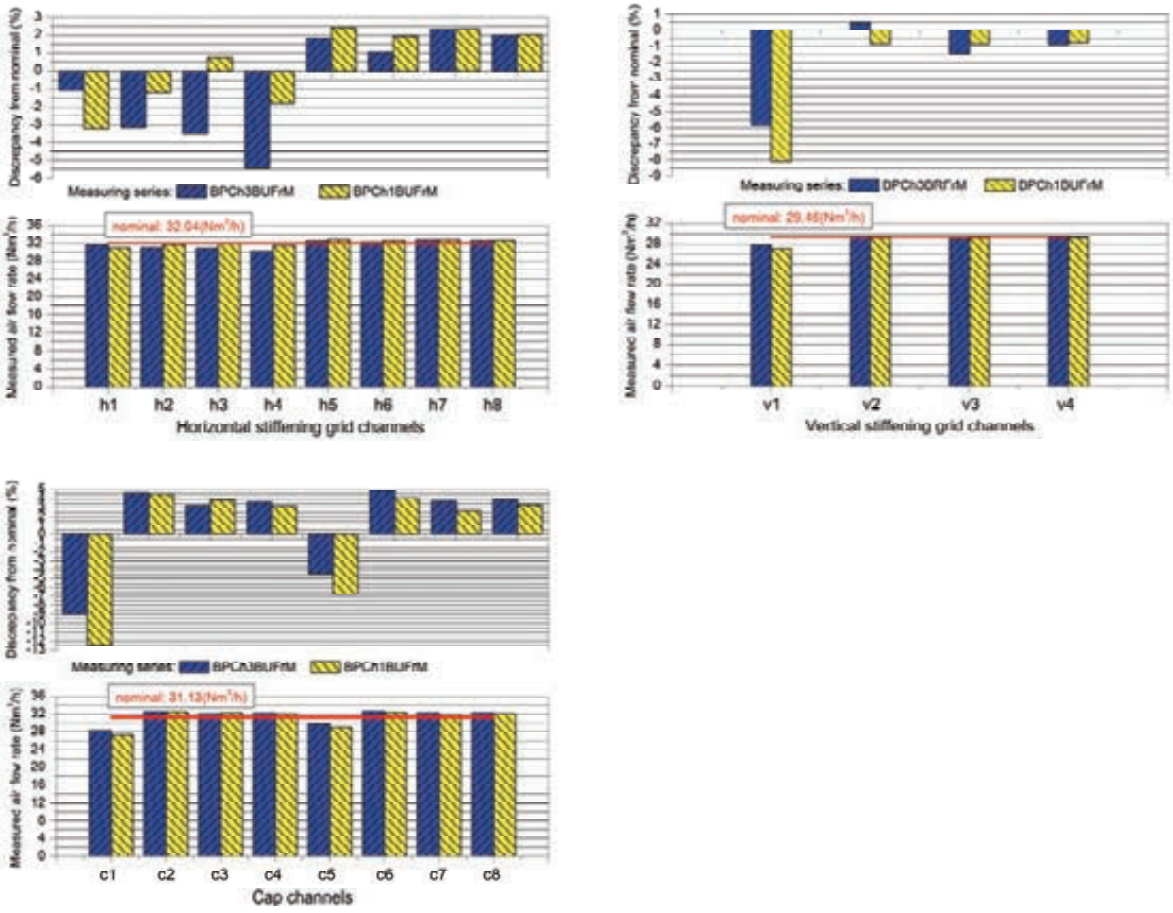

Fig. 2: Air flow rates measured in equivalent horizontal/vertical grid and cap channels for two different positions of the By-pass attachment (measuring series BPCh1BUFrM and BPChBUFRM). Upper diagrams show the discrepancy of measured flow rates from the nominal value.

Therefore, from the aforementioned it might be concluded that only chamber 1 is critical for flow distribution in manifold 2. Right in this chamber extremely non-uniform pressure distribution has been measured. These strong pressure variations are due to high velocities of fluid exiting the first wall channels. In the vicinity of the first wall the low pressure domains occur, which causes the aforementioned poor supply of channels attached to the chamber 1. In central chambers pressure variations are significantly dampened. This is especially true for chambers 3 and 4 (which are farthest from the first wall) where almost flat pressure profiles have been observed. Pressure distribution in the intermediate chamber 2 measured in series BPCh1BUFrM is more homogeneous than in series BPCh3BUFrM. This situation is due to less amount of fluid which in the former case has to be transported towards central part of manifold 2 since in this measuring series By-pass outlet is attached to the chamber 1.

A detailed analysis of pressure profiles has revealed an extremely important role of perforated rails which separate individual manifold chambers and in GRICAMAN mock-ups represent

penetrations of horizontal stiffening grids through manifold volumes in HCPB TBM V2.1-W. By making flow resistance these perforated rails slows down the high velocity flow coming from the first wall and in that way homogenize the pressure field in manifold 2. This statement could be demonstrated by an analysis of pressure profiles in longitudinal and cross direction of manifold 2: after passing the perforated rail separating chamber 1 and chamber 2 extreme pressure variations next to the first wall, have been dampened giving almost flat pressure distribution in the rest of manifold 2.

In relation to this, for an improvement of flow distribution in manifold 2 it is of crucial importance to avoid attaching channels to domains with low pressures. This can be achieved either by introduction of some elements which make drag and decelerate high velocity streams exiting from the first wall (an example of such an element is the perforated rail in the actual design) and/or eventual alternation of locations at which inlet/outlet channel legs are attached. In the actual design this alternation would be beneficial for the aforementioned channels c1 and c2, because the inlet cross sections of these channels could be placed in domains with higher pressures. This benefit would be larger for measuring series BPCh3BUFrM. Taking into account this possibility for an improvement of flow distribution, we state that By-pass attachment to the chamber 3 is advantageous in comparison to its attachment to the chamber 1.

Experimental results for flow rate distribution in Manifold 3 obtained in the aforementioned two series have shown negligible discrepancies of measured flow rates in individual breeding unit channels (maximal discrepancy from the mean value was ~1%). However, measured pressure distribution has shown an unexpected situation. Therefore, although at most of measuring positions very small values of differential pressures have been found, at pressure profiles in front of breeding unit inlets in the lower part of manifold 3 strong pressure peaks (~-1000Pa) have been recorded (see Figure 3). Analysing pattern of attached channel outlets and the internal structure of manifold 3 volume we came to the following conclusion: These pressure peaks are associated with local flow structures which occur as a result of complicated interplays of several perpendicular fluid streams with local flow obstacles which represent penetrations of outlet breeding unit legs through the volume of manifold 3. Therefore, since in the lower part of manifold 3 these flow obstacles are distributed in vicinity of outlets of cap channels, they influence flow directions of fluid streams exiting form these channels and lead to further interactions with fluid streams exiting from grid channels. In the upper part of manifold 3 these flow obstacles are staggered and do not stay on the way of fluid streams exiting from the outlet legs of attached grid/cap channels (that is likely the reason why in this part of manifold 3 no pressure peaks have been measured).

The emergence of the pressure peaks made it necessary to reconsider the flow rate distribution in manifold 3. The aforementioned results for series BPCh1BUFrM and BPCh3BUFrM have been measured at equivalent breeding unit channels which have significantly higher flow resistance than real cooling channels in breeding units of HCPB TBM. This high flow resistance is due to small diameter of applied flow meters. In relation to this we defined an additional measuring series (named BPCh3BUFrE) in which flow meters have been disassembled from equivalent breeding unit channels so that hydraulic resistance was reduced to the level of real breeding unit channels. Flow rate distribution has been determined indirectly - from experimentally derived hydraulic characteristic of each channel and measured pressure loss.

Results of pressure measurements in this series confirmed the existence of peaks at the same measuring positions and of the same magnitude (see Figure 3). Flow rate measurements have shown that the effect of these peaks on the flow rate distribution in manifold 3 is quite weak: maximal discrepancy of the flow rate from the mean value is ~3.4%, i.e. the difference of ~6% between the minimal and maximal flow rates has been found. Nevertheless, by designing the manifold system it would be worth to reconsider the pattern of inlet/outlet

locations of breeding unit channels and when possible not to locate the outlet legs of these channels in the vicinity of cap channel outlets.

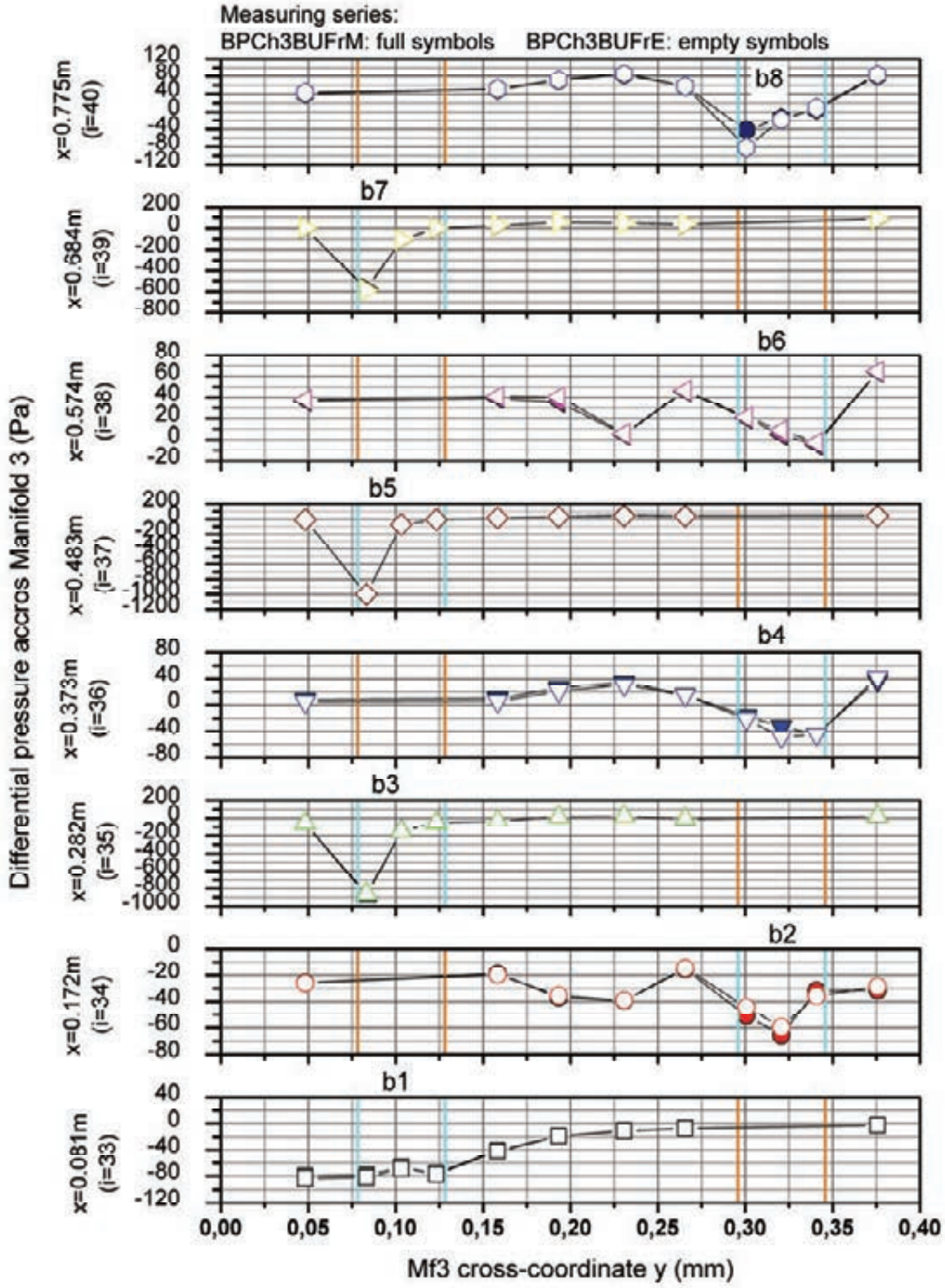

Fig. 3: Comparison of cross pressure profiles measured at longitudinal positions of breeding unit inlets in Manifold 3 for two arrangements of equivalent breeding unit pipes: with mounted flow meters i.e. high resistance (measuring series BPCh3BUFrM) and with no flow meters i.e. low resistance (measuring series BPCh3BUFrE). Cyan colored lines represent cross coordinate range of breeding unit inlets (denoted as b1-b8). Orange colored lines represent cross coordinate range of penetrations of outlet legs of breeding unit channels through manifold 3.

Conclusions

The report deals with the GRICAMAN experimental facility for the investigation of the flow distribution in the coolant system of HCPB TBM. The considered flow domain is the upper poloidal half of TBM bounded at the outlets of FW channels, at the outlets of by-pass pipes and at the inlets of BU's. The facility is constructed keeping real geometry of manifold 2 and manifold 3 and replacing complicated grid and cap cooling channels with simple pipes having the same flow resistance as the real channels. The facility has been experimentally tested by measuring flow rate distribution through equivalent channels and pressure distribution within manifold boxes. The draft version of the Final report for this Task has been submitted in December 2012.

Staff:

O. Albrecht
O. Bitz
M. Ilić
T. Kuhn
G. Schlindwein
R. Schmidt
K. Zinn

Acknowledgment

This work supported by the European Communities under the contract of Association between EUROATOM and Karlsruhe Institute of Technology, was carried out within the framework of the European Fusion Development Agreement. The views and opinions expressed herein do not necessarily reflect those of European Commission.

Production of Advanced Breeder Pebbles by a Modified Process (BMBF Reference No. 03FUS0012)

As part of the BA DEMO activities, the KALOS facility (KArlsruhe Lithium OrthoSilicate) was assembled to investigate a modified fabrication process for lithium orthosilicate pebbles [1]. Recently, a larger platinum crucible, able to process a three times larger amount of melt, was procured and the two standard crucibles were restored.

Lithium orthosilicate pebbles with a lithium metatitanate content of up to 40 mol% have been fabricated. The fabrication of this material is studied as it is a promising alternative to the reference material because of its higher mechanical rigidity [2]. Figure 1 shows SEM images of chemically etched cross sections for 10, 20, 30 and 40 mol%. The cross section for 10 mol% shows the dominant orthosilicate grains, while the metatitanate phase appears only as small inclusions at the grain-boundaries. As the metatitanate content increases, the grain size of the orthosilicate decreases and the metatitanate phase becomes more obvious. Between contents of 20 and 30 mol%, a clear change in the crystallization behavior can be recognized. At a content of 30 mol%, the lithium metatitanate dominates the crystallization, indicating that it solidifies first, and at 40 mol% its dendritic crystallization behavior becomes evident. This indicates an eutectic point between 20 and 30 mol% metatitanate, which is in agreement with an observed minimum in the melting temperature between 20 and 30 mol%. Measurements of the density by helium pycnometry confirmed the already observed tendency of an increase in the closed porosity with increasing metatitanate contents.

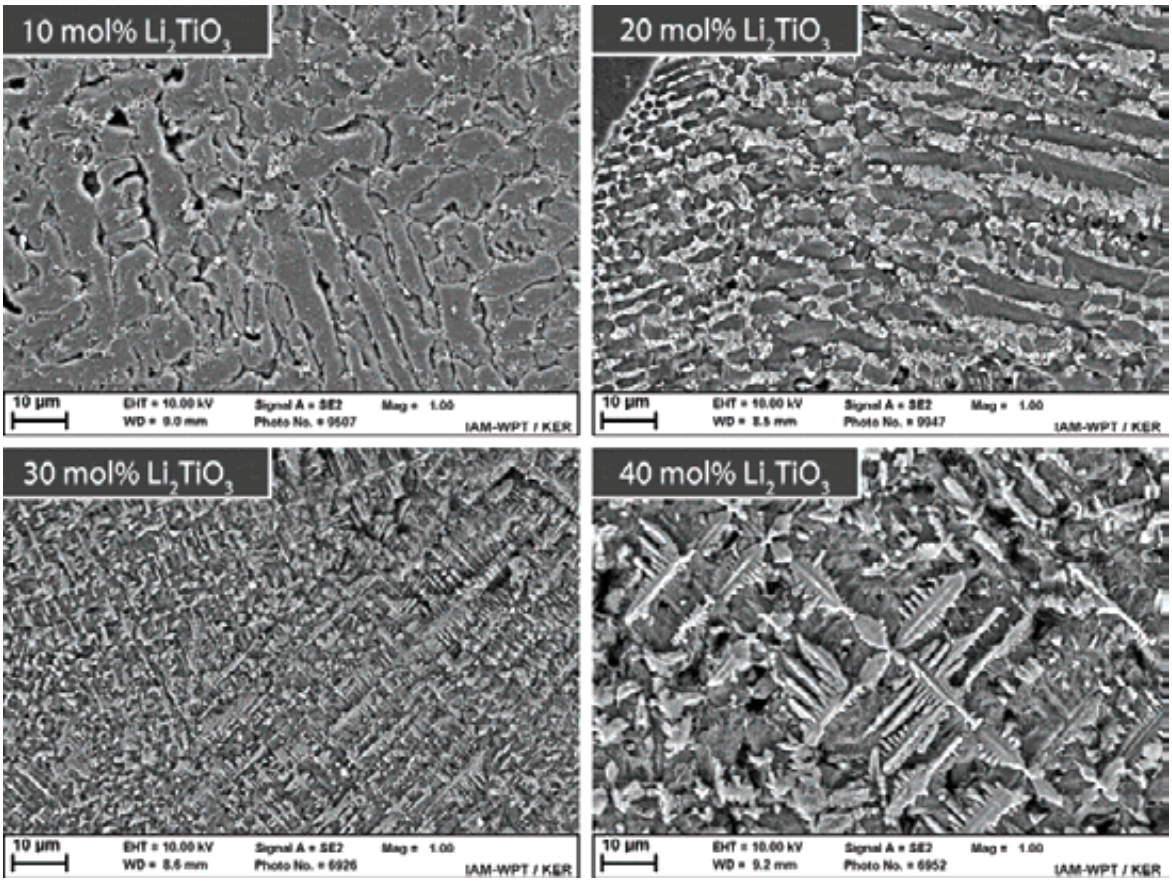

Fig. 1: SEM image showing cross sections for pebbles containing 10, 20, 30 and 40 mol% lithium metatitanate.

The noticeable influence of the drop height on the pebble quality [1] shows that the pebble quality significantly depends on the cooling speed of the droplets.

To mimic the slow cooling of the 14 m dropping distance experiments of 2010 and to avoid the quenching of the pebbles, a new cooling system was developed and put into operation in 2012 (see figure 2) instead of the formerly used liquid nitrogen bath. This system uses 4 copper pipes to spray liquid nitrogen homogenously in a Plexiglas tube through which the melt is dropping. Each of the 2-meter long copper pipes is equipped with multiple nozzles which are directed at their counterparts on the opposite side of the Plexiglas tube to prevent a distinct direction of gas flow in the Plexiglas tube.

Blended breeder ceramics consisting of 80 mol% lithium orthosilicate and 20 mol% lithium metatitanate were used as showcase to study the influence of the spray cooling on the pebble quality and the fabrication parameters of the process for the blended material in more detail. It has been proven that the liquid nitrogen spray cooling is cooling the droplets sufficiently so that they are solid when they reach the receptacle, rendering a liquid nitrogen batch redundantly.

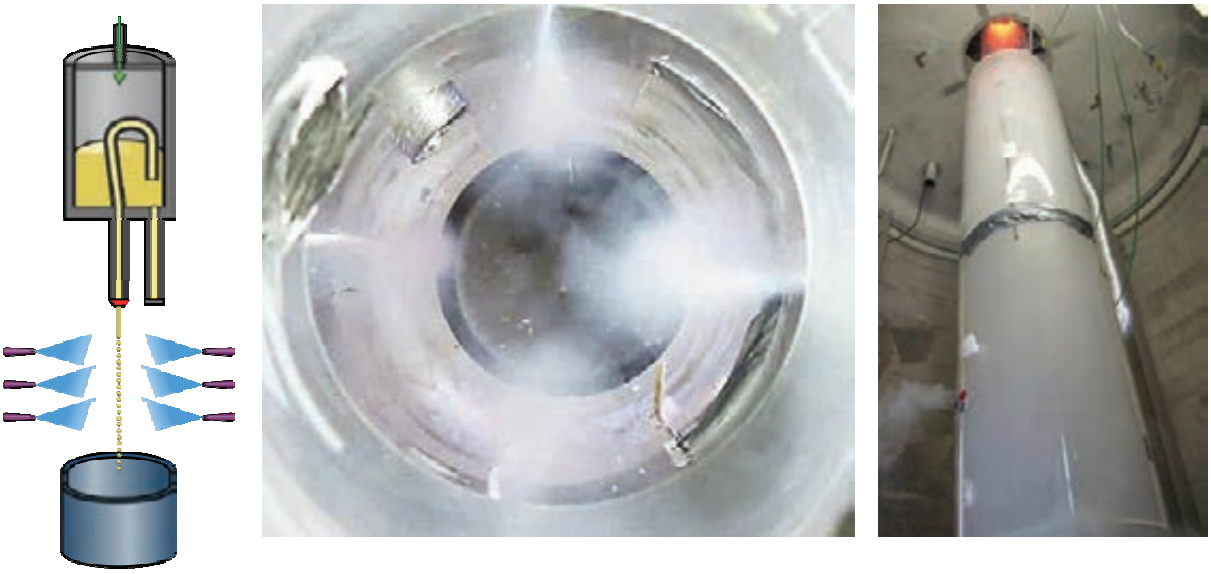

Fig. 2: Experimental setup – test facility (drawing), top view of the multi-jet liquid nitrogen spray in operation and the liquid nitrogen spray section during pebble fabrication.

Weibull Analysis of different cooling methods

The strength distribution of ceramics follows a continuous Weibull probability distribution. The distributions generate a Weibull modulus (m) which is typically used as an indication of the production process stability. Crush-loads are related to the size of defects such as cracks and pores that arise during production. The larger the modulus, the lower the amount of variation in the crush-loads, implying that there are less random factors present in the process. In Figure 3 are examples of the Weibull modulus for the three investigated cooling regimes.

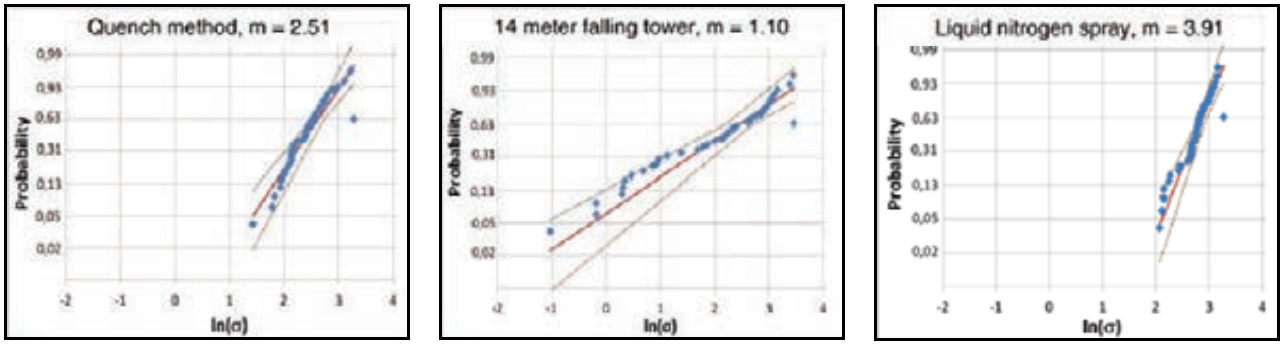

Fig. 3: Weibull analysis – Comparison of the Weibull graphs of pebbles cooled by the quench method (left), in air during 14 meters of falling (middle) and the lately implemented liquid nitrogen spray method (right).

As can be expected, the lowest Weibull modulus is found when using an increased height for the cooling. This is due to the fact that every pebble solidifies slightly differently to the next one. Over a 14-meter falling distance, there are many different paths that the pebbles can take as well as different impact scenarios. Overall this will increase the variation in crush-loads due to the various weaknesses introduced to the pebbles during cooling.

The liquid nitrogen quench method introduces the pebbles to a rapid change in temperature. As all pebbles are a slightly different size and slightly different temperature, the amount they are affected by the quench will also vary, again having an effect on the crush load variation. Initial results for the liquid nitrogen spray show that it results in an increased Weibull modulus. This can be due to the fact that rather than quenching the pebbles, the heat is slowly removed by the combination of cooled air and liquid nitrogen micro-droplets which gives the pebbles more time to adapt to the new temperatures resulting in less thermal cracking.

Not only does the liquid nitrogen spray increase the Weibull modulus, but it also increases the average crush-load. In Figure 4 a comparison of the average crush-loads can be seen for the three different cooling methods. The liquid nitrogen quench method has the lowest value due mainly to the size of cracks formed when quenching. The 14-meter falling distance removes the quench, but introduces more impacts and collisions, again resulting in cracks but not to the extent of the quench. The liquid nitrogen spray on the other hand reduces the effects of collisions and minimizes the thermal quench resulting in improved crush-loads.

As the increase in falling height was only possible to perform whilst still testing lithium orthosilicate, a direct comparison between the increased falling height and the liquid nitrogen spray is not possible. However, as the increased height is not practically realistic and displays a low Weibull modulus, the liquid nitrogen spray will be the preferred method for the future.

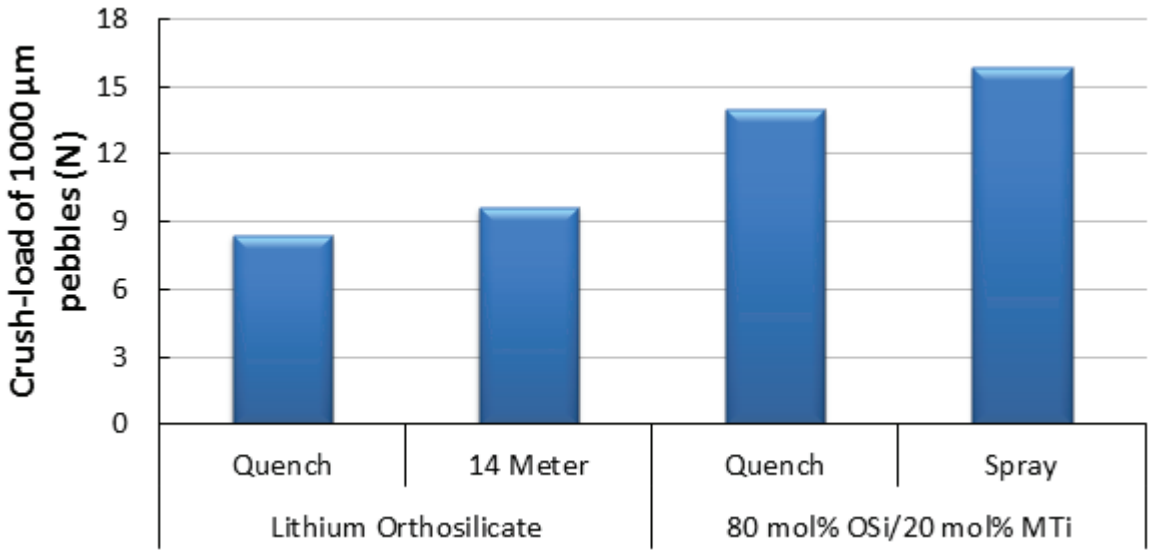

Fig. 4: Comparison of the mean crush-load of 1000 µm pebbles cooled by one of the three cooling methods.

Analysis of droplet formation

The process aims to use the principles of the Rayleigh-Plateau instability of a falling liquid jet to form droplets [1] which then solidify to form pebbles. The instabilities originate from minute external disturbances which increase exponentially as the waves move further away from the nozzle. Eventually, when the pinched area becomes small enough, the jet will rupture causing the formation of droplets, which become spherical due to surface tension.

A high-speed camera directed at the nozzle during pebble fabrication examines the droplet formation. It was possible to prove that the process operates in the desired way (see figure 5). It could also be verified that the droplets soon start to capture each other to form larger droplets.

Experiments were conducted in which samples were periodically taken throughout the discharge. The results are shown below as intensity maps which show the percentage of pebbles formed in each size range against the percentage of batch complete. This allows the stability of the process to be analyzed over time and the comparison of pebble size distributions for different operating pressures. For these experiments, the liquid nitrogen spray cooling was turned off for safety reasons.

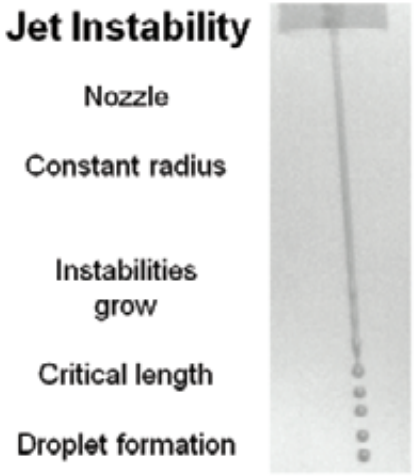

Fig. 5: Image of the nozzle taken by the high-speed camera during pebble fabrication, showing the droplet formation by the Rayleigh-Plateau instability.

At low pressures, the jet is allowed to decay naturally resulting in each droplet forming individually without being greatly affected by the other droplets that are formed. However, a slightly visible secondary peak at a slightly larger pebble diameter can be found. Its diameter corresponds to double the volume of pebbles from the main peak, which strongly indicates that capturing of at least two droplets during the falling is happening to some degree. As the pressure increases though, it can be assumed that it will cause an increase in the turbulence around the nozzle and hence more variation in the velocity of the jet. This means that the droplets are significantly less independent of one and other and many collisions occur. This leads to a higher output of large pebbles between 1500 µm and 2000 µm as shown in figure 6. At 1200 mbar, a secondary peak can be seen at approximately 800 µm for the same reason as explained above. At high pressures, many undersized pebbles are also formed when droplets split due to the increase in air resistance upon ejection. The pebble size distribution for high pressures like this are in general much less stable than for low pressures.

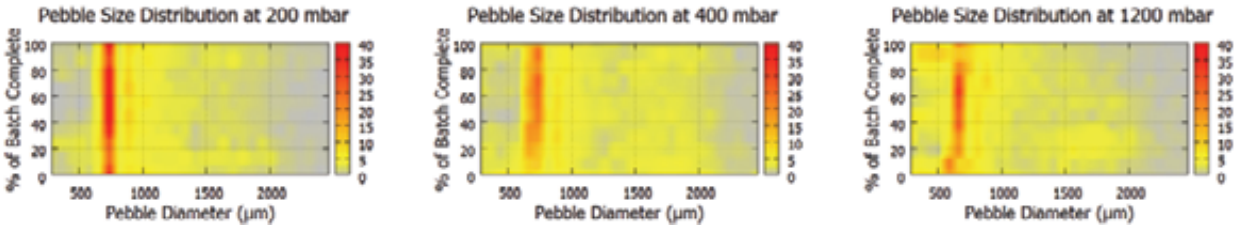

Fig. 6: Pebble size distribution as a function of process completion and process pressure.

By reducing the pressure, the control over the formation of individual pebbles is improved which in turn increases the amount of pebbles in the desired range or in other words, the yield.

In combination with the liquid nitrogen cooling the yield can be further increased, as it prevents the capturing of droplets once the droplets solidified on the outside (Fig. 7). The carried out modifications of the process led to significant improvement of the yield and the pebble quality. Also the capabilities of investigating the pebble fabrication over time and at the nozzle have been improved significantly.

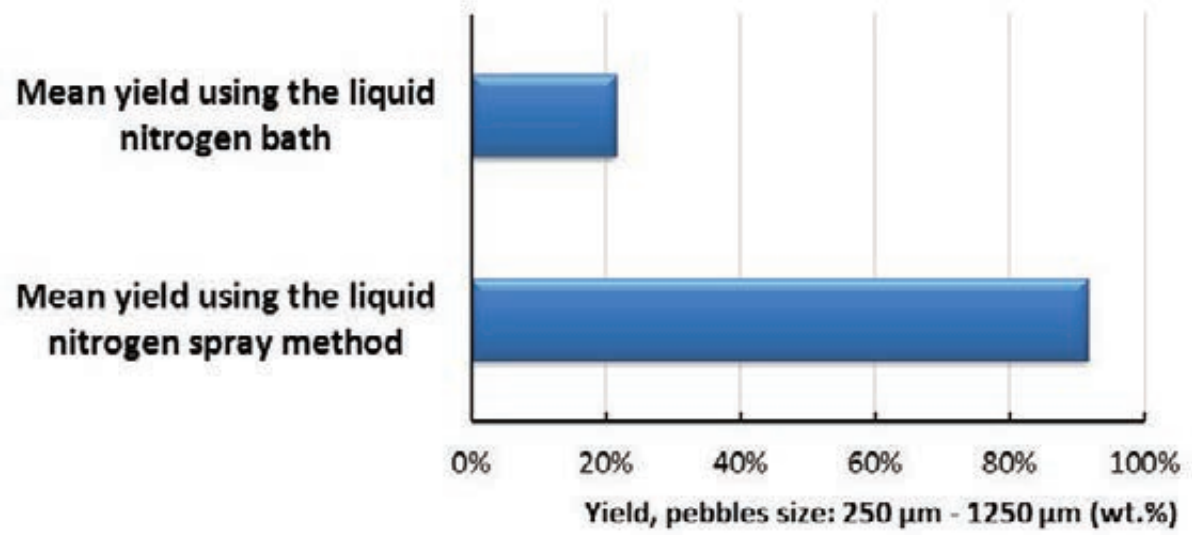

Fig. 7: Comparison of the yield for the two different cooling systems.

Cooperation with industry

The company Goraieb Versuchstechnik, Karlsruhe, Germany, is involved in the BMBF project to develop an alternative production route for advanced lithium orthosilicate pebbles. The company is responsible for the technical setup and the operation of the facility. The optimization of the facility and the material development is carried out in cooperation with KIT.

Staff:

R. Knitter
M. Kolb
O. Leys
U. Maciejewski
C. Odemer
M. Offermann

Literature:

[1] Kolb, M.; Knitter, R.; Kaufmann, U.; Mundt, D.: Enhanced fabrication process for lithium orthosilicate pebbles as breeding material. Fusion Eng. Design 86 (2011) 2148-2151.

[2] Knitter, R., Kolb, M., Kaufmann, U., Goraieb, A.A., Fabrication of modified lithium orthosilicate pebbles by addition of titania, J. Nucl. Mater., http://dx.doi.org/10.1016/j.jnucmat.2012.10.034.

[3] Knitter, R.; Kolb, M.H.H.; Odemer, C., Synthesis of tritium breeder ceramics from metallic lithium, Journal of Nuclear Materials, 420 (2012) 268-272

[4] Kolb, M.H.H.; Bruns, M.; Knitter, R.; van Til, S., Lithium orthosilicate surfaces: Characterization and effect on tritium release, Journal of Nuclear Materials, 427(2012) 126-132

[5] Zarins, A.; Supe, A.; Kizane, G.; Knitter, R.; Baumann, L., Accumulation of radiation defects and products of radiolysis in lithium orthosilicate pebbles with silicon dioxide additions under action of high absorbed doses and high temperature in air and inert atmosphere, Journal of Nuclear Materials, 429 (2012) 34-39

[6] Kolb, M.H.H.; Annabattula, R.K.; Knitter, R.; Kamlah, M., Determination of friction coefficients of tritium breeders and their influence on pebble bed mechanics, 27th Symposium on Fusion Technology (SOFT 2012), Liege/Belgium, 24.-28.09.2012

[7] Leys, O.; Kolb, M.; Goraieb, A.; Knitter, R., Melt-based breeder pebbles: effect of cooling and analysis of droplet formation, 27th Symposium on Fusion Technology (SOFT 2012), Liege/Belgium, 24.-28.09.2012

[8] Mukai, K.; Kolb, M.; Knitter, R.; Hoshino, T.; Suzuki, A.; Terai, T., Investigation of crush load and microstructure on $Li_{2+x}TiO_{3+y}$ pebbles after annealing in a reducing atmosphere, 27th Symposium on Fusion Technology (SOFT 2012), Liege/Belgium, 24.-28.09.2012

Acknowledgement

This work was financially supported by the Ministry of Research and Education (BMBF) under the grant No. 03FUS0012. The views and opinions expressed herein do not reflect necessarily those of the BMBF or the European Commission.

Screening of an Alternative Production Route/Capacity for Be Pebbles (F4E-2009-GRT-30 (PNS-TBM) Action 2)

Introduction

The general objective of the Action 2 of this Grant is the characterization of Be pebbles produced by various fabrication routes and their qualification with respect to the applicability for fusion reactor blankets.

- Characterization of three batches of Be pebbles with different sizes of grains produced by Bochvar Institute, Russia has been performed. Mechanical milling of beryllium hot-pressed blocks or ingots was used for the production of these batches.
- Small batch of impact ground vacuum cast beryllium was purchased from MATERION Company (former Brush Wellman Inc., USA) and characterized following similar investigation program as Russian pebbles.
- The work program of the grant was successfully completed.

Characterization of Be pebbles

Investigations of microstructure

Investigations of microstructure of three batches of Be pebbles produced by Bochvar Institute with various sizes of grains (10-30 μm, 30-60 μm and >100 μm) and impact ground (IG) vacuum cast beryllium have shown differences in surface morphology, internal porosity and crack propagation behavior.

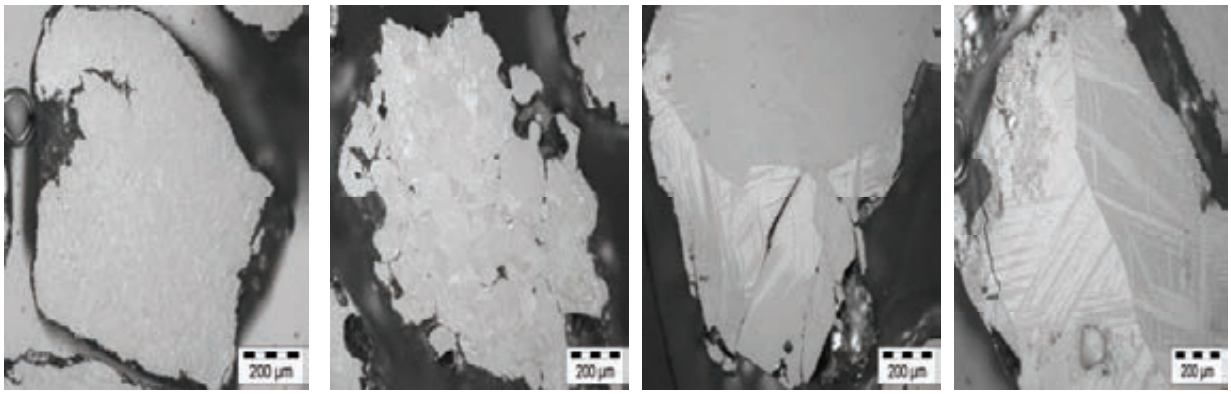

a) **b)** **c)** **d)**

Fig. 1: Optical microscopy of investigated Be pebbles with different grain sizes a) 10-30 μm, b) 30-60 μm, c) >100 μm and d) impact ground pebbles.

1. Be pebbles with the smallest grains (10-30 μm) are practically free of pores and cracks. Some surface defects and cracks attached to them were observed.
2. Be pebbles with the grain sizes in the range of 30-60 μm have rather loosely bound grain structure, which resulted in the fallout of individual grains of the matrix during grinding and polishing.
3. Be pebbles with the grain sizes exceeding 100 μm contain a great number of small pores and inclusions presumably referring to the history of material fabrication. Compared to beryllium pebbles with the grain sizes ranging 30-60 μm, a change of the behavior of crack propagation from intergranular to transgranular takes place.
4. IG pebbles have microstructure which is similar to the coarse-grained pebbles (> 100 μm). Large number of cracks and pores in the inner parts of individual pebbles were observed.

All batches of investigated Be pebbles have some properties in common:

- No obvious preferred grain orientation (texture) in the matrix was observed.
- The presence of surface oxide was observed by EDX analysis of the pebble surfaces.
- Contamination with iron and aluminum was observed on the surface of Be pebbles. Presumably, these impurities originate from the process of material fabrication.

Analysis of tritium release characteristics of Be pebbles

Three major release peaks were observed. Positions of the peaks depend on the temperature ramping rate due to a presence of a certain delay needed for tritium diffusion before outgassing. At heating rate of 15°C/min all peaks are shifted to higher temperatures by about 100-150°C in comparison to lower heating rates of 5 and 7°C/min. This fact suggests that hydrogen diffusion in the bulk of grains takes place. This also indirectly confirms that hydrogen is not trapped at the surface of pebbles exclusively, but penetrates inside the grains during thermal loading.

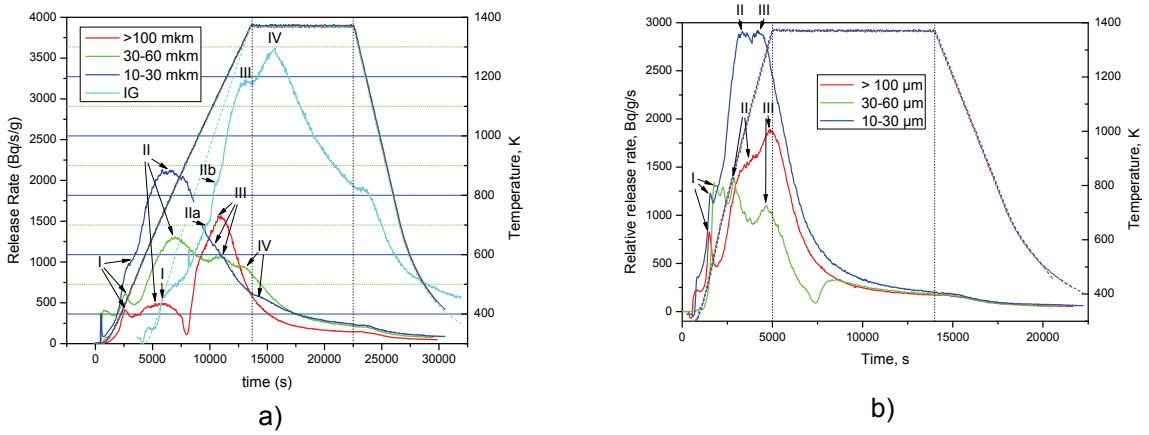

Fig. 2: Tritium release rate from Be pebbles with different sizes of grains at heating rate (a) 5°C/min or 7°C/min (IG Be) and (b) 15°C/min.

At slow heating rate (5°C/min) the heights of the first and second peaks are increasing with decreasing of the grain size, while the height of the third peak is decreasing. In particular, the third peak for the batch with the grain size of 10-30 μm is observed as a small shoulder, while for the batch with the largest grain size (>100μm) it dominates tritium release. For the faster temperature ramps this clear tendency versus grain size is not observed.

Investigations of packaging densities of Be pebbles

The largest packing factors (γ ≈ 63%) were obtained when testing pebbles with grain sizes more than 100 μm. This packing factor is comparable with that of 1 mm NGK pebbles investigated previously. These pebbles are characterized by smooth surfaces; irregular pebble shapes (rather brick-type than spherical) and wide size distribution (fractions of mm to several mm). At flat walls, mostly, the largest pebble surface is in contact with the wall, which is probably favorable for better heat transfer.

The batches with grains more than 100 μm, 10-30 μm and NGK pebbles behave in a very similar way showing relatively close values of the packing factors for different container heights.

Compared to the batches with grains more than 100 μm and 10-30 μm pebbles, the batch having 30-60 μm grains differs significantly in the surface roughness, although pebble shape and size distribution are not very distinct. However, larger surface roughness reduces the packing factor remarkably.

Preliminary conclusions on a potential suitability of the investigated Be pebbles for TBM purpose

Different characteristics of Be pebbles examined in the frame of this grant are summarized in Table 1. The judgment on chemical composition is based on information on contamination with iron which is a highly-activated element under neutron irradiation.

Table 1: Comparison of different properties of Be pebbles from the point of view of TBM application.

Characteristic of material/Material batch	Be pebbles with the grain sizes of 10-30 µm	Be pebbles with the grain sizes of 30-60 µm	Be pebbles with the grain sizes exceeding 100 µm	IG Be
Packing density	best	worst	best	best
Chemical composition	best	medium	bad	worst
Tritium release measurement	best	medium	bad	worst
Material density	medium	best	bad	worst
Pebble size, mm	1.32	1.34	1.37	1.21

These preliminary considerations show the advantages of Be pebbles with the grain sizes ranging from 10 to 30 µm. Good performance was also shown by the pebbles with the grain sizes of 30-60 µm, although their packing density was slightly lower than packing densities of other types of pebbles. Coarse-grained Be pebbles have a good performance only by investigations of packing density. Other characteristics (tritium release measurements, chemical composition and pebble density) are not in favor of the large-grained Be pebbles. The influence of the grain sizes of pebbles on the stable and reliable work of TBM is still under discussion.

Analyses of the results have shown that IG pebbles have acceptable size and pebble bed packing density. On the other hand the material density of individual pebbles is the lowest among tested beryllium grades. Chemical composition is characterized by high amounts of impurities such as aluminum, silicon and iron located mainly on the surface. Investigation of the microstructure of pebble cross sections revealed numerous voids and cracks. The major tritium release peak for this material is delayed above 1373 K, while for the other Be grades it occurs at temperatures below 1200 K. Therefore the IG material cannot be recommended for TBM applications.

After characterization in unirradiated state the pebbles with the smallest grain sizes (10-30 µm) seem to be a major candidate in addition to the present reference NGK pebbles produced by rotating electrode method for the use in ITER and DEMO blanket modules.

Staff:

A. Abou-Sena
V. Chakin
P. Kurinskiy
A. Möslang
R. Rolli
H.-C. Schneider
P. Vladimirov

List of External Contributors:

E. Alves (ITN)
J. Reimann (KBHF)

Acknowledgement

This work was supported by Fusion for Energy under the grant contract No. F4E-2009-GRT-030(PNS-TBM) - Action 2 - with collaboration by ITN Portugal. The views and opinions expressed herein reflect only the author's views. Fusion for Energy is not liable for any use that may be made of the information contained therein.

Breeder and Neutron Multiplier Materials: Development of Beryllium and Beryllium Alloy Pebble Beds with Improved Tritium Release Characteristics (BMBF Reference No. 03FUS0012)

Introduction

$Be_{12}Ti$ is considered to be one of the candidate materials for neutron multiplier of TBM in future fusion power plants.

One should note that beryllium and its compounds are high toxic materials (especially, fine particles in air) so that special glove-boxes under controlled argon atmosphere were used for R&D works. Also, investigations of neutron-irradiated $Be_{12}Ti$ specimens which were fabricated at the beryllium laboratory are described in this report.

Equipment

Two glove-boxes for works with beryllium-based materials were under preparation in 2012. The first glove-box consisting with three sections was tested in order to prove its impermeability. As it was reported in 2011, this glove-box system contains a wet ball milling device from the company NETZSCH and high-temperature sintering oven. Fig. 1 shows an updated view of this glove-box.

Fig. 1: Glove-box system consisting of three sections (electrical sintering oven is on the top of this system).

The second glove-box is designed for investigations of milled Be powders by means of KEYENCE optical digital microscope (see Fig. 2). One should note that adapters for optical cable were done through the wall of the glove-box.

Fig. 2: KEYENCE digital microscope inside of a new-built glove-box.

Due to technical problems related to the tightness of the glove-boxes, technological works with beryllium and its compounds were not performed during the reporting period.

Characterization of neutron-irradiated titanium beryllide samples

Cylinder-shaped $Be_{12}Ti$ samples (diameter of 3 mm) fabricated at the beryllium laboratory by an arc-melting of cold-pressed Be-Ti tablet were irradiated in the frame of HIDOBE-01 campaign in High Flux Reactor in Petten, Netherlands. The parameters of neutron irradiation corresponded to $6{,}94\times10^{25}$ neutrons/m^2 (E>1 MeV) with a damage dose of 13,9 dpa for titanium beryllide samples irradiated at 740 K, and to $8{,}07\times10^{25}$ neutrons/m^2 with a damage dose of 16,3 dpa for irradiation temperature equaled to 873 K. Helium production was 2300 and 2680 appm for irradiation temperatures 740 and 873 K, correspondingly.

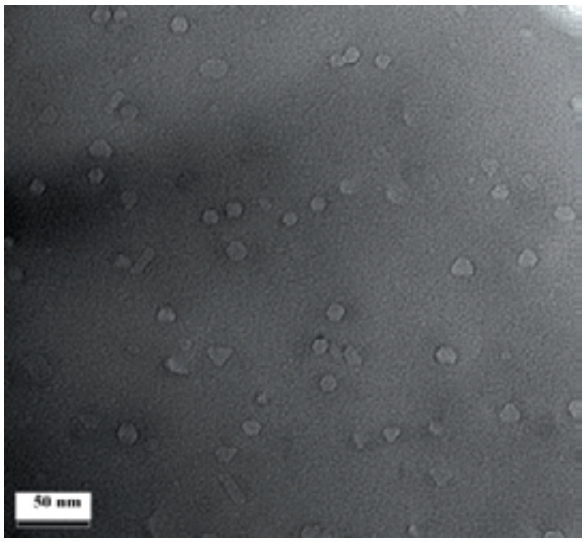

Fig. 3: High-resolution TEM image of titanium beryllide irradiated at 873 K.

The sizes and shapes of radiation-induced gas bubbles as well as swelling of samples were evaluated by means of TEM. Also, the mechanical behavior of titanium beryllide specimens in initial and irradiated states was investigated using compression tests under constant loading [1]. Fig. 3 shows radiation-induced gas bubbles with the sizes of 15-20 nm after neutron irradiation at 873 K.

Swelling of neutron-irradiated titanium beryllide samples was evaluated using high-resolution TEM images. Estimated values of swelling of specimens irradiated at 740 and 873 K were 0,08 and 0,28%, accordingly.

One should note that the values of swelling of neutron-irradiated beryllium pebbles are much higher under the same irradiation conditions [2].

Both, titanium beryllide samples in unirradiated state and after irradiation at 740 K, showed very similar parameters of a brittle failure at uniaxial compression tests using constant loading (1000 N) at 923 K. These experimental results allow making the conclusion that the high-dose neutron irradiation at 740 K did not lead to a further degradation of mechanical properties of beryllide samples which consist, mainly, of $Be_{12}Ti$ phase.

All works with neutron-irradiated titanium beryllide specimens were performed in the Fusion Materials Laboratory (FML) at IAM-WBM.

Cooperation with industrial partners

Several $Be_{12}Ti$ and $Be_{12}V$ specimens for investigations of their fusion-relevant properties were supplied by company Materion Corp., USA (http://materion.com/). Materion Corp. is a world's wide leader in the manufacturing of beryllium-based materials for nuclear applications.

Staff:

V. Chakin
M. Klimenkov
P. Kurinskiy
A. Möslang
R. Rolli

Literature:

[1] P. Kurinskiy, A. Moeslang, V. Chakin, M. Klimenkov, R. Rolli, S. van Til, A.A. Goraieb, Characteristics of microstructure, swelling and mechanical behavior of titanium beryllide samples after high-dose neutron irradiation at 740 and 873 K, Fusion Engineering and Design, accepted for publishing, 2012.

[2] V. Chakin, R. Rolli, A. Moeslang, P. Vladimirov, P. Kurinskiy, S. van Til, L. Magielsen, M. Zmitko, Characterization of constrained beryllium pebble beds after neutron irradiation at HFR at high temperatures up to helium production of 3000 appm, Fusion Engineering and Design, accepted for publishing, 2012.

Acknowledgement

This work was financially supported by the Ministry of Research and Education (BMBF) under the grant No. 03FUS0012. The views and opinions expressed herein do not reflect necessarily those of the BMBF or the European Commission.

Post Irradiation Examination of Be Materials Irradiated in HIDOBE-01 Campaign (F4E-2009-GRT-030 (PNS-TBM) - Action 3)

KIT has successfully finished all the planned post-irradiation examinations of Be materials within the F4E-2009-GRT-030 (PNS-TBM) - Action 3 and the final report from KIT was sent to NRG and F4E on 14.11.2012.

The HIDOBE-01 irradiation experiment was performed at HFR, Petten, Netherlands. Within the experiment advanced beryllium materials including not-alloyed Be and also Be-Ti alloys in forms of pebbles and pellets have been irradiated at target temperatures of 425, 525, 650, 750 ℃ up to helium production of 3 000 appm [1]. Within the contract GRT-030-Action 3 Post Irradiation Examinations (PIE) of the irradiated samples were performed by the EU consortium partners NRG, KIT, ITN, and UL. In the beginning of the Grant the irradiated samples were distributed among the partners according to their investigation equipment and economic feasibility [2]. KIT has received a part of the irradiated samples from HIDOBE-01 for the PIE by two transports coordinated by NRG as a leading organization of the consortium. The full test matrix for KIT included matrixes for unconstrained Be pebbles, constrained Be pebble beds – both loose pebbles and namely pebble beds, and Be and Be-Ti pellets. Creep and thermo-desorption tests, microstructure investigations by optical metallography (OM), scanning (SEM) and transmission electron microscopy (TEM) have been performed according to the “HIDOBE-01: Detailed PIE plan” [2].

Creep tests of individual Be pebbles with diameters of 1 and 2 mm have been made on a creep machine located in a glove box which is purged with nitrogen. The pebbles were tested at non-irradiated and irradiated states at temperatures which were equal to irradiation temperatures using three different loadings per each temperature. Fig. 1 shows examples of creep curves for 1 mm Be pebbles. Finally, it was obtained that for the two lowest irradiation temperatures of 425 °C and 525 °C no creep behaviour was observed. At these temperatures probably radiation hardening takes place which manifests itself in the reduction of the initial deformation under loadings of the pebbles. At higher irradiation temperatures of 650 and 750 °C significant creep values are fixed. The creep rates strongly depend on testing temperatures and loadings. The calculated creep rates vary in the range of $5x10^{-8}$ – $2x10^{-7}$ s^{-1}. The ability of high temperature irradiated Be pebbles to be easily deformed under applied loading means a possibility to relax internal stresses in the pebbles that occur when swelling arises. It is known that swelling in Be significantly increases above 650-700 °C. At the same temperatures creep phenomena start in Be pebbles compensating the volume increase and causing the relaxation in the internal stresses. No doubt, this is a positive effect in the HCPB concept of the DEMO blanket.

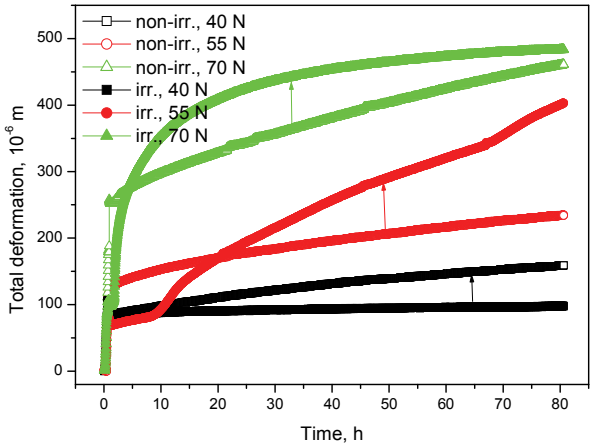

Fig. 1: Creep curves of 1 mm Be pebbles irradiated and tested at 650 ℃.

Vickers hardness (HV 0.4) measurements allow to estimate radiation-induced hardening of the Be pebbles after neutron irradiation. It was obtained that the highest hardening (290) takes place at the lowest irradiation temperature of 425 °C (see Fig. 2). The increase of irradiation temperatures causes the linear decrease of the hardening with full recovery of Vickers hardness values to non-irradiated ones at the highest irradiation temperature of 750 °C. The scattering of the hardness values reaches 20 % and can be explained by different orien-

tation of grains in the pebble during the Vickers hardness measurements. The recovery of the hardness values to non-irradiated state at high temperatures occurs due to annealing of both the internal stresses caused at production of the Be pebbles by Rotating Electrode Method (REM) and the radiation defects formed under irradiation. The formation of high strength intermediate layer in contact zones between Be pebbles and platinum foil was observed. This intermediate layer has hardness values around 1100-1200 which is much higher than the hardness of all irradiated components of the irradiated pebble bed such as Be (200), Pt (60-80) and stainless steel (up to 230).

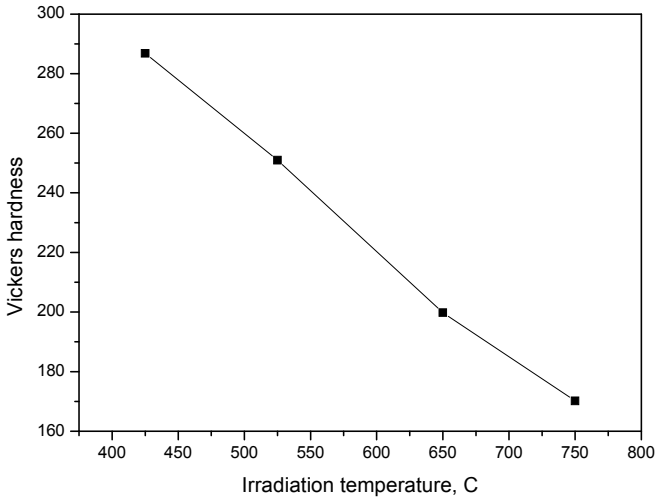

Fig. 2: Vickers hardness of the irradiated Be pebbles versus irradiation temperature.

The tritium/helium release behaviour of the irradiated Be materials were investigated using proportional counter (PC), ionization chamber (IC), and quadrupole mass-spectrometer (QMS). Fig. 3 shows an example of a TPD curve for 1 mm Be pebbles irradiated at 650 °C. In principle, the main features of the TPD measurements are as follows. For all Be pebbles independently on the irradiation temperature and state (unconstrained or constrained pebbles) only one major single peak has been observed for both Mass 4 (possible ^{4}He or $^{1}H^{3}H$) by QMS and release activity measured by IC. The peak is located at temperatures of 900-1100 °C. It is generally accepted that tritium most likely is located in the helium bubbles in a molecular form therefore the release took place approximately at the same temperatures. The increase of the heating rate from 1 to 7 °C/min causes a shift of the peak to the right on 30-50 °C. Considering measured cumulative tritium released activities in relative units versus irradiation temperature a sharp drop of its value can be allocated above the irradiation temperature of 650 °C. At the maximum irradiation temperature of 750 °C the residual measured tritium is 6-8 times lower than at other irradiation temperatures. Obviously, tritium in this case was mainly released from the Be pebbles already during irradiation. A direct conclusion from these analyses is that at irradiation temperatures higher than 650 °C a quite significant part of the produced tritium is able to escape already during neutron irradiation. Above this temperature the tritium remaining in the pebbles decreases further substantially with temperature. This strong decrease of the residual tritium in the irradiated beryllium pebbles above 600-650 °C is of outstanding importance for the HCPB pebble bed concept. Be pellets show similar results as the Be pebbles, while the BeTi samples show significant differences. The QMS measurements for Mass 4 reveal the presence of two peaks which are located at 730-830 °C and above 1130 °C respectively. The peak of release activity by IC which is much broader than the peaks for Be pebbles is located at the same temperatures as first peak obtained by QMS starting already since 400 °C (700 K).

The microstructure data obtained by OM, SEM and TEM can be characterized as follows. The microstructures of irradiated unconstrained Be pebbles strongly depend on irradiation temperatures. No significant pore or bubble formations occur at 425 and 525 °C. Irradiations at 650 and 750 °C lead to intensive pore formation resulting swelling up to the highest value of 7 %. No compact oxidation layer is observed in the surface regions at 425 and 525 °C but an initial oxidation by means of formation of small BeO particles on the pebble surface already started. Strong oxidation occurs after irradiation at 650 and 750 °C. The thickness of BeO layers on the pebble surfaces can reach 10-25 µm. The formation of an open porosity

network was observed for unconstrained Be pebbles at 750 °C while for constrained pebbles the network was formed already at 650 °C (see Fig. 4). Internal stresses in Be pebbles from the pebble beds caused by swelling are mainly localized in the regions close to contact zones between pebbles. This effect is accompanied by intensive formation of pores in the near surface regions what is probably induced by a stress-enhanced diffusion of vacancies and helium atoms towards stressed zones. Defragmentation of Be pebbles at high irradiation temperatures was observed in some cases. This could be explained by a weakening of grain boundaries and sub-boundaries when condensation of helium atoms in parallel with bubble formation occurs. A transfer of fragments from Be pebbles from one part of the pebble bed to another one through free gaps could happen. Strong oxidation of the external surfaces of Be pebbles with formation of thick brittle beryllium oxide layers was observed. Peeling and destruction of the brittle oxide layers can lead to a transfer of small beryllium oxide particles through the gaps between pebbles. Strong interaction between Be pebbles and platinum foil at contact zones takes place. This process is accompanied by a significant damage of the platinum foil caused by beryllium diffusion into platinum with the formation of pores. Strong interaction between Be pebbles and austenitic stainless steel with formation of thick corrosion damage layer occurs [3].

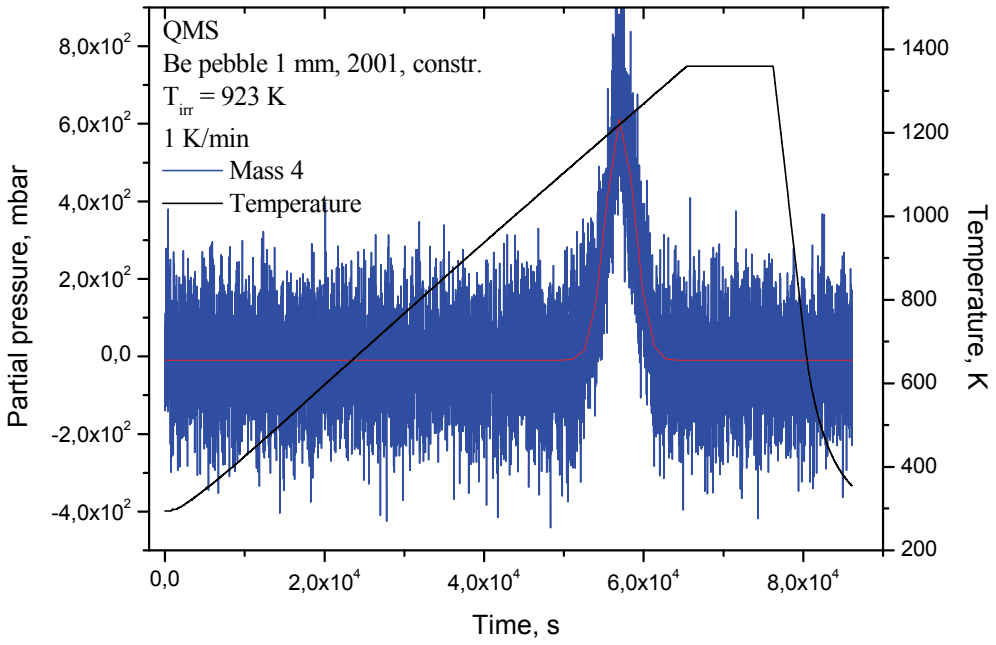

Fig. 3: Release curve for constrained Be pebbles Ø 1 mm irradiated at 650 °C as partial pressure of ^{4}He versus time using heating rate of 1 K/min.

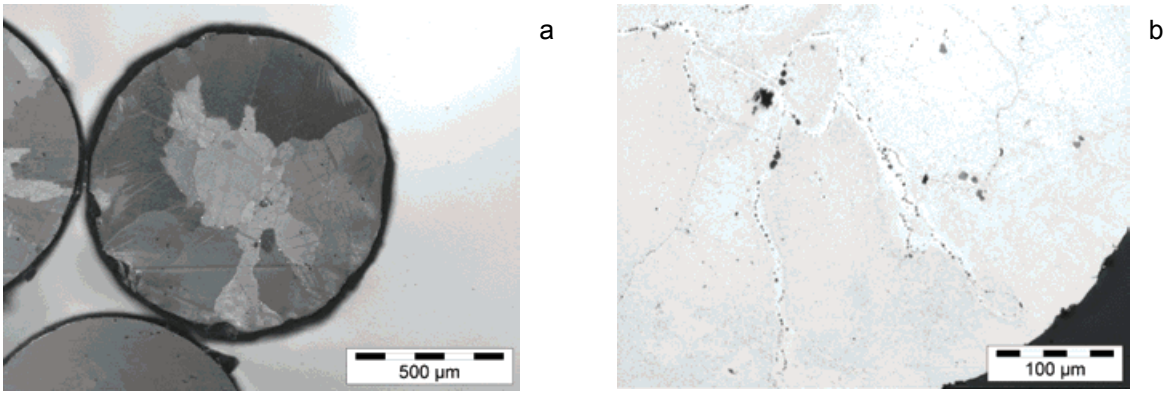

Fig. 4: Cross sections of 1 mm Be constrained pebbles irradiated at 650 ºC and investigated by OM: overview (a) and internal channels which lead outside the pebble (b).

TEM observations allow to conclude that the main radiation defects in the Be pebbles independently of irradiation temperature is flat pores or bubbles with a hexagonal shape in the basal plate (0001). Fig. 5 presents a TEM image of a pebble microstructure after irradiation at highest temperature of 750 °C. The sizes of the pores depend on irradiation temperature and vary from 7 nm at 425 °C to 150 nm at 750 °C. These results are quite important because they present the information about radiation damage of Be microstructure in the nano-scale that provide an opportunity to create or develop microstructure codes for radiation-induced changes of mechanical characteristics, TPD tests etc. for irradiated Be pebbles [4].

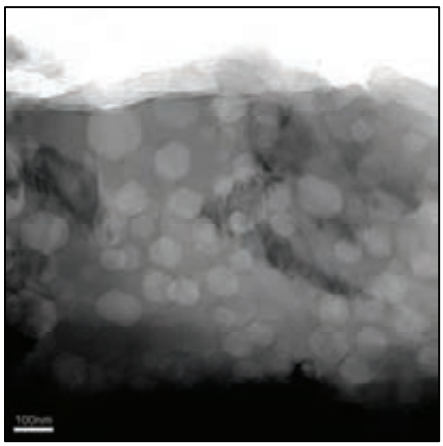

Fig. 5: TEM image of microstructure of 1 mm Be pebble irradiated at 750 °C.

Staff:

P. Barié
V. Chakin
J. Ehrmann
A. Erbe
M. Gilpert
M. Holzer,
H. Jackisch
M. Klimenkov
A. Moeslang
S. Lautensack
H. Ries
M. Rietschel
G. Rösch
R. Rolli
I. Sacksteder
R. Schmidt
H.-C. Schneider

Literature:

[1] A. Sugonyako, S. van Til, HIDOBE: final report on irradiation up to 3000 appm He, NRG-20296/09.96239/P, TW2-TTBB-004b D4b.

[2] S. van Til, HIDOBE-01: Detailed PIE plan, Under the contract of Fusion for Energy F4E-2009-GRT-030 (PNS TBM) - Action 3, NRG, the Netherlands, 14 October 2010.

[3] V. Chakin, R. Rolli, A. Moeslang, P. Vladimirov, P. Kurinskiy, S. van Til, A.J. Magielsen, M. Zmitko, Characterization of constrained beryllium pebble beds after neutron irradiation at HFR at high temperatures up to helium production of 3000 appm, Presented to 27th Symposium on Fusion Technology, September 24-28, 2012, Liege, Belgium.

[4] V. Chakin, R. Rolli, M. Klimenkov, A. Moeslang, P. Vladimirov, P. Kurinskiy, H.-C. Schneider, S. van Til, A.J. Magielsen, M. Zmitko, Microstructure characterization of beryllium pebbles irradiated at HFR up to 3000 appm helium production within HIDOBE-01 experiment, Presented to 10th IEA International Workshop on Beryllium Technology, September 19-21, 2012, Karlsruhe, Germany.

Acknowledgement

This work was supported by Fusion for Energy under the grant contract No. F4E-2009-GRT-030(PNS-TBM) - Action 3 - with collaboration by NRG Petten, The Netherlands; ITN Sacavém, Portugal and ISSPI, Riga, Lativa. The views and opinions expressed herein reflect only the author's views. Fusion for Energy is not liable for any use that may be made of the information contained therein.

Effect of Hydrogen on Morphology of Beryllium Surface (HPC-FF 2012 HySuBe)

Introduction

After the end of life of the DEMO fusion reactor blanket about 7 kg of tritium will be generated within 300 tons of beryllium pebbles used in the helium-cooled pebble bed. Therefore the prediction of the tritium inventory retained in beryllium pebbles is very important both for safety during reactor operation and utilization of radioactive beryllium pebbles after the end of life of the reactor. Associative desorption of the accumulated tritium occurs at the surface of material therefore behaviour of hydrogen on beryllium surface is studied in this work.

Calculation method

In this work static and dynamic first principles density functional theory (DFT) calculations were used for revealing of possible hydrogen configurations at the surface and determination of adsorption and desorption barriers. *Ab initio* calculations are performed with plane-wave VASP computer code [1]. Full geometry optimization is carried out using Generalized Gradient Approximation (GGA) with Perdew-Wang non-local exchange-correlation functional [2] and the scalar relativistic PAW [3]. The calculations involve typically 13x13x13 Monkhorst-Pack k-point mesh [4] and cutoff energy of 450 eV. Migration barriers were estimated by means of the drag and/or nudged elastic band methods. Rhombohedral supercells with 64 and 96 lattice sites are applied.

Results

It was found previously that being at beryllium surface hydrogen molecules dissociate immediately. Individual hydrogen atoms cannot desorb from the surface before they form hydrogen molecule again. Our previous results on adsorption barrier for hydrogen molecule on (0001) Be surface were improved. The results obtained by *ab initio* molecular dynamics confirmed the existence of the adsorption barrier for hydrogen molecule of 0.75 eV, but also revealed the existence of a shallow physisorption state (see Figure 1). The barrier for associative desorption (i.e. desorption after formation of hydrogen molecule) is about 1 eV. We also confirmed that hydrogen surface coverage affects the adsorption barrier. Indeed at critical surface coverage of 0.5 ML (ML stands for monolayer. It is defined relative to the total number of the available places for hydrogen adsorption at the (0001) Be surface; only one type of H surface adsorption sites is filled in this case) the adsorption barrier increases by 0.1 eV up to 0.85 eV. Both results for pure and H-covered (0001) surfaces are very close to the value of 0.8 eV deduced from experiments.

In contrast no adsorption barrier exists for a single hydrogen atom which is adsorbed exothermally. Hence the adsorption of atomic hydrogen, which is not hindered by the surface barrier, is significantly higher for atomic than for molecular hydrogen. This explains contradictory experimental data on solubility of atomic and molecular hydrogen.

To clarify the effect of the hydrogen surface coverage on the mechanism of associative desorption several *ab initio* molecular dynamics simulations have been performed at 900K, with varying hydrogen surface coverage.

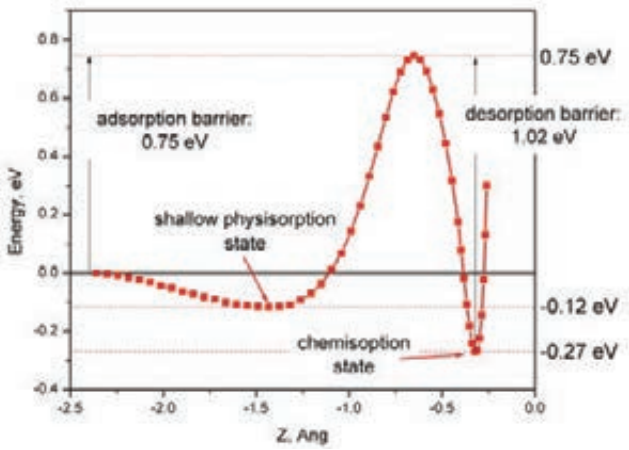

Fig. 1: Energy profile for hydrogen molecule impinging beryllium (0001) surface with an energy slightly above the adsorption barrier.

In one case only hcp adsorption sites were occupied with hydrogen atoms (0.5 ML). After 33 fs significant surface changes have occurred (several beryllium atoms are slightly above the surface being ready to evaporate), but no hydrogen desorption occurs (see Figure 2a). On the contrary in the run were both hcp and fcc positions were filled (1 ML), hydrogen atoms from adjacent fcc and hcp positions make a pair and desorb as a molecule after 22 fs (Figure 2b). The H-H distances are in the range of 0.66-0.84 Å (cf 0.74 Å for H-H distance in H_2 molecule). Due to desorption the surface occupancy dropped down to 0.5 ML. It should be noted that all the hydrogen molecules formed consist of one hydrogen from fcc and one from hcp sites. The pair making process is random and some hydrogen from fcc sites were left at the surface.

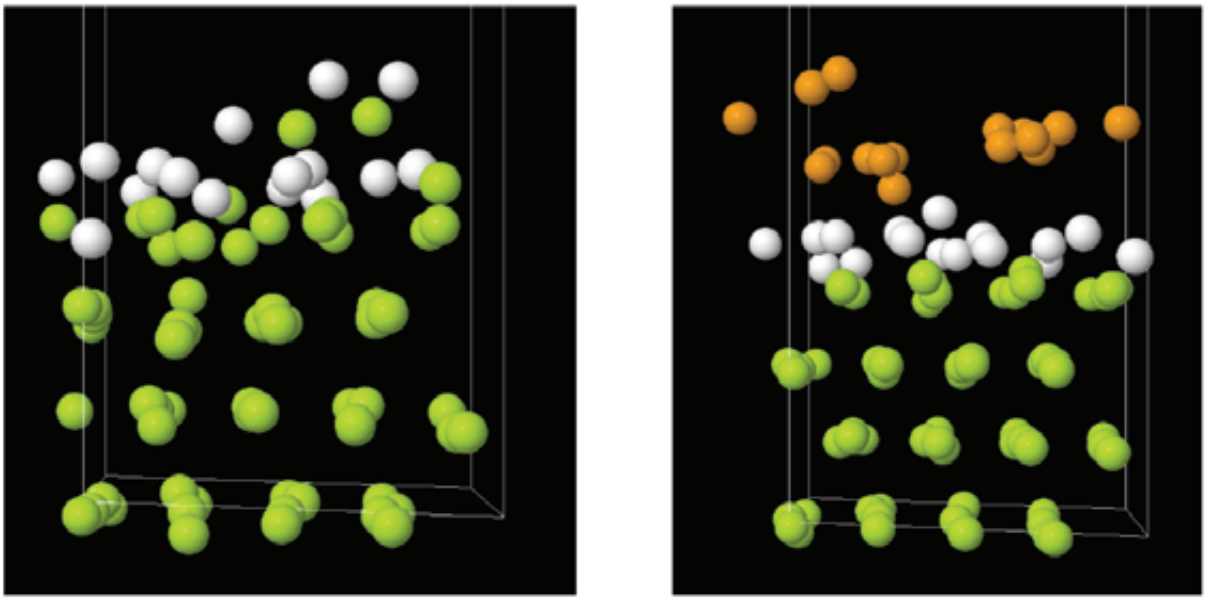

Fig. 2: Side view of hydrogen on the Be (0001) surface: (a) 0.5 ML, (b) 1.0 ML. Hydrogen atoms are colored white, while H_2 molecules are orange.

As was found previously the pair of H atoms can desorb from the surface only if they are located close to each other (within one surface crystal unit cell) and there are no vacant places for hydrogen to escape. It makes the surface coverage of 0.5 ML a critical one as far as if one additional hydrogen atom comes to the surface there is no empty place for it and it will with necessity share a unit cell with another H-atom that should result in desorption of a H_2 molecule.

We tried to simulate this kind of associative desorption act when additional H-atom comes from the bulk of material as it should be in the case of T-release after neutron irradiation. *Ab initio* molecular dynamics runs were performed with H-atom put in subsurface octahedral position, while the whole surface was covered with 0.5 ML of hydrogen. To our surprise no desorption event occurred during 750 fs. Hydrogen stays in the subsurface layer but results in a shift of one regular Be-atom to ad-atom position above octahedral channel. It seems that hydrogen promotes surface diffusion of Be by reducing cohesion of Be atoms with surface, which can lead to lighter Be evaporation. However, additional investigations are required. These facts may shed light on the possible mechanism of surface reconstruction observed at high surface hydrogen coverage.

Conclusions and future prospects

Behaviour of hydrogen on beryllium (0001) surface was investigated. It was found that hydrogen can occupy two types of positions: hcp and fcc sites. After dissociation hydrogen atoms seem to repel each other so that formation of hydrogen molecule and it's desorption is effectively prevented until a critical hydrogen surface concentration (0.5 ML) is reached.

Then the appearance of one additional hydrogen atom at the surface seems to result in formation of close hcp-fcc pair, creation of hydrogen molecule followed by it's desorption from the surface. However, formation of complex arrangements of hydrogen and beryllium atoms was observed instead. This behaviour will be carefully studied in more detail.

Staff:

P. Vladimirov

Literature:

[1] G. Kresse, J. Hafner, Abinitio Molecular-Dynamics for Liquid-Metals, Phys Rev B, 47 (1993) 558-561.

[2] J.P. Perdew, Y. Wang, E. Engel, Liquid-Drop Model for Crystalline Metals - Vacancy-Formation, Cohesive, and Face-Dependent Surface Energies, Phys Rev Lett, 66 (1991) 508-511.

[3] G. Kresse, D. Joubert, From ultrasoft pseudopotentials to the projector augmented-wave method, Phys Rev B, 59 (1999) 1758.

[4] H.J. Monkhorst, J.D. Pack, Special points for Brillouin-zone integrations, Phys Rev B, 13 (1976) 5188.

Acknowledgement

This work, supported by the European Communities under the contract of Association between EURATOM and Karlsruhe Institute of Technology, was carried out within the framework of the European Fusion Development Agreement. The views and opinions expressed herein do not necessarily reflect those of the European Commission.

Modeling of Pebbles and Pebble Beds (CoA)

Objective

The mechanical response of a crushable pebble assembly is investigated. A continuum damage mechanics approach has been used to investigate the influence of individual pebble failure on the over-all stress-strain response of a pebble assembly subjected to uni-axial compression. The nature of damage law (sudden to gradual) and its influence on macroscopic response is studied.

Crush experiments and damage law

Figure 1 shows the probability distribution of critical failure energy of single Lithium Orthosilicate (OSi) pebbles [2]. Fig. 2 shows the assumed damage evolution (D_i) as a function of normalized stored elastic energy (φ_i/φ_i^{cr}) in the pebble. The damage evolution law is given by

$$D_i = 1\text{-}\exp(-a((\varphi_i/\varphi_i^{cr})\text{-}1)).$$

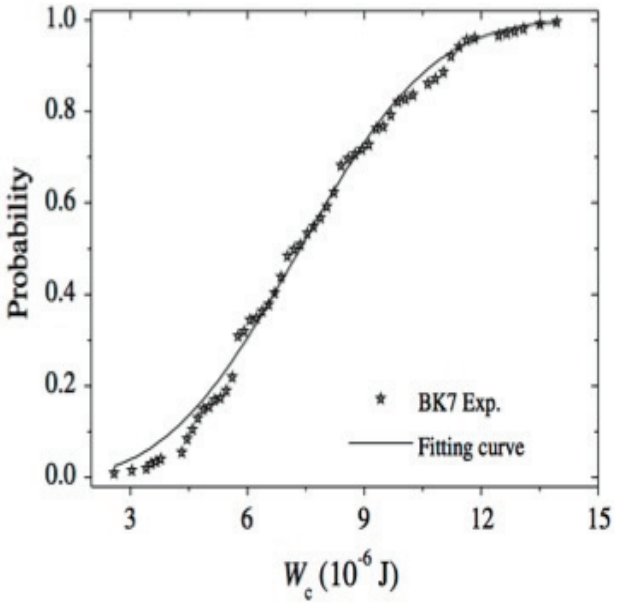

Fig. 1: Probability of critical failure energy of OSi pebbles obtained from crush tests on single OSi pebbles.

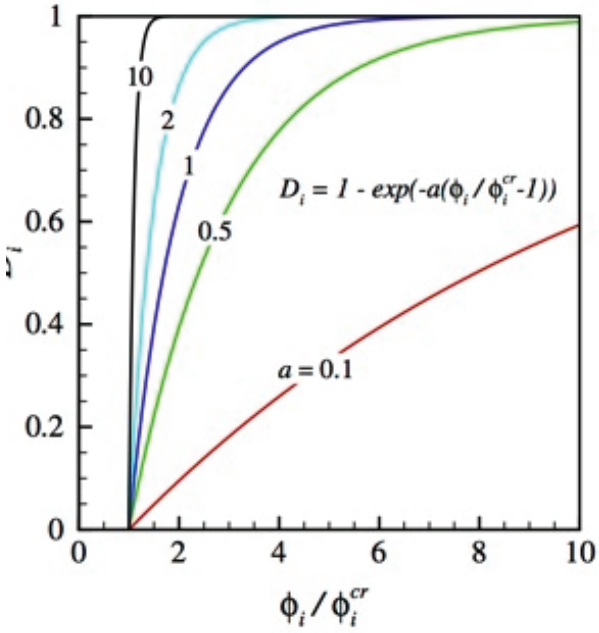

Fig. 2: Evolution of damage (D_i) as a function of normalized stored elastic energy in the pebble.

Crushable pebble assembly simulation

We use Discrete Element Method (DEM) to study the influence of crushable pebbles on the overall stress-strain response of the pebble assembly [1]. The model system consists of 5000 spherical pebbles with periodic boundary conditions. Each pebble in the assembly is assigned a critical failure energy following Weibull distribution as shown in Figure 1. Then the assembly is subjected to uni-axial compression up to 1.5% strain and then unloaded to a stress-free configuration. During the loading, the stored elastic energy in each pebble is monitored and the corresponding damage value (D_i) is calculated according to the damage evolution law mentioned before (see Figure 2). The elastic modulus of the pebble is reduced according to $E = (1\text{-}D_i)E_0$, where E_0 is the initial elastic modulus of the pebble.

Fig shows the average stress-strain response of a crushable pebble assembly. The assembly comprises of 5000 spherical pebbles of size 0.5 mm each in a cubical box with periodic boundary conditions. The results correspond to the case of uni-axial compression up to 1.5% strain followed by unloading to a stress-free state. Each curve in the figure corresponds to a specific value of damage coefficient (*a*) indicating the nature of damage accumulation in the pebble. Large value of "*a*" corresponds to sudden damage and a small value corresponds to gradual damage as shown in Fig. 2. The value of *a*=0 corresponds to the case of a non-crushable pebble assembly. Clearly, with increase in the value of damage coefficient "a", the system starts to show compliant response finally showing a stress-plateau for large values of "a" shown here.

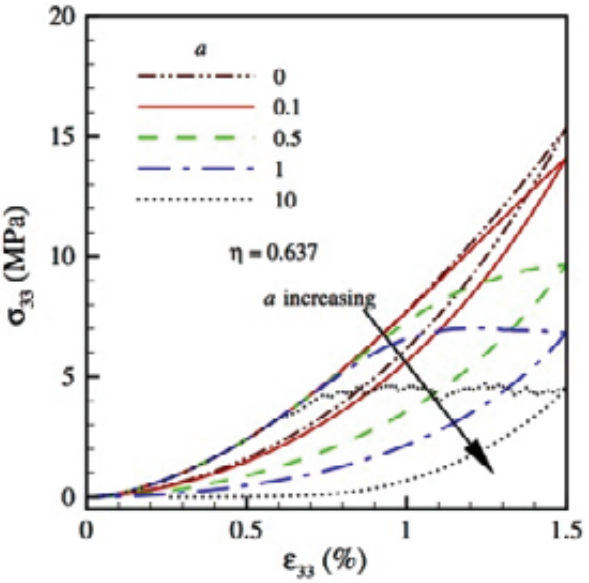

Fig. 3: Stress-Strain response of a crushable pebble assembly.

Also, note that the residual strain after unloading increases with increase in the value of "a". This may be related to the net reduction in compliance of the assembly due to large number of failed pebbles at an early stage of loading unlike the gradual damage case, where individual pebbles continue to fail until the end of loading. The packing factor of the assembly also has influence on the over-all stress-strain response of a crushable assembly. For a detailed study, the reader may refer to [3].

Conclusions

A micromechanical approach to the simulation of a crushable pebble assembly has been developed. The results show that the damage accumulation law adopted for individual pebble failure has considerable influence on the macroscopic response of the assembly. The residual strain after unloading depends on the overall compliance of the assembly at the end of loading which eventually depends on the type of damage.

Staff:

R. K. Annabattula
M. Kamlah

Literature:

[1] Y. Gan & M. Kamlah, Discrete element modelling of pebble beds: With application to uniaxial compression tests of ceramic breeder pebble beds. Journal of the Mechanics and Physics of Solids 58, 129-144(2010).

[2] S. Zhao, Multiscale modeling of Thermomechanical properties of ceramic pebbles, Ph.D. Thesis, Karlsruhe Institute of Technology (2010).

[3] R. K. Annabattula, Y. Gan, S. Zhao and M. Kamlah, Mechanics of a crushable pebble assembly using discrete element method, Journal of Nuclear Materials, 430, 90-95 (2012).

Supply of Preliminary Fabrication & Welding Procedure Specifications and Feasibility Mock-ups for TBMs EUROFER Subcomponents: Lot 3: HCPB CP FMU and pF/WPS (F4E-OPE-305-03 (TBM-MD))

Objective

The design of the cooling plate for the HCPB TBM concept bases on an arrangement with a 180° bending of the front part. The subcomponent fabrication strategy proposed by KIT for the realization of a Cooling Plate Feasibility Mockup (CP FMU) bases on machining cooling channel structures into a plane plate by Wire Spark Erosion. After the fabrication of the channels the plate will be bent. The scope of this task is to develop a set of preliminary fabrication procedure specifications. The fabrication parameters will be demonstrated by a relevant scale Feasibility Mock Up.

The achievements in 2012 have been summarized in a series of reports:

- HCPB CP FMU Design package for approval prior to fabrication
  - Detailed 2D and 3D CAD drawings, parts list of the FMU;
  - Workshop layouts of the FMU;
  - CAD editable files of the FMU.

- HCPB CP - Fabrication Development Plan
  - Update of description of fabrication processes/ technologies for fabrication of the FMU.
  - Technical plan detailing the foreseen development activities (incl. duration and time sequence).
  - Updated tentative usage plan of EUROFER semi-finish products up to the fabrication of the FMU.

- HCPB CP Reference codes & standards to be used as basis for the development of pF/WPS
  - Reference set of codes & standards to be used as basis for the development of pF/WPS.

- HCPB CP pF/WPS, as planned to be implemented for the fabrication of FMU
  - Set of fabrication parameters as planned to be used for the FMU on basis of past developments.

On basis of the above mentioned reports, the intermediate fabrication experiments have been started (drilling of starting holes for wire spark erosion and bending of the cooling plate). The intermediate fabrication experiments will be continued and concluded in order to define the fabrication parameters for the Feasibility Mock Up (FMU).

In this activity the following Industrial companies / external associations are involved:

Krüger Erodiertechnik, Heimerdinger Oberflächentechnik, Institut für Umformtechnik / Forschungsgesellschaft Umformtechnik (Stuttgart).

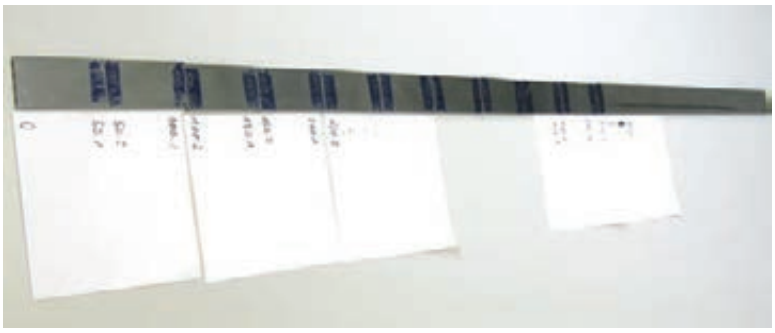

Fig. 1: Accuracy test of HCPB TBM Cooling Plate MU with 4 cooling channels (length full scale).

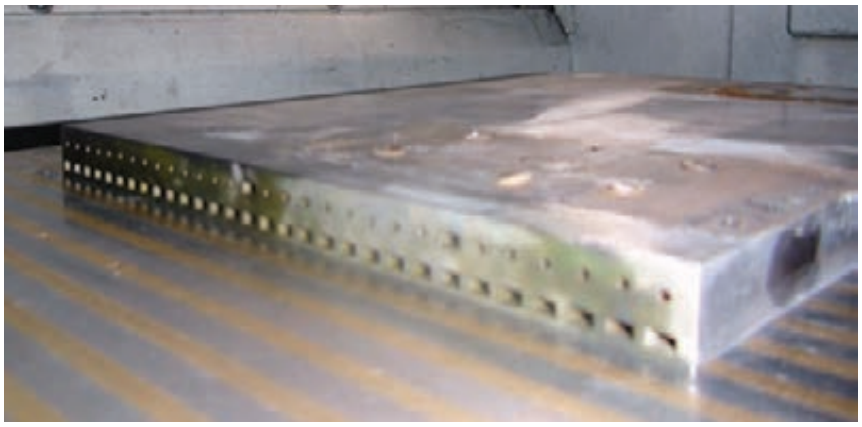

Fig. 2: Running process of HCPB TBM Cooling Plate MU with 30 cooling channels (length 300mm).

Fig. 3: Contract adapted wire cutting spark erosion machine. Max. cutting length about 1000 mm.

Fig. 4: 180° HCPB cooling plate U-bending tool

Fig. 5: Several HCPB TBM Cooling Plate bending experiments (until real scaled MU below).

Staff:

J. Rey
P. Freiner
A. von der Weth
H. Neuberger

Non-destructive Testing (NDT)

Objectives

The uniaxial diffusion-welded cooling plate of a stiffening grid (U-DW-Ar-welded cooling plate) and material for Mock Up (MU)-components in as-received condition is investigated by means of non-destructive ultrasonic immersion testing and using 3D software visualization for the quality assurance and defect quantification with higher accuracy.

Task current status

For quality assurance of the diffusion bending and materials characterization MU cooling plates were non-destructively tested using the ultrasonic immersion technique. For testing the immersion system KC- 200 was used by GE Inspection Technologies. The ultrasonic examinations were performed by straight-beam and using the frequency of 20MHz. The uni-axial diffusion-welded cooling plate of a stiffening grid (Fig. 6) was scanned with the focus on different levels (from the surface till the diffusion bending-area) and at the sound velocity C_l = 5820 mm/s for EUROFER.

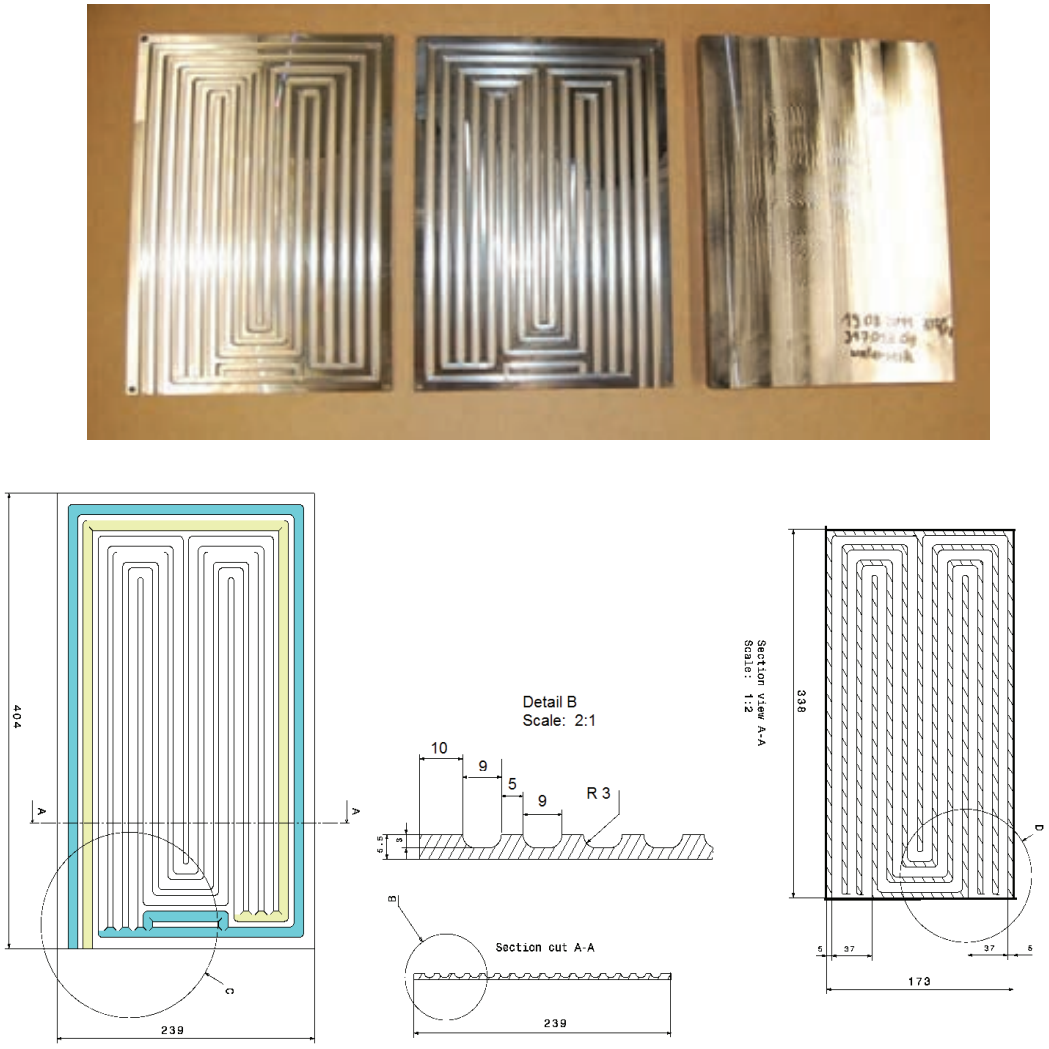

Fig. 6: Overview of U-DW-Ar-welded cooling plate of a stiffening grid.

The ultrasonic immersion testing of the diffusion bond and webs showed that they contain no imperfects or chamfer except material defects such as pores or non-metallic inclusions, which are located almost at the diffusion bonding plane.

In the depth of 4 mm, ca. every 2-3 mm, many defects exist in the materials (non-metallic inclusions or pores) in the size of 50 to 150µm (Fig. 7).

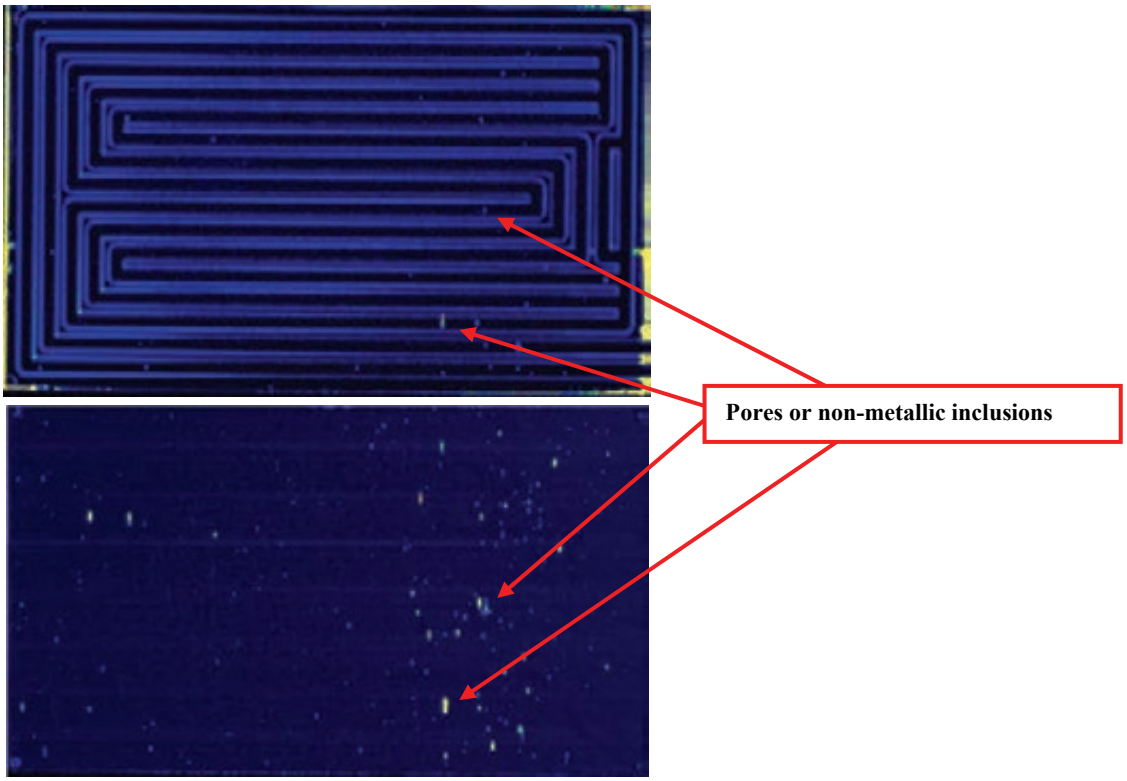

Fig. 7: C-Scan image of U-DW-Ar-welded cooling plate of a stiffening grid.

Ultrasonic immersion testing data are used as input for 3D visualization software programmed by I-Deal Technologies. Using 3D visualization software, all detected flaws can be visualized clearly. The results are presented on the fig. 8.

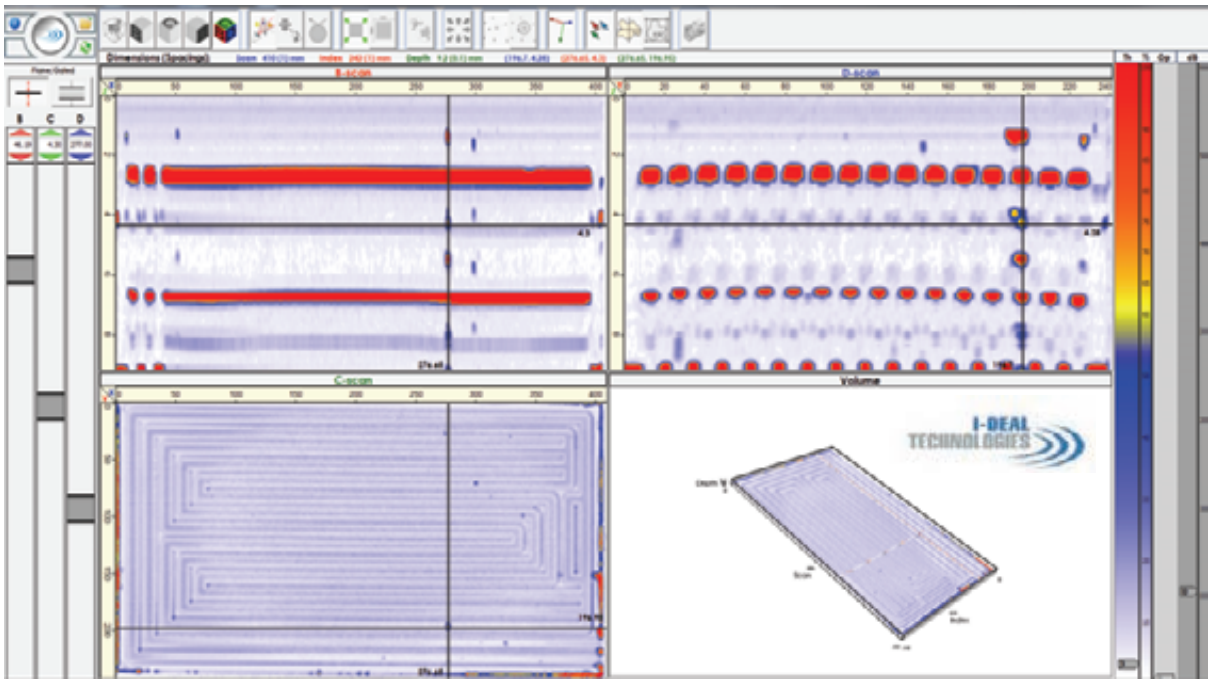

Fig. 8: Screen-shot of 3D visualization of U-DW-Ar-welded cooling plate of a stiffening grid.

In the last non-destructive ultrasonic testing, it was observed that the material used for the MU-components contained a lot of defects e.g. pores or non-metallic inclusions. This is not expected for the used material. Therefore the other four work pieces (100 x 100(80) x 50(30)

mm from Chromelso 92 (so-called P92) fabricated by MAN (Diesel & Turbo) were non-destructive investigated in as-received condition. During the ultrasonic testing, inclusions or impurities are determined at all four test pieces and located in a depth range from 5 to 10 mm. (Fig. 9).

Hence, it has been decided to investigate the defect sources. For these investigations, samples are cut from the work piece at the depth, at which the defects are found. These samples were ground and polished and then investigated by light microscope. During metallographic examination some inclusions are identified and measured (Fig. 10).

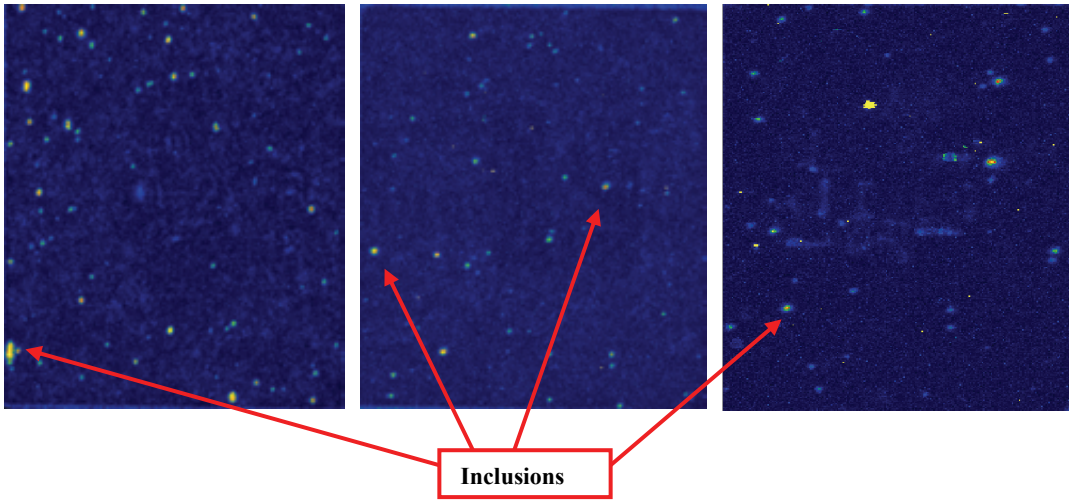

Fig. 9: C-Scan image of work pieces in as-received condition.

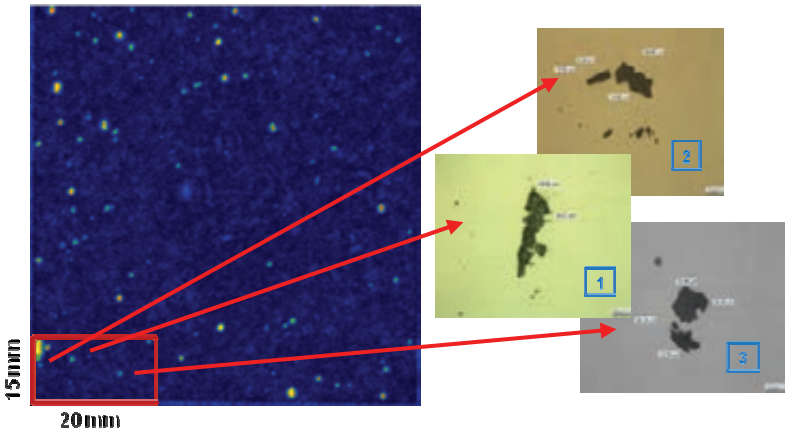

Fig. 10: Metallographic examination of inclusions.

The determined inclusions were examined by SEM (scanning electron microscope) and their element distribution is analyzed by EDX (energy dispersive X-ray spectroscopy). The results can be seen in Fig. 11. The EDX results show that the detected inclusions consist of various oxides of Al, Si, Ca, Mg and Mn base.

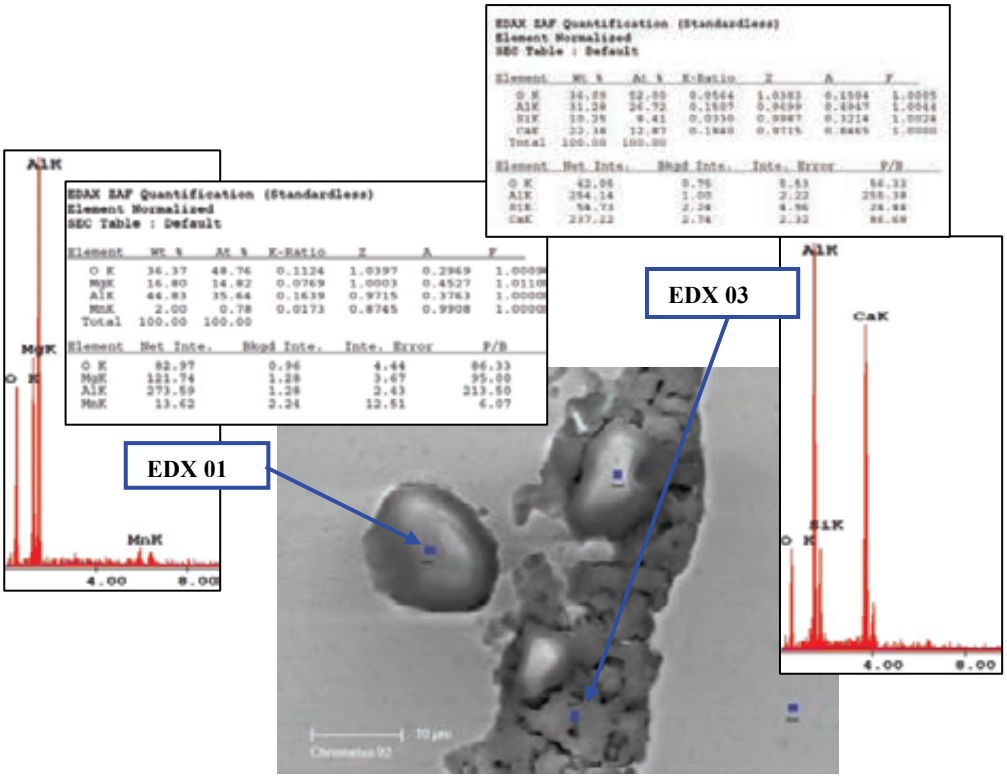

Fig. 11: EDX analysis of the inclusion No. 1 (lower part).

Currently, the Breeder Unit Cooling Plates were examined using the non-destructive ultrasonic immersion technique to optimize the wire EDM process for evenly run of internal cooling channels.

Staff:

J. Aktaa
W.W. Basuki
S. Knaak
T. Martin

Acknowledgement

This work was supported by Fusion for Energy under the service contract No. F4E-OPE-305-03 (TBM-MD). The views and opinions expressed herein reflect only the author's views. Fusion for Energy is not liable for any use that may be made of the information contained therein.

Study Regarding the Use of Liquid Metal as Blanket Coolant (WP12-DAS-02-T14-01)

Liquid metals like PbLi are promising candidates for coolants and breeder materials in thermonuclear power reactors. The DCLL blanket considered in a recent design study represents a very attractive design option for a liquid metal blanket and could yield high thermal efficiency. This is achieved by a thermal insulation (flow channel inserts (FCI)) between the very hot liquid metal and the duct walls. The latter are internally cooled by helium to keep their temperature below the compatibility limit of the structural material. The ceramic material SiC/SiC, which is foreseen as thermal insulation, has poor electrical conductance and interrupts the electric current path from the fluid into wall, when insulating FCIs are fitted into the steel ducts. As a result, electric currents induced by the interaction of the moving liquid metal with the strong plasma-confining magnetic field are reduced to a minimum and magnetohydrodynamic (MHD) pressure drop, resulting from electromagnetic Lorentz forces, becomes acceptable.

Due to the complex geometry FCIs will be fabricated in pieces and inserted into the channels of the blanket modules. At junctions between FCIs as well as at locations where the pipes have to be remotely cut and rewelded for blanket maintenance it is expected that gaps in the insulation are present. The impact of the sudden variation of material conductivity on MHD pipe flow has been investigated and a detailed parametric study quantifies the additional MHD pressure drop $\Delta p3D$ depending on the size (length) l of the non-insulated gap regions. Fig. 1a shows details of the geometry near the insulation gap. At sufficient distance from the gap the pressure distribution reaches fully developed conditions with a uniform slope while the extra pressure drop $\Delta p3D$ due to Lorentz forces is caused near x=0 by additional 3D current loops. Further details can be found in [1].

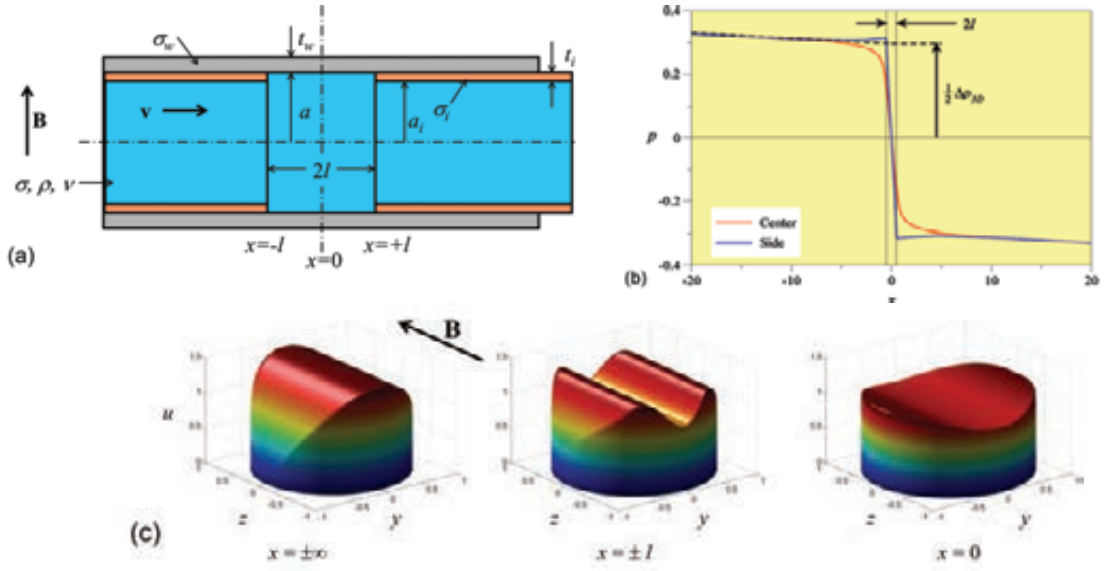

Fig. 1: Gap between two FCIs (a) geometry; (b) dimensionless pressure distribution along the pipe axis y=0 and along the side wall y=±1; (c) typical velocity profiles in fully developed regions (x→±∞), at the beginning and end of the gap (x=±l) and in the middle of the gap (x=0).

Staff:

L. Bühler
H. -J. Brinkmann
V. Chowdhury
S. Ehrhard
C. Mistrangelo

Literature:

[1] L. Bühler; MHD pressure drop at bare welding positions in pipes of DCLL blankets. KIT Scientific Report 2012, submitted.

Acknowledgement

This work, supported by the European Communities under the contract of Association between EURATOM and Karlsruhe Institute of Technology, was carried out within the framework of the European Fusion Development Agreement. The views and opinions expressed herein do not necessarily reflect those of the European Commission

Magneto-hydrodynamic Flows in a HCLL Blanket Mock-up (CoA)

Numerical analysis

Liquid metal flows in two connected breeder units (BU) of a Helium Cooled Lead Lithium (HCLL) test blanket module are investigated by asymptotic analysis and numerical simulations for strong magnetic fields $B(x)$ with variations in radial direction x, as present in ITER. The flow is characterized by the Hartmann number Ha that is proportional to the magnetic field strength and by the interaction parameter N which measures the ratio of electromagnetic to inertia forces. Figure 1(a) shows the axial distribution of pressure along the external stiffening plate (SPE) and the central one (SPC). A strong pressure drop occurs across the entrance gap for $x<0$ due to higher velocities and 3D effects near the expansion. In the BU the pressure drop is moderate. When approaching the first wall (FW) the pressure along SPC drops rapidly due to strong modifications of the flow. Along SPE the pressure gradient becomes weaker because the fluid velocities along this wall are strongly reduced. The remaining relatively high pressure level at the FW is required to accelerate the flow along the FW before it passes the narrow gap to reach BU2. The complete variation along the FW is shown in Fig. 1(b). The pressure drop at the first wall gap may reach a similar order of magnitude as the one along the radial extension of the module. It strongly depends on the distribution of the magnetic field $B(x)$ and its value at the first wall. Surprisingly, the distribution of flow rates in layers parallel to B remains practically unchanged in comparison with the case of a uniform magnetic field.

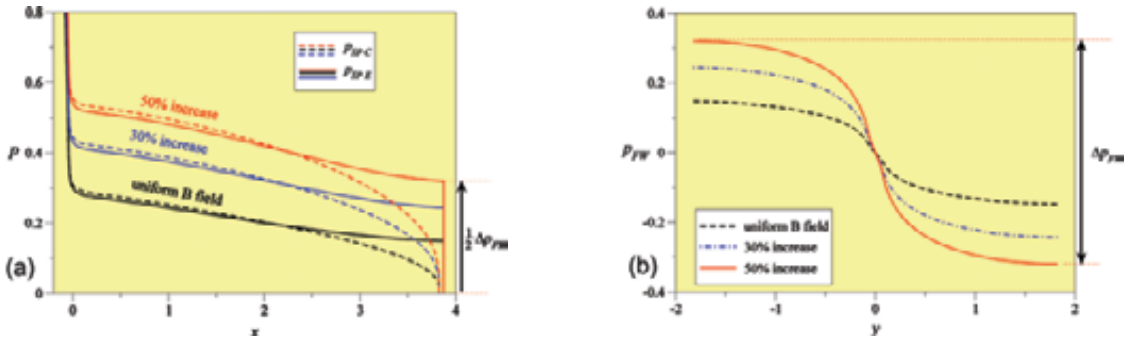

Fig. 1: MHD flow in two BUs for Ha = 1000, $N \rightarrow \infty$. Variation of pressure p, (a) along the central (SPC) and external stiffening plate (SPE), and (b) along the first wall for uniform magnetic field and varying fields with 30% and 50% increase towards the FW.

In order to confirm the asymptotic calculations, complete 3D numerical simulations (HPC-FF) have been performed by taking into account inertial forces and proper thickness and conductivity of the walls. For very high interaction parameters N, i.e. for very small velocities, numerical simulations show that the flow in the 2 BUs exhibits almost perfect symmetry as in the asymptotic analysis for $N \rightarrow \infty$ (Fig. 2(a)). With decreasing N flow separation occurs near the first wall due to stronger inertia forces as can be seen in Fig. 2(b) for N=1200.

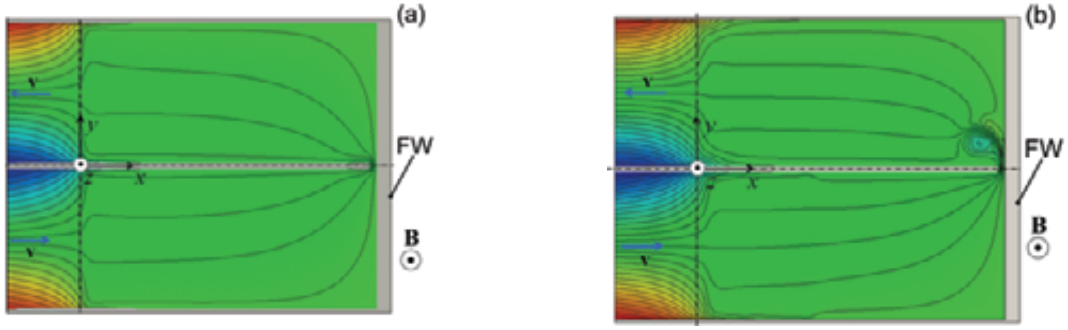

Fig. 2: MHD flow in two BUs for Ha = 1000, N = 18000 (a) and N = 1200 (b). Colored contours of electric potential in the central symmetry plane z = 0 serve as approximate flow streamlines.

Staff:

L. Bühler
H. -J. Brinkmann
V. Chowdhury
S. Ehrhard
C. Mistrangelo

Numerical Studies of MHD Flows with Strong Magnetic Fields (HPC-FF-FSNMHD)

Parallel numerical simulations have been performed on the HPC-FF in Jülich. The project FSNMHD is a continuation of project FSNHPCM.

The solver is based for the hydrodynamic part on the open source code OpenFOAM and MHD equations have been implemented separately [6]. Large computational resources are required to predict MHD flows in complex geometries. Different topics have been investigated. We studied MHD flows in HCLL blankets as described in section 2, for various applied magnetic fields and values of inlet velocity. We carried out simulations to analyze the influence of internal volumetric heating on temperature distribution in liquid metal flows in blanket breeder units. First results are summarized in the following. They are also the starting point for further numerical calculations that will be performed on the Helios supercomputer at the International Fusion Energy Research Center (IFERC) in Rokkasho.

Liquid metal HCLL blanket flows are expected to be mainly driven by buoyancy forces caused by non-isothermal operating conditions due to neutron volumetric heating and cooling of walls, since only a weak forced flow is required for tritium extraction. The present numerical study aims at clarifying the influence of electromagnetic and thermal coupling of adjacent fluid domains on magneto-convection in geometries related to the HCLL blanket.

Only few studies are available for MHD buoyant flows in horizontal ducts with internal heat sources and for control parameters relevant for fusion blankets. A phenomenon that has not been studied yet is the thermal and electromagnetic coupling of flows in sub-channels that form the blanket module, caused by the finite electric and thermal conductivity of walls.

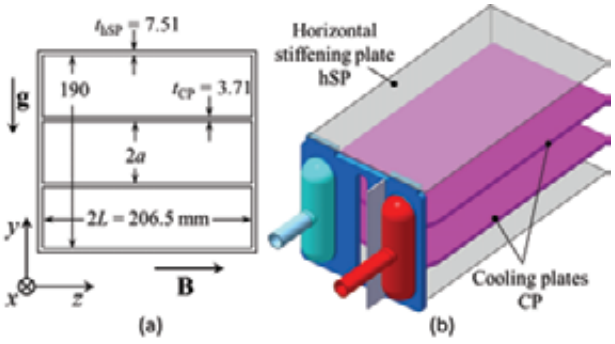

Fig. 1: (a) Geometry used for numerical simulations and reference dimensions. (b) Design of back plate and cooling plates for a breeder unit of a HCLL test blanket module

We consider MHD flows in electrically and thermally conducting horizontal ducts where non-homogeneous thermal conditions are caused by heat sources distributed uniformly within the fluid and by heat extraction through the walls. The considered geometry is shown in Fig. 1. It consists of three flat channels electrically and thermally coupled. The dimensions and properties of fluid and wall materials are taken according to the last design of a HCLL test blanket module. We investigate MHD flows for intense magnetic fields expressed in terms of the non-dimensional Hartmann number $Ha \geq 2000$. The magnitude of the volumetric heat source is quantified by the Grashof number Gr that is varied in a range corresponding to volumetric heating of 0.04÷5 MW/m³. The order of magnitude of the selected heat sources is close to average values expected in HCLL and DCLL blanket modules. We carried out both 2D simulations with the purpose of understanding the basic state of the flow and 3D calculations to define the way in which temperature perturbations develop in the channels. The numerical study shows that when the Grashof number exceeds a critical value Gr_c a well-organized convective motion sets in.

The development of 3D magneto convection can be summarized as follows:

- For $Gr < Gr_{c1}$ i.e. if the internal heating is smaller than a critical value a 2D stable steady regime dominated by conduction is found.
- For $Gr_{c1} < Gr < Gr_{c2}$ i.e. for moderate heat sources, temperature perturbations develop in the upper half of the duct, where an unstable thermal stratification is present. Convection

sets in as spatially periodic pairs of counter-rotating rolls with their axis aligned with the magnetic field (Fig. 2).

- For $Gr > Gr_{c2}$ the amplitude of temperature disturbances becomes large, convective rolls lose their periodicity, increase in size and become time dependent.

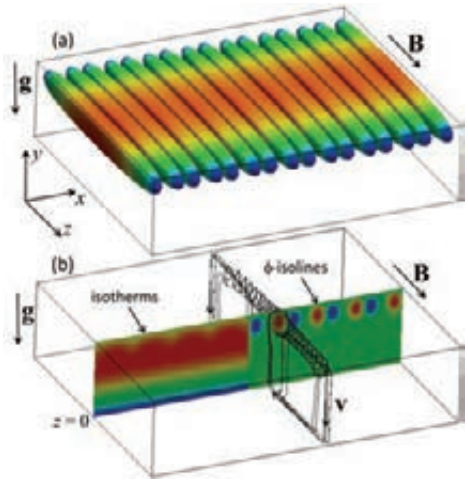

Fig. 2: Flow at *Ha* = 2000 and Gr = 2.2 10^7. (a) Isosurfaces of electric potential, colored by temperature, to visualize convective rolls. (b) 3D velocity streamlines drawn in black. Temperature (left) and potential (right) on the plane $z = 0$.

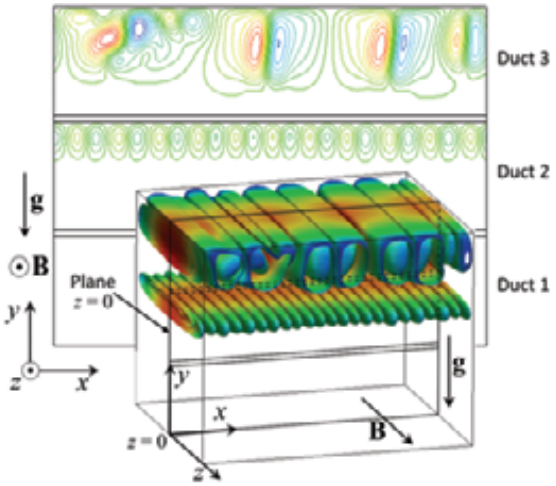

Fig. 3: Isolines and isosurfaces of electric potential for *Ha* = 2000 and *Gr* = 2.2 10^7 in three coupled channels. The flow in the lowest duct 1 is still stable.

In multiple electrically and thermally coupled ducts a significant temperature difference between horizontal stiffening plates (SP) is observed. Instabilities start as periodic rolls along the upper SP. The flow in the other two ducts is stable and 2D in *yz* planes. For larger heat sources the convective pattern is complex as visualized by potential isosurfaces in Fig. 3. In the upper duct there are large structures, while in the middle channel smaller convective rolls develop. By further increasing *Gr* temperature perturbations extend to the lowest duct. Further studies are required to quantify the temperature difference between stiffening plates and to clearly predict stability conditions of 3D MHD-buoyant flows under ITER operating conditions.

Applications of the developed code have been published and presented by the MHD group at IKET in references [1] – [5].

Staff:

L. Bühler
H. -J. Brinkmann
V. Chowdhury
S. Ehrhard
C. Mistrangelo

Literature:

[1] L. Bühler and C. Mistrangelo; Magnetohydrodynamic flows in breeder units of a HCLL blanket with spatially varying magnetic fields. Fusion Engineering and Design, under review.

[2] L. Bühler and C. Mistrangelo; Influence of a spatially varying magnetic field on liquid metal flows in in the European concept of a test blanket. Magnetohydrodynamics, 48(1), 169–176, 2012.

[3] C. Mistrangelo and L. Bühler; Magneto-convective flows in electrically and thermally coupled channels. Fusion Engineering and Design, under review.

[4] C. Mistrangelo and L. Bühler; Numerical study of fundamental magneto-convection phenomena in electrically conducting ducts. IEEE Transactions on Plasma Science, Vol. 40(3), 584-589, 2012.

[5] C. Mistrangelo and L. Bühler; Buoyancy-driven MHD flows in electrically and thermally coupled ducts. European GDR Dynamo & MHD Days, 1st - 4th October 2012, Nice.

[6] C. Mistrangelo and L. Bühler; Development of a numerical tool to simulate magnetohydrodynamic interactions of liquid metals with strong applied magnetic fields. Fusion Science and Technology, 60(2):798-803, 2011.

Acknowledgement

This work, supported by the European Communities under the contract of Association between EURATOM and Karlsruhe Institute of Technology, was carried out within the framework of the European Fusion Development Agreement. The views and opinions expressed herein do not necessarily reflect those of the European Commission.

Divertor

Identification of Alternative He-cooled Divertor Concepts (WP12-DAS-02-T06-01)

The He-cooled reference design uses W-1wt% La_2O_3 (WL10) as material for the thimble, which has a structural function. The operating temperature window for this material is dictated at the lower boundary by the Ductile to Brittle Transition temperature and the upper temperature by the Recrystallization temperature being assumed between 600 °C and 1300 °C, respectively. The dilemma of the divertor design is, however, that irradiated material data for the used tungsten and tungsten-based materials are unknown. The recommendation of the material specialists for the lower operating temperature window of the refractory metals are based on conservative estimates under expectations of large increase in hardening at low neutron irradiation temperatures < 0.3·Tm. This seemingly makes the design problematic, and even critical.

The goal of this task is given by the desire to find a way for an extension of the DBTT limit downwards, while still meeting the design requirements. For this reason the tantalum-base alloy T-111 (Ta-8%W-2%Hf) is being investigated as an alternative to WL10 as thimble material, not least because of its many excellent qualities, among others, an extremely low DBTT of -196 °C. The result of the study showed that the T-111 material chosen may satisfy the requirements, when working at a coolant temperature of between 350 °C and 450 °C. As shown in Figure 1, the calculated maximum stress in T-111 thimble in a case with $T_{He,\ in}$ = 350 °C, mfr = 6.8 g/s, p_{He} = 10 MPa, and $q_{max,\ PPPT\ DEMO\text{-}1}$ = 8.7 MW/m2, amounts to 368 MPa at 949 °C, which remains well below the acceptable value of approximately 423 MPa. This solution even offers the advantage that the use of ODS type of Eurofer is dispensable.

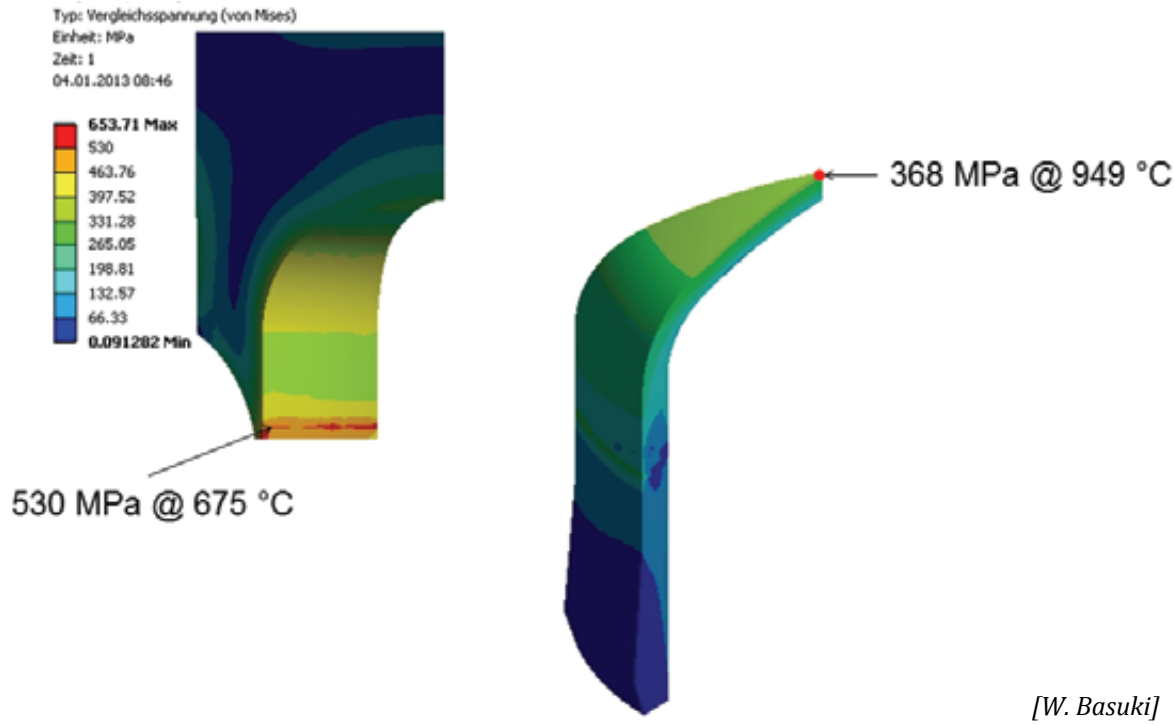

Fig. 1: ANSYS stress calculations for a study case with T-111 thimble at a reduced He temperature of 350 °C, 10 MPa, and 6.8 g/s, under maximum surface heat load (PPPT DEMO-1) of 8.7 MW/m^2.

Staff:

W. Basuki
P. Norajitra
L. Spatafora

Acknowledgement

This work, supported by the European Communities under the contract of Association between EURATOM and Karlsruhe Institute of Technology, was carried out within the framework of the European Fusion Development Agreement. The views and opinions expressed herein do not necessarily reflect those of the European Commission.

Hexagonal Finger - Divertor Integration Study (WP12-DAS-02-T05-02)

A modular He-cooled divertor concept for DEMO has been developed at KIT under the EU PPCS with the goal of reaching 10 MW/m^2. The reference design is based on the use of small tungsten-based cooling fingers. The status of design development has been reported in detail. Subject of this task is to investigate the integration of the 9-finger modules to an entire target plate (TP) including the design of a collector and distributor system for helium as well as the attachment of the TP to the divertor cassette backbone structure. The results of the present study show that the integration of the nine-finger modules (Figure 1) to a target plate is possible, despite the relatively inflexible hexagonal tiles geometry and the large number of more than 400 9-finger modules per TP. A sophisticated system for optimum cooling of the entire plate using hydrant principle with multi-stage ring channel system and multi-level helium coolant routing was designed. Further investigation with respect to a shading of the TP edges to prevent damage to edges by the incident particles have shown that even a minimal inclination of the TP of far less than 1° is sufficient, despite the additional gaps created by the hexagonal tile shape. A load-suitable and function-oriented suspension system for the TP has been developed which is based on the principle of a double-crank mechanism. In this context, special consideration was given that the helium inlet and outlet lines are largely protected against any relative displacement and deformation of the components. Outstanding issues that need further investigation are:

- Thermal-hydraulic analysis of the entire cooling system in the TP, including throttling of the flow rates of the cooling zones.
- Thermo-mechanical analysis of the entire TP structure, including the TP attachment.
- Simplification of the integration through the use of simpler square tile form, which, however, must first be checked thermo-hydraulically and thermo-mechanically.
- The choice of material, investigation of the strength and the life of the bearings.
- Technological study on manufacturing the entire plate.

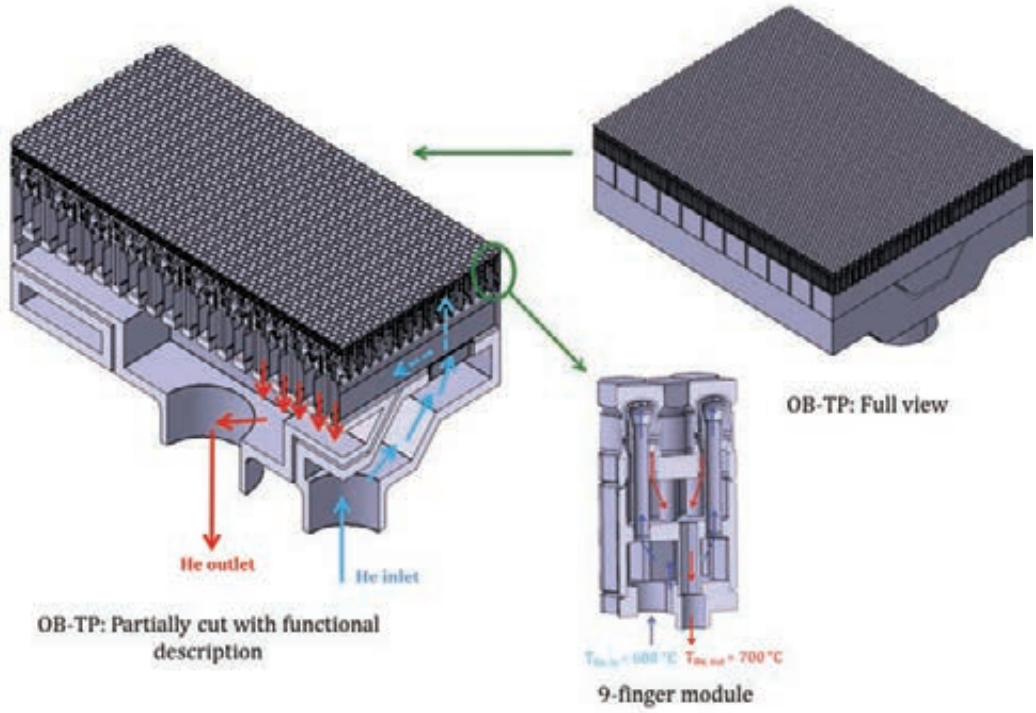

Fig. 1: Full view and partially cut of an OB-TP with functional description.

Staff:

P. Norajitra
L. Spatafora

Acknowledgement

This work, supported by the European Communities under the contract of Association between EURATOM and Karlsruhe Institute of Technology, was carried out within the framework of the European Fusion Development Agreement. The views and opinions expressed herein do not necessarily reflect those of the European Commission.

Prototype Cooling Structures: 9-Finger Module Production for the NDE and HHF Tests (WP12-MAT-01-HHFM-05-02)

Since the development of the 1-finger module has progressed so far, the work is mainly focused on the production of larger units, starting with the tungsten 9-finger modules. Figure 1 shows the successfully fabricated 9-finger modules in versions with brass fingers (far right) and tungsten fingers (middle). The former is intended for NDE testing. The use of brass, which has a similar thermal conductivity as that of the tungsten, facilitates the mechanical generation of artificial defects for NDE studies. The production and assembly technology for such 9-finger modules of tungsten is described in detail in [1]. Two manufactured 9-finger modules, which are equipped with tungsten cooling fingers, are planned for the HHF tests in Efremov and KIT-HELOKA facility, respectively.

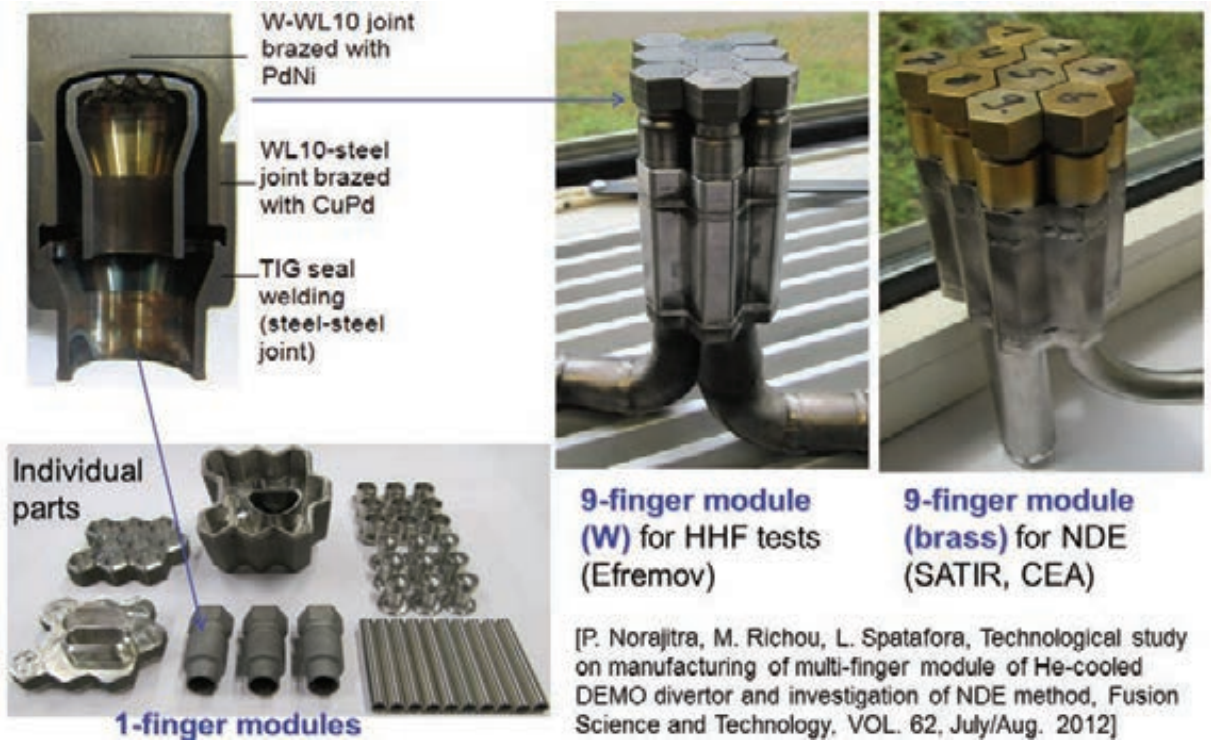

Fig. 1: HEMJ – Finger modules manufactured at KIT.

Non-destructive experiments

First non-destructive testing experiments on a 9-finger module made of brass were successfully performed at the SATIR facility, CEA, using the same method as for the ITER divertor tests. It is based on the detection of a time delay of the surface temperature evolution measured by IR thermography during a fast decrease of the water temperature flowing though the mock-up. The result shows that the method is promising and applicable for testing He-cooled modules.

HHF tests on multi-finger modules

A tungsten 9-finger module was passed to Efremov for HHF tests. The experiments will start in mid-2013.

Staff:

P. Norajitra
L. Spatafora

Literature:

[1] P. Norajitra, M. Richou, L. Spatafora, Technological study on manufacturing of multi-finger module of He-cooled DEMO divertor and investigation of NDE method, Fusion Science and Technology, VOL. 62, July/Aug. 2012.

Acknowledgement

This work, supported by the European Communities under the contract of Association between EURATOM and Karlsruhe Institute of Technology, was carried out within the framework of the European Fusion Development Agreement. The views and opinions expressed herein do not necessarily reflect those of the European Commission

Structural Materials – Steels

Handling and Storage Services for the EUROFER-97-HEAT 3 Semi Finished Products (F4E-OPE-412)

This task includes the documentation of the storage and handling of the boxes of EUROFER-97#3 semi-finished products in KIT, intended to be used for F4E-OPE-305. In 2012 a series of draft reports has been issued to F4E documenting the first opening of the EUROFER storage boxes, the material inventory and the packing of the different lots of material for transport to the fabrication locations.

Inventory report of EUROFER-97#3 semi-finished products at the time of first access

- Documentation of the opening of the sealed wooden boxes presently stored at KIT premises.
- “One by one” extraction of the semi-finished products and Identification of EUROFER-97#3 semi-finished products.
- Dimensional measurement/comparison with list of manufacturers list including visual inspection of each semi-finished product in order to detect any flaw or scratch.
- Inventory checkout of the content of the boxes at the time of first access.
- Check of relevancy/matching of boxes content with the original manufacturer’s identification.
- Material certificate (provided by manufacturer in a separate accompanying documentation).

Inventory report of EUROFER-97#3 semi-finished products leftover

- This document summarizes the inventory report of EUROFER-97#3 semi-finished products leftover.

Materials Checkout Note signed by the supplier and ATMOSTAT/F4E:

- Identify and extract one by one the required plates for LOT_A.
- Check together with ATMOSTAT/CEA personnel the items of the checklist given in Appendix D.
- Pack all the required plates for LOT_A as specified by F4E.

Materials Checkout Note signed by the supplier and KIT/F4E.

- Identify and extract one by one the required plates for LOT_B.
- Check together with KIT personnel the items of the checklist given in Appendix D.
- Pack all the required plates for LOT_B as specified in [R3.5].
- If necessary, load the box containing LOT_B in the truck of the carrier designated by KIT.
- Procedure for handling of Plates.

Fig. 1: Vacuum lifter gripping of 50mm plate EUROFER.

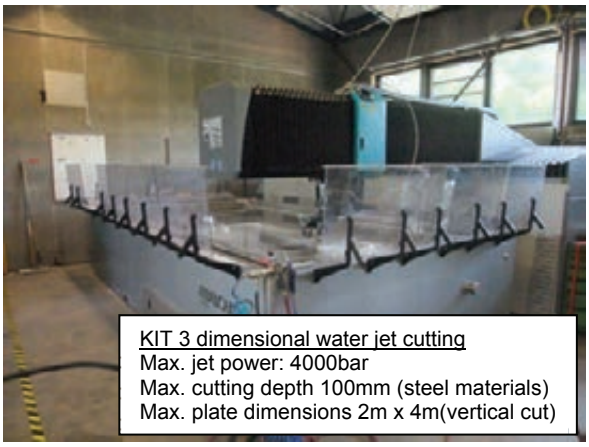

Fig. 2: KIT water jet cutting machine (installed August 2012).

Fig. 3: Cut of 50mm EUROFER steel plate.

Fig. 4: Precision water cut of >F4E< Logo with 50mm P92 heat-resisting steel material.

Staff:

P. Brecht
St. Fischer
P. Freiner
K. Gross
M. Heilig
F. Hohmann
S. Linke
H. Neuberger
J. Rey
A. von der Weth

Acknowledgement

This work was supported by Fusion for Energy under the service contract No. F4E-OPE-412. The views and opinions expressed herein reflect only the author's views. Fusion for Energy is not liable for any use that may be made of the information contained therein.

Production and Characterization of Laboratory-scale Batches of Nano-structured ODS Ferritic Steels (WP12-MAT-01-ODSFS-01-01)

Introduction

Future generation reactor concepts are based on materials that can withstand higher temperatures and higher neutron doses in corrosive environments. 9 to 14 wt.% oxide dispersion strengthened (ODS) steels – produced by mechanical alloying - are typical candidate materials for future structural materials in fusion and fission power plants due to their excellent high temperature strength and good corrosion resistance. Only materials with excellent properties in terms of swelling and irradiation resistance as well as excellent mechanical properties are likely to meet these requirements.

Yttrium has proven to be an excellent addition to ferritic steels to form nano-sized dispersion oxide particles inside the material. However, there might be potential for improvements by choosing different oxides. One of the main causes for choosing yttrium as dispersion oxide is the high thermal stability and low diffusion speed in an iron chromium matrix. Alternative oxides need to have similar properties.

In this work different variations of ODS alloys were produced by milling pre-alloyd gas-atomized steel powder of the composition Fe13Cr1W0.3Ti by mixing the powder with different oxide powders and milling in an attritor ball mill for several hours. The powders were consolidated by hot-isostatic-pressing followed by an additional thermo-mechanical treatment (hot-rolling). Thermo-mechanical treatment of ODS alloys is essential for the reduction of the porosity and homogenization of the microstructure [1].

Materials and Methods

Four different alternative oxides where chosen by looking at their Gibbs-Free-Enthalpy (GFE) and comparing it to the one of yttrium oxide. The GFE over temperature for various oxides and nitrides is shown in Fig. 1. According to this data, Ceria (Ce_2O_3), Lanthana (La_2O_3), Magnesia (MgO) and Zirconia (ZrO_2) have sufficient thermal stability at the desired operating temperatures and were included as promising candidates. An overview of the produced alloys is given in Table 1.

Table 1: Materials, fabrication details and experiments performed/planned

Material	Milling-time	Process	Experiments performed / planned
Fe13Cr1W0.3Ti + Y_2O_3	80h	MA+HIP+HR	Charpy, tensile, TEM characterization, ,EBSD
Fe13Cr1W0.3Ti + La_2O_3	80h	MA+HIP+HR	Charpy, tensile, TEM characterization,
Fe13Cr1W0.3Ti + Ce_2O_3	80h	MA+HIP+HR	Charpy, tensile, TEM characterization,
Fe13Cr1W0.3Ti + ZrO_2	80h	MA+HIP+HR	Charpy, tensile, TEM characterization,
Fe13Cr1W0.3Ti + MgO	80h	MA+HIP+HR	Charpy, tensile, TEM characterization,

Steel powder of the composition Fe13Cr1W0.3Ti was gas-atomized at NANOVAL GmbH & Co. KG and then mixed with the different oxide powders. The final composition (Fe13Cr1W0.3Ti+0.3 M_xO_y) was mechanically alloyed (MA) in a attritor ball mill at 1200/800 rpm for 80 h. The optimized milling-time has already been determined in earlier works by

Hoffmann et al. [3]. All processing after MA was done in argon inert gas atmosphere without exposing the powders to air. Following, the material was put into steel cans and HIPped for 2 h at 1150°C with an applied pressure of 100 MPa. After HIPing, the cans were hot-rolled (HR) at 1100°C from a diameter of 40 mm to 6 mm thickness in 5 passes with reheating after each pass at TU Clausthal.

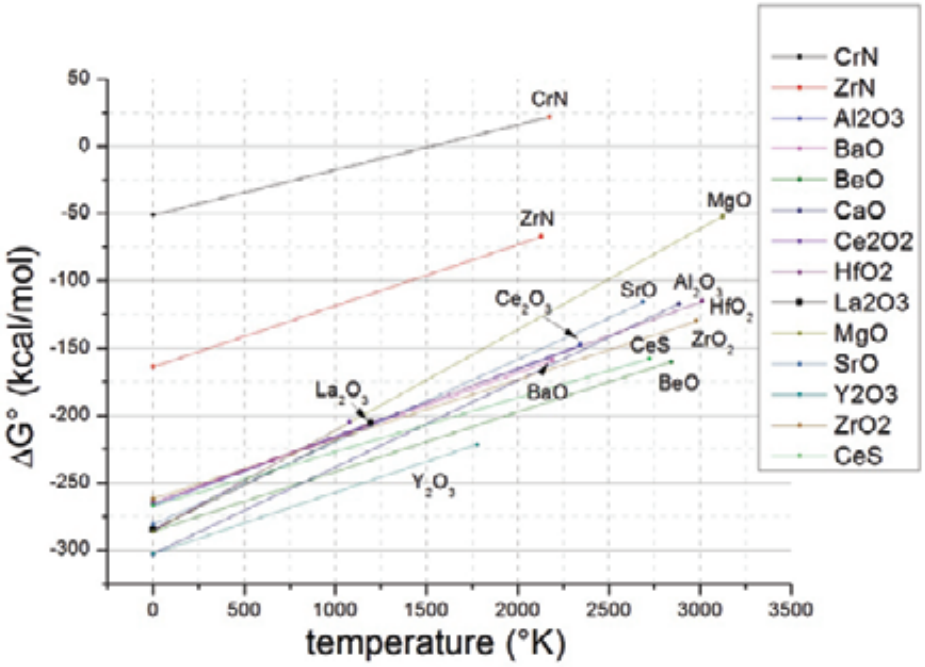

Fig. 1: Gibbs-Free-Enthalpy of various oxides and nitrides [2].

All specimens for mechanical testing and characterization were cut by electro-discharge-machining (EDM) in the rolling-direction (L-T). Microstructural characterizations were done using a FEI Tecnai F20 transmission electron microscope (TEM) and a high-angle annular dark field (HAADF) detector combined with an energy dispersive X-ray spectometer (EDX) to determine the chemical composition. Charpy-impact tests were done on KLST specimens and mini-LCF specimens were used for tensile-testing.

Electron backscatter diffraction mappings were performed using a JEOL-6500F field emission gun scanning electron microscope (FEG-SEM) operating at 15 kV with a step size of 80 nm. Samples were measured in the T-S orientation in the rolling direction. Texture analysis was conducted by automated acquisition and further indexing of Kikuchi patterns after image processing in a TSL system interfaced to the SEM [4].

Results

Mechanical tests

The different ODS alloys show major differences in the mechanical tests. Brittle behavior of ODS alloys in terms of charpy impact-tests strongly depend on the morphology of the nano-sized oxide particles. Micro-meter sized particles at the grain boundaries may produce the brittle behavior of some alloys (e.g. ZrO_2). Also, it is clearly visible when comparing Y_2O_3-alloys in as-hipped and as-rolled condition, that thermo-mechanical treatment is essential for ODS alloys. Fig. 2 shows the results of the Charpy impact tests

Alloys containing ZrO_2 have poor properties in terms of impact-energy compared to other ODS alloys. Figs. 3, 4 and 5 show the vast differences between the alloys. 100% brittle fracture did not occur even at -100°C with MgO, whereas ZrO_2 has no ductile fracture at the in-

vestigated temperature range (-100°C to 400°C) and performed in the same order of magnitude as the as-HIPped material.

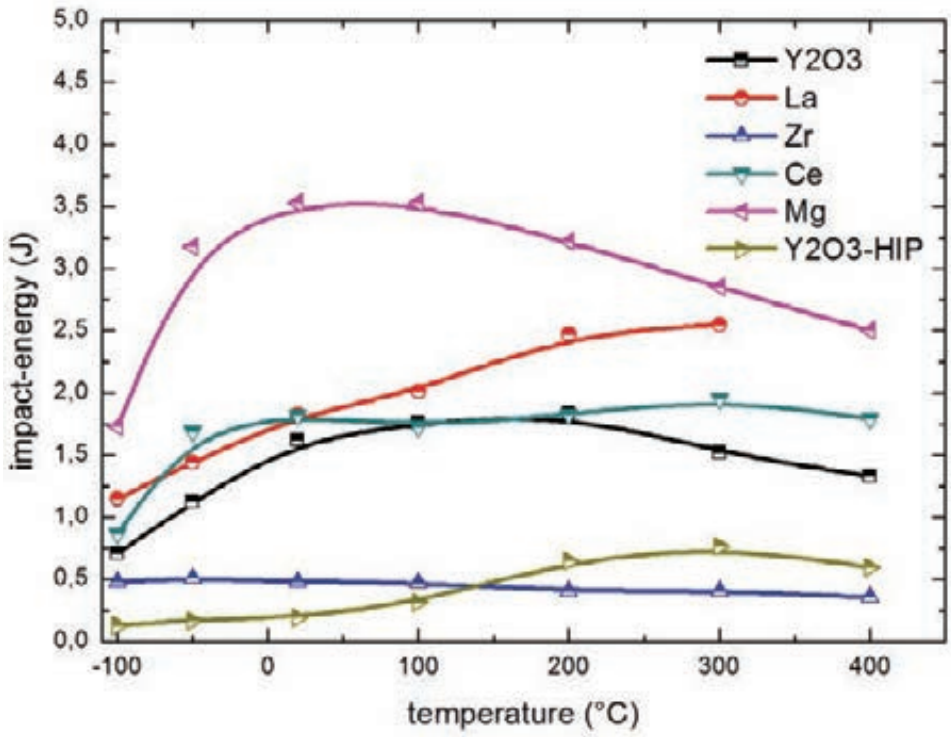

Fig. 2: Results of charpy-impact test at different temperatures.

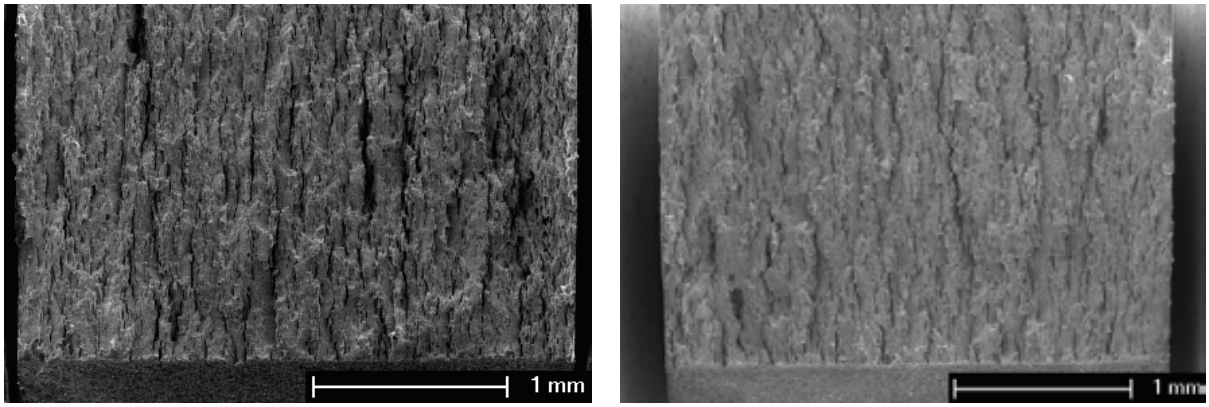

Fig 3: KLST (ZrO_2) sample after charpy-impact-test at room-temperature and 300°C.

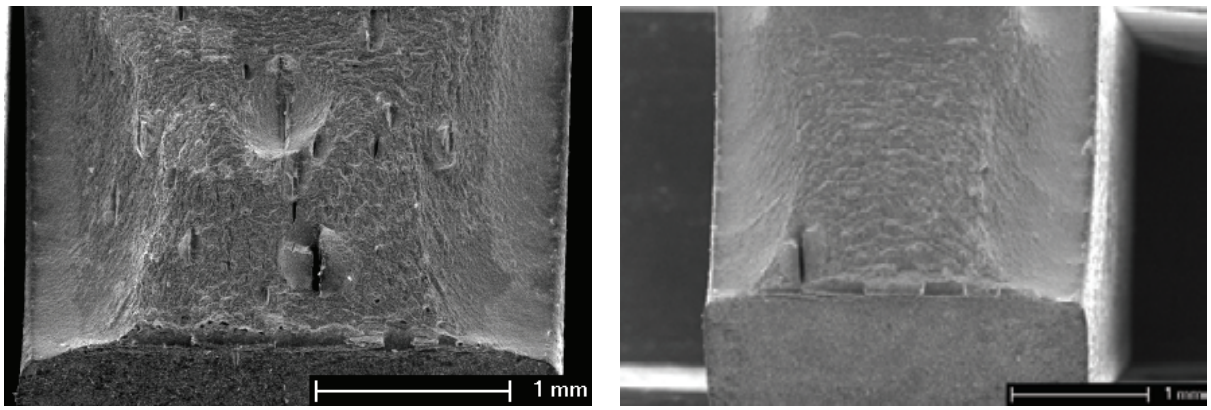

Fig 4: KLST (MgO) sample after charpy-impact-test at room-temperature and 300°C.

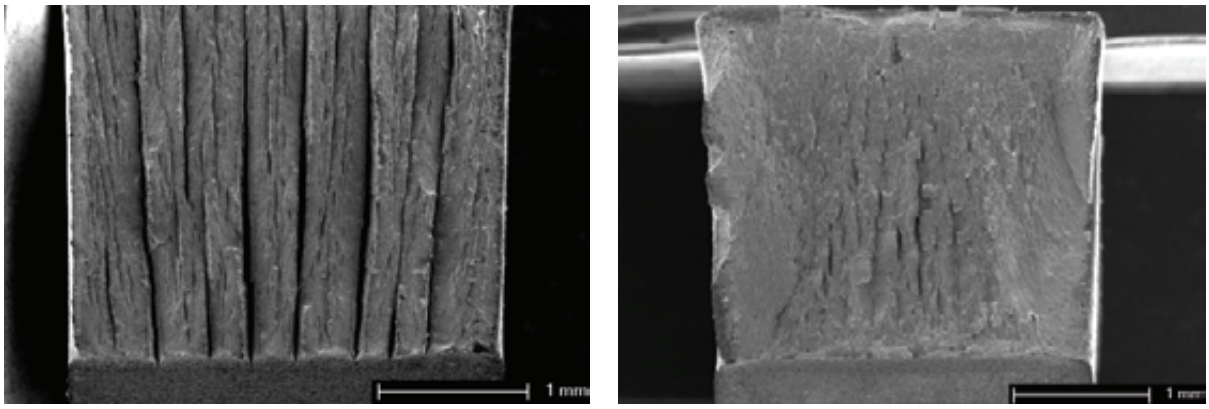

Fig 5: KLST (Y_2O_3) sample after charpy-impact-test at room-temperature and 300°C.

In opposite to the charpy-impact properties, minor differences were observed in the general behavior of the alloys during tensile tests. Fig. 6 shows the results of the ultimate tensile strength (UTS) over temperature. It can be clearly seen, that yttrium-alloys have the best tensile properties. There is a difference of up to 200 MPa between the weakest alloy (MgO) and yttrium-based material. All the other materials have an ultimate tensile strength between MgO and Y_2O_3-alloys.

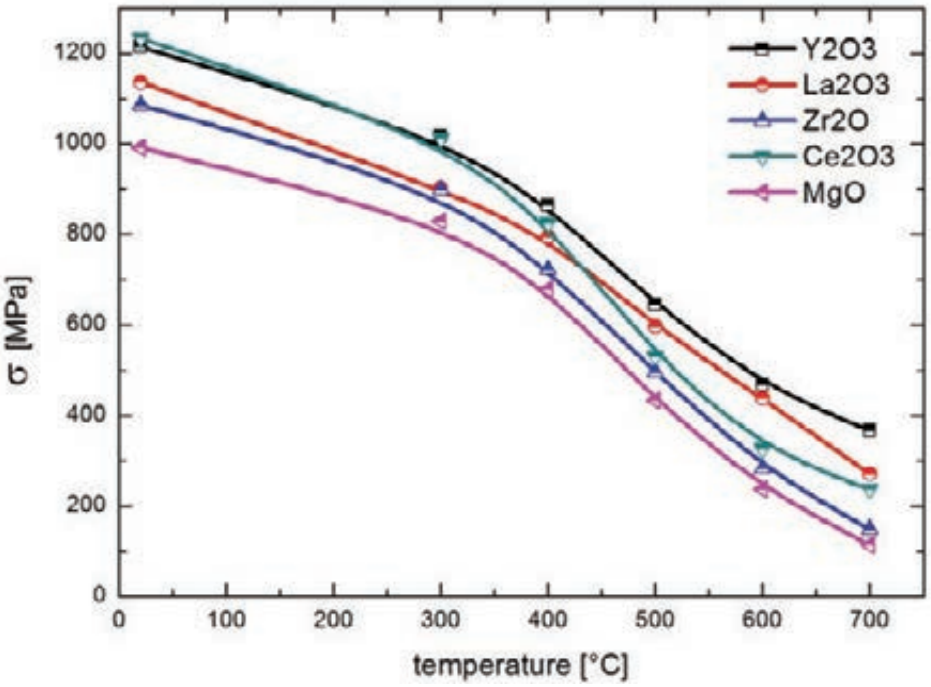

Fig. 6: Ultimate tensile strength of different alloys.

Microstructural characterization

The TEM images of the microstructure show a clearly visible rolling-texture. Micrometers-long lamellar grains with some hundred nano-meters thickness can be seen. A fine distribution of La_2O_3-ODS particles could be achieved (Fig. 7). Both dark-field and bright-field were used to show the presence and distribution of the particles.

The Ce_2O_3-added alloys also show a similar texture in the TEM-images with oxide particles clearly visible (Fig. 8). The distribution of the oxide particles inside the grains and on the grain boundaries could be observed in all the images (Figs. 7 + 8).

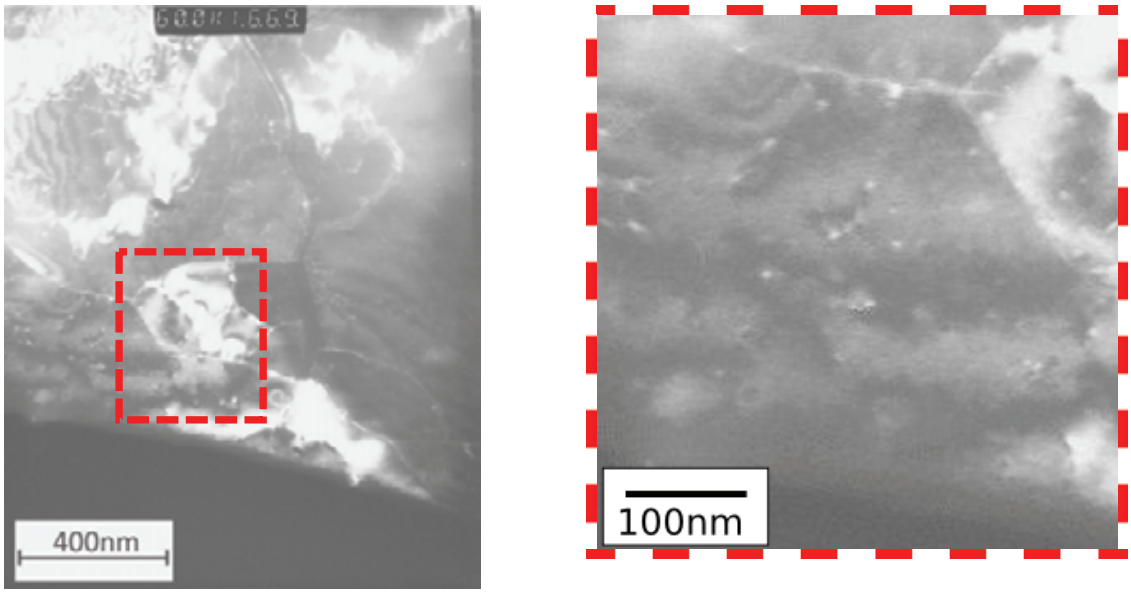

Fig. 7: TEM DF image and enlarged area with oxide particles of La_2O_3-added alloy.

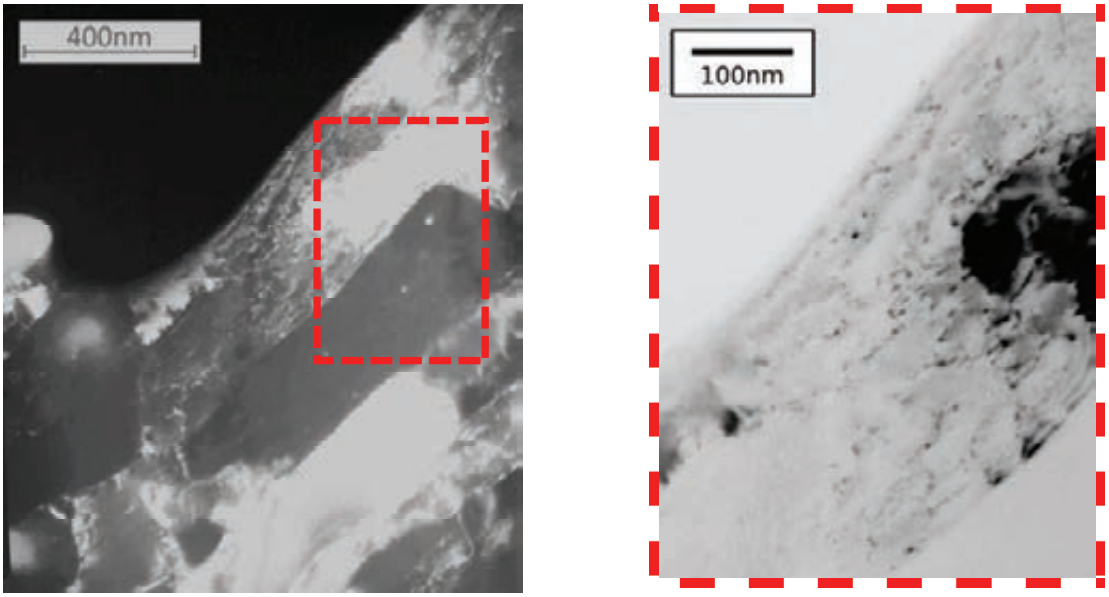

Fig. 8: TEM DF and enlarged BF image of Ce_2O_3-added alloy.

The results of the EBSD-mappings (Fig. 9) show a partially recrystallized microstructure in the hot-rolled condition. Areas containing clusters of fine recrystallized grains with sizes in the nano-meter range and coarser elongated grains are noticeable in the microstructure. The grain size distribution is shown in Fig. 10 where all points with a misorientation greater than 2° are considered different grains. This is due to an intrinsic limitation of the technique.

Summary

Mechanical tests show, that all of the selected oxides are potential candidates to produce oxide dispersion strengthening ferritic steels. Some alloys (MgO, Ce_2O_3) even performed better than the reference material in terms of Charpy impact tests. Regarding the tensile behavior, Y_2O_3-added alloys display the best performance among all the investigated materials. This is due to the excellent high-temperature stability and more uniform size distribution of the oxide particles. Further, detailed TEM examinations of the different oxide particles which formed after HIPing are likely going to explain the differences in in the tensile properties.

EBSD scans are an essential technique for full a characterization of the microstructure. The examined material (Y_2O_3-added ferritic-ODS) shows a strong texture after hot rolling with a predominance of α-fiber grains. In the hot-rolled condition, the microstructure is not uniform and displays partial recrystallization.

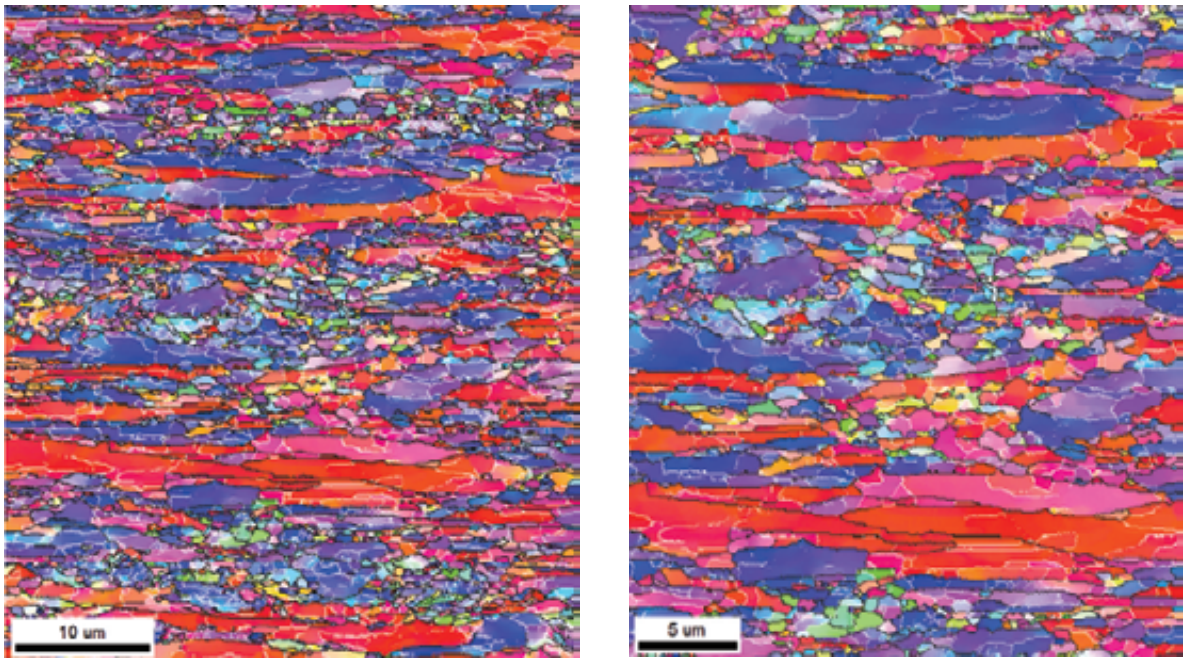

Fig. 9: EBSD-map of Y_2O_3-added alloy.

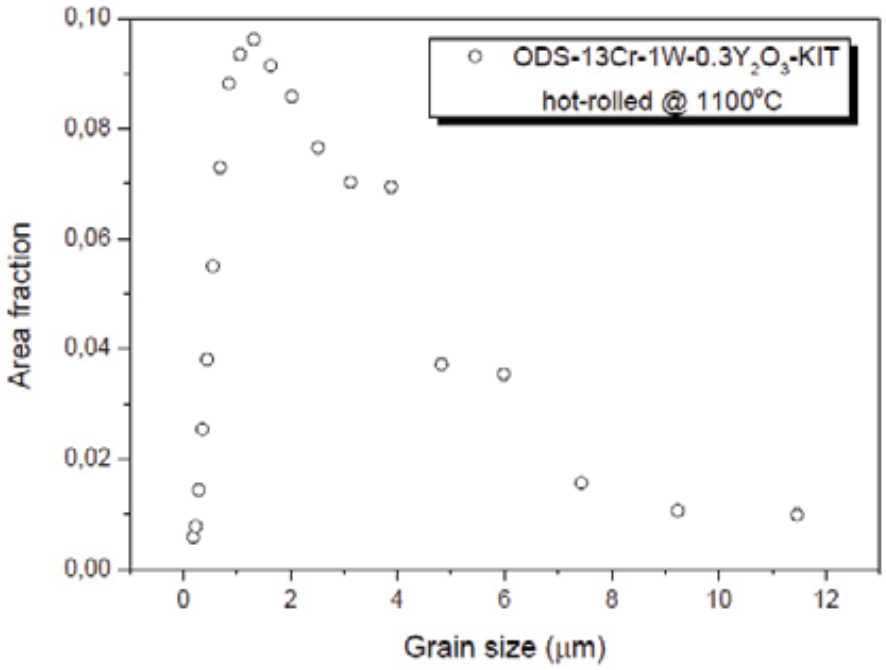

Fig. 10: Grain-size-distribution of Y_2O_3-added alloy.

The present results show that stable oxides other than Y_2O_3 are able to form fine ODS-particles in ferritic steels.

However, future work is needed to determine the optimal processing conditions to obtain a rather uniform microstructure. The approach of choosing different oxides is very promising in terms of material costs (minimizing the need for rare-earth metals) and the design of low-

activation-materials for fission and fusion applications since MgO, for instance, has very low activation under neutron irradiation.

Staff

S. Baumgärtner
L. Commin
B. Dafferner
S. Heger
J. Hoffmann
U. Jäntsch
M. Klimenkov
R. Lindau
A. Möslang
J. Reiser
M. Rieth
V. Widak
R. Ziegler
H. Zimmermann

Literature:

[1] Z. Oksiuta , P. Mueller, P. Spätig, N. Baluc, Effect of thermo-mechanical treatments on the microstructure and mechanical properties of an ODS ferritic steel, Journal of Nuclear Materials, 412 (2011)

[2] T.B. Reed, Free Energy formation of Binary Compounds, The MIT Press Cambridge, Massachusetts and London, England, 1971.

[3] J. Hoffmann, M. Klimenkov, R. Lindau, M. Rieth, TEM study of mechanically alloyed ODS steel powder, Journal of Nuclear Materials, (2011).

[4] C.C. Eiselt, M. Klimenkov, R. Lindau, A. Möslang, H.R.Z. Sandim, A.F. Padilha, D. Raabe, High-resolution transmission electron microscopy and electron backscatter diffraction in nanoscaled ferritic and ferritic–martensitic oxide dispersion strengthened–steels, Journal of Nuclear Materials, 385 (2009) 231-235.

[5] J. Hoffmann J., Klimenkov M., Lindau R., Rieth M., *TEM study of mechanically alloyed ODS steel powder*, Journal of Nuclear Materials (2012), DOI: 10.1016/j.nucmat.2011.09.034

[6] Hoffmann, J.; Rieth, M.; Lindau, R.; Klimenkov, M.; Möslang, A.; Armstrong, D.;Britton, B. *Current status of the KIT ODS steel development programme*, KIT-CCFE Divertor Technology Workshop, May 29, 2012 Culham, UK,

[7] Hoffmann, J.; Armstrong, D.E.J.; Britton, B.E.; Rieth, M. *Recrystallization of ODS alloys*, ODS Alloys for Nuclear Applications Workshop, September 24-26, 2012, Oxford, UK,

[8] Hoffmann, J.; Rieth, M.; Lindau, R.; Klimenkov, M.; Möslang, A.; Zschommler Sandim, H.R .*Investigation on different oxides as candidates for nano-sized ODS particles inreduced-activation ferritic (RAF) steels,* 2nd Joint IAEA - EC Topical Meeting on Development of New Structural Materials for Advanced Fission and Fusion Reactor Systems, April 16-20, 2012, Ispra, I,

[9] Hoffmann, J. *Investigation on different oxides as candidates for nano-sized ODS particles in reduced-activation ferritic (RAF) steels*. Ajou-KIT-Kyoto University Joint International Symp., January 31 - February 1, 2012, Kyoto, J,

Acknowledgement

This work, supported by the European Communities under the contract of Association between EURATOM and Karlsruhe Institute of Technology, was carried out within the framework of the European Fusion Development Agreement. The views and opinions expressed herein do not necessarily reflect those of the European Commission.

Nano-structured ODS Ferritic Steels Development
Production and Characterization of Industrial Batches of Nano-structured ODSFS (WP12-MAT-01-ODSFS-02-01 + WP12-MAT-01-ODSFS-02-02)

Abstract

This activity is focused on the fabrication of ODS FS using semi-industrial or industrial scale-methods. Therefore, the goal of this line of work is to probe the feasibility of production of ODSFS in large batches around 5-15 kg.

In the large scale production of 5kg slabs of an ODS steel unexpectedly cracks occurred during hot rolling. Metallographical examinations and chemical analyses were performed to identify the possible reasons for cracking. It was shown that high porosity can be regarded as main reason for this failure. Chemical analyses of materials from the different production steps supported the assumption that leaking of the HIP containers during the consolidation process was the most likely reason.

Basing on the results of preceding work a chemical composition for the large scale production was determined. Mechanically alloyed powder to produce a 5-10kg batch is now available.

Introduction

The developmental work on nano-structured ODS steels in Europe is carried out at universities and research centres at laboratory scale, i.e. small batches of a few grams to about 200 grams. The presently identified applications in future nuclear fusion reactors require instead amounts of material that are orders of magnitude larger and need therefore an industrial-scale fabrication. Among others, the transferability of the results gained in lab-scale to industrial scale production has also to be proven. Unfortunately a cooperation of a research centre with a single industrial partner as it was the case in the past in the ODS-Eurofer development performed by KIT (formerly FZK) with PLANSEE is no longer possible due to the decision of PLANSEE to give up the ODS production.

This very fruitful cooperation lead in several developmental steps to a reduced activation ferritic martensitic 9Cr ODS-steel with acceptable mechanical properties that allow to increase the operational temperature compared to the non-ODS Eurofer 97 steel by about 100°C to 650-700°C making the material suitable for application in the blanket and divertor of a DEMO-type reactor.

Due to the α-γ phase transformation in these steels, the application temperature of this ODS-steel is limited to temperatures of about 800°C. To avoid this drawback the development of ODS ferritic steels (ODSFS) which do not show such a phase transformation is pursued.

To establish a production route in industrial scale it was decided to divide the fabrication process into single steps and to find industrial partners for each production step. In preceding studies each step was analysed in laboratory scale in view of scalability to industrial scale.

This task is strongly interwoven with other tasks in which the influences of composition and production parameters on the properties of ODSFS are investigated.

Objectives

This activity is focused on the fabrication of ODS Ferritic Steels using semi-industrial or industrial scale-methods. Therefore, the goal of this line of work is to probe the feasibility of production of ODSFS in large batches around 5-15 kg.

Following the identification of chemical composition and manufacturing conditions, production of one or several batches and preliminary characterization of the batch(es) in the unirradiated condition have to be carried out.

As reported in the task report of 2011, problems with a large scale test production occurred due to crack formation in the rolling step of 5kg slabs.

It was decided to make further investigations to clarify the reasons. Therefore the cracked slabs were investigated by metallurgical means and chemical analyses were taken from samples of the produced material to find the possible reasons for failure.

From the preliminary production of small 0.2 to 1kg batches it could be deduced, that an alloy containing 2.0 wt-% W has a higher strength and similar ductility than a 1.1 wt.-% W containing alloy. If Ti is added, which should decrease the oxide particle size and increase their spatial distribution, 0.3 wt.-% Ti seems to be the optimum amount. In any case pre-alloyed powder is to be preferred to elemental powder.

Regarding all this, it was decided to order a larger batch of 13.5%Cr-2.0%W-0.3%Ti steel powder. This powder was gas-atomized in Argon and yielded a particle diameter d_{50} of about 40 microns.

The mechanical alloying of this steel powder was performed during the reporting period in cooperation with an industrial partner according to the procedure developed at KIT in the lab scale.

Results

The production route for the production of a large-scale batch of ODSFS was described in earlier reports. It consists of mechanically alloying of gas-atomized steel powder with Yttria in a high-energy ball mill. The consolidation process is done by Hot Isostatic Pressing (HIP).

Fig. 1 shows a comparison of large scale and small scale ODSFS production before and after HIP. The usual production steps following the HIP are hot cross rolling and a final heat treatment.

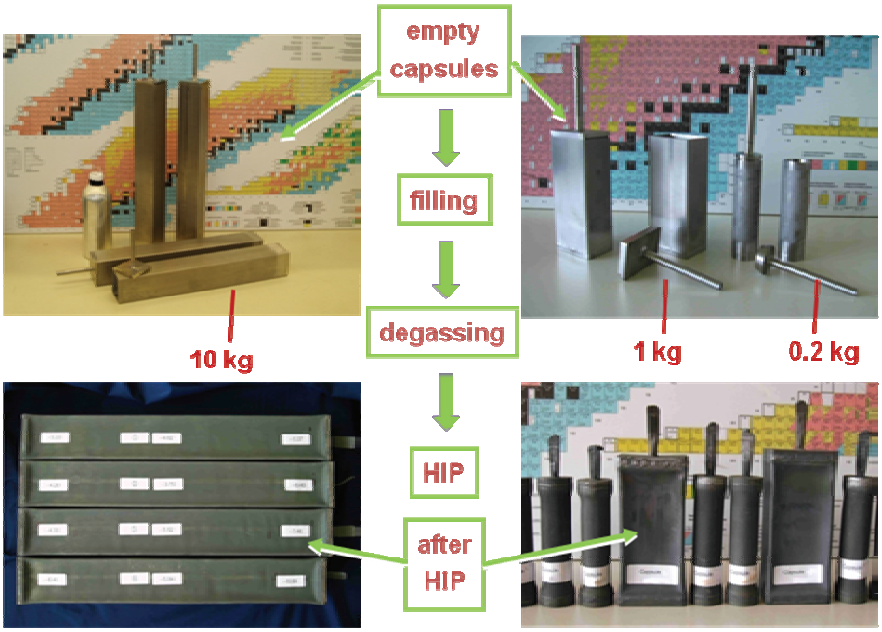

Fig. 1: Comparison of large scale and small scale ODSFS production route until HIP step.

Prior to the hot-rolling the capsules are machined to defined shape and dimensions by milling. For better handling and to allow cross roll in the available rolling mill, the long slabs were cut into 2 pieces. Up to this point no abnormalities were seen in the large scale production compared to earlier small scale (0.2 - 1kg) batches. During the hot rolling of the 5 kg slabs cracks occurred even after little reductions in thickness. After first very small reduction stages, cracks occurred in the slabs. Changes in rolling temperature and rolling speed did not improve the situation. The rolling was stopped and it was decided to first investigate the reasons for the failure. The following Fig. 2 shows the significantly different behaviour during hot-rolling of 1kg and 5kg slabs. While the test rolling of small slabs did not show any cracks during rolling, the 5kg slabs cracked immediately.

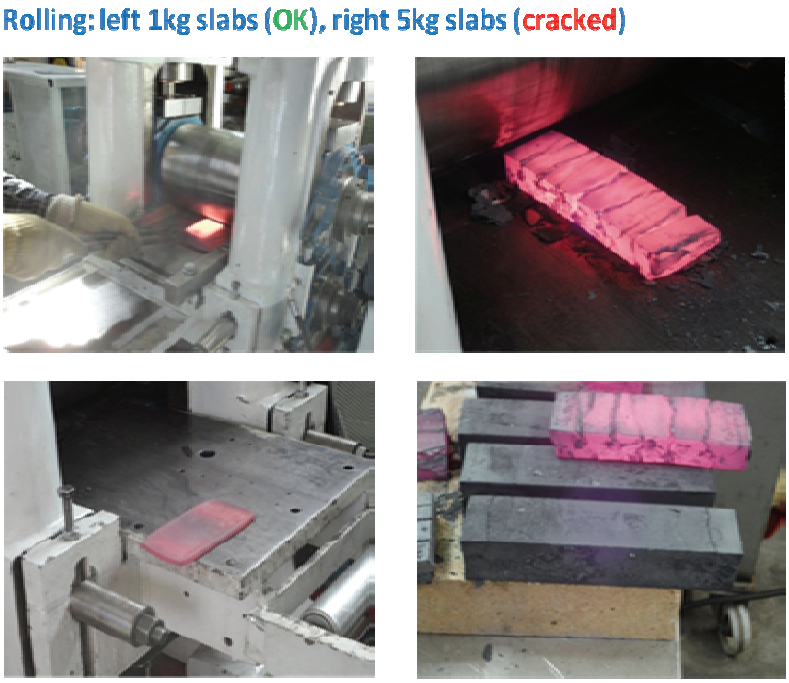

Fig. 2: Comparison of the rolling results of 1kg (left) and 5kg slabs (right).

In order to clarify the possible reasons for the failure, metallographic examinations and chemical analyses were planned and performed. To check the homogeneity over the total length of the HIP capsule, metallographic cuts were made from samples close to the upper and bottom cap, i.e. from the transition region between hipped ODS and stainless steel cap as well as from the respective centre regions. For the chemical analyses little cubes of 3-4 mm edge length were taken from the same regions. Numerous elements were measured applying inductively coupled plasma atomic emission spectroscopy (ICP-AES) and inductively coupled plasma mass spectroscopy (ICP-MS) after dissolution of the steel samples in acids by microwave digestion.

Nevertheless it was expected that the oxygen and perhaps the nitrogen content, which were measured by carrier gas heat extraction (CHE), would contribute most to the elucidation of the failure reasons.

Figure 3 gives the results of the metallographic examinations of bottom and top region of the hipped capsule. The austenitic stainless steel caps of the hip capsules can be easily identified in the upper left and lower right micrograph. Of greatest importance is of course the occurrence of a very high porosity in all pictures. There seems to be also no significant difference in the porosity of top and bottom. This finding is most likely the reason for the low resistance against cracking during the rolling procedure.

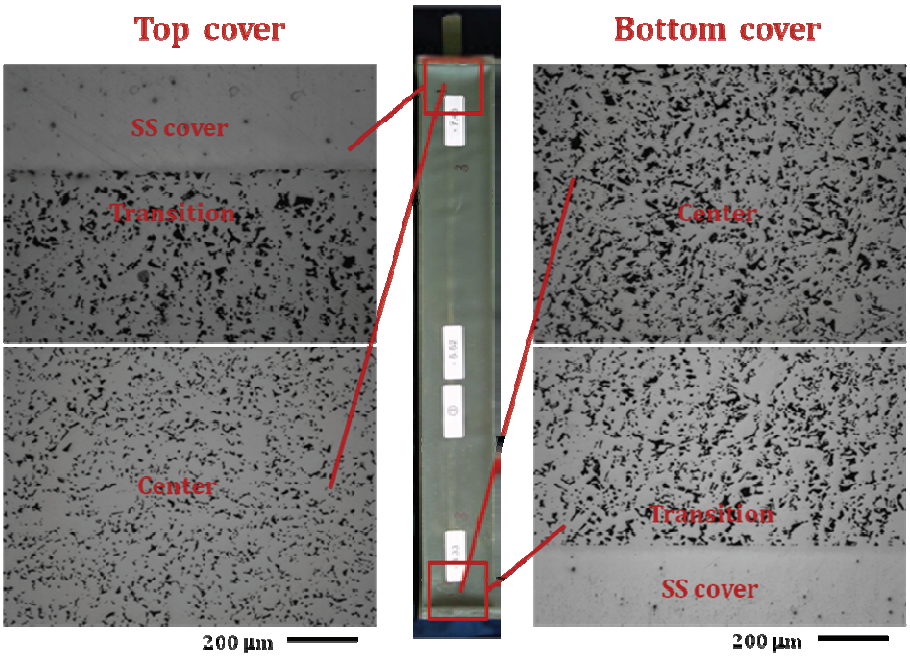

Fig. 3: Metallography of hipped samples.

A piece of the rolled and terribly cracked slab (s. Fig. 2, right) was also cut to perform metallographic examinations and chemical analyses (s. Tab. 1, H3T). A large degree of porosity could also be observed.

According to the findings two possible reasons for the failure can be assumed:

1. The degassing procedure was not perfect and a leak might have occurred during the evacuation, crimping and seal welding of the suction pipe.
2. Cracking of the HIP containers might have occurred during the HIP process.

Both reasons cannot be excluded from the very beginning. Usual deformation of the HIP containers was observed, but no obvious cracking.

The results of the chemical analyses, especially the oxygen content were supposed to give hints on the failure reason.

The steel powder which was used for the above described test production was on the basis of a conventional 9Cr steel (DIN 1.4903) which was available in large amounts. Table 1 gives the oxygen contents of differently treated 9wt.-% Cr steel powders, hipped and rolled ODS steel. Of special importance is the so-called excessive oxygen (exO), i.e. oxygen which is not bound to the Yttria compound $O(Y_2O_3)$. The values for exO can be calculated by subtracting the latter from the total (measured) oxygen content O_{tot}. For the calculation a nominal Yttria content of 0.3 wt.-% was assumed.

The as-received steel powder (C00) contains after gas atomization in argon about 260 ppm of oxygen. When this powder is milled in the CM02 attritor in the usual manner without any addition of Yttria, the total oxygen (O_{tot} = exO) content increase to 945 ppm (C01). Mechanical alloying under the same conditions with nominally 0.3 wt.-% Yttria leads to an increase of the total O content of 1600 ppm and exO of 953 ppm, respectively (C02). That means that both powders C01 and C02 contain the same amount of excessive oxygen.

The large slabs were produced from powder, which was mechanically alloyed by our industrial partner.

The powder C03 has a surprisingly low excessive O-content of about 600 ppm which did not increase significantly in the samples taken from the bottom (H3B) and top (H3T) of the hipped samples. It should be noted that there is a difference between bottom and top of the HIP capsule of 144 ppm O. Hot rolling at 1000-1100°C with pre-warming in a furnace without protecting gas leads to a moderate increase of exO in the same order (H3R).

All these findings support the assumption that the capsules were leaking during the HIP process, presumably not from the beginning, because that would have prevented any densification.

Nevertheless it should be taken note that all oxygen contents are in the usual magnitude and also similar to the measured values of earlier 9-14Cr ODS steels produced at KIT.

Table 1: Evolution of the oxygen content of differently treated 9wt.-% Cr steel powders, hipped and rolled ODS steel.

	Alloy	Y_2O_3 wt.%	O_{tot} wt.%	ΔO_{tot} wt.%	$O(Y_2O_3)$ wt.%	exO wt.%	Remarks
C00	P91 as-rec.	0	0.0260	0	0	0.0260	powder as-received
C01	P91 M	0	0.0945	0.0685	0	0.0945	powder milled
C02	P91Y MA	0.3	0.1590	0.1330	0.0638	0.0953	powder mechanically alloyed
C03	P91ZY MA	0.3	0.1251	0.0991	0.0638	0.0614	powder mechanically alloyed
H3B	P91ZB MA	0.3	0.1217	0.0957	0.0638	0.0580	powder mechanically alloyed HIP
H3T	P91ZT MA	0.3	0.1361	0.1101	0.0638	0.0724	powder mechanically alloyed HIP
H3R	P91ZR MA	0.3	0.1511	0.1251	0.0638	0.0874	powder mechanically alloyed HIP, Roll

Chemical Analyses by Ms. Dr. Ch. Adelhelm and Dr. T. Bergfeldt

In order to avoid such failure in future large scale ODS productions; the capsule design should be optimized to avoid leaking during HIP process. In the frame of WP12-MAT-01-ODSFS-02-02/KIT/PS supporting further experiments have been performed to optimize the fabrication process.

Since the production of 1 kg batches where the biggest amount of ODS alloys was reliably encapsulated, degassed, hipped and hot rolled without problems it was decided to use this size for these studies. Sufficient 9%Cr steel powder (1.4903) and also some MA powder on this basis were available.

Five capsules of 1kg capacity were produced in the usual manner from stainless steel tubes with rectangular cross section (60x40x2 mm). The HIP capsules were filled inside the glove box with mechanically alloyed 9Cr ODS powder. During the filling the capsules were agitated and pressed in order to get a high filling density. The glove box system at the KIT powder metallurgy lab allows to TIG-weld the upper cap with the suction tube onto the filled container under inert gas atmosphere. This procedure should prevent additional oxygen uptake of the MA powder. A ball valve is then being mounted on the suction tube and closed.

The filled capsules can then be removed through the airlock system for degassing in a furnace with a vacuum pump system consisting of rotary and turbo-molecular pumps. The degassing takes usually place at 400-450°C for 2-3 hours.

After the degassing procedure the suction pipe is crimped with a special tool in a hydraulic press. The final seal welding of the crimped pipe is being performed by electron beam welding. This has the advantage that the capsules are under vacuum during welding and no oxygen or other gases can find a way through the melt into the capsule as it could happen with EB-welding in the workshop.

After the seal welding the capsules were shipped to an industrial company which has so far made all the HIP consolidations for KIT in the last years. The HIP pressure was 100 MPa which were applied for 2.5 hours hold time at 1100°C.

After hipping the bottom and cap were cut off. Fig. 4 shows the typical "cushion"-like deformation of the rectangular HIP capsules. A first inspection did not show any abnormalities.

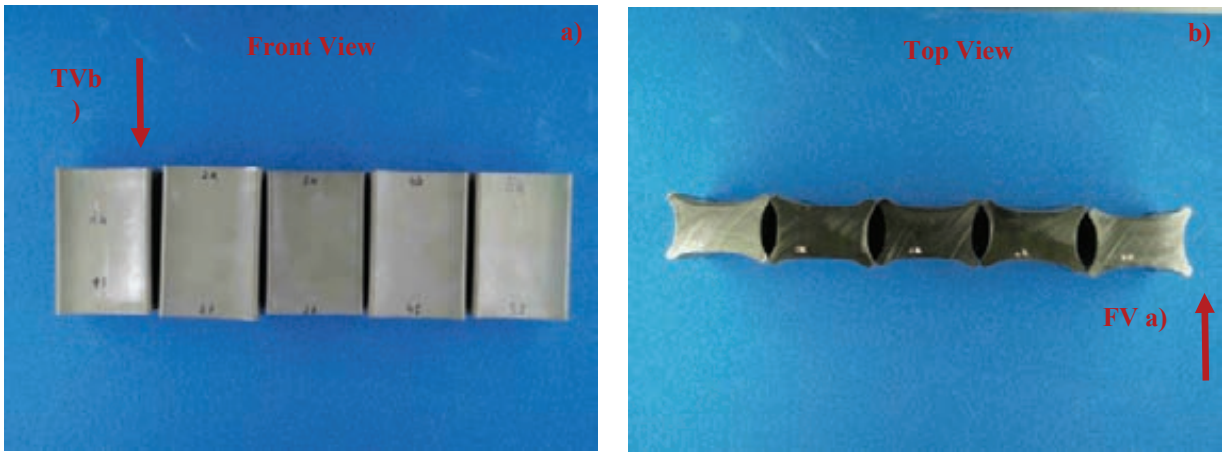

Fig. 4: HIP capsules after hot-isostatic pressing and cutting off bottom and top cap.

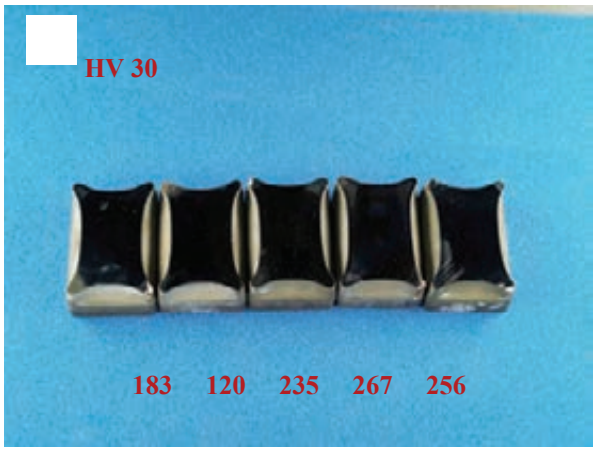

Fig. 5: Vickers hardness measurement on bottom of HIP capsules.

A simple test to check the quality of the HIP is Vickers hardness measurement. The bottom of the capsules was ground and mechanically polished. The values of the Vickers hardness measurements are given in Fig. 5. Obviously two of the bottom pieces show significantly lower hardness values. Since hipped samples have no defined heat treatment after hipping and cooling slowly down, this is normally no reason to worry, since post-HIP heat treatment must be performed anyway to adjust the microstructure.

Slices were cut from the top and bottom of each specimen for metallography and heat treatment trials.

The micrographs in Fig. 6 clearly show non-negligible porosity. Capsule 2 looks very similar. Since a well established production method and a capsule size were used, that did not cause any problems in earlier productions, this behaviour was absolutely unexpected.

A second slice was cut from the bottom of sample 1 to check whether the porosity decreases in longitudinal direction. Unfortunately this was not the case. So it can be assumed that the samples 1 and 2 are fully porous over the whole capsule volume (s. Fig. 6 left).

The examination of the capsules 3, 4, and 5 showed only very few pores. The different appearance is shown in Fig. 6 in the right and left halves in the polished and etched condition. The etched micrographs show the typical microstructure for ferritic martensitic steels. The round white features are presumably unmilled steel particles with a coarser martensitic structure. It should be noted, that the grey spots in 3F are no pores but carbides which can be clearly seen in higher magnification.

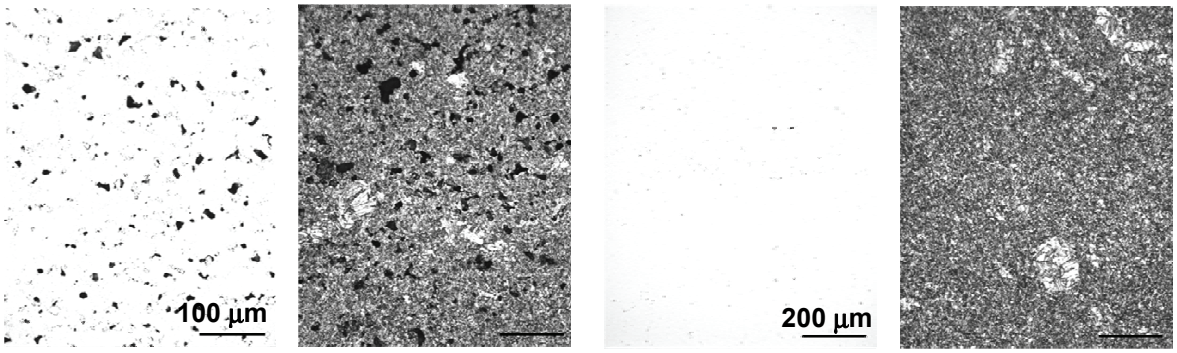

Fig. 6: Micrographs of sample 1F and 3F heat treated (left) and etched (right).

The findings from the described examinations gave no clear indication for the failure reason. It seems that the suction pipe is a critical point. The transition from the thin pipe to the thick top cap is very abrupt and may cause the formation of small cracks and leaks during hipping. So the design should be improved.

On the other hand, due to the machining of the capsules after hipping in order to get a rectangular shape for rolling, there is no protecting and supporting sleeve around the slab which could prevent crack formation during hot rolling. Therefore it was decided to fabricate a kind of "sardine cans" and integrate the milled slabs into this can (s. Fig. 7).

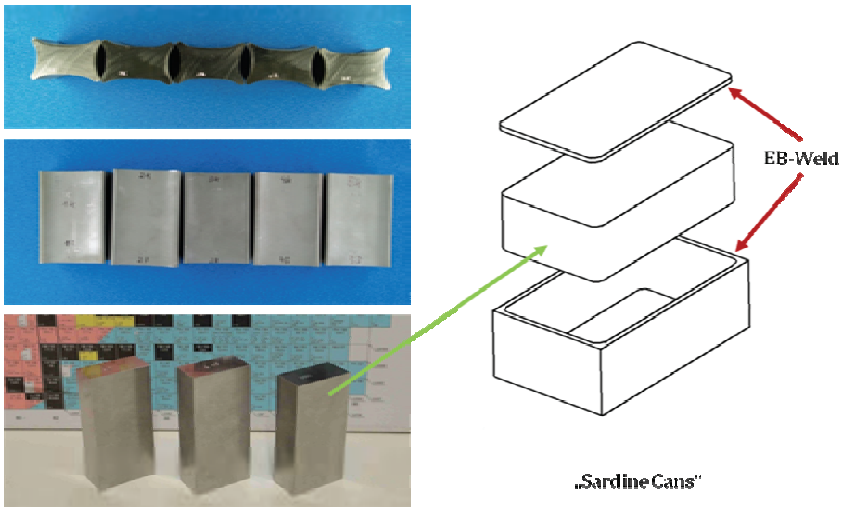

Fig. 7: "Sardine can" like HIP capsules as protection and support for rolling.

Currently the fabrication of these containers is under way. It is foreseen to make a degassing in the EB-device prior to EB welding.

These cans will then be hipped prior to hot rolling. Besides the supporting function of the can it would be interesting also to see whether this method with a second HIP before rolling would have an effect on the porous slabs. It cannot be excluded that the porosity can be closed to some extent.

Summary

In the large scale production of ODS unexpectedly cracks occurred during hot rolling. Metallographic examinations showed that high porosity can be regarded as reason for this failure.

Chemical analyses of materials from the different production steps supported the assumption that leaking of the HIP containers during the consolidation process was the most likely reason. A downsizing of the HIP capsules was only partly successful.

Conclusions

In order to avoid such failure in future large scale ODS productions; the capsule design needs further optimization to avoid leaking during HIP. It is proposed to encapsulate the slabs after shaping and perform a second HIP before hot rolling.

Staff:

C. Adelhelm
S. Baumgärtner
T. Bergfeldt
D. Bolich
B. Dafferner
P. He
M. Hoffmann
U. Jäntsch
T. Kaiser
M. Klimenkov
R. Lindau
A. Möslang
R. Ziegler
H. Zimmermann

Literature:

[1] He, P.; Klimenkov, M.; Lindau, R; Möslang, A.; Characterization of precipitates in nano structured 14% Cr ODS alloys for fusion application; J. Nucl. Mater. (428) 2012, 131-138.

[2] Commin, L.; Rieth, M.; Widak, V.; Dafferner, B.; Heger, S.; Zimmermann, H.; Materna-Morris, E.; Lindau, R.; Characterization of ODS (Oxide Dispersion Strengthened) Eurofer/Eurofer dissimilar electron beam welds; J. Nucl. Mater. in press.

[3] He, P.; Liu,T.; Möslang, A.; Lindau, R.; Ziegler, R.; Hoffmann, J.; Kurinskiy, P.; Commin, L.; Vladimirov, P.; Nikitenko, S.; Silveir, M.; XAFS and TEM studies of the structural evolution of yttrium-enriched oxides in nanostructured ferritic alloys fabricated by a powder metallurgy process; Mater. Chem. and Phys., 136 (2012), 990-998

[4] Ryazanov, A.I.; Chugonov, O.K.; Latushkin, S.T.; Lindau, R.; Möslang, A.; Prikhodko, K.E.; Semenov, E.V.; Unezhev, V.N., Vladimirov, P.; Investigations of High Concentration of Helium Atoms Effects on Microstructure and Mechanical Property Changes in EUROFER ODS Materials; J. Nucl. Mater. in press.

[5] Lindau R., Möslang A.; Nanoscaled Materials for Fusion Power Plants; 5th German-Japanese Symposium on Nanostructures, 5th International Symposium on Nanostructures OZ 12, Wenden-Olpe, Germany, March 4-6, 2012.

[6] Lindau, R., Commin, L., Jäntsch, U., Klimenkov, M., Möslang, A., Norajitra, P., Bergman, L., dos Santos, J.F.; Investigations on the joining of 9-20 Cr ODS and Non-ODS steels applying Diffusion, Electron Beam and Fric-

tion Stir Welding; 2nd Joint IAEA - EC Topical Meeting on Development of New Structural Materials for Advanced Fission and Fusion Reactor Systems, Ispra, I, April 16-20, 2012.

[7] Rogozhkin S., Aleev A., Klimenkov, M., Lindau, R., Möslang, M., Nikitin, A., Vladimirov, P., Zaluzhnyi, A.; Tomographic Atom Probe study of un- and irradiated ODS EUROFER steel; 2nd Joint IAEA - EC Topical Meeting on Development of New Structural Materials for Advanced Fission and Fusion Reactor Systems, Ispra, I, April 16-20, 2012.

Acknowledgement

This work, supported by the European Communities under the contract of Association between EURATOM and Karlsruhe Institute of Technology, was carried out within the framework of the European Fusion Development Agreement. The views and opinions expressed herein do not necessarily reflect those of the European Commission.

Helium Behavior in Beryllium (WP12-MAT-01-IREMEV-01-01)

Introduction

Beryllium is an effective neutron multiplier material widely exploited both in conventional nuclear and fusion reactor applications. It is considered as functional material for the helium cooled beryllium pebble bed of fusion reactor blankets for increasing the efficiency of tritium production. On the other hand such macroscopic effects as, e.g., swelling of beryllium, are greatly influenced by the amount of accumulated transmutation helium. Thorough atomic scale simulations of beryllium behavior under irradiation are necessary for understanding of basic mechanisms and reliable prediction of microstructural changes.

This activity is being performed in the frame of EFDA modeling program IREMEV while computer time is provided within the grant HeliBery on HPC-FF.

Calculation method

In this work static and dynamic first principles density functional theory (DFT) based calculations are used for the identification of possible defect configurations and their diffusion pathways.

Ab initio calculations are performed with plane-wave VASP computer code [1]. Full geometry optimization is carried out using Generalized Gradient Approximation (GGA) with Perdew-Wang non-local exchange-correlation functional [2] and the scalar relativistic PAW [3]. The calculations involve typically 13x13x13 Monkhorst-Pack k-point mesh [4] and 450 eV for cut-off energy. Migration barriers were estimated by means of the drag method. Rhombohedral supercells with sizes of 64 and 96 lattice sites are applied.

First principle molecular dynamics calculations were performed using a time step of 3 fs it is possible to perform 3,000-4,000 step simulation (9-12 ps), which lasts about three days on powerful computer cluster (HP XC3000 at SCC, KIT, in our case). To speed up the calculations we downsized the requirements as follows: 7x7x7 Monkhorst-Pack k-point mesh and 250 eV energy cut off were used for the first principles molecular dynamics (FPMD) calculations. This choice was justified by the fact that FPMD were used to elucidate helium diffusion pathways and defect cluster configurations qualitatively. We have relaxed helium and defect cluster configurations observed in FPMD simulations using static first principles calculations with higher requirements and found that all configurations were stable. This confirms that the reduction of the requirements does not produce artificial configurations which would not be found with a more demanding set of parameters.

Results

In this study we investigated the behavior of interstitial and substitutional helium, its diffusion pathways and interaction with point defects present in irradiated beryllium by means of static and molecular dynamics *ab initio* simulations. It was shown that a mixed dumbbell consisting of self-interstitial and helium atoms represents the ground state configuration for interstitial helium. At low temperatures the mixed dumbbell migrates in the basal plane through a series of in-basal-plane rotations, while at higher temperatures jumps between adjacent basal planes were observed as well.

It was revealed that as in many other metals interstitial helium atoms are bound to each other (E_b ~1 eV). In beryllium two mixed dumbbells meet each other so that helium atoms are the nearest neighbors whereas the helium pair can be oriented either in- or out-of-basal plane.

In addition it was found that helium is very strongly bound to vacancies: the binding energy of more than 3 eV found by static ab initio calculations suggests that helium can be hardly released from a mono-vacancy at temperatures below the melting point.

As it was shown previously vacancy clusters are unstable in beryllium. We have shown that addition of helium stabilizes di-vacancies. Thus it is confirmed that the presence of transmutation gas is the necessary condition for the development of a porous microstructure in beryllium.

Diffusion of smallest mobile He-vacancy cluster $HeVc_2$ was studied using ab initio based molecular dynamics. One type of diffusion jumps has been observed in this computer experiment. For precise determination of the migration barriers nudged elastic band method implemented in the density functional theory code VASP was used. Various energy profiles are shown for possible jumps within (see Fig. 1) and out of (Fig. 2) basal plane.

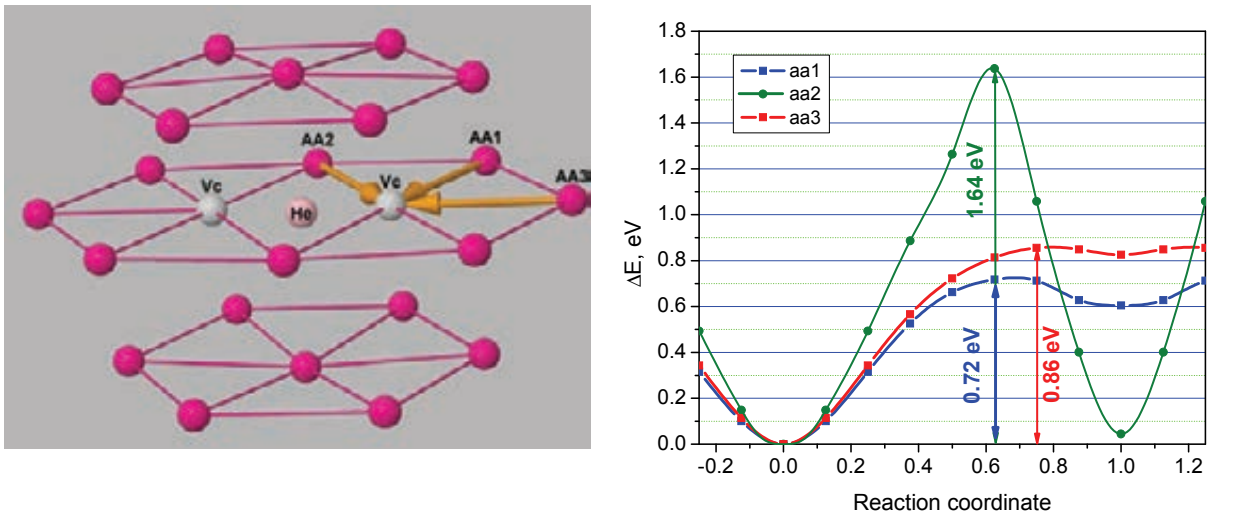

Fig. 1: (a) Three possible in-basal-plane jumps of beryllium atoms labeled as aa1, aa2 and aa3 into He_1Vc_2 complex situated in the same basal plane. In the cases aa1 and aa3 dissociation of basal $(He_1Vc_2)_{aa}$ complex occurs: $(He_1Vc_2)_{aa} \rightarrow HeS + Vc$, while in the case of aa2 jump $(He_1Vc_2)_{aa}$ complex changes its orientation.
(b) Energy profiles corresponding to these migration pathways.

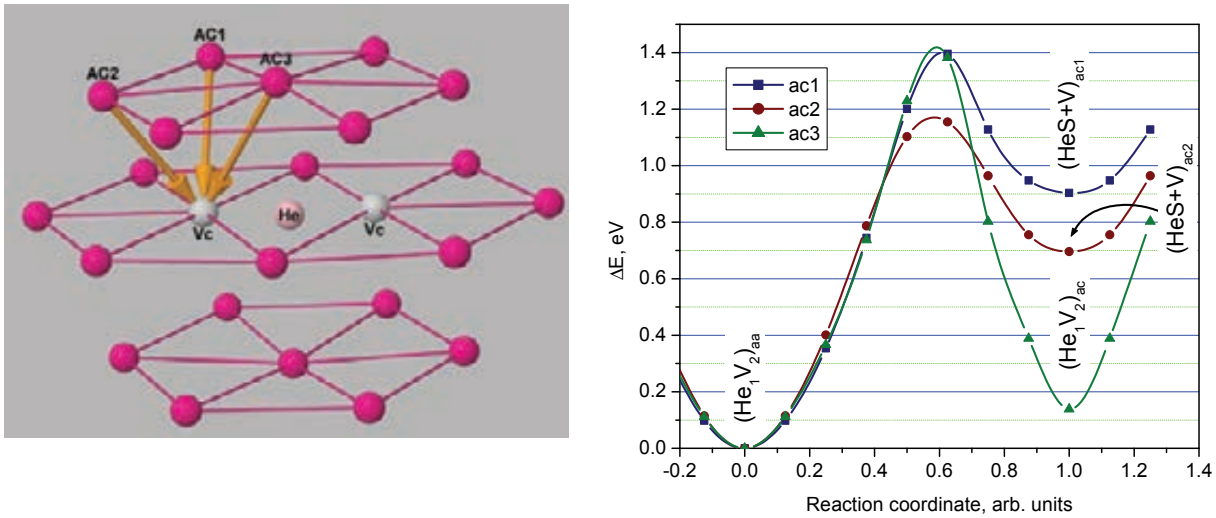

Fig. 2: (a) Three possible jumps of beryllium atoms labeled as ac1, ac2 and ac3 from one basal plane into He_1Vc_2 complex situated in the adjacent basal plane. In the cases ac1 and ac2 dissociation of basal $(He_1Vc_2)_{aa}$ complex occurs, while in the case ac3 a new $(He_1Vc_2)_{ac}$ non-basal complex is formed.
(b) Energy profiles corresponding to these migration pathways.

This analysis suggests that $HeVc_2$ cluster is migrating preferentially in basal plane with approximately the same rate as vacancy (0.7 eV), while it needs to overcome the two times higher barrier (1.4 eV) to move between basal planes. On the other hand the barrier for dissociation (ac2) is slightly lower (1.2 eV). This suggests that $HeVc_2$ cluster rather dissociates than jumps out of basal plane. Calculations of diffusion coefficient for this cluster are on the way.

Conclusions and future prospects

Valuable information about helium behaviour in irradiated beryllium was obtained using static and dynamic *ab initio* methods. Of special importance is the revealing of the diffusion pathways of interstitial and substitutional helium atoms. This information will be used for development of kinetic Monte Carlo and rate theory models for description of helium induced swelling of irradiated beryllium.

Staff:

P. Vladimirov

Literature:

[1] G. Kresse, J. Hafner, Abinitio Molecular-Dynamics for Liquid-Metals, Phys Rev B, 47 (1993) 558-561.

[2] J.P. Perdew, Y. Wang, E. Engel, Liquid-Drop Model for Crystalline Metals - Vacancy-Formation, Cohesive, and Face-Dependent Surface Energies, Phys Rev Lett, 66 (1991) 508-511.

[3] G. Kresse, D. Joubert, From ultrasoft pseudopotentials to the projector augmented-wave method, Phys Rev B, 59 (1999) 1758.

[4] H.J. Monkhorst, J.D. Pack, Special points for Brillouin-zone integrations, Phys Rev B, 13 (1976) 5188.

Acknowledgement

This work, supported by the European Communities under the contract of Association between EURATOM and Karlsruhe Institute of Technology, was carried out within the framework of the European Fusion Development Agreement. The views and opinions expressed herein do not necessarily reflect those of the European Commission

Analysis of Grain Boundary Segregation and Precipitation in Neutron Irradiated EUROFER97 (WP12-MAT-01-IREMEV-04-01)

Objectives

The current task aims at continuation of analysing the neutron irradiation induced evolution of the microstructure in the RAFM steel EUROFER97 and its boron doped variants addressing (a) irradiation dose dependence of *sizes* and *volume densities* of radiation defects (e.g. defect clusters, dislocation loops, voids, helium bubbles, precipitates); (b) neutron flux dependence of *sizes* and *volume densities* of radiation defects. A long term goal is the correlation of the neutron irradiation induced changes in the microstructure to the changes in the mechanical properties, as well as verification of models for the evolution of radiation defects. The specimens to be studied in this task stem from SPICE (15 dpa/300 °C, HFR, NRG, Petten), WTZ (15 dpa/330 °C, Bor-60, JSC "SSC RIAR", and Dimitrovgrad), ARBOR 1 (32 dpa/ 330 °C, Bor-60, JSC "SSC RIAR", and Dimitrovgrad) and ARBOR 2 (70 dpa/ 330 °C, Bor-60, JSC "SSC RIAR", and Dimitrovgrad) irradiation programmes. The neutron fluxes (>0.1 MeV) for Bor-60 and HFR irradiations were 1.8×10^{19} $m^{-2}s^{-1}$ and 4.0×10^{18} $m^{-2}s^{-1}$, respectively.

Task Current Status

The microstructure of EUROFER97 irradiated to 32 dpa in the ARBOR 1 irradiation programme was analysed with the high resolution FEI Tecnai G² F20 X-TWIN TEM installed in the hot cells of the FML. TEM specimens were prepared from the undeformed parts of impact tested KLST specimens. After investigating the dose dependence of size distributions of defect clusters and dislocation loops, and quantitative analysis of voids and helium bubbles; the emphasis was put on the determination of irradiation induced grain boundary segregation in combination with analysing the precipitate structure.

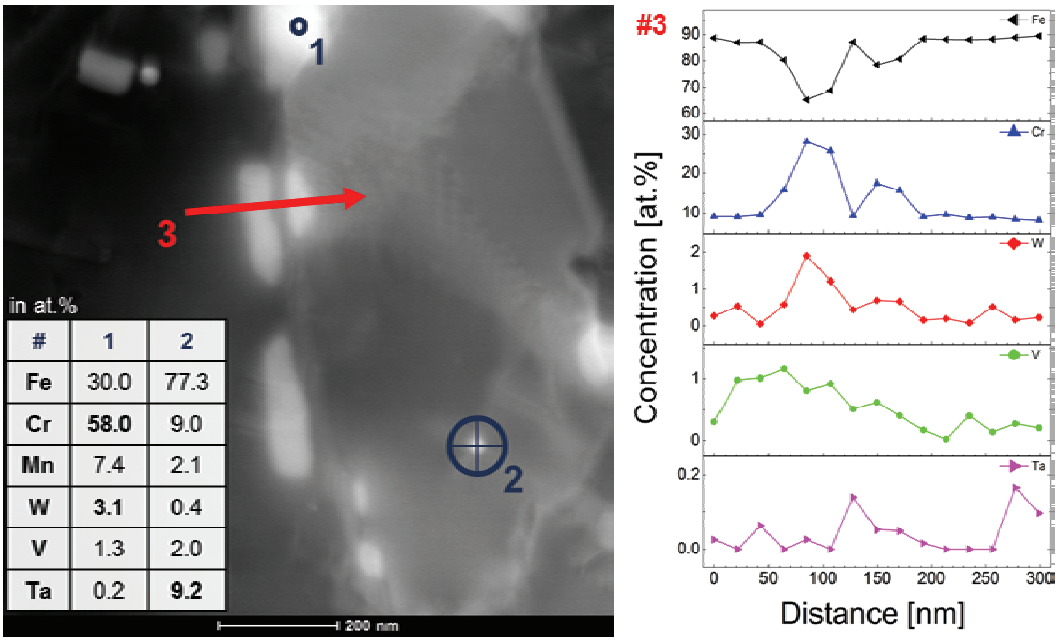

Fig. 1: STEM-HAADF micrograph of unirradiated EUROFER97. Precipitates show bright contrast. Elemental concentrations determined by EDX point (#1 and 2) and line (#3, following the red arrow) scans are shown in table and diagram, respectively.

Fig. 1 shows a TEM micrograph recorded in STEM mode using a HAADF detector. Due to the high Z sensitivity of the detector, precipitates composed of a high amount of heavier elements appear bright in the micrograph due to a larger scattering cross section. A typical distribution of precipitates in unirradiated EUROFER97 can be observed: large elongated precipitates are located along grain or lath boundaries, their sizes account for hundreds of

nanometres in length and tens of nanometres in width. Elemental analysis by EDX was performed on marked precipitates.

All line scans and elemental maps were performed in STEM-EDX nanoprobe mode (probe diameter of ~1 nm) using drift correction during measurements. On the right-hand side of Fig. 1 the result of a line scan following the red arrow is presented. The precipitates that were crossed by the measurement are shown to be enriched in chromium and tungsten, and complementarily depleted in iron. Other elements show no significant concentration change during the line scan. Additionally, results of EDX point measurements at positions #1 and #2 are given in the table within Fig. 1. By calculating the relative elemental concentrations of the precipitate at position #1, it can be shown to be of $M_{23}C_6$ type with a composition of $Cr_{14.4}Fe_{7.5}(W_{0.8}V_{0.3})C_6$. It is assumed that all measured elements are contained in the precipitate except Mn and Ta. For Mn quantitative EDX measurements are proven to be difficult since the Mn-Kα peak is strongly influenced by the Cr-Kβ peak leading to erroneously high concentrations of Mn. This effect can also be seen when comparing Cr and Mn concentrations in point measurements #1 and #2. Therefore, Mn concentrations (bulk concentration of 0.48 at.%) are disregarded in further diagrams. Furthermore, C concentration was not considered due to low measuring accuracy of EDX for light elements and possible C surface contamination despite of using plasma cleaning surface treatment before TEM analysis. Future analyses will involve EELS measurements with high accuracy for quantifying light elements as C. A second kind of precipitate is shown in Fig. 1 and marked with #2. This type of precipitates with a spherical shape and diameters of about 20 nm were found to be distributed homogeneously in the matrix. The precipitate (at position #2) was identified as Ta enriched, and is most likely TaC.

Fig. 2 shows an example of precipitates found in irradiated samples of EUROFER97 from ARBOR 1. These large precipitates analysed by EDX (line scan following red arrow) demonstrate a distinct increase in Cr, W, and V, with an atomic fraction for Cr of more than 50%. Also in this case the composition indicates precipitates of type $M_{23}C_6$. No significant changes in the precipitate structure could be observed after irradiation of EUROFER97 to 32 dpa at 330 °C: large and mostly elongated precipitates of type $M_{23}C_6$ are decorating grain boundaries while small Ta rich precipitates show no preferential position in the microstructure. The search for α' precipitates in irradiated EUROFER97 specimens has not been successful so far, further investigations by means of EDX and EFTEM mapping will be performed.

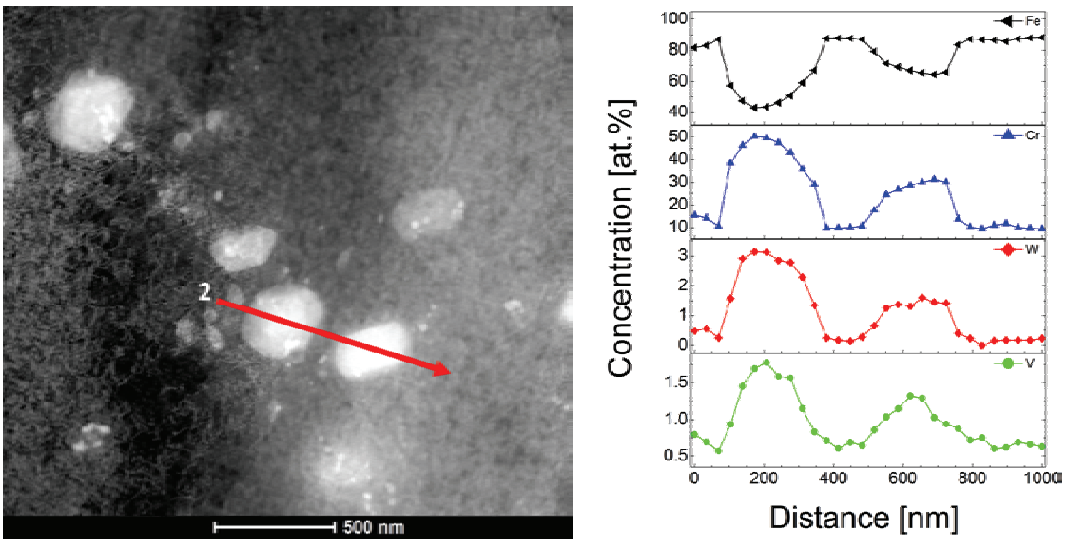

Fig. 2: STEM-HAADF micrograph of EUROFER97 irradiated to 32 dpa at 330 °C in ARBOR 1. Analysis by EDX was performed following the red arrow, results of the line scan for relevant elements are given in the diagram.

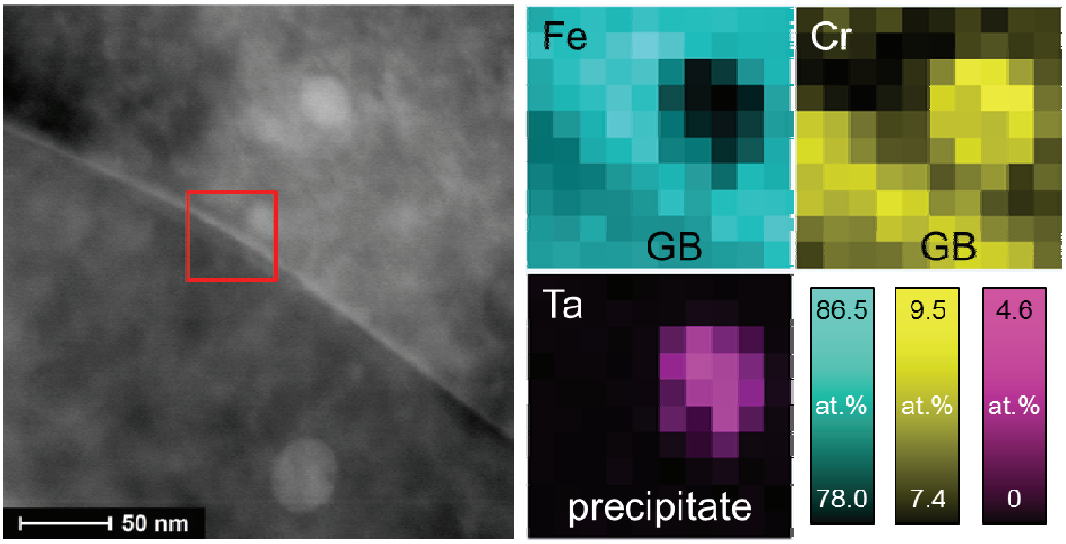

Fig. 3: STEM-HAADF micrograph of EUROFER97 irradiated to 32 dpa at 330 °C in ARBOR 1. Red square marks grain boundary area analysed by EDX providing elemental maps shown on the right.

Grain boundary segregation of chromium in EUROFER97 was investigated by using EDX elemental mapping. For analysis a grain boundary was chosen that showed a distinct contrast in the HAADF micrograph, with no $M_{23}C_6$ precipitate located close to the measuring area. In the unirradiated state Cr segregation at grain boundaries could not be detected so far. The TEM micrograph in Fig. 3 presents an investigated grain boundary in irradiated EUROFER97 after 32 dpa from ARBOR 1. EDX elemental maps were determined within the red square. Results show segregation of Cr along the grain boundary with a concentration increase of up to 2 at.% compared to the surrounding matrix. The Fe concentration on the other hand shows depletion in the same region. In addition a precipitate rich in Ta and Cr was detected close to the grain boundary which is only slightly visible in the TEM micrograph. In this measurement elements W and V showed no significant concentration change.

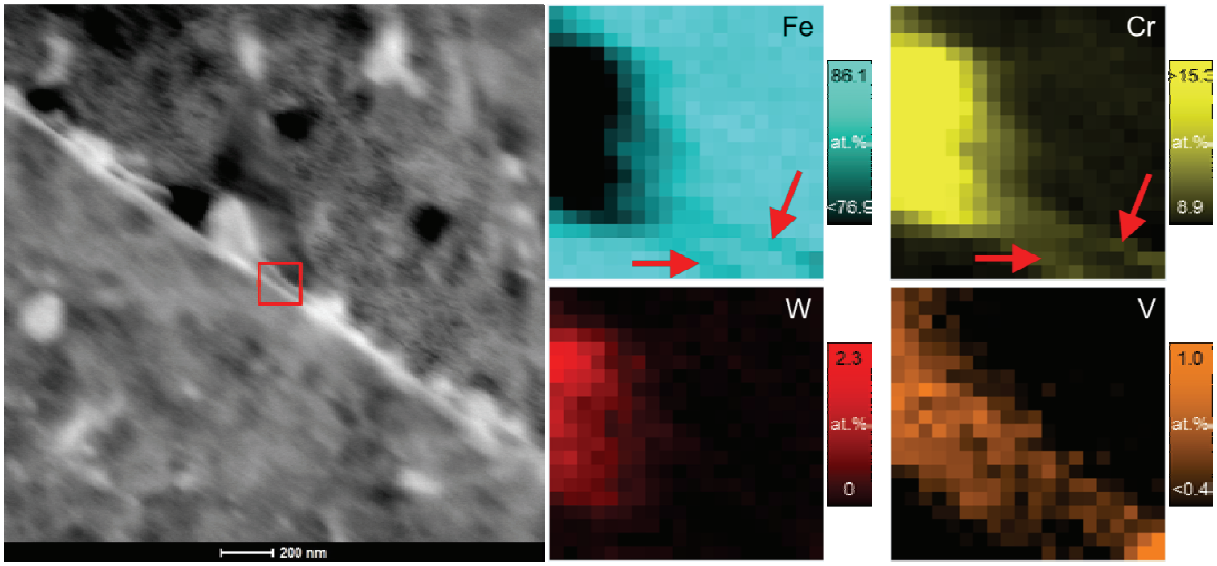

Fig. 4: STEM-HAADF micrograph of EUROFER97 irradiated to 32 dpa at 330 °C in ARBOR 1. Red square marks grain boundary area analysed by EDX providing elemental maps shown on the right. Besides the large Cr and W rich precipitate depletion of Fe and segregation of Cr are observed at GB as marked by red arrows. V map reveals a presence of V rich precipitate at GB.

A second grain boundary shown in Fig. 4 was investigated. In the HAADF micrograph a bright contrast at the grain boundary was observed, to some extent appearing as two bright lines.

The red square including the double bright contrast was analysed by EDX elemental mapping. First of all a precipitate could be detected which showed no pronounced contrast in the HAADF micrograph. Since it is clearly composed of Cr and W (up to 24.6 at.% and 2.3 at.%, respectively), it is assumed to most likely be of $M_{23}C_6$ type. Furthermore, the EDX maps in Fig. 4 show Cr segregation (red arrows) following the double bright contrast in the TEM micrograph. The Cr concentration in this regions is about 2 at.% higher compared to the adjacent darker areas in the elemental map. As a consequence Fe is depleted where the Cr concentration is high. To visualize the small concentration increase of 2 at.% in comparison to the large Cr concentration of 24 at.% in the precipitate, the intensity scale of Cr was adapted resulting in blooming of the precipitate (maximum brightness level set to 15.3 at.%). An analogue procedure was performed on the Fe map. V increase at the grain boundary is observed: besides the occurrence of V in the detected precipitate, which also supports the assumption of being of $M_{23}C_6$ type, the V concentration is slightly increased by 0.5 at.% along the grain boundary. The presence of elongated VN precipitates at grain boundaries is possible in accordance with measurements in the unirradiated state.

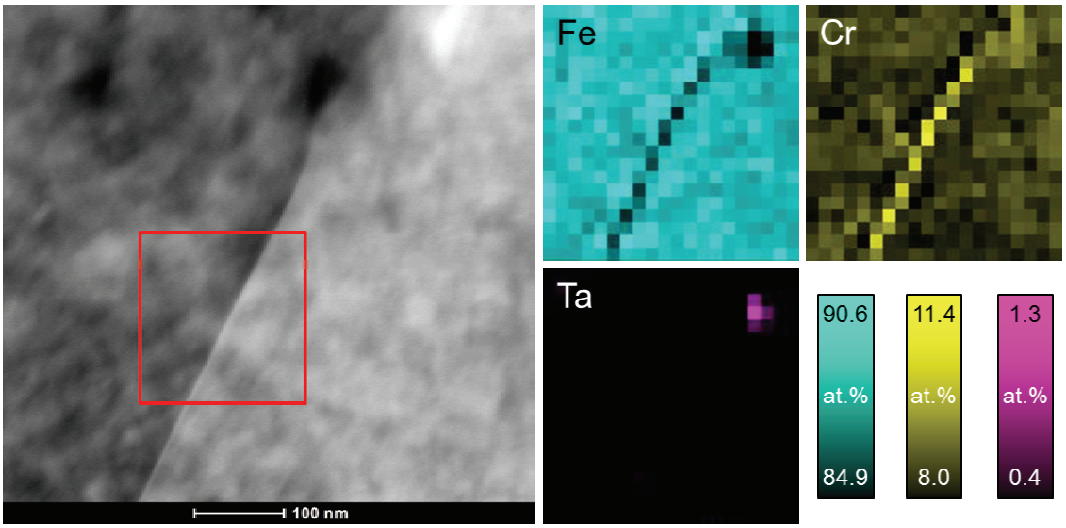

Fig. 5: STEM-HAADF micrograph of EUROFER97 irradiated to 32 dpa at 330 °C in ARBOR 1. Red square marks grain boundary area analysed by EDX providing elemental maps shown on the right.

A narrow segregation profile of Cr at a grain boundary is presented in Fig. 5. The increase of the Cr concentration only occurs at a width of one measuring point when crossing the grain boundary, while the distance between EDX spots corresponds to 9.1 nm. The range of the Cr concentration in the measured area is between 8.0 at.% and 11.4 at.% while the highest and lowest values are located next to each other forming an adjacent bright and dark line at the grain boundary. The grain boundary region is free of precipitates except for a small Ta enriched one that in this case does not affect the resulting elemental map.

Conclusion and Outlook

Precipitation and segregation at grain boundaries in EUROFER97 were investigated by TEM. STEM-HAADF micrographs showed two types of precipitates: (1) large elongated precipitates located along grain boundaries, (2) small spherical precipitates distributed randomly throughout the matrix. EDX analysis showed them to be of type $M_{23}C_6$ and Ta enriched, respectively, in accordance with literature results on unirradiated EUROFER97. An influence of irradiation (ARBOR1: 32 dpa, 330 °C) on the precipitation structure could not be detected.

Segregation of Cr at grain boundaries was studied. In unirradiated specimens of EUROFER97 no segregation could be detected by means of EDX measurements.

After ARBOR 1 irradiation to 32 dpa at 330 °C segregation of Cr and depletion of Fe were observed at several grain boundaries. Increase of Cr concentration was up to 3.4 at.% when compared to the surrounding matrix.

Further TEM investigations of irradiated EUROFER97 will provide quantitative analysis of dislocation loops (SPICE), precipitate size distributions and determination of precipitate compositions complemented by EELS measurements (WTZ, ARBOR 1). The search for Cr-rich α' precipitates will be continued by means of EDX and EFTEM analysis. Furthermore, TEM investigations will be conducted on irradiated EUROFER97 and boron doped variants at high damage doses (ARBOR 2) with respect to quantification of sizes and volume densities of radiation induced defects (e.g. defect clusters, dislocation loops, voids/bubbles, precipitates). The results of quantitative microstructure analysis will be used for verification of models for evolution of radiation defects in RAFM steels.

Staff:

C. Dethloff
E. Gaganidze

Literature:

[1] O. J. Weiß, E. Gaganidze, J. Aktaa, Quantitative characterization of microstructural defects in up to 32 dpa neutron irradiated EUROFER97, J. Nucl. Mater. 426 (2012) 52-58.

[2] C. Dethloff, E. Gaganidze, V. V. Svetukhin, J. Aktaa, Modeling of helium bubble nucleation and growth in neutron irradiated boron doped RAFM steels, J. Nucl. Mater. 426 (2012) 287-297.

[3] C. Dethloff, Modeling of Helium Bubble Nucleation and Growth in Neutron Irradiated RAFM Steels, PhD thesis, KIT Scientific Publishing, 2012.

[4] E. Gaganidze, C. Dethloff, O. J. Weiß, V. Svetukhin, M. Tikhonchev, J. Aktaa, Modeling and TEM Investigation of Helium Bubble Growth in RAFM Steels under Neutron Irradiation, J. ASTM Int. (2012), accepted for publication.

Acknowledgement

This work, supported by the European Communities under the contract of Association between EURATOM and Karlsruhe Institute of Technology, was carried out within the framework of the European Fusion Development Agreement. The views and opinions expressed herein do not necessarily reflect those of the European Commission.

EUROFER97: Post-irradiation Examinations of Tensile and LCF Specimens after Neutron Irradiation up to 16.3 dpa in the Range Irradiation Temperatures at 250°C, 350, and 450°C (CoA)

Objectives

The loading of first-wall and blanket structures of Tokamak-type fusion reactors includes, besides the plasma surface interactions, a combined effect of oscillating mechanical load and temperature gradients giving rise to thermo-mechanical and thermal fatigue and damage due to high fluxes of fusion neutrons. For lifetime predictions and for the design of structural components, it is therefore important to quantify the irradiation-induced changes on material properties such as LCF and tensile behavior. In the framework of the European steel developing program the RAFM steel EUROFER97 was irradiated up to 16.3 dpa in the mixed-spectrum reactor HFR of Petten, The Netherlands.

Work performed in previous reporting periods

A comprehensive post-irradiation program was performed which included tensile, impact and LCF tests. A special wrapper, with irradiation capsules all specimens, was inserted in the central part of the reactor core of HFR. The irradiation was set to 250, 300, 350, 400, and 450 °C. The cumulative neutron fluence E>0.1 MeV m^{-2} was 22.85 x 10^{25}. The neutron irradiation was carried out in 771 FPD up to nominal dose of ~15 dpa. The experimental obtained damage levels for monitor set positions in the specimen holder varied between 13.4 to 18.1 dpa. Neutronic calculations have shown that the volume-average displacement dose of all specimens was ~16.3 dpa for stainless steel.

Irradiation effect on mechanical properties of EUROFER97

Results of tensile and LCF tests

The post-irradiation examinations were performed in the hot cell facility of the Fusion Material Laboratory at KIT. A universal testing machine equipped with a high-vacuum furnace was used. Fully instrumented tensile tests were carried out with a strain rate of 0.1 mm/min at T_{test} = T_{irrad}, the test temperatures were the same as the irradiation temperatures. The unirradiated specimens were in the as-received condition. LCF tests have been performed also at T_{test} = T_{irrad} = 250, 350, and 450 °C in high vacuum. During these tests, complete fatigue cycles with hysteresis loops were recorded, allowing a detailed monitoring of the stress amplitude, $\Delta\sigma(N)$, as a function of cycles, and of the elastic, $\Delta\varepsilon_{el}(N)$, and plastic strains, $\Delta\varepsilon_{pl}(N)$, respectively. The fatigue tests were performed under symmetric push-pull conditions until specimen failure, N_f.

Tensile properties

Figures 1 – 2 show the tensile properties of irradiated and non-irradiated specimens. As expected, a significant irradiation-induced strength increase, $\Delta\sigma_{irr}$, has been observed at the lowest irradiation temperatures, 250 and 300 °C, while above about 400 °C even a minor softening appears. This temperature behavior is expected and is a general feature of ferritic-martensitic steels, and is due to smaller dislocation loops and nanoscaled precipitates that are stable only below about 400 °C. As they are not formed above about

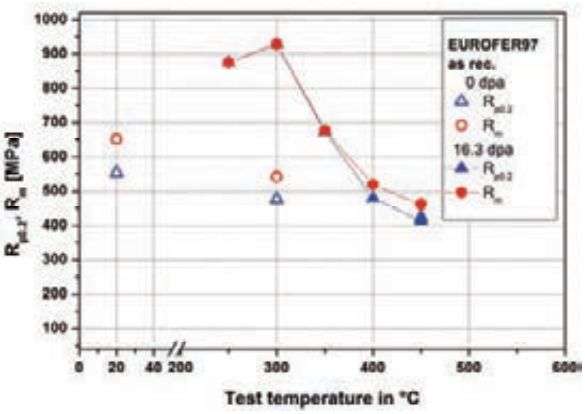

Fig. 1: Yield strength $R_{p0.2}$ and tensile strength R_m.

400 – 420 °C, at least in a helium-free bcc matrix, uniform and total elongation are nearly the same at 450 °C for irradiated and unirradiated specimens.

However, that 250 °C irradiation reveals a smaller $\Delta\sigma_{irr}$ of about 60 MPa compared to the 300 °C irradiation. This observation might be surprising, but is in agreement with hardness measurements that have been done after the same irradiation on F82H-mod and different EUROFER97 heats. A general feature of mixed-spectrum neutron-irradiated ferritic-martensitic steels is also the serrated yielding or dynamic strain aging observed at the selected strain rate around $T_{test} = T_{irrad} = 250$ °C, Fig. 1, which is due to the repeating interaction between moving dislocations and solute carbon atoms. Despite the pronounced strain localization observed after irradiation below about 400 °C and the related small uniform elongation, A_g, of about 1% or even less, the total elongation after fracture, A, is in the range of 10% and therefore still about 50% of the unirradiated value, Fig. 2. Consequently, low-temperature irradiated RAFM steels begin to deform around 1% in an irreversible manner by strain localization. Whether dislocation channeling observed in other laboratories as origin of the strain localization is the dominant deformation mode also under the present conditions which has to be analyzed further.

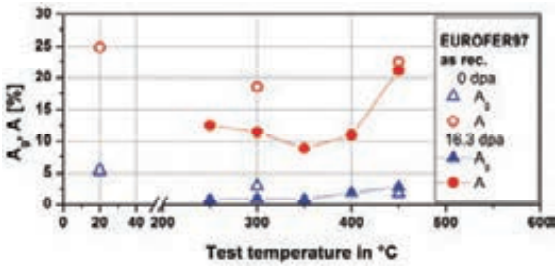

Fig. 2: Uniform elongation A_g and elongation after fracture A.

LCF properties

The stress-strain hysteresis curves at 250 °C revealed a distinct irradiation-hardening corresponding to the tensile tests. An increase in strength of about 70% could be detected at 250 °C and about 60% at 350 °C, while at 450 °C the stress amplitudes of the irradiated and the unirradiated specimens are almost identical, as expected from tensile tests. In all diagrams of Fig. 3, the gradient in the stress amplitudes showed the typical cyclic softening of the RAFM steels. It is important to note that this cyclic softening is most pronounced at high strength that is at low irradiation temperatures: e.g., after 250 °C irradiation and at a strain amplitude of 0.7% the stress amplitude collapses from about 750 MPa during the first cycles continuously down to about 500 MPa. Despite this cyclic softening, the stress amplitude of the irradiated specimens remains always significantly above that of the unirradiated specimens at irradiation temperatures below about 400 °C. From this behavior it can be concluded that even the continuous cyclic motion of dislocations does not yet sweep out the vast majority of the irradiation-induced defects on their gliding planes.

Figure 3 shows another common feature of LCF testing that so far has been only observed in unirradiated specimens: e.g. all stress amplitudes of 250 °C-tests follow one single common curve and are practically identical beyond about 200 cycles, despite the wide range of applied strain amplitudes. Consequently, large strain amplitudes show more cycling softening at small strain ranges. That is, the deformation response on individual fatigue loading occurs specifically in the early phase of fatigue testing.

Remarkable for the 250 °C irradiation is also that with decreasing strain amplitude the irradiated specimens achieved a considerable increase in fatigue life, Fig. 4. At the lowest $\Delta\varepsilon$ of 0.5%, the number of cycles to failure, N_f, is about ten times higher than in the unirradiated control. In contrast to the 250 °C irradiations, the irradiation hardening is much less pronounced after 350 °C irradiation. This might be the reason that, for this irradiation temperature, no clear irradiation effect on fatigue life could be determined within the data scatter. Also for the 450 °C irradiation, the irradiated and unirradiated controls have similar fatigue lifes within the experimental uncertainties, despite the somewhat different slopes. The fatigue

life results reported here on the 350 °C irradiation are consistent with the ones reported on the same material after fast-breeder irradiation up to 71 dpa at about 330 °C.

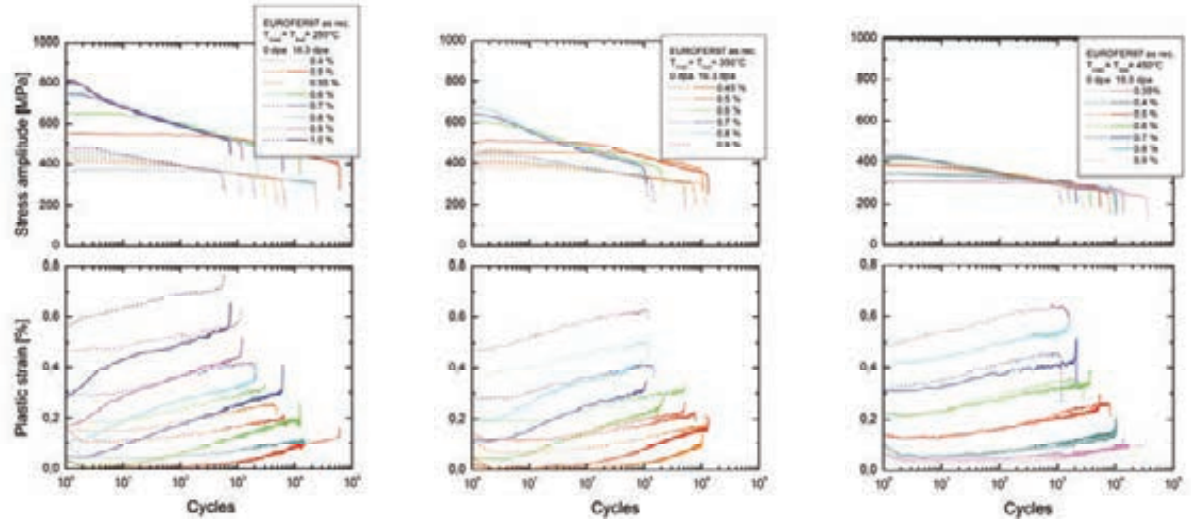

Fig. 3: Stress amplitudes and plastic elongations vs. number of cycles; unirradiated and irradiated EUROFER97 at Tirrad = Ttest = 250, 350, and 450 °C.

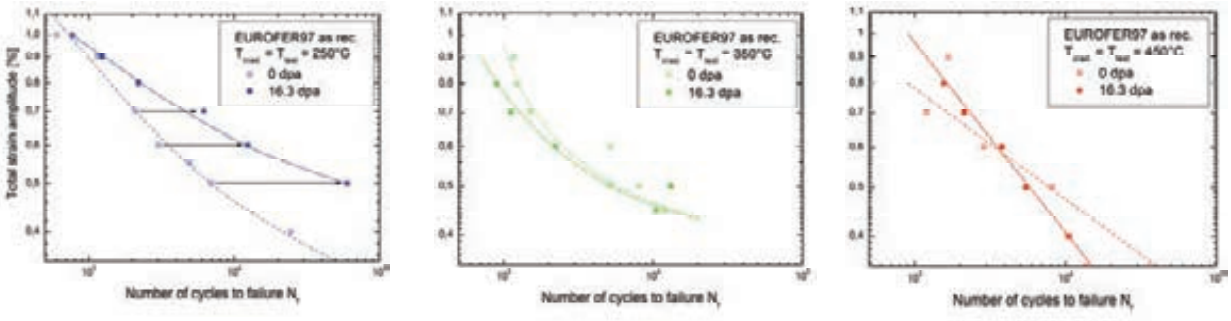

Fig. 4: Effect of irradiation temperature on fatigue lifetime N_f at $T_{irrad} = T_{test}$t = 250, 350, and 450 °C.

Structural and fractographic properties

The irradiation-induced hardening could be quantified by Vickers hardness measurements. The steel had an initial hardness of 214 – 226 HV0.1 in the unirradiated state. The high increase was measured as expected at 250 °C, 16.3 dpa, with 308 – 328 HV0.1 and at 300 °C with 321 – 356 HV0.1. At 350 °C the hardness was lower again, between 265 – 282 HV0.1, and at 450 °C, the thermal effect on the material could be determined with 221 – 237 HV0.1. All hardness measurements were performed at non-deformed material of impact specimens, which were in the same irradiation program. Also, selected specimens were cut to investigate the microstructure of unirradiated or irradiated conditions. The characteristic microstructures were documented by TEM. A homogeneous distribution of dislocation loops, point defects and/or α`-precipitates of about $2 \times 10^{15}/cm^{-3}$ was determined in EUROFER97 at 250 °C and 16.3 dpa. These irradiation-induced microstructures are significantly responsible for the irradiation hardening. Some helium bubbles or voids having diameters of 1–2 nm were observed, but their density was insufficient to influence the material property.

After tensile tests at 250 °C, an orientation mechanism of the dislocation loops and point defects was often observed. The comparison with tensile-tested material at 450 °C and 16.3 dpa showed a completely recovered material without any irradiation-induced loops or point defects, but with a homogeneous sub-grain formation. Further microstructural changes were found after LCF tests. The thin foils for TEM were cut near the fracture. Sub-grain or sub-cell formation was found independent of the former microstructure with lath structure, as other laboratories found, too. The sub-cells in the unirradiated state were nearly free of dislocations. There was a clear difference to the irradiated material. Beside dislocation free sub-cells, sub-cells with a high density of irradiation induced defects and dislocation loops were observed. This development was seen especially after 250 °C irradiation, Fig. 5a, but much less after 350 °C. Practically free of dislocation loops was the LCF-tested specimen after 450 °C irradiation, Fig. 5b. Independent of the irradiation temperature, TEM analysis of irradiated specimens reveals also pronounced sub-cell formation similar to the unirradiated controls. That is, a significant fraction of dislocations move to the lath and grain boundaries, leaving behind a cell interior with low dislocation density. This is a major reason for the cyclic softening observed during fatigue testing.

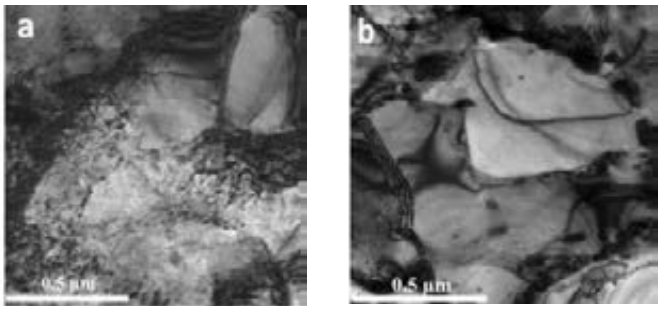

Fig. 5: Cell formation in LCF-tested sample after 250 °C, 16.3 dpa (Fig. 5a), and after 450 °C, 16.3 dpa (Fig. 5b).

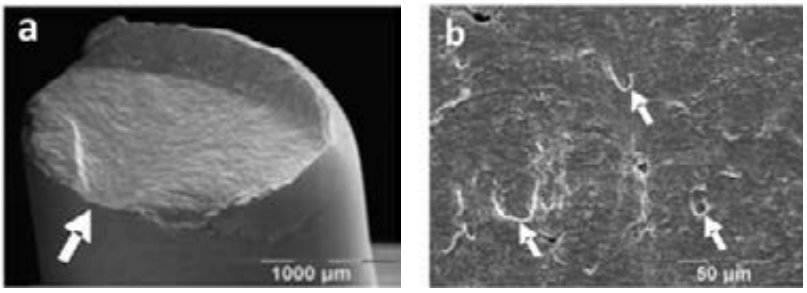

Fig. 6: Fracture surface of post-irradiated LCF tests at 450 °C. 6a shows the macroscopic view and the arrow marks the fracture origin. Details of the fracture are presented in Fig. 6b: striation formation with cyclic formed dimples around small inclusions, shown by arrows.

The fractures of the tensile specimens all had a ductile character with uniformly distributed dimple formations. The difference between unirradiated and irradiated was quite evident. The irradiated samples showed less reduction of area compared with unirradiated ones. The samples after LCF tests exhibited the typical flat fracture surface with striations which reflect the push-pull load on this material. The crack propagation is observable by fatigue paths and striations. In this way, the fracture origin of every LCF sample was clearly detectable at the outer face as shown in Fig. 6. The first cracks are always initiated at specimen surface. It depends on the applied highest stress state at the surface. Further surfaces are in the bulk material, too, between, e.g., inclusions and matrix. The cyclic load influences these interfaces, and large dimples with striations occurred around the inclusions, Fig. 6 b.

Conclusions

Tensile tests

- Irradiation-induced hardening and strengthening could be confirmed at <300 °C.
- Thermally induced recovery and the hardening effect of dislocation loops and small precipitates was dissolved at temperatures >400 °C.

Fatigue tests

- In all specimens of EUROFER97, the typical cyclic softening of martensitic steel was observed in unirradiated as irradiated state and reflected by the continuous decrease of stress amplitude.
- EUROFER97 after neutron of 250 °C showed an increase of lifetime to a factor of about ten at $\Delta\varepsilon$=0.5%.
- After irradiation at higher temperatures, unirradiated and irradiated specimen had lifetimes in the same range.
- Cell structures were formed in the microstructure after a few hundred cycles.

The HFR-irradiation program and other irradiation programs, e.g. Bor 60, are still in work. Further mechanical and structural investigations are implemented to characterize the irradiation behavior of different RAFM steels to determine their possible applications.

Staff:

J. Aktaa
S. Baumgärtner
J. Ehrmann
E. Gaganidze
M. Holzer
S. Lautensack
E. Materna-Morris
A. Möslang
H. Ries
R. Rolli
H.-C. Schneider

Literature:

[1] E. Materna-Morris, A. Möslang, and H.-C. Schneider: Tensile and Low Cycle Fatigue Properties of EUROFER97-Steel after 16.3 dpa Neutron-Irradiation at 523, 623, and 723 K. Proceedings and lecture: ICFRM-15, October 16-22, 2011, Charleston, SC, USA. J. Nucl. Mater. in press.

Analytical TEM Characterization of He Bubbles in Boron-alloyed Steel after Neutron Irradiation (WP12-MAT-01-IREMEV-04-02)

Introduction

Electron energy loss spectroscopy (EELS) was used to detect and study the spatial distribution of He and Li on the nanoscale in boron-alloyed steel after neutron irradiation. Li and He are the products of the $^{10}B(n, \alpha)^{7}Li$ nuclear reaction and knowledge of their distribution is important to understand their influence on mechanical properties. Here, a new method is presented for the direct detection of Li in Fe, which is based on the analysis of the plasmon structure of Fe/Cr matrix its comparison with the structure of Li particles/drops and its separation from the He signal. The linear extrapolation of the Fe plasmon background allows for the calculation of Li and He two-dimensional maps and the measurement of their spatial distribution. From the plasmon structure, conclusions can be drawn with respect to the chemical composition of Li nano particles and rhe characterization of He bubbles in boron-alloyed steel after neutron irradiation.

Method

The boron-alloyed specimens were prepared from a ferritic martensitic 9CrWTaV steel (EUROFER 97) with the addition of 0.116% wt ^{10}B. After fabrication, the ferritic-martensitic alloy was treated thermally at 1040 °C for 30 min and normalized at 750°C for 90 min to obtain the tempered martensite structure. The specimen was neutron-irradiated up to 16.3 dpa at 400°C in the HFR mixed-spectrum reactor, Petten. After complete transmutation (approximately corresponding to a displacement damage dose of 1 dpa), this amount of boron produces 5800 appm He and Li.

Samples with a thickness of 0.2-0.3 mm were thinned by electro polishing in a TENUPOL device. TEM investigations were performed using an FEI Tecnai 20 FEG microscope with an accelerating voltage of 200 kV, the scanning unit for performing scanning TEM (STEM) equipped with a high-angle annular dark field (HAADF) detector and an energy-dispersive X-ray (EDX) detector for elemental analysis.

Results

<u>Li and He detection in the Fe matrix using plasmon excitation energy</u>

Numerous studies reveal the applicability of EELS for the detection of He and Li in TEM. The EELS studies dealing with He detection and distribution were performed mainly on the He-implanted material, such as Al or Fe, and revealed that the He line is well detectable on the plasmon signal from the base material. The different methods were developed for calculation of shape of matrix plasmon in order to separate the He signal for calculation of density in individual bubbles. The blue shift of the He 1s-2p line was used to estimate the He pressure inside single bubbles. The results of the EELS line scan experiment through two bubbles of 56 and 100 nm in size are shown in Fig. 1. The bubbles investigated are located in the area of enhanced Li concentration approximately 1.5μm away from the middle of the former BN particle that disappeared during irradiation. The bubbles formed in this area are significantly larger than the bubbles statistically distributed in the specimen. Detailed TEM characterizations of their morphology in the halos around BN particles were published elsewhere. The damaging halo can be divided into three shells exhibiting different bubble sizes and distributions.

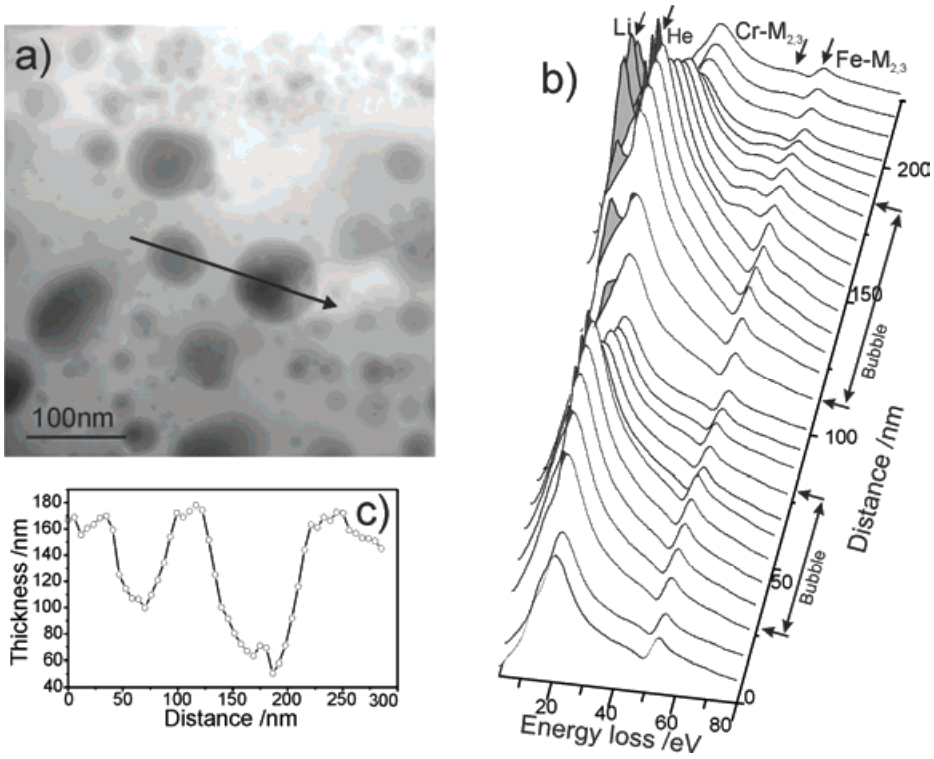

Fig. 1: Line-scan experiment across two bubbles. (a) shows the HAADF image of the investigated area, (b) presents the EELS spectra obtained at each point of the scan, and (c) presents the thickness profile across the line.

The well-pronounced He line was detected in both bubbles (Fig. 1b). Fig. 2b shows a spectrum with the He line at 21.7eV and this line after background subtraction. The background of the Fe/Cr plasmon was calculated as a Gauss curve. The He 1s-2p EELS line is characterized by a 3eV width peak (insert Fig. 2b). In the 100 nm bubble, the He line shows a higher intensity than in the smaller one. Apart from the He line, an intense peak at 12eV can be observed clearly in the bubble of 90 nm size (Fig. 1b, Fig. 2c). The peak or in some cases, the pre-shoulder on the Fe/Cr plasmon, can be attributed to the Li effect (Fig. 2c). The intensity of this peak varied for different experiments as a factor of local Li concentration. In some bubbles, it can be observed with the He signal, as is shown in Fig. 2d. In the experiment shown in Fig. 1, Li was observed in the bubble of 100 nm only.

The analysis of the plasmon structure yields the 2-dimensional distribution of Li and He. Fig. 3 presents an area with numerous bubbles that appear dark in the HAADF image (Fig. 3a). The Fe and Cu EDX Kα maps are shown in Figs. 3 b,c. The copper forms the thin Cu-rich layer of 1-3 nm thickness around the bubbles.

Coating of the bubble surface with Cu differs from previous investigation results of this material. Copper forms nanometer-sized precipitates after neutron irradiation, which serve as nucleation sites for He bubbles. Coating of the bubble surface with copper was not observed. Such radiation-induced precipitation behavior of Cu appeared to be limited to the area around the BN precipitates. Presumably, this is due to the strong irradiation damage caused by recoil products of the B^{10}(He,Li) reaction, which significantly exceeds the 16.2 dpa caused by the external neutron source. Other possible reasons may be the presence of Li and formation of the Li-Cu solid solution. The intensity distribution of the Li plasmon line shows that Li is located as small drops inside the bubbles and on the bubble surface (Fig. 3e). Investigations show that He is not present in all bubbles. Some bubbles are well visible in the 2d map of the He 1s-2p line (Fig. 3d). Several bubbles do not contain He, because they are located on the specimen surface – for example, the large bubble at the bottom right of the scanned area.

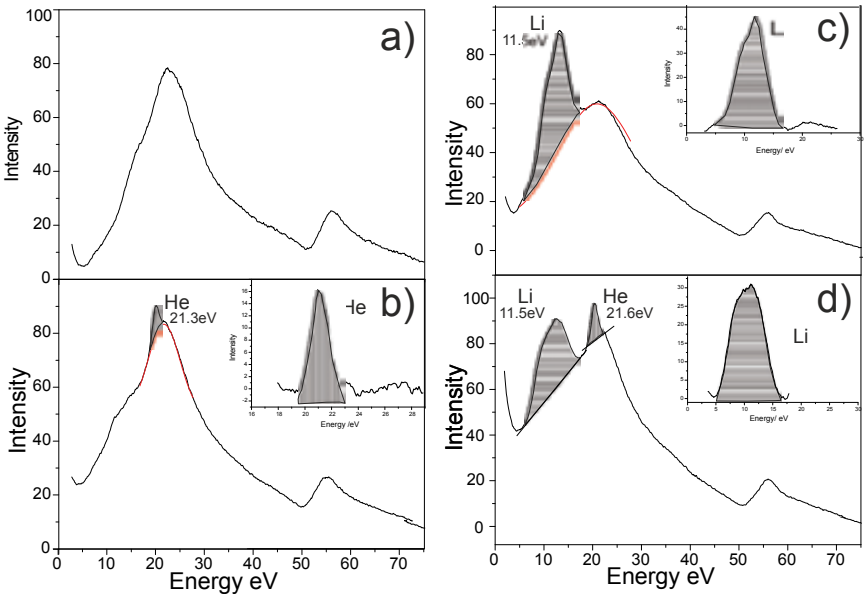

Fig. 2: The four different spectra reveal the location of Li and He features in the plasmon area. (a) shows the spectrum of the pure matrix, (b) presents the matrix with the He feature, (c) shows the matrix with the Li peak, and (d) shows Li and He in the same spectrum.

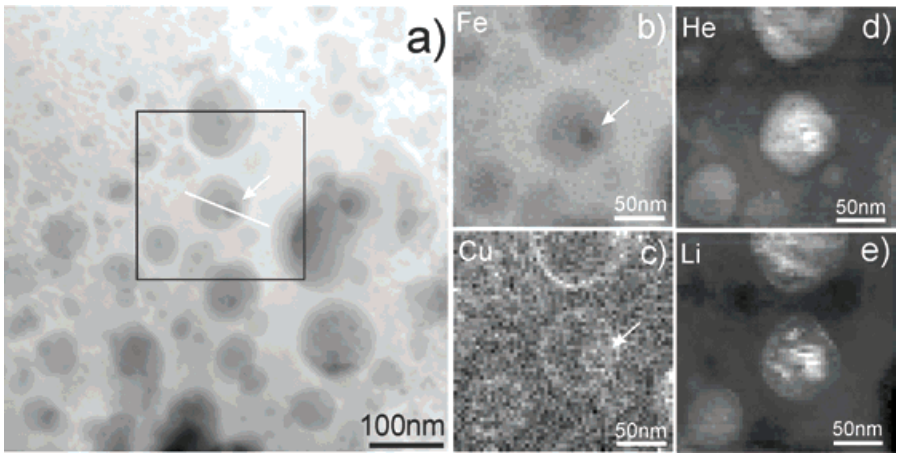

Fig. 3: Analytical TEM investigation of the area with numerous bubbles. The HAADF image of the investigated area is shown in (a), the Fe, Cu, He, and Li maps are shown in b, c, d, and e, respectively.

So far, no publication has been found, which deals with the plasmon structure of lithium precipitates in iron and steel. The assumption that Li can be detected and investigated without any proof based on the Li K edge is due to the following arguments:

A. In the investigated area Li concentration is high enough to form small precipitates.

B. The published EELS investigations of metallic Li show the presence of a sharp plasmon peak at 12eV.

C. The simultaneously acquired EDX spectra as well as EELS spectra in the energy range of up to 300eV do not indicate the presence of any other element (Be or B), which can be connected to the plasmon peak at 12eV.

D. The influence of He can be excluded. The difference between the measured plasmon Li peak and the He 1s-2p line is clearly obvious.

All these factors allow the conclusion to be drawn that the plasmon peak at 12eV indeed originates from Li precipitates or drops in He bubbles.

Spectroscopic He and Li imaging

This section will highlight several results revealing the spatial distribution of Li and He inside bubbles or cavities. The characterized areas are located in regions near the former BN precipitates, where the Li and He concentration is higher than in the specimen average. This area is characterized by bubbles of larger size compared to the specimen average. In some cases, He bubbles with sizes of up to 100 nm were detected.

The observation of numerous bubbles with Li drops or Li/He-filled cavities shows that the width of Li plasmon peak is a variable value. It shows in the mostly cases a FWHM of 5 eV (Fig. 2c). In some cases, the FWHM of the plasmon peak was measured to be at 7.5 eV (Fig. 2d) and in some cases, two maxima were observed. A plasmon peak with an FWHM of 2.5eV can also be measured. Such a variety of plasmon fine structure suggests that Li exists in different chemical states. Li may oxidize or form some other chemical compound inside the bubble. Calculation of maps with few eV energy windows allows studying the spatial distribution of different phase. In the bubble shown in Fig. 4 is presented a Li drop 22nm located in a 50nm large He filled bubble. The Li drop fills approximately ¼ of bubble volume. This is clearly visible in Fig. 4 part (b) He map and (c) Li map. The map obtained by 2.5eV window positioned at 8.0 eV show the increased plasmon intensity at drop's surface (part d), whereas the map obtained at 12eV (part e) reflect nearly the same spatial distribution as entire Li plasmon shown in part (c). This result suggests that Li drop could show some other chemical compound on the surface. It is unlikely that some surface effects could play a role here. Due to lacking reliable experimental data and references, however, only assumptions can be made for the correlation of chemical Li state and shape of Li plasmon. The low energy peak at 8eV corresponds to the plasmon position measured for metallic lithium.

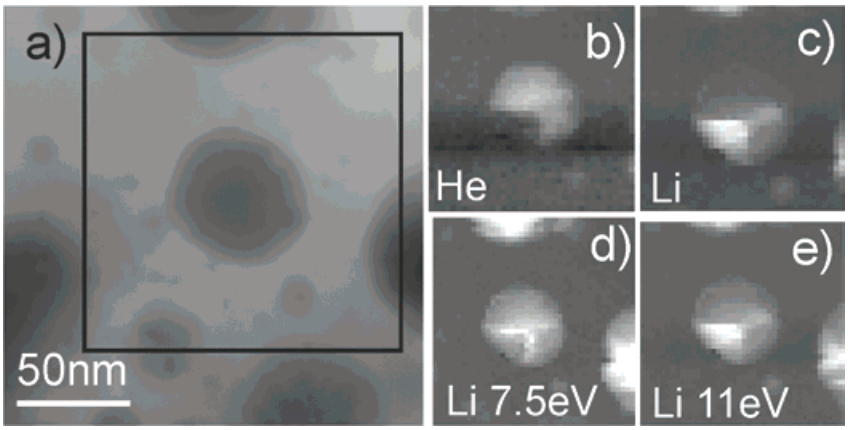

Fig. 4: Analytical TEM investigation of the individual bubble. The HAADF image of the investigated area is shown in (a), He and Li maps are shown in parts b and c. The Li map obtained by a 2.3eV energy window at 7.7eV and 10.7eV are shown in parts d and e respectively.

As ^{10}B alloying beyond 400wt.ppm has a significant impact on ductility and dynamic fracture toughness of neutron irradiated ferritic-martensitic steels, the morphology of Li nanoclusters and He bubbles and their interaction is of primary importance to predict the steel behaviour after long neutron expose. The interaction of dislocations with these Li-He obstacles is underway to analyze their barrier strength as input for nano-scale modelling.

Conclusion

The spatial distribution of Li inside the Fe matrix was detected and investigated by means of EELS plasmon spectra. The new method appears to be more reliable and informative than analysis of the Li-K edge at 54eV, which overlaps with the Fe-$M_{2,3}$ edge. It was found that changes of thicknesses of the Fe matrix in the investigated area and the associated dynamic effects on the intensity of the scattered electrons hardly allow for any clear separation of Li and Fe signals. Using linear background subtraction, spatial distribution of Li inside He-filled

bubbles may be imaged and these elements separated by 11eV from each other may be distinguished clearly. Investigations of bubbles and cavities show the formation of He-filled bubbles with some Li drops inside. Some bubbles are half filled with Li and half with He. The He-filled bubbles are not stable during TEM investigations. In some cases, cracking of bubbles and He disappearance were observed during the experiment. The fine structure of the Li plasmon peak suggests the presence of Li in the different chemical compounds.

Staff:

U. Jäntsch
M. Klimenkov
E. Materna-Morris
A. Möslang
R. Rolli
H.-C. Schneider

Acknowledgement

This work, supported by the European Communities under the contract of Association between EURATOM and Karlsruhe Institute of Technology, was carried out within the framework of the European Fusion Development Agreement. The views and opinions expressed herein do not necessarily reflect those of the European Commission.

Experimental Validation of Models (WP12-MAT-01-IREMEV-04-03)

The mechanical behavior of specific reduced-activation martensitic steels (Eurofer97, F82H-mod) will be further investigated in the present task by means of indentations at high temperature. A previous study had shown the ability of the instrumented indentation technique to both determine at room temperature the irradiation damage in irradiated samples (15 dpa, HFR-SPICE irradiation program) and recovery effects after thermal annealing.

Further characterizations of such irradiated steels at high temperature by indentations at the macro- and microscale are required for a more complete description of the mechanical behavior. The use of a newly constructed instrumented indentation device operating at up to 650 °C and capable of testing up to 200 N will enable such investigations on irradiated specimens. Its installation in a Hot Cell is planned in nearest future.

With a view to determine the effective impact of the temperature on the recovery of irradiation damages and decrease of strength in the previously mentioned irradiated specimens, the mechanical behavior including elasticity and plasticity properties of unirradiated Eurofer97 and F82H-mod specimens at different temperatures has to be analyzed in advance. For that purpose, first operations of the high temperature device will be performed and preliminary tests will be analyzed.

Characterization of RAFM steels up to 650 °C by means of the indentation technique

The operating ability of the high temperature instrumented indentation device has been verified according to the initial requirements. Different aspects have been taken into account. Those are mainly related to the capability of inducing cyclic indentation and measuring the corresponding force and displacement of the indenter, generating a high vacuum testing atmosphere, and heating both the sample and the tip.

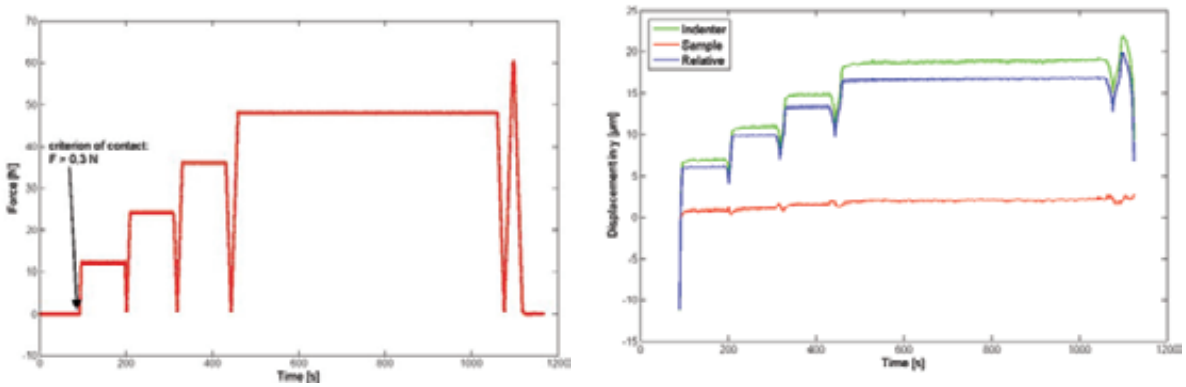

(a) (b)

Fig. 1: (a) Force-displacement data of a cyclic force application, (b) Corresponding displacement-time data.

In this machine, the indentation force is measured on the upper part of the loading shaft inside the vacuum chamber and an additional load cell external to the vacuum chamber is suited for compensation of vacuum forces. In this way, the force-signal measured during the experiment is not influenced by forces resulting from the vacuum. Additionally, a force criterion was defined for the contact detection between the tip and the sample, this one was set to 0.3 N. As displayed in Figure 1(a), cyclic force controlled ball indentations required for identification of mechanical properties by a specific post-processing data tool were achieved. The measurement of displacement or indentation depth is realized during the test by means of an optical setup. This one combines a long-distance microscope connected to a digital camera used for 10 Hz acquisition of pictures of the indenter´s and sample´s motion and a Digital Image Correlation (DIC) code implemented in MATLAB which helps calculate the displacement of the indenter relatively to the sample. Thanks to this contactless measuring method,

influences of frame stiffness and thermal drift are minimized. From the contact detection, the relative displacement can be calculated, i.e. the indentation depth is set to h=0. Figure 1(b) illustrates the absolute position of both indenter and sample, relative displacement results from the subtraction of both displacements at the same acquisition time, which finally gives the indentation depth. The vacuum generation was also evaluated. As required, the turbo-membrane pumping system is able to achieve high vacuum atmosphere with a pressure in the chamber of at least 10^{-5} mbar after approximately 45 min.

First experiments at room and higher temperatures were carried out with the device on unirradiated Eurofer97 samples. Both the tip and the sample are heated locally to avoid substantial heat flow due to a temperature gradient when the contact is realized. A combination of two datasets (force-time and displacement time), using a synchronized time signal, leads to required force-displacement dataset. Figure 2 illustrates a comparison of multicyclic indentation curves measured at several temperatures. The trend is as expected: with rising temperature the material gets softer and therefore, the indentation depth is increased. However, at high temperatures an unexpected behavior of the measured displacement is observed which is mainly illustrated by the oscillation of the displacement values in the unloading part in Figure 2. This phenomenon is highly related to the accuracy of the thermal regulation. Therefore, efforts will be focused on the enhancement of thermal stability during the heating process.

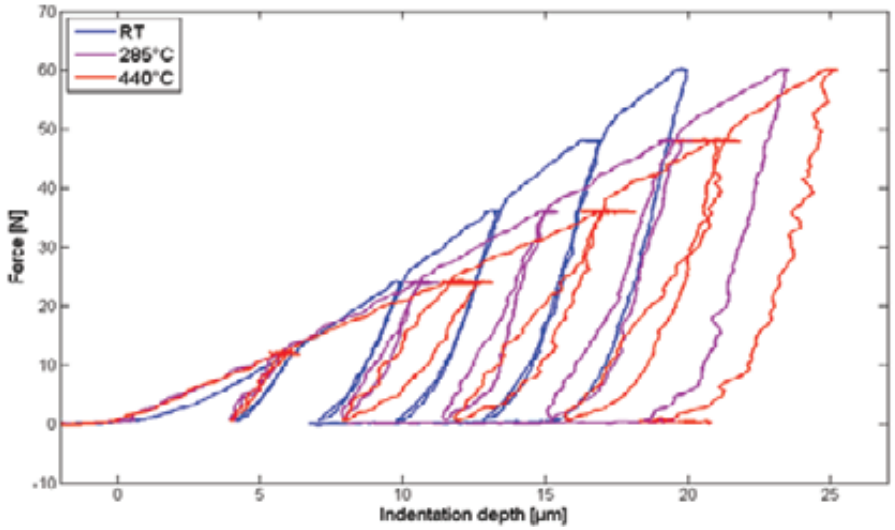

Fig. 2: Multicyclic indentation curves on Eurofer97 at high temperatures.

Additionally, hardness values were calculated by means of the spherical diamond tip (diameter of 400 µm) according to the testing method from standard DIN EN ISO 6506 "Brinell" and the following equation:

$$\mathrm{HBW} = 0.102\,\frac{2P}{\pi D\left(D-\sqrt{D^2-d^2}\right)}$$

where *P* is the applied (here 47,06 N), *D* is the indenter diameter, and *d* the residual impression. A hardness of 2,6 GPa was found at room temperature, and a drop by ca. 30 % is expected when heating up to 440 °C.

After a complete characterization of the temperature-depending mechanical behavior of unirradiated RAFM steels, the indentation device will be installed in a Hot Cell of the Fusion Materials Laboratory to allow investigations on irradiated specimens.

Staff:

B. Albinski
I. Bernstein
M. Holzer
W. Ibbe
S. Lautensack
I. Sacksteder
H.-C. Schneider

Literature:

[1] Sacksteder, I., "Characterization of tungsten from room temperature up to 1000°C by means of the indentation technique" (Lecture), EFDA WP12-MAT-01-IREMEV Monitoring Meeting 3.-5. December 2012, Garching, Germany

[2] Sacksteder, I. ; Albinski, B. ; Bernstein, I. ; Schneider, H.-C. ; Kraft, O., "Une utilisation de l´indentation instrumentée à haute température pour tester des échantillons irradiés" Lecture), Indentation2012, Lyon, 29-31 October, 2012, France

[3] Sacksteder, I,; Hostettler, S.; Charbonneau, G.; Albinski, B.; Schneider, H.-C., "An evaluation of requirements for investigating the temperature dependent fracture behavior of irradiated materials by indentation" (Poster), SOFT 2012 Conference 24.-28. September 2012, Belgium

[4] Albinski, B.; Sacksteder, I.; Schneider, H.-C.; Kraft. O., "High-Temperature Indentation Experiments on Fusion-related Materials" (Poster), SOFT 2012 Conference 24.-28. September 2012, Belgium

[5] Sacksteder I., Albinski, B., "Characterization of RAFM steels up to 650°C by means of the indentation technique" (Lecture), EFDA WP12-MAT-01- IREMEV Monitoring Meeting 13.-21. June 2012, Ljuljana, Slovenia

[6] Albinski, B.; Sacksteder, I.; Schneider, H.-C., "Ein fernhantierter Hochtemperatur-Indenter zur Untersuchung von Materialien für den Fusionsreaktor" (Poster), InnoMateria in Köln, 14.-15. Mai 2012, Germany

Acknowledgement

This work, supported by the European Communities under the contract of Association between EURATOM and Karlsruhe Institute of Technology, was carried out within the framework of the European Fusion Development Agreement. The views and opinions expressed herein do not necessarily reflect those of the European Commission.

Operation of the KIT Fusion Materials Laboratory (CoA)

The Fusion Materials Laboratory provides the infrastructure for the performance of tasks defined in the EFDA and F4E work programmes related to the characterisation and testing of irradiated and non-irradiated materials. Methods such as optical and electron microscopy, tritium adsorption and desorption,, crush load, micro hardness, creep, charpy impact, tensile, LCF and instrumented indentation tests as well as long-time annealing tests are applied. The work includes Post Irradiation Examinations (PIE) of Reduced Activation Ferritic Martensitic (RAFM) steels (reference material for DEMO and ITER-TBMs) and tungsten as well as investigations on materials relevant for the HCPB blanket (ceramic breeder materials, beryllium) and technical aspects (glasses).

PIE on selected samples from the HFR IIB and BOR 60 experiments were performed. For this purpose, in 2012 mostly LCF tests were performed. Tested specimens' small cuts were prepared for LOM, SEM, and TEM and examined. Broken halves of charpy specimens were prepared for instrumented indentation and served for identifying material parameters and Vickers hardness. The aim of the investigations is to study the irradiation effects on the mechanical and structural properties of these materials and to investigate the possibilities of a post-irradiation heat-treatment in order to reduce irradiation defects.

The investigation of functional blanket materials was continued. Lithium orthosilicate pebbles were investigated by LOM and crush-load tested on a newly installed testing device. In addition their porosity and deformation hardness were determined. Different batches of materials were characterised with respect to the influence of parameters of the fabrication process on the mechanical and structural properties. Tritium adsorption / desorption tests and creep tests were done on irradiated and unirradiated beryllium, beryllium vanadium, and beryllium titanium alloys and on BeO-doped beryllium, both on single pebbles and on pebble beds.

Adsorption and desorption experiments were also done with unirradiated beryllium titanium pebbles. Furthermore different beryllium titanium alloys were characterized by LOM and SEM. Porosity measurements and creep tests were performed. Activated beryllium from the HIDOBE irradiation was investigated by LOM and SEM. To produce cross-cuts for LOM and SEM, a multi-step embedding and grinding process of very small and highly radiating Beryllium was developed. For TEM investigations, another new preparation method for the extremely brittle irradiated beryllium was developed, producing thin fragments by crush-test and fixing them on ultra-fine meshes, furnishing images of a quality never reached before on irradiated Be.

The new quadrupole mass spectrometer, able to identify the tritium release and retention of fusion-relevant materials, was used for quantitative analysis of a high number of tritium release experiments (Be of HIDOBE).

For the PIE the following equipment was used:

Charpy impact, LCF and tensile testing devices, indentation device for instrumented ball-indentation, Vickers hardness-test;

LOM, SEM, and TEM with analysis of chemical elements.

Desorption device with high temperature furnace for tritium and helium release measurements, quadrupole mass spectrometer.

He-pycnometer and new sphere crush and creep testing apparatus

Operation of the new 200 kV high resolution TEM for investigation of radioactive material down to atomic scale was continued. Various results, identifying the damage mechanisms in highly irradiated steel an Beryllium, could be published.

The SEM was equipped with a completely new power supply, operating system and analyzing software, combining the adapted handling unit, shielding and transfer-system for highly activated material with state-of-the-art electronics.

Results

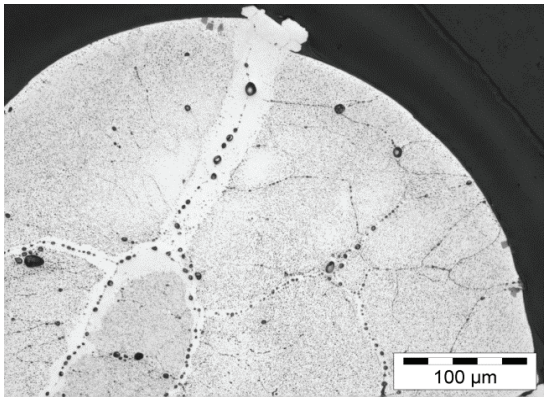

Fig. 1: Open porosity (He) network in irradiated Beryllium pebble, LOM picture after special preparation in metallographic Hot Cell.

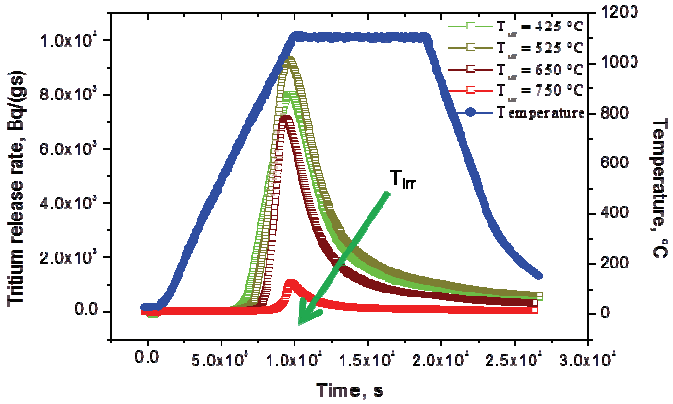

Fig. 2: Tritium release tests on Beryllium for different irradiation temperatures.

Fig. 1 shows the result of the metallographic preparation of Beryllium developed at FML. Clearly visible is open porosity by irradiation-induced forming of Helium/Tritium.

Fig. 2 indicates the Tritium-release by heating the irradiated Beryllium. The tritium-inventory's dependence on the irradiation temperature is obvious: at higher temperatures, "self-release" occurs during the irradiation and the released amount of tritium is comparably low.

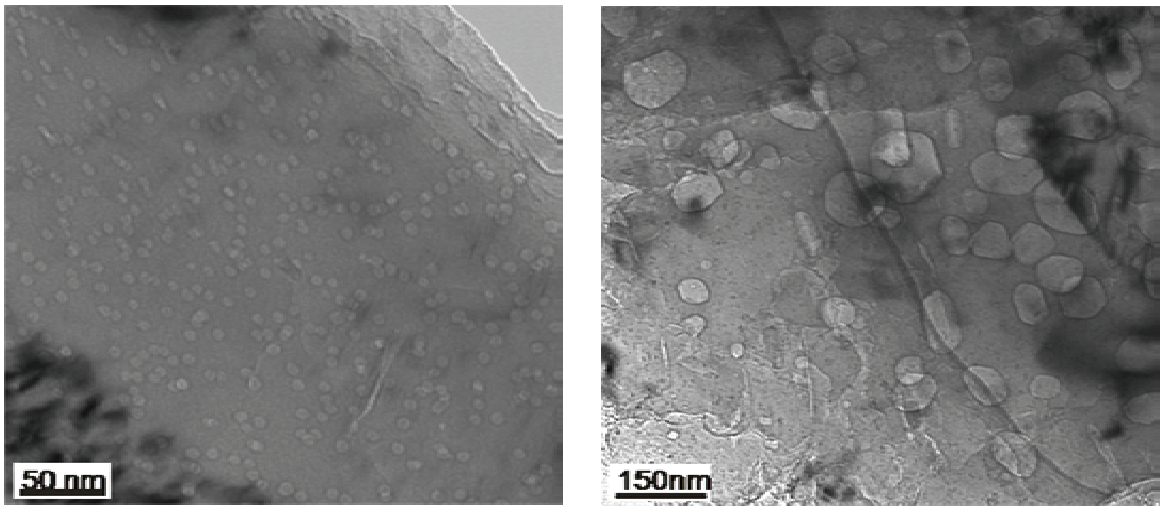

Fig. 3: TEM-Studis of He-Bubbles in 1 mm Ø Be-Pebbles. Left: T_{irr} = 357 °C. Right: T_{irr} = 675 °C.

Fig. 3 shows the dependence of the He formation in Tritium on the irradiation temperature. After irradiation at 357 ºC, helium bubbles have typical diameters of 8 nm, they homogenously distributed in the microstructure forming sometimes chains of bubbles. Some bubbles show an elongated narrow shape of about 4 nm thickness.

After irradiation at 675 ºC helium bubbles are much larger, ranging from 10 to 130 nm. These large bubbles mostly show a hexagonal faceted shape, however unlike the irradiation temperature of 357 ºC only the small part of the bubbles can be identified as disk like shape.

Fig. 4: Indentation device for indentation up to 3 N / 1000 °C.

Fig. 5: Indentation device for indentation up to 200 N / 650 °C.

Fig. 4: the new testing device for high temperature indentation is a unique, custom-designed machine. It was delivered in December 2011 and is actually in validation.

It furnishes first results in tests at elevated temperatures

- up to 1000°C
- in the mN-range
- In the nm-range

The second Example for a new testing device for high temperature indentation is given in Fig. 5. It is a complete FML-development; it is actually to be validated.

It furnishes first results in tests at elevated temperatures

- up to 650°C
- in the 200 N range
- In the 40 µm range by ball-or Vickers-indents

The machine is adapted to sophisticated experiments, furnishing material parameters by neural-network based analysis.

Both machines are designed for remote-handled use in the Hot Cell with highly active specimens.

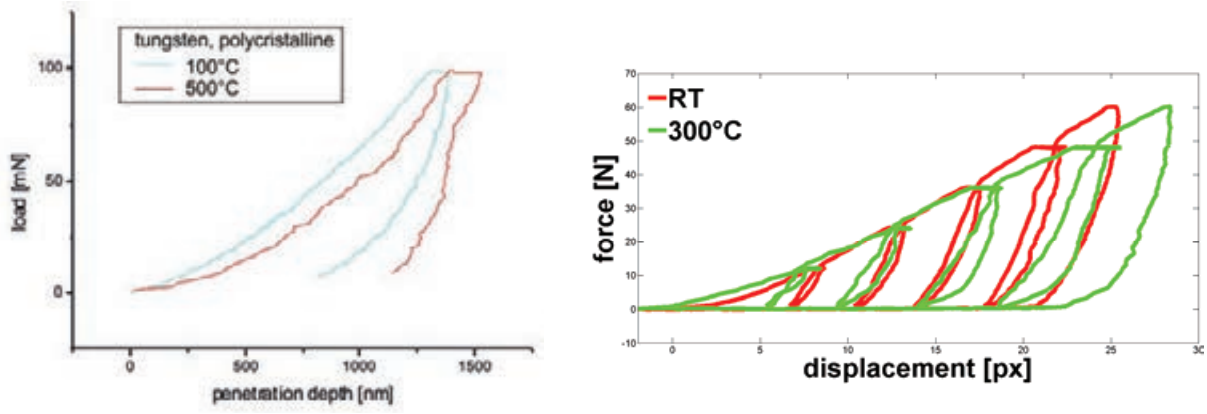

Fig. 6: High-temperature indents in tungsten (left) and in EUROFER97 (right).

Fig. 6 shows on left side first results of high-temperature indentation on polycristalline Tungsten at 2 different testing temperatures, performed on the 3 N / 1000 °C machine.

On the right side, indentation results for EUROFER97, performed on the 200 N / 650 °C machine are displayed.

Staff:

B. Albinski
P. Barié
I. Bernstein
J. Ehrmann
A. Erbe
M. Gilpert
M. Holzer
W. Ibbe
S. Lautensack
G. Mangei
U. Meyer
H. Ries
M. Rietschel
R. Rolli
I. Sacksteder
M. Scherwitz
R. Schmidt
H.-C. Schneider
M. Weber

Literature:

[1] Albinski, B.; Schneider, H.C.; Kraft, O.: Entwicklung und Aufbau einer Hochtemperatur-Indentationsanlage zur Charakterisierung bestrahlter Werkstoffe, Jahrestagung Kerntechnik 2012, INFORUM GmbH, CD-ROM

[2] Annabattula, R.K.; Gan, Y.; Zhao, S; Kamlah, M.: Mechanics of a crushable pebble assembly using discrete element method. Journal of Nuclear Materials 430, 2012, 90 95.

[3] Annabattula, R.K.; Gan, Y; Kamlah, M.: Mechanics of binary and polydisperse spherical pebbles assembly. Accepted, Fusion Engineering and Design, 2012

[4] Klimenkov, M.; Lindau, R.; Materna-Morris, E.; Möslang, A.: TEM characterization of precipitates in EUROFER 97. Progress in Nuclear Energy 57 (2012) 8–13

[5] Weiß, O.J.; Gaganidze, E.; Aktaa, J.: Quantitative microstructural investigation of neutron-irradiated RAFM steel for nuclear fusion applications. Böllinghaus, T. [Hrsg.] Materials Challenges and Testing Supply of Energy and Resources Berlin [u.a.] : Springer, 2012 Part 1, 13-22

[6] Sacksteder, I,; Hostettler, S.; Charbonneau, G.; Albinski, B.; Schneider, H.-C.: An evaluation of requirements for investigating the temperature dependent fracture behavior of irradiated materials by indentation (Poster). SOFT 2012 Conference 24.-28. September, Belgien

[7] Weiß, O.J.; Gaganidze, E.; Aktaa, J.: Quantitative characterization of microstructural defects in up to 32 dpa neutron irradiated EUROFER97. Journal of Nuclear Materials, 426(2012) S.52-58

[8] Materna-Morris, E., Möslang, A., Schneider, H.C.: Tensile and Low Cycle Fatigue Properties of EUROFER97 after 16.3 dpa Neutron Irradiation between 250 and 450 °C. Journal of Nuclear Materials, in press

[9] Gaganidze, E.; Dethloff, C.; Weiß, O.J.; Svetukhin, V.; Tikhonchev, M.; Aktaa, J.: Modeling and TEM Investigation of Helium Bubble Growth in RAFM Steels under Neutron Irradiation. J. ASTM International (2012), DOI:10.1520/STP103972.

[10] Neitzert, E. et al.: FEMaS - CA: Fusion Energy Materials Science - Coordination Action; Final Report, Max-Planck-Institut für Plasmaphysik, Garching

[11] Ying, A.; Reimann, J.; Boccaccini, L.; Enoeda, M.; Kamlah, M.; Knitter, R.; Gan, Y.; Van der Laan, J.; Magielsen, L.; Di Maio, P.A.; Dell'Orco, G.; Annabattula, R.K.; Van Lew, J.T.; Tanigawa, H.; Van Til, S. Status of ceramic breeder pebble bed thermo-mechanics R&D and impact on breeder material mechanical strength. Fusion Engineering and Design, 87(2012), 1130-113

[12] Zhao, S.; Gan, Y.; Kamlah, M.: Spherical ceramic pebbles subjected to multiple non-concentrated surface loads. International Journal of Solids and Structures, 49(2012) S.658-671

[13] Zhao, S.; Gan, Y.; Kamlah, M: Failure initiation and propagation of Li4SiO4l pebbles fusion blankets. Accepted, Fusion Engineering ånd Design. 2012

Corrosion Testing in PICOLO Loop and Development of Coatings as Anti-corrosion and T-permeation Barriers (CoA)

Introduction

In a future fusion reactor with a He-cooled liquid lithium-lead blanket (HCLL), reduced activation ferritic-martensitic steels (RAFM) are considered as structural materials, which are in direct contact with the breeding liquid metal material Pb-15.7Li. For application in DEMO, two critical issues might affect the acceptance of this material. The first one is the compatibility with the breeder and the second one the permeation of tritium into the coolant through the walls. Corrosion testing at the envisaged ITER-TBM operation temperature near 550°C in flowing Pb-15.7Li, showed dramatic corrosion attack of roughly 400 µm/year at a flow velocity of 0.22 m/s [1]. At cooler system areas, precipitations are formed which lead after a short operation time of approx. 3000 h to line plugging. Performed calculation by MATLIM code verified this behavior due to the temperature dependent solubility of corrosion products in liquid Pb-15.7Li [2] very well. However, reliable extrapolation towards system relevant small flow velocities requires additional data points at lower testing velocities. These lacks will be closed by testing of the bare RAFM steel Eurofer at the lower velocities of 0.1 m/s in the present test campaign and later at planned flow velocities near some 0.01 m/s.

In general, by considering all corrosion data available, it is obvious that corrosion attack is always present in a system working with flowing Pb15.7Li at elevated temperatures. Wall thinning, transport of corrosion products and precipitate formation will be present and has to be considered as potential risk as discussed in [3]. A reduction may be seen and given by application of corrosion barriers. As known from earlier examinations Al-based scales [4] may fulfill such criteria and thus more industrial relevant electrochemical Al plating of Eurofer is under progress as well as qualification of processed scales. In this report both topics 1) compatibility testing of bare Eurofer in Picolo and 2) processing of Al-based barriers on Eurofer will be reported.

Corrosion testing in Picolo

The HCLL concept for blankets is based on the application of the liquid breeder Pb-15.7Li which is in direct contact with the structural components, e.g. RAFM-steels. The breeder Pb-15.7Li is circulating in a closed loop with warm and cool components. The compatibility of the steels applied will mainly be determined by their corrosion resistance. At high flow velocities high dissolution rates of ca. 400 µm/year were evaluated at 550°C leading to a high amount of dissolved corrosion products in the Pb-15.7Li. In a TBM system or also in a testing loop, e.g., PICOLO these components are transported with the breeder flow to sections with cooler temperature and will form precipitates as known due to oversaturation. A good data base is existing for low (480°C) and higher operation temperatures (550°), however reliability of corrosion data at medium and small flow velocities are scarce for the preferred Eurofer steel. Qualification of risks and validation of modeling tools need such corrosion data. Thus, a testing program was set up to analyze the material behavior at 0.1 m/s flow velocity and testing times up to 12,000 h.

Operation of Picolo and testing program

Picolo is a Pb-15.7Li testing loop with a total length of ca. 12 m and an inventory of roughly 20 kg Pb-15.7Li. The test section is designed to operate at 550°C and is fabricated from a ferritic-matensitic steel (DIN 1.4914) as well as the other parts in the hot sections. The cooler parts are machined from austenitic steels (e.g., 1.4571). The Pb-15.7Li flow is powered by an electromagnetic pump and is adjustable in the range of roughly 0.01 to 1 m/s. The lowest temperature is about 350°C in the surrounding of the pump, the flow meter and the magnetic trap. The latter is installed to collect magnetic particles moving with the melt.

Cylindrical samples (diameter 8 mm) are exposed in the test section in an arrangement concentric with the Pb-15.7Li flow. The test section has an inner diameter of 16 mm and a length of roughly 450 mm. About 12 samples are screwed together to a testing stack.

The actual test campaign was started in 2011. The test program for this campaign was mainly focused on testing of Eurofer, however, other materials as the Chinese low activation steel CLAM, and Al-coated samples were also exposed to Pb-15.7Li flow at 0.1 m/s. The Al-coated samples were processed using the formerly developed ECA process (**E**lectro-**C**hemical plating by **A**l deposition applying an organic toluene based electrolyte). The longest exposed samples with 12.000 h ware removed at the end of 2012.

Corrosion results

Corrosion attack at 550°C testing temperature and 0.22 m/s flow velocity of Pb-15.7Li was evaluated to be near 400 µm/year of material loss. This corresponds to an amount of roughly 4 kg dissolved Fe/Cr from a square meter Eurofer plate in one year. Some of the Eurofer samples exposed at 0.1 m/s were analyzed in 2012. These short–term exposed samples were analyzed by applying two different methods for diameter determination. The first method was based on a conventional technology by measuring the diameter of the metallographically processed sample (analyzing the cross cutting) after removal from the testing loop. This diameter was set in correlation to the measured value of the fresh sample. The second method used a laser scanning technology for diameter determination. However, the samples had to be etched to remove adherent Pb-15.7Li scales from the cylindrical sample. Both methods delivered comparable values. Fig. 1 shows the evaluated corrosion attack for samples exposed up to 1500 h at 0.1 m/s in comparison with the earlier measured attack at 0.22 m/s. These values coming from short-term exposure are approx. ~250 µm/year. The analyses of the long-term exposed samples will improve the accuracy of the number given above. The evaluation of the first CLAM-steel samples showed, that the corrosion attack for this material is rather similar. All coated samples were designed for long-term exposure and their analyses are now under completion.

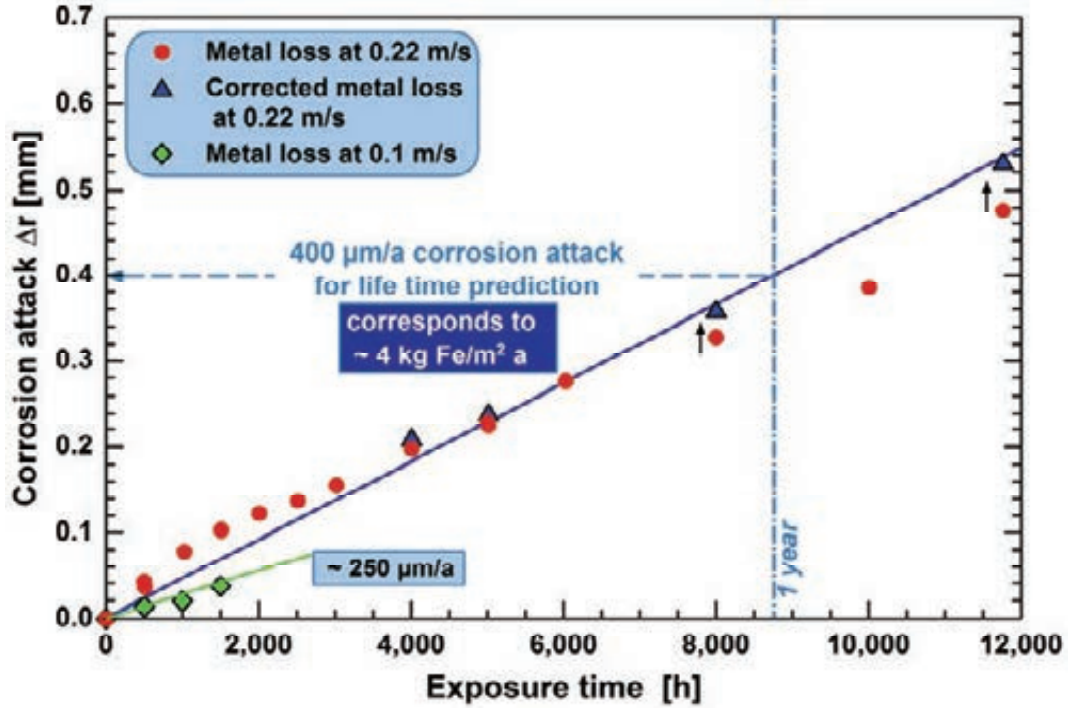

Fig. 1: Corrosion attack of Eurofer dependent on flow velocity at 550°C testing temperature.

Conclusions

The corrosion testing campaign at 0.1 m/s was successfully finished in 2012 with removing long-term exposed samples after 12,000 h as designed. The short-term bare samples were analyzed and showed corrosion attack near 250 µm/year. These values are smaller than the numbers evaluated for 0.22 m/s flow velocity. This behavior (smaller values) is in full agreement with expectations and predictions based on modeling work using the MATLIM code. However, the reliability under long-term view has to be improved by analyzing the other samples with exposure time up to 12,000 h applying the same methods. A first prescreening was done for samples with exposure times near 9000 h. This indicates that corrosion attack was present and that the materials take off is not overestimated by the values given above. The corrosion products are still present at 0.1 m/s flow velocity and the risk of precipitate formation with line plugging is not significantly reduced looking on the ratios in corrosion attack of 400 vs. 250µm/year, respectively.

Corrosion and T-permeation barriers by electrochemically deposited Al coatings and progress in ECX process development

Former research activities had shown the possibility to protect Eurofer steel from corrosion in liquid Pb-17.5Li environment by applying aluminum-based coatings. The first samples were fabricated by dipping the steel into an Al melt for coating and the process was named Hot Dip Aluminization (HDA) [5]. During this process protective scales are formed by appropriate metallurgical reaction and heat treatment. However, coating of Eurofer by HDA exhibited some technological restrictions, especially in the fields of homogeneity, layer thickness distribution and industrial application with complex geometries. To overcome these difficulties an evaluation process indicated that electrochemical deposition processes are an interesting alternative to HDA by providing low deposition temperature and a good control of layer thicknesses (low thicknesses <50µm possible), due to time and current depended layer growth . Therefore the amount of deposited aluminium is highly controllable (low activation criteria).

Due to its high electronegativity, aluminum could not be deposited from common water-based electrolytes, like other common metals e.g. Cu, Ni, Fe and Zn. Therefore water-free (aprotic) electrolytes are required to electroplate aluminum. Such electrolytes should provide electrochemical stability in the envisaged potential window, thermal stability and electrical conductivity. Two promising types of water-free electrolytes were identified in the last years. One is based on toluene and an Al-organic compound, what led to the development of the so called ECA process, while the other one is based on an imidazolium based ionic liquid and $AlCl_3$. The second, rather new process is referred to as ECX process, which promises to be more flexible regarding to deposition parameters and safety issues. The ECX process depicts the latest status of electrolyte development for electrochemical aluminum deposition for fusion applications. However, in both cases, either ECA or ECX, it is necessary to heat-treat the coated steel samples to enable the desired formation of protective aluminide based barrier scales.

Al deposition

In the last years, various scales on Eurofer test samples for corrosion testing in PICOLO loop were produced by ECA and were heat-treated, while optimization of heat treatment is still an ongoing task [6]. These ECA - samples proved the ability of electrochemically deposited scales (generally 20 µm Al) to protect Eurofer steel in flowing Pb-15.7Li in PICOLO loop, during exposition times of up to 5,300 hours. Long-term exposure up to 12,000 h in flowing Pb-15.7Li was executed and the analyzing of the samples is under progress. These results may be used as reference values for the new ECX process with higher ability in coating of inner surfaces.

The investigation of the new and more flexible ECX process focused on determination of proper deposition conditions e.g. suitable current densities, temperatures and surface treatments. In the beginning of the development, electrolytes used were based on lewis-basic mixtures of [Emim]Cl and AlCl3 (0,78:1) However, aluminum layers deposited from such electrolytes tend to form dendrites at edges (Fig. 2 left) and coated Eurofer samples showed nonhomogeneous heat treatment behavior (partial delamination, see Fig 2 right). For this reason lewis-acidic mixtures (1:2, 1:1,5) were introduced. They exhibit a better long-term stability compared to lewis-basic ones and a wider range of applicable current densities. This should lead to shorter deposition times and therefore an enhancement of the efficiency of the ECX process.

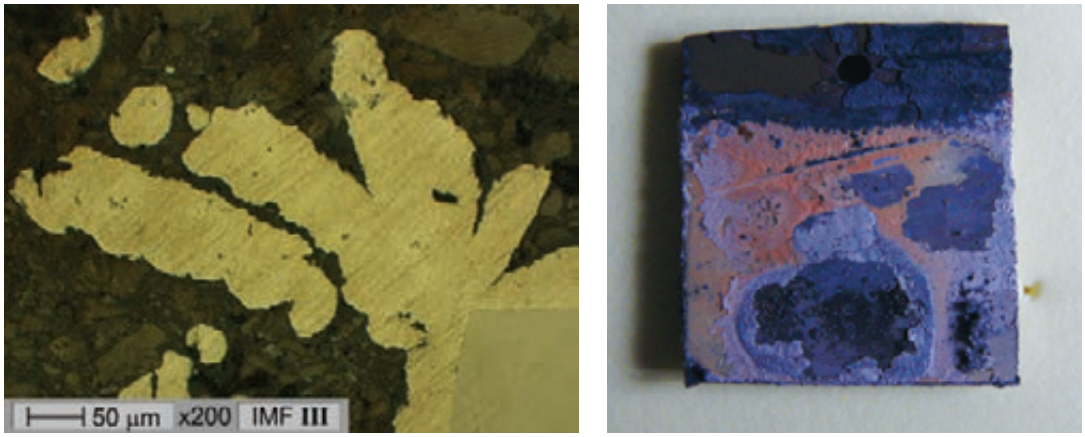

Fig. 2: Electrodeposition from lewis-basic electrolytes: Dendrite growth at edges (left), partial delamination of coating and nonhomogeneous heat treatment behaviour (right).

Results

Al deposition from lewis basic electrolytes

The deposition of Al layers in the field development of barriers applying ECX process was shifted to the application of lewis basic electrolytes due to the facts given above. The work with lewis basic electrolytes showed, that morphologies of the deposited aluminum coatings from ionic liquids strongly depend on deposition conditions as temperature, current density and type of applied current (direct current or pulsed current). As an example Fig. 3 shows the influence of current density on the surface morphology for three different current densities (10, 20 and 25 mA/cm²), while in that case the electrolyte was not agitated. As it could be seen the aluminum morphology by ECX could vary from feather-like structures (left), over more flat, homogeneous structures to cauliflower-like structures (right). These findings lead to the conclusion, that only dense, flat and homogeneous aluminum deposits (by ECX) would be suitable for further heat treatment for producing protective scales on Eurofer steel samples. Therefore on-going work in this field should focus on the control of deposition conditions and process stability. To ensure more homogeneous and dense aluminum deposits first attempts on the application pulsed current (Pulse plating, PP) during Al deposition were made. These experiments provided promising results indicating, that more homogeneous coatings could be produced, compared to samples plated with the same mean current density at direct current conditions (Fig. 4).

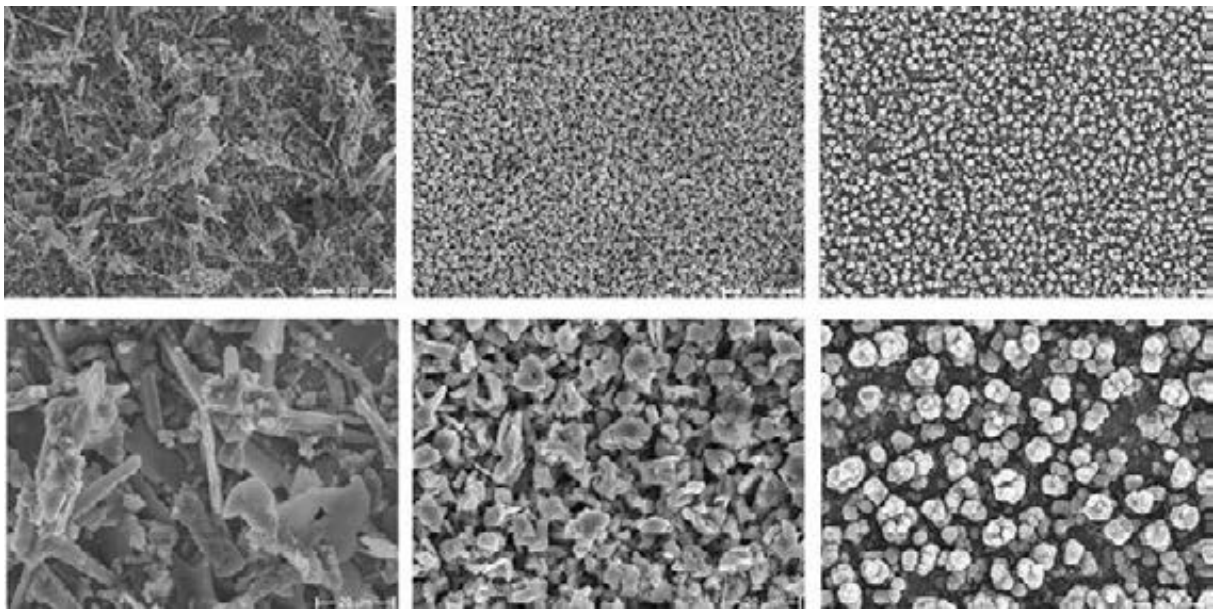

Fig. 3: Influence of current density on the surface morphology of electrodeposited aluminium coatings, from [Emim]Cl:$AlCl_3$ (1:1,5) at 100°C, 10 mA/cm² for 60 min (left), 20 mA/cm² for 30 min (middle) and 25 mA/cm² for 24 min (right). Bottom line: increased magnification.

By choosing the optimized deposition conditions flat and relatively smooth aluminum layers could be achieved by electroplating aluminum from ionic liquids on Eurofer steel (cross section, Fig. 5). Thereby the amount of deposited aluminum (layer thickness) was easily controllable by varying the deposition time (Fig. 5). Clearly visible is that the layers are well adherent on the substrate and that the thickness is proportional to deposition time.

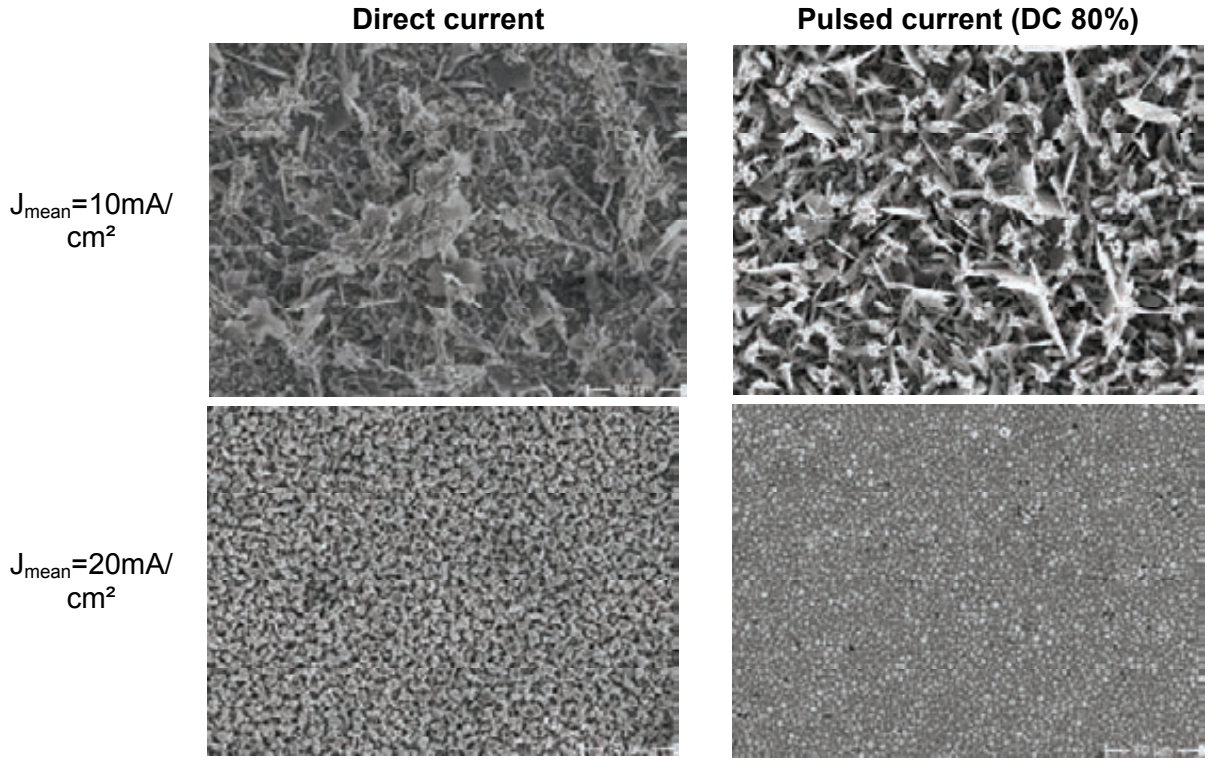

Fig. 4: Dependence of morphology on deposition current.
Left: constant DC; right pulsed DC with same mean current density.

Heat-treating of flat and homogeneous electrodeposits on Eurofer made by ECX process in *lewis-acidic* ionic liquids exhibit better performance of the samples compared to samples deposited from *lewis-basic* electrolytes. However this step is still under intense development and has to be adapted to the morphology of deposited Al layers and geometries, e.g., cylindrical samples as required for corrosion testing in Picolo. First pre-test samples were processed and showed that Al can be deposited homogeneously on the cylindrical surface. The first heat treated samples showed no tendency of spalling. However, more detailed characterization needed is under execution.

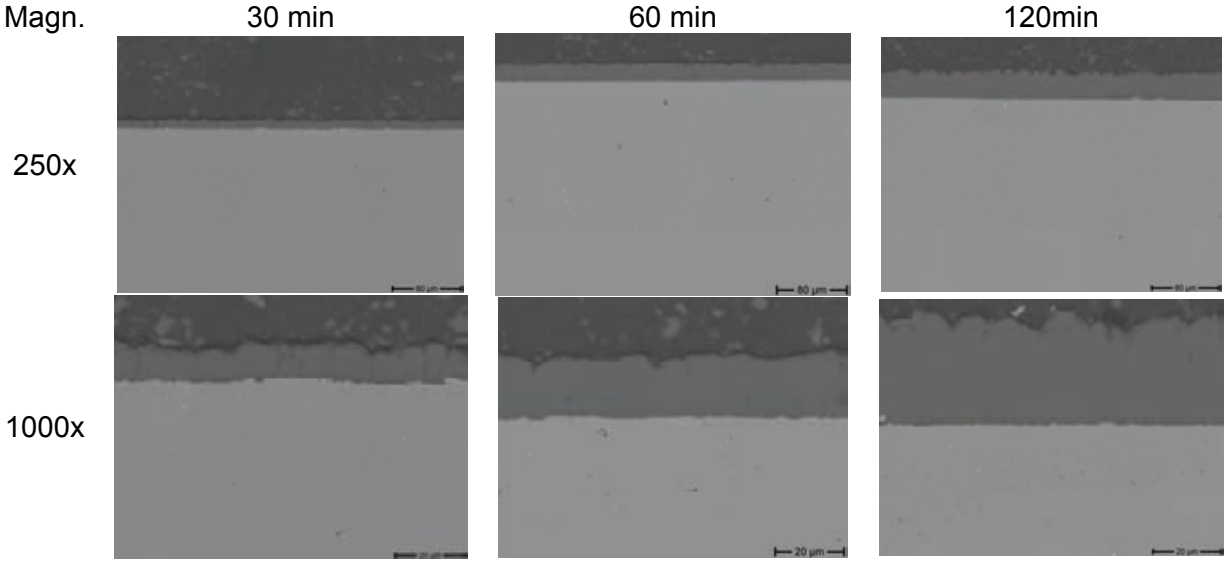

Fig. 5: Time dependence of layer thickness during electrodeposition from [Emim]Cl:$AlCl_3$;used method was Pulse Plating (j_m=20 mA/cm²); substrate: Eurofer (sheet)

Conclusions

The corrosion testing program of Eurofer which was earlier performed at flow velocities of 0.22 m/s at 480 and 550°C exposure temperature was successfully enlarged on a flow velocity of 0.1 m/s at the testing temperature of 550°C. The data evaluated show that corrosion attack is a serious concern and reaches high values of 400 and 250 µm/year at flow velocity of 0.22 and 0.10 m/s, respectively. These data show that corrosion resistant barriers have to be considered for reliable operation of a TBM. Earlier work showed that barriers based on Al scales as fabricated, e.g., by HDA can fulfill the issue corrosion protection and reduction of T-permeation. The development in the field Eurofer coating by electroplating showed that this technology is a real tool to coat steel with Aluminum. Both processes, ECA and ECX, were successfully developed and tested. They outline that Al layer thickness can be controlled and reduced to levels acceptable under low activation criteria. Additionally, with the development of electro-chemically based deposition technologies ECA and ECX a clear step towards industrially relevant coating technologies was done. With the application of pulsed current deposition technology for ECX process a significant progress was achieved in the field controlling of the morphology of Al layers deposited. The heat treatments performed showed that fine grained coating convert to more homogeneous surface scales. This may eliminate defect centers seen in characterization of ECA processed samples. Surely, additional development work is absolutely necessary e.g. in the field of metallurgical heat treatment and optimization of electrolyte parameters with special view on reduced but homogeneous Al scale thickness. Additional measures to be taken up will be initiated by first exposure tests in flowing Pb-15.7Li performed in the Picolo loop, which are the necessary first qualification steps concerning compatibility and stability of the formed barriers.

Staff:

M. Heck
N. Holstein
J. Lorenz
J. Konys
W. Krauss
J. Novotny
O. Wedemeyer
S.-E. Wulf

Literature:

[1] J. Konys, W. Krauss, J. Novotny, H. Steiner, Z. Voss, O. Wedemeyer, Compatibility behavior of EUROFER steel in flowing Pb–17Li, J. Nucl. Mat., 386–388, (2009), 678–681.

[2] H. Steiner, W. Krauss, J. Konys, Calculation of dissolution/deposition rates in flowing eutectic Pb–17Li with the MATLIM code, J. Nucl. Mat., 386-388, (2009), 675-677.

[3] W. Krauss, J. Konys, A. Li-Puma, TBM testing in ITER: Requirements for the development of predictive tools to describe corrosion-related phenomena in HCLL blankets towards DEMO, Fus. Eng. Design, 87 (2012) 403–406.

[4] J. Konys, W. Krauss, Z. Voss, O. Wedemeyer, Comparison of corrosion behavior of bare and hot-dip coated EUROFER steel in flowing Pb–17Li, J. Nucl. Mat. 367-370, (2007) 1144-1149.

[5] J. Konys, W. Krauss, Z. Voss and O. Wedemeyer, Comparison of corrosion behavior of bare and hot-dip coated EUROFER steel in flowing Pb–17Li, J. Nucl. Mat., Vol. 367-370, (2007), 1144-1149.

[6] J. Konys, W. Krauss, N. Holstein, J. Lorenz, S. Wulf, K. Bhanumurthy, Impact on heat treatment on surface chemistry of Al-coated Eurofer for application as anti-corrosion and T permeation barriers in a flowing Pb-15.7Li environment, Fus. Eng. Des. 87, (2012), 1483.

[7] S.-E. Wulf, N. Holstein, W. Krauss J. Konys, Influence of deposition conditions on the microstructure of Al-based coatings for application as corrosion and anti-permeation barrier, 27th Symposium on Fusion Technology (SOFT), Liège, Belgium, Sept. 24-28 (2012).

[8] W. Krauss, J. Konys, N. Holstein, J. Lorenz, Electro-chemical processing for tungsten fabrication and joining by layer deposition, Challenges to Developing W-Based Materials for Fusion Applications, UCSB, Santa Barbara, CA, USA, February 13 – 15, 2012

[9] W. Krauss, J. Lorenz, J. Konys Performance of electro-plated and joined components for divertor application, 27th Symposium on Fusion Technology (SOFT), Liège, Belgium, Sept. 24-28 (2012)

Goal Oriented Training Programme "Fabrication and Characterization of Materials" (WP10-GOT-FabriCharMe (FU07-CT-2010-00065))

The EFDA 2010 Work Programme covers a training activity in the field of Materials Science and Technology called FabriCharMe (Fabrication and Characterization of Materials). The general aim of the training programme is to prepare engineers and scientists for activities to support the ITER project and the long-term fusion programme within the Associations, Fusion for Energy and ITER Organization. The special aim of this training is to provide knowledge and to develop expertise of young engineers to fulfil future duties of structural materials foreseen for in-vessel components in DEMO and TBM of ITER. These materials include the low activation ferritic/martensitic steel EUROFER (foreseen to be used on the ITER TBM), nano-structured low activation Fe-Cr steels and tungsten and copper alloys as structural, heat sink or protective elements. Thus training is needed in the procurement of these materials, managing qualification programmes and guiding the development of the materials. To achieve this, the training includes practical and/or theoretical laboratory activities and educational tasks (formal courses and conferences).

The main activities according the priority area "Materials Science and Technology" are specific issues of structural materials in fusion, e.g. selection of materials, alloy compositions and tailoring of properties, properties and failure mechanism under radiation (hardening, fracture, creep) and the role of gaseous transmutations, especially helium. In addition, modern tools for modelling and simulation of radiation e.g. methods to simulate evaluation of microstructure, advanced characterization methods including electron microscopy, energy dispersive spectroscopy, diffraction methods, and micro-mechanical testing are covered as well as practice in materials technology, e.g. overview on different fabrication processes and joining techniques, qualification of base materials and welds according to nuclear standards, and non-destructive testing.

The whole network consists of 5 associations from 5 different European countries. KIT is hosting the two trainees working in this programme under WP1 and WP2, training topics are focussed on KIT's activities in post-irradiation testing, determining of irradiation damages, appropriate advanced characterization and microstructural investigation techniques, continuum mechanics modelling and design rules including radiation damage, selection and fabrication of materials, and joining techniques. CEA provides the opportunity to work with the SYSWELD analysis software (WP2) and on the Jannus beam line (WP1). IPPLM-WUT is providing training on nanoscale microstructural characterization. CRPP qualified a trainee on small and ultra-small specimen test techniques. CCFE-Oxford gave a training unit on focused ion beam-machined micromechanical specimens.

In 2012, there was the yearly network meeting - with presentations by the trainees and by the mentors of the host associations - on November 12th and 13th, held at CEA. The next network meeting is scheduled for July, 2013 at WUT.

Work package No. 1 (WP1)

Irradiation damage - advanced characterization and modelling
L. Commin, hosted at KIT since April 2011, supervised by A. Möslang
Associated Partners in this programme: CEA, IPPLM-WUT, CRPP
Secondments in 2012: CRPP

In fusion reactors, due to pulsed operation, the combined creep and fatigue loading of structural materials will occur. Therefore, fatigue, creep and creep–fatigue analysis of the candidate structural materials must be performed. Pure fatigue tests have been conducted on Eurofer97 base material and similar electron beam welds, and then fatigue pre-stressed samples at different number of cycles were produced. Microstructural analysis of the samples was done using optical microscopy and SEM.

In a second step, creep analysis on these pre-stressed samples will be performed until fracture occurs. Hence, the damage contributions of fatigue and creep will be studied.

In nuclear fusion reactors, the copper grades currently used for ITER water-cooled divertor will no more be usable, because of their lack in irradiation resistance and thermal strength. Investigation of new copper-based material was then performed and small scale samples produced. The materials investigated are Cu-Mn alloys (Fig. 1 and Fig. 2) and Cu Y_2O_3 dispersed material. Several processing routes (sintering, induction melting, HIP) were studied and the resulting microstructure, microhardness and thermal conductivity were determined [1].

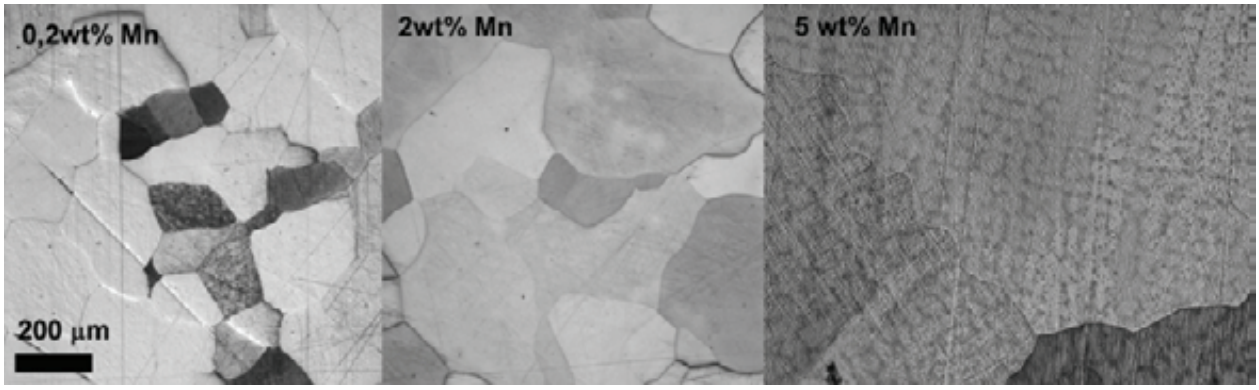

Fig. 1: Microstructure of the Cu-Mn alloys produced by induction melting.

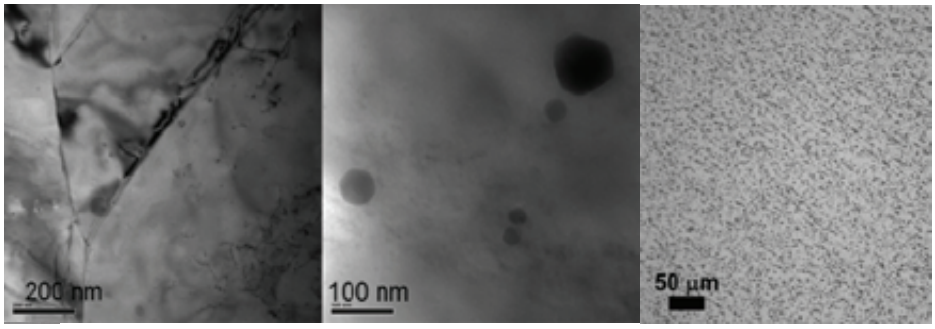

Fig. 2: Microstructure of the Cu-ODS alloys after HIP.

Experiments and finite element simulations have been carried out to assess the warm pre-stressing effects on the effective fracture toughness Eurofer97. The experiments have been conducted on sub-sized compact tension specimens in the low ductile to brittle transition region. The specimens have been pre-loaded at room temperature before being tested at low temperature. The role of the residual compressive stress field, triaxiality level and accumulated equivalent plastic strain respectively on the fracture toughness increase after warm pre-stressing was analyzed [2].

Conclusions

Creep-Fatigue study of Eurofer base materials and welds was initiated. Sample production and fatigue loading was performed. The creep loading will be performed next. A first step concerning processing issues of copper based materials was done. Solution hardened Mn-Copper alloys and Y_2O_3 dispersion strengthened copper alloys were successfully produced. A first composition selection could be drawn from these results and the thermal conductivity capabilities were kept. A further investigation on the irradiation resistance and mechanical properties will be performed. The warm pre-stressing effects on the effective fracture toughness Eurofer97 was assessed and highlighted the role of the residual compressive stress field, triaxiality level and accumulated equivalent plastic strain.

Work package No. 2 (WP2)

Structure Materials and joining development
M. Scherwitz, hosted at KIT since October 2010, supervised by H.-C. Schneider
Associated Partners in this programme: CEA, CCFE-Oxford
Secondments in 2012: CEA

The RAFM steel Eurofer97 is a potential candidate as structural material for in-vessel components of future fusion power plants. During operation it will be subjected to cyclic thermo-mechanical loading and therefore it is necessary to characterize its LCF behaviour. Beside lifetime investigations on the base material, it is also important to characterize the behaviour of its welding joints by considering the various bonding techniques.

In 2012, sub-sized specimens of Eurofer97, including different types of welds as well as without welds, were tested at an application relevant temperature of 550 °C. Diffusion-, Electron Beam-, and Tungsten Inert Gas welds were placed in the centre of the specimens to investigate the influence of welding joints on the fatigue lifetime of components. The semi-finished goods underwent PWHT (760 °C/2 h) before specimen fabrication. All test series were conducted in strain controlled mode with a strain rate of 3*10−3 s−1 and total strain range between 0.4 % and 1.6 %.

PWHT of the EB and TIG joints lead to a reduction of the hardness, but still reveal significant higher strength values compared to the base material. The hardness map of an EB welded joint is shown in Figure 3. The map illustrates several hardness measurements in the welded zone and the surrounding base material. The sample on the left hand side shows the sample in the “as-welded” state. On the right hand side, the sample was PWH treated. The hardness of the base material was not affected by this heat treatment. The hardness values are within the same range. In contrast to the measurements in the base material, the values of the weld zone could be significantly reduced by this heat treatment.

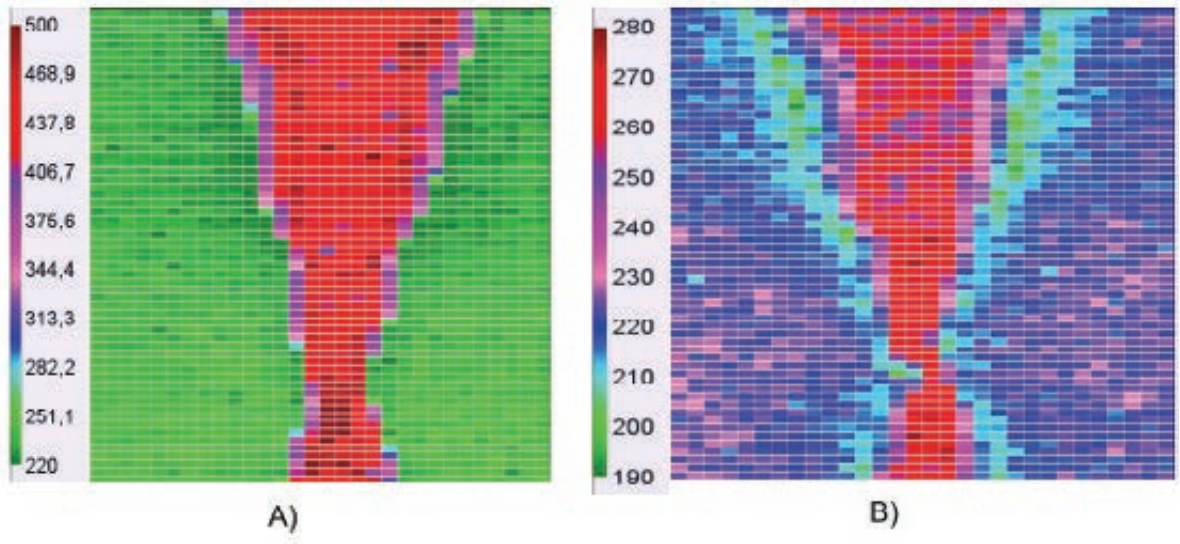

Fig. 3: Hardness maps (HV1) of Electron Beam welded sample for A) “as-welded” and B) heat treated at 760 °C for two hours.

The various LCF tests under equal test conditions showed, that lifetime of specimens, including diffusion- and EB welds, is almost as high as specimens of the base material. TIG specimens showed lower lifetimes compared to the other welds. This can be traced back on clearly higher stress levels monitored during testing, since the controlled gauge length is mostly occupied by the TIG weld (including HAZ).

In comparison, the gauge length of the EB welded specimen includes the narrow welding zone, the HAZ, as well as base material. At diffusion welded specimens the bonding interface is not detectable anymore and the diffusion bonded joints behave almost like base material. Those samples failed statistically distributed along the entire nominal length. According to the different material sections and the respective different local stress-strain fields, TIG and EB welded samples failed within the transition regions of the HAZs and the base material. Further investigations on TIG welded samples are planned for 2013. These tests will show the influence of the weld width within the gauge length.

During a 6 month secondment at CEA Saclay in France the trainee performed some heat treatment simulation by SYSWELD and following experimental validation. The simulations and experiments were carried out on Eurofer97.

The fabrication of joints by welding always results in welding deformation. Deformation can be reduced by clamping, however often not completely prevented. For welding processes with low welding speeds, like TIG, often arises some deformation. This handicaps the adherence of fabrication tolerances. Therefore it is important to get a better understanding of the deformation evolution and the investigation of deformation reduction by local heat treatment. The FEM simulations are carried out with the software SYSWELD. In this calculation thermal and mechanical material properties are respected.

The dimensions of the simulated part are 170 x 50 x 1.6 mm³. Due to the symmetric boundary condition along the weld, the finite element model was reduced to half of the real plate. This saves calculation time. The plate was clamped on one side transversal to the welding direction. This allows the evolution of deformation.

In a first step the TIG weld was simulated to achieve a deformed plate. The deformation depends on the thickness of the welded plate. A thin plate was chosen to obtain large deformations. This simplified the evaluation of the local heat treatment. Afterwards the deformation was reduced by multiple local heat treatment simulations.

The experimental results were validated by real experiments. The plate was fixed by the same clamping conditions and the total dimensions of the real plate are 170 x 100 x 1.6 mm³. We used the same welding equipment for the weld fabrication and the local PWHTs. The speed of the welding gun for the heat treatment was much higher than for the welding. This prevents melting of the material. Additionally, the grain structure was not changed by this heat treatment. Figure 4 shows the fixed plate without welding (A), after welding with large bending deformation (B), and after three local thermal heat treatments (C). It can be seen, that most of the bending deformation could be eliminated by this local heat treatment.

A B C

Fig. 4: Deformation of the plate before welding A, after welding B and after three times of local heat treatment C.

Future activities:

- Continuation of the ongoing work
- Exchange with IPPLM-WUT / PL for WP1
- Exchange with CEA (Jannus) / F for WP1

Staff:

J. Aktaa
L. Commin
A. Möslang
M. Rieth
M. Scherwitz
H.-C. Schneider
P. Vladimirov

Literature:

[1] L. Commin, S. Antusch, et al., Nuclear Materials Conference, Osaka, Japan, Oct 22-25, 2012

[2] N. Ilchuk, L. Commin, P. Spätig, G.R. Odette, SOFT, Liege, Belgium, Sept 24-28, 2012

[3] Antusch, S.; Commin, L.; Müller; M. Piotter V.; Weingärtner, T.: Two component tungsten powder injection moulding – an effective mass production process (Vortrag). 2nd Joint IAEA-EC Topical Meeting, Ispra, Italy, April 16-20, 2012

[4] He, P.; Liu, T.; Möslang, A.; Lindau, R.; Ziegler, R.; Hoffmann, J.; Kurinskiy, P.; Commin, L.; Vladimirov, P.; Nikitenko, S.; Silveir, M.: XAFS and TEM studies of the structural evolution of yttrium-enriched oxides in nanostructured ferritic alloys fabricated by a powder metallurgy process, Materials Chemistry and Physics, 136(2012), 990-998

[5] Reiser, J., Commin, L.; Rieth, M.; Hoffmann, A.: Ductile tungsten (W) pipes for divertor applications (Poster). SOFT, Liege, Belgium, Sept 24-28, 2012

[6] Widak, V.; Commin, L.; Grydin, O.; Rieth, M.: Investigations of dissimilar welds of the high temperature steels P91 and PM2000 (Poster). SOFT, Liege, Belgium, Sept 24-28, 2012

[7] Scherwitz, M.; Walter, M.; Aktaa,J.; Schneider, H.-C.: Low cycle fatique behavior of Eurofer97 welding joints (Poster). SOFT 2012 Conference 24.-28. September, Belgium

Acknowledgement

This work, supported by the European Communities under the contract of Association between EURATOM and Karlsruhe Institute of Technology, was carried out within the framework of the European Fusion Development Agreement. The views and opinions expressed herein do not necessarily reflect those of the European Commission.

Structural Materials - Refractory Alloys

Coordination of the EFDA Fusion Materials Topical Group (WP12-MAT-01-HHFM-03-05)

During the reporting period the EFDA program 2012 on high heat flux materials development was compiled and evaluated. The according proposals were assessed. In several working and monitoring meetings the progress was monitored and discussed. The results of the Topical Group were published in a review article [1]. The final activity was the formulation of the next program for 2013 and the coordination of the calls for participation and task agreements.

Staff:

M. Rieth

Literature:

[1] M. Rieth, S.L. Dudarev, S.M. Gonzalez de Vicente, et al., Recent progress in research on tungsten materials for nuclear fusion applications in Europe, Journal of Nuclear Materials 432 (2013) 482–500.

Acknowledgement

This work, supported by the European Communities under the contract of Association between EURATOM and Karlsruhe Institute of Technology, was carried out within the framework of the European Fusion Development Agreement. The views and opinions expressed herein do not necessarily reflect those of the European Commission.

Armour Materials - Fabrication of Different Armour Prototype Materials by PIM (WP12-MAT-01-HHFM-01-01)

Objectives of the task

This activity is in close cooperation with WP12-MAT-01-HHFM-04-04/KIT/PS. The task includes the fabrication of a variety of different armour prototype materials by Powder Injection Molding (PIM) and the basic characterization.

State of the art PIM R&D

In 2011 two new tungsten alloy feedstocks (W-2La_2O_3 and W-2Y_2O_3) were developed and parts via PIM produced. The results of the characterization are promising [1]. But both materials are produced by mechanical alloying. This needs a lot of time and is expensive. The idea for this investigation was therefore to produce the materials only by mixing, without mechanical alloying. Two new materials by using promising ODS powders are developed and small prototype plates produced via PIM. Also a new heat-treatment process, consisting only of high temperature sintering was used. The basic characterization of the mechanical and physical properties, the microstructure as well as the high heat flux testing in progress.

Development of Feedstock

Two powders of pure tungsten, with an average grain size distribution in the range of 0.7 µm (W1) to 1.7 µm (W2) Fisher Sub-Sieve Size (FSSS) were used for preparation of binary tungsten powder particle systems. The mixtures consist of 50% W1 + 50% W2. The particle size of the powders for the preparation of the doped tungsten alloys was for the Lanthanum Oxide (La2O3) powder, 2.50 µm and for the Yttrium Oxide (Y2O3) powder, 1.50 µm. The characteristic data of the powders are summarized in Table 1.

Table 1: Particle Size Distribution and BET Surfaces of the Used Powders.

Powder	Particle Size µm FSSS	D10 µm	D50 µm	D90 µm	BET Specific Surface m^2/g
Tungsten (W1)	0.70	0.14	0.47	1.25	1.27
Tungsten (W2)	1.70	0.55	1.80	4.91	0.43
Lanthanum oxide (La_2O_3)	<1.50	0.41	1.17	4.32	11.10
Yttrium oxide (Y_2O_3)	<2.50	0.35	1.58	3.67	13.91

The two different doped tungsten alloys were produced only by mixing. For the first composition (W-2La_2O_3) the binary tungsten powder particle system (50% W1 + 50% W2) was doped with 2 wt.% La_2O_3 powder and for the second (W-2Y_2O_3) with 2 wt.% Y_2O_3.

The most critical point of the feedstock preparation is a homogeneous distribution of agglomerate free powder in the binder matrix. After heating the powders at 80 °C for removing moisture a portion was mixed with a 50 vol.% wax/thermoplastic binder system in a kneader (Brabender, Germany) at 120 °C. After that, the feedstocks were then compounded and granulated.

Producing of parts

The injection molding of the small plates was carried out on an ELEKTRA injection molding machine at a feedstock temperature of 160 °C and a mold temperature of 50-60 °C.

After injection molding and before heat-treatment the green parts have undergone solvent debinding. At first solvent debinding in n-Hexane for 48 hours at 50 °C followed by thermal

debinding for ½ hour at 550 °C in dry H_2 atmosphere. The sintering was realized by PLANSEE SE (Reutte, Austria). The debinded plates are sintered at 2400 °C in dry H_2 for 2 hours. Figure 1 shows the green parts and finished parts after heat-treatment.

Fig. 1: Finished plates: green parts (left) and after heat-treatment (right). The shrinkage is nearly 20%.

Results of the basic characterization

The basic characterization was part of a short stay programme (October until December 2012) at the University of Oxford in the Department of Oxford Materials and is in progress. That includes the following methods of analysis: microstructure (FIB), crystal orientation (EBSD), hardness (Nanoindentation) and mechanical testing (4-Point-Bending-Tests). First results of the microstructure, performed by using a Zeiss AURIGA FIB (Carl Zeiss AG, Germany) are shown in Figures 2 and 3. In both materials the embedded particles (La_2O_3, respectively Y_2O_3) are homogeneous around the tungsten grain boundaries and act as grain grow inhibitor.

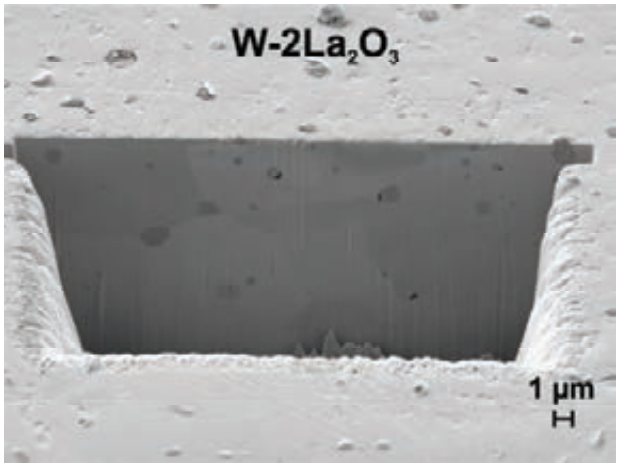

Fig. 2: SEM image of the W-2La_2O_3 microstructure.

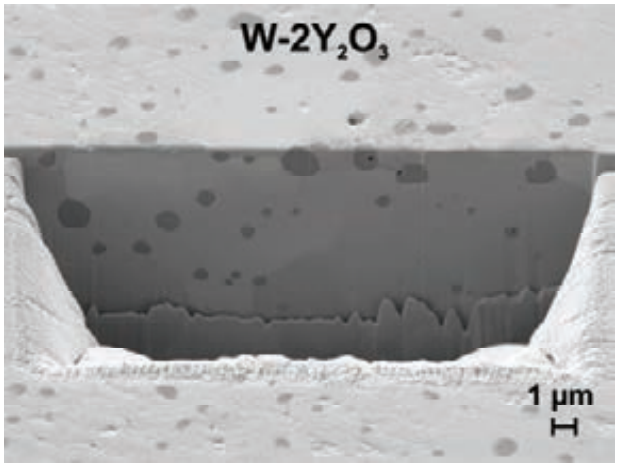

Fig. 3: SEM image of the W-2Y_2O_3 microstructure.

Conclusions and outlook

The motivation for this work was the investigation of prototype materials produced by PIM. The microstructure of the finished samples shows a homogeneous allocation of the embedded particles in the tungsten matrix. The tungsten grains are small, because the embedded particles acts as grain grow inhibitor. These first results show that the producing of the powders only by mixing was successful.

The basic characterization is ongoing. Also further steps on the investigation of the material properties via HHF-tests in cooperation with the colleagues from FZ Jülich and IPP Garching is envisaged.

Industrial cooperation

The high temperature sintering was realized by the PLANSEE SE Company (Reutte, Austria).

Staff:

S. Antusch
D.E.J. Armstrong (Oxford Materials, Oxford, UK)
L. Commin
T. Hanemann
W. Knabl (PLANSEE SE, Reutte, Austria)
M. Offermann
V. Piotter
M. Rieth
S.G. Roberts (Oxford Materials, Oxford, UK)
H. Walter

Literature:

[1] S. Antusch, M. Müller, P. Norajitra, G. Pintsuk, V. Piotter, H.-J. Ritzhaupt-Kleissl, T. Weingärtner, Two component tungsten Powder Injection Molding for mass production of He-cooled DEMO Divertor parts. Journal of Fusion Science and Technology 62 (2012), 110-115.

Acknowledgement

This work, supported by the European Communities under the contract of Association between EURATOM and Karlsruhe Institute of Technology, was carried out within the framework of the European Fusion Development Agreement. The views and opinions expressed herein do not necessarily reflect those of the European Commission.

Mechanical Characterisation of W-armour Materials (WP12-MAT-01-HHFM-01-02)

Background and Objectives

Tungsten and tungsten alloys are presently considered for helium cooled divertor and possibly for the protection of the helium cooled first wall in DEMO designs, mainly because of their high temperature strength, good thermal conductivity, and low sputter rates. There are two types of applications for these materials which require quite different properties: one is the use as plasma-facing armour or shield component, the other is for structural purposes. An armour material needs high crack resistance under extreme thermal operation condition while a structural material has to be ductile within the operation temperature range. Both material types have also to be stable with respect to high neutron irradiation doses and helium production rates.

The protection materials development part focussed on an optimisation of armour materials and high heat flux testing. Candidate materials have to be characterised by fatigue and shock tests for an assessment of their possible lifetimes. Additionally, basic mechanical characterisations have to be performed on new developed materials, to support the alloys optimisation processes.

Activity 1, Armour Materials, Characterisation of W-ODS alloys: The objective is a mechanical characterization of selected W-ODS materials, based on tensile tests, LCF tests and TMF xtests in the interesting temperature region for fusion applications (up to 1600 °C).

Status

The first new developed W-ODS materials: W-2Y (provided by PSI-CRPP), WCr10Si10 and WCr12Ti2.5 (both provided by CEIT, Spain) were mechanically investigated by tensile and 3-point-bending tests.

In the first Quarter of 2012 CEIT provided a second small ingot from WCr12Ti2.5 for validation of the previous results. The material was manufactured by mechanical alloying in combination with a post HIP process (1300°C, 1h, 200 MPa). Sub-sized specimens for 3-point-bending tests were fabricated by EDM technique and tested.

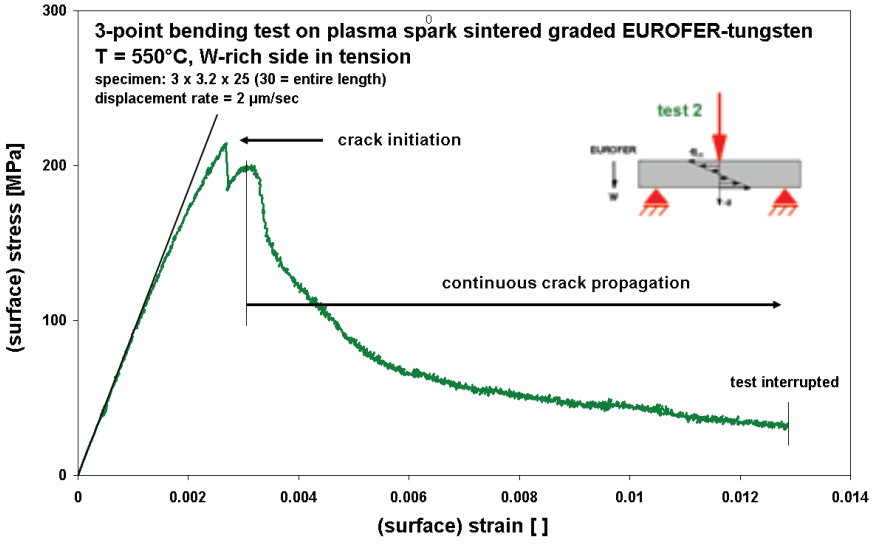

Fig. 1: Results of 3-point bending tests on WCr12Ti2.5.

Compared to the first charge it is found, that the second charge reveals a lower strength. However, when analysing the results from both charges one may assume, that the ductile to brittle transition behaviour is not significantly affected by manufacturing depending fluctuations of the mechanical properties. Accordingly, the DBTT (ductile to brittle transition temperature) can be determined within the range of 900° and 950°C as one can see in the following diagram, Fig. 1.

Besides, two small samples from plasma spark sintered graded EUROFER-tungsten were provided by MEdC (Romania). In order to get a first impression of the mechanical behaviour of the graded alloy, 3-point-bending tests were performed at an application relevant temperature of 550°C. In the first test, the specimen was mounted within the test set-up in a way that the W-rich side was loaded in compression and the EUROFER-rich side was loaded in tension. In the second test, the specimen was turned so that the W-rich side was loaded in tension and the EUROFER-rich side was loaded in compression (see insertion [Fig. 2]). It is found, that an increasing loading of the W-rich side in compression is leading to a continuous hardening of the material after yielding without any damage (Fig. 2 – blue curve). In contrast, an increasing loading of the W-rich side in tension is leading to an onset of failure after low plastic deformation at a significantly low stress level (Fig. 2 – green curve).

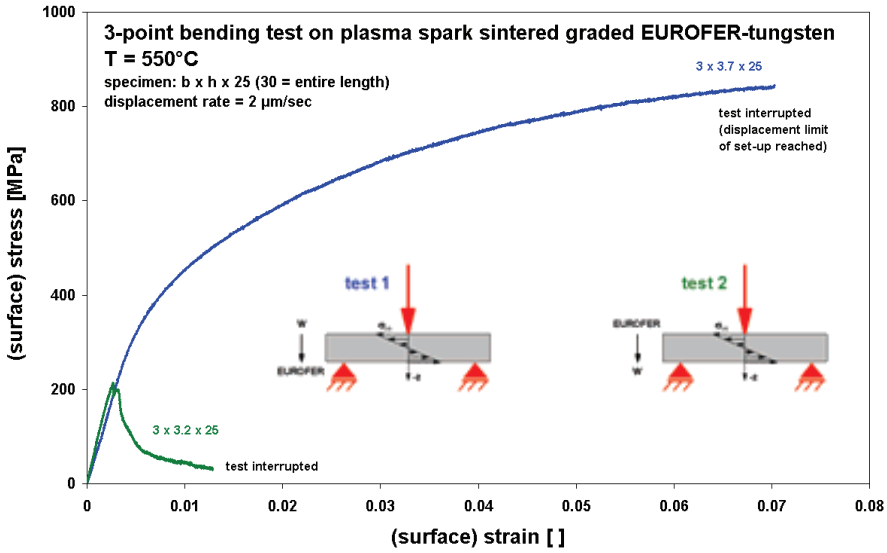

Fig. 2: Results from 3-point-bending tests on a graded EUROFER-tungsten alloy.

However, the specimen does not fail abrupt. After crack initiation, a continuous crack propagation with increasing loading is observable as illustrated in (Fig. 3) in more detail. Based on the general mechanical behaviour of both EUROFER and tungsten one may assume, that the fracture toughness is increasing from the W-rich side towards the EUROFER-rich side. Accordingly, the crack is growing stepwise with increasing load.

Conclusion and Outlook

For validation, 3-point-bending tests on samples from a second charge from WCr12Ti2.5 were performed. It is found, that the second charge reveals a lower strength compared to the first charge. However, when analysing the results from both charges one may assume, that the ductile to brittle transition behaviour (DBTT: 900°-950°C) is not significantly affected by manufacturing depending fluctuations of the mechanical properties.

Additionally, 3-point-bending tests on samples from plasma spark sintered graded EUROFER-tungsten were conducted at 550°C. Based on the test performance it is found, that an increasing loading of the W-rich side in compression leads to a continuous hardening of the material after yielding without any damage, whereas an increasing loading of the W-rich side in tension leads to an onset of failure after low plastic deformation at a significantly low stress level, followed by a stepwise crack growth.

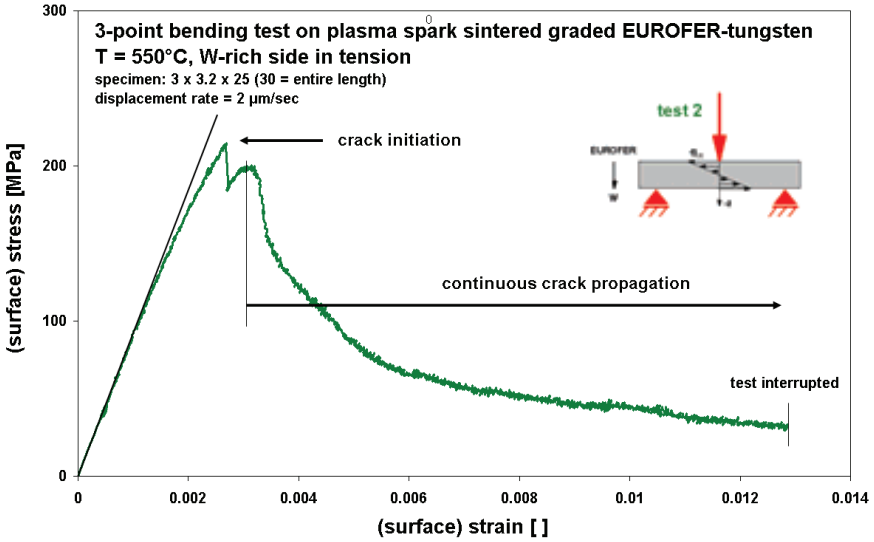

Fig. 3: Deformation and failure behaviour of a graded EUROFER-tungsten alloy under 3-point-bending loading – W-rich side in tension.

It is planned to continue the mechanical characterization of the investigated tungsten alloys in 2013. Beside additional bending tests on the alloys provided by CEIT, in particular WCr12Ti2.5 should also be tested in tensile experiments. Therefore, CEIT currently tries to manufacture some bigger ingots.

Staff:

M. Walter

Acknowledgement

This work, supported by the European Communities under the contract of Association between EURATOM and Karlsruhe Institute of Technology, was carried out within the framework of the European Fusion Development Agreement. The views and opinions expressed herein do not necessarily reflect those of the European Commission.

Mid-term Structural Materials (WP12-MAT-01-HHFM-02-01)

This activity is aimed at studying copper based materials for water cooling divertor applications.

Introduction

In a fusion reactor, the structural lifetime of pure copper would be limited by its high creep and swelling rate as well as by irradiation hardening and possibly helium embrittlement. Therefore, high strengthening and irradiation resistance improvement of copper-based materials is required. At the same time, this should not be too detrimental to the thermal conductivity of the material since copper alloys are used as heat sinks.

The copper alloys considered as candidates for fusion applications can be divided into two groups: (1) precipitation hardened alloys and (2) dispersion strengthened alloys. The high density of small particles is used to improve void swelling and mechanical strength and to provide high sink strength for the recombination of vacancies and interstitials produced during neutron irradiation.

Precipitation hardened alloys like Cu-Cr-Zr grades have been chosen for ITER and they can likely be used as a structural material in the temperature range of 200-350°C. However, under irradiation conditions the same problems will arise as with pure copper above 280°C due to radiation-enhanced precipitate over-aging and softening effects.

Dispersion strengthened alloys using alumina particles (GlidCop types) were investigated and could present better properties such as a high stability under irradiation and under higher temperatures. The fine particles are hard and thermally stable even at temperatures approaching the melting point of the copper matrix. The fine dispersion of the alumina particles in the copper matrix also prevents from recrystallization (with a dependence on the particles size and distribution). However, it has been reported that the ductility and low cycle fatigue properties of GlidCop alloys are weak at elevated temperatures.

Materials, Study and Results

Solution hardened Mn-Copper alloys (Figure 1) were produced using induction melting for several Mn content from 0.2 to 5 wt%. The analysis of the resulting materials showed a good density (98%) and dissolution of Mn in the Cu matrix. The thermal conductivities of the alloys produced were measured in the range of room temperature to 1000°C. It proved that up to 1 wt% Mn the thermal conductivity is still in the range of the alloys currently considered for ITER. Microhardness measurements showed about 25% increase compared to pure copper.

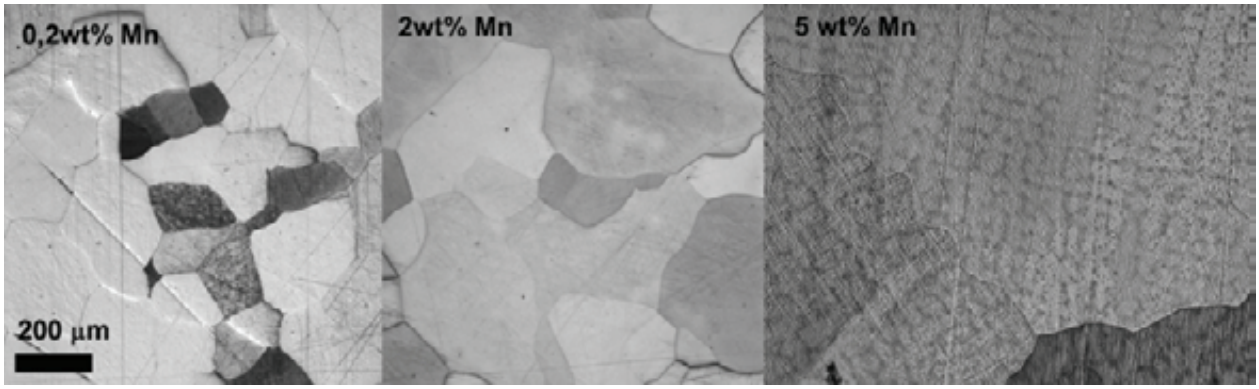

Fig. 1: Microstructure of the Cu-Mn alloys produced by induction melting.

2wt% Y_2O_3 dispersion strengthened copper alloys were produced using mechanical alloying and HIP at 900°C, 100MPa (Figure 2). The analysis of the resulting material showed a density of 95% and TEM exhibited a good dispersion of the nanoparticles (Figure 2). Microhardness measurements showed about 90% increase compared to pure copper.

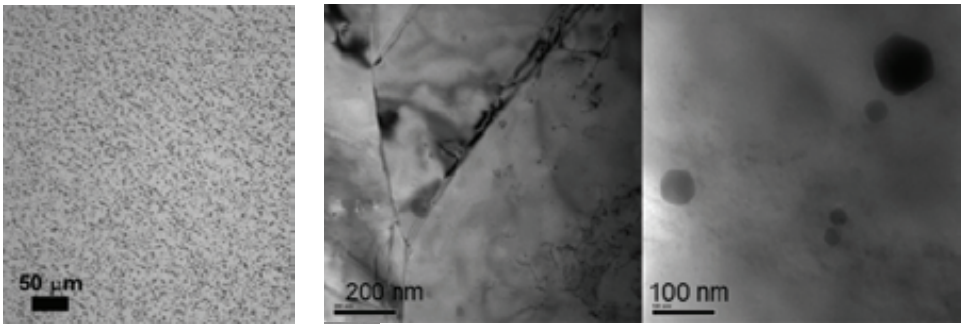

Fig. 2: Microstructure of the Cu-ODS alloys after HIP.

Conclusions

A first step concerning processing issues of copper based materials was done. Solution hardened Mn-Copper alloys and Y_2O_3 dispersion strengthened copper alloys were successfully produced. A first composition selection could be drawn from these results and the thermal conductivity capabilities were kept. A further investigation on the irradiation resistance and mechanical properties will be performed.

Staff:

S. Antusch
D. Bolich
L. Commin
B. Dafferner
W. Goldacker
M. Hoffmann
U. Jäntsch
P. Lukits
M. Rieth
H. Zimmermann

Literature:

[1] L. Commin, S. Antusch, W. Goldacker, P. Lukits, M. Rieth, D. Bolich, M. Hoffmann, Nuclear Materials Conference, Osaka, Japan, Oct 22-25, 2012

Acknowledgement

This work, supported by the European Communities under the contract of Association between EURATOM and Karlsruhe Institute of Technology, was carried out within the framework of the European Fusion Development Agreement. The views and opinions expressed herein do not necessarily reflect those of the European Commission.

Reduced Activation Stainless Steels (WP12-MAT-01-HHFM-02-02)

Introduction

In the new EFDA DEMO roadmap a water-cooled divertor, based on the ITER design (CuCrZr pipes with attached tungsten monoblocks), is specified as base-line concept. To mitigate the risks due to the unknown behavior of CuCrZr under fusion-relevant neutron irradiation, in the roadmap backup solutions are strongly recommended. Therefore, the investigation and development of copper composite materials is considered as an important part of the DEMO divertor R&D programme.

High heat flux (HHF) tests with prototype cooling structures (MAT-HHFM-05-01/KIT/PS) have shown that austenitic stainless steels could meet the requirements necessary to reinforce CuCrZr pipes. The restrictions are: (1) Due to their high thermal expansion and low heat conductivity, such steels can be used in thin layers only. (2) They have to be stabilized (i.e. precipitation hardened) in order to avoid swelling. (3) The available commercial grades are high activating. While the first point can be addressed by design, the remaining issues were part of the present activity.

Commercial Materials

The most used austenitic stainless steels are part of the AISI series 304 (Cr-Ni steels) and 316 (Cr-Ni-Mo steels) which come in many variants whith slightly changed compositions and/or additions. The basic variants, 1.4301/304 and 1.4401/316, are within the same strength regime and both are qualified and licensed for pressure vessel construction. The 316 steel with its higher Ni content and Mo addition shows better corrosion resistance compared to the 304 steel. 316LN (or 1.4429) is the variant with the highest strength, operating temperature, and corrosion resistance while 316Ti (or 1.4571) shows the lowest swelling rate under neutron irradiation which is the main reason for its preferred use in nuclear applications. Another group of austenitic steels are the so-called 15-15 steels (it means 15 wt.-% Cr + 15 wt.-% Ni) which have been considered and modified for their use as cladding materials in nuclear fission reactors. Within this group, the steel 1.4970mod was optimized for low swelling rates and high temperature strength. While in the 1.4970mod steel Ti and small amounts of B were added to form stabilizing carbide precipitates, the 1.4981 steel is alloyed with Nb which forms NbC precipitates.

Table 1: Specifications of the chemical composition (without trace elements and impurities) for some commercial austenitic steels (in wt. %). The European standard notation (1.4XXX) and the ASTM/AISI denominations (where defined) are given in the head line.

	1.4301 304	**1.4401 316**	**1.4429 316LN**	**1.4571 316Ti**	**1.4981**	**1.4970 mod**
C	≤0.07	≤0.07	≤0.03	≤0.08	≤0.1, ≥0.04	0.08 – 0.10
Si	≤1	≤1	≤1	≤1	0.3 – 0.6	0.7 – 0.9
Mn	≤2	≤2	≤2	≤2	≤1.5	1 – 2
Cr	17 – 19.5	16.5 – 18.5	16.5 – 18.5	16.5 – 18.5	15.5 – 17.5	14 – 16
Ni	8 – 10.5	10 – 13	11 – 14	10.5 – 13.5	15.5 – 17.5	14 – 16
Mo		2 – 2.5	2.5 – 3	2 – 2.5	1.6 – 2	1.3 – 1.7
Nb					10 x %C, ≤1	
B						0.004 – 0.008
N			0.12 – 0.22			
Ti				5 x %C, ≤0.7		0.3 – 0.5

The specifications of these austenitic steels are given in Table 1. Their phase points are indicated in the Schaeffler diagram in Fig. 1.

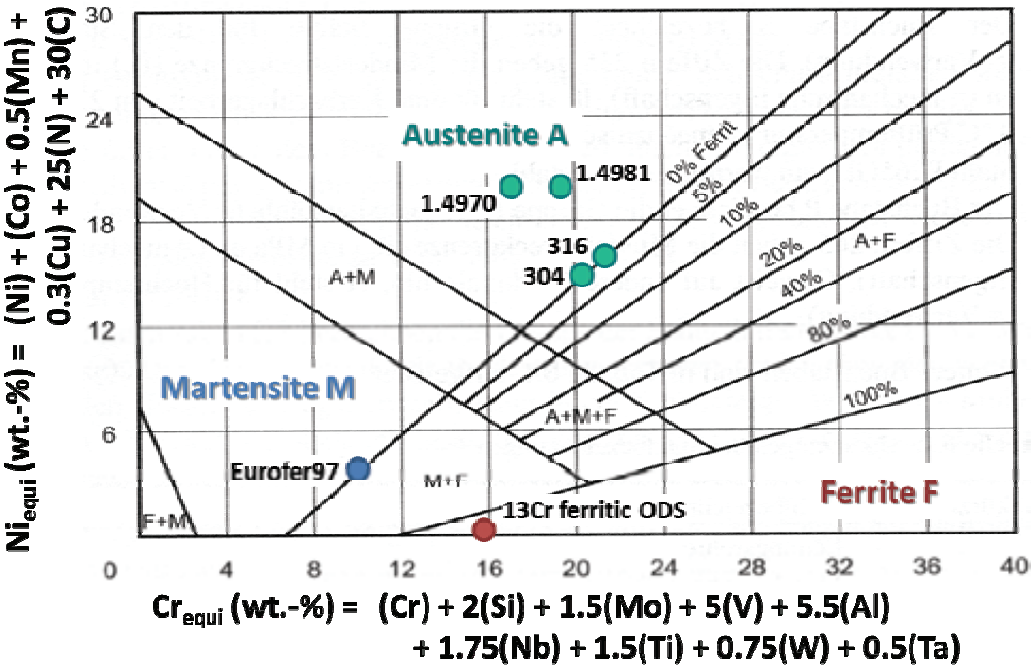

Fig. 1: Schaeffler diagram (chrome and nickel equivalents). The phase points of typical steels for nuclear applications are indicated in the diagram.

It can be clearly seen that the chemical compositions of the 304 and 316 steels are tailored to meet the minimum requirements for a complete formation of the austenite phase. That is, their phase points appear directly at the verge to ferrite formation. As a consequence, the austenite phase is not quite stable. Especially after deformation (e.g. cold work), but also under neutron irradiation, 304 and 316 steels can develop significant ferrite fractions. This is useful for large batch fabrication of semi-finished products (the soft ferrite phase suppresses hot-cracking) but it also restricts the applicability. The situation is different for the 15-15 steels. Their phase points are placed well within the stable austenite regime (see Fig. 1). Therefore, they are more stable under irradiation but the production of large-scale semi-finished products is limited.

Irradiation Data

One of the most significant drawbacks of austenitic steels in nuclear applications is their high swelling rate (compared to ferritic steels). Swelling of austenitic steels is strongly temperature dependent and shows a peak between 550 °C and 650 °C (see Fig. 2, upper diagram). Figure 2 shows also that swelling can be clearly reduced by two methods: (1) by cold work, typically in the range of 5-20 % and (2) by the formation of small precipitates, that is, by specific additions in the chemical compositions. The effect of the second point is demonstrated in Fig.2 (lower diagram). The addition of Ti (in 316Ti and 1.4970) or Nb (in the 1.4981 steel) leads to the formation of TiC or NbC and more complex precipitates which stabilize the steels. Therefore, compared to the 316 steel, swelling is much lower in 316Ti, and is even more suppressed in the 1.4970 and 1.4970mod steels.

Reviews of irradiation tests on 304 and 316 (316L and 316LN) steels have been reported, for example, in [1, 2] from which the following important conclusions can be drawn. (1) Above 400°C annealing of irradiation damage occurs and uniform elongation (a measure for ductility) starts to increase. (2) Below 500 °C irradiation hardening and above 500 °C softening is observed with a saturation dose of 20 dpa. (3) A minimum of uniform elongation appears around 325 °C. (4) At about 200 °C and below, ductility (uniform elongation) starts to improve

slowly. Table 2 gives some values in the lower temperature and dose range. It is remarkable that after neutron irradiation to 10 dpa at 200 °C the 316L steel shows still ductility (uniform elongation) of more than 10 % while its yield strength has increased from 250 MPa (unirradiated) to over 700 MPa.

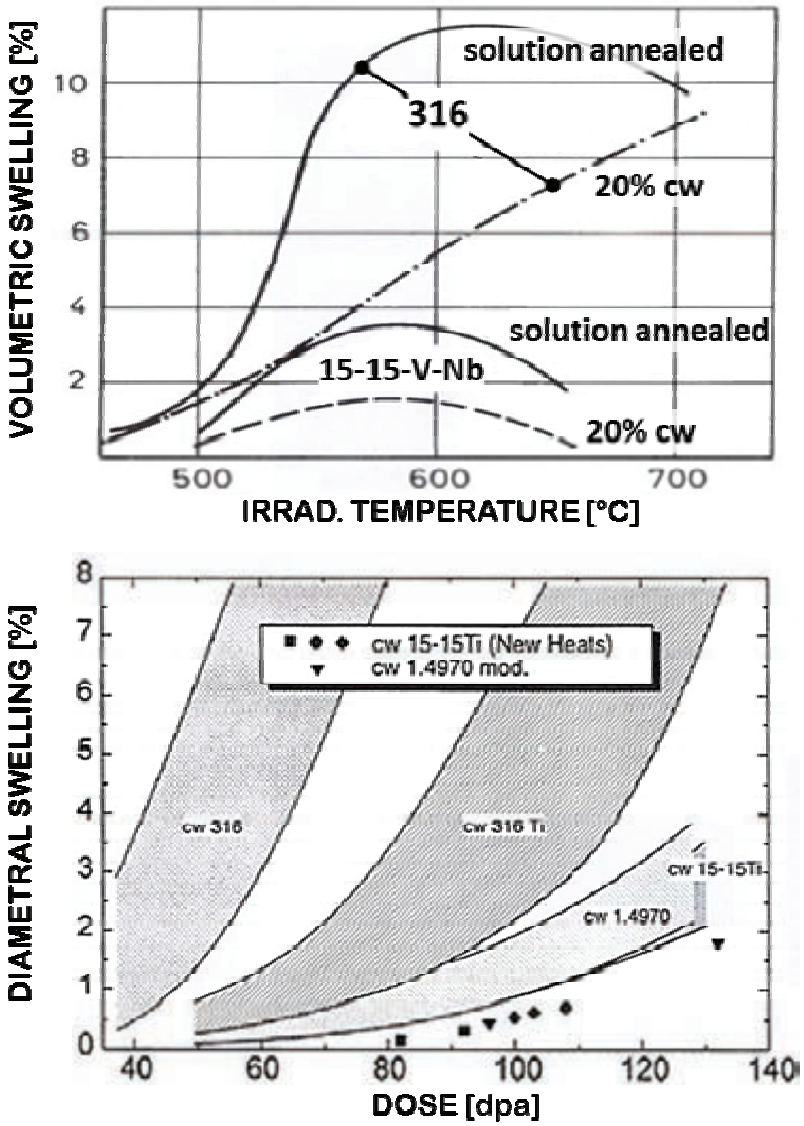

Fig. 2: Upper diagram: Swelling of austenitic steels depending on irradion temperature during ion irradiation (40 dpa, 10 appm He). Swelling is clearly reduced in cold-worked (cw) compared to solution annealed steels. The steel 15-15-V-Nb (1.4988) steel belongs to the same steel class as 1.4970 or 1.4981.
Lower diagram: Swelling of austenitic steels depending on dose during fast neutron irradiation at 500 °C. All steels have been cold-worked (cw) prior to irradiation. Source: H.-J. Bergmann, W. Dietz, K. Ehrlich, G. Mühling, M. Schirra, FZKA 6864, ISSN 0947-8620, 2003.

Table 2: Uniform elongation (i.e. strain to necking) before and after neutron irradiation of 316L(N) steels. Parameters are irradiation temperature and neutron dose (details are given in [1, 2]).

Irrad. Dose	**Irradiation Temperature**					
	60 °C	80 °C	200 °C	225 °C	325 °C	400 °C
unirrad.	0.5	0.4	0.33	0.31	0.3	0.32
5 dpa	0.35	0.22	0.18	0.08	0.09	0.14
7 dpa	0.3		0.13		0	0.05
10 dpa	0.28		0.11	0.05	0	0.04
15 dpa	0.26		0.08		0	0.03

Reduced Activation

The radwaste of the different regions of a reactor are usually evaluated according to the NRC 10CFR61 waste-disposal concentration limits. The waste-disposal rating (WDR) is defined as the sum of the ratio of the concentration of a particular isotope to the maximum allowed concentration of that isotope taken over all isotopes and for the particular class. According to the NRC 10CFR61 regulation, if the waste contains a mixture of nuclides, then waste-disposal must meet the requirement of WDR < 1 (low-level waste, Class C).

The remote maintenance rating (RMR) is defined as the dose rate at the surface of a uniformly activated, thick, infinite slab with the same composition and density as the machine component. Based on current Nuclear Regulatory Commission (NRC) regulations, if the RMR is less than or equal to 2.5×10^{-5} Sv/h, the unprotected radiation worker can have unrestricted access to the component. Frequently, the hands-on limit is defined as RMR $\leq 10^{-5}$ Sv/h and the recycling limit by RMR $\leq 10^{-2}$ Sv/h.

The results of activation calculations [3] for several fusion materials are compiled in Table 3. WDR values are calculated for a divertor in the ARIES design, 100 years after shut-down. It is evident that Mo leads to unacceptable high activation levels and, therefore, has to be avoided in reduced or low-activation alloys. This is the reason why Mo is replaced by W in reduced activation ferritic-martensitic steels like Eurofer or F82H. Nb is a natural impurity in iron as well as tungsten.

Table 3: Waste-disposal rating (WDR) of fusion materials; Calculations have been performed for a divertor following the ARIES design, 100 years after shut-down. For WDR < 1, materials can be considered as low-level waste.

Material	WDR	main contributing isotopes
8-9CrWVTa (F82H)	0.4	Nb-94
MoTiZr (TZM)	4026	Tc-99 from Mo
pure W	0.08	
commercial W	0.98	Nb-94, Ag-108
316	84	Tc-99 from Mo
RASS	1.03	Ni-63, Ni-59 from Ni
CuCrZr	9.7	Ni-63 from Cu

It increases activation significantly and has to be restricted to ppm levels or even lower. As a result, 316 steels with Mo as alloying element and Nb as impurity are high activating materials which have to be treated as high-level waste.

For designing a reduced activating (austenitic) stainless steel (RASS) the most important step is the replacement of Mo and a reduction of impurities (like Nb). The WDR value (1.03) for such a RASS in Table 3 results from the following chemical composition: 15% Cr-15% Ni-2% W-1.7% Mn-0.5% Si-0.5% Ti-0.1% C (in wt.%) and all other impurities as in the F82H steel. It demonstrates that such a steel could just qualify as low-level waste by only minor adjustments of the composition. Finally, the result for CuCrZr shows clearly that any ITER-like divertor design can never meet the low-level waste criterion.

Powder Metallurgy

The microstructure (i.e. grain size) of austenitic stainless steels (produced by the usual melt metallurgy route) can be controlled only by recrystallization after prior cold-working. In principle, powder metallurgy (PM) could provide alternative measures. Therefore, a basic study

was performed to determine feasibility, consequences, and possible drawbacks of this fabrication route. Since larger quantities of the steel 1.4981 were available in the form of forged rods with diameters of about 40 mm, this alloy was selected as reference material for the study.

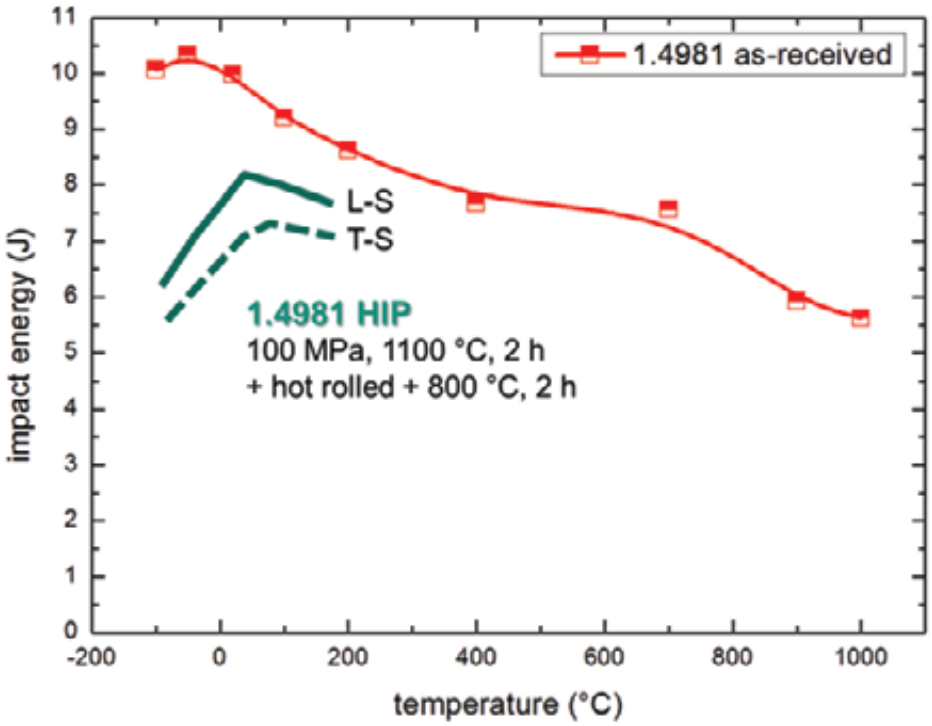

Fig. 3: Charpy tests with the austenitic steel 1.4981. Miniaturized Charpy specimens (4 mm x 3 mm x 27 mm, notch 1 mm) were fabricated from a 40 mm forged rod in the condition as received from the manufacturer (red squares). For comparison, the results with powder metallurgically produced 1.4981 steel (powder was mixed, HIPed and hot-rolled) are indicated by green lines (solid: parallel to RD, dashed: perpendicular to RD).

First, powder was fabricated from the base material by atomization. During the process the chemical composition was changed mainly by a loss of Mn (a drop from 1.3 to 0.5 wt.%) and by an increase of oxygen (from 0.02 to 0.1 wt.%). Then the powder was blended with Y_2O_3 and ZrO_2 (<1 wt.%), encapsulated, degassed at 500 °C, HIPed at 100 MPa / 1100 °C for 2 hours, hot-rolled, and finally annealed at 800 °C for 2 hours. The influence of the fabrication route on the mechanical properties was determined by Charpy tests (see Fig. 3). A slightly reduced toughness (a reduction by 1-2 J) of the PM material is observed for testing temperatures above RT. This can be mainly contributed to the higher content of oxygen and to the addition of oxides. In the lower temperature range, however, the PM material loses a significant amount of ductility. Nevertheless, a complete embrittlement as observed with ferritic steels doesn't appear.

Discussion and Conclusions

It has been shown that 15-15-steels with Ti stabilization perform best at temperatures above 500 °C. In this regime they can be used up to more than 70 dpa in a fast breeder environment due to their good swelling behavior. However, in water-cooled divertor designs, swelling would not be the main issue due to the lower operating temperatures. In addition, the stabilizing precipitates are not stable under neutron irradiation below 500 °C. Therefore, the use of Ti stabilization is questionable.

First calculations have shown that a RASS could be relatively easy obtained by the simple replacement of Mo by W and by the same reduction of impurities (mainly Nb, Al and Co) that has been applied for Eurofer and F82H steels. For that reason an extensive development

programme as has been already performed in the past by replacing Ni by Mn seems not to be strictly necessary.

The fact that 316 steels experience severe irradiation hardening at lower temperatures but still provide a remarkable amount of ductility at temperatures below 200 °C enables potential applications in water cooled divertor designs. Unfortunately, the required low cooling temperatures would disable electricity production. Due to irradiation embrittlement, the other optional application of a RASS (i.e. to reinforce CuCrZr pipes) is restricted to operating temperatures above 400-500 °C.

As a conclusion, for low temperature and medium neutron dose applications, swelling is not a pressing issue. Since Ti stabilization becomes ineffective at lower irradiation temperatures, and since Eurofer/F82H-type steels perform better at temperatures above 350 °C, it seems to be unnecessary to follow the Ti stabilizing concept for RASS. Therefore, future activities will be restricted to investigate RASS with simple chemical compositions, that is, Fe-Cr-Ni-Mn-W plus variations or minor contents of other elements (C, Si, and N).

From the technological point of view, there are almost no restrictions. It has been demonstrated that the fabrication of thin walled semi-finished products (pipes, sheets, etc.) is possible with all potential RASS candidates. Even PM fabrication routes are thinkable and feasible, should they be required.

Collaborations

M. Gilbert, S. Dudarev (CCFE), L. El-Guebaly (University of Wisconsin)

Staff:

L. Commin
B. Dafferner
S. Heger
J. Hoffmann
M. Hoffmann
U. Jäntsch
M. Rieth
R. Ziegler
H. Zimmermann

Literature:

[1] P. Robertson, I. Ioka, A.F. Rowcliffe, M.L. Grossbeck and S. Jitsukawa, Temperature dependence of deformation behavior of type 316 stainless steel after low temperature neutron irradiation, ASTM STP (1997) 1325.

[2] P.H. Dubuisson, J.L. Seran, P. Soulat, Irradiation Embrittlement of Reactor Internal Materials, in “Effect of Irradiation on Water Reactor Internals,” Study Contract COSU CT94-074, Vol.3, June 1997, p.15.

[3] Laila A. El-Guebaly, University of Wisconsin – Madison, USA, private communication.

Acknowledgement

This work, supported by the European Communities under the contract of Association between EURATOM and Karlsruhe Institute of Technology, was carried out within the framework of the European Fusion Development Agreement. The views and opinions expressed herein do not necessarily reflect those of the European Commission.

Long-term Structural Material (WP12-MAT-01-HHFM-03-01)

Introduction

A divertor is a plasma facing, high heat flux component in a fusion reactor. The expected heat load for a divertor in a future fusion power reactor (DEMO) in a short-term scenario is expected to be about 10 MW/m^2 with peaks of up to 20 MW/m^2 due to plasma instabilities. As a divertor has to deal with such extreme heat loads it is quite obvious that tungsten, the material with the highest melting point of all metals (3420°C [1]), is considered as a candidate for several divertor applications. One application asks for a tungsten material that can be used for structural cooling pipes [2–4]. As these pipes are meant to be pressurized pipes (e.g. helium coolant, 600°C, and 100bar) the tungsten material must fit the needs of a structural material. In this case the tungsten material must have a low brittle-to-ductile transition temperature (BDTT) as well as high fracture toughness (e.g. 20 MPa m$^{1/2}$). Unfortunately tungsten is very brittle and until now has mostly been used as a functional and not as a structural material. So in this context the question of how to make tungsten ductile and how to shift the brittle-to-ductile transition (BDT) to lower temperatures arises.

The approach that in this work was assessed is the ductilization of tungsten by synthesizing a tungsten laminate. The idea is as follows. Tungsten foil is ductile; it can be bent plastically even at room temperature (RT). Through the assembly and appropriate joining of several layers of tungsten foil it is possible to extend the ductile properties of the foil to the bulk [5, 6] (see Fig. 1). The reason for and sources of the extraordinary ductility of tungsten foil are widely discussed. One reason might be the foil effect, according to which the dislocations that move to the free surface are annihilated.

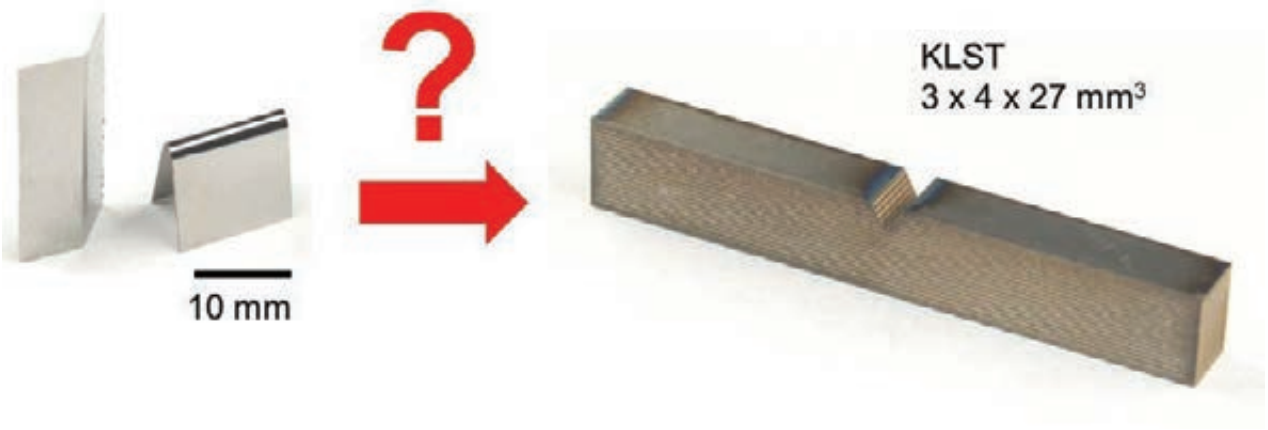

Fig. 1: Main question of the tungsten laminate project: Tungsten foil is ductile in a bending test even at room temperature. Is it possible to synthesize a tungsten laminate with a high dynamic fracture toughness measured by Charpy?

In this report the special mechanical properties of tungsten foil are assessed by tensile tests. The following chapters will address these questions:

1. How can it be explained that the tensile test properties in the rolling direction (0°) and perpendicular to it (90°) are the same?
2. Is there a reason why the most ductile material behaviour can be obtained on a tensile test sample tested in the 45° direction?
3. Is there a proof that the foil effect really takes place during a tensile test?

Experimental: Setup of the tensile tests

All tensile tests were performed in an electro-mechanical test device (Zwick100). This test device was modified and combined with a furnace (RT to 1400°C) and a vacuum chamber (operation pressure: 10^{-6} mbar). The experiments were carried out using subsized specimens (gauge length: 7 mm; width: 2 mm). The test specimens were fabricated by electrical discharge machining (EDM) and all tests were displacement controlled with a strain rate of 0.1 mm/min.

Results

Tensile tests at 600°C, foil, as-received

Tensile tests were performed at 600°C. Fig. 2 shows the stress-strain curve of 100 µm tungsten foil in the as-received condition tested at 600°C. As expected, due to the 90° rotation symmetry of the texture of the foil, {100} <011>, the plastic material behaviour in the rolling direction (0°) and perpendicular to the rolling direction (90°) is congruent. The influence of the grain boundaries and the grain shape cannot be observed at 600°C. Most ductile material behaviour, combined with a decrease of the tensile strength of about 10%, can be measured on a tensile test sample orientated in the 45° direction. This material behaviour might be attributed to the texture of the foil in {100} <011>. This texture allows the main slip direction of bcc metals, the <111> direction, to appear at an angle of 45° to the direction of tension. It is well known from Mohr's circle of stress that the maximum shear stress appears at an angle of 45°. This means that for a tensile test sample orientated in the 45° direction, the preferred slip direction of bcc metals and the direction where the maximum shear appears are congruent. This is why the plastic formability of tensile test samples orientated at 45° to the rolling direction of the foil is favoured.

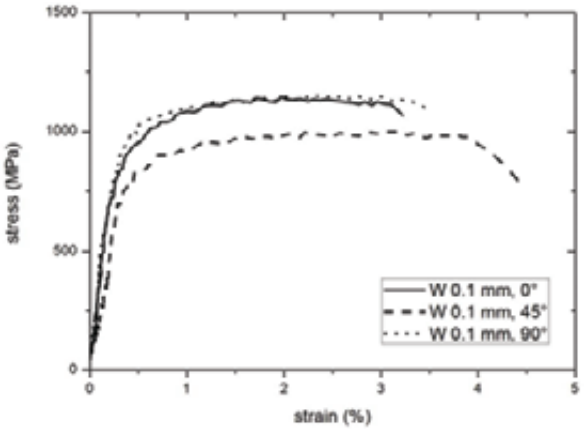

Fig. 2: Stress-strain curves of tensile tests performed on 100-µm-thick tungsten foil in the as-received condition at 600°C. As expected the plastic material behaviour in the rolling direction (0°) and perpendicular to the rolling direction (90°) is congruent.

It can be concluded that at 600°C the anisotropic material behaviour can easily be explained by the texture of the foil. At this test temperature the grain shape and the grain boundaries no longer influence the mechanical properties. Furthermore it can be determined that none of the stress-strain curves show any necking, which means that the uniform elongation (elongation without necking) is congruent to the total plastic strain.

Tensile tests at 600°C, foil, recrystallized

Up to now the tensile tests have been performed only on tungsten foil in the as-received condition. In a new test series presented in this section, annealed tungsten foil will be assessed. The annealing conditions were 1 h at 2000°C and 1 h at 2700°C in hydrogen, respectively.

As can be seen from Figure 3, the tungsten foil in the recrystallized condition shows extreme plastic strain in a tensile test at 600°C. Plastic strain of 25 to 45% can be measured. Comparing these results with the results obtained for tungsten foil in the as-received condition (also tested at 600°C), the plastic strain increases by a factor of ten together with a decrease of the tensile strength by a factor of five. The decrease in the tensile strength of recrystallized tungsten was expected as it is well known that the tensile strength decreases when (i) the

dislocation density decreases, (ii) the amount of grain boundaries decreases, and (iii) the grain size increases (see also Hall–Petch [7,8]). What is astonishing is the very large plastic strain of up to 45%. The reason for this incredible material behaviour might be that the dislocations can move out of the foil surface: this is known as dislocation annihilation or the 'foil effect'. Assessing the surface of the test sample after the test, it can be seen that the surface is now rough over the whole gauge length. This roughness is a hint that dislocation activity takes place at the surface and that the dislocation annihilation takes place over the whole gauge length. Figure 4 shows a comparison of tensile test samples tested at 600°C in the as-received (Fig. 4, left) and recrystallized condition (Fig. 4, right).

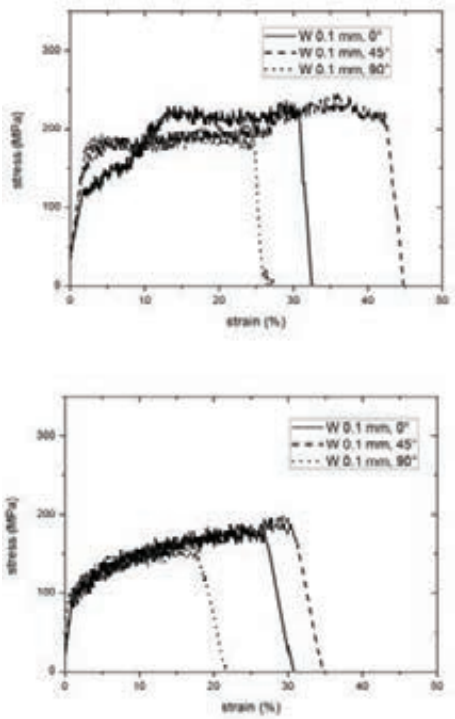

Fig. 3: Results of tensile test on 100-µm-thick tungsten foil in the recrystallized condition at 600°C. Top: foil was annealed for 1 h at 2000°C. Bottom: foil was annealed for 1 h at 2700°C. Extreme plastic strain of up to 40% combined with serrated flow can be observed.

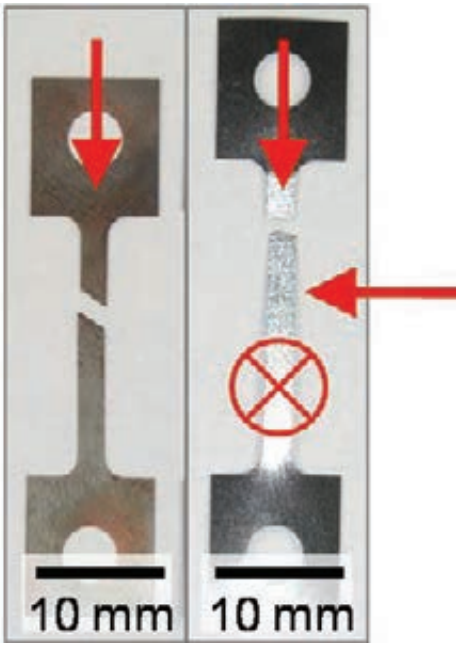

Fig. 4: Picture of tensile test samples of 100-µm-thick tungsten foil tested at 600°C. Left: foil in the as-received condition. Right: foil in the recrystallized condition (1 h / 2000°C). Even by the naked eye, the incredible plastic strain of the recrystallized foil as well as the rough surface can be seen. The rough surface is the evidence that dislocations moved out of the foil surface – the 'foil effect'.

The results show that the mechanical properties of tungsten foil are anisotropic and can be explained by considering (i) the texture of the tungsten foil of {100} <011>, (ii) the anisotropic grain shape (0.5 µm × 3 µm × 15 µm), (iii) the preferred slip direction of body-centred cubic (bcc) metals, the <111> direction, as well as the preferred cleavage plane of tungsten at room temperature, the {100} plane (see Fig. 5).

After the analyses and the mechanical assessment of 100-µm tungsten foil in different conditions the preliminary conclusion is that the ductility of tungsten foil is caused by (i) the high amount of mobile edge dislocation, (ii) the small grain size, which may lead to (ii-a) multiple slip at the grain boundaries [9] or (ii-b) nano-crystalline effects such as grain boundary sliding [9,10], and (iii) the foil effect – the dislocation annihilation on the free surface. In particular, the extreme plastic deformability of tungsten foil in the recrystallized condition seems to benefit from the foil effect.

Summary and conclusion

The main point of the tungsten laminate project is to assess whether the ductile properties of a tungsten foil can be extended to the bulk.

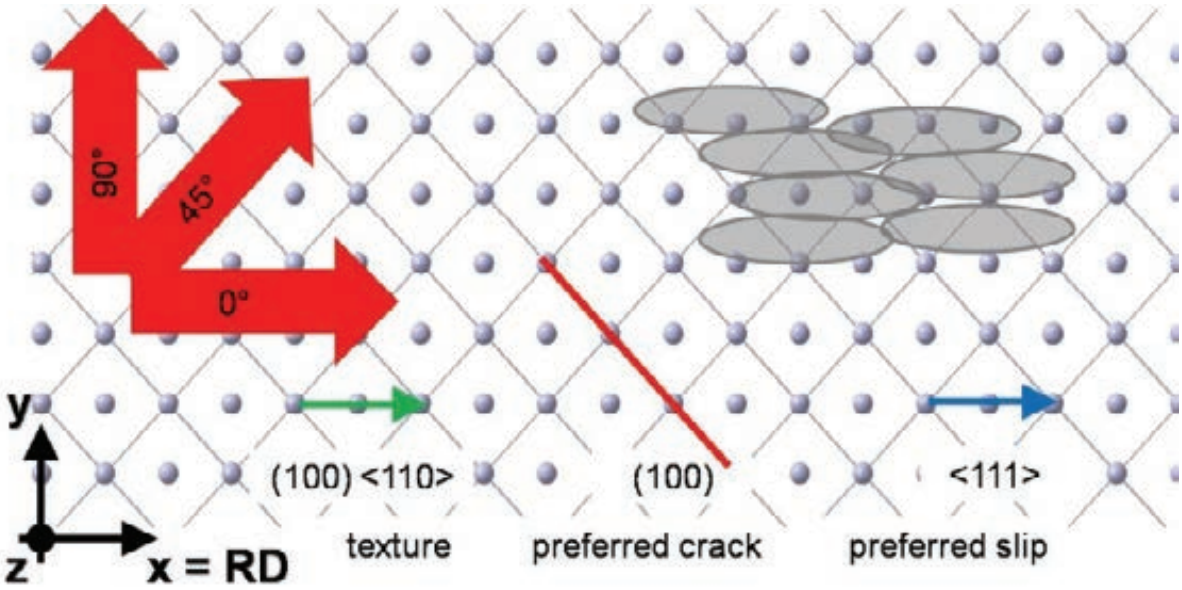

Fig. 5: This figure shows a top view of a tungsten foil (the x-axis is the rolling direction; the x-y plane is the flat surface of the foil). The texture of the tungsten foil, {100} <011>, is symmetric for a rotation of 90° around the z-axis, which is the out-of-plane axis. The mechanical properties of tungsten foil can be explained considering (i) the {100} <011> texture of the tungsten foil, (ii) the anisotropic grain shape (0.5 μm × 3 μm × 15 μm), and (iii) the preferred slip direction of bcc metals, the <111> direction, as well as the (iv) preferred cleavage plane of tungsten at room temperature, the {100} plane.

By synthesizing a tungsten laminate using the right combination of interlayer and joining technology it is possible to produce a tungsten laminate which shows improved properties in a Charpy impact test compared to pure tungsten plate material. So it is possible to extend the properties to a bulk.

Tungsten foil is an extraordinary semi-finished product with curious ductile material behaviour. Discussing about the ductility of 100-μm-thick tungsten foil in the as-received condition as well as in the recrystallized condition size effects have to be considered. In the as-received condition the 100-μm-thick tungsten foil has very small grains, so nano-crystalline effects have to be considered, discussing about the sources and mechanism of the ductile material behaviour. In the recrystallized condition (e.g. annealing for 1 h at 2000°C) the 100-μm tungsten foil has only one grain over the thickness of the foil. In this case the foil effect becomes relevant. In any case, tungsten foil is an excellent semi-finished product for the synthesis of tungsten laminates, especially tungsten laminate pipes for structural applications.

Staff:

S. Baumgärtner
D. Bohlich
B. Dafferner
M. Hoffmann
U. Jäntsch
A. Möslang
J. Reiser
M. Rieth
R. Ziegler
H. Zimmermann

Literature:

[1] www.plansee.com (2012).

[2] M.S. Tillack et al., Fusion Eng. Des. 86 (2011) 71.

[3] P. Norajitra et al., Fusion Eng. Des. 82 (2007) 2740.

[4] J. Reiser, M. Rieth, Fusion Eng. Des. 87 (2012) 718.

[5] J. Reiser, M. Rieth, B. Dafferner, A. Hoffmann, J. Nucl. Mater., 423 (2012) 1.

[6] J. Reiser, M. Rieth, B. Dafferner, A. Hoffmann, J. Nucl. Mater., 424 (2012) 197.

[7] E.O. Hall, Proc. Phys. Soc., B 64 (1951) 747.

[8] N.J. Petch, J. Iron Steel Inst., 174 (1953) 25.

[9] J. Koike, Mater. Sci. Forum, 449–452 (2004) 665.

[10] M.A. Meyers, A. Mishra, D.J. Benson, Prog. Mater. Sci., 51 (2006) 427.

[11] J. Reiser, M. Rieth, B. Dafferner, et al., Tungsten foil laminate for structural divertor applications - basics and outlook; J. Nucl. Mater., 423 (2012) 1.

[12] J. Reiser, M. Rieth, B. Dafferner, et al., Tungsten foil laminate for structural divertor applications - analyses and characterisation of tungsten foil.; J. Nucl. Mater., 424 (2012) 197.

[13] J. Reiser, M. Rieth, A. Möslang, et al., Recent progress in research on tungsten materials for nuclear fusion applications in Europe; J. Nucl. Mater., 432 (2012) S.482-500.

Acknowledgements

This work, supported by the European Communities under the contract of Association between EURATOM and Karlsruhe Institute of Technology, was carried out within the framework of the European Fusion Development Agreement. The views and opinions expressed herein do not necessarily reflect those of the European Commission.

The authors are grateful to our colleagues from Plansee Metall GmbH, the University of Oxford, Department of Materials, and the Karlsruhe Institute of Technology (KIT), Institute for Applied Materials (IAM), for their support and valuable contributions.

Fracture-Mechanical (FM) and Microstructural Characterization of Tungsten Alloys (WP12-MAT-01-HHFM-03-02)

Objectives

Inherent low fracture toughness of tungsten combined with the high DBTT are major drawbacks for structural application of tungsten alloys. Furthermore, fracture-mechanical properties are expected to exhibit strong anisotropy due to (i) different grain shape/ orientation with respect to the rolling direction and (ii) texture. The current task aims at fracture-mechanical characterization of different laboratory and industry scale W-alloys and their ODS variants (W-1%La_2O_3, W-2%Y_2O_3) in the interesting temperature window for fusion applications (RT-1300 °C). The emphasis is put on the investigation of microstructure and load rate dependence of the fracture toughness (K_{IC}). The investigations are accompanied by fractographic and microstructural investigations.

Performed Work

Fracture-Mechanical (FM) behaviour of W-2wt%.Y_2O_3 manufactured at CRPP-EPFL in collaboration with PLANSEE by MA and HIPping has been investigated in a temperature range between 200 and 600 °C and under high vacuum condition. Miniaturized 3PB specimens of KLST geometry with dimensions of 27x4x3 mm^3 and with a V shaped notch of 1 mm depth have been manufactured from two areas A and C of a disk shaped ingot. The specimen extraction orientation with a longitudinal direction parallel to a disk circumferential orientation and with an expected crack propagation direction parallel to radial direction corresponds to a C-R orientation according to the ASTM E399 nomination. To increase the stress triaxiality at the notch sharp crack starter notches with a final radius of 20-25 µm have been introduced by a razor blade polishing of the notch tip. The initial crack lengths varied in the range of 1040-1200 µm. The quasi-static three-point bending was performed in a deformation controlled way at a deformation rate of 2 µm/s, which corresponds to a stress intensity factor rate of 0.6-0.9 $MPam^{1/2}$. The fracture surface morphology of the specimens has been investigated by a scanning electron microscopy (SEM).

Load vs. displacement curves for selected FM 3PB specimens tested in a temperature range between 200 and 600 °C are shown in Fig. 1. At 200 °C the specimens failed in a brittle manner. The SEM images of fracture surface in Fig. 2a revealed a failure by a transgranular cleavage. It has to be noted that no substantial differences in fracture behaviour have been observed between specimens manufactured from the areas A and C of the ingot indicating a homogeneous microstructure throughout the ingot. An onset of inelastic deformation in load vs. displacement curves has been observed already at 250 °C. At a test temperature of 300 °C and above the FM specimens exhibited large plastic deformation as seen in Fig. 1. The partial unloading of selected FM specimens at elevated temperatures, see Fig. 1, showed an increase of unloading compliance under load increase indicating a stable crack grows under three-point bending. The SEM image of fracture surfaces of FM specimens tested above 300 °C, see e.g. Fig. 2b, revealed a complex fracture behaviour. Namely, crack propagation took place in mutually, orthogonal planes, i.e. in an initial crack plane and in a plane being transverse to the initial crack plane. The crack propagation

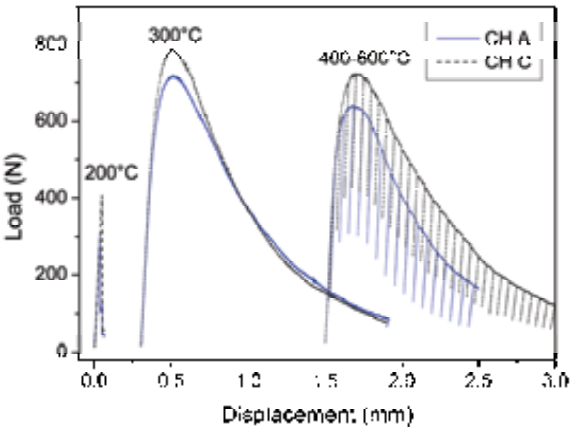

Fig. 1: Load vs. displacement curves for FM W-2wt.%Y_2O_3 specimens. For a better visualization the abscissa is shifted for selected curves. The test temperature is indicated next to the curves. Label CH A and CH B refer to area A and area B of ingot, respectively.

in the initial crack plane was accompanied by pronounced dimple formation being characteristic to ductile tearing of a material above ductile-to-brittle transition.

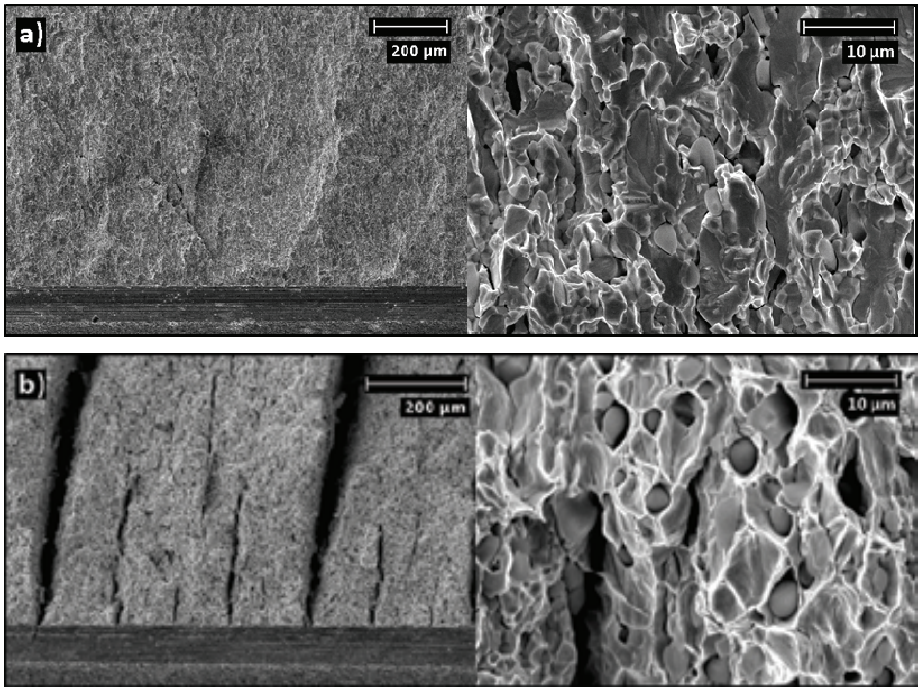

Fig. 2: Fracture surfaces of FM W-2wt.%Y_2O_3 specimens tested at a) 200 °C and b) 300 °C. Right part images show fracture morphology at a higher magnification.

The analysis of load vs. displacement curves with respect to Fracture Toughness (FT) was performed in accordance to ASTM E399. The obtained FT values are summarized in Fig. 3 for the two investigated ingot areas. On increasing temperature the stress intensity factor loses its validity with increasing ductile behavior and the calculated values give only a lower bound of FT. The corresponding invalid FT values are denoted by open symbols in Fig. 3. It has to be noted that the absolute levels of the FT at a test temperature of 200 °C and for adequate specimen orientation (C-R) are comparable to that of polycrystalline round blank tungsten of technical purity produced by Plansee by sintering of tungsten powder into rods and subsequent forging. The ductile deformation manifested in dimple formation, however, is attained at much lower temperature for the case of yttria reinforced tungsten.

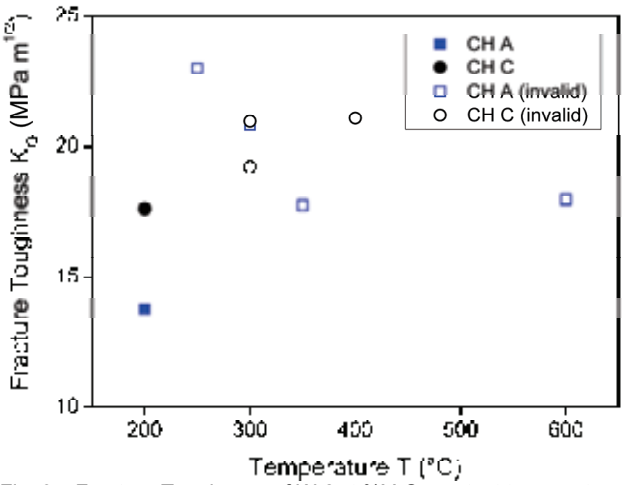

Fig. 3: Fracture Toughness of W-2wt.%Y_2O_3 vs. test temperature for two different ingot areas A and C. Values denoted by open symbols do not satisfy ASTM E399 validity criteria. Load rate 0.6-0.9 MPam$^{1/2}$/s.

The upper shelf FT of W-2wt%.Y_2O_3 was analyzed in the frame of elastic-plastic Fracture Mechanics. A single specimen methodology was followed for a construction of a crack resistance J(Δa) curve. An unloading compliance analysis was implied for the assessment of the in-plane crack advancement under three-point-bending. A critical value of J integral (J_{IC}) of 48.78 N/mm was determined according to ASTM E813. The mode I fracture toughness was then estimated through $K_{IC}=\{J_{IC}E/(1-\nu^2)\}^{1/2}$ relationship, with E=380 GPa being the Young's modulus of tungsten at 600 °C and ν=0.28 being its Poisson ratio. The upper shelf

FT value calculated this way was 141.8 MPa $m^{1/2}$ which is a rather high value for tungsten. Comparatively, an upper shelf fracture toughness value of 72.9 MPa $m^{1/2}$ was determined for tungsten with 1 wt.% La_2O_3 (WL10) at 600 °C by application the critical crack tip opening displacement approach in [B. Gludovatz et al., Int. J. Refract. Metals Hard Materials 28 (2010) 674].

In contrast to W-2wt%.Y_2O_3 no stable crack growth was observed for round blank polycrystalline tungsten and W-1%La_2O_3 tungsten alloys in the upper shelf. The strong ductile deformation without advancement of crack prevented the analysis of the upper shelf fracture toughness in these alloys.

Conclusion and Outlook

Fracture mechanical and microstructural characterization of tungsten alloys provided within EFDA HHFM Task Agreement has been performed. The FM investigation of yttria reinforced tungsten alloys manufactured at CRPP-EPFL in collaboration with PLANSEE yielded very promising results. In the investigated C-R orientation large plastic deformation and onset of ductile dimple formation was observed at test temperatures above 300 °C. Fracture behaviour in the upper shelf was complex being characterised by crack propagation in mutually orthogonal planes, i.e. in an initial crack plane and in a plane being transverse to the initial crack plane. Upper shelf fracture toughness of 140 MPa $m^{1/2}$ determined via analysis of crack resistance curve is very promising and superior to that of La_2O_3 reinforced tungsten alloy reported in literature. Investigation for other specimen orientations is mandatory in order to study the influence of the material anisotropy on the fracture mechanical behaviour. Strong ductile deformation without advancement of crack for round blank polycrystalline tungsten and W-1%La_2O_3 tungsten alloys prevented the analysis of upper shelf fracture toughness of this alloys.

FM characterization of different novel laboratory and industry scale W-based structural materials that are being developed under EFDA HHFM Task Agreement will be performed in the interesting temperature window for fusion applications (RT-1300 °C). The J-Integral and/or COD methods will be applied for the investigation of upper shelf fracture toughness. FM experiments will be accompanied by fractographic and microstructural investigations.

Staff:

E. Gaganidze
M. Klotz
S. Knaak
M. Walter

Literature:

[1] E. Gaganidze, M. Walter, U. Bürkle, M. Klotz, *Fracture-Mechanical and Microstructural Characterization of W- alloys*, EFDA MAT-W&Walloys Monitoring Meeting, February 7-9, 2012, Garching, Germany

[2] E. Gaganidze, *Fracture-Mechanical and Microstructural Characterization of W- alloys*, EFDA MAT-HHFM Monitoring Meeting, June 19-21, 2012, Ljubljana, Slovenia

[3] M. Rieth et al., *Recent progress in research on tungsten materials for nuclear fusion applications in Europe,* J. Nucl. Mater. 432 (2013) 482-500

Acknowledgement

This work, supported by the European Communities under the contract of Association between EURATOM and Karlsruhe Institute of Technology, was carried out within the framework of the European Fusion Development Agreement. The views and opinions expressed herein do not necessarily reflect those of the European Commission.

Long-term Structural Materials (WP12-MAT-01-HHFM-03-07)

Acquisition of knowledge on the mechanical behavior of tungsten at high temperature is the focus of this project. The high temperature nanoindentation technique will be used in a Hot Cell environment for that purpose. This technique requires only small testing volumes and offers the possibility to reuse already tested specimens. Hence, it remains an attractive testing tool for the characterization of irradiated materials especially when considering the high costs of irradiation volume.

A preliminary task of this study consists in making a reliable choice concerning the material of the indenter tip operating at elevated temperatures in order to prevent any significant modifications of its structural properties during long-term heating. For that purpose, a comparison study of the mechanical properties obtained on a reference sample material will be made with different tip materials.

The mechanical behavior resulting from indentation of unirradiated samples made of pure, single and polycrystalline tungsten will be investigated from room temperature up to 1000 °C with a view to compare it later on with the one resulting from irradiated specimens. For both series of specimens, analyses of the temperature-dependant changes in elastic and plastic properties will be accomplished in accordance with the corresponding materials microstructure. Analyses of irradiation-induced hardening is here of particular interest.

The ability of the indentation technique to generate cracks will be utilized to examine the temperature-dependant changes in the fracture mechanisms of tungsten and determine the ductile to brittle transition temperature based on the indentation method. The requirements for the choice of an adapted geometry of the indenter tip will also have to be investigated for that purpose.

Characterization of tungsten from room temperature up to 1000°C by means of the indentation technique

The instrumented indentation device to be used for investigating the high-temperature behavior of tungsten up to 1000°C was brought into service. The HTIIS (ONERA, Michalex) is currently calibrated with different materials such as fused silica and aluminum. Contrary to diamond, a Berkovich tip made of sapphire is adapted for a calibration study up to 1000°C. Another tip made of cubic boron nitride (cBN) will be used for investigation of harder materials such as tungsten. Such a tip was already manufactured and tested. However, the sensibility of the cBN crystal to wear is relatively high; as a consequence, defects on the tip are rapidly induced. Thus, the quality of the crystal has to be further enhanced.

A base frame adapted for use in the Hot Cell as well as an antivibration system were installed to enhance the mechanical stability of the whole device and minimize its sensitivity to external vibrations disturbing the measurement.

The following pictures show several indentation curves resulting from measurements performed in an inert gas and high vacuum atmosphere at different temperatures. The data were generated by means of Berkovich sapphire tip loaded up to 500 mN on a fused silica sample with a size of 10×10×5 mm^3. In all figures, the green and red curves are measured curves while the blue one is the theoretical one. The indentation behavior at room temperature is in good accordance with the theory; the creep behavior is clearly visible and becomes more significant by increasing the temperature. At higher temperature effects due to compliance and thermal drift are still occurring. Efforts are currently focused on the correction of such phenomena.

Further steps for calibration of the device will be focused both on testing at indentation force lower than 500 mN and up to 1000°C.

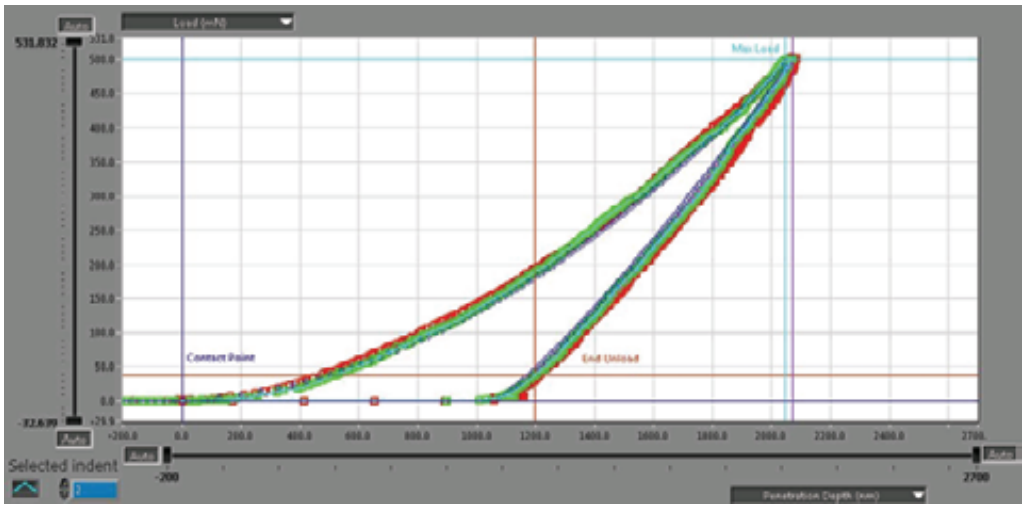

Fig. 1: Indentation on fused silica at room temperature (with Berkovich sapphire tip)

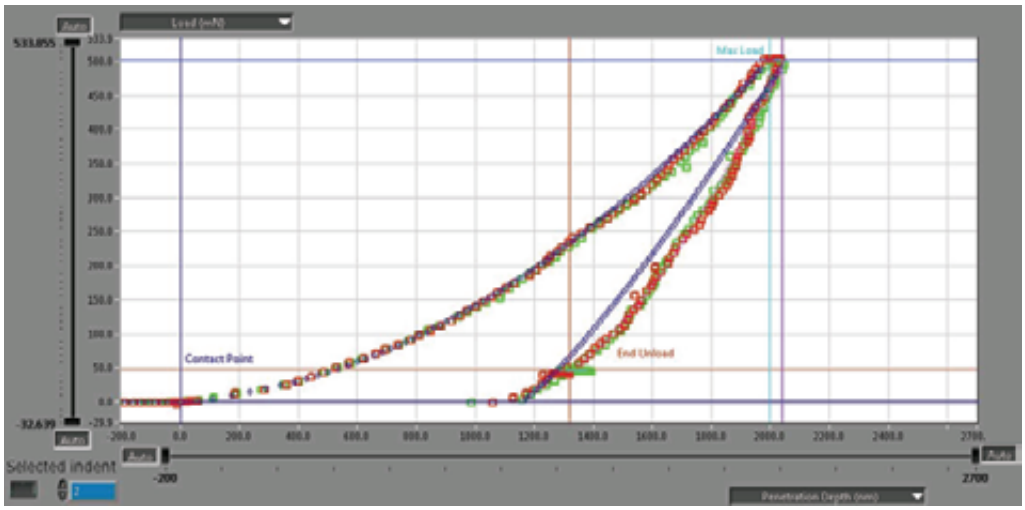

Fig. 2: Indentation on fused silica at 500 °C (with Berkovich sapphire tip)

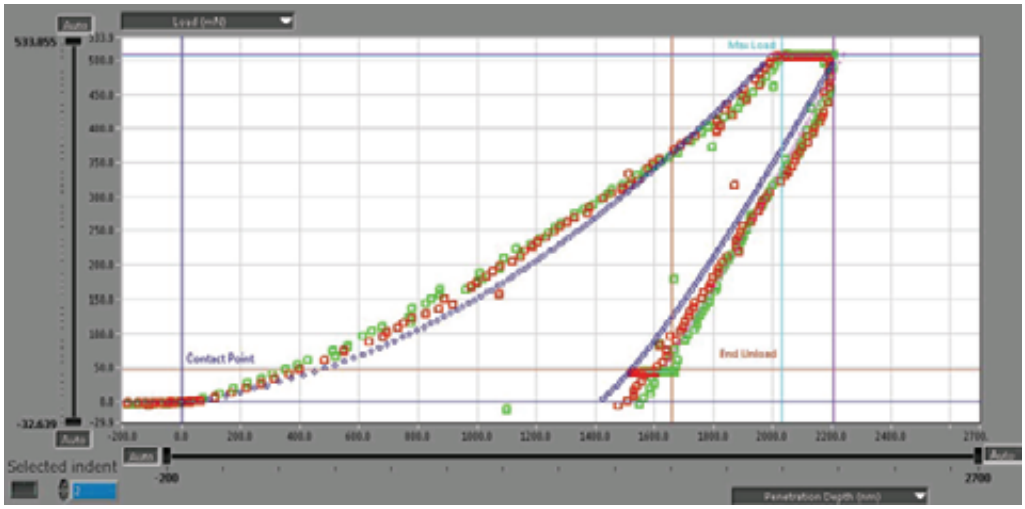

Fig. 3: Indentation on fused silica at 800 °C (with Berkovich sapphire tip).

Future activities:

- Enhancement of the thermal testing conditions in the 650°C indentation device
- Further steps for calibration of the device with series of tests up to 650°C
- Characterisation of unirradiated RAFM steels by instrumented indentation up to 650°C
- Further steps for calibration of the HTIIS indentation machine with series of tests at indentation force lower than 500 mN and up to 1000°C.
- Characterisation of unirradiated tungsten by instrumented indentation up to 1000°C.

Staff:

B. Albinski
I. Bernstein
M. Holzer
W. Ibbe
S. Lautensack
I. Sacksteder
H.-C. Schneider

Literature:

[1] Sacksteder, I. ; Albinski, B. ; Bernstein, I. ; Schneider, H.-C. ; Kraft, O., "Une utilisation de l´indentation instrumentée à haute température pour tester des échantillons irradiés" Lecture), Indentation2012, Lyon, 29-31 October, 2012, France

[2] Sacksteder, I,; Hostettler, S.; Charbonneau, G.; Albinski, B.; Schneider, H.-C., "An evaluation of requirements for investigating the temperature dependent fracture behavior of irradiated materials by indentation" (Poster), SOFT 2012 Conference 24.-28. September 2012, Belgium

[3] Albinski, B.; Sacksteder, I.; Schneider, H.-C.; Kraft. O., "High-Temperature Indentation Experiments on Fusion-related Materials" (Poster), SOFT 2012 Conference 24.-28. September 2012, Belgium

[4] Sacksteder, I., "Characterization of tungsten from room temperature up to 1000°C by means of the indentation technique" (Lecture), EFDA WP12-MAT-01-HHFM Monitoring Meeting 13.-21. June 2012, Ljuljana, Slovenia

[5] Albinski, B.; Sacksteder, I.; Schneider, H.-C., "Ein fernhantierter Hochtemperatur-Indenter zur Untersuchung von Materialien für den Fusionsreaktor" (Poster), InnoMateria in Köln, 14.-15. Mai 2012, Germany

Acknowledgement

This work, supported by the European Communities under the contract of Association between EURATOM and Karlsruhe Institute of Technology, was carried out within the framework of the European Fusion Development Agreement. The views and opinions expressed herein do not necessarily reflect those of the European Commission.

Material and Joining Process Development by Electro-chemical Plating Brazing and Coating (WP12-MAT-01-HHFM-04-02) SS and Cu Joining (WP12-MAT-01-HHFM-04-03)

Introduction

A general challenge in divertor development, independently of design type and cooling medium water or Helium, is the reliable and adapted joining of components. Depending on the design variants, the characteristics of the joints will be focused on functional or structural behavior to guarantee e.g. good thermal conductivity and sufficient mechanical strength. All design variants is common that tungsten is the plasma facing material. However, the structural material underneath may vary depending on design variants. Thus, material combinations to be joined will range from Cu base over steel to tungsten. Especially tungsten shows lacks in adapted joining due to its metallurgical behavior ranging from immiscibility over bad wetting up to brittle intermetallic phase formation. Joining assisted by electro-chemical deposition of functional and filler layers showed that an encouraging progress was achieved in wetting, applying nickel interlayers. However, although nickel is a good model element and reference material but due to the high activating under irradiation less preferred in fusion technology. Hence, alternative elements (e.g. Pd, Fe) are favored and are under investigation to manufacture suitable joints. Beyond the development of deposition technology the mechanical characterization of the processed joints was an evaluation area.

Electroplating as tool for joining and material development

Element selection for joints

In the He cooled divertor design tungsten is selected as armor and as structural material, whereas in other e.g. water cooled variants tungsten is considered as armor material and cooling pipes may be from steel as shown in Fig.1. Interface temperatures between structural component steel and tungsten may be for both designs similar, e.g., below roughly 700°C. In the He cooled layout the W – W joint will be operated near 1200°C. In all cases the filler alloy should not contain elements which form brittle intermetallic phases. The STEMET alloy 1311 is such a Ni-based filler with additions of 16% Co, 5% Fe, 4% Si, 4% B and 0.4% Cr as used in first technological tests [1] due to the melting temperature near 1050°C and increasing remelting temperature after joining. This alloy exhibits excellent wetting but forms brittle phases after short time at operation temperature which lead to failure, e.g., by detachment. Similar behavior was also present when tungsten was brazed to steel due to the large expansion mismatch between both materials. Steel-tungsten connections conducted by copper seemed to balance the expansion but showed bad wetting of tungsten. Active interlayers deposited by electro-chemical technology promised to be a solution and guided the path for development of filler systems to be applied in W-steel and W-W alloy joining or for development of W-composites with laminate structure.

Clearly visible by the operation condition is that all low melting and brittle phase forming elements are excluded such as e.g. Al, Si, Cd or Sn. Thus, filler components applied for this purpose will come from the transition elements and should possess not too high melting temperatures to avoid steel melting or recrystallization of tungsten. Additionally, at least one of the filler components should have an extended solubility range with tungsten. V and Ti form solid solutions and would fulfill one criterion but have rather high melting temperatures above 1600°C. Other elements like Ni and Pd also react with W and exhibit lower melting temperature. Additionally, alloying them with Cu, which showed some advantage for mismatch adjustment in W-steel casting, is possible and can be used to adapt brazing temperature. For example the melting temperature of Ni – Cu varies rather linearly with composition of the filler between the melting temperatures of the pure elements.

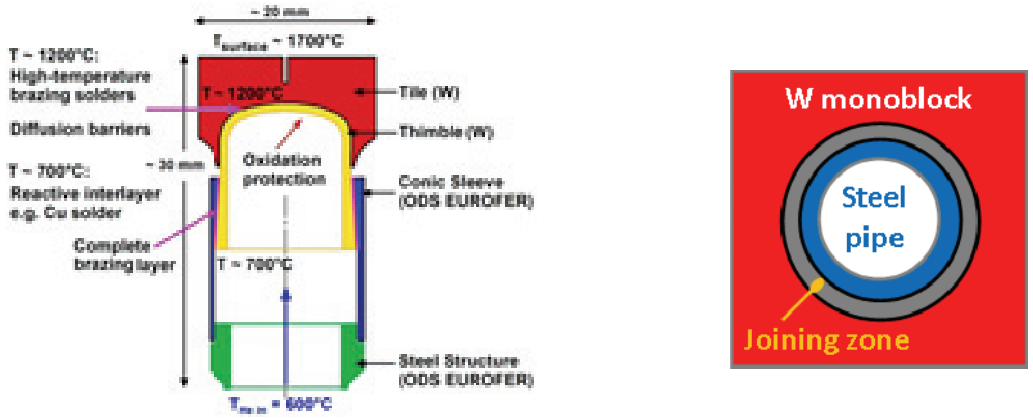

Fig. 1: Components of He cooled divertor with required joints as well as water cooled layout in mono block configuration.

Electroplating

Electrochemical processes allow the deposition of metallic layers on a solid substrate from a liquid system. Commonly, water-based systems are used in technology if molten salt methods working at several 100°C are neglected. However, new investigations showed that also water sensitive metals (e.g. Al and W) can be deposited from systems working at nearly room temperature [2] applying water free solvents. Classifying the elements mentioned above, Cu, Ni, Pd or Fe belong to the group which can be handled in aqueous systems. Other elements like W, Al, or V are water sensitive and require water free systems for deposition.

Neither W-W nor W-steel brazing with good wetting and mechanical characteristics is possible with pure Cu. To form suitable joints, reactive interlayers are required. Both elements Ni and Pd can assist there and they have the advantage to be deposited from aqueous solvents.

Joints by Ni and Cu plating

Deposition of Ni proved to be a suitable technology to deposit a reactive interlayer on tungsten, if the work pieces are cleaned and adherent oxygen containing surface scales and impurities from manufacturing processes are removed as described in [3]. Performed tests showed also, that Ni coating of steels (e.g. Eurofer) works well and increases the wettability for Cu as filler metal. Under both substrate conditions homogeneous and well adherent Ni layers are deposited. Additionally performed tests to modify the filler composition after brazing revealed that multilayer deposition with the sequence Ni – Cu – Ni – Cu can be done with the aim to increase the remelting temperature towards e.g. 1250°C for a ~1 :1 composition. Fig. 2 shows the micrograph of a W-W joint processed by electrochemical deposition of Ni as reactive component directly on both W (20 µm) pieces before plating the surface of one piece with roughly 50 µm Cu as filler component. The optical inspection shows good wetting and a defect-free brazing

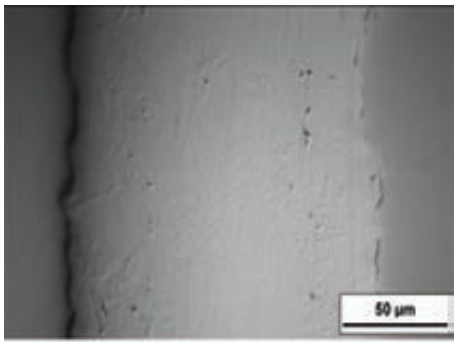

Fig. 2: Micrograph (polarized light) of two brazed tungsten pieces with Cu-Ni filler in the centre.

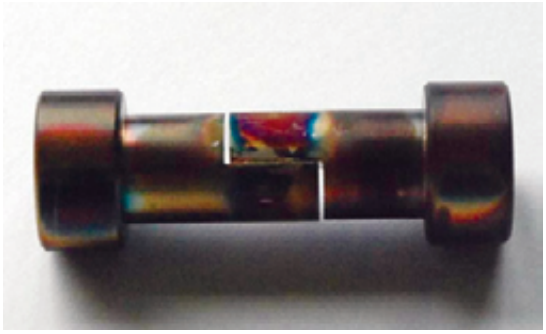

Fig. 3: Joint steel sample for shear testing with a central brazing zone of roughly 12 x 12 mm².

zone. This qualified process was then used to fabricate samples for mechanical shear testing. A sample fabricated from ferritic-martensitic steel is depicted in Fig. 3 with a brazing zone parallel to the load axe under testing condition.

Joints by Ni and Pd plating

Deposition of Pd was similarly performed to Ni plating by applying water-based electrolytes. However, the technical application of Pd electroplating is less widespread compared to Ni plating. Thus, first plating tests for Pd were based on the experience gathered from W coating by Ni. To remove impurity scales from W the developed cleaning processes with alkaline hexacyanoferrate solution for Ni coating [3] were also applied for Pd deposition on tungsten.

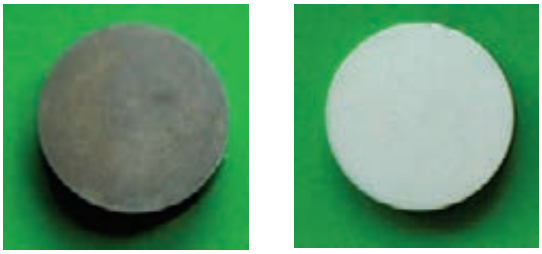

Fig. 4: Macroscopic view of cleaned tungsten disc (left) and Pd coated piece (right).

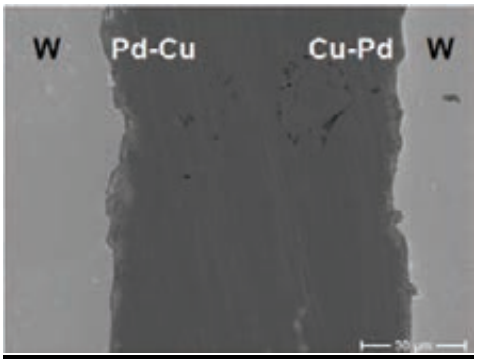

Fig. 5: SEM picture of W parts brazed by Pd and Cu.

The used electrolyte contained the Palladium in form of an ammonia complex and deposition was performed at. T = 40°C and pH range of 7 to 8. In contrast to Ni plating no consumable anode was used. Homogeneous coating was obtained for current densities in the range i = 10-80 mA/cm². The Layer thickness can be controlled by the deposition time and can be easily varied in the range of 10 to 100 µm. Fig. 4 shows a W disc before and after Pd coating, visualized by the even silvery brightness homogeneous coating and adherence to the substrate. However, it has to be mentioned that the successfully performed Pd plating is much more difficult due to hydrogen production, especially in contact with W compared to Ni deposition. Sample fabrication for joining tests with Pd as reactive interlayer was done in the same manner as applied in Ni – Cu joining. This means, that both W pieces were first coated by roughly 15 µm Pd and then one of these parts was plated in the desired joining zone by about 80 µm Cu layer. The clamped parts were brazed in a furnace under Ar flow at 1100°C for about 10 min. From the brazed pieces cross sections were fabricated and underwent microstructural analyses for qualification of the joint. Optical microscopy and SEM showed no defects (cracks, incomplete wetting) in the contact zone between W discs and filler metal as illustrated by Fig. 5. The different gray shadows may give hints that a mixing of the elements W – Pd – Cu took place. This indicates that Pd has a similar ability compared to Ni in activation of W surfaces for brazing with Cu, which is as pure metal normally not able to wet tungsten and form resistant fittings.

Mechanical testing of joints

Metallurgical analyses showed that W – W, W – steel and steel-steel joints can be fabricated by Ni – Cu electro plating technology with good wetting at the brazing temperature of 1100°C. Applying these parameters first samples for shear tests were fabricated as depicted in Fig. 3. These samples were tested in a shear rig and showed shear strength of braze comparable to values known from commercial Ni-Cu fillers tested at room temperature. Clearly visible is that no detachment of the Ni interlayer from the substrate

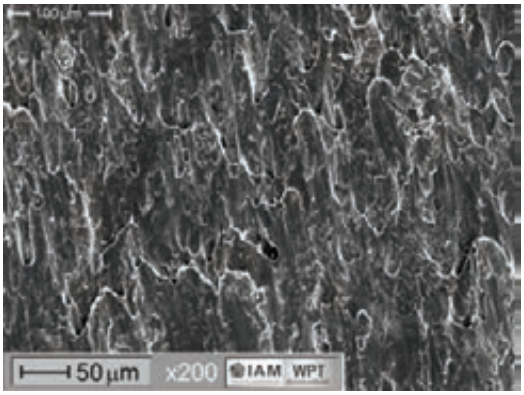

Fig. 6: Cracking zone of filler after shear test.

took place and that the crack was inside the filler as depicted in Fig. 6 and that no brittle failure occurred. These mechanical characterization of joints will be continued to improve statistics and collect values for W – W joints.

Electroplating as tool for composite materials

Tungsten and tungsten alloys are currently considered as candidate materials for various divertor applications, however, they exhibit all the disadvantage of low fracture toughness and a high brittle to ductile transition temperature. Application of W-alloys as structural material, e.g., as pressurized components will require improved properties in these fields.

Development in the field of W composite materials by combination of thin W foils and interlayers of, e.g., Cu foils showed, that such an improvement seems to be possible [4]. However, several open issues are present in this development area, ranging from thinner interlayers up to industrial relevant processing. Electroplating of W foils seems to be a promising tool due to the ability of thickness control of layers during deposition by time or deposition current.

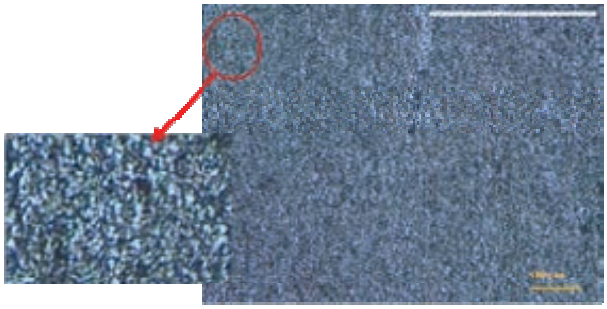

Fig. 7: W foil etched in solution of $K_3[Fe(CN)_6]$ * KOH for 3 min.

Based on the experience in W coating for joining, a development program was set up to coat W foils. In the first stage surfaces were characterized in as delivered and etched conditions to evaluate suitable agents for electroplating. Alkaline hexacyanoferrate solution was used as etching agent to remove surface impurities as described in [3] and to achieve a surface roughening. Fig. 7 shows the morphology of a 0.1 mm thick tungsten foil after etching. The first tests showed, that deposition behavior of Cu on foils is different to plating of massive parts, e.g., cut from rods. Cyanidic electrolytes showed unfavorable behavior despite their better ability in micro scattering. In contrast, sulfatic electrolytes formed more bright and stable layers. By the latter process foils were coated by Cu layers and are now under processing for laminate formation.

Discussion

The performed high heat flux tests under development of He cooled divertor components showed clearly that improvement of brazing technology is absolutely necessary to manufacture reliable joints between armor material tungsten and structural cooling components beneath. This finding is independent of design or cooling variants helium or water. The defects analyzed in high heat flux testing guided the path towards development of joining technology based on electro plating, e.g., by observed strong deficits in homogeneous wetting of the components applying common technology and not adapted fillers.

The development of tools based on electro plating for brazing showed that the deposition of metallic well adherent layers on tungsten is possible if surfaces are cleaned. Copper as main filler component can be used if reactive interlayers are first deposited on tungsten to allow metallurgical reactions. The application of electro plating eliminated here the main risk of inhomogeneous wetting and formation of defects, responsible for failure under load.

Ni has proven to be an excellent activator for brazing and possesses industrial relevance in common technology. Different types of joints, e.g., W to W and W to steel were successfully manufactured by Ni - Cu. The amount of Ni may underlie ‘neutron restrictions’ and has to be kept low. However, the performed tests showed that Ni-Cu is an excellent model system which defines quality for other filler compositions. Further development in joining by electro

plating showed that Pd can successfully overtake the part of Ni in brazing with Cu. However, more stable Pd deposition under industrial view is required for transferring successfully performed lab tests to manufacturing.

First performed mechanical load tests indicated that joints fabricated by electro plating have high potential in joining fusion relevant components. Surely, additional development and qualification work is necessary in both fields mechanical tests and filler adjustment. Activities in the field of W laminate processing indicated that W in shape of foils shows a more complex surface behavior which may be correlated to the high degree of deformation. Application of sulfatic electrolytes indicated that Cu layers can be deposited and that the layer thickness can be controlled by the deposition parameters current and time very well. The electroplating showed the ability to fabricate W laminates with thin ductile interlayers. The whole work on laminates by electroplating needs of course additional development.

Staff:

Dr. J. Konys
Dr. W. Krauss
Dr. N. Holstein
DI J. Lorenz
DI O. Wedemeyer
DI S.-E. Wulf
M. Heck
J. Novotny

Literature:

[1] P. Norajitra, R. Giniyatulin, T. Hirai, W. Krauss, V. Kuznetsov, I. Mazul et al., Current status of He-cooled divertor development for DEMO, Fus. Eng. Design., 84 (2009), 1429-1433.

[2] W. Krauss, J. Konys, N. Holstein, Development of advanced Al-coating processes for future application as anti-corrosion and T-permeation barriers, Fus. Eng. Design, 85, (2010). 2141-2262.

[3] W. Krauss, J. Lorenz, N. Holstein, J. Konys, Alternative electro-chemically based processing routes for joining of plasma facing components, Fus. Eng. Design, 86, (2011), 1607-1610.

[4] J. Reiser, M. Rieth, B. Dafferner, A. Hoffmann, Charpy impact properties of pure tungsten plate material in as-received and recrystallized condition (1 h at 2000°C (2273 K)), J. Nucl. Mater., (2012), http://dx.doi.org/10.1016/j.jnucmat.2012.10.037

[5] S.-E. Wulf, N. Holstein, W. Krauss J. Konys, Influence of deposition conditions on the microstructure of Al-based coatings for application as corrosion and anti-permeation barrier, 27th Symposium on Fusion Technology (SOFT), Liège, Belgium, Sept. 24-28 (2012).

[6] W. Krauss, J. Konys, N. Holstein, J. Lorenz, Electro-chemical processing for tungsten fabrication and joining by layer deposition, Challenges to Developing W-Based Materials for Fusion Applications, UCSB, Santa Barbara, CA, USA, February 13 – 15, 2012

[7] W. Krauss, J. Lorenz, J. Konys Performance of electro-plated and joined components for divertor application, 27th Symposium on Fusion Technology (SOFT), Liège, Belgium, Sept. 24-28 (2012)

Acknowledgement

This work, supported by the European Communities under the contract of Association between EURATOM and Karlsruhe Institute of Technology, was carried out within the framework of the European Fusion Development Agreement. The views and opinions expressed herein do not necessarily reflect those of the European Commission

Material Technologies - 2Component-Powder Injection Molding (2C-PIM) (WP12-MAT-01-HHFM-04-04)

Objectives of the task

Powder Injection Molding (PIM) is a powder metallurgy (PM) near net shape fabrication process for metals and ceramics with tight tolerances and good surface finishes. This process enables the mass production of low cost and high performance parts with complex geometries. Materials with high melting points such as tungsten or tungsten alloys can be effectively fabricated with this process. The PIM process for tungsten, developed at KIT, comprises five stages: design and engineering of a PIM tool (including filling simulation), kneading or extrusion of suitable feedstocks (combination of powder and binder), injection molding of green parts, debinding and the final heat-treatment process. The KIT divertor design for the future DEMO fusion power plant is based on a modular concept of He-cooling finger units. More than 250,000 single parts are needed for the whole divertor system where the most promising divertor material tungsten must withstand the steady state heat loads of up to 10 MW/m².

PIM is a mass production process – but can it also be used for joining? The motivation for this work was the development and investigation of an alternative joining method for two different materials by using 2Component-Powder Injection Molding (2C-PIM).

State of the art PIM R&D

First successful experiences at KIT with pure W-PIM were made in 2009 - 2010. In 2011 two new tungsten alloy feedstocks (W-2La_2O_3 and W-2Y_2O_3) are developed and two-component parts via insert PIM successful produced. The resulting qualities of the joining zones were remarkably fine and the seam was without gaps or cracks. In other words, joining tungsten to W-2La_2O_3 or to W-2Y_2O_3 was very successful [1]. To further apply and investigate this idea, a real 2C-PIM tool was developed, optimized by simulations, and fabricated. This new 2C-PIM tool allows now the fully automatic replication of fusion relevant components, such as the tungsten tile and the tungsten alloy thimble, in one single step and without additional brazing [2; 3]. The microstructural investigation of the joining zone was performed by scanning electron microscopy (SEM) and Auger electron spectroscopy (AES).

<u>Design and Engineering of the new 2C-PIM tool: Filling simulation</u>

Computer simulation tools to design the part, the gating system and the thermal processing of the injection molding tool are very helpful for the successful production of PIM parts. For the simulation of the injection molding process, the software tool SIGMASOFT® was used. The material data of the feedstock like heat capacity, heat conductivity, pVT data (pressure, volume, temperature) and rheology must be known before starting the simulation. A CAD model of the future part including gating system must be imported into the simulation software. After creating the mesh

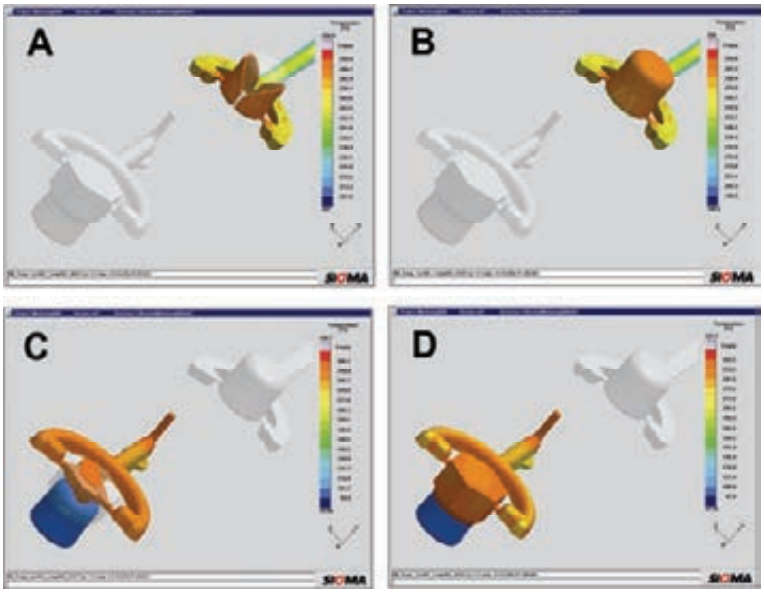

Fig. 1: Filling simulations of the thimble and the tile.

of the model, the type of feedstock, the temperature of the feedstock, the temperature of the injection molding tool and the injection filling time could be selected. The filling simulation allows the definition of the future gating system parameters (position, size, shape) and is very helpful to detect problems (air inclusions, mold filling, premature settings, shearing rate) before the building of the tool is realized. Fig. 1 shows the final and optimized filling simulation of the mockup. A half point gaiting system is used for the filling. Fig. 1 (A) – (B) shows the first step, the filling of the thimble and Fig. 1 (C) – (D) shows the second step, the filling of the tile on top of the finished thimble. The result is the finished mockup which consists of the tile and the thimble (see Fig. 1 (D)).

Producing of parts

Fig. 2 shows the open new tool, left the ejection side and right the nozzle side. This tool allows the fabrication of the tungsten tile and the tungsten alloy thimble in one step, fully automatic, without additional brazing.

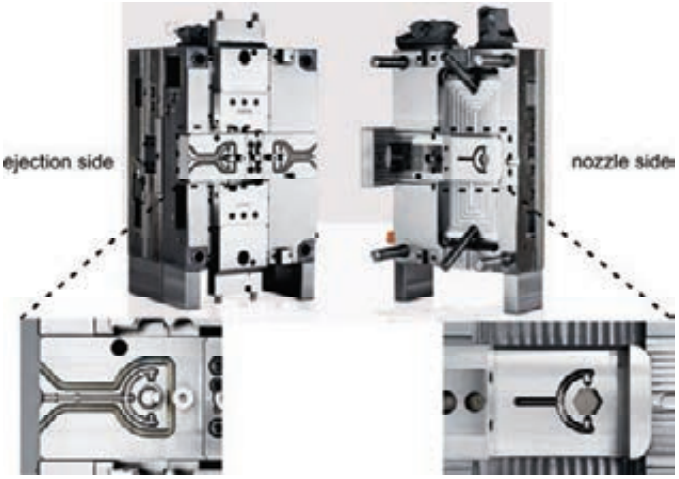

Fig. 2: The new fully automatic 2C-PIM tool: ejection side (left) and nozzle side (right).

To replicate the divertor mockup granulated, homogeneous and agglomeration free tungsten and tungsten alloy feedstock is used. The tile is made of pure tungsten and for the thimble are two different tungsten alloys used. For the composition of W-2La_2O_3, the tungsten was doped with 2wt.-% La_2O_3 powder and for W-2Y_2O_3 with 2wt.-% Y_2O_3 powder. The details of the powder preparation are reported elsewhere [1]. The injection molding was carried out on an FERROMATIK MILACRON K50 injection molding machine (FERROMATIK MILACRON, Germany) at a feedstock temperature of 160 °C and a mold temperature of 50-60 °C. At the first step the pre-mold thimble is replicated, after that, the tool is moved around 180 ° and in the second step the tile is mold on top of the thimble. This process is very quick and effective. The tool could be also used to replicate one component mockups within one process step. After injection molding and before heat-treatment the green parts have undergone solvent debinding. At first solvent debinding in n-Hexane for 48 hours at 50 °C followed by thermal debinding for ½ hour at 550 °C in dry H_2 atmosphere. The developed heat-treatment process is a two-step procedure, first pre-sintering in a sinter furnace from MUT, Germany at 1800 °C in dry H_2 for 2 hours in order to reach a state where the material contains only closed porosity which is necessary for the HIP treatment.

Fig. 3: Finished two-component mockups: green parts (left) and after heat-treatment (right).

After that, the samples were compacted by the use of a suitable HIP-cycle, performed by a HIP 3000 (Dieffenbacher, Germany). The samples were heated up to 2000 °C at 200 MPa pressure and argon atmosphere for 3 hours. Figure 3 shows the green parts and finished parts after heat-treatment.

Results of the joining zone quality of the finished 2C-PIM divertor mockups

Metallographic investigations reveal that the material connection of the two-component powder injection molding combinations W + W-2La_2O_3 and W + W-2Y_2O_3 are successful (see Fig. 4, for example the material combination W+W-2Y_2O_3). No cracks or gaps in the seam of the joining zone between the W tile and the W-2Y_2O_3 thimble are visible. The Auger electron measurements (Fig. 4 right) show the elemental concentration of tungsten across the interface of the finished parts. The color of the W matrix is shown in red and the color of the embedded Y_2O_3-particles is black. A solid bond of the material interface was achieved.

The resulting microstructure (metallographic section) of the finished mockup is also shown. The embedded spherical Y_2O_3-particles in the tungsten matrix are marked by white arrows. Pure PIM tungsten parts achieve a density of 98.6 – 99% T.D., a Vickers-hardness of 457 HV0.1 and a grain size between 5 and 7 µm. The grain size for the material composition W-2La_2O_3 is smaller, with an average value of 3 µm and the relative density is over 97% T.D. and the Vickers-hardness 586 HV0.1. Once again is the grain size smaller for W-2Y_2O_3 with values below 3 µm. These composition achieves also a density of over 97% T.D. but the Vickers-hardness is 617 HV0.1 and still higher than for W-2La_2O_3. Density, hardness and grain size results for the finished parts after heat-treatment are summarized in Table 1. For both doped materials the embedded particles act as grain growth inhibitor and generate a small grain size in comparison to pure PIM tungsten. The effect of the grain boundary strengthening is also seen in the results of the Vickers-hardness. These results are very significant for W-2Y_2O_3.

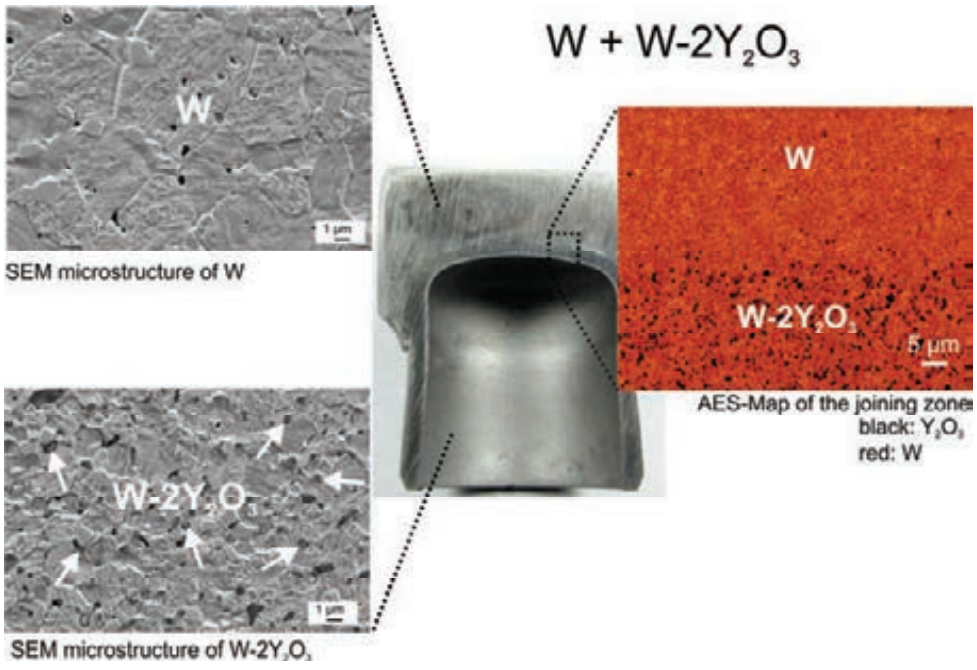

Fig. 4: Quality analyses of the joining zone in a 2C-PIM divertor mockup via SEM and AES.

The materials in this case are pure tungsten for the armour tile and W-2Y_2O_3 for the thimble. The embedded spherical Y_2O_3 particles in the tungsten matrix are marked by white arrows.

Table 1: Results of density, hardness and grain size of the finished parts after heat-treatment.

Material	Theoretical density (% TD)	Vickers-hardness (HV0.1)	Grain size (µm)
W	98.6 - 99.0	457	5 - 7
W-2La_2O_3	96.5 - 97.2	586	>3
W-2Y_2O_3	96.3 - 97.1	617	<3

Integration of interlayer within the 2C-PIM process

Fig. 5 shows the microstructure of the integrated W-mesh into the W-PIM matrix. The idea is to have an interlayer between the W tile and the W alloy thimble which acts as a crack stopper. The W-mesh is enclosed from the W-PIM matrix and increases the strength. This is a first promising result and will be further investigated in 2013.

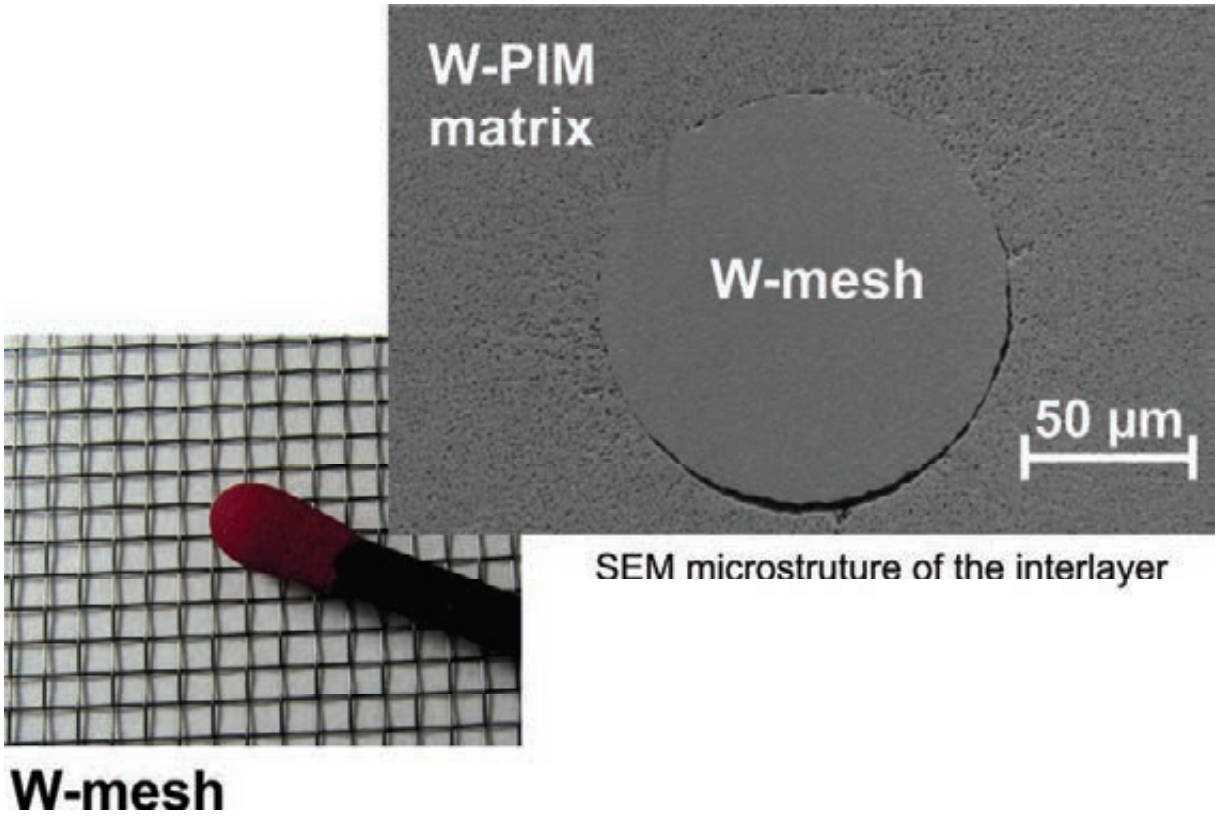

Fig. 5: The W-mesh before (left) and after embedding in the W-PIM matrix (right).

Conclusions and outlook

The motivation for this work was the investigation of a suitable manufacturing method for divertor components consisting of different tungsten materials. Based on the previous results of the tungsten PIM divertor part tile and pretests of basic 2C-PIM parts a newly developed fully automatic 2C-PIM tool allows the replication of fusion relevant components such as the tungsten tile and the tungsten alloy thimble in one step without additional brazing. The microstructure of the finished samples, and the quality of the joining zone, were characterized and found to be remarkably fine.

Further steps are the investigation of the integration of interlayer within the 2C-PIM process and the material characterization via HHF-tests. These tests are in cooperation with the colleagues from FZ Jülich and IPP Garching.

In conclusion, it has been demonstrated that PIM is a powerful process for mass production as well as for joining even complex shaped parts.

Staff:

S. Antusch
L. Commin
T. Hanemann
J. Heneka
N. Denker
M. Müller
M. Offermann
K. Plewa
V. Piotter
M. Rieth
H. Walter
T. Weingärtner

Literature:

[1] S. Antusch, M. Müller, P. Norajitra, G. Pintsuk, V. Piotter, H.-J. Ritzhaupt-Kleissl, T. Weingärtner, Two component tungsten Powder Injection Molding for mass production of He-cooled DEMO Divertor parts. Journal of Fusion Science and Technology 62 (2012), 110-115.

[2] S. Antusch, L. Commin, M. Müller, V. Piotter, T. Weingärtner, Two component tungsten Powder Injection Molding – an effective mass production process. 2nd Joint IAEA-EC Topical Meeting, Ispra, 2012, to be published in Journal of Nuclear Materials (submitted).

[3] S. Antusch, L. Commin, J. Heneka, V. Piotter, K. Plewa, H. Walter, A new fully automatic PIM tool to replicate two component tungsten DEMO divertor parts. 27th SOFT, Liège, 2012, to be published in Journal of Fusion Engineering and Design (submitted).

Acknowledgement

This work, supported by the European Communities under the contract of Association between EURATOM and Karlsruhe Institute of Technology, was carried out within the framework of the European Fusion Development Agreement. The views and opinions expressed herein do not necessarily reflect those of the European Commission.

Long-term Structural Materials: Investigating and Developing W Deep Drawing (WP12-MAT-01-HHFM-04-06)

Continuing the recent deep drawing experiment within the EFDA MAT-HHFM framework, some important parameters in deep drawing tests were studied. In these experiments (round or flat) punch and (sharp or flat) die shapes (Figure 1) were varied. In contrast to the first deep-drawing experiments with force-controlled process a new series of experiments with path-controlled process has been started in another vacuum furnace at KIT. This device operates with path-controlled axial compression. Good deep-draw results were achieved at 700 °C process temperature. Figure 2 shows an example of successfully deep drawn thimble from tungsten disk of Ø 28 mm size with a new flat tool. The cracks on the thimble opening occurred when knocking out the sample from the tool. The entire wall thickness of the thimble remains largely uniform. An axial forming speed ~1 µm/s and a maximal force of ~ 14 kN were measured, being regarded as material-friendly. In comparison, much higher values in the previous experiments with a force-controlled process of up to ~30 µm/s and 20 kN, respectively, were determined. An achieved thimble height of ~12 mm from this last experiment would be sufficient for a complete assembly of a 1-finger module and therefore a good basis for further development of bigger divertor components.

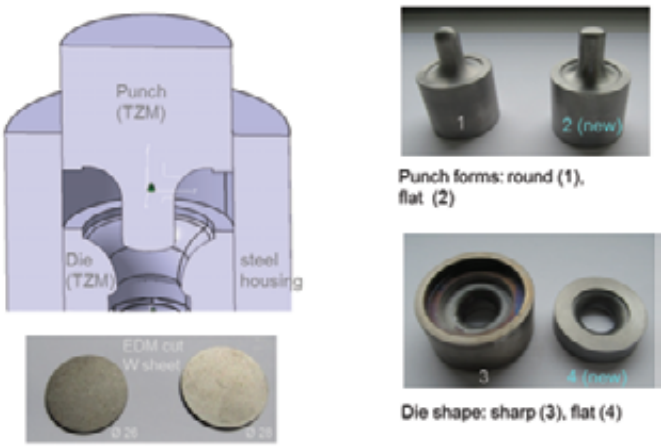

Fig. 1: New deep-drawing tool.

Fig. 2: Deep-drawn thimble from Ø 28 mm initial W slice with new flat tool.

Staff:

W. Basuki
P. Norajitra
L. Spatafora
V. Toth

Acknowledgement

This work, supported by the European Communities under the contract of Association between EURATOM and Karlsruhe Institute of Technology, was carried out within the framework of the European Fusion Development Agreement. The views and opinions expressed herein do not necessarily reflect those of the European Commission.

Long-term Structural Materials: Development of W-WL10 Joint Brazing using Titanium Filler (WP12-MAT-01-HHFM-04-07)

The brazing of tungsten and WL10 with titanium interlayer is under investigation within the EFDA MAT-HHFM framework. Titanium is low activating and has a sufficiently high melting point of 1668 °C, therefore very suitable for a high demanding braze joining of divertor components especially regarding the relatively high operating temperature.

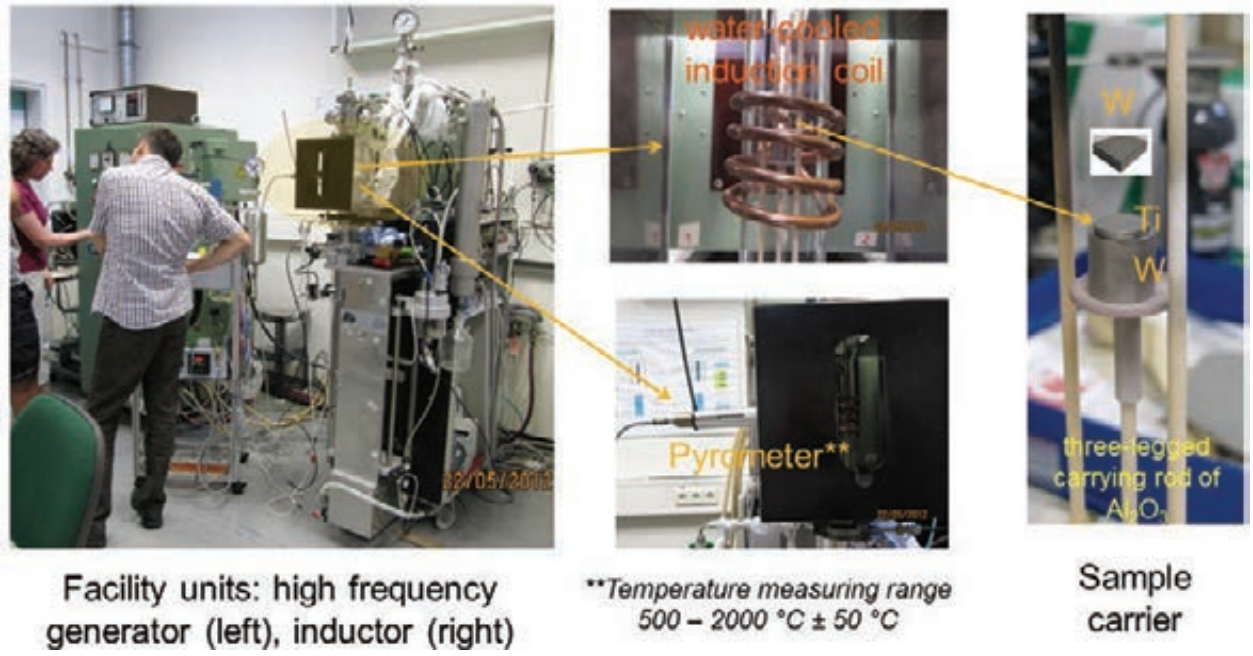

Fig. 1: Induction furnace (left) with inductive heating coil and pyrometer (middle), and sample arrangement (right).

Continuing the recent trials in normal oven, wetting tests were carried out in an induction furnace (Figure 1) at KIT-IAM-AWP. The furnace (left) has an inductive heating coil (center, above), which is driven with a high frequency generator (far left), and a Pyrometer for temperature measurement in the range of 500–2000 °C (center, bottom). The stacked samples (right, from the bottom upwards Ø10 mm W cylinder, Ti sheet (Ø8 mm x 1 mm, 99.999% purity from GoodFellow), and 1 mm thick tungsten slice) are located in a three-legged holder device within a glass bulb, which was first purged with Ar and then evacuated down to 1 mbar. The process parameters used are: Tbr ~ 1820 °C (W surface), no pressing weight, heating rate ~ 120 K/min, and holding time ~ 2.5 min.

Figure 2 shows a relative rapid temperature sequence, as measured on the surface of tungsten, such as a rise in temperature from ~1000 °C to ~1700 °C within about 6 min can be clearly seen. Light microscopic examination (Figure 3) shows a perfect wetting of titanium on tungsten surfaces.

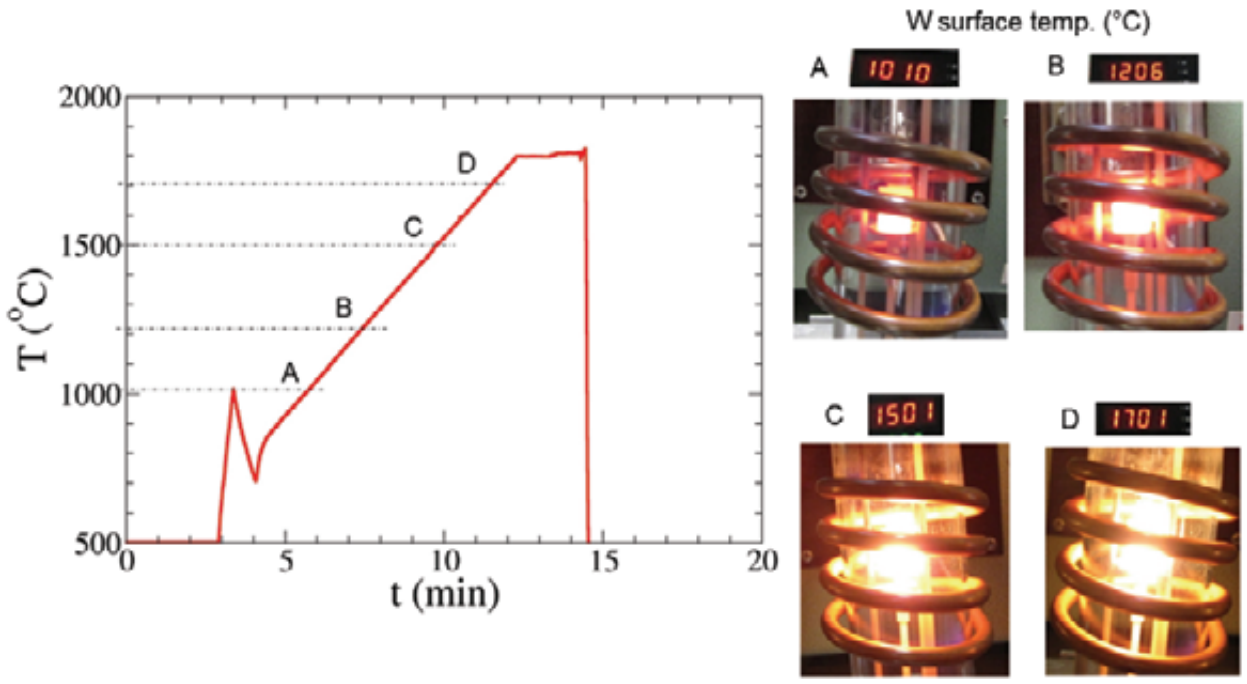

Fig. 2: Temperature sequence of the samples (W surface).

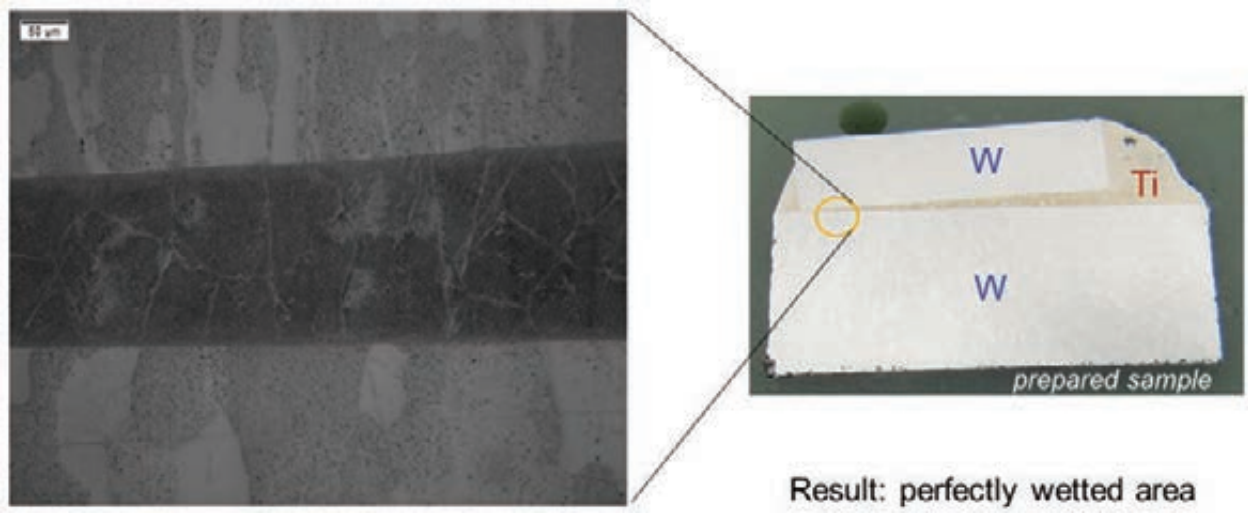

Fig. 3: Light microscopic examination.

Staff:

S. Antusch
S. Berberich
W. Basuki
P. Norajitra
L. Spatafora
U. Stegmaier

Acknowledgement

This work, supported by the European Communities under the contract of Association between EURATOM and Karlsruhe Institute of Technology, was carried out within the framework of the European Fusion Development Agreement. The views and opinions expressed herein do not necessarily reflect those of the European Commission.

Prototype Cooling Structures (WP12-MAT-01-HHFM-05-01)

Introduction

There are several tasks a divertor has to fulfill. These are for example (i) to remove particles, e.g. He, T, Fe, C, which is realized by pumps; (ii) to remove dust caused by tungsten armour erosion; as well as (iii) to deals with the heat load. This paper will focus on the last task; dealing with the heat load.

The expected heat load for a DEMO divertor in a short-term scenario is about 10 MW/m^2, with expected peaks as a result of plasma instabilities up to 20 MW/m^2. The basis of this short-term scenario is plasma in pulsed operation condition. A long-term scenario makes use of continuous burning plasma. In this case, the requirement is to deal with 7 MW/m^2. A heat load that defines the absolute plasma physical minimum is expected to be 5 MW/m^2.

The setup of an ITER divertor can deal with a heat load of 20 MW/m^2. Such a divertor consists of a pipe made of CuCrZr (precipitation hardened: Cu, 0.5–1.2 wt.% Cr and 0.03–0.3 wt.% Zr) that is surrounded by a tungsten armour in a monoblock shape. The coolant is water with an inlet temperature of 100°C, an outlet temperature of 120°C and a pressure of 40 bar. Such an ITER divertor can be regarded as a best case configuration for the removal of heat loads, as it combines the excellent thermal conductivity of copper (Cu = 305 W/(m*K) at RT) with the excellent heat transfer coefficient of water (H_2O= 100 kW/(m^2*K), using swirl or hypavapotron). As one expects much higher neutron loads and neutron damage for a DEMO divertor [1] it is worth to develop alternative concepts and to assess other combinations of materials for the cooling pipe and coolants.

The whole assessment of the matrix of material for the cooling pipe (copper, austenitic steel (316Ti), ferritic-martensitic steel (Eurofer, F82H), tungsten laminate pipe) and coolant (water, helium) will be discussed in another paper. In this paper, we want to focus on the use of a tungsten laminate for divertor applications.

The idea of the tungsten laminate project is that tungsten foil is ductile and can be bent plastically even at room temperature. Within the framework of the tungsten laminate project we succeed in expanding the ductile properties of the foil to the bulk, by assembling and joining of several layers of the ductile tungsten foil [2,3]. Such a tungsten laminate can be used for divertor applications in the case of: (i) a transition piece between the steel pipe and the tungsten armour, in order to deal with the different thermal expansion coefficients of the structural steel pipe and the tungsten monoblock armour; or (ii) as a structural material, especially in the shape of a tungsten laminate pipe. Both applications will be discussed in the following sections.

Divertor: structural steel pipe, W armour

In this application, the tungsten laminate is used as a transition piece between a structural steel pipe and tungsten armour, in order to deal with the different thermal expansion coefficients of steel and tungsten.

The geometry of the divertor target consists of a pipe that is surrounded by tungsten armour. The material for the structural steel pipe is either austenitic steel (e.g. 316Ti (1.4571) or 15/15Ti (1.4970)) or reduced activation ferritic martensitic (RAFM) steel, such as Eurofer or F82H. The coolant might either be water or helium. For water cooling, the heat transfer coefficient can be increased by using a swirl of a hypavapotron. If the coolant is helium the heat transfer coefficient can be increased by either jet impingement [4, 5] or a foam.

The problem of using steel as a structural material for a divertor is, on the one hand, its bad thermal conductivity. For austenitic steel, the thermal conductivity at RT is 15 W/(m*K), for Eurofer the thermal conductivity at 500°C is 30 W/(m*K) [6].

On the other hand, the different thermal expansion coefficients of the steel pipe and the tungsten armour make this connection a challenge. The thermal expansion coefficient of steel, for example, is about 12 * 10^{-6} 1/K at RT, whereas the thermal expansion coefficient of tungsten is about 4 * 10^{-6} 1/K at RT. Here a tungsten laminate can help.

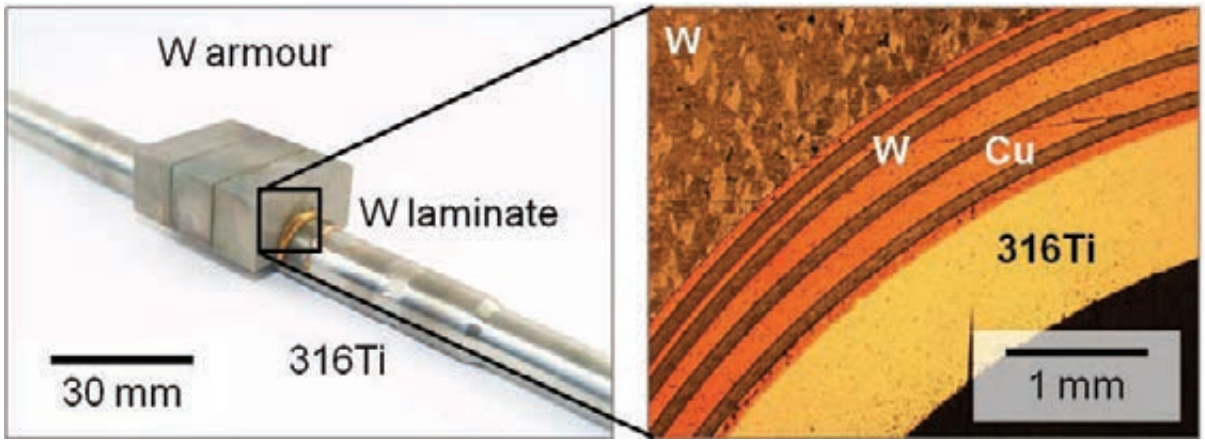

Fig. 1: Left: Divertor mock-up for high heat flux tests. The mock-up consists of a structural steel pipe (austenitic steel, 316Ti) surrounded by tungsten armour in a saddle-type shape. Between steel pipe and tungsten armour, a tungsten laminate, made of four layers of tungsten foil and five layers of copper, compensates the different thermal expansion coefficients of steel and tungsten.

Fig. 1 (left) shows a testable mock-up made of an austenitic steel pipe (316Ti, 1.4571) that is surrounded by tungsten armour. In this case, the tungsten armour is not in the monoblock shape, but in a saddle-type shape. Between the steel pipe and the tungsten armour there is a tungsten laminate that consists of four layers of tungsten foil and five layers of copper in between. The steel pipe, the tungsten laminate and the tungsten armour were joined in one step by brazing. The optical micrograph shown in Fig. 1 (right) gives an impression of how the tungsten laminate surrounds the steel pipe.

As a result, we can summarize that we succeeded in producing a testable steel mock-up made of austenitic steel (316Ti). The connection of the tungsten laminate to the steel pipe, as well as the connection to the tungsten armour, works. This mock-up can now be used for high heat flux (HHF) tests.

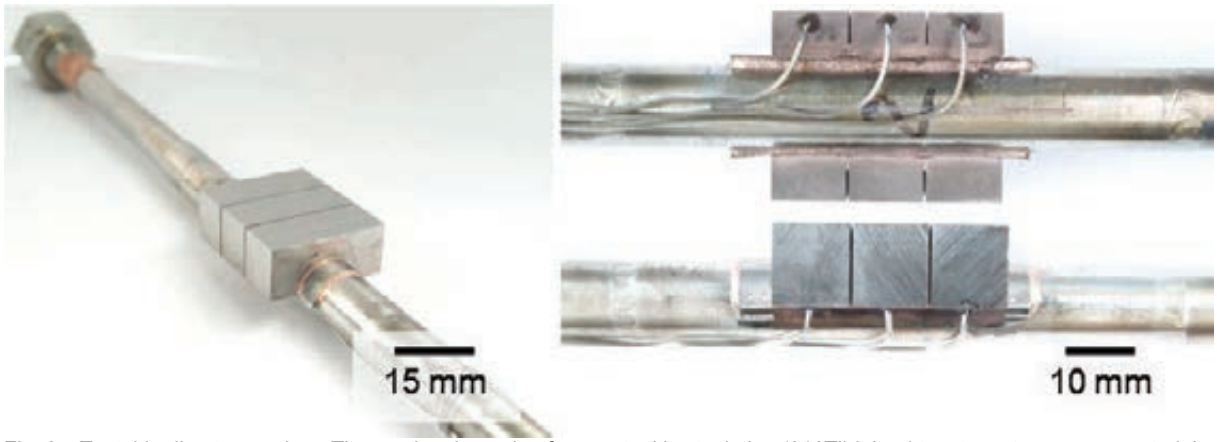

Fig. 2: Testable divertor mockup. The mockup is made of an austenitic steel pipe (316Ti) joined to a tungsten armour material in the saddle type shape. A tungsten laminate is used as a transition piece between the steel pipe and the tungsten armour dealing with the different thermal expansion coefficients of steel and tungsten. Right: The picture shows the position of the thermo couples.

High heat flux tests were performed at the IPP, Garching (Mr. H. Greuner, and Mr. Böswirth). Thermocouples used were type K (NiCr-Ni) that were positioned 2 mm below the plasma facing surface (Fig. 2). The coolant was water, RT, 10 m/s and 1.13 l/s. The mockup was exposed to a heat load of 6 MW/m^2. One cycle took 1 min: 20 s beam on, 40 s beam off. Until now the mockup was tested for 100 cycles and shows no damage at all (Fig. 3). The Mock-up Tests will continue in 2013.

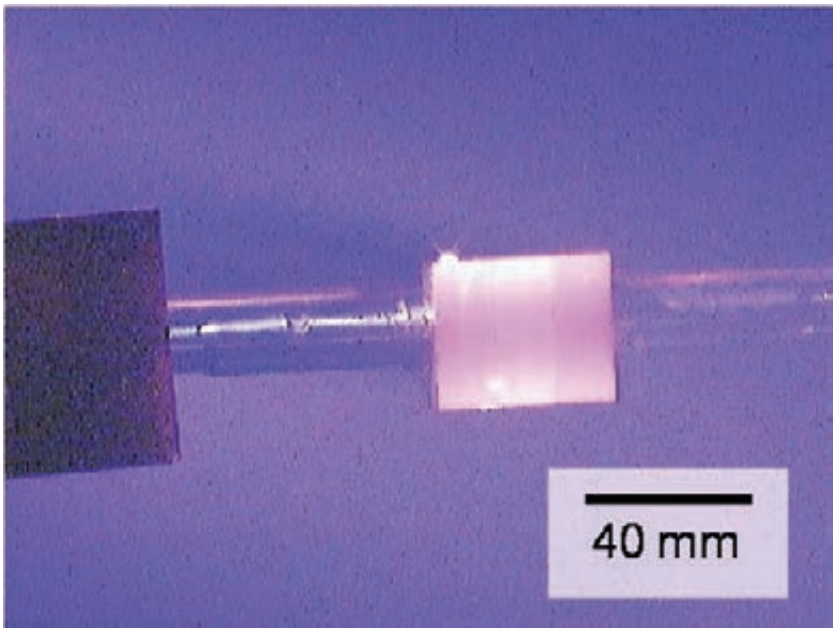

Fig. 3: Mockup from Fig. 2 during the high heat flux test (HHF). The coolant was water at RT. After 100 cycles at 6 MW/m^2 the test was stopped. The mockup shows no damage at all (IPP, Garching, Mr. Henri Greuner and Mr. Böswirth).

Divertor: structural tungsten laminate pipe, W armour

In this application, the tungsten laminate is used as a structural material. By rolling up and joining a tungsten foil, a tungsten laminate pipe can be realized.

Again the geometry of the divertor target consists of a pipe that is surrounded by tungsten armour. The material for the structural pipe is now a tungsten laminate pipe. The coolant might either be water or helium. Especially for a helium coolant, the jet impingement has to be integrated into a pipe design. Such a divertor concept for a helium-cooled divertor, using a tungsten laminate pipe with an integrated jet impingement, can be found in a former publication [7].

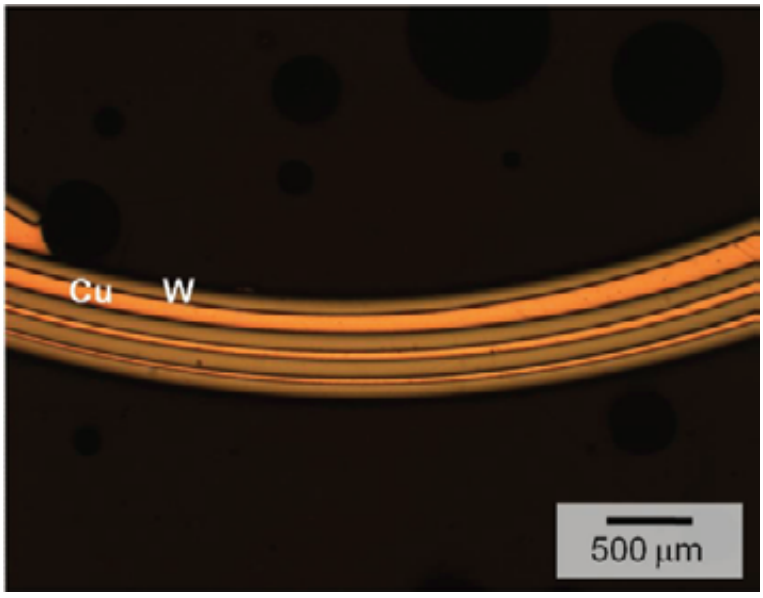

Fig. 4: Optical micrograph of a tungsten laminate pipe made by rolling up and joining of a tungsten foil. The interlayer is copper, the joining technology is brazing. In this case the tungsten laminate pipe is used as a structural material for pressurized pipes.

The problem of using tungsten as a structural material can be divided into two issues. The first question is how to find a tungsten material that fits the need of a structural material,

which means finding a tungsten material with a low brittle-to-ductile transition temperature. The second question is how to produce a pipe made of tungsten.

Tungsten pipes can be produced by hot extrusion. However, this fabrication route is really challenging. Another possibility is to drill a hole into a tungsten rod. What we did in our research was to synthesize a tungsten laminate pipe by rolling up and joining a tungsten foil. Fig. 4 shows an optical micrograph of a cross-section of a tungsten laminate pipe. In this special case, the interlayer was a copper foil and the joining technique was brazing. Such laminate pipes can then be characterized by a mechanical test, e.g. Charpy impact tests.

Charpy impact test were performed on the basis of the EU standards 528 DIN EN ISO 148-1 and 14556:2006–10. The pipe samples had dimensions of 27 mm length, 15 mm outer diameter, 1 mm wall thickness, 22 mm span. Benchmark experiments were performed on tungsten pipes, produced by drilling a hole in a tungsten rod. The results of the Charpy impact test can be found in Fig. 5. Fig. 5 (left) shows the fractured pieces of a Charpy impact test on a tungsten pipe, made by drilling a hole into a tungsten rod. The test temperature was 300°C. The dissipated energy was nearly zero. It is obvious that such a pipe cannot be used for safety relevant and pressurized pipes. Much more promising are the results obtained from the Charpy impact test performed on tungsten laminate pipes (see Fig. 5, right). In this case, the tungsten laminate pipe was produced using an interlayer made of a copper alloy, joined by brazing. The Charpy impact test temperature was 300°C. The dissipated energy was at least 20 J; the striker got stuck in the sample.

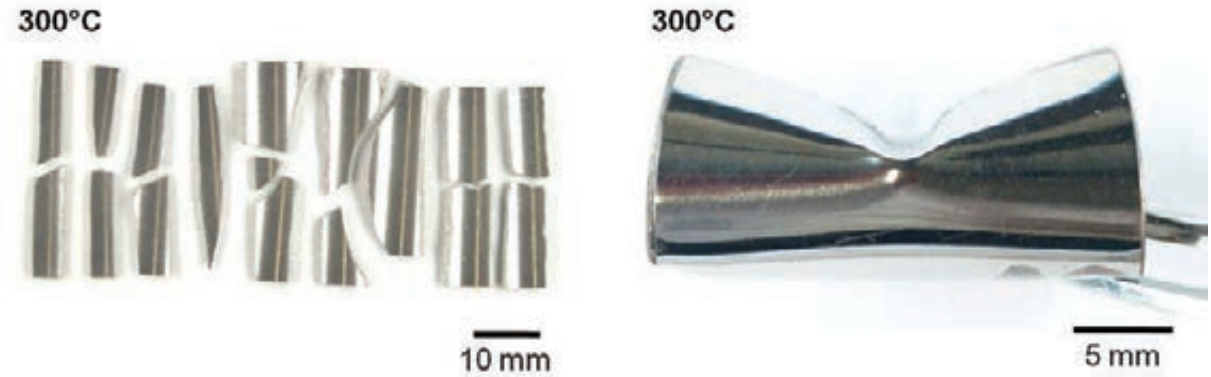

Fig. 5: Left: Charpy impact test of a tungsten pipe made by drilling a hole in a rod. The test was performed at 300°C, the dissipated energy is nearly null. Right: Charpy impact test of a tungsten laminate pipe. The test was performed at 300°C, the dissipated energy is at least 20 J. The tungsten laminate pipe is deformed plastically but not fractured.

It can be summarized that a tungsten laminate pipe has extraordinary properties and is a serious candidate for a structural tungsten material. It is obvious that the properties of a tungsten laminate, as well as a tungsten laminate pipe, strongly depend on: (i) the condition of the tungsten foil (as-received, recrystallized); (ii) the interlayer (copper, palladium, titanium, zirconium, vanadium or no interlayer); (iii) the interface between tungsten and interlayer (wettability, solid solution, intermetallics); and (iv) ageing (continuous diffusion, Kirkendall-effect).

Besides these issues, the type of joining technology is essential too. Here we can distinguish among: (i) brazing; (ii) diffusion boning; (iii) hot pressing; and (iv) other. This wide matrix of (i) kind of tungsten foil, (ii) interlayer, and (iii) joining technology, allows us to assess a wide range of tungsten laminate materials, and allows tailoring of the required properties.

Fig. 6 gives an impression of how a testable mock-up might look like one day. This picture shows a tungsten laminate pipe that is joined at both ends to steel pipes made of austenitic steel. The joining of the tungsten laminate pipe to the steel pipe is realized by copper brazing. It can be concluded that the connection of a tungsten laminate pipe to steel pipes works.

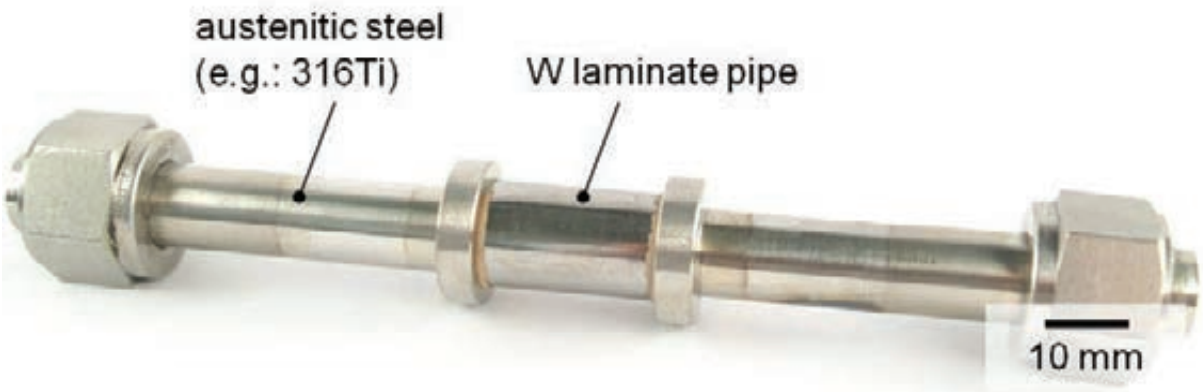

Fig. 6: This picture shows a tungsten laminate pipe that is joined at both ends to a pipe made of austenitic steel (316Ti). This configuration was tested in a burst test device using water at RT, perform at PLANSEE SE. The test was successfully stopped at 1000 bar.

In a next step, the tungsten armour monoblocks, as well as a steel cartridge for the jet impingement, have to be added. After that, a testable helium cooled divertor mock-up using a tungsten laminate pipe is ready for high heat flux tests.

Fig. 6 shows the result of a burst test using water at RT, perform at PLANSEE SE (Mr. Thomas Huber and Mr. Anton Zabernig). The test was successfully stopped at 1000 bar. The laminate pipe did not explode. This is curious as it was estimated different from numerical calculations. It might be that the laminate pipe benefits from self friction.

Summary and conclusion

By assembling and joining several ductile tungsten foils we succeeded in expanding the ductile properties of the foil to the bulk. Such a tungsten laminate can be used for divertor applications in terms of: (i) a transition piece for a structural steel divertor, dealing with the different thermal expansion coefficients of steel pipe and tungsten armour. First HHF tests at the IPP (Garching) show that at least 6 MW/m^2 can be removed.

By rolling up and joining of a tungsten foil, a tungsten laminate pipe can be synthesized. Such pipes can be used for divertor applications in terms of: (ii) a structural material, meaning for safety relevant, pressurized pipes. The Charpy impact test results as well as burst tests at RT look promising.

Staff:

S. Baumgärtner
D. Bohlich
B. Dafferner
M. Hoffmann
U. Jäntsch
A. Möslang
J. Reiser
M. Rieth
R. Ziegler
H. Zimmermann

Literature:

[1] M.R. Gilbert, S.L. Dudarev, S. Zheng, L.W. Packer and J.-Ch. Sublet, Nucl. Fusion, 52 (2012).

[2] J. Reiser, M. Rieth, B. Dafferner, A. Hoffmann, J. Nucl. Mater., 423 (2012) 1.

[3] J. Reiser, M. Rieth, B. Dafferner, A. Hoffmann, X. Yi, D. E.J. Armstrong, J. Nucl. Mater., 424 (2012) 197.

[4] V. Widak, P. Norajitra, Fusion Eng. Design, 84 (2009) 1973.

[5] R. Krüssmann, G. Messemer, K. Zinn, Fusion Eng. Design, 84 (2009) 1119.

[6] K. Mergia, N. Boukos, J. Nucl. Mater., 378 (2008) 1.

[7] J. Reiser, M. Rieth, Fusion Eng. Design, 87 (2012) 718.

[8] Jens Reiser, Michael Rieth, Anton Möslang, et al., Fusion Engineering and Design, Ductile tungsten laminate pipes for divertor applications, under review.

Acknowledgements

This work, supported by the European Communities under the contract of Association between EURATOM and Karlsruhe Institute of Technology, was carried out within the framework of the European Fusion Development Agreement. The views and opinions expressed herein do not necessarily reflect those of the European Commission.

The authors are grateful to their colleagues from PLANSEE Metall GmbH, University of Oxford, Department of Materials, and the Karlsruhe Institute of Technology (KIT), Institute for Applied Materials (IAM), for their support and valuable contributions.

Issues Related to Radiation on Blanket and Divertor Materials (WP12-MAT-02-M02-01)

Objectives

Structural materials for the in-vessel components of future energy generating Fusion Reactors (FR) will be exposed to high neutron and thermo-mechanical loads. Degradation of microstructure of structural materials under neutron irradiation as a result of displacement damage accumulation up to damage doses of 150 dpa and production of transmutation products i.e. helium and hydrogen will strongly influence materials performance. The Reduced Activation Ferritic/Martensitic (RAFM) steels and their Oxide Dispersion Strengthened (ODS) variants are considered as primary candidate structural materials for the First Wall (FW) and helium cooled Breeding Blanket (BB). The current work aimed at assessment of the influence on the neutron irradiation on the blanket and divertor materials. The effects on the mechanical properties of RAFM steels were assessed by retrieving the experiments simulating He production. Also the issue of swelling has been addressed. Assessment of blanket design limitations due to mechanical properties degradation under neutron irradiation and He production was performed.

Task Current Status

At KIT the effects of helium were simulated by the irradiation of boron doped EUROFER based steels. The evolved helium microstructure and its influence on the mechanical properties turned out to depend strongly on the irradiation temperature. At irradiation temperatures below 340 °C and at helium contents below 420 appm the steel microstructure is characterized by the presence of helium bubbles which are nearly homogeneously distributed in the steel matrix. At an irradiation temperature of 450 °C, however, helium bubbles are predominantly nucleated at line dislocations. At T_{irr} ≤350 °C a progressive material embrittlement with produced helium amount was found up to 420 appm He. On the base of these experiments the helium embrittlement rate between 0.5 and 0.6 °C/appm He is estimated at T_{irr} ≤350 °C and up to 420 appm. This embrittlement rate is slightly higher than the embrittlement rate of 0.40 °C/appm He obtained at T_{irr}=250 °C up to 300 appm He by comparative studies of neutron irradiation induced embrittlements in 11B and 10B isotope doped F82H steels by a JAEA group [E. Wakai et al., J. Nucl. Mater. 398 (2010) 64]. The helium influence on the impact properties is found to be strongly reduced at T_{irr}=450 °C by investigation of neutron irradiated ERUOFER97 based boron doped model steels by KIT. These estimations can be considered conservative as the boron doping technique most probably overestimates helium embrittlement as a result of possible non-homogeneous distribution of boron e.g. due to precipitation of boron nitrides and partial segregation of boron at grain boundaries.

The DBTT-shift of the steels irradiated in spallation targets at T_{irr} <380 °C was found by Dai and coauthors [Y Dai et al, J. Nucl. Mater. 389 (2009) 288, Y Dai et al, J. Nucl. Mater. 415 (2011) 306] to be much higher than that of neutron irradiated steels and the difference increased with irradiation dose which was attributed to the He-induced embrittlement. At irradiation temperatures below 380 °C the shifts in the DBTT due to synergy of helium and dpa effects was shown to linearly increase with helium concentration up to 1600 appm. For the case of EUROFER97 the embrittlement due to 18 dpa and 1400 appm helium under spallation target irradiation was a DBTT increase of about 600 °C. Taking into account the dpa damage (18 dpa) induced low temperature (T_{irr} ≤335°C) embrittlement of about 190 °C under fission neutron environment, helium induced embrittlement under spallation target environment can be estimated to be about 410 °C for 1400 appm which corresponds to the helium embrittlement rate of about 0.3 °C/appm He at T_{irr} < 380 °C. The helium embrittlement rate is, however, not constant and is reduced for lower helium contents. So up to 600 appm He the embrittlement rate due to helium is reduced down to 0.13-0.15 °C/appm He at T_{irr} <380°C.

The swelling of RAFM steels is sensitive to irradiation or implantation temperature, helium and dpa production rates and steel virgin microstructure. The neutron irradiation of boron and nickel doped F82H to 51 dpa at 300 °C yielded in nearly no swelling up to 504 appm He [E. Wakai et al., J. Nucl. Mater. 283-287 (2000) 799].

After irradiation at 400 °C, however, 1.2% and 1.1% volumetric swelling was observed in 60 wppm nat. B and 58 wppm 10B doped F82H steels due to production of 77 and 332 appm He, respectively [E. Wakai et al., J. Nucl. Mater. 283-287 (2000) 799]. Remarkably, about 0.5% swelling was determined in reference F82H std. steel due to only 25 appm He. Such a large swelling was attributed to a non-controlled helium production-to-dpa rate under neutron irradiation of boron doped steels [E. Wakai et al., J. Nucl. Mater. 356 (2006) 95]. In contrast to boron doped steels the nickel doped F82H +1.31 at% 58Ni steel exhibited no swelling even though about 504 appm He was generated due to transmutation of 58Ni isotope. The absence of tempering heat treatments on Ni doped F82H steels were considered as a main reason for swelling suppression under neutron irradiation in [E. Wakai et al., J. Nucl. Mater. 283-287 (2000) 799]. Single, dual and triple beam irradiation of F82H specimens were performed for the study of the effects of gas atoms and displacement damage on the mechanical properties and microstructure of F82H [E. Wakai et al., J. Nucl. Mater. 356 (2006) 95]. The peak temperature of swelling induced by dual beam irradiation (10.5 MeV Fe3+ and 1.05 MeV He+) to 50 dpa at helium to dpa ratio of 10 appm He/dpa was at about 430 °C in the temperature range from 360 to 600 °C and the value of swelling was 0.6 %. A well pronounced bimodal distribution observed at 430 °C indicated advanced bubble to void transformation. The observed swelling of 0.6% is still in the acceptable range according to the French design code RCC-MRx. It has to be emphasized that whereas He/dpa ratio of 10 studied is adequate for fusion condition, the dpa production rate of $1.0x10^{-3}$ dpa/s is at least three orders of magnitude larger than the damage accumulation rate under fusion neutron spectrum. The absence of an irradiation facility with fusion relevant neutron spectrum does not allow the assessment of swelling under in-service condition and so still an uncertainty remains concerning the helium content and the irradiation temperature for the onset of pronounced swelling for fusion relevant dpa and helium production rates.

Blanket design limitations due to DPA & helium

EUROFER97 shows excellent mechanical properties in the unirradiated condition from -80 to 550 °C [A. Möslang et al., Nucl. Fusion. 45 (2005) 649]. Above this temperature range the structural application of the steel is limited mainly by the considerable loss of tensile and creep strengthes. Strong hardening and correlated embrittlement induced by low temperature neutron irradiation (T_{irr} ≤335 °C) imposes a lower limit of application temperature for EUROFER97. Only minor hardening and embrittlement observed at T_{irr} =350 °C indicates considerable healing of radiation damage at this temperature. Neutron irradiation at T_{irr} ≥400 °C has nearly no impact on the mechanical properties. On the basis of these experiments EUROFER97 is highly suited for fusion reactor design with an operating temperature range between 350 and 550 °C for the First wall (FW) and Breeding Blanket (BB) structures.

In the irradiation temperature range between 350 and 550 °C the application of EUROFER97 is further limited by helium effects. By assessment of helium embrittlement of between 0.15 and 0.25 °C/appm He on the base of helium simulation experiments and for fusion reactor relevant helium to dpa ratio of 10 appm He/dpa, helium effects are expected to be tolerable up to a damage dose of at least 40 dpa. Beyond this limit the DBTT of the structural steel will be raised above RT. Consequently application temperature range, DPA and He limits for EUROFER97 are proposed between 350 and 550 °C, 40 dpa and 400 appm He, respectively.

The mechanical performance of RAFM steel at low irradiation temperatures (T_{irr} <350 °C) will be mainly limited by dpa induced embrittlement. By utilizing post irradiation annealing of FW and BB structures for the recovery of dpa effects at low irradiation temperatures and for fu-

sion reactor relevant helium to dpa ratio of 10 appm He/dpa the helium effects will be tolerable up to a damage dose of at least 40 dpa on the basis of spallation proton irradiation experiments.

Advanced ODS EUROFER steels with 0.3 wt.% Y_2O_3 exhibit good mechanical properties in the unirradiated state in the temperature range from -50 to 650 °C [R. Lindau et al., Fusion Eng. Des. 75-79 (2005) 989]. Yield and tensile strength are about 35% higher than for EUROFER97 up to 700 °C. The impact properties are somewhat worse than that of EUROFER97 but still in an acceptable range, i.e. DBTT at around -50 °C and USE between 6.5 and 8.5 J for KLST specimens [R. Lindau et al., Fusion Eng. Des. 75-79 (2005) 989], [J. Henry, J. Nucl. Mater. 417 (2011) 99], [N. Luzginova, J. Nucl. Mater. 428 (2012) 192]. Low temperature neutron irradiation (T_{irr}≤340 °C) leads to strong embrittlement of ODS EUROFER steels. Irradiation at 450 and 550 °C of recently developed ODS EUROFER steel yielded nearly no changes of the mechanical properties [N. Luzginova, J. Nucl. Mater. 428 (2012) 192]. Consequently, experimentally validated lower application temperature for ODS EUROFER is 450 °C. Having in mind a strong recovery of the radiation damage in base EUROFER97 steel above 350 °C, the operation temperature window between 350-400 and 650 °C can be proposed for ODS EUROFER (9%Cr) steel. The influence of helium on the mechanical properties of ODS EUROFER is not available yet and a dedicated study is required in the future.

Staff:

J. Aktaa
E. Gaganidze

Literature:

[1] J. Weiß, Ermile Gaganidze, J. Aktaa, Quantitative characterization of microstructural defects in up to 32 dpa neutron irradiated EUROFER97, J. Nucl. Mater. 426 (2012) 52-58.

[2] E. Gaganidze, C. Dethloff, O. J. Weiß, V. Svetukhin, M. Tikhonchev and J. Aktaa, Modeling and TEM Investigation of Helium Bubble Growth in RAFM Steels Under Neutron Irradiation, J. ASTM International, DOI:10.1520/STP103972, (2012).

[3] E. Gaganidze and J. Aktaa, Issues Related to Radiation on Blanket and Divertor Materials, Final Report for EFDA WP12-MAT-02-M02-01/KIT and EFDA WP12-MAT-02-M03-01/KIT, KIT Internal Report, FUSION Nr. 404, 2012.

[4] E. Gaganidze and J. Aktaa, Assessment of neutron irradiation effects on RAFM steels, accepted for publication in Fusion Engineering and Design, (2012).

Acknowledgement

This work, supported by the European Communities under the contract of Association between EURATOM and Karlsruhe Institute of Technology, was carried out within the framework of the European Fusion Development Agreement. The views and opinions expressed herein do not necessarily reflect those of the European Commission.

Assessment of Mechanical Properties of Neutron Irradiated RAFM Steels (WP12-MAT-02-M03-01)

Objectives

Structural materials for the in-vessel components of future energy generating Fusion Reactors (FR) will be exposed to high neutron and thermo-mechanical loads. Degradation of microstructure of structural materials under neutron irradiation as a result of displacement damage accumulation up to damage doses of 150 dpa and production of transmutation products i.e. helium and hydrogen will strongly influence materials performance. The Reduced Activation Ferritic/Martensitic (RAFM) steels and their Oxide Dispersion Strengthened (ODS) variants are considered as primary candidate structural materials for the First Wall (FW) and helium cooled Breeding Blanket (BB) with operating temperatures between 350 and 650 °C. The current work aimed at compilation and assessment of mechanical properties of neutron irradiated RAFM steels. The emphasis was put on the assessment of Charpy impact, fracture toughness, tensile and low cycle fatigue properties of EUROFER97 and EUROFER ODS (9% Cr) steels irradiated up to a displacement damage dose of 80 dpa. The effects of the neutron irradiation temperature and dose were investigated.

Task Current Status

The influence of the neutron irradiation on tensile, impact, low cycle fatigue (LCF) and fracture-mechanical properties of EUROFER97 and other reference RAFM steels were investigated by SCK-CEN, NRG, KIT and CEA up to damage dose of 80 dpa.

Tensile properties

Tensile properties of EUROFER97 and other RAFM steels are severely degraded under neutron irradiation at irradiation temperatures below 340 °C as found in different European irradiation programmes carried out by SCK-CEN, NRG, KIT and CEA. Neutron irradiation leads to substantial increases in the Yield Stress which is sensitive to the irradiation parameters i.e. irradiation dose and temperature. The Yield Stress increase is rather steep at doses below 10 dpa for different Heats of EUROFER97 as well as for other investigated RAFM steels for irradiation temperatures between 300 and 335 °C and for test temperatures between 300 and 350 °C. The hardening rate is significantly decreased at the achieved damage doses of 70-80 dpa for all investigated steels. At achieved damage doses the hardening indicates a clear tendency towards saturation for EUROFER97 (Heat E83697). A comparison of high dose irradiation results obtained on EUROFER97 (Heat E83697), pre-irradiation heat treated EUROFER97 HT (heat E83697) and EUROFER97 (Heat E83698) reveals, however, that high dose hardening behaviour can be observably modified by variation of different metallurgical variables (Thermal Treatment, Heat, etc.). A plate material of EUROFER97 (Heat E83698) did not reached saturation at 80 dpa, though hardening rate per dose increment is substantially reduced compared to hardening rate below 10-15 dpa. Hardening quantified for F82H-mod and 9Cr2WTaV (British Steel, Heat VS3104) steels at 70 dpa is comparable to that of EUROFER97 (Heat E83697). Furthermore, similar to EUROFER97 (Heat E83697) F82H-mod steel indicates saturation of hardening at the achieved damage doses. The limited number of available irradiated specimens does not allow detailed statistical analysis of the results.

Close values of the Ultimate Tensile Strength (R_m) and Yield Stress ($R_{p0.2}$) of EUROFER97 and other RAFM steels after low temperature irradiation (T_{irr} <340 °C) indicate a strong suppression of the strain hardening capability. The Uniform Strain and Total Strain of ERUOFER97 show a strong reduction from their values in the reference unirradiated state already at 2.1 dpa. The Uniform Strain is scattered mostly below 0.5% in the irradiated state. Though strongly reduced, the Total Strain remains mostly at or above 10% for irradiated specimens. In contrast to EUROFER97 (heat E83697) the Total Strain of about 6.0% is ob-

served for EUROFER97 (Heat E83698) after irradiation to 42 and 78 dpa. From RAFM steels irradiated to 71 dpa at 332 °C and at a test temperature of 350 °C the highest Uniform Strain of 1.7% was shown by ODS EUROFER (0.5 wt.% Y2O3). At a test temperature of 20 °C, however, ODS EUROFER (0.5 wt.% Y_2O_3) failed by a brittle fracture whereas EUROFER97 and F82H steels showed Total Strains above 10%.

The irradiation temperature dependence of the Yield Stress of EUROFER97 and other RAFM steels was intensively studied within SPICE irradiation programme by KIT through irradiation of RAFM steels at multiple temperatures from 250 to 450 °C to a volume average damage dose of 16.3 dpa. The Yield Stress increase depends strongly on the irradiation temperature, exhibiting high values at low irradiation temperatures of T_{irr} ≤300 °C. Yield Stress increase is considerably lower at T_{irr} =350 °C indicating substantial recovery of radiation defects at this irradiation temperature. At irradiation temperatures of 400 and 450 °C the Yield Stress exhibits values that are comparable to those of in the unirradiated state, indicating nearly complete recovery of the irradiation damage. Irradiation temperature dependence of the Yield Stress of F82H and other RAFM steels resembles to that of EUROFER97. The influence of the irradiation temperature (300, 450, 550 °C) on the tensile properties of recently developed ODS EUROFER steel (EU batch, 0.3 wt.% Y_2O_3) up to a damage dose of 3 dpa was studied by NRG. Significant hardening was found for ODS EUROFER at irradiation temperature of 300 °C which was comparable to the hardening of the base EUROFER97. In contrast, no changes of Yield Stress in comparison with unirradiated state were observed for irradiation temperatures of 450 and 550 °C.

Impact properties

Low temperature (T_{irr} <340 °C) neutron irradiation leads to a severe degradation of impact properties of RAFM steels. EUROFER97 and other RAFM steels show steep increase in the ΔDBTT with dose below 15 dpa. With farther increasing the damage dose the embrittlement rate decreases and a clear tendency towards saturation is observed at the achieved doses. Indeed, for 70 dpa/ 335 °C irradiation the ΔDBTT of EUROFER97 is found to be 233 °C, which is only 15 °C higher than the ΔDBTT after 32 dpa/332 °C irradiation. F82H irradiated to 65 dpa at 337 °C behaves somewhat poorly compared to the EUROFER steels with respect to the embrittlement. The embrittlement of OPTIFER XI and OPTIFER XII steels after irradiation to 12 dpa (and 31 dpa in case of OPTIFER XI) confirms the embrittlement trend of EUROFER97. The pre-irradiation HT of EUROFER97 leads to considerable improvement of the irradiation resistance up to 30 dpa. At the achieved doses, however, the embrittlement of EUROFER97 HT becomes comparable to that of EUROFER97.

The role of irradiation temperature on the impact properties of EUROFER97 and other RAFM steels was studied in SPICE programme by KIT through irradiation of RAFM steels at multiple temperatures from 250 to 450 °C to a volume average dose of 16.3 dpa. The results on ERUOFER97 irradiated to 15 dpa at 330 °C within WTZ programme allowed further refinement on the irradiation temperature role on the embrittlement. The DBTT of EUROFER97 and other RAFM steels is influenced most at low irradiation temperatures (T_{irr} ≤330 °C). Remarkably, the DBTT of EUROFER97 HT at T_{irr} =250 °C is smaller than the DBTT of EUROFER97 by 50 °C. The DBTT of reference F82H-mod and OPTIFER-Ia materials is comparable to that of EUROFER97 at T_{irr} =300 °C. The DBTTs of the steels irradiated at or above 350 °C remain below -24 °C and, hence, well below the material application temperature. On the basis of this study a temperature window between 350 and 550 °C is proposed for operation of the FW and Blanket components. The influence of the irradiation temperature (300, 450, 550 °C) on the impact properties of recently developed ODS EUROFER steel (0.3 wt.% Y_2O_3) up to a damage dose of 3 dpa was studied by NRG. Significant DBTT shifts of 56 °C and 151 °C were reported after irradiation at 300 °C to 1 and 3 dpa, respectively. The DBTT shifts after irradiation at 450 and 550 °C were marginal.

Fracture-Mechanical properties

The influence of the low temperature (300 °C) neutron irradiation on the Fracture-Mechanical (FM) properties of ERUOFER97 and other RAFM steels were intensively studied by SCK and by NRG up to 3 and 10 dpa, respectively. Compilation and detailed assessment of Fracture-Mechanical experiments on irradiated EUROFER97 and F82H specimens was performed by KIT. Progressive material embrittlement with dose is found for EUROFER97 after irradiation at 300 °C which does not show saturation of Fracture Toughness Transition Temperature (FTTT) up to 10 dpa. The irradiation induced shifts in FTTT are significantly larger than the shifts in Charpy DBTT which indicates a non-conservative estimation of the embrittlement by Charpy tests. The lack of high dose data on FTTT of EUROFER97 indicates the need for high dose FM experiments.

Low Cycle Fatigue properties

The influence of the neutron irradiation on the LCF properties of RAFM steels were investigated by NRG and KIT. The low temperature (≤330 °C) neutron irradiation has only minor influence on the fatigue behaviour of RAFM steels. Irradiation induced hardening may differently affect LCF behaviour and can yield i) enhanced lifetime in comparison to the unirradiated state as a result of reduction of the inelastic strain amplitude especially at low strain ranges or ii) reduced lifetime as a result of accelerated fatigue damage accumulation due to enhanced stress levels especially at high strain ranges. No influence of the high temperature (400 °C) neutron irradiation on the fatigue behaviour was observed by KIT.

Post-irradiation annealing

The post-irradiation annealing (PIA) leads to a substantial recovery of the mechanical properties of neutron irradiated RAFM steels. The neutron irradiation induced hardening of ERUOFER97 is substantially reduced after annealing at 550 °C already for one hour. Recovery in the hardening is accompanied with the recovery in the ductility properties, i.e. a complete recovery of the Uniform Strain and substantial recovery of the Total Strain is observed. The impact properties of EUROFER97 can be also substantially recovered by PIA. The PIA of e.g. 70 dpa irradiated EUROFER97 HT at 550 °C for 3 h leads to a reduction of the DBTT from 135 to -43 °C resulting in a residual embrittlement (shift in DBTT) of just 48 °C compared to the unirradiated state. Comparatively, after PIA at 550 °C for 3 h the residual embrittlement of 65 dpa irradiated F82H-mod is about 106 °C.

Conclusions

The assessment of the mechanical properties of European reduced activation ferritic/martensitic steel EUROFER97 and it's ODS variants has been performed up to a damage dose of 80 dpa. The main conclusions of the assessment can be summarized as follows

- Low temperature neutron irradiation (T_{irr} ≤335 °C) leads to strong hardening and embrittlement of EUROFER97 and other international RAFM steels. Minor hardening and embrittlement observed at T_{irr} =350 °C indicates considerable healing of radiation damage. Neutron irradiation at T_{irr} ≥400 °C has nearly no impact on the mechanical properties.
- The increase of the Yield Stress of RAFM steels is rather steep at doses below 10 dpa at T_{irr} ≤335 °C. In spite of large scattering of low temperature, high dose hardening data a clear reduction of the hardening per dose increment is observed at achieved damage doses of 70-80 dpa. Selected RAFM steels (e.g. EUROFER97, Heat E83697) show saturation of hardening at 70 dpa. Ductility properties (uniform strain, total strain) seem to saturate already above 2.5 dpa. Lack of irradiated specimens does not allow detailed statistical analysis of the results.

- All investigated RAFM steels show steep increase in the ΔDBTT with dose below 15 dpa at T_{irr} ≤335 °C. At 70 dpa EUROFER97 and other RAFM steels indicate saturation behaviour of low temperature embrittlement.
- Progressive material embrittlement, quantified as increase in FTTT, observed for EUROFER97 indicate no saturation of FTTT for the achieved damage doses of 10 dpa. Comparison of low temperature neutron irradiation (T_{irr} ≤335 °C) induced shifts in FTTT and in Charpy DBTT reveals non-conservative estimation of the embrittlement by Charpy impact test. There is a need for high dose fracture toughness experiments on EUROFER97.
- Post irradiation annealing at 550 °C for 3 h leads to a nearly complete recovery of the impact and tensile properties of low temperature (T_{irr} =335°C) irradiated EUROFER97 indicating substantial healing of radiation defects.
- Helium effects are not sufficiently understood due to absence of an irradiation facility with fusion reactor relevant neutron spectrum and have to be a subject of future investigations. Helium effects cannot be healed out by post irradiation annealing.
- The conclusions given above are made on the basis of irradiation behaviour of base RAFM steels. Qualification of advanced joining technologies (e.g. Diffusion bonding, EB/TIG welding) under high dose irradiation damage is an important requirement for disturbance free operation of DEMO and belongs to the key priorities within structural materials R&D.

Staff:

J. Aktaa
E. Gaganidze

Literature:

[1] J. Weiß, Ermile Gaganidze, J. Aktaa, Quantitative characterization of microstructural defects in up to 32 dpa neutron irradiated EUROFER97, J. Nucl. Mater. 426 (2012) 52-58.

[2] E. Gaganidze, C. Dethloff, O. J. Weiß, V. Svetukhin, M. Tikhonchev and J. Aktaa, Modeling and TEM Investigation of Helium Bubble Growth in RAFM Steels Under Neutron Irradiation, J. ASTM International, DOI:10.1520/STP103972, (2012).

[3] E. Gaganidze and J. Aktaa, Issues Related to Radiation on Blanket and Divertor Materials, Final Report for EFDA WP12-MAT-02-M02-01/KIT and EFDA WP12-MAT-02-M03-01/KIT, KIT Internal Report, FUSION Nr. 404, 2012.

[4] E. Gaganidze and J. Aktaa, Assessment of neutron irradiation effects on RAFM steels, accepted for publication in Fusion Engineering and Design, (2012).

Acknowledgement

This work, supported by the European Communities under the contract of Association between EURATOM and Karlsruhe Institute of Technology, was carried out within the framework of the European Fusion Development Agreement. The views and opinions expressed herein do not necessarily reflect those of the European Commission.

Nuclear Data

Nuclear Data Studies/Experiments in Support of TBM Activities (F4E-2010-GRT-056-02 (ES-AC) - Action 2, NUDATA_Exper)

Overall objective

The overall objective of the grant agreement was to provide the experimental data base required for the validation of the nuclear data libraries EFF and EAF developed in the frame of the EU Fusion Technology Programme. The focus of the KIT tasks was on experimental validation activities of ITER and TBM design calculations and on development of detectors and measuring techniques.

Task 2.2
Measurement of neutron spectra with a proton recoil detector in the HCLL TBM mock-up irradiated with DT neutrons

In previous experiments with the HCLL mock-up, TPR, neutron and gamma-ray spectra have been measured. A well characterized NE213 scintillator was applied to obtain neutron spectra in two locations in the mock-up under DT neutron irradiation at TUD-NG. However, the accessible neutron energy range in the proton-recoil based scintillator starts around 2 MeV. Below these energies the influence on carbon recoils on the primarily measured pulse height spectra is too high and these energies had to be excluded from previous measurements. Hydrogen-filled proportional counter tubes can be used to measure neutron spectra in the range of several tens of keV up to approximately 1 MeV depending on their size and pressure of the filling gas which determines the H density and hence the mean free path of the recoil proton.

We have used a commercially available proton recoil tube for the measurement of neutron spectra in the HCLL TBM mock-up. The device was a LND 281 fabricated by LND Inc. Its active volume had a radius of 1.82 cm and a length of 17.78 cm. The tube was filled with a mixture of hydrogen (3040 torr), nitrogen (100 torr) and methane (100 torr) according to the manufacturers' data sheet. With these values it is possible to measure neutron fluxes from approx. 300 keV to 1 MeV via collisions with the hydrogen nuclei in the detector.

The reaction $^{14}N(n,p)^{14}C$ + 625.9 keV has been used to calibrate the primary pulse height spectrum of protons.

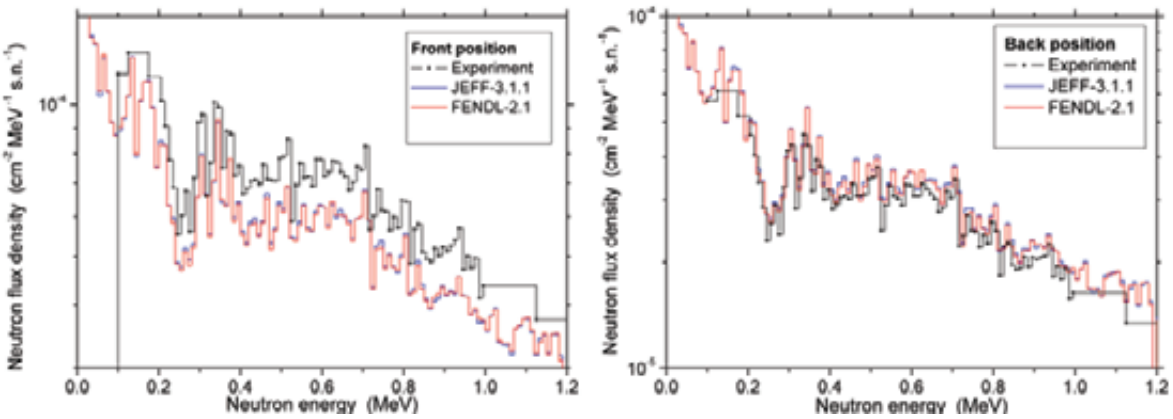

Fig. 1: Measured and calculated neutron spectra in the HCLL TBM mock-up.

The response matrix was calculated with MCNPX Version 2.6 [1]. The detailed geometry including gas amplification effects are taken into account.

The calculated response matrix and the measured pulse height spectrum of the proton recoil counter in two positions were used as input for the unfolding procedure with the MAXED

code from the UMG-3.3 package [2]. The unfolding procedure requires also a spectrum estimate which was calculated with MCNP [3].

The results of the neutron spectrum measurement together with MCNP calculation of the neutron spectrum in the two measurement positions are shown in Fig. 1. For the MCNP calculations data from the JEFF-3.1.1 [4] and FENDL-2.1 [5] nuclear data libraries were used.

Staff:

U. Fischer
D. Förster
D. Gehre
A. Klix

Literature:

[1] J.S. Hendricks, G.W. McKinney, M.L. Fensin, M.R. James, R.C. Johns, J.W. Durkee, J.P. Finch, D.B. Pelowitz, L.S. Waters, M.W. Johnson, “MCNPX 2.6.0 Extensions”, LA-UR-08-2216, LANL, 2008

[2] M. Reginatto and P. Goldhagen. Maxed, a computer code for maximum entropy deconvoltion of multisphere neutron spectrometer data. Health Physics, 77(5):579–583, November 1999.

[3] “MCNP—A General Monte Carlo N-Particle Transport code”, Version 5, Report LA-UR-03-1987, Los Alamos, 2008

[4] A. Santamarina, D. Bernard, Y. Rugama (Eds.), "The JEFF-3.1.1 Nuclear Data Library, JEFF Report 22, Validation Results from JEF-2.2 to JEFF-3.1.1", NEA Data Bank (2009), ISBN 978-92-64-99074-6

[5] D. Lopez Aldama, A. Trkov, "FENDL-2.1 -- Update of an evaluated nuclear data library for fusion application", INDC(NDS)-467, IAEA, 2004

Task 3.1.1
Self Powered Neutron Detectors

In this Task self-powered neutron detectors (SPND) were studied to see whether this type of detector can be proposed for neutron flux monitoring in an ITER-TBM. SPND have a number of interesting properties such as small dimensions, capability to operate in harsh environments, absence of external bias, simplicity etc. so they are attractive neutron monitors for TBM in ITER. However, several draw-backs must be considered, among them the most important is the fact that present available SPND are optimized for operation in a thermal nuclear reactor where the neutron spectrum is much softer than that expected in a TBM. This fact can limit the use of SPND in a TBM since the effective cross sections for the production of beta emitters are much lower in a fast neutron spectrum.

This work represents the first attempt to study SPNDs as neutron flux monitors for TBM. Several state-of-the-art SPND available on the market were bought and tests performed using fast neutrons available at TAPIRO fast neutron source of ENEA Casaccia and with 14 MeV neutrons at the Frascati neutron generator (FNG). Three SPND with different emitters (V, Co, Rh) where inserted into the TAPIRO reactor and the current generated from the induced beta activity in the emitter was measured with a Keithley 6485 picoammeter. An example of such a current measurement is shown in Fig. 2. The oscillations during the irradiation period were caused by electromagnetic noise from a helium pump of the reactor.

The results clearly indicate that in fast neutron spectra, the response of SPNDs is much lower than in thermal neutron flux. Activation calculations were also performed using the European Activation System EASY [6] to find out possible material candidates for SPND suitable for operation in TBM neutron spectra.

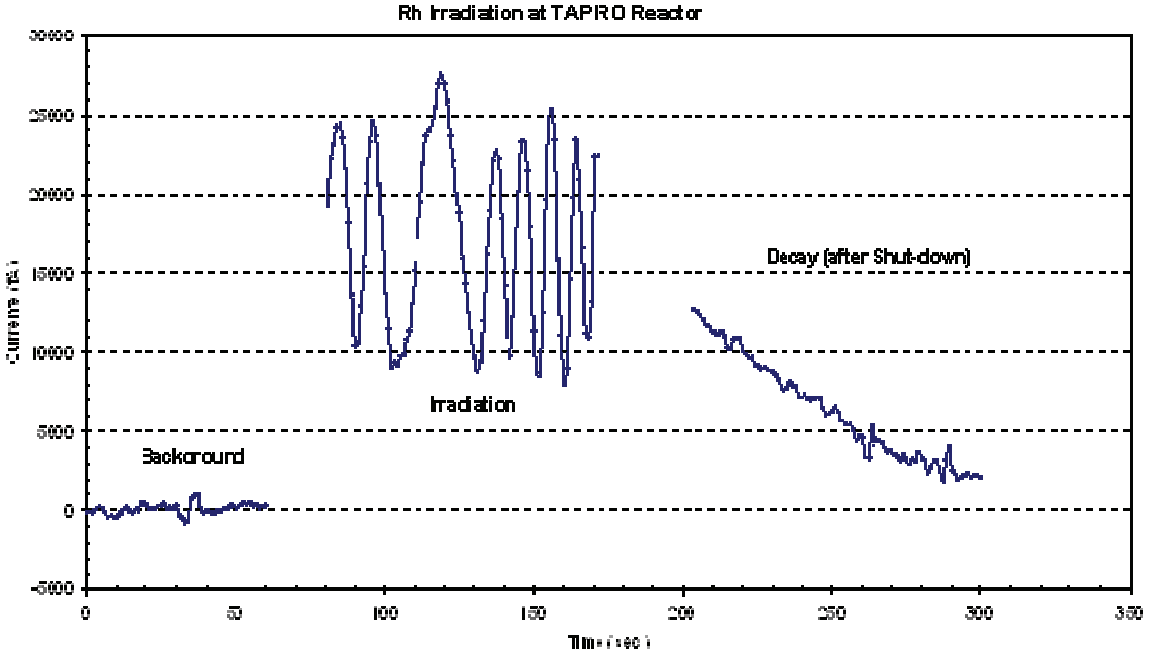

Fig. 2: Results of Rh-SPND irradiation at TAPIRO Reactor.

Staff:

M. Angelone
U. Fischer
A. Klix

Literature:

[6] R.A. FORREST, The European Activation System: EASY-2007 overview, Report Culham Science Centre, UKAEA FUS 533, (2007).

Task 3.2
Assessment of a Li glass detector coupled to a photodiode via optical fiber for use in the ITER TBM

Neutronics experiments with the TBM in ITER will face several severe challenges. Any kind of detectors will have to withstand an extremely harsh environment which is characterized by intense fields of ionizing radiation, temperatures on the order of several hundred ^{o}C, strong magnetic fields etc. In addition, the access to the TBM will be very limited so that any kind of diagnostics system might have to stay in the TBM for many plasma pulses and experimental campaigns before it could be replaced in the event of a failure.

This task is devoted to preliminary investigations of the suitability of a combination of lithium glass scintillators, optical fibers and photodiodes as candidates for TBM diagnostics. At this point we do not address the radiation hardness of the system, we test only the principal functionality.

The detector used in these tests was a ^{6}Li-enriched lithium glass GS2 from Nuclear Enterprises. The cylindrical scintillator had a diameter of 1 cm and a height of 1 cm. In a first step it was coupled to a custom design avalanche photo diode from Hamamatsu. The APD had a sensitive area of 5 mm by 5 mm and a peak sensitivity at 450 nm. It was operated at a bias voltage of 384.7 V. Under these conditions it produced a pulse signal approximately proportional to the energy deposition by the charged particles in the scintillator.

Figure 3 shows the test assembly which consisted of a charge-sensitive preamplifier, the APD in an aluminium housing, an optic fiber bundle and a GS 2 lithium glass. The optic fiber was a BFH22-550 containing a bundle of 7 strands from Thorlabs. The used lengths were 1 and 2 meters.

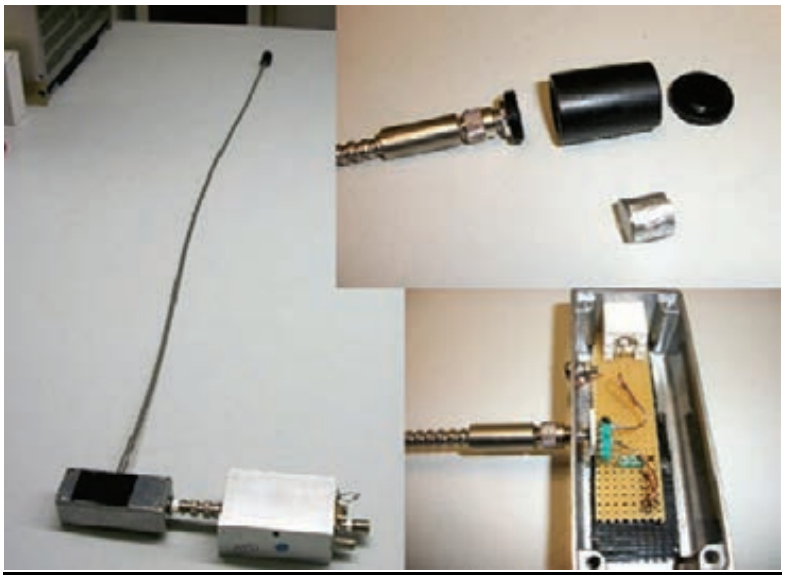

Fig. 3: Assembly for testing of a lithium glass scintillator coupled to an avalanche photodiode via a glass fiber bundle.

Recorded pulse height spectra under neutron irradiation with and without Cd cover are presented in Fig. 4. The scintillation signal in such a lithium glass is generated from gamma interactions and the tritium-breeding reaction of low-energy neutrons on ^{6}Li. Gamma-rays lead to low pulses which can be separated from the distinctive peak caused by the tritium breeding reaction in the pulse height spectrum.

Recorded pulse height spectra are shown in Fig. 4. In the first case the lithium glass was directly attached to the APD without the optical fiber. The peak from the tritium breeding reaction can be seen very clearly. A Cd cover suppresses the slow neutron flux, hence the peak disappears mostly if the lithium glass is covered with Cd.

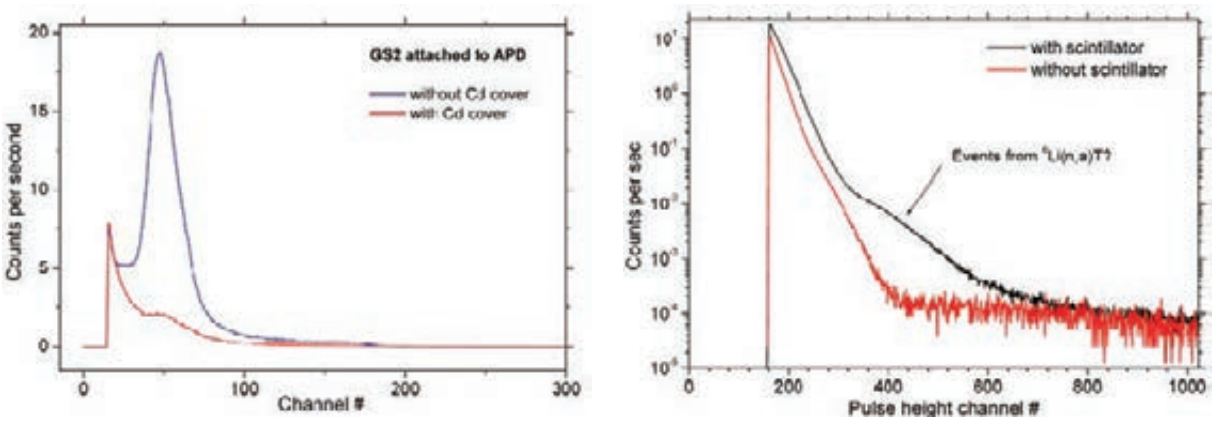

Fig. 4: Recorded pulse height spectra from the lithium glass scintillator coupled directly to the APD (left) and via the glass fiber bundle (right).

When using the combination lithium glass – optical fiber – APD the peak due to the tritium breeding reaction could not be seen clearly. Further work would be necessary to optimize the design.

Staff:

U. Fischer
A. Klix
Th. Lafargue
W. Hansen

Acknowledgement

This work was supported by Fusion for Energy under the grant contract No. F4E-GRT-056-02 (ES-AC) - Action 2 with collaboration by ENEA, Italy; AGH-UST, Poland; JSI, Slovenia and ASCR, Czech Republic. The views and opinions expressed herein reflect only the author's views. Fusion for Energy is not liable for any use that may be made of the information contained therein.

Nuclear Data Improvements and Development of Tools – Nuclear Data Evaluation (F4E-FPA-GRT-168.01)

Overall objective

The overall objective of the Framework Partnership Agreement F4E-FPA-168 on "Development of Nuclear Data Files" between F4E and the "Consortium on Nuclear Data Development and Analysis" is to contribute to the generation, maintenance and validation of nuclear data libraries relevant for ITER, IFMIF and DEMO. The Consortium, consisting of the research institutions of KIT (Germany), CCFE (UK), NRG (The Netherlands), JSI (Slovenia), TUW (Austria), CIEMAT (Spain) and IFIN-HH (Romania), combines available European expertise to provide the services requested by F4E to meet their objectives in the field of nuclear data development.

These services include nuclear data evaluations relevant to the various fusion applications encompassing neutron, proton and deuteron induced reactions, the generation of associated co-variance data for uncertainty assessments, the development of advanced nuclear models and codes, the processing and benchmarking of the evaluated data against integral experiments, as well as the development of suitable software tools for sensitivity and uncertainty analyses of fusion systems.

The first specific grant, F4E-FPA-GRT-168.01 on "Nuclear Data Improvements and Development of Tools - Nuclear Data Evaluation" started May 1, 2012, with activities on the evaluation of neutron induced reactions on ^{55}Mn, ^{63,65}Cu and ^{181}Ta, benchmark analyses for neutron (Fe, Pb) and deuteron (Cu, Al) induced reactions, the evaluation/generation of damage energy/displacement cross-section data, the evaluation of deuteron induced activation cross-section data, the development of optical model potentials for the emission of alpha-particles over a wide target nuclide mass range, the development of consistent TALYS model based activation/transmutation and transport neutron sub-libraries as well as the processing of photo-nuclear data libraries and thermal scattering data tables for Monte Carlo applications. Codes and software tools related activities are conducted on the further development of the stochastic and deterministic sensitivity/uncertainty approaches (MCSEN and SUSD3D codes), associated pre- and post-processing tools, and the MCUNED extension of MCNPX for the use of deuteron cross-section data in Monte Carlo transport calculations.

KIT is leading the Consortium and is co-ordinator of the FPA-168 and the associated grants. It contributes to the FPA-168.01 grant activities with the following tasks:

Task 1.2
Generation of genuine EFF/JEFF evaluated general purpose nuclear data files for n + ^{63,65}Cu including covariance data up to 150 MeV

Objective

Cu is an important heat sink material for fusion power reactors which is also used for diagnostics, microwave waveguides and mirrors in ITER. As there are no genuine JEFF data evaluations available for Cu, complete new evaluations of the cross-section data are performed for n+ ^{63,65}Cu up to 150 MeV using consistent approaches for the cross-section evaluation and co-variance generation.

Computer codes and nuclear models

Simulations of the n+^{63,65}Cu interactions are performed making use of the TALYS code [1] in the energy range from 1 keV up to 200 MeV of the neutron incident energies. The analysis

performed for the n+^{63,65}Cu reactions revealed some deficiencies of the nuclear models included in latest version TALYS-1.4.

In some cases the set of the experimental data could be fitted with TALYS-1.4 only by changing nuclear model parameters to unphysical values. Improvements can be achieved by inclusion in TALYS of an additional model for the pre-equilibrium reactions description, namely the Geometry Dependent Hybrid model (GDH) [2]. The previous version TALYS-1.2 was already properly modified and well globally tested against experimental data for incident neutrons and protons. The modified TALYS-1.2 gives more accurate results for n+Cu reactions compared to TALYS-1.4. The GDH model was involved in calculations by making use of the new option of the keyword *preeqmode* 5. The nuclear level density was described with a phenomenological generalized superfluid model [3] (*ldmodel* 3).

The nuclear model calculations were done using TALYS built-in global Optical Model Potentials (OMPs) for neutrons and protons. The global OMPs for deuterons [4] and alphas [5] were used in the TALYS calculations. For tritons and helions, new OMPs were elaborated using a large experimental data base and available OMPs for some target nuclides [6]. The parameters of the global OMPs for d, t, ^{3}He and alphas were separately calculated and used in TALYS calculations as external data files invoking *optmod* commands. All OMPs have the same valid incident energy range from keVs up to 200 MeV. Therefore the evaluated data are continuous and consistent in the full energy range of the incident neutrons. The results for total, elastic and inelastic scattering cross sections were obtained with the optical model making use of the local OMPs for both copper isotopes. All uncertainties arising during the evaluation process due to a possible adaptation of the reaction cross sections which do not come from nuclear model simulations (for example, already existing evaluated data) are accounted for in the elastic scattering cross section, keeping the total cross section unchanged.

Results of the nuclear model calculations

Resonance parameters

A complete resolved resonance parameter data set was evaluated for n+^{63}Cu and ^{65}Cu reactions at Oak Ridge National Laboratory (ORNL) using the SAMMY code [7]. This evaluation is based on the new low energy measurements performed at the Massachusetts Institute of Technology on ^{63}Cu and ^{65}Cu for the total cross sections and for the neutron transmission (energy range 0.01 eV- 0.1eV). Making use of the available experimental data for higher energies from EXFOR and the newly measured ones, new resonance parameters and their covariances were prepared for the stable copper isotopes. For both nuclei the resonance region was set from 10^{-5} eV to 99.5 keV. The results of the evaluation for ^{63}Cu are shown in Fig. 1.

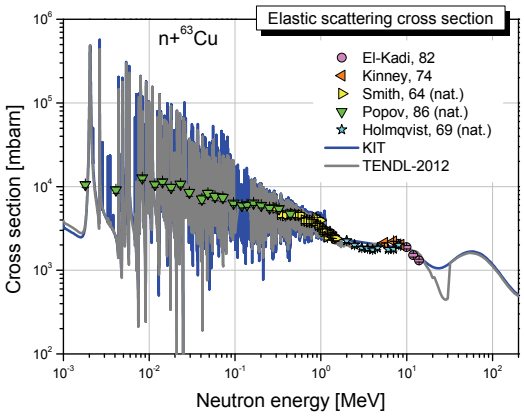

Fig. 1: Evaluated elastic scattering cross section for n+^{63}Cu.

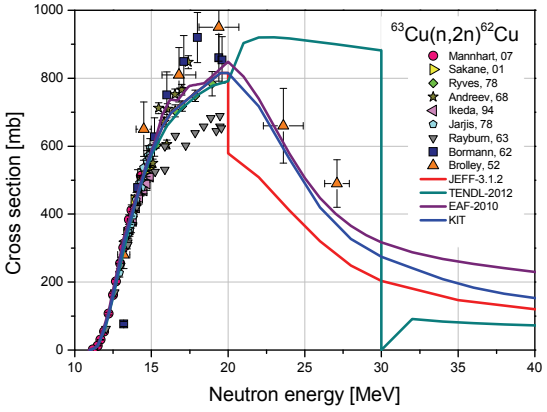

Fig. 2: Evaluated ^{63}Cu(n,2n)^{62}Cu cross section.

Nuclide production cross sections

The nuclear data evaluation using the TALYS code is based on a sequential iteration procedure. Starting with default nuclear parameters, the results of the nuclear model simulations were consequently adjusted to the available experimental data by changing accordingly the parameters. Shown in Fig. 2 is the newly evaluated $^{63}Cu(n,2n)^{62}Cu$ cross section compared to the measurements and other evaluations from JEFF-3.1.2, TENDL-2012 and EAF-2010 libraries.

Particle emission spectra

The equilibrium part of the particle emission spectra is calculated in TALYS in the framework of the multiple Hauser-Feshbach statistical model [1]. The pre-equilibrium part of the particle spectra is described in the modified TALYS-1.2 code within the GDH model accounting for multiple pre-equilibrium processes [2].

The results of the present evaluations for the neutron emission spectra are shown in Fig. 3 for natural copper at 14 MeV. Results for the alpha emission spectrum are compared in Fig. 4 to JEFF-3.1.1 [8] and TENDL-2012 [9]. Invoking the GDH model in TALYS calculations gives more consistent results with the measurements as compared to JEFF and TENDL data.

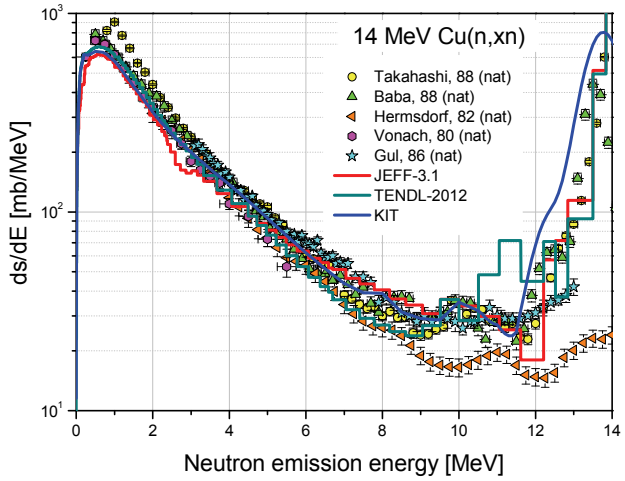

Fig. 3: Evaluated neutron emission spectra at 14 MeV incident neutron energy.

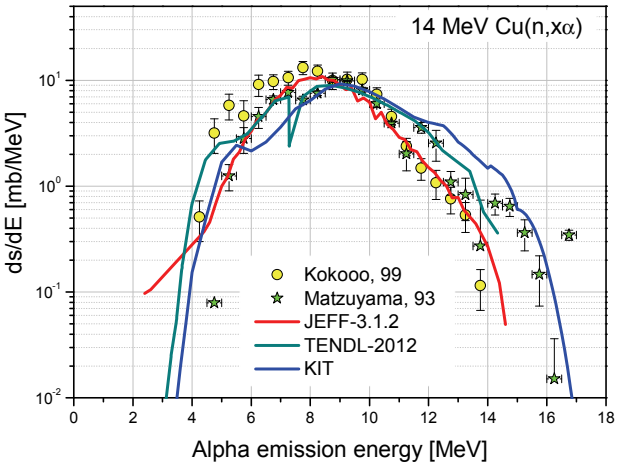

Fig. 4: Evaluated α-emission spectrum for n+^{nat}Cu at 14 MeV incident neutron energy.

Related to the particle emission spectra are the total particle production cross sections, i.e. the integrals over the emission spectra for the particular neutron incident energy. Fig. 5 presents the newly evaluated total hydrogen production cross section (the sum of p, d and t production cross sections). Due to the absence of experimental results we show here measured data for other elements close to Cu (Cr, Co, Ni, Fe) and for heavy Tl to get some general trend for the total gas production cross sections. The results of the evaluation seem to be reasonable and show real improvements compared to JEFF-3.1.1 and TENDL-2012 libraries.

Calculations of the data covariances

As a requirement, the newly evaluated general purpose files must include covariance data to enable the assessment of the uncertainty of the final particle transport results related to the nuclear data. In the present work, the co-variances were prepared making use of the BEKED [10] and the modified TALYS-1.2 codes. The BEKED code utilizes a Monte Carlo approach for calculations of the covariance matrices for the cross-sections. The principal steps of this method are as follows: set up of the uncertainties of the nuclear model parameters, preparation of the input files and execution of TALYS using the Monte Carlo technique for the model

parameters sampling, finally calculations of the data covariances for the chosen reaction channels.

The BEKED code carries out the random sampling of the optical model parameters, deformation parameters for coupled channels calculations and nuclear level density parameters. With this method experimental uncertainties are also taken into account in the calculations of the final evaluated nuclear data covariances. The Monte Carlo samplings are performed until the deviation of the final results for two sequential runs becomes negligible. Reliable results can be obtained with several thousand TALYS runs for each copper isotope. An example of the covariance data evaluation for ^{65}Cu using BEKED code is shown in Fig. 6.

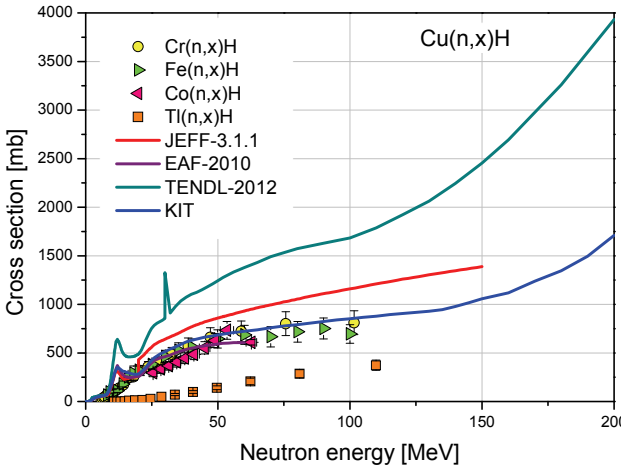

Fig. 5: Evaluated total hydrogen production cross section.

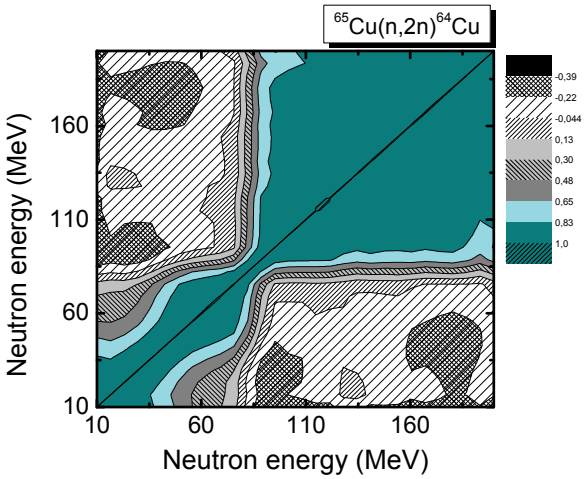

Fig. 6: Evaluated covariance matrix for ^{65}Cu(n,2n)^{64}Cu reaction cross section.

Evaluated data files

The evaluated nuclear data files for n+^{63}Cu and n+^{65}Cu particle transport calculations were output in the standard ENDF-6 data format. The most severe problem for storing of the high energy data is the limitation of the ENDF-6 format for the number of the explicitly given reaction channels. In case of the n+Cu interactions the possible number of the open channels at 200 MeV can exceed several hundreds. The data file becomes extremely large and complicated for handling if such information like particle spectra is presented for each reaction channel. Furthermore, at high energies the experimentally measured cross sections are usually a sum of all possible channels leading to the formation of a particular nuclide. For the present evaluation, we adopted the following structure of the data files: below 20 MeV of the neutron incident energy we give the full detailed information for all open reaction channels and above 20 MeV we present total particle emission spectra, total cross sections for the production of the residual nuclides and their recoil spectra. To this end, we use the MT5 section on the file above 20 MeV that is treated as a sum of all possible nuclear reactions except total and elastic scattering cross sections. The particle spectra and residual production cross sections can be restored using combination of the information for the section MT5 in the MF=6 and MF=3 files. The covariance data are presented in the evaluated data files in MF=32 for the resonance data, and MF=33 for all explicitly given reaction channels.

Staff:

U. Fischer
P. Pereslavtsev
A. Konobeev

Literature:

[1] A.J. Koning, S. Hilaire, M.C. Duijvestijn, Proceedings of the International Conference on Nuclear Data for Science and Technology (ND2007), April 22-27 2007 Nice France (2008).

[2] A.Yu. Konobeyev, U. Fischer, A.J. Koning, P.E. Pereslavtsev, M. Blann, Journal of the Korean Physical Society v. 59, No. 2, 935 (2011)

[3] A.V. Ignatyuk, R. Capote, Nu, IAEA-TECDOC-1506 (2006) p.85, http://www-nds.iaea.org/RIPL-2/handbook.html

[4] Haixia An, Chonghai Cai, Phys. Rev. C73, 054605 (2006)

[5] V. Avrigeanu, P.E. Hodgson, Phys. Rev. C49, 2136(1994).

[6] P.Pereslavtsev, U. Fischer, EFFDOC-974, NEA Data Bank, Paris, May 2006

[7] V. Sobes, B. Forget, L. Leal, K. Guber, et.al, this conference.

[8] A. Santamarina et. al, JEFF Report 22, NEA No. 6809, Nuclear Energy Agency, 2009

[9] A.J. Koning et. al, NRG Petten, The Netherlands, ftp://ftp.nrg.eu/pub/www/talys/tendl2012/tendl2012.html

[10] A.Yu. Konobeyev, U. Fischer, P.E. Pereslavtsev, Journal of the Korean Physical Society v. 59, No. 2, 923 (2011)

Task 2.1
Benchmark analyses of the general purpose data evaluations of Pb to assess their quality for design analyses of the HCLL breeder blanket concept

Objective

Pb is a material of highest importance for the European breeder blanket development programme which includes irradiation tests of Test Blanket Modules (TBM) in ITER and conceptual design studies for DEMO power reactors. The HCLL (Helium-Cooled Lithium-Lead) breeder blanket design utilizes Pb as neutron multiplier material. A neutronic experiment has been recently performed on a mock-up of the HCLL TBM to check and validate the capability of the neutronic tools and data to predict reliably the Tritium production and other nuclear responses of interest in the TBMs.

The benchmark analyses performed on Pb under Task 2.1 of FPA-168-01 build on the results obtained in the analyses of this experiment and complement them by analyses of benchmark experiments on pure material assemblies. The focus of the analyses is on the performance of the Pb data evaluations contained in the JEFF general purpose data library. Furthermore, cross-checks to data evaluations from other sources are included.

This activity has started in 2012 with a search on available integral 14 MeV neutron experiments on lead which are suitable for the benchmark analyses.

Staff:

U. Fischer
K. Kondo

Task 3.1
Upgrading of the MCSEN sensitivity software to comply with the current standard of the MCNP-5 Monte Carlo code

Objective

The Monte Carlo sensitivity code MCSEN has been developed in the frame of previous EFDA tasks and the F4E Nuclear Data Grant F4E-2008-GRT-014 (ES-AC) as extension to the MCNP-4C code to enable the Monte Carlo based calculation of sensitivities and uncertainties of nuclear responses in arbitrary 3D geometry. In the frame of this task, the MCSEN software is upgraded to comply with the MCNP5 standard. This upgrading enables the user to apply MCSEN as software patch to the current state-of-the-art production Monte Carlo code MCNP-5 thus providing access to all of MCNP's latest features.

The work on the MCSEN adaptation to MCNP-5 has been started in 2010 by analysing the programme flow in MCNP-5, coded in Fortran 90, as compared to the previous code versions of MCNP and MCSEN which utilized the obsolete Fortran 77 programming language.

Staff:

U. Fischer
D. Leichtle
R. Perel (Hebrew University of Jerusalem)

Task 3.3
Tools for pre- and post-processing of data for the S/U codes MCSEN and SUSD3D

Objective

The MCSEN and SUSD3D codes have been developed for Monte Carlo and deterministic sensitivity/uncertainty (S/U) calculations by KIT and JSI, respectively. The codes have been benchmarked against each other and qualified for fusion technology applications.

This task aims at unifying the data streams and processes for both approaches. To this end, suitable pre- and post-processing tools with visualisation capabilities are developed based on common standard data formats.

The work performed by KIT is on the adaptation of the processing module for the sensitivity data provided by MCSEN. The sensitivity profiles are prepared in a format which is suitable for the processing tools and interfaces developed by JSI for the co-variance data generation and the visualisation.

Staff:

U. Fischer
D. Leichtle
R. Perel (Hebrew University of Jerusalem)

Task 4.2
Evaluation of advanced damage energy and displacement cross-sections for the major EUROFER constituents based on an atomistic modelling approach

Objective:

Reliable assessments of radiation induced damage in fusion reactor materials require the use of advanced simulation techniques for the underlying displacement damage mechanisms. The calculation of radiation damage rates (dpa per second) for the EUROFER reduced activation steel is, therefore, based on improved displacement cross-sections based on Molecular Dynamics (MD) and Binary Collision Approximation (BCA) simulation methods for the calculation of the number of lattice defects. This approach shows a better agreement with available experimental data of point-defect production in materials than the standard Norgett-Robinson-Torrens (NRT) approximation used e. g. by the NJOY code. Neutron induced damage energy and displacement cross-section are evaluated for the main EUROFER constituents (Fe, Cr, W, Ta) up to 150 MeV utilizing the advanced atomistic modelling approach.

In 2012, various available MD simulation sets were analysed to choose an appropriate interatomic potential and modelling results as input for combined BCA and MD simulations of EUROFER. The results from Ref. [11] were selected for the further BCA-MD calculations. In addition, analyses were performed on the recoil energy distributions obtained with data from the ENDF/B-VII.0, ENDF/B-VII.1, JENDL-4, JEFF-3.1.2, and TENDL-2011 data libraries to define the most complete, reliable, and appropriate data to be used for the calculation of displacement cross-sections together with results of the atomistic modelling for the number of defects produced under irradiation. JEFF-3.1.2 and TENDL-2011 data were selected for the further use at energies below and above 20 MeV.

Staff:

U. Fischer
A. Konobeev

Literature:

[11] K. Vörtler, C. Björkas, D. Terentyev, L. Malerba, K. Nordlund, “The Effect of Cr Concentration on Radiation Damage in Fe–Cr Alloys,” J. Nucl. Mat. 382, 24 (2008).

Acknowledgement

This work was supported by Fusion for Energy under the Framework Partnership Agreement F4E-FPA-168.with collaboration by CCFE, UK; NRG, Netherlands; JSI, Slovenia; TUW, Austria; CIEMAT, Spain and IFIN-HH, Romania. The views and opinions expressed herein reflect only the author’s views. Fusion for Energy is not liable for any use that may be made of the information contained therein.

Neutronic Analysis of ITER Diagnostic Components (ITER/IO/12/4300000548)

Objective

The objective of this contract was to provide neutronics computational service for the ITER Organization (IO) Diagnostics Division in order to improve the shielding performance of the Diagnostic Generic Equatorial Port Plug (EPP) in ITER. The aim was to guide and assist the EPP design developers with optimal shielding solutions which are characterised of maintain the main diagnostics purposes of the EPP together with adequate radiation shielding performance. The crucial parameter for the optimization was the possible minimum of shutdown dose rate inside the ITER bioshield, in interspace at the port back-side. The aim was reached by parametric neutronic analyses of the shielding geometry and material composition, mitigating direct streaming of neutrons from the plasma by arranging the labyrinths and horizontal rails.

Introduction

Nuclear safety and machine reliability are among the first priority tasks in the ITER project. The ITER machine must withstand the 14 MeV neutrons generated on the D-T fusion nuclear reactions in the plasma chamber and impinged on the blanket First Wall (FW) shown in Fig. 1 causing materials radioactivity. The ITER machine is very large (height of 30 m, the same in diameter inside its cryostat), with complex shaped geometry and tight mm-tolerance for components assembly. For instance, gaps around the EPP massive 45-ton diagnostic drawers are 2 cm, and every centimeter counts if such gaps have direct view to the plasma neutron source, as neutronics analyses [1-3] have proved. The ITER diagnostic equipment is supposed to be packed inside the three vertical diagnostic shield module (DSM) drawers are separated in the toroidal direction by narrow inter-drawer gaps (~5 mm). The DSM drawers are shown in Fig. 2. Such separation provides an assembly tolerance and cuts eddy currents induced during plasma disruptions.

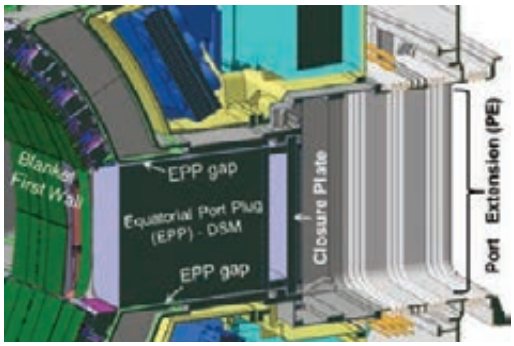

Fig. 1: Vertical cut through the Computer Aided Design (CAD) model of the Equatorial Port.

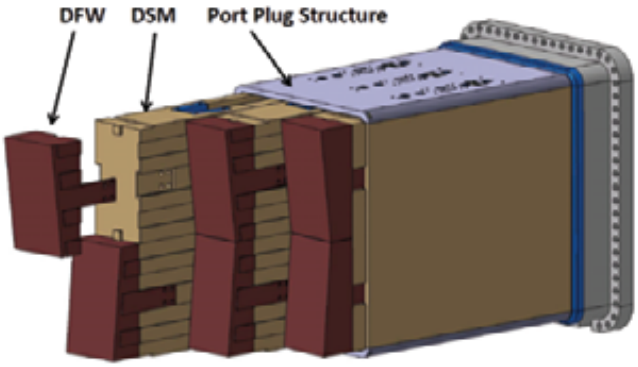

Fig. 2: CAD view of Equatorial Port Plug (EPP) showing the assembly of Diagnostics FW to the DSM, then insertion the DSM drawers into the port plug structure.

The importance of this service contact consists in guarantee of personnel safety along maintenance of the diagnostics equatorial port in ITER and after its shutdown. The nuclear safety target is to limit the radiation exposure of the ITER personnel by 100 μSv/h of Shut-Down Dose Rate (SDDR) at 10^6 s after neutron irradiation, reducing the potential biological damage. It was demonstrated in works [1-3] that in case of Diagnostic Equatorial Port Plug (EPP) this SDDR limit is difficult to meet, because of neutron streaming through the gaps arranged around the EPP Diagnostic Shield Module (DSM). As the outcome of [1-3], the optimal design of EPP has been established [4] which is practically feasible.

The challenging problem to mitigate the radiation streaming is discussed in [5], where a double labyrinth configuration of the EPP all-round gaps was chosen as a preferable EPP design solution.

Methodological approach

The methodological approach for the EPP neutronic analysis persuaded the aim of the development of radiation shielding within the limited time. The ITER design encompasses many engineering parts. Some of them, such as gaps and channels provide streaming paths for neutron and secondary photon radiation, and they must be explicitly modeled as presented in Figs. 1, 2. While for other ITER components (blanket bulk shield, vacuum vessel shield, EPP drawers) the homogenization of shield materials is possible for the neutronics modeling. The Monte Carlo code MCNP5 [6] was used with the ITER-global MCNP5 model called B-lite version 2 supplied by the ITER Organization (IO). For this analysis, the R2Smesh interface system [7] has been applied, which couples the MCNP5 transport and FISPACT-2007 [8] activation calculations through the common use of mesh-tally distributions. In the R2Smesh scheme, the results of neutron fluxes, generated decay photon sources and the final results of shutdown dose rates are calculated on a 3D mesh, which can have a high spatial resolution. In this contract the effect of mutual dependence of three ITER ports (upper, equatorial, and lower) was quantified by presenting separate SDDR contributions inside each of the port interspace. The radiation leakage from one port volume to another port volume is called as “radiation cross-talk”. The computational scheme was devised to quantify the radiation cross-talk effect between the interspace volumes F1-F5 pinpointed in Fig. 3. The mostly shielded version of the ITER port configuration is characterized by the totally closed ports in the Ultimate Baseline B-lite model presented in Fig. 4, where only the gaps between the ITER blanket modules (so called inter-blanket gaps) are open.

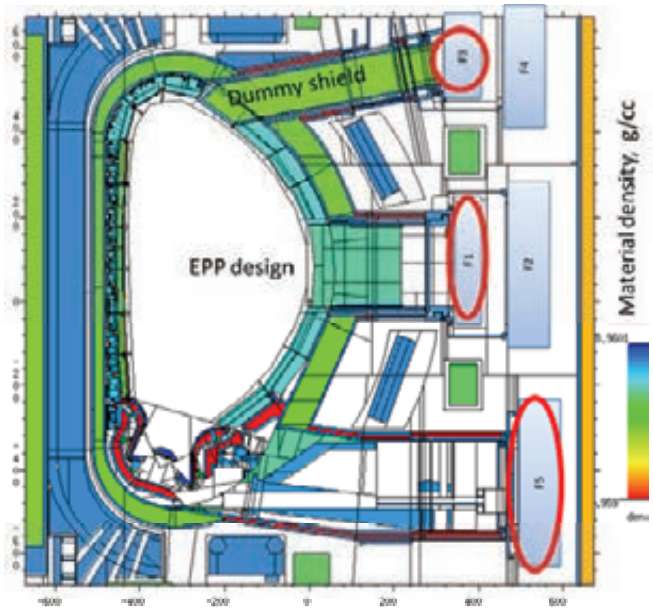

Fig. 3: Vertical cut of the B-lite model with integrated EPP double labyrinth design and five interspace volumes F1-F5 to examine the cross-talk effect.

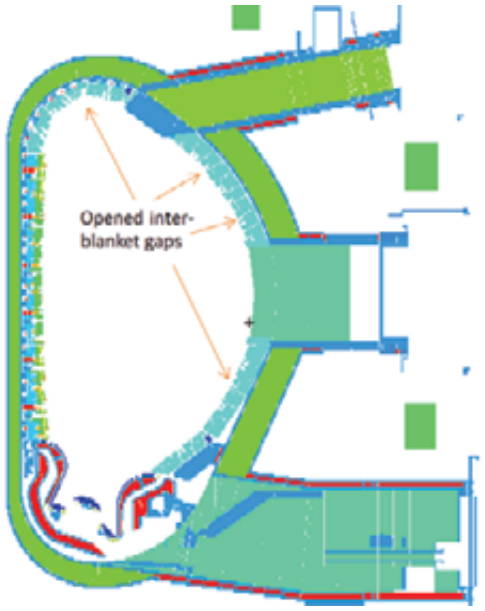

Fig. 4: Vertical cut of the Ultimate Baseline B-lite MCNP model with completely blocked Upper, Equatorial, and Lower Ports.

Results of EPP neutronics analysis

Following to the outcomes of a parametric neutronics analyses [1-3], the optimized double labyrinth configuration was devised and integrated into the ITER-global MCNP5 model called B-lite ver.2. The schematic view of such double labyrinth is depicted in Fig. 5, in which the distinguishable parameters of the EPP all-round gaps are pinpointed, such as gap thickness, length, and shift.

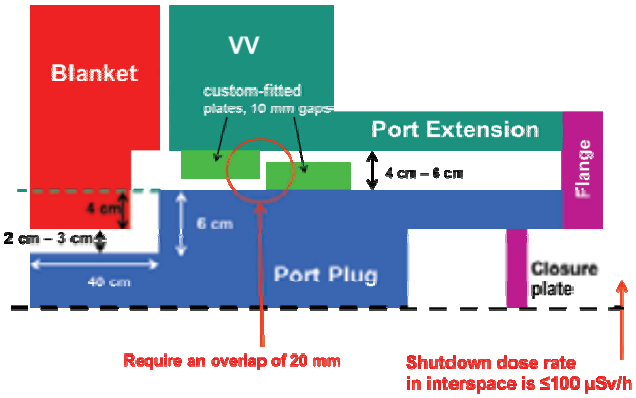

Fig. 5: Schematic view of the optimized double labyrinth EPP gap configuration (vertical cut).

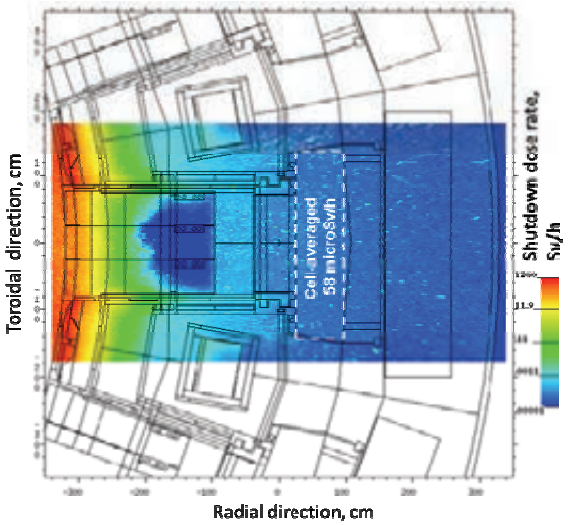

Fig. 6: Map of shut-down dose rate (SDDR) in the vicinity of the equatorial port plug (with shielded upper and lower ports) B-lite MCNP model horizontal cut.

Figure 6 visualizes the Shut-Down Dose Rate (SDDR) in the vicinity of the equatorial port plug (with shielded upper and lower ports) on the horizontal cut of B-lite MCNP model with fully closed inter-drawer gaps. The EPP interspace SDDR is counted to 58 μSv/h. The horizontal rails arranged inside the DSM inter-drawer 0.5-cm gaps reduce the neutron streaming inside them, as it is quite noticeable in Fig. 7 in comparison with much stronger streaming through the all-round EPP 6-cm gaps. In correspondence to flux distribution in Fig.7, the next Figure 8 shows the map of shutdown dose rate distribution plotted on high resolution mesh around the Diagnostics EPP. The SDDR map has been calculated using the R2Smesh interface and taking advantage of the HPC-FF and HELIOS high performance computational resources [9, 10]. The 3D dose map is plotted with ParaView visualization tool [11] between the thresholds at 10^{-5} Sv/h and 10^{-2} Sv/h at the EPP back-side. The personnel access is possible inside the ITER ports where dose rate is less than 10^{-4} Sv/h, that is the mentioned 100 μSv/h radiation design limit of SDDR at 10^{6} s of cooling time.

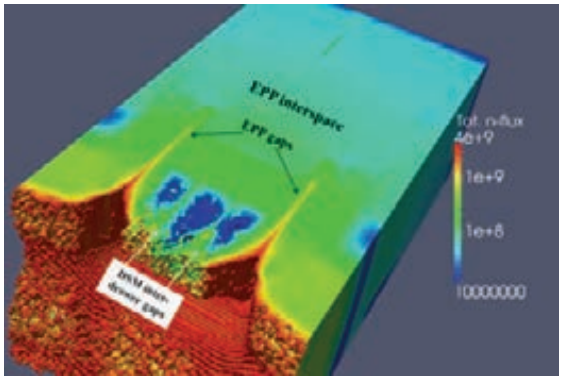

Fig. 7: Map of total neutron flux (n/cm^2/s) for B-lite model with railed inter-drawer gaps inside the EPP DSM.

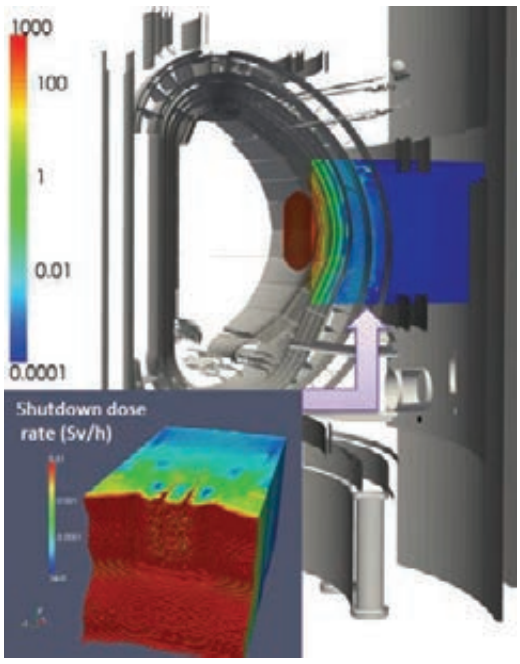

Fig. 8: Map of shutdown dose rate (Sv/h) at 10^{6} s cooling time for Diagnostic Equatorial Port Plug (EPP).

To estimate the radiation cross-talks between the three ITER ports (upper, equatorial, and lower), four MCNP models have been run with the following modifications of the Ultimate Baseline model, corresponding to four rows in Table 1 of four different contributors to SDDR inside the port interspaces:

1. Ultimate Baseline model with all ports including all gaps (except of blanket inter-module gaps) “closed” with a steel:water mixture of 80%:20%, as shown in Fig. 4;
2. Only the lower port “opened”, i.e. using the standard B-lite ITER model lower port;
3. Only the equatorial port “opened”, i.e. the equatorial port plug has been replaced with the diagnostic version of the double-labyrinth, depicted schematically in Fig. 5;
4. Only the upper port “opened”, i.e. using the standard B-lite ITER model upper port.

The voids of the blanket manifolds and the in-vessel coils of the original B-lite model have been filled with 80% of steel and 20% of water. From the results of SDDR cross-talks presented in Table 1 it follows that half of total SDDR in the Equatorial Port interspace (78 μSv/h) is coming from other ITER parts, mainly from the original B-lite Lower Port (18 μSv/h) and general leakage of the blanket and VV of the Ultimate Baseline model (17 μSv/h) depicted in Fig. 4. It is assumed in this analysis that the EPP DSM drawers themselves do not include the diagnostics apertures, which could contribute an additional 50 μSv/h. Therefore, taking into account these DSM apertures and plus 50 μSv/h to EPP SDDR, the 100 μSv/h access limit is exceeded in current global ITER model, and farther steps for improvement of the radiation shielding design are required. This should be done in a synergistic manner for the whole ITER, especially its Lower Port.

Table 1: Shut-Down Dose Rate (SDDR) cross-talks between interspaces of three ports of B-lite global ITER model.

Contribution to SDDR from the following ITER components	SDDR, μSv/h F5 **Lower Port**	SDDR, μSv/h F1 **Equatorial Port**	SDDR, μSv/h F3 **Upper Port**
1. Ultimate Baseline (all ports closed)	9	17	19
2. Original Lower Port	189	18	6
3. Diagnostics Equatorial Port Plug with double labyrinth and closed inter-drawer gaps	10	41	9
4. Original Upper Port	1	2	48
TOTAL	209	78	82

Nuclear heating distributions have been calculated for the critical locations of EPP, particularly inside the custom-fitted steel plate connected to VV which represents a part of second labyrinth shown in Fig. 5. The highest nuclear heating equaled 0.23 W/cc was found in front of that custom-fitted VV-plate. The rate of displacements per atom (dpa) of steel located in critical positions of EPP have been calculated using the MCNP5 code in accordance with the standard Norgett–Robinson–Torrens (NRT) model and FENDL-2.1 damage cross-section library, see details in Ref. [3]. The damage expressed as rate per full power year (fpy) has reached maximum value 0.3 dpa/fpy at the same location as the peak of nuclear heating was observed. All the results were normalized on the 500 MW of DT fusion power, 80% of which is released with 14 MeV neutrons. The SDDR results have been provided at 1e6 s after the ITER shutdown in order to compare with the 100 μSv/h access limit. The ICRP74 photon-to-dose conversion factors [12] are used to convert decay gamma spectra to SDDR at the final step of the R2Smesh scheme.

The ITER SA2 neutron irradiation scenario [13] has been applied for the FISPACT part of the R2Smesh interface; it assumes 0.3 MWa/m^2 of accumulated fluence on the blanket FW.

Staff:

U. Fischer
D. Leichtle
A. Serikov

Literature:

[1] A. Serikov, U. Fischer, D. Leichtle, C.S. Pitcher, A. Suarez, Local modeling approach for Monte Carlo parametric neutronic analysis in ITER, Proc. German Annual Meeting on Nuclear Technology (Jahrestagung Kerntechnik 2012), May 22 – 24, 2012, Stuttgart, Germany (2012).

[2] A. Serikov, U. Fischer, D. Leichtle, C.S. Pitcher, A. Suarez, Verification of the local Monte Carlo modelling approach for fusion neutronics applications in ITER," Transactions of the American Nuclear Society, Vol. 106, pp. 641-644, Chicago, Illinois, USA, June 24–28, 2012.

[3] A. Serikov, U. Fischer, et al., "Monte Carlo radiation shielding and activation analyses for the Diagnostic Equatorial Port Plug in ITER," Fusion Engineering and Design, vol. 87, 690–694 (2012).

[4] C.S. Pitcher, et al., Port-Based Plasma Diagnostic Infrastructure on ITER, TOFE-2012 conference, Nashville, to be published in Fusion Science and Technology.

[5] A. Serikov, et al., Mitigation of radiation streaming inside the ITER ports, ICRS-12 & RPSD-2012 conference, Nara, Japan, Sep 2-7, 2012, to be published in Progress in Nuclear Science and Technology.

[6] X-5 Monte Carlo Team, "MCNP—A general Monte Carlo N-particle Transport Code, Version 5, Vol. I: Overview and Theory," LA-UR-03-1987, Los Alamos National Laboratory (Apr. 24, 2003).

[7] M. Majerle, D. Leichtle, U. Fischer, A. Serikov, "Verification and validation of the R2Smesh approach for the calculation of high resolution shutdown dose rate distributions," Fusion Engineering and Design 87, 443-447 (2012).

[8] R. A. Forrest et al., "FISPACT 2007 user manual," UKAEA FUS 534 report, March 2007.

[9] A. Serikov, U. Fischer, et al., "Computational Challenges of Fusion Neutronics for ITER Ports," submitted to Joint International Conference on Supercomputing in Nuclear Applications and Monte Carlo 2013 (SNA + MC 2013), La Cité des Sciences et de l'Industrie, Paris, France, October 27-31, 2013.

[10] A. Serikov, U. Fischer, et al., "Toolkit for High Performance Monte Carlo Radiation Transport and Activation Calculations for Shielding Applications in ITER," Proc. M&C 2011, Rio de Janeiro, RJ, Brazil, May 8-12, 2011, Latin American Section / American Nuclear Society (2011); http://mathematicsandcomputation.cowhosting.net/MC11/_pdf/mc27_256_paper.pdf

[11] ParaView visualization application: http://www.paraview.org

[12] ICRP Publication 74, Conversion Coefficients for use in Radiological Protection against External Radiation, Ann. ICRP, vol. 26, no. 3/4, Elsevier, Amsterdam, 1996.

[13] M. J. Loughlin, N. P. Taylor, Recommended Plasma Scenarios for Activation Calculations, ITER Internal Report ITER_D_2V3V8G v 1.1, (28 Oct. 2009).

Acknowledgement

This work was supported by ITER Organization under the service contract No. ITER/IO/12/4300000548. The views and opinions expressed herein reflect only the author's views. The ITER Organization is not liable for any use that may be made of the information contained therein.

Monte Carlo Radiation Transport Calculations for Nuclear Fusion Facilities (HPC-FF-FSNMCFU)

Objective

The objective of the HPC-FF-FSNMCFU project was to exploit the capabilities of the High Performance Computational (HPC) system for massive parallel Monte Carlo transport computations and extend their application range to challenging problems in the field of nuclear design analyses for the development and optimization of specific systems/components of the ITER tokamak.

The computational simulations play important role in development of thermonuclear fusion devices. In that development, there is a great demand for computations in field of fusion neutronics. Only large, powerful multi-hundred CPU clusters, such as the HPC-FF system for fusion applications at Jülich Supercomputing Centre [1] could provide necessary resources for massive parallel Monte Carlo particle transport simulations for challenging tasks of shielding and activation analyses in ITER and DEMO fusion reactors. It was demonstrated that the parallel use of hundreds of the HPC-FF CPUs allows substantially accelerate the Monte Carlo calculations with the MCNP5 code [2]. The challenging tasks of deep-penetration radiation transport for fusion neutronics in ITER were addressed successfully, e.g. nuclear heating and helium production rate have been calculated with high spatial resolution using the MCNP5 mesh tally capability. The experience of performing the neutronics analyses for the ITER Upper Electron Cyclotron Heating (ECH) launcher [3] has shown that some tasks could be solved only on supercomputers. The Monte Carlo statistical errors associated with the mesh-tally results were reduced by applying variance reduction techniques and by taking the advantages of massive parallel computations on the HPC-FF system. The HPC-FF powerful computational resources allowed extending the range of ITER applications for neutronics analyses with inclusion of In-Vessel Viewing System (IVVS) and the Glow Discharge Cleaning (GDC) unit to be installed in the equatorial port [4], as well as the upper ports in the Neutral Beam Cell of ITER [5].

One of the recent applications of HPC-FF performed in a frame of this project was nuclear analysis of Diagnostics Equatorial Port Plug [6]. The computational challenges of neutronics analysis are resolved by applying the Monte Carlo OpenMP/MPI parallelization for radiation transport and number of CAD geometry conversion tools and interfaces for activation analysis and shutdown dose rate calculations. The mesh-tally of shutdown dose rates superimposed over the MCNP5 geometry calculated with the R2Smesh interface [7] allows exploring radiation pathways and pinpointing critical locations. It was concluded from the EPP neutronics analysis [8] that direct radiation streaming from the plasma should be excluded or mitigated by blocking the gaps with the labyrinths, rails, and shielding plates made of steel or boron carbide.

As shows practice of the MCNP5 MPI parallel computations [9-11], there is a need to decrease the amount of time allowed for communications between the CPU cluster nodes regulated by number of “rendezvous” in the MCNP5 settings. The optimal number of CPUs used in MCNP5 parallel calculations is dependent on the complexity of the model, physical process involved in particle tracks and the particle histories lengths. An important issue for scaling is keeping or increasing the calculation load on each processor: the higher ratio of computation per communication, the closer speed-up scaling to linear law. From the experience of the MCNP5 parallel runs for the ITER fusion neutronic applications, the optimal number of CPUs depends on the size of the MCNP5 task and the number of available processors. The maximum speed-up was found on HPC-FF at around 700 with 1600 CPUs.

Staff:

U. Fischer
D. Leichtle
A. Serikov

Literature:

[1] HPC-FF system: http://www.fz-juelich.de/ias/jsc/EN/Expertise/Supercomputers/JUROPA/JUROPA_node.html

[2] X-5 Monte Carlo Team, "MCNP—A General Monte Carlo N-Particle Transport Code, Version 5, Volume I, MCNP Overview and Theory," LA-UR-03-1987, Los Alamos National Laboratory (Apr. 24, 2003; revised Oct. 3, 2005).

[3] A. Serikov, U. Fischer, et al., "Evolution of shielding computations for the ITER upper ECH launcher," Nuclear Technology, vol. 175, no. 1, pp. 238-250, July 2011.

[4] A. Serikov, U. Fischer, D. Leichtle, "Neutronic Analyses for the IVVS/GDC System in ITER," Transactions of the American Nuclear Society, vol. 104, (2011) pp. 637-638.

[5] A. Serikov, U. Fischer, et al., "Neutronic Analyses for the Upper Ports in the Neutral Beam Cell of ITER," Fusion Science and Technology, vol. 60, no. 2, pp. 708-714, Aug. 2011.

[6] A. Serikov, U. Fischer, et al., "Monte Carlo radiation shielding and activation analyses for the Diagnostic Equatorial Port Plug in ITER," Fusion Engineering and Design, vol. 87, 690–694 (2012).

[7] M. Majerle, D. Leichtle, U. Fischer, A. Serikov, "Verification and validation of the R2Smesh approach for the calculation of high resolution shutdown dose rate distributions," Fusion Engineering and Design 87, 443-447 (2012).

[8] A. Serikov, U. Fischer, et al., "Neutronics for equatorial and upper ports in ITER," Proc. of the 27th SOFT conference, Liege, Belgium, Sep. 24-28, 2012, to be published in Fusion Engineering and Design.

[9] A. Serikov, U. Fischer, et al., "High performance computations of Monte Carlo radiation transport for ITER fusion neutronics," Proceedings of the Workshop "Computational Methods in Science and Engineering" (SimLabs@KIT 2010), November 29 - 30, 2010, Karlsruhe, Germany, KIT Scientific Publ., 2011, ISBN 978-3-86644-693-9, http://digbib.ubka.uni-karlsruhe.de/volltexte/1000023323; http://books.google.de/books?id=KgGCchbdi6MC&lpg=PA3&dq=SimLab%40KIT%20workshop%2C%20Karlsruhe%2C%20Nov.%2029-30%2C%20KIT%20Scientific%20Publishing%202010&hl=de&pg=PA135#v=onepage&q&f=false.

[10] A. Serikov, U. Fischer, et al., "Toolkit for High Performance Monte Carlo Radiation Transport and Activation Calculations for Shielding Applications in ITER," Proc. M&C 2011, Rio de Janeiro, RJ, Brazil, May 8-12, 2011, Latin American Section / American Nuclear Society (2011); http://mathematicsandcomputation.cowhosting.net/MC11/_pdf/mc27_256_paper.pdf

[11] A. Serikov, U. Fischer, D. Grosse, "High Performance Parallel Monte Carlo Transport Computations for ITER Fusion Neutronics Applications," Progress in Nuclear Science and Technology, Vol. 2, pp.294-300 (2011).

Acknowledgement

This work, supported by the European Communities under the contract of Association between EURATOM and Karlsruhe Institute of Technology, was carried out within the framework of the European Fusion Development Agreement. The views and opinions expressed herein do not necessarily reflect those of the European Commission.

Monte Carlo Calculations of Covariances for Nuclear Reactions in Fusion Technology Applications (HCP-FF-FSNMCCO)

Objective

The objective of the FSNMCCO project was to use the HPC-FF parallel super computer for calculations of reaction cross-sections and their covariances using the Monte Carlo method as a part of uncertainty assessments in fusion neutronic applications.

Calculation of reaction cross-sections and covariances using the Monte Carlo method

The calculations of covariance matrices for nuclear cross-sections were performed using a set of computer programs, named BEKED, which has been elaborated in KIT [1].

The computation of reaction cross-sections and corresponding covariances includes following steps: the definition of the basic set of parameters for the nuclear models used for the cross-section calculation, based on the available measurements, the definition of uncertainties of model parameters, the Monte Carlo sampling of N number of input data sets for the code implementing selected models, the performing of calculations for obtained input data files, and the calculation of cross-sections and covariance matrices for particular reactions

$$\sigma_i^{eval} = (1/K)\sum_{k=1,K}^{K} \sigma_{ik} \pm \sqrt{V_{ii}}, \quad (1)$$

$$V_{ij} = N^{-1}\sum_{k=1}^{N}(\sigma_{ik} - \sigma_{i0})(\sigma_{jk} - \sigma_{j0}) \quad (2)$$

where σ_{ik} is the cross-section corresponding to the "*i*"-th primary neutron energy in the "*k*"-th Monte Carlo history, σ_{i0} is the cross-section obtained using the basic set of model parameters.

Fig.1 shows the covariances matrix for neutron inelastic scattering for ^{52}Cr calculated using the TALYS code [2], ALICE/ASH code [3], and the BEKED package.

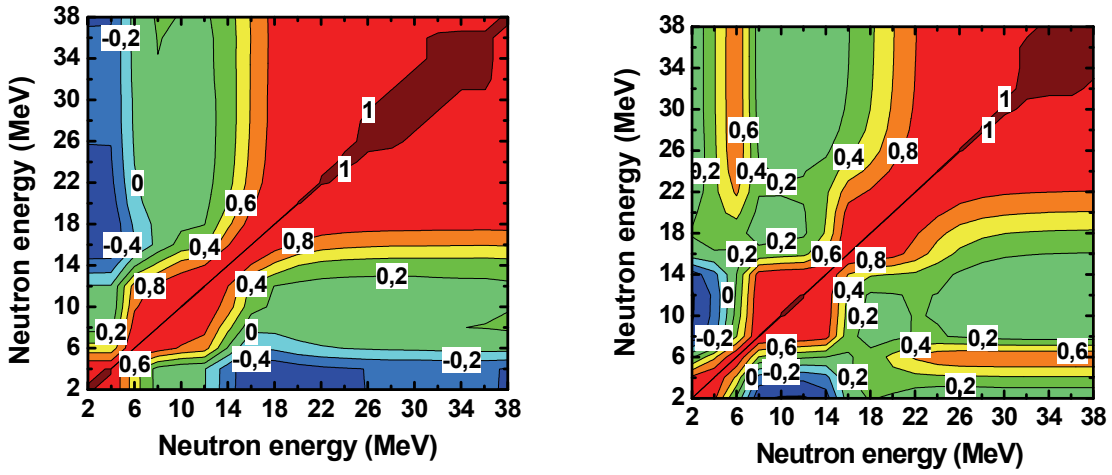

Fig. 1: Correlation matrix for the ^{52}Cr(n,n') reaction cross-section calculated using BEKED and nuclear models implemented in the TALYS code (left figure) and ALICE/ASH code (right figure).

The search of optimal nuclear model parameters for copper

The search was performed for nuclear level density parameters providing the best description of available measured reaction cross-sections for nucleon induced reactions on 63Cu and 65Cu isotopes. Experimental data were taken from EXFOR.

The method, close to Hastings-Metropolis algorithm [4,5], was used to find the optimal nuclear level density parameters providing the minimal value of the following expression

$$H(a_0,a_1,a_2,...,a_N)=\sum_{j=1}^{N_{\exp}}\left((\sigma_j^{calc}(a_0,a_1,a_2,...,a_N)-\sigma_j^{\exp})/\Delta\sigma_j^{\exp}\right)^2 . \quad (3)$$

Additionally the value of the S-deviation factor [6] was calculated for the control of obtained deviations:

$$S(a_0',a_1',a_2',...,a_N')=10^{\left\{\left(\sum_{j=1}^{N_{\exp}}\left[\frac{\lg(\sigma_j^{\exp})-\lg(\sigma_j^{calc})}{(\Delta\sigma_j^{\exp}/\sigma_j^{\exp})}\right]^2\right)\left(\sum_{j=1}^{N}\left[\sigma_j^{\exp}/\Delta\sigma_j^{\exp}\right]^2\right)^{-1}\right\}^{1/2}}, \quad (4)$$

where a_0, a_1, …, a_N are nuclear level density parameters for X_0, X_1, … X_N nuclei; $\sigma_j^{\exp}$ and $\Delta\sigma_j^{\exp}$ are measured value of cross-section and its error.

The method of the search of optimal parameters assuming parallel computer calculations is described in details in Ref.[6]. Table 1 shows the gain in H1/2 and S-values after the search of the minimum of Eq.(3) for copper isotopes.

Table 1: The values showing the gain in the values of $H^{1/2}$ and S values after the search of "optimal" nuclear level density parameters for copper. Nuclear level density is calculated using the generalized superfluid model (GSM), Gilbert-Cameron model combined with Ignatyuk-Smirenkin-Tishin model (GC-IST), and back-shifted Fermi gas model (BSM)

Ratio of final and initial values	GSM	GC-IST	BSM
$(H/H_0)^{1/2}$	0.858	0.917	0.843
S/S_0	0.971	0.985	0.963

Staff:

U. Fischer
A. Konobeev
P. Pereslavtsev

Literature:

[1] A.Yu. Konobeyev, U. Fischer, P.E. Pereslavtsev, Computational Approach for Evaluation of Nuclear Data Including Covariance Information, Journal of the Korean Physical Society 59 (2011) 923

[2] A.J. Koning, S. Hilaire, M. Duijvestijn, TALYS-1.0, Int. Conf. Nucl. Data for Sci. and Technology, Nice, France (2007) 058 DOI: 10.1051/ndata:07767

[3] C.H.M. Broeders, A.Yu. Konobeyev, A.Yu. Korovin, V.P. Lunev, M. Blann, ALICE/ ASH - Pre-Compound and Evaporation Model Code System for Calculation of Excitation Functions, Energy and Angular Distributions of Emitted Particles in Nuclear Reactions at Intermediate Energies, FZKA 7183, Forschungszentrum Karlsruhe (2006)

[4] W.K. Hastings, Biometrika 57 (1970) 97.

[5] R. Capote, D.L. Smith, Nuclear Data Sheets, 109 (2008) 2768

[6] A.Yu. Konobeyev, U. Fischer, P.E. Pereslavtsev, R.Capote, Second International Workshop on Accelerator Radiation Induced Activation (ARIA 2011), Ma'ale Hachamisha, Israel, May 15-19, 2011

Acknowledgement

This work, supported by the European Communities under the contract of Association between EURATOM and Karlsruhe Institute of Technology, was carried out within the framework of the European Fusion Development Agreement. The views and opinions expressed herein do not necessarily reflect those of the European Commission.

Design Tools and Methodologies - Neutronic Studies (WP12-DTM-04)

Overall objective

The design of nuclear DEMO components such as blanket, shield, divertor, ports, etc. depends to a large extent on the results of neutronic analyses. Neutronic studies are required, iteratively with plasma physics and system analyses, and engineering design activities, to develop a mature DEMO design.

Task DTM-04 of the EFDA 2012 work programme on Power Plant Physics & Technology (PPPT) aimed at performing first neutronic scoping studies to assess the nuclear performance of DEMO1 and provide important nuclear responses which are required for the engineering design and its verification. A dedicated part of the programme was devoted to the evaluation and further development of neutronic tools which are required for applications to DEMO nuclear analyses.

The nuclear analyses strand of the activities comprised the development of a provisional MCNP model of DEMO, shielding analyses for the definition of the radial build, the assessment of the Tritium breeding capability and of radiation loads to the TF coil taking into account neutron streaming effects, the calculation of the nuclear heating, radiation induced damage and gas production in the steel structure at different locations in the DEMO plant, as well as calculations of the activation inventory and the afterheat production.

The activities in the tools development strand focussed on the evaluation of available tools with the main objective to identify further development needs towards mature, robust and flexible European software tools for DEMO nuclear analyses. These included, first of all, suitable Monte Carlo codes for particle transport simulations in DEMO, second, coupling schemes of radiation transport and activation codes with the capability to provide shut-down dose radiation maps, and, finally, geometry conversion tools which enable the import of CAD data in the Monte Carlo codes.

The Task DTM-04 activities were conducted in a joint effort by CCFE (UK), CEA (France), CIEMAT (Spain), ENEA (Italy), HAS (Hungary), IPPLM (Poland), JSI (Slovenia), and KIT (Germany). KIT co-ordinated the DTM-04 activities (Task T-01), conducted tasks on the “Development of a provisional DEMO model” (Task T-02), on the “Shielding analyses in response to system code studies“ (Task T-03), and contributed to Tasks 12 and 13 on “Tools for CAD geometry import in Monte Carlo codes” and “Tools for coupled radiation transport and activation calculations”, respectively.

In the following summaries of the related task activities are given.

Task T01 - Task Co-ordination

Objective

The objective of the task co-ordination was to guide and monitor the DTM-04 activities to ensure the analyses and the development works are performed in a consistent manner and in agreement with the prescribed task specifications. The DTM-04 task co-ordination also included the responsibility for the DEMO model provided to the participating associations and any modification applied for specific purposes. Analyses results are checked for their validity and consistency. Care was taken in merging the various efforts on the CAD conversion tools, the Monte Carlo codes, and the approaches for shut-down dose rate calculations in the most efficient way with the ultimate goal to arrive as much as possible at joint European neutronic tools for the future application to DEMO nuclear analyses.

The following reports were provided by the DTM-04 Task coordinator:

Nuclear Analyses Report

This report summarizes the nuclear analyses conducted in the frame of WP12-DTM-04 on the basis of a provisional MCNP DEMO1 model.

The **provisional DEMO model** was developed on the basis of the available MCNP model elaborated in the frame of the 2006/2008 EFDA DEMO study and taking into account the results of the shield dimensioning analyses conducted under WP12-DTM-04, Task T-03, and the recommendations of the WP11 Remote Handling (RH) handling studies. This model was provided to the WP12-DTM-04 Task participants as MCNP input deck together with a FORTAN90 source routine describing the plasma neutron source for conducting the nuclear analyses **(Task T02, KIT)**.

The **dimensioning of the shield** of the provisional DEMO was performed on the basis of 3D Monte Carlo shielding calculations. The radial build was defined in accordance to the results of the system code analyses performed by CCFE with the PROCESS code for DEMO1. The radial thickness assumed for the inboard mid-plane amounts to 80 cm, for the blanket and the manifold region, and 65 cm, for the shield and the vacuum vessel (VV), summing up to a total thickness of 145 cm for the entire inboard blanket/shield/VV system. The shielding calculations showed that the assumed radial build is sufficient to satisfy the radiation design limits as specified for DEMO. This applies also for the peak nuclear heating which is well below the recommended limit of 50 W/m^3 **(Task T03, KIT)**.

The **TBR calculations**, performed with MCNP using the provisional DEMO model with HCLL blanket modules, revealed a global TBR of 1.08. This is considered sufficient to ensure Tritium self-sufficiency when taking into account uncertainties involved in the TBR-calculations due to uncertainties of the nuclear data, the effect of the ^{6}Li burn-up during the blanket lifetime, the presence of ports without breeder blanket (e. g. for plasma heating) as well as Tritium losses in the fuel cycle **(Task T04, HAS)**.

Radiation loads to the inboard TF coil were calculated for vertical gaps between the blanket modules with widths of 20, 10 and 5 mm. These gaps extend over the entire poloidal length of the inboard blanket segment in the DEMO model. The effect of the gap width on the radiation loads to the TF coil was shown to be rather modest. Decreasing the gap width from 20 to 5 mm reduces the peak values of the fast and total neutron fluences by no more than 30 and 25 %, respectively. This is due to the fact that the neutron radiation streaming through the blanket gaps impinges, at the bottom of the gaps, on a bulk shield system with no penetrations included. The neutron fluences are about two orders of magnitude lower than the specified DEMO design limits **(Task T05, CIEMAT)**.

The **nuclear heating data** were provided for the blanket/shield system including calculations of the power density profiles across the blanket, shield and vacuum vessel in the central inboard and outboard blanket modules. The calculation of the total nuclear power production showed that 84 % is generated in the breeding blanket modules, 8 % in the divertor, 6% in the shield/VV system, and 2% in the manifold region. The resulting energy multiplication factor is at 1.17, as it is typical for a fusion power reactor based on a liquid metal (Pb-Li) blanket with steel structure **(Task T06, ENEA)**.

The **radiation damages to steel** structures were calculated for irradiation times from 1 to 20 fpy. The maximum damage rate at the inboard side is 13 dpa/fpy at the first wall and decreases to 0.2 dpa/fpy at the front of the shield. In the region of the vacuum vessel, the displacement damage accumulates to less than 10^{-2} dpa over 20 fpy, and thus is very moderate. The shield can be operated over 5 fpy resulting in a maximum displacement damage of slightly more than 1 dpa. At the outboard side, the damage at the back of the manifold region, due to the larger blanket thickness, is less than 1 dpa over 20 fpy **(Task T06, ENEA)**.

The **He production in steel** is a crucial issue for power reactors since the re-weldability of components and connections/pipes made of steel must be assured. The calculations showed that the inboard shield could be operated up to 5 fpy before the 1 appm re-weldability limit is reached. The vacuum vessel need not be replaced during an assumed lifetime of 20 fpy. At the outboard side, the He production behind the breeder module is lower due to the larger breeder zone. Even for 20 fpy, the He production is well below the 1 appm limit in the entire manifold region **(Task T06, ENEA)**.

The **decay heat produced in the blanket modules** was calculated for irradiations of 1.57 fpy, assuming a detailed DEMO operation scenario over 5 calendar years, and a continuous irradiation over 5 fpy. For the 1.57 fpy irradiation the total decay heat power amounts to 9.51 MW at shutdown which corresponds to less than 1% of the nuclear power produced during operation. With the 5 fpy irradiation, the production of medium and long-lived radio-nuclides is increased resulting in a slight increase of the decay heat power at short decay times after shut-down (≈ 20%) and a significant increase (≈ factor 3) at decay times longer than some 1000 years **(Task T08, CIEMAT, HAS)**.

For the region of the inboard divertor rail, the nuclear heating and the He production in the steel structure were calculated assuming two divertor configurations with different shielding capabilities. For the reference case of the provisional DEMO model, the peaking values for the nuclear heating and the He production are around 1.2 W/cm^3 and 5 appm, respectively. The related hot spot areas are located at the back of the void interspace between the bottom blanket module and the divertor cassette where no shielding of the impinging radiation is provided. With the inclusion of an additional shielding/supporting structure behind the inboard divertor plate the resulting maximum He production in the steel structure of the rail is reduced to a level of 0.5 appm and therefore must not be exchanged over the assumed lifetime **(Task T09, IPPLM)**.

For the upper vertical port, through which the blanket cooling pipes will go, shielding calculations were performed to analyse and optimise the shielding. It was shown that additional needs to be applied to reduce the neutron fluxes to a tolerable level in the range of 10^{10} to 10^{11} n/cm^{2}s. This could be achieved by an additional shield of 50 cm thickness assuming an efficient shield material such as water/borated steel (40%/60%) mixture **(Task T10, CIEMAT, JSI)**.

Tools for Nuclear Analyses of DEMO

This report summarizes the work conducted in the frame of DTM-04 on the evaluation and further development of neutronic tools which are required for the nuclear analyses of DEMO.

This included, first of all, an evaluation of suitable (European) Monte Carlo (MC) codes which may serve as alternative to the US code MCNP which is the current reference for fusion neutronics calculations (Task T-11), and, second, coupling schemes of radiation transport and activation codes which are required for safety and waste related analyses (Task T-13), and, finally, CAD to MC geometry conversion tools which provide (indirect) access to engineering CAD geometry data in MC transport simulations (Task T-12).

Task T11 - Evaluation of Monte Carlo (MC) transport codes for application to DEMO

There are several candidates which comply with the long-term goal to provide a European MC code which, on the one hand, is open source and freely available, on the other hand, is well suitable and validated for fusion neutronics applications (in particular to DEMO), and thus could actually replace MCNP. Along this guideline, TRIPOLI 4, SERPENT 2, and GEANT4 were prioritised for further consideration, taking into account that TRIPOLI is a mature code which is already validated for fusion neutronics and verified for DEMO application, that SERPENT will require a substantial future development effort, and that GEANT is a toolkit which needs to be adapted. The FLUKA code should be also further investigated for its capabilities to handle the DEMO geometry and the plasma neutron source and the use of data libraries from external sources.

Task T12 - („Evaluation of CAD to MC geometry conversion tools“)

Available approaches for the import of CAD geometry in MC codes were evaluated with respect to their suitability for fusion applications and further development needs. A benchmark exercise was conducted with this objective on a complex CAD DEMO Cad model with HCLL blankets. The benchmark exercise included the CAD to MC geometry conversion tools McCad, developed by KIT, Germany, and MCAM, developed by the Chinese FDS team. The primary aim was to check McCad’s capabilities for the DEMO model conversion by independent users and thereby identify the further developments needs for establishing McCad as European software tool for the CAD import in Monte Carlo codes.

The MCAM conversion tool was shown to be an already mature software which is available upon a license agreement with the Chinese FDS team with no access to the source code. McCad, on the other hand, is under development at KIT as open source software project. It is available as test version upon request. User support is still required for the implementation of the software and its use it for the conversion of complex models. It is thus recommended to further improve and develop McCad towards a mature and robust European software tool for the CAD import in MC codes such as MCNP and TRIPOLI.

With regard to the preparation of suitable DEMO CAD neutronics model it is recommended to devise this model in two steps. First a simple generic model needs to be set up with empty blanket boxes. This model can be easily converted and completed by void cells as required for the neutronic calculations. In as second step, a complete blanket module needs to be devised with detailed internal geometry. This model can be converted, again easily, and subsequently filled in the empty blanket boxes of the already available generic model by using the repeated structure feature of MCNP. Following this procedure, a much less complex geometry model will be generated which is much more suitable for the neutronics calculations than the benchmark model considered.

Task T13 - („Evaluation and further development of coupled radiation transport and activation calculation schemes for DEMO“)

The different schemes available for coupled radiation transport and activation calculations were evaluated for their suitability and applicability to DEMO. To this end a DEMO benchmark exercise was performed including the R2S (Rigorous 2-Step) systems developed by CCFE, KIT and UNED, and the Direct 1-Step (D1S) approach developed by ENEA. In addition, methods for the estimation of uncertainty propagation in R2S type calculations were conceptually designed and evaluated.

A blind comparison was performed on a DEMO benchmark model with HCLL blankets and a specified irradiation history. Shut-down dose rate (SDR) results, provided with the different approaches, showed good agreement within 25% for the specified in-vessel positions.

From the experience gained in the course of this exercise, some benchmark specific recommendations were made regarding the calculation of requested responses such as the absorbed dose and traceability tallies. As for the D1S approach, it is recommended to extend the database with libraries for more DEMO-relevant nuclides and for nuclides relevant at a wider range of decay times.

The analyses also served to identify shortcomings in the algorithms and normalisation parameters of some of the tools, which were corrected during the course of the exercise. This highlights the importance of performing regular inspections of the performance of the tools via this kind of computational inter-comparison. To complement these exercises, and enhance quality assurance, it is recommended that European SDR tools continue to be validated against available experimental data, and particularly against those from large-scale tokamak geometries such as JET.

Finally, it is recommended to combine the various development efforts in the field of SDR calculation tools towards a single European tool based on the R2S approach which need to be complemented by a D1S tool for quick SDR assessments. The R2S tool should include suitable means which allow the estimation of SDR uncertainties by propagating these in a proper way from the neutron transport through the activation to the decay photon calculation.

Staff:

U. Fischer
D.Leichtle
P. Pereslavtsev

Literature:

U. Fischer, Nuclear Analysis Report for DEMO1, EFDA_D_2CXWZV v1.2 - WP12-DTM04, January 2013

U. Fischer, Tools for Nuclear Analyses of DEMO, EFDA_D_2M8PH6 v1.1 - WP12-DTM04, January 2013

Task T02 - Provisional DEMO MCNP Model

Objective

The objective was to develop a provisional DEMO model on the basis of the available MCNP model developed in the frame of the 2006-2008 EFDA DEMO study. This model was to be provided to the DTM-04 participants for the nuclear analyses to be conducted in Tasks T-04 to T-10, and other urgent WP12 tasks, as required e. g. for the assessment of radiation fields in DEMO for remote handling investigations.

The following revisions were applied to the 2006/08 DEMO model to provide a provisional MCNP model for the WP12-DTM-04 nuclear analyses:

- The radial build has been adjusted to the results of the shield dimensioning analyses, WP12-DTM-04, Task 03, confirming essentially the radial build assumed in the system code analyses for DEMO1. There was also included a casing of the TF magnet at the in-board side of the reactor.
- In accordance with the recommendations of the WP11 RH handling studies, the lower blanket module at the outboard side was cut to enable the removal of the divertor cassette through the divertor port.

The global reactor parameters were not changed for this provisional model. Fig. 1 shows vertical and horizontal cross-sections of the provisional MCNP model of DEMO generated with the MCNP plotter.

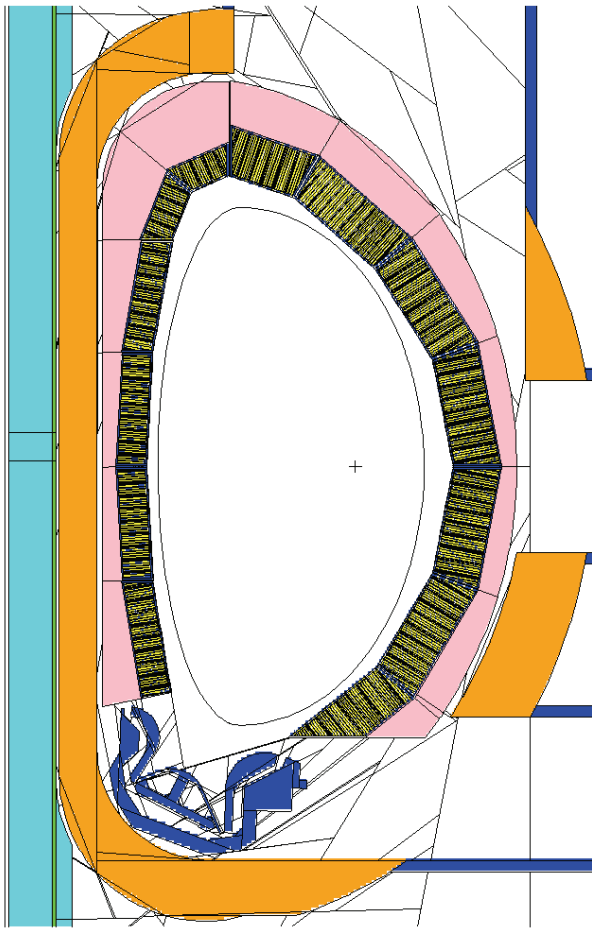

Fig. 1a: Vertical cross-section of provisional MCNP model for HCLL DEMO.

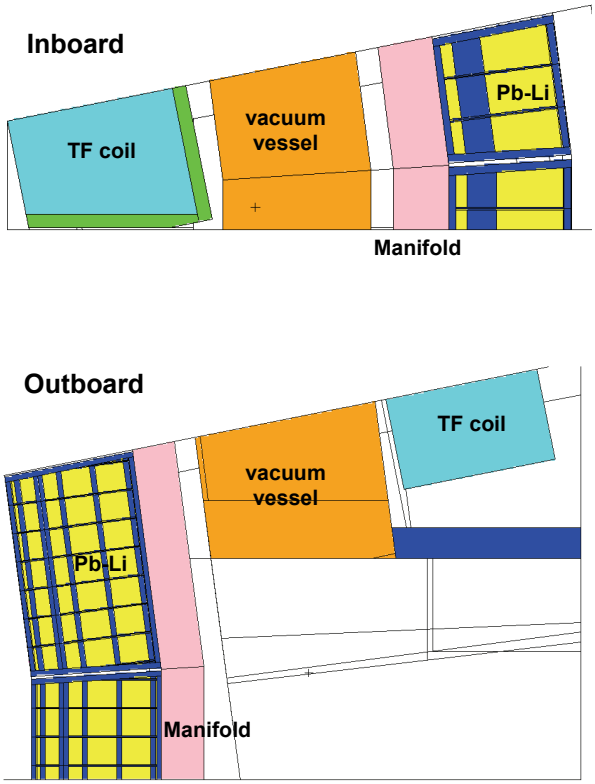

Fig. 1b: Horizontal cross-sections of provisional MCNP model for HCLL DEMO.

The currently preferred DEMO version, called DEMO1, is a near-future technology, pulsed version of DEMO assuming major and minor radii of 9.0 and 2.25 m, respectively, and a fusion power of 2119 MW. To cope with such conditions, the neutron wall loading of the provisional DEMO model was adjusted. The average neutron wall loading of the 2006/08 model is 1.76 MW/m^2 while the corresponding value of DEMO1, as provided by the PROCESS code, is 1.269 MW/m^2. With the fusion power of 2385 MW for the 2006/08 DEMO, resulting in a normalization factor of 8.468 10^{20} neutrons/s, a re-normalisation factor of 1.269/1.76 = 0.721 was derived and recommended for application with the nuclear analyses in order to be consistent with DEMO1 assumptions.

The model was provided to the DTM-04 task participants as MCNP input deck together with a FORTAN90 source routine describing the plasma neutron source.

Staff:

U. Fischer
P. Pereslavtsev

Literature:

U. Fischer, P. Pereslavtsev et al, Final report on the EFDA task TW6-TRP-005, Deliverable 1a: “Model Generation and Neutronic Design Analyses for the European DEMO Conceptual Study”, July 2008.

U. Fischer, P. Pereslavtsev, Description of the provisional DEMO1 MCNP model, EFDA_D_2L6X4U v1.1 - WP12-DTM04-T02, January 2013

Task T03 - Shielding Analyses in Response to the System Codes Studies

Objective

The objective of this task was to dimension the shield of the provisional DEMO on the basis of 3D Monte Carlo shielding calculations, and, iteratively to the system code analyses performed, to define the radial build.

The shielding calculations were performed with the MCNP Monte Carlo code using the DEMO 2006/08 model with the HCLL blanket ("HCLL Demo Reactor Variant") and a radial build according to the DEMO1 parameters provided by the PROCESS code analyses of CCFE.

The calculations were performed in the torus mid-plane to check if the assumed radial build, as shown in Table 1, is sufficient to satisfy the radiation design limits of the TF coil at the inboard side. To this end radial profiles of the nuclear power and the neutron flux densities were calculated across the inboard torus mid-plane, as well as the radiation loads to the TF coil at the central inboard side. The results were normalised to an average neutron wall loading of 1.38 MW/m^2 as provided by the PROCESS code for DEMO1. With the assumed poloidal distribution, taken from the DEMO 2006/08 analyses, this results in a neutron wall loading of 1.49 MW/m^2 at the inboard mid-plane.

Table 1: Radial build assumed for the shielding calculations of DEMO.

Component	IB thickness (mm)	OB thickness (mm)	Material composition
FW armor	2	2	W
FW	30	30	Eurofer 63.5%, He 37.5%
Breeding zone Cooling plates Stiffening plates Breeder material	475 6.5 11 475	775 6.5 11 775	Eurofer 51%, He 49% Eurofer 57.6%, He 42.4% Pb-15.8Li, 90% ^{6}Li
Manifold	300	400	LiPb 5%, Eurofer 28% , He 67%
Shielding	300	400	WC 65%, Eurofer 10%, H_2O 25%
VV	350	800	SS316 61%, H_2O 37%, B 2%
TF casing	60		SS316

Fig. 2 shows the radial profile of the nuclear power density across the inboard torus mid-plane, from the first wall down to the TF coil. It is revealed that the peak nuclear is well below the recommended limit of 50 W/m^3 for the maximum power density in the TF coil - already in the region of the vacuum vessel.

It is thus indicated that the assumed radial build is sufficient for protecting the superconducting coils sufficiently. This was confirmed with the directly calculated radiation loads to the inboard TF-coils given in Table 2.

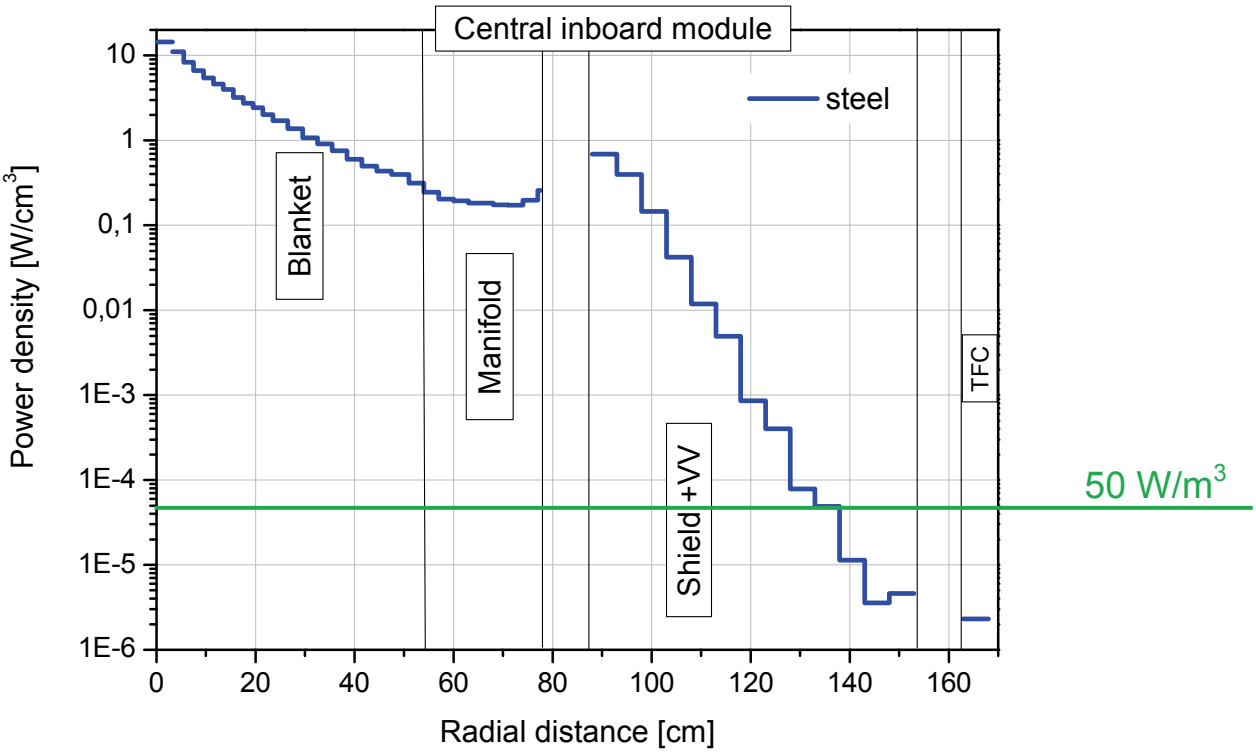

Fig. 2: Radial profile of the nuclear power density [W/cm^3] across the inboard mid-plane.

Table 2: Radiation design limits and radiation loads as calculated for the TF coil at the inboard mid-plane of DEMO.

	Radiation design limits		**Calculated radiation loads**	
	ITER(*)	**DEMO(**)**	**1 FPY**	**20 FPY**
Integral radiation dose in insulator (Epoxy) [Gy]	$1.0 \cdot 10^{7}$	$1.0 \cdot 10^{7}$	$3.6 \cdot 10^{4}$	$7.2 \cdot 10^{5}$
Peak fast neutron fluence (E>0.1 MeV) to the Nb_3Sn superconductor [1/cm^2]	$1.0 \cdot 10^{19}$	$1.0 \cdot 10^{19}$	$3.3 \cdot 10^{15}$	$6.6 \cdot 10^{17}$
Peak displacement damage to copper stabiliser, or maximum neutron fluence, between TFC warm-ups [dpa]	$1.0 \cdot 10^{-4}$	$1.0 \cdot 10^{-4}$	$2.2 \cdot 10^{-6}$	$4.3 \cdot 10^{-5}$
Peak nuclear heating in winding pack [W/cm^3]	$1.0 \cdot 10^{-3}$	$5.0 \cdot 10^{-5}$	$1.8 \cdot 10^{-6}$	

(*) Based on D. Maisonnier, P. Sardain, EFDA, December 2006
(**) Revised DEMO values according to J.-L. Duchateau, November 2011

The shielding calculations, performed for the inboard torus mid-plane, showed that the assumed radial build is sufficient to satisfy the radiation design limits as specified for DEMO. The radial thickness assumed for the inboard mid-plane amounts to 80 cm, for the blanket and the manifold region, and 65 cm, for the shield and the vacuum vessel (VV), summing up to a total thickness of 145 cm for the entire inboard blanket/shield/VV system.

The provisional MCNP model of DEMO, developed in the frame of Task WP12-DTM-04-02, is based on this radial build.

Staff:

U. Fischer
P. Pereslavtsev

Literature:

U. Fischer, P. Pereslavtsev, Recommendations for the DEMO Radial Build, EFDA_D_2M4CQP v1.1 - WP12-DTM04-T03, January 2013

Task T12 - Tools for CAD Geometry Import in Monte Carlo (MC) Codes

Objective

The objective of this task was to evaluate available approaches for the import of CAD geometry models in MC codes with respect to their suitability for DEMO fusion neutronics applications, the user-friendliness, availability and further development needs. To this end a benchmark exercise was conducted on the conversion of a complex CAD neutronics model of the 2006/08 DEMO with HCLL blankets integrated.

The benchmark exercise included the CAD to MC geometry conversion tools McCad, developed by KIT, and MCAM, developed by the Chinese FDS team. The primary aim was to check McCad's capabilities for the DEMO model conversion by independent users and thereby identify the further developments needs for establishing McCad as European software tool for the CAD import in Monte Carlo codes. CCFE and CIEMAT participated in the benchmark with MCAM, ENEA and JSI with McCad. KIT provided the McCad conversion tool and support in implementing and employing the McCad software package for the conversion process. The benchmark model and the related specifications for performing subsequent validation and test calculations were also provided.

The MCAM conversion tool was shown to be an already mature software which is available upon a license agreement with the Chinese FDS team, however, with no access to the source code. McCad, on the other hand, is under development at KIT as open source software project. It is available as test version upon request. User support is still required for the implementation of the software and its use for the conversion of complex models. In the course of the WP12-DTM-04-12 benchmark exercise, McCad was significantly improved to facilitate the conversion process for complex geometry models like the HCLL DEMO. It is thus recommended to further improve and develop McCad towards a mature and robust European software tool for the CAD import in MC codes such as MCNP and TRIPOLI. Of particular importance towards this goal is the implementation of an efficient material management system for the assignment of materials to the converted models.

With the CAD to MC geometry translation approach, the input geometry is converted in two steps into a geometry description suitable for MC particle transport codes. In the first step, the input geometry is decomposed into volumes that can be described by the Boolean combination of algebraic half-spaces. The overall geometry is not affected by the decomposition, i.e. the total volume content and the shape before and after the conversion are identical. In the second step, the void space is generated which is not available in the CAD system but mandatory for the particle transport simulation codes. This step requires suitable void generation algorithms which are different in MCAM and McCad. Due to the complexity of the DEMO CAD neutronics model, both MCAM and McCad users had to apply dedicated approaches for the completion of the converted DEMO model with void spaces. This process implied some manual work and additional manipulations with the interface data files. The different approaches applied with the MCAM and McCad processes resulted in MCNP geometry models with different degrees of complexity.

The void generation algorithm in McCad implies a large number of Boolean operations which are time-consuming and unstable. Especially when processing a model with a complex geometry such as the HCLL DEMO, the conversion process becomes very inefficient. Thus a new void filling algorithm was developed with the objective to decrease the required number of Boolean operations. The improved algorithm detects the collision between bounding boxes and the boundary surfaces of material solids and then describes the geometry of a void cell using these boundary surfaces. The improved void generation algorithm has been introduced in the latest McCad version 0.32 which reduced the conversion time from about 3 hours to 11-15 mins. This McCad version was provided by KIT to the benchmark participants ENEA and JSI.

The following two step approach was elaborated for the conversion of the HCLL DEMO model. It is based on the following steps:

1. Use of the simple (generic) DEMO model with empty blanket segment boxes (void space interior) as input CAD model, generation of the void cells and output to the MC file.
2. Decomposition of the HCLL blanket segment model, conversion and output to the MC file without void generation.

The interior blanket cells of the simple (generic) DEMO model (step 1) then have to be removed manually from the MCNP input file and replaced by the HCLL blanket segment model from step 2. Fig. 3 illustrates the integration process.

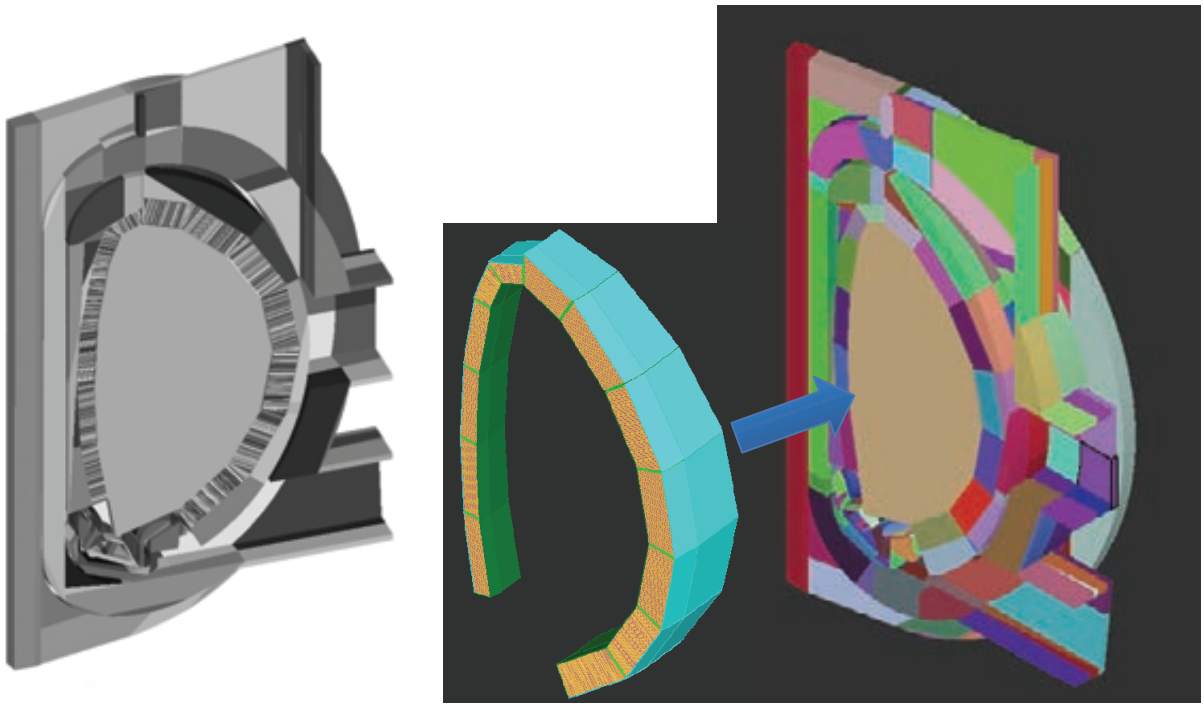

Fig. 3: CAD neutronics benchmark model with integrated HCLL blanket modules (left). Right side: Simple generic model with empty blanket module boxes and HCLL blanket internal geometry separated.

The comparison of the converted models in terms of their complexity (Table 3) showed consistency with regard to the void cells generated by MCAM and McCad. On the other hand, McCad generates about two times more material cells than MCAM which are, however, of significant less complexity.

Table 3: Results of the CAD to MC model conversion by MCAM and McCad.

	Original **CAD**	**MCAM**		**McCad**		
		CIEMAT	CCFE	KIT	ENEA	IJS
Number of material cells	6302	6302	6399	14190	14216	14090
Number of void cells		242	215	262	268	158
Total number of cells	6302	6544	6614	14452	14484	14248
CPU time required		~ 7 min.	~14 min.	~12 min.	~15 min.	~13 min.

Verification calculations to check the correctness of the converted model were performed for the volumes of the geometry cells by performing stochastic volume calculations with MCNP and comparing the results to the volumes provided by the CAD software. These comparisons showed extremely good agreement, in general within the very low statistical uncertainties, for

all of the many geometry cells. Further test calculations referred to the neutron wall loading (NWL) distribution which was calculated at the first wall of the thirteen blanket models.

There is good agreement for the NWL distributions as obtained by CIEMAT, ENEA and KIT. A bit larger difference was seen with the CCFE results, which was addressed to the way the NWL is calculated, i. e. it is not an issue of the converted model.

The use of the converted model in full neutron transport calculations is hindered by the necessity to assign materials to all non-void geometry cells of the model. MCAM has already implemented a functionality which enables the material assignment in a convenient way with an integrated material management system. Yet many manual interactions are still required which are error prone. Discrepant results observed for the full neutron transport calculations with the MCAM converted model indicate such problems.

With regard to the preparation of suitable DEMO CAD neutronics model it was recommended to devise this model in two steps. First a simple generic model needs to be set up with empty blanket boxes. This model can be easily converted and completed by void cells as required for the neutronic calculations. In as second step, a complete blanket module needs to be devised with detailed internal geometry. This model can be converted, again easily, and subsequently filled in the empty blanket boxes of the already available generic model by using the repeated structure feature of MCNP. Following this procedure, a much less complex geometry model will be generated which is much more suitable for the neutronics calculations than the benchmark model considered in WP12-DTM-04-012.

Staff:

U. Fischer
L. Lei
I. Lengar (JSI)
F. Moro (ENEA)
I. Palermo (CIEMAT)
P. Pereslavtsev
S. Zheng (CCFE)

Literature:

U. Fischer, L. Lu, P. Pereslavtsev, I. Palermo, J. M. Gomez-Ros, F. Mota, S. Zheng, D. Taylor, F. Moro, R. Villari, I. Lengar, L. Snoj, Evaluation and development of tools to import CAD data into Monte-Carlo codes, EFDA_D_2D4AJN v1.0 - WP12-DTM04-T12, March 2013

Task T13 - Tools for Coupled Radiation Transport and Activation Calculations

Objective

The objective of this Task was to evaluate the different available schemes for coupled radiation transport and activation calculations for their suitability and applicability to DEMO. To this end a DEMO benchmark exercise was performed including the R2S (Rigorous 2-Step) systems developed by CCFE, KIT and UNED, and the Direct 1-Step (D1S) approach developed by ENEA. In addition, methods for the estimation of uncertainty propagation in R2S type calculations were to be conceptually designed and evaluated. The long-term goal of this activity aims at a robust, reliable and flexible single European system for MC based R2S shut-down dose rate (SDR) calculations complemented by a D1S tool for quick SDR assessments. This includes means to estimate the uncertainties propagating from the neutron transport through the activation to the decay photon calculation.

Table 4 summarizes the features and capabilities of the coupled tools which are currently available in the EU. Both the three R2S based and the D1S approaches have been, to different extents, validated using available experimental data or computational inter-comparisons. Note that all R2S tools have the capability to calculate the material activation on superimposed meshes. The D1S approach, which does not apply activation calculations, provides also mesh tally based SDR distributions.

Table 4: Available European coupled tools for MCNP mesh-based shut-down dose rate calculations.

	MC-R2S	R2Smesh	R2S-UNED	advanced-D1S
developer	CCFE	KIT	UNED	ENEA
method	R2S	R2S	R2S	D1S
neutron transport	MCNP	MCNP	MCNP	MCNP + built-in decay photon libs + decay factors
activation	FISPACT	FISPACT	ACAB	
photon transport	MCNP	MCNP	MCNP	
parallelisation	N+A+P: MPI	N+P: MPI, A: batch	N+P: MPI, A: batch	N+P: MPI (no A)
mesh	rect	rect	rect + cyl	N.A.
individual material activation	x	✓	✓	✓
individual material γ sample	x	x	✓	✓
γ source resolution (spatial)	mesh	mesh (fine/coarse)	mesh	pointwise
γ source resolution (energy)	24g	24g	user-spec	gamma lines
component discrimination	✓	✓	✓	✓
portable source definition	✓	✓	✓	x
radiological data	✓	x	x	x
validation	FNG-SDR-2000 ITER-SDR-2010*	JET-SDR-2010 ITER-SDR-2010*	ITER-SDR-2010*	FNG-SDR-2000 JET-SDR-2003, 2005, 2007, 2010 ITER-SDR-2010*

**computational*

A blind comparison was performed on a benchmark model of the 2006/08 DEMO with HCLL blankets and a specified irradiation history. SDR results were requested from the benchmark participants for several in-vessel positions.

The biological SDR results show good agreement within 25% as shown in Fig. 4 below. The absorbed dose in steel, however, show larger discrepancies - up to 50% for results obtained with the same R2S based methodology. This discrepancy might be addressed to the use by CCFE of F4 tallies in void with tally multiplier cards, as opposed to F6 in steel as specified in the problem description. This method is known to overestimate the dose due to lack of self-shielding.

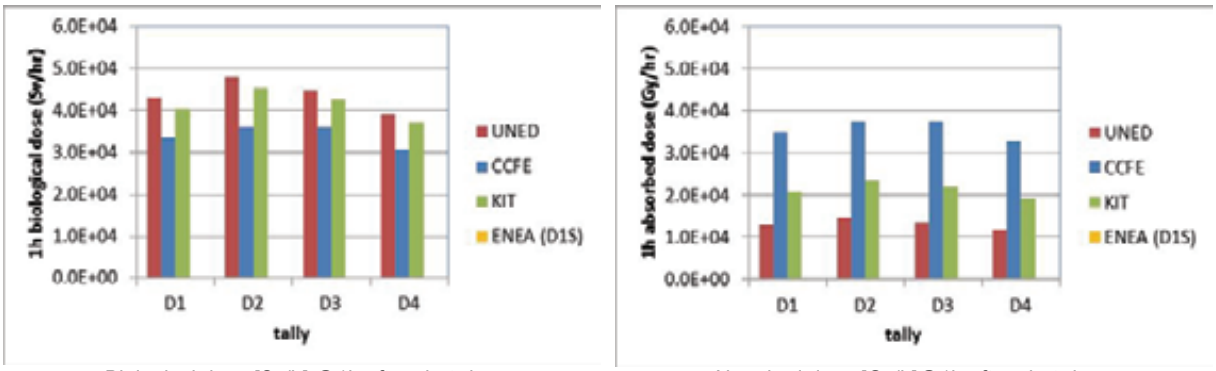

Biological dose [Sv/h] @1h after shut-down

Absorbed dose [Gy/h]@1h after shut-down

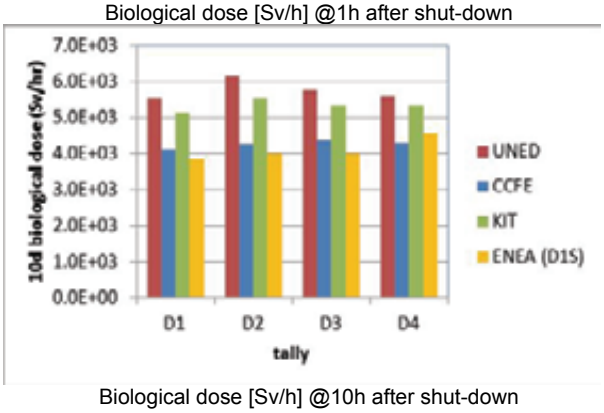

Biological dose [Sv/h] @10h after shut-down

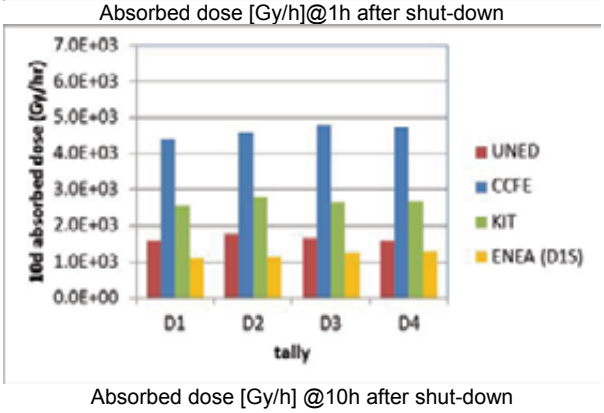

Absorbed dose [Gy/h] @10h after shut-down

Fig. 4: Comparison of calculated biological and absorbed dose rates in specified in-vessel positions of the DEMO HCLL model.

Both CCFE and ENEA reported that small underestimations of the decay dose field from their respective methods were to be expected. The former would be due to the homogenised and uniform activation source and sampling across mesh voxels, and to limitations in voxel resolution, whereas the latter is caused by the lack of appropriate D1S libraries for all nuclides of significance to the decay dose field and the simplified nature of the activation treatment. These reports are consistent with the observations made of biological SDR results.

Traceability results were of great assistance in the identification of the causes for discrepancies observed in preliminary results, and are consistent with the agreement in SDR data. The observations made are generally positive and provide confidence in the reliability of these methods to map the SDR field in-vessel in a large tokamak model. Capabilities for ex-vessel calculations have not been tested.

From the experience gained in the course of this exercise, some benchmark specific recommendations were made regarding the calculation of requested responses such as the absorbed dose and traceability tallies. As for the D1S approach, it is recommended to extend the database with libraries for more DEMO-relevant nuclides and for nuclides relevant at a wider range of decay times.

The cumbersome nature of the model selected for this exercise, and the exclusion of ex-vessel tallies, prevented testing some features of the mesh-based R2S methods which are rather important to ex-vessel SDR computations.

The analyses also served to identify shortcomings in the algorithms and normalisation parameters of some of the tools, which were corrected during the course of the exercise.

This highlights the importance of performing regular inspections of the performance of the tools via this kind of computational inter-comparison.

To complement these exercises, and enhance quality assurance, it is recommended that European SDR tools continue to be validated against available experimental data, and particularly against those from large-scale tokamak geometries such as JET.

It was recommended to combine the various development efforts in the field of SDR calculation tools towards a single European tool based on the R2S approach, which needs to be complemented by a D1S tool for quick SDR assessments. The R2S tool should include suitable means which allow the estimation of SDR uncertainties by propagating these in a proper way from the neutron transport through the activation to the decay photon calculation.

Staff:

J. Catalan (CIEMAT)
D. Leichtle
R. Pampin (CCFE)
A. Turner (CCFE)
R. Villari (ENEA)

Literature:

R. Pampin, J.P. Catalan, D. Leichtle, A. Turner, S. Villari, Evaluation and development of schemes for coupled radiation transport and activation calculations, EFDA_D_2LGNUM v1.0 - WP12-DTM04-T13, January 2013

Acknowledgement

This work, supported by the European Communities under the contract of Association between EURATOM and Karlsruhe Institute of Technology, was carried out within the framework of the European Fusion Development Agreement. The views and opinions expressed herein do not necessarily reflect those of the European Commission.

Shutdown Dose Rate at JET with the New ILW and Prediction of the Expected Dose Level after Future Tritium Experiment (JW12-FT-5.43)

Overall objective

The objective of this Task is to validate 3-D shutdown dose rate calculations with the new ITER-like wall through radiation dose measurements performed during the 2012 off-operational periods of JET. The computational analysis of these measurements will be performed in 2013 using the Advanced D1S (ENEA), the mesh-based R2Smesh (KIT), and the MC-R2S (CCFE) approaches for the shut-down dose rate calculations. In addition, estimations of the shutdown dose rates following hypothetical DT irradiations will be performed in preparation of the future tritium experiment on JET.

D3b and D4b (KIT)
Preparation and installation of a dose rate meter, and measurement of dose rates during short shutdown in Summer 2012

Local shut-down dose rate assessments for areas near a fusion reactor vessel are necessary input for the design of maintenance schemes and accident scenarios and hence also of importance for the licensing procedure. These assessments are based on calculations with particle transport and inventory codes using evaluated nuclear data libraries. Experimental checking of their performance is therefore required.

Parts of the task JW12-FT-5.43 are devoted to measurements of shut-down dose rates with several instruments. KIT prepared an OD-02 dose rate meter (STEP GmbH Pockau) which is based on a calibrated open ionization chamber. The design of the instrument allows to measure the ambient dose equivalent H*(10) alone and together with the directional dose equivalent H'(0.07). It is suitable for dose rate levels above 1 µSv/h. Actual measurements with the OD-02 have been performed by JET personnel in August 2012. The OD-02 measurements agree well with values measured with the other dose rate meters. Results are shown in Fig. 1.

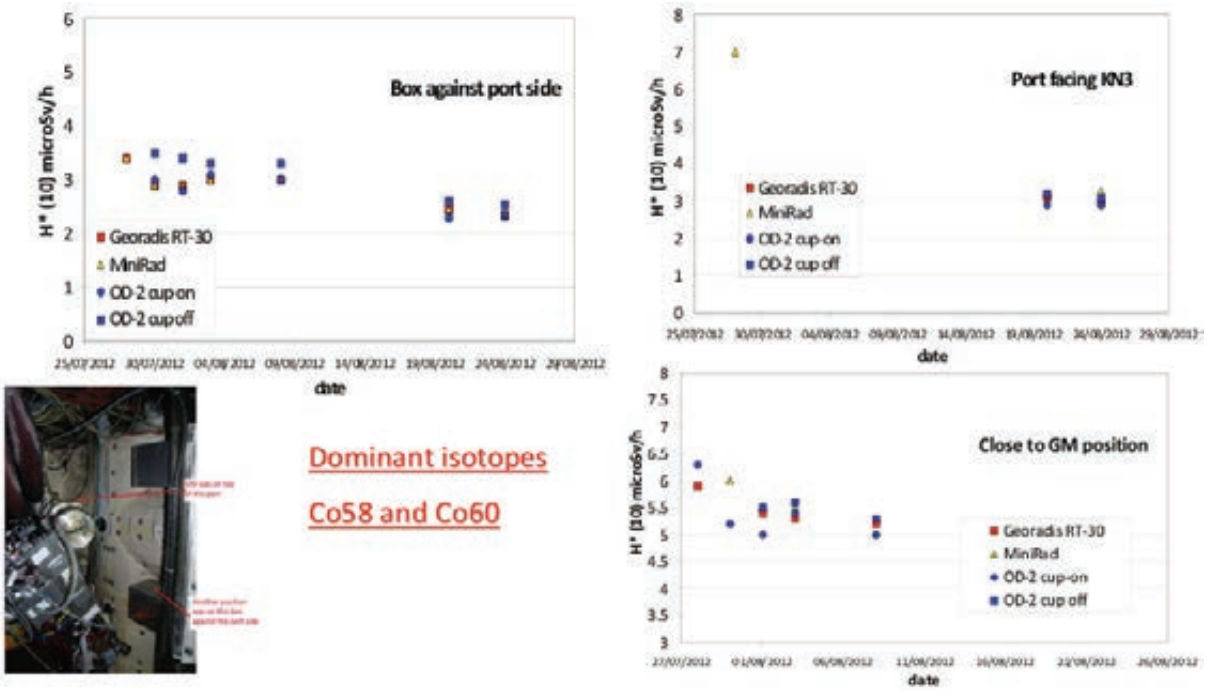

Fig. 1: Dose rate measurements from August 2012. The data marked with "OD-02 cup-on" represent H*(10) while "OD-02 cup-off" represents H*(10)+H'(0.07).
(Diagrams from R. Villari's presentation at the TF-FT Semi-Annual Monitoring Meeting, 11-14 Dec. 2012, JET Culham Science Center).

Staff:

U. Fischer, KIT
A. Klix, KIT
M. Angelone, ENEA
R. Villari, ENEA
P. Batistoni, EFDA JET
S. Popovichev, JET, CCFE
B. Syme, JET, CCFE
L. Mercedes, CCFE
L. Packer, VVFE
I. Lengar, JSI

Acknowledgement

This work, supported by the European Communities under the contract of Association between EURATOM and Karlsruhe Institute of Technology, was carried out within the framework of the European Fusion Development Agreement. The views and opinions expressed herein do not necessarily reflect those of the European Commission.

International Fusion Materials Irradiation Facility (IFMIF)

Broader-Approach Activity: IFMIF Testcell and High Flux Test Module (BMBF Reference No. 03FUS0008)

Introduction

Scope of work

In the Engineering Validation and Engineering Design Activities (EVEDA) for the International Fusion Material Irradiation Facility IFMIF, which is an element of the Broader Approach activities launched jointly by several European countries and Japan, the german contribution includes engineering tasks for the IFMIF Testcell and the IFMIF irradiation experiments. This report covers tasks performed at the Institute for Neutron Physics and Reactor technology at the KIT attributed to the following procurement arrangements (PAs):

- PA TF-1 EU : Engineering design and Validation of the IFMIF High Flux Test Module
- PA TF-2: Irradiation in fission reactor (Responsible SCK-CEN, contribution by KIT)
- PA TF-4: Other irradiation modules (Responsible CIEMAT, contribution by KIT)
- PA ED-04: Test Cell, Access Cell, Test Module Handling Cell and Technology Rooms

According to the planning for EVEDA, these tasks will be performed in the timeframe up to 12/2013. In this report, the progress for the year 2012 is described.

System overview

The IFMIF facility is dedicated to fusion-relevant irradiation of structural and functional material specimens, with the objective to create an experimentally validated material properties database suitable for design and licensing of future fusion power plants. The facility is composed of several subsystems, namely the 40MeV 250mA deuteron accelerator facility (AF), the lithium target facility (LF) and the test facilities (TF). The target- and testcell (TTC) is part of the test facilities, containing the lithium target neutron source and the test modules. It has the primary function to shield the environment against the intense radiation generated by the target, and to safely contain all hazardous materials. Inside the TTC, the target and test modules are arranged, as shown in Fig. 1.

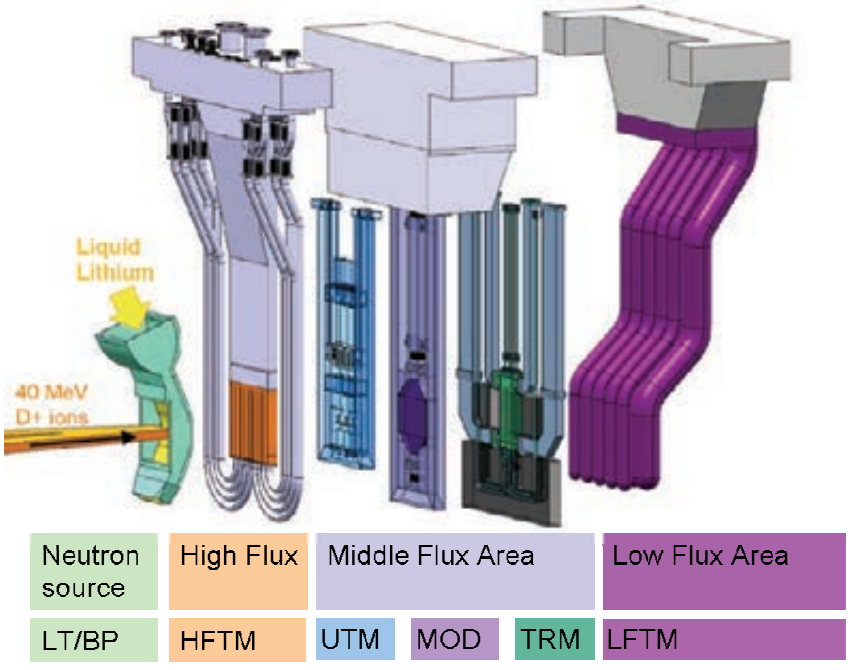

Fig. 1: Overview on the irradiation experiments inside the IFMIF Target- and Testcell (TTC).

The High Flux Test Module (HFTM) is the irradiation device for miniaturized SSTT samples of structural materials. The HFTM is positioned immediately behind the neutron source inside the TTC. The HFTM contains up to 24 irradiation rigs/capsules with approximately 80 SSTT samples. It is possible to adjust individual temperatures for the specimens in each rig, in the range of 250 – 550°C (A high temperature option 650°C is additionally investigated).

The Tritium Release Test Module (TRM) is filled with specimen of tritium breeding materials, such as Li_2SiO_4, Beryllium, and others. The tritium release can be measured in situ during the irradiation, and the change in specimen structure (porosity etc.) can be examined after the irradiation.

Engineering Design and Validation for the HFTM

HFTM Irradiation Capsule and Rig

The three previously produced capsules have been filled with liquid NaK-78 metal. The following QA procedures however revealed, that the achieved NaK level was outside of the tolerances necessary for reactor irradiation. The capsules have therefore been re-opened and analyzed. It was found, that the wetting of the liquid metal in tight gaps prevented the complete filling of large voids which are distant from the filling fittings. Improvements to the NaK filling procedure (concerning temperature, predetermined NaK volumes and filling times) have been decided, and a new set of three capsules was produced.

Other capsules without specimens and NaK filling were prepared for the experiments in helium loops. The manufacturing techniques to equip their surfaces with a knop pattern was successfully proven and applied to three capsules. The parts for the improved rig design were fabricated, as shown in Figure 2. Also, large pressure vessel parts needed to integrate the HFTM mockups in the HELOKA-LP helium loop were fabricated and tested.

Fig. 2: Capsules with knop pattern, completed rig and HFTM container.

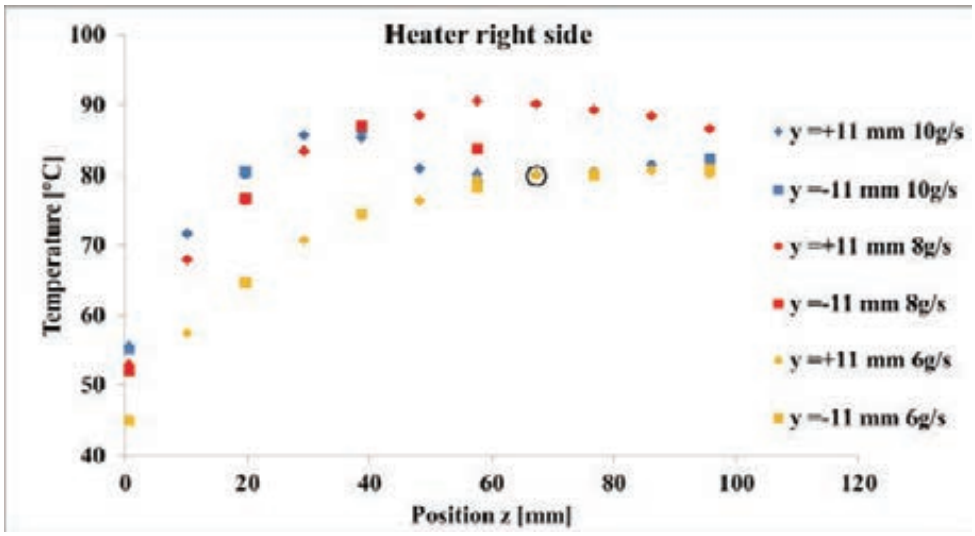

Fig. 3: Axial surface temperature profile on the rig companion heater surface showing laminar-to-turbulent transition features: At potentially turbulent flow conditions (10g/s), generation of turbulence at z>40mm increases local heat transfer and decreases surface temperature.

HFTM Mockup experiments

The HFTM single rig experiment aims to investigate the behaviour of a 1:1 rig inside a compartment mockup. The experiment was operated with heating under operation cooling conditions. The thermocouple pattern under the cooled surface revealed a distinctive pattern, showing the spatial laminar-to-turbulent transition phase of the minichannel coolant flow (Fig. 3). CFD calculations were able to re-produce this feature.

Engineering Design of the Target- and Testcell

The TC design followed the previously decided rectangular concept. Details in the routing of media and signal lines have been engineered. The overall sealing concept was detailed. In the final stage, the integration into the IFMIF building was arranged.

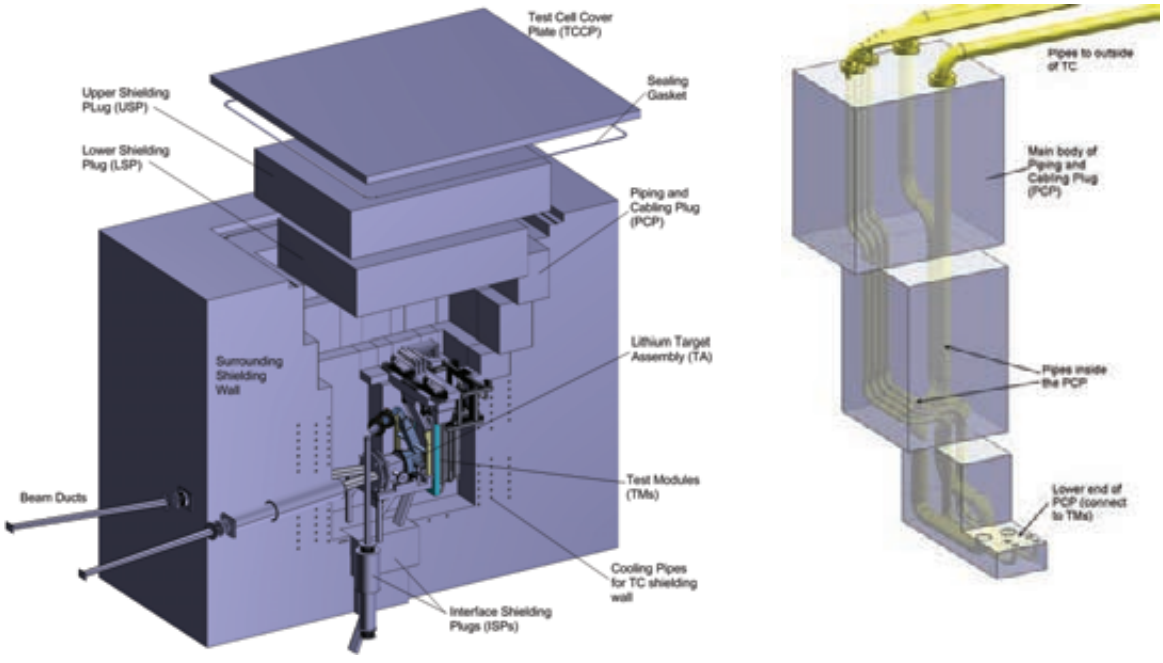

Fig. 4: Design of the IFMIF Test Cell, on the right a detail of the removable Piping and Capeling Plug with bent pipes to reduce the neutron streaming.

Based on process descriptions, functional models of several key maintainance processes have been implemented. Simulations on the needed process times were performed for several scenarios.

Engineering Design of the Tritium Release Test Module

The design of the Tritium Realease Test Module (TRM) was matured, and a 3D CAD model, as well as manufacturing drawings were produced. Engineering analyses were performed for thermal and mechanical issues. Neutronic and tritium transport calculations were done to assess safety issues. From the engineering CAD model, a 3D model was derived suitable as input for more detailed neutronic (MCNP) analyses, to assess the local heat release and tritium production. 3D CFD simulations are in preparation. For the future tritium transport simulation, a MATLAB code based on FUS-TCP has been customized to the TRTM topology.

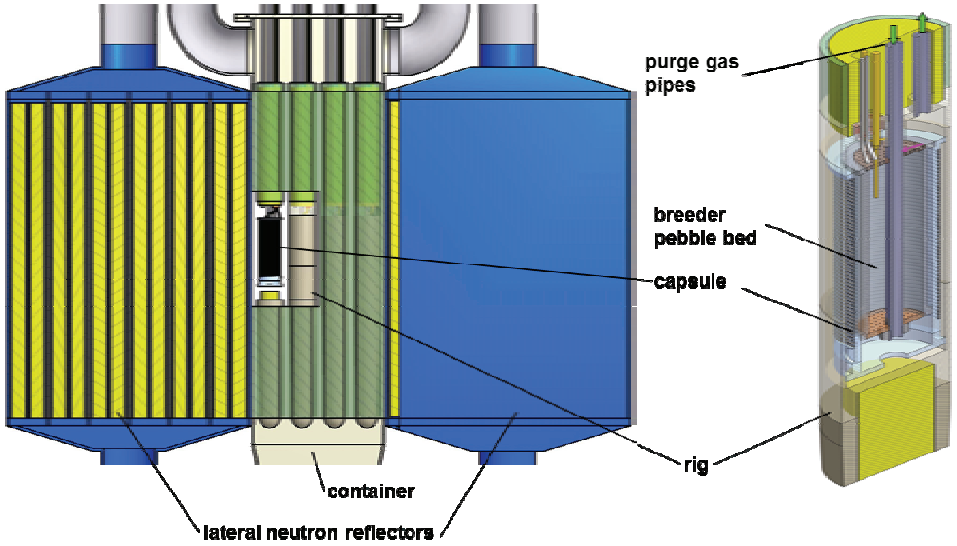

Fig. 5: Overview of the TRTM module and detail from capsule CAD model.

Staff:

A. Abou-Sena
F. Arbeiter
Y. Chen
B. Dolensky
J. Freund
T. Heupel
Ch. Klein
M. Mittwollen
A.-L. Muche
G. Schlindwein
N. Scheel
P. Schubert
K. Tian
K. Zinn

Acknowledgement

This work was financially supported by the Ministry of Research and Education (BMBF) under the grant No. 03FUS0008. The views and opinions expressed herein do not reflect necessarily those of the BMBF or the European Commission.

Broader Approach Activity: Neutronics Analysis for the IFMIF Test Facility and High Energy Beam Transport Section (BMBF Reference No. 03FUS00008)

Objective

The objective of this work was to support the engineering design of the IFMIF Test Facility (TF) with the Test Cell (TC) and the high energy beam transport (HEBT) section within the EVEDA/BA framework. The TC is the central part of IFMIF where two deuteron beams react with the liquid lithium target and the Test Modules (TMs) are placed for irradiation. The HEBT section is required to transport two deuteron beams accelerated to 40 MeV with the beam current of 125 mA from the exit of the accelerator to the lithium target. Neutronic analyses are performed to provide various nuclear responses which are required for the engineering design of the facility (material damage, gas productions, heating, etc.) and for safety related assessments (activation of various components, air and gas, biological doses to work personnel and the public).

Computational approach

In the IFMIF lithium target, neutrons are generated through d-Li(d,xn) reactions. The McDeLicious Monte Carlo code [1] was developed as an enhancement to MCNP in order to simulate the neutron and photon generation in the transport calculation with the comprehensive evaluated d + ^{6,7}Li cross-section data. A standard set based on the LA150 evaluated library was used in previous IFMIF nuclear analyses. Currently a new FENDL-3 library is prepared by the IAEA with an energy range of incident particles up to 150 MeV. The version of FENDL-3 Starter Library, release 4 (FENDL-3/SLIB4) has been prepared as a working file to conduct verification and validation. This release is expected to be the almost final form before the official release of FENDL-3.0. The library has been extensively tested through IFMIF design and shielding analyses in KIT. Some problems detected during the analyses have been reported to IAEA and fixed.

Nuclear analysis for IFMIF Test Cell

A very detailed Monte Carlo geometry model including a detailed representation of the Test Modules has been generated [2] from engineering CAD models using the McCad conversion software developed at KIT [3]. A final geometry model based on the reference Test Cell design (the rectangular shape with liner) of the EVEDA phase has been successfully developed and is now fully functional with the McDeLicious Monte Carlo code. The integral Target Assembly without replaceable back plate proposed by Japan has been integrated into the TC model. The final Monte Carlo geometry model includes the deuterium beam ducts, the lithium target assembly with the back plate, lithium loop components within the TC, three TMs and biological shielding (Fig. 1).

Detailed nuclear responses (2-dimensional distributions for neutron / photon flux, nuclear heating, dpa, gas production for the TC liner, 3-dimensional distribution for neutron / photon flux, biological dose rate and nuclear heating in the TC biological shielding) have been evaluated with the final geometry model. Fig. 2 shows the biological dose rate distribution around the TC during full power operation. The necessary thickness for the TC biological shielding has been determined based on the present analysis.

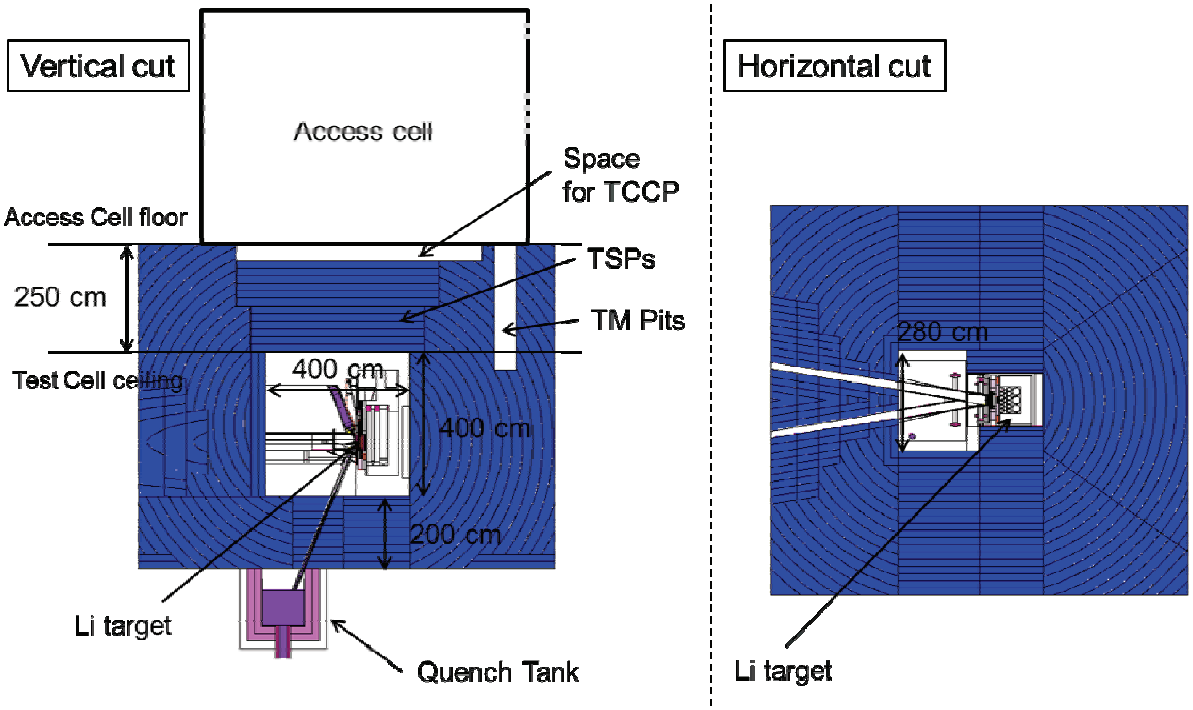

Fig. 1: Final IFMIF TC neutronic model based on the EVEDA reference TC design.

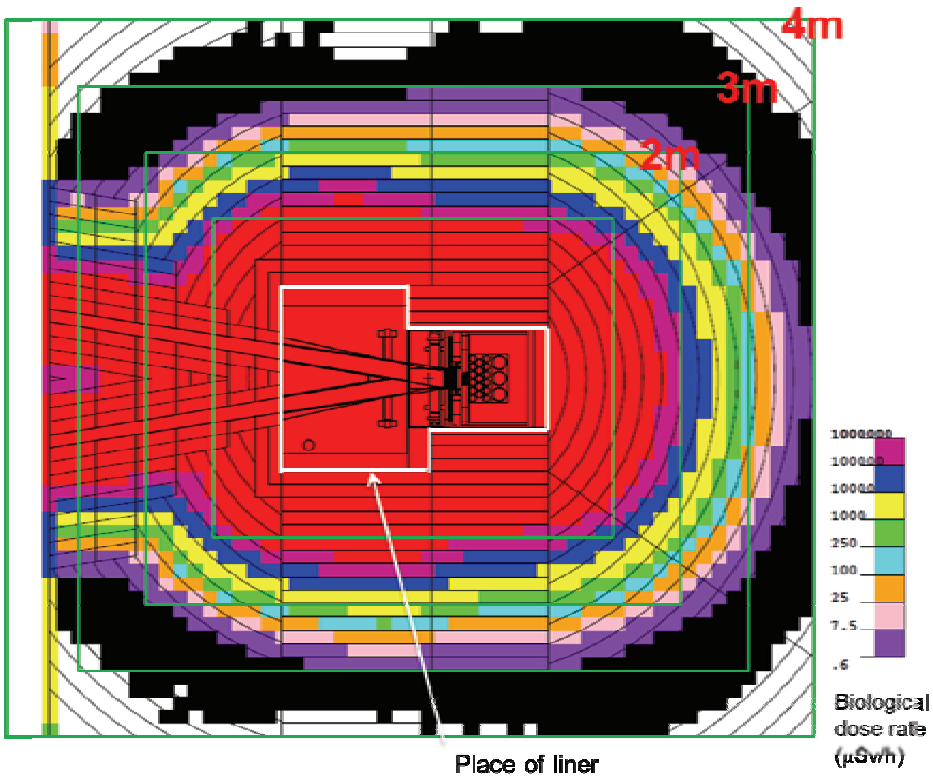

Fig. 2: Biological dose rate distribution around TC during full power operation (horizontal cut at the beam level).

Nuclear analysis for IFMIF HEBT section

In the HEBT section, neutrons back streaming from the lithium target can cause significant damage to accelerator components and result in their activation. In order to estimate the re-

sulting radiation doses, detailed neutron and photon flux distributions inside the Target Interface Room (TIR) and the Radiation Isolation Room (RIR) during operation were evaluated.

A calculation model for the IFMIF accelerator building up to 41.2 m upstream from the Li target was prepared considering the latest HEBT system design. Fig. 3 shows the geometrical configuration of the present calculation model. Shutdown dose rate calculations were performed utilizing the mesh-tally based rigorous 2-Step approach (R2Smesh) which has been developed at KIT [4] and the FISPACT-2007 inventory code. Fig. 4 shows the shutdown dose distribution at several decay times after 11-months operation calculated for TIR with/without a polyethylene beam duct shield. The dose analysis and optimization for the local shielding structure has been carried out for the TIR and the RIR.

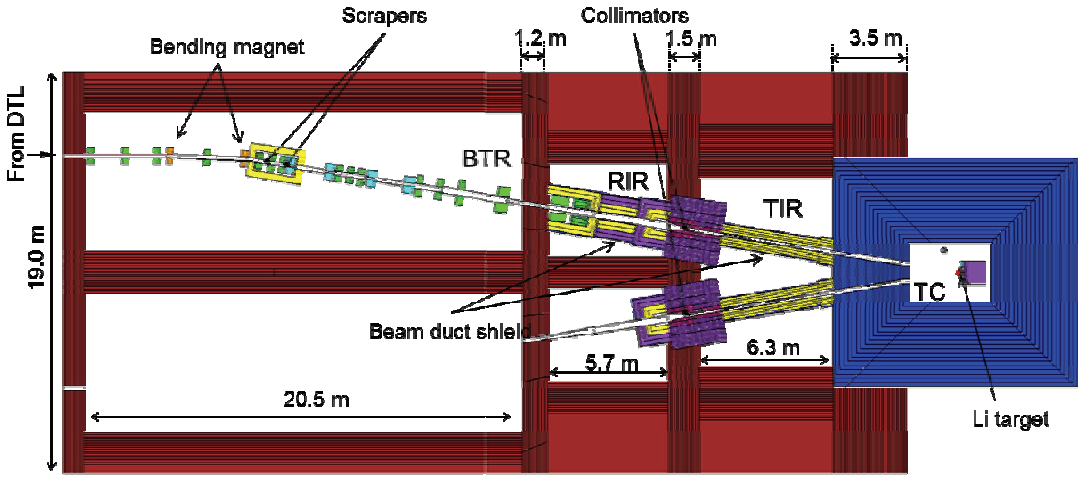

Fig. 3: Geometrical configuration of the present analysis for the IFMIF HEBT section.

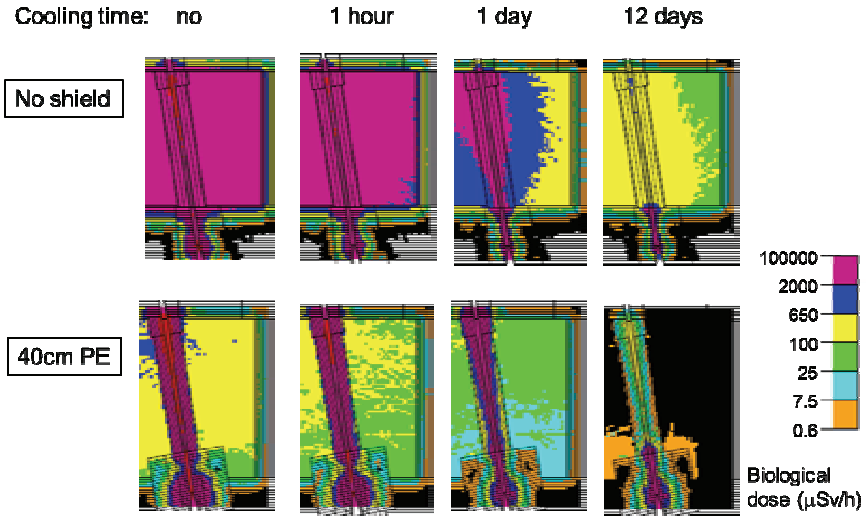

Fig. 4: Shutdown dose distribution at different cooling times calculated for the TIR.

Staff:

U. Fischer
A. Klix
K. Kondo
A. Serikov

Literature:

[1] S. P. Simakov, U. Fischer, K. Kondo and P. Pereslavtsev, “Status of the McDeLicious Approach for the D-Li Neutron Source Term Modeling in IFMIF Neutronics Calculations”, Fusion Science and Technology, 62, 1, 240-245 (2012).

[2] K. Kondo et al., Neutronic analysis for the IFMIF target and test cell using a new CAD-based geometry model, Fusion Eng. Des. 87 (2012), pp. 983-988.

[3] D. Große and H. Tsige-Tamirat, Current Status of the CAD Interface Program McCad for MC Particle Transport Calculations, Proceedings of International Conference on Mathematics, Computational Methods & Reactor Physics (M&C 2009), on CD-ROM, American Nuclear Society, 2009.

[4] K. Kondo et al., “Shutdown Dose Calculations for the IFMIF Test Facility and the High Flux Test Module”, to be published in *Progress in Nuclear Science and Technology*.

Acknowledgement

This work was financially supported by the Ministry of Research and Education (BMBF) under the grant No. 03FUS0008. The views and opinions expressed herein do not reflect necessarily those of the BMBF or the European Commission.

Fuel Cycle –
Vacuum Pumping

High-performance Computation of Vacuum Flows (HPC-FF-SIMVAC, IFERC-CSC-VACKIT)

Background and objectives

The prediction and calculation of vacuum gas flows is of key importance for the design and operation of fusion machines and the specific vacuum pumps used there. The gas flows in such systems vary from the free molecular regime to the hydrodynamic limit, with corresponding Knudsen numbers covering the whole range of rarefaction.

KIT has developed the ProVac3D (Profile of the Vacuum system of 3D complexities) software, which is a Monte Carlo simulation code for gas flow based on the time-of-flight accumulation method [1]. This versatile software has been used much for the designs of the ITER cryopump and the Neutral Beam Injection systems. This success encouraged us to investigate the feasibility of ProVac3D to study transient flow problems and to simulate a diffusion pump.

Transient gas flow studied by ProVac3D

A typical example of the transient process associated with rapid pressure changes in a fusion machine is the pellet gas injection to control the plasma instabilities. Due to the underlying idea of monitoring a single particle travel path and velocity, ProVac3D is intrinsically able to describe transient phenomena. However, in the transient cases, the simulations usually demand a significantly larger number of simulation particles in order to achieve sufficient time resolution. Therefore, parallel calculations are highly desirable. This is accomplished by using the Message Passing Interface (MPI) parallelization approach. This parallelization approach is very suitable for the supercomputer with distributed memory, such as HPC-FF (the High Performance Computer for Fusion) at Jülich Supercomputing Centre (JSC), Germany, and Helios at IFERC-CSC (International Fusion Research Centre - Computational Simulation Centre), Japan. Although the speed-up efficiency cannot be 100% because there exist delay times and communication times between different processors, the obtained speed-up efficiencies on both supercomputers are still above 90% by using hundreds processors.

The feasibility of ProVac3D to study transient gas flow was demonstrated by simulating a cylindrical tube of the length L = 0.6428 m and the inner diameter D = 0.016 m and comparing the simulation result with experimental results from our test rig TRANSFLOW shown in Figure 1 [2].

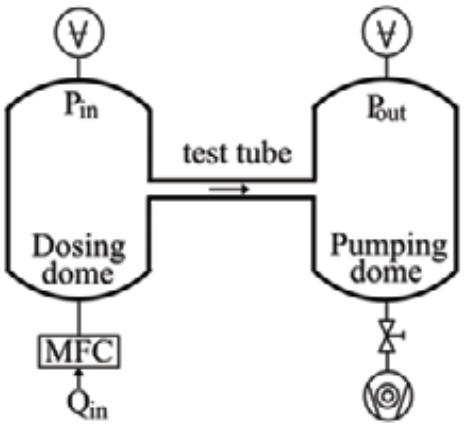

Fig. 1: Scheme of the TRANSFLOW test rig.

In the simulation, nitrogen molecules at 0°C are injected into the tube inlet with Maxwellian velocity distribution. The first 0.2 s are divided into 20000 time windows, so the resulting time resolution is 0.01 ms. One hundred equally distributed virtual discs along the tube axis are implemented to record the time-dependent incident hits. In order to obtain such extremely high time resolution, the total number of molecules in the simulation is 10 billion in parallel either with 640 cores or 6400 cores on HPC-FF and on Helios, respectively. Figure 2 shows the time-dependent incident hits on the tube outlet. The first (quicker) small peak caused by the direct flight of the molecules without wall reflection has been well resolved.

The comparison of the simulated conductance and the measured conductance in the experiment is shown in Figure 3. We can see that, although the measured conductance decreases more rapidly than the simulated one, their relative difference at long term is still less than 4%. The reason of the deviation from the simulation side could be that the gas flow is not totally free molecular. The Knudsen number at the tube inlet is about 1.3, which means that the collisions between gas molecules is not negligible and we are exactly at the Knudsen minimum. From the experimental side, the measurement of the tube dimensions is very critical. The measured flow rate has an experimental error in the order of several percent as well. In conclusion, the found deviation of 4% is according expectation and the qualitative agreement with the experimental result is good [3].

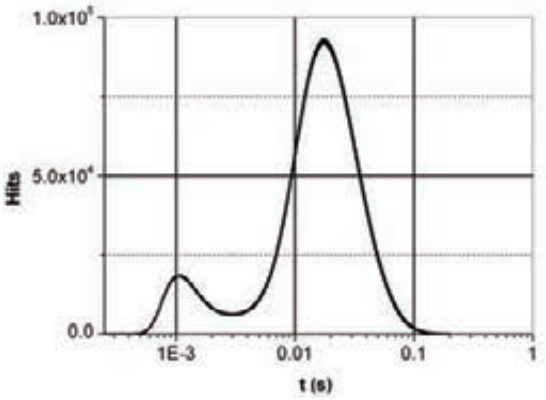

Fig. 2: Time-dependent incident hits on the tube outlet.

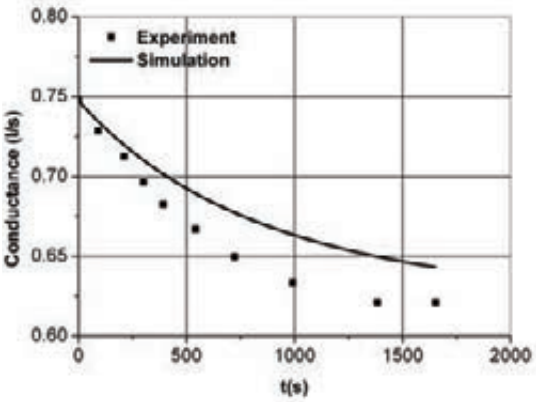

Fig. 3: Comparison of the simulated conductance and measured conductance.

Simulation of a diffusion pump by ProVac3D

For DEMO, a new divertor pumping concept has been proposed recently, that would replace the cryogenic torus pumps, as used in ITER, by a liquid metal diffusion pump [4, 5]. Mercury, being one candidate working fluid, is known to be perfectly tritium compatible. Vapour diffusion pumps have no problems with dust and magnetic fields as they have no moving parts.

The pumping principle of diffusion pumps is given by the momentum transfer from the liquid jet onto the particles being pumped. Due to this working principle the molecular simulation approach of ProVac3D is most suitable. As there are no other simulation codes for diffusion pumps existing, the first step in developing such a one must be to benchmark the code. This has been tried for a linear jet mercury diffusion pump, for which a number of well defined experimental data points together with a good description of the design including dimensions was found in literature, see Fig. 4 [6]. Such linear diffusion pumps can be scaled to the desired pumping speed simply by its length, which gives this pump type a high relevance for this work.

Some necessary simplifications and assumptions had to be introduced in the ProVac3D model, such as (i) there is no inlet leak valve and the corresponding diffusion baffle is neglected, (ii) the molecules of the gas load (nitrogen at 15°C) are injected into the pump with homogeneous space distribution and Maxwell velocity distribution, (iii) the bottom of the pump is considered as a sink for the gas load with a certain sticking probability (parametric variation between 0.2 and 0.5 to mimic the backing pump), (iv) the structure of the jet nozzle is simplified, but the open angles and the effective nozzle areas are kept, (v) the jet speed inside the pump is constant (parametric variation between Mach 3 and 5).

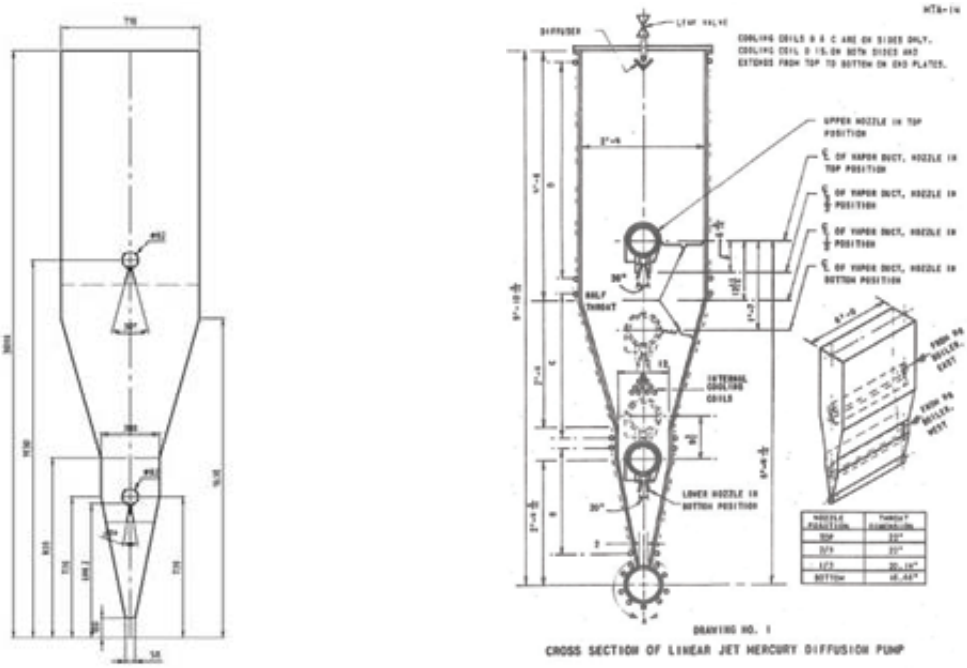

Fig. 4: ProVac3D model (left) and sketch (right) of a mercury diffusion pump.

The calculation is done in three steps. First, we calculate the background density of the mercury molecules established by the mercury jets. The temperature of the mercury molecules is 160°C, the corresponding saturation pressure is 5.6379 mbar. This leads to the number density of the mercury gas inside the injection tube of 9.43×10^{22} /m^3. If we assume the jet is choked, the jet speed at the nozzle will be at the sound speed. Then we know the number flow rates of the upper jet and the lower jet by multiplying the nozzle area, the sound speed and the aforementioned number density. These flow rates are used to normalize the simulated time-of-flight [1] into the background mercury density inside the pump. In the second step, the gas molecules of the gas load coming from the pump inlet will be simulated. The interaction between incoming gas particles and the jet is characterised by a pumping probability, which can already be interpreted as a capture coefficient of the pump. A preliminary result is shown in Figure 6. The collisions between the molecule of the gas load (probe particle A) and the mercury molecule in the background (target particle B) will be considered in the third step. However, this has not yet been achieved in 2012.

Conclusions and outlook

The ProVac3D code has been found to be a very versatile and powerful code for molecular modelling of vacuum flows. The code development for the vapour diffusion pump is a central element of the programme towards a fusion power plant. Further code validation and application of the code to derive refined pump designs will be the major objective of next year´s work in this area.

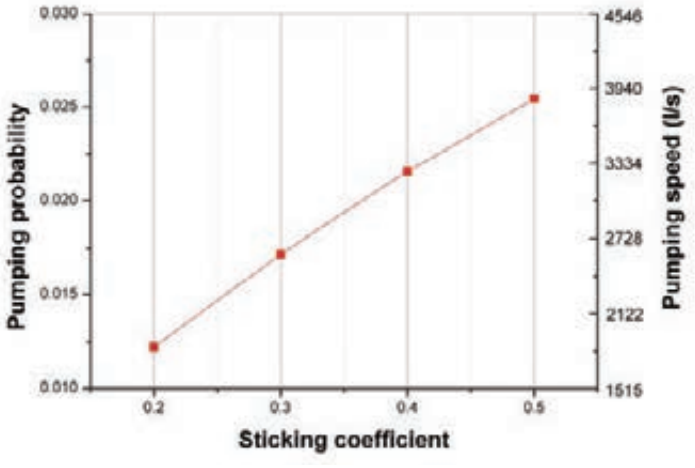

Fig. 5: Pumping probability and pumping speed for the validation case

Staff:

X. Luo

Literature:

[1] X. Luo, Chr. Day, Investigation of a new Monte Carlo method for transitional gas flow, Proc. 27th Int. Symp. on RGD, AIP Conference Proceedings 1333, Melville, W, USA, 2011, pp. 272-276.

[2] St. Varoutis, Th. Giegerich, V. Hauer, Chr. Day, TRANSFLOW: an experimental facility for vacuum gas flows, J. Physics Conf. Ser 362 (2012) 012027.

[3] X. Luo, T. Giegerich, and Chr. Day, Transient Gas Flow Studied by a Test Particle Monte Carlo Approach with ProVac3D, Proc. 28th International Symposium on Rarefied Gas Dynamics, Zaragoza, Spain, July 2012.

[4] Chr. Day, Th. Giegerich, D. Valougeorgis, Assessment of the pumping systems for DEMO, EFDA WP11-DAS-HCD-FP final report, Dec. 2011.

[5] Th. Giegerich, Chr. Day, Conceptuation of a continuously working vacuum pump train for fusion power plants, SOFT 2012, Liege, Belgium, September 2012.

[6] E. Lind, F. Steinhaus, Development of a large linear jet mercury diffusion pump, Scientific report of Livermore Research Laboratory, Livermore, CA, USA, January 1953.

Acknowledgement

This work, supported by the European Communities under the contract of Association between EURATOM and Karlsruhe Institute of Technology, was carried out within the framework of the European Fusion Development Agreement. The views and opinions expressed herein do not necessarily reflect those of the European Commission.

Assessment of the Down-time of the Divertor Cryopumping Systems due to Massive Gas Injection (WP12-IPH-A07-1-2-02)

Background and objectives

Disruptions are sudden terminations of the plasma current in a tokamak due to MHD instabilities or high plasma density operation, resulting in a rapid deposition of the thermal energy content of the plasma onto the divertor and other plasma facing components. The thermal quench is followed by a current quench leading to large electromagnetic forces on vacuum vessel, blanket modules, first wall and in-vessel coils. The current quench can also generate runaway electrons that can potentially create serious damages to the first wall. Therefore, above other means, disruptions in ITER are planned to be mitigated by rapid and massive injection of particles into the plasma to reduce its energy and increase its resistivity and suppress runaway electrons. Different disruption mitigation systems using various gases or gas mixtures have been suggested for ITER but more investigations are needed to find the best candidate systems.

The large quantities of material injected in the tokamak will have a direct impact on the divertor cryopumping system, which includes 6 primary vacuum torus cryogenic pumps (TCP). The objective of this task is to identify the limitations and potential down-times of the ITER cryopumping system in case of massive gas injection (MGI).

Gas throughputs at the divertor and gas pressure in the tokamak after MGI

Table 1 summarizes the MGI gas parameter used as input for the gas flow calculations [1]. The resulting gas amounts injected and the pressures in the tokamak (1400 m³, including associated volumes) are reported in the last two columns. A gas temperature of 420 K was assumed. The assimilation of the injected gas into the plasma has been found to be limited to about 20% in present experiments, therefore the required gas amount to be injected could be five times higher [1].

Table 1: Calculated gas amounts and pressures from [1].

Gas species	Particle number required with 100% assimilation	Gas amount injected assuming 20% assimilation [kPa.m³]	Pressure in the tokamak [Pa]
Helium	2.80E+25	812	580
Neon	5.60E+24	162	116
Argon	3.00E+24	87	62
10% Neon / 90% Deuterium	1.60E+25	464	331
10% Argon / 90% Deuterium	1.50E+25	435	311

The gas throughput calculations have been performed using ITERVAC [2], which can model gas flows for a wide range of flow regimes (molecular, transitional, and viscous) in the complex network of conductances of the ITER divertor vacuum system, including the gas passages through the divertor cassettes and the torus pumping duct (see Fig.1 which shows an axial cut of a pumping port).

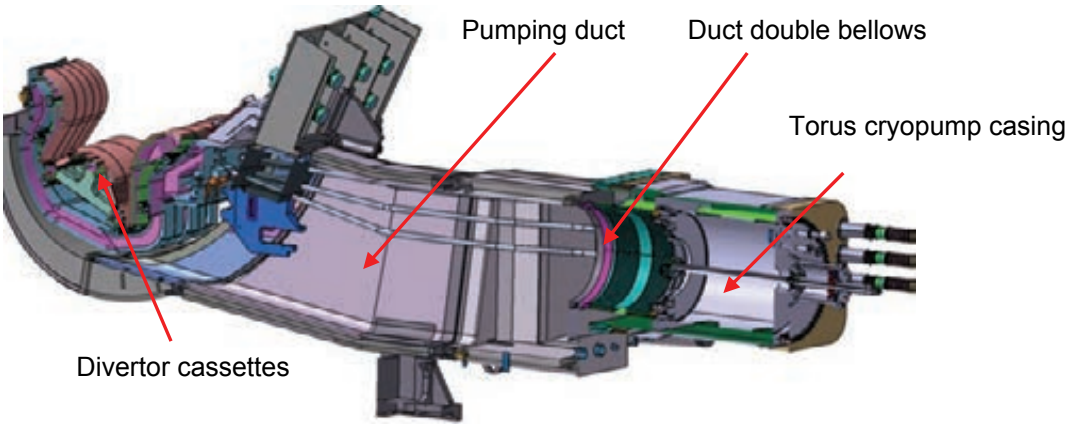

Fig. 1: Axial cut through one pumping port. Only the casing of the TCP is represented.

Maximum gas throughput at the divertor

At an event which triggers the MGI event, the gas will be injected in a very short time, in the range of ms. The inlet valve of the TCP needs minimum 10 s for a full closing. Therefore, it can be assumed that the TCP cannot be protected by closing the valve.

The calculations of the throughput have been divided in two cases: throughput driven by the pumping speed of the TCPs or driven by the pressure difference between the divertor dome and the pumping duct. For the first case, it was assumed that the pumping speed of the TCP is limited to a value at which the resulting heat loads to the TCP's cryogenic circuits can be transferred by the cryogenic supply system. The pumping speeds for the various gases were estimated by scaling factors resulting from the pumping tests performed in the TIMO facility with a smaller scale model pump [3]. In the second case, the throughputs calculated based on the pressure difference (see Table 2) are way larger than in the first case (by factors 4 to 6). It means that the TCPs will be overloaded. In comparison, the typical fuelling rates in ITER during a "normal" operation are between 120 and 200 Pa·m³/s at a divertor pressure in the range of 1-10 Pa.

Table 2: Maximum throughputs (driven by pressure difference) for different gases calculated with ITERVAC. The throughputs are given at the temperature of 420 K and not at the norm temperature of 273.15 K.

Gas species	Divertor dome pressure [Pa]	Maximum throughput [kPa·m³/s]
Helium	580	1545
Neon	116	129
Argon	62	49
Deuterium	280*	735

*The deuterium pressure is taken as 90% of the argon/deuterium injection (see Table 1).

Heat loads to the TCP after MGI and consequences

In order to describe the TCP behaviour after MGI, a complete assessment of the various heat loads to the TCP has been performed. It includes the heat loads to the cryosorption panels and thermal radiation shield of the TCP by thermal radiation, solid conduction, gas conduction (in molecular and viscous pressure regimes), convection, and the heat loads by the cooling of the gas throughput and by adsorption to the cryopanels.

According to the very large throughput previously calculated, it was assumed that the pumping ducts will be rapidly filled by the large amount of injected gas and thus the pressure in front of the TCPs will rise from 1-10 Pa up to a value in the range of the value at the divertor pressure dome (see Table 2) in a very short time. The pressure in front of the TCP is the main input parameter for the heat loads calculations.

The limit pumping speed value of the TCP (including the upstream duct double bellows) in molecular flow regime can be very well predicted by means of Monte Carlo simulation. But the interrelations between the pumping speed, the gas throughput, and the pressure inside and in front of the TCP in transitional regime and viscous pressure regime (which is dominating under MGI) is very difficult to predict or to scale from one pump to another, especially for the high pressure considered. Nevertheless, in this task the experimental results taken from the ITER model pump experiments performed at KIT with the smaller scale model pump [3, 4] were used wherever possible to come up with simple correlations predicting the pump behaviour. After a MGI, the pumping speed will increase drastically with the pressure and drop down to zero after a short time when the pump limit capacity (particularly limited for helium and deuterium which are pumped by cryosorption, unlike for neon and argon which are mainly pumped by condensation/re-sublimation) is reached and/or the cryopanel temperature is too high due to the large increase of the heat loads (most critical for helium which is totally released at temperature above ~12 K).

Depending on the cryopanel temperature and the type and amount of gases previously pumped, a variable quantity of gas is released from the pumping surfaces into the regeneration volume of the pump (~14 m³) and the vacuum vessel (tokamak + pumping duct) if the TCP valve is still open. In MGI cases studied, it was found that at the high heat fluxes involved, the TCP heat capacity takes a minor role, it will be heated rapidly. For helium and deuterium, the high heat fluxes to the cryopumps are leading to the spontaneous regeneration of the previously accumulated gases, while the pressure inside the torus remains high. On the other hand, the cryopumps can pump the quantities of neon and argon injected without going into spontaneous regeneration. Nevertheless, a regeneration of the accumulated neon and argon could be suitable before starting a new pumping cycle.

The total down-time of the cryopumping system is defined by the time needed to perform the complete regeneration of the TCPs (exhaust of the released gases from the crypump volume by the rough pumps and cool-down of the interior components) and the rough pumping of the vacuum vesssel down to the cross-over pressure (~10 Pa) at which the TCP can be switched on again. Therefore, the down-time also strongly depends on the roughing pump system performances. For the helium and deuterium cases, additional time is needed to pump down the torus down to the cross-over pressure (~10 Pa) at which the cryopumps can be switched on again. As a consequence, from cryopumping point of view, argon and neon seems to be the best gas candidate for the disruption mitigation systems.

Example: Massive neon injection

Figures 2 and 3 show the evolution of the heat loads, temperatures (separate for the cryopanel system (CP) and the thermal shield system (TRS)), pressures and gas throughput for one TCP after a massive neon injection. The gas throughput is calculated at the norm temperature of 273.15 K. It is seen that the CP temperature increases rapidly. Nevertheless, the pumping limit temperature for neon (~41 K) is much higher than it would be for helium for example and it was shown that the injected neon can be pumped by 4 TCPs down to a pressure in the vacuum vessel of about 0.1 Pa in about 53 seconds without reaching the pumping limit temperature for neon.

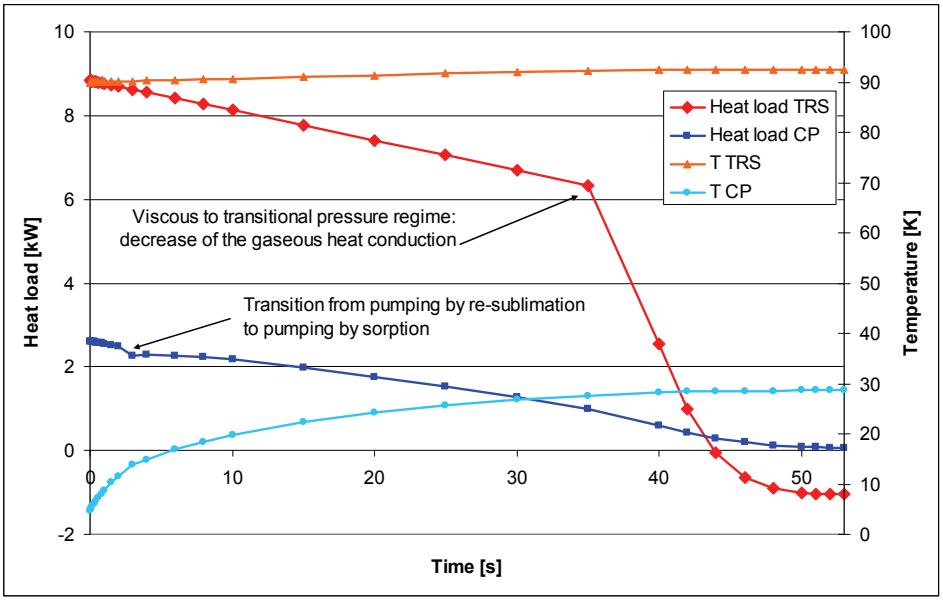

Fig. 2: Heat loads and temperature evolutions of the TRS and CP after massive neon injection.

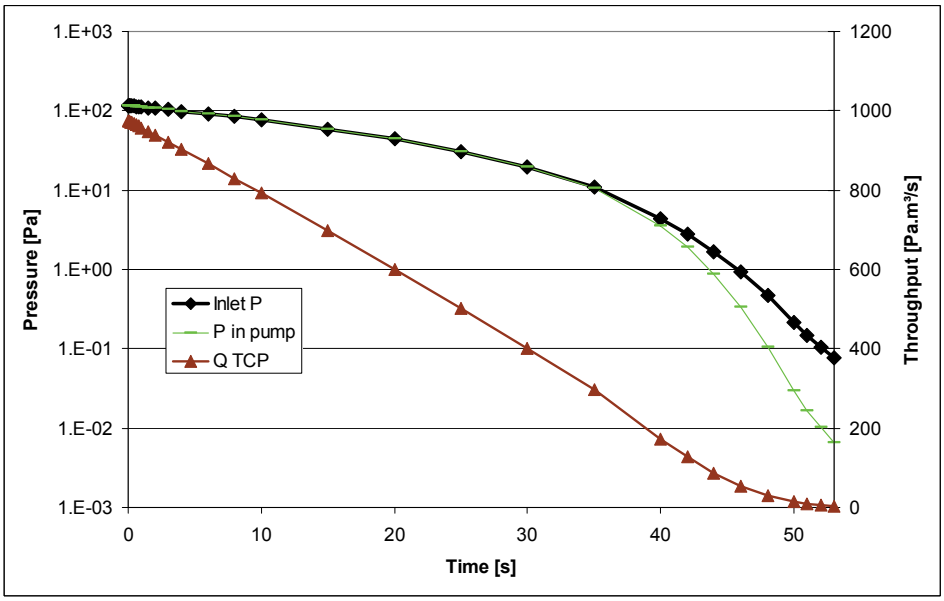

Fig. 3: Pressure in front and inside the pump and gas throughput to the TCP evolutions after massive neon injection.

After 35 seconds, the transition between viscous and transitional pressure regimes is accompanied with a sharp decrease of the heat load to the TRS because gaseous heat conduction, which is the dominating heat load to the TRS, is decreasing rapidly with the pressure in transitional pressure regime. This effect is less visible for the CP because the heat loads are dominated by the cooling and pumping of the gas. After 3 seconds, the CP temperature is too high to pump neon by re-sublimation, and it is then pumped by adsorption. It results in a small but sharp decrease of the heat load due to the fact that the enthalpy of sorption is smaller than the enthalpy of re-sublimation at the same temperature. Note that after 43 seconds, the heat load to the TRS becomes negative because the heat transferred by the cryogenic supply is higher than the heat load deposited on the TRS. From this point, the temperature of the TRS starts to decrease.

The final temperature of the CP is 29 K. Note that the ratio of the inlet pressure over the pressure inside the pump is increasing from a pressure of 10 Pa (illustrated on Fig. 3 by the

detachment of the two pressure curves in black and green), which is characteristic of a change from viscous to transitional flow.

At the end, the neon gas load for one TCP is 26.4 kPa·m³ (related to the norm temperature of 273.15 K) which is most probably below the maximum gas load. Nevertheless, after a neon injection it could be suitable to regenerate the TCP because the adsorbed/frozen neon could have a negative impact on the pumping of DT gases. However, there is no need to pump the torus with the roughing system, and they can be fully used for the regeneration of the TCPs only.

Conclusions and outlook

The quantities of gas injected for disruption mitigation are large enough to have potentially a significant impact on the TCP. This task for the first time clarified and quantified the chain of events occurring after a MGI and is therefore helpful to define what could be the best disruption mitigation system and gas candidate.

In the perspective of the continuation of this task for 2013, further activities are planned to be performed in order to refine the calculations. Firstly, the rough pump performance will have to be taken into account, then, the divertor ITERVAC model will be updated to the newest ITER design, and, thirdly, the thermodynamics properties used in the calculations will be re-visited and the fundamental pumping phenomena (adsorprtion vs condensation) re-considered.

Staff:

V. Hauer
M. Scannapiego

Literature:

[1] L. R. Baylor et al., Disruption-mitigation-technology concepts and implications for ITER, IEEE Transactions on Plasma Science 38 (2010) 419-424.

[2] Chr. Day et al., The use of flow network tools for geometrically complex vacuum gas dynamics problems, 6th Europ. Congr. On Computational Methods in Applied Sciences and Engineering, Vienna, Austria, Sept. 2012.

[3] A. Mack et al., First operation experiences with ITER-FEAT model pump, Fusion Engineering and Design 58-59 (2001) 365-369.

[4] H. Haas et al., Performance tests of the ITER model pump, Fusion Engineering and Design 69 (2003) 91-95.

Acknowledgement

This work, supported by the European Communities under the contract of Association between EURATOM and Karlsruhe Institute of Technology, was carried out within the framework of the European Fusion Development Agreement. The views and opinions expressed herein do not necessarily reflect those of the European Commission.

Co-ordination of the Activities in the EFDA ITER Physics Research Area A10 - Particle Transport, Fuelling and Inner Fuel Cycle Modelling (WP12-IPH-A10-1)

Background and objectives

The EFDA ITER physics programme is divided in eleven research areas. The topic of research area 10 is the particle transport, fuelling and inner fuel cycle modelling. In 2012, this area contained nine tasks from five different Associations (TEKES, CCFE, Hellenic Republic, DTU and KIT) working in this area. KIT was providing the project leadership co-ordinating the task and reporting to the responsible officer at EFDA.

The understanding of particle and impurity transport in plasma and the control of it with source and sink terms (gas puffing, pellets, vacuum pumping) is important for the operation of tokamaks. At normal operation, deuterium and tritium will be re-fuelled while helium and impurities should be removed from the core plasma via the divertor pumping system. Many efforts were investigated in the modelling of inner plasma transport processes in the past whereas the fuelling and pumping is only one simplified boundary condition in these models. An integrated modelling of fuelling, pumping and linked actuators to the inner fuel cycle is needed for better understanding of the requirements to the fuel cycle components and predictive plasma control. The inner fuel cycle including a detailed balance of particle and impurity transport as well as a characterization of in-vessel inventories, pumping capabilities and plasma wall interactions is a large and in many aspects not yet fully addressed field, where plasma physics and engineering problems meet. It has been recognized that in order to progress, very specific parts of the larger problem have to be addressed.

In the working year 2012, the divertor is primarily looked at from the point of view of gas exhaust. This is looked from the physics side (high density operation and detachment conditions) and from the engineering side (neutral gas recycle flow pattern modelling). Main objectives of this project are to develop a physics-based understanding of the ITER divertor neutral gas exhaust and to study the influence of fuelling parameters on core plasma composition close to ITER conditions. As dedicated support of ITER, the divertor cryopumps were treated in terms of pumping in different operations and plasma control.

Co-ordination and monitoring

To develop of a physics-based understanding of the ITER divertor neutral gas exhaust, two experiments in ASDEX Upgrade with focus on detachment and density limit (hydrogen, deuterium), and in MAST with focus on high density plasma conditions achieved by means of gas puffing and pellet fuelling (deuterium) were planned (in ASDEX the experiment was finally shifted to 2013). In MAST, high density plasma was reached by strong gas fuelling only, see Fig. 1. The upstream conditions were measured with Thomson scattering and simulated with OSM-EIRENE. Data and modelling suggest that strong fuelling raises the density and lowers the temperature in vicinity of the fuelling source. The results of SOLPS simulations are showing that the neutral flux across the separatrix increases with the density and is roughly linearly depending on the plasma ion mass. The

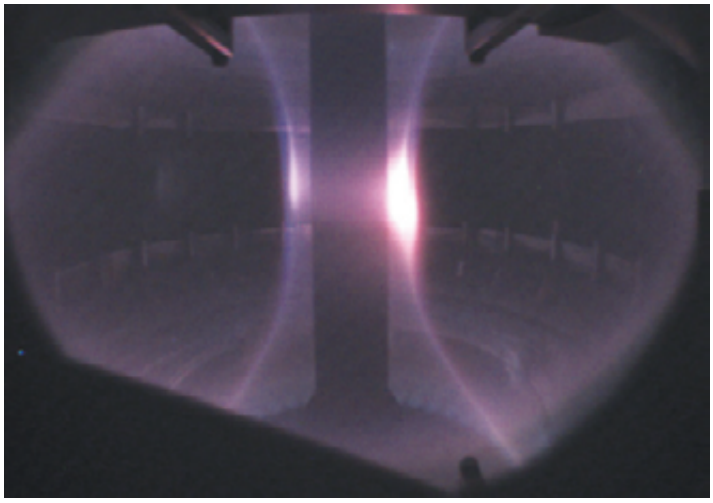

Fig. 1: Gas fuelling to the discharge in MAST.

dense region attenuates neutrals which increases the SOL fuelling source but reduces the core fuelling. The “density limit” in MAST is caused by a reduction in confinement at higher density together with reduced core fuelling. Probably, pellet fuelling will allow overcoming this “density limit”.

Different experiments have been performed to investigate pellet fuelling of plasmas with ELM mitigation by resonant magnetic perturbations and the microstability analysis of the discharges in MAST. Simultaneous pellet fuelling and ELM mitigation were successfully demonstrated. The experiments for the microstability analysis of pellet fuelled discharges were complemented by Thomson scattering measurements and simulation with gyrokinetic codes (GS2). A stabilisation on the positive density gradient region of the pellet deposition profile was seen whereas the outer part of the pellet deposition profile needs more investigations. An asymmetric evolution of the pellet deposition profile was found which probably based on microinstabilities was leading to diffusion of pellet material towards the plasma core.

The Collective Thomson scattering (CTS) diagnostic was also installed in ASDEX. A proof-of principle experiment was performed which demonstrate that CTS can be used for determination of plasma composition. Further experiments are planned to demonstrate the technique for spatially resolved measurements across the plasma to study the effects of hydrogen gas puffs and neutral beam injection.

The Direct Simulation Monte Carlo method (DSMC) was used for simulation of gas flows. The input for these simulations was provided with B2-EIRENE for an ITER-like divertor geometry. Meshing and CFD simulations were done but further work for running DSMC simulations is needed. The attempt to simplify the computations by replacing the real geometry with channels instead was tested. This simplification of geometry brings advantages in performance but leads to higher uncertainties. Results show that the effort required for these simulations is very high. An open issue is the input from plasma simulation codes (like SOLPS or B2-Eirene). However, these codes provide pressure or particle fluxes in 2D not considering gaps between divertor cassettes. The high pressure gradients inside cassettes (several orders of magnitude) are leading to backflow of neutrals to the plasma boundary.

To support the understanding of the interplay within the fuelling cycle, a zero-d functional block diagram of the ITER fuel cycle was developed.

Current status and outlook

This project will go in its second year in 2013. In the end of the 2-year programme, a fully integrated understanding of the fuel cycle with a physics-based description of the interlinks between neutral gas and plasma (fuelling and pumping) will be developed. It will also be investigated how pumping speed variation at ITER can influence detachment/attachment conditions.

Staff:

Chr. Day
V. Hauer

Acknowledgement

This work, supported by the European Communities under the contract of Association between EURATOM and Karlsruhe Institute of Technology, was carried out within the framework of the European Fusion Development Agreement. The views and opinions expressed herein do not necessarily reflect those of the European Commission.

Advanced Numerical Modelling of the Neutral Gas Flow to the Divertor Pumping System (WP12-IPH-A10-1-1-02)

Background and objectives

Over the last few years much effort has been invested in modelling the complex geometry of a divertor in tokamak type fusion reactors. The main difficulty, which should be faced accordingly, is that in this specific lower region of a fusion reactor there is a common presence of ionized (plasma) and neutral particles and therefore different mathematical/numerical approaches have to be applied for its thorough theoretical description. In addition, the definition of the boundary conditions in the interface is not trivial and straightforward. Until nowadays, there is no numerical code available for describing the interaction between plasma and neutral gas particles, although it is obvious that such a code is an essential and urgently needed scientific and engineering tool for the design and the optimization of the divertor in future fusion reactors like DEMO. This is why KIT has started to develop such a code. The proposed algorithm will give the chance to study in detail the flow behaviour in different operational conditions of the reactor and how this flow affects the efficiency of the related vacuum system.

The present work mainly focuses on the numerical simulation of the flow field and the calculation of overall quantities of practical interest inside the complex geometry of the divertor by coupling two well established and reliable stochastic numerical approaches: the B2-EIRENE (SOLPS) and the Direct Simulation Monte Carlo (DSMC) algorithms. The main challenge is the definition of interfaces and the boundary conditions between plasma and neutral particles, which requires deep knowledge of plasma and neutral gas physics. In addition, the complex geometry of such a system is another difficulty which should be overcome.

Numerical approaches

The numerical code B2-EIRENE is a linear Monte-Carlo solver of the Boltzmann kinetic equation with fixed background for test particles. Primary application is to model the interaction of neutral gas with plasma. This package was further developed at IPP Garching under the name SOLPS and nowadays it represents the main code package which is used in modelling the ITER divertor. Different kinds of grid (e.g 2D triangular, 3D tetrahedral) may be implemented and various surface interactions can be modelled (e.g. reflection, sputtering). The model can include various atomic and molecular processes: ionization, recombination, dissociation, charge-exchange and elastic collisions. The BGK model [1] is used in EIRENE to describe neutral-neutral collisions. The main shortcoming of this model is that the correct expressions for the viscosity and thermal conductivity cannot be proved simultaneously (the obtained Prandtl number is wrong) so that the BGK model is not suitable of describing accurately non isothermal flows.

On the other hand, the DSMC approach is based on a particle method for use in rarefied gas dynamics. In this method, the solution of the kinetic equation is circumvented by simulating groups of model particles that statistically mimic the behaviour of real molecules. The primary approximation of DSMC is to uncouple the molecular motion and intermolecular collisions over small time intervals. The DSMC method, due to its simplicity, is widely used in many applications including vacuum gas dynamics and has been successfully implemented in modelling rarefied gas flows (e.g. [2]).

Based on the work plan presented in Figure 1 the following scheme was developed (to be continued next year):

- Definition of complex geometrical parameters of the ITER divertor.
- Development of a numerical code capable of coupling the above two described approaches. Here, the following requirements are included:

- Definition of interfaces/boundary conditions (e.g. distribution functions) between plasma and neutral gases.
- Benchmarking of adaptive unstructured mesh generators
- Code parallelization.

- Simulation of neutral single gas or gas mixture flows.

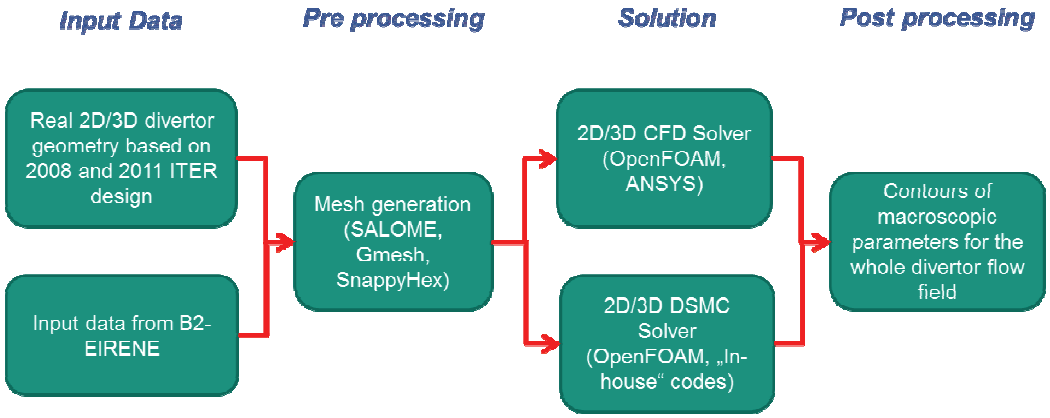

Fig. 1: Simplified work plan of the present investigation.

Code development

Input data from B2-EIRENE code

In preparation of the present task it was agreed with FZJ, who is heavily involved in the ITER divertor physics development, to receive their output data obtained by the B2-EIRENE code and use as input parameters for DSMC simulations. The data which were provided include distributions of particle flux, partial pressure and temperature of D, D_2 and He along the walls of the divertor, given with the exact x and y coordinates of a simplified divertor contour (e.g. no lower part of the divertor) used by them. All data correspond to three reference DT ITER discharges with different levels of divertor neutral pressure under the dome. From the above numerical data the average pressure in the corresponding x and y positions in the dome and the inner/outer targets was calculated and used as input parameter for the DSMC calculations.

ITER divertor geometry and mesh generation

Due to the fact that the current ITER divertor detailed design could not be delivered from ITER in time, the already available 2008 ITER CAD files were initially used for understanding and visualising the geometrical configuration of the ITER divertor, see Fig. 2. After electronic processing of the CAD files, the corresponding 2D case was extracted (Figure 3) in order to be applied as a simplified test case for preliminary DSMC/CFD calculations. It is noted that a 2D flow configuration is expected to be unable to describe in detail the real flow divertor conditions, since there is no symmetry in the toroidal direction, but on the other hand, it is assumed to be a first preliminary case for applying the provided B2-EIRENE boundary conditions.

In order to increase the resolution of the results, especially close to the walls of the divertor, a high quality mesh should be adopted. In that framework, three open-source free available generic mesh generators were examined (namely the Gmesh, SALOME and the SnappyHexMesh). SALOME was found to have a significant advantage over the other two platforms, especially in the functions of editing/modifying STEP and IGES files and mesh adaptation in complex geometries. In additions, SALOME seems to be more powerful in cre-

ating 3D meshes and this makes it more preferable when the 3D geometry of the divertor will be introduced.

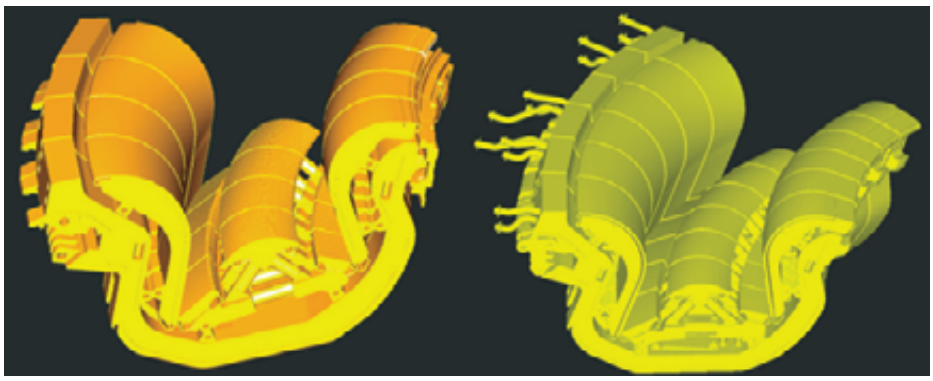

Fig. 2: 3D CAD drawings of the ITER divertor for the case of 2008 (left) and 2011 (right) designs.

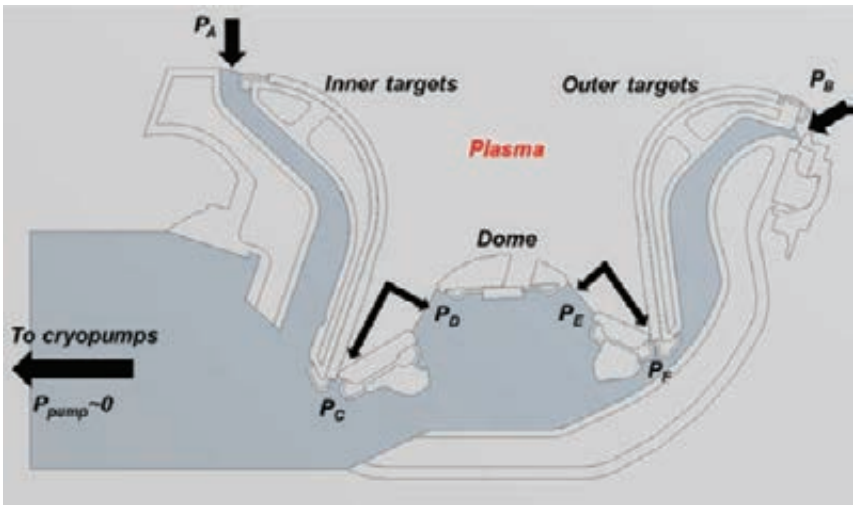

Fig. 3: Flow configuration which was introduced as initial simplified case for DSMC simulations. The geometry is based on a 2D cut of the 2008 divertor. The data for the input pressures through the various gaps around the divertor are provided by B2-EIRENE simulations.

Preliminary simulations

In the framework of this task some preliminary simulations only for the case of the 2D flow configuration presented in Figure 3 were performed. In all the simulations the OpenFOAM software was used and the laminar, compressible CFD solver was applied. Due to the fact, that the OpenFOAM DSMC solver needs some modifications in the source code in order to be able to run pressure driven flows, no DSMC calculations have been conducted and presented yet. This issue is under work and will be elaborated in next year´s work programme.

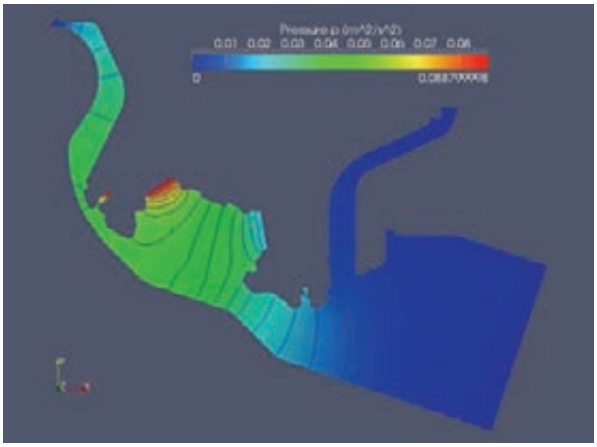

Fig. 4: Indicative pressure contours based on OpenFOAM CFD simulations.

Indicative pressure contours for the whole area of the divertor are presented in Figure 4. It is noted that all the performed CFD simulations mainly were focusing on checking and benchmarking the capabilities of the OpenFOAM

platform in solving complex geometries and not on providing accurate results. Since our main goal is to use the DSMC solver in order to be able to describe low pressure cases, first open issues regarding mesh import and definition of boundary conditions could be clarified.

Conclusions and outlook

This work represents a major step towards the goal of simulating the 3D divertor geometry, since many technical open issues have been well understood and clarified. The next step is the modification of the OpenFOAM DSMC algorithm for modelling pressure driven flows. Then, the simulation of the 2D case and later the 3D case will become possible. Furthermore, it is believed that since OpenFOAM software is already parallelized, the speed-up of the simulations especially in the 3D case will be easily achieved.

Staff:

C. Gleason-Gonzalez
S. Varoutis

Literature:

[1] P. Bhatnagar, E. Gross, M. Krook, A model for collision processes in gases I, Physical Review 94 (1954) 511–525

[2] S. Varoutis, C. Day, F. Sharipov, Rarefied gas flows through channels of finite length at various pressure ratios, Vacuum 86 (2012) 1952-1959.

Acknowledgement

This work, supported by the European Communities under the contract of Association between EURATOM and Karlsruhe Institute of Technology, was carried out within the framework of the European Fusion Development Agreement. The views and opinions expressed herein do not necessarily reflect those of the European Commission.

Fuel Cycle Simulator Development (WP12-SYS01-T02-02 and WP12-IPH-A10-1-3-03)

Background and objectives

The most important requirement on the fusion fuel cycle is on one hand to ensure proper functioning of the interfaces with the plasma, i.e. supply of the fuel species and other gases (also non-hydrogenic) at the requested flow rates, and transfer of the torus exhaust gas at the requested throughput and divertor pressure. On the other hand, tritium breeding and coolant purification from permeated tritium is another core function provided by the fuel cycle. An important overall requirement is to work within a given administrative tritium inventory limit. It is a general aim for a power plant to keep this number reasonably low.

The fuel cycle can be considered as a complex plant. To enable a well defined design development of the fuel cycle for a fusion power plant and its sub-systems, a fuel cycle simulator tool that is able to describe all actuators in a quantitative way would be very beneficial but is still missing. It was therefore decided in 2012 to make a first step in this direction by elaborating a block diagram which allows to meet three objectives: (i) assess the sub-system contributions to the overall tritium inventory, (ii) assess the dependency and the sensitivity of fuel throughput from parameters like fusion power, burn-up fraction and others, and (iii) develop a (simple) set of equation as input for a system code. The latter is an important aspect as the fuel cycle is practically non-existent in the currently used European PROCESS system code. The module was also developed with a capability to be used for sensitivity studies, i.e. to find how the overall performance of the fuel cycle is changing, if the performance of a sub-system is changing. This information is essential as it provides the operational limits of the system and helps to identify potential bottlenecks and, thus, justify where future R&D efforts shall be placed first to resolve.

The work was organised in two phases. First, the ITER fuel cycle structure was studied in detail and performance data checked (WP12-IPH-A10-1-3-03). As most of the sub-systems are in advanced phases of the design, this allowed using ITER as a benchmark case. In the second phase, following positive benchmark, the ITER block diagram was expanded so as to describe the full fusion fuel cycle, i.e. including the outer fuel cycle structures with the blanket systems and introducing further improvements to the inner fuel cycle (WP12-SYS01-T02-02).

Fuel cycle block diagram

The final block diagram structure of the fuel cycle, see Fig. 1, originates from a functional decomposition of the fuel cycle, resulting in 30 sub-systems which are characterized by in- and outcoming flows (considering composition changes) and by their retention time, so that information on steady-state inventories can be deduced. The flowchart is not limited to tritium or tritiated species alone. The colours and arrows describe the gas species and the flow directions exchanged between the different systems (yellow: H, orange: D, red: T, green: He, blue: coolant and impurities). The diagram has been programmed as Visio sheet. The model is programmed as a simple Excel spreadsheet with macros. The choice of the subsystems has been made reflecting previous approaches in this direction, as reported in literature.

On the first page of the simulator xls sheet (the control page), two groups of input parameters have to be defined: ‘Reactor Parameters’ and ‘Engineering Parameters’, see the screenshot in Fig. 2. Reactor parameters are the interface to the plasma physics: Here, plasma volume, Greenwald density, fusion power, impurity seeding or burn-up ratio are defined. These parameters are independent of the technical realization of the fuel cycle. In the second group, engineering parameters are defined. These parameters have no effect to the plasma or the reactor itself but they define the requirements to all technical gas processing systems. As can be seen in the lower part of figure 2, each system has to be given a specific retention

time. This mainly classifies the systems in continuous (there, an arbitrary retention time of 10 s is chosen) and batchwise (e.g. cryogenic distillation).

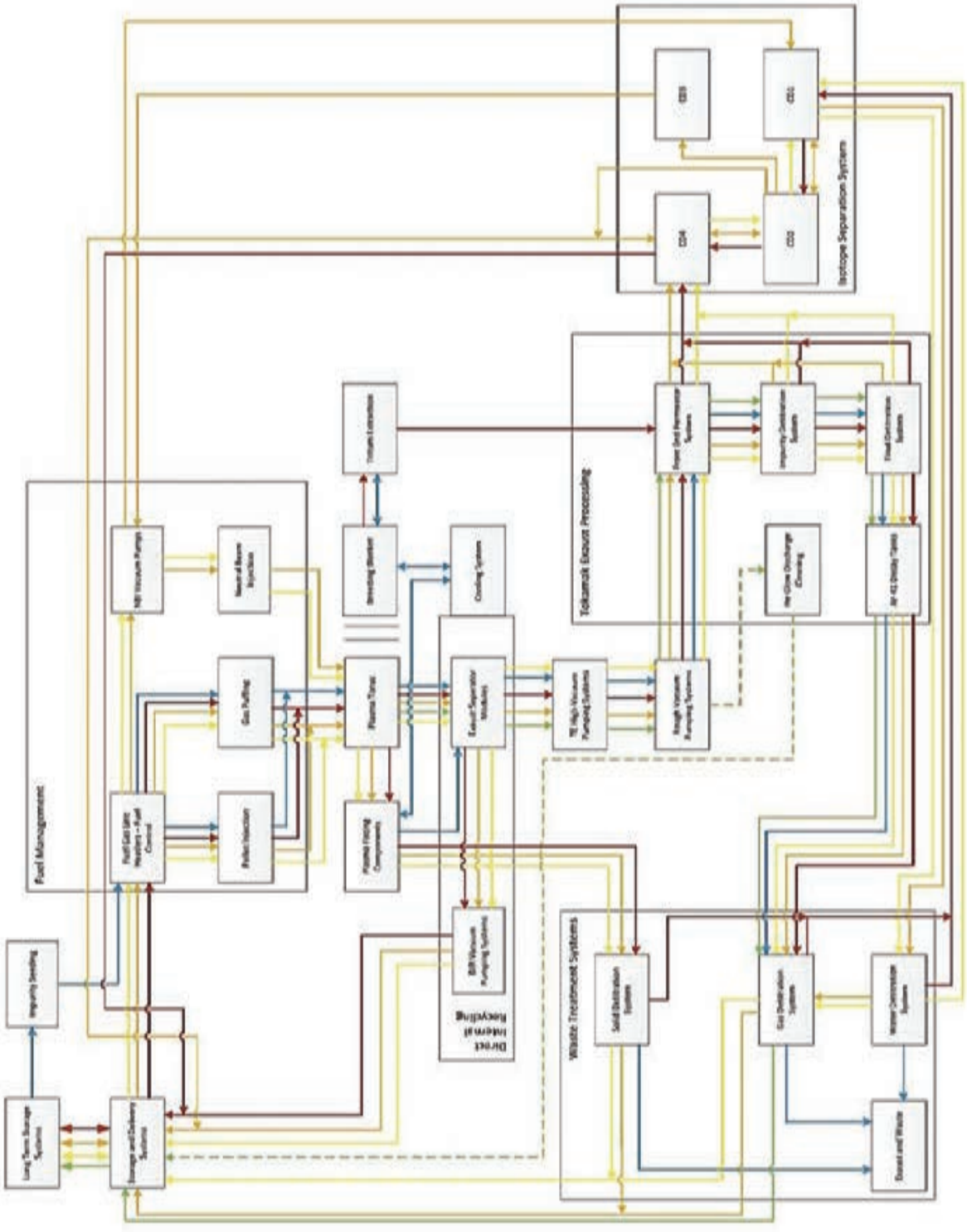

Fig. 1: Block diagram of the fuel cycle.

Each of the 30 sub-systems is given an own spreadsheet in the Excel file. Here, the balance equations for every gas species considered in the system are solved, based on input parameters defined on the control page, and additional information is given.

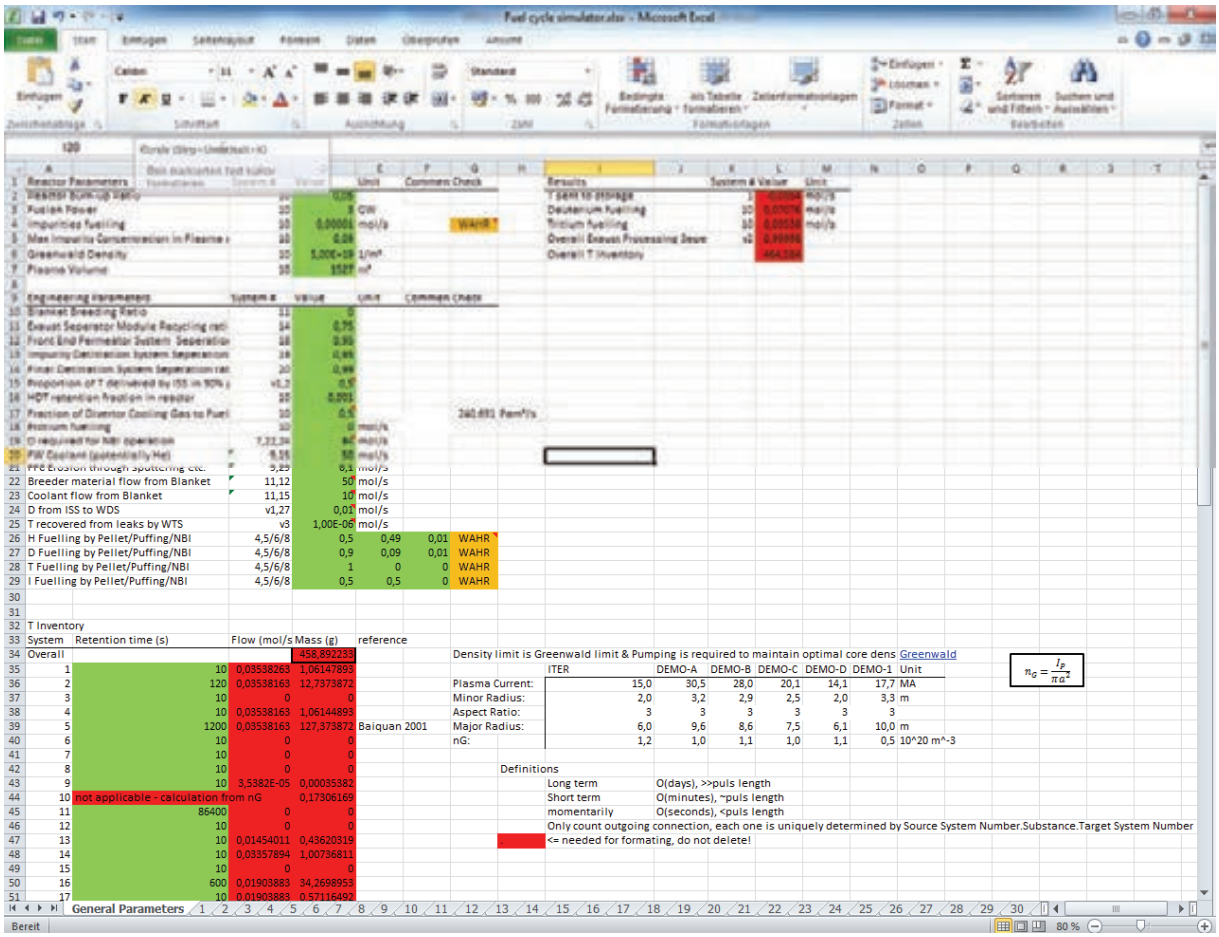

Fig. 2: The control page of the fuel cycle simulator Excel sheet.

Optimisation of the DEMO fuel cycle

By using the fuel cycle simulator, the main contributors to the overall tritium inventory can be quantified. Figure 3, which holds for an ITER-style fuel cycle, illustrates the four main contributors which make up for 97% of the total tritium inventory (no storage systems, no wall inventory, the blanket inventory shown is a generic number used at the lower side of expectation).

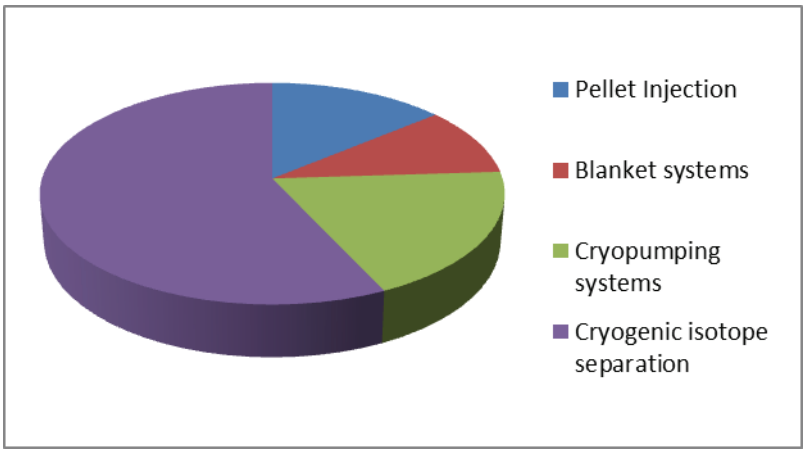

Fig. 3: Main contributors to the overall tritium inventory of an ITER-style fusion device (isotope separation 57%, cryopumping 19%, pellet injection 14%, blankets 10%).

The two most relevant systems are the cryogenic isotope separation system and the cryogenic pumping systems.

Both processes are basically batch-wise and, thus, directly resulting in large inventories and large processing times. Hence, R&D has started since a few years to develop customized continuous processes for the tritium plant, based on inorganic membranes. Already existing

continuous processes like the PERMCAT in the tokamak exhaust processing unit add just in the per mille range to the total inventory.

For a 2 GW fusion power DEMO machine which results just by extrapolation of the ITER systems, the total tritium inventory that was calculated under the assumptions above, is of the order of 3100 g-T (the burn-up fraction was assumed to be 1%, and the tritium breeding ratio to be 1.1). This inventory number is very high and may turn out to be critical for the licensing process. This is the reason for developing the Direct Internal Recycling (DIR) concept, which can minimise the potential issue of too high inventory build-up at DEMO [1- 3]. It is based on a separation of hydrogen isotopes from the torus exhaust gas stream to be directly recycled into the reactor, see Figure 4. This shortcut, close to the plasma vessel, would have several advantages for a fusion reactor:

- Significant reduction of tritium start-up inventory,
- Meeting administrative tritium inventory limitations,
- Drastic decrease of gas load on any hydrogen processing system, especially on tritium processing systems, reduction of the tritium plant size and inventories.

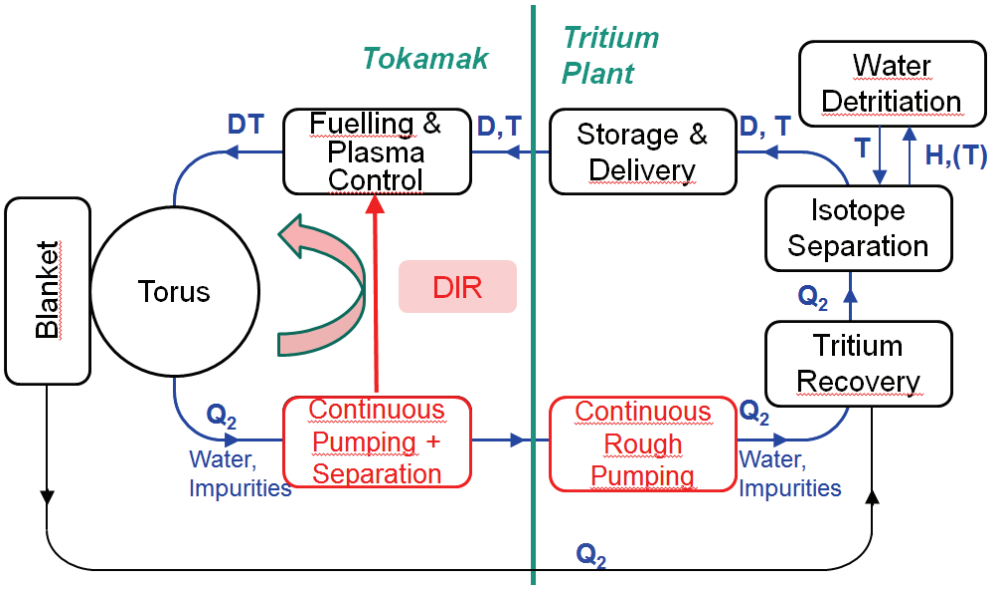

Fig. 4: Improved fuel cycle for DEMO: The DIR concept.

As this concept is novel and the exhaust separator module has not yet been demonstrated to work, the fuel cycle model contains an engineering parameter, the exhaust separator module recycling ratio, or DIR ratio, which is defined as follows:

$$DIR\ ratio = \frac{directly\ recycled\ hydrogen\ isotopes}{amount\ of\ gas\ pumped\ out\ of\ the\ machine}$$

By setting this parameter to 0, the standard ITER-case without any separation can be described. By giving it a value between 0 and unity, different performance characteristics of the exhaust separation can be studied.

In addition to the separation, the complete DIR concept contains another change compared to existing technology. It replaces the ITER-style batchwise primary and rough pump systems by continuous pumping systems. This can be considered by a corresponding reduction of the retention times of the pumping systems.

Figure 5 below is illustrating this potential by plotting the inventory as a function of increasing DIR ratio. The technical solution for such a system is currently under proof-of-principle testing, details can be found elsewhere in this annual report (WP12-DAS05).

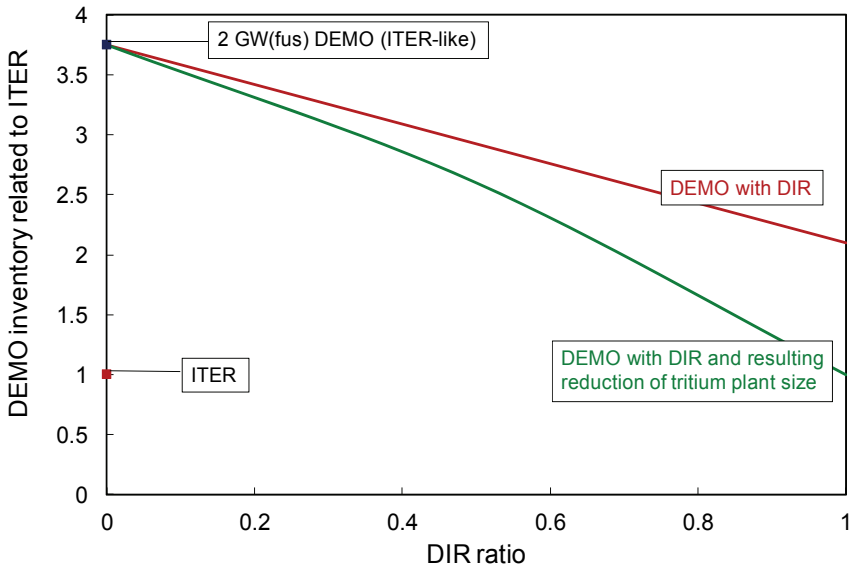

Fig. 5: Estimation of the dependence of tritium inventory in a fusion device on the DIR-fraction. The chart is assuming a burn-up fraction of 1% and a tritium breeding ration of 1.1.

Conclusions and outlook

A functional block diagram of the fusion fuel cycle was elaborated as a working platform with the aim to investigate inventories and flows in the different sub-systems and to derive the time constants for tritium processing. This simulation tool was benchmarked against the ITER fuel cycle. Based on an ITER-like solution, the DEMO systems with and without DIR have been investigated. It was found that, if the DIR solution works as expected, DEMO could be operated with a tritium inventory similar to the ITER inventory.

This work also acts as a first step towards system integration of the complete fuel cycle, which is the major milestone of the upcoming work year.

Staff:

Chr. Day
Th. Giegerich

Literature:

[1] Chr. Day, Th. Giegerich, D. Valougeorgis, Assessment of the pumping systems for DEMO,

[2] EFDA WP11-DAS-HCD-FP final report, Dec. 2011. Chr. Day et al., Technology gaps for the fuel cycle of a fusion power plant, 24th Fusion Energy Conf., San Diego, CA, US, Oct 2012.

[3] Chr. Day, The direct internal recycling concept to simplify the fuel cycle of a fusion power plant, SOFT 2012, Liege, Belgium, Sept. 2012.

Acknowledgement

This work, supported by the European Communities under the contract of Association between EURATOM and Karlsruhe Institute of Technology, was carried out within the framework of the European Fusion Development Agreement. The views and opinions expressed herein do not necessarily reflect those of the European Commission.

Numerical Model of an ITER Type Cryogenic Pump (WP12-IPH-A10-1-3-02)

Background and objectives

The primary pumping system of ITER is based on six specially developed cryogenic pumps, since no standard commercial vacuum pumps meeting the ITER design criteria are available. These large-scale cryopumps provide for a high pumping speed and feature an integral inlet valve, which can be closed to perform regeneration and to throttle the torus exhaust gas flow. To check the basic pump concept and examine its performance under ITER-relevant operating conditions prior to designing the prototype cryopump, a model pump of reduced scale was manufactured and studied in the TIMO facility at KIT.

Contrary to the normal application of a cryopump, the high-performance cryopump for ITER is not required to generate a very high vacuum, but to pump a high gas throughput of the fusion exhaust. The open questions in the design of these cryopumps are the scale-up from the model size to the 1:1 scale pump with more cryosorption panels and the impact of higher gas loads currently expected during ITER operation. To address these, a simulation tool to predict the operational characteristics of the cryopumps (such as pumping speed and pressure as a function of gas throughput) should be developed. This simulation tool could also be used to identify the optimum regeneration point of the cryopumps, which might eliminate the inflexible concept of strict regeneration patterns and introduce a philosophy of pump regeneration on-demand, i.e., only when the limiting amount of gas has really been reached. Based on the present investigation, it is demonstrated how such a pump can be modelled in a predictive way under normal and adverse conditions. It is also suggested to develop this code further for ITER, in order to become a reliable control software for predicting the cryopump behaviour.

Modelling approach

When one deals with rarefied gas flows, usually the Direct Simulation Monte Carlo (DSMC) or Test Particle Monte Carlo (TPMC) methods are employed. The former one can be used for arbitrary Knudsen number, but it requires the simulation of a huge number of model particles simultaneously. Such computational effort is justified when the intermolecular collisions must be taken into account. The latter method consists of simulation of individual particle trajectories, where the particle-particle interactions are neglected, so that the method requires less computational effort. This simplicity also allows describing very complex geometries whereas the corresponding computational effort for the DSMC is several orders of magnitude higher.

The cryovacuum pump design elaborated for the torus pumping system of ITER is characterized, on one side, by geometrically very complex parts forming the cryogenic circuits in regions, where the intermolecular collisions can be neglected, and, on the other side, by geometrically simpler parts in regions where the collisions have to be taken into account. This is why a combination approach of the two methods above and thereby adding their individual advantages has been applied. To be more specific, the flow between the cryopanels is simulated by the TPMC method and then these results are introduced as input parameters for the DSMC method applied in the remaining volume with a virtual boundary surface to the cryopanel volume. The treatment with TPMC has already been done previously [1] where it was found that the distribution of the capture coefficient along the virtual surface depends mainly on the gas species and is independent of the valve position.

The chosen pump geometry is a good representation of the ITER torus cryopump; actually, it exactly corresponds to a 1:2 model of the ITER torus cryopump of the 1998 design. This has been chosen because this cryosorption pump for ITER was designed, manufactured and tested in KIT [2]. The chosen simulation model presented in Figure 1 (bottom) is a simplified

one, but still complex in geometry and for that reason the implementation of the DSMC method becomes a challenging task.

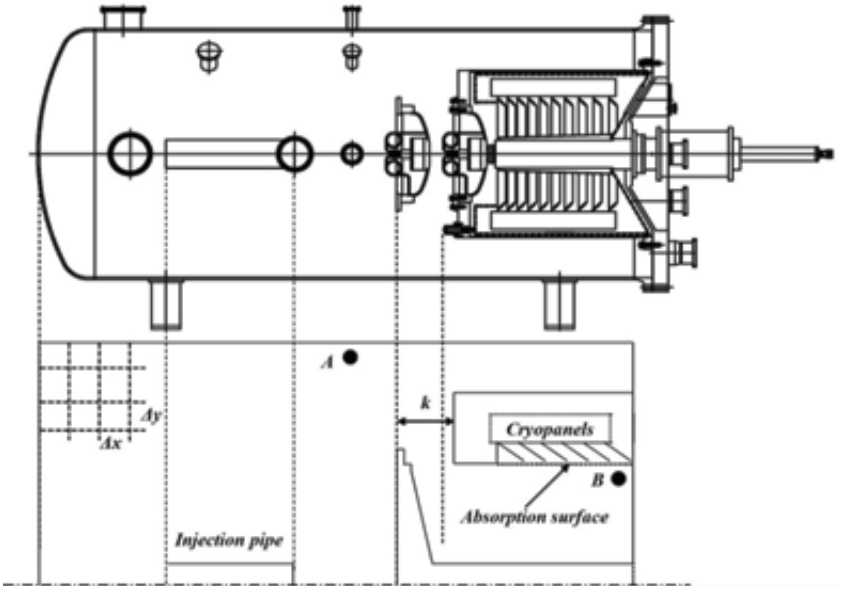

Fig. 1: Geometrical configuration of the cryopump (top) and the corresponding simulated model (bottom).

The vacuum chamber represents a cylinder of diameter 1.8 m and length 4.0 m. During the operational phase of the pump, gas with a fixed throughput q is injected in the axis of the chamber through a pipe. The molecules of the gas travel throughout the flow field interacting with other molecules as well as with the stationary walls until finally to be captured by the cryosorption panels. The access of the gas to the cryopanels is restricted by a movable valve, which has a maximum valve stroke of k=0.4 m. The temperature of the injected gas and the pump walls is assumed to be equal to T_0=300 K, while the temperature in the adsorption surface (dotted line in Figure 1-bottom) in front of the cryopanels and the valve shaft is equal to T_c= 80 K. During the simulations, the local pressure was measured in two different points A upstream and B inside the cryopump. The positions of the gauges are shown in Figure 1 (bottom).

Results and discussion

Calculations have been carried out for a wide range of input parameters: (i) the injected gas flow rate ranges between 500 and 5000 sccm, b) the valve position varies from $0-100\,\%$ of the maximum opening and c) for two different gases, helium and deuterium. It is noted that the obtained results cover actually the whole range of Knudsen number. The case of q=500 sccm is proven to correspond to the free molecular regime, while the case of q=5000 sccm is an ITER relevant case.

As an example, in Figure 2 the temperature contours in the area close to the valve and inside the pump for gas helium and two gas throughputs and valve positions are presented. It is seen that the temperature field in the area of the valve is not uniform and strongly depends on the valve position and the throughput of the gas. On the other hand, in the area towards the end of the pump the temperature decreases and is independent of the valve opening and the gas throughput. Based on this information, temperature measurements can be scaled in a more general way with the injected throughput in order to assess the pumped amount of gas over a time period. This idea illustrates nicely that the presented calculations can be used for tritium monitoring and thus provides a very important safety function purpose as well.

The elaborated calculations provide detailed information of the gas flow field such as pressure and temperature distribution, number of particles absorbed by each cryopanel, heat fluxes, etc [3].

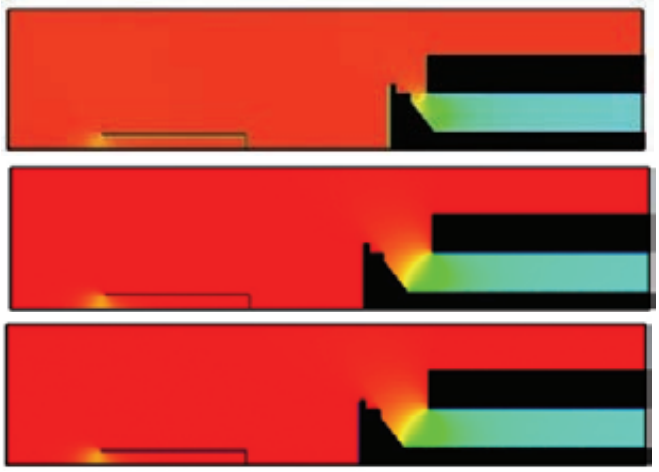

Fig. 2: Temperature contours [K] for two different gas throughputs (q=500 sccm and 5000 sccm) and two different valve positions (50% and 100%), for gas helium.

Conclusions

A numerical modelling of the ITER model cryopump combining both DSMC and TPMC methods has been developed. The importance of such a tool is based on the fact that it can provide information for macroscopic quantities, which cannot be measured during an operation phase. One can use this approach as design supporting tool within future pump development. For instance, the influence of valve positions on the distribution of the pumped gas amount along the cryopanels surfaces can be studied. In conclusion, the presented code could be further developed towards the control of an operational pump in a fusion reactor.

Staff:

S. Varoutis
X. Luo

Literature:

[1] X. Luo, Chr. Day, H. Haas, S. Varoutis, Experimental results and numerical modeling of a large-scale cryopump I, J. Vac. Sci. Technol. A 29 (2011) 041601/1-7.

[2] H. Haas, Chr. Day, A. Mack, D. Murdoch, Performance tests of the ITER model pump, Fusion Eng. Des., 69 (2003) 91-95.

[3] St. Varoutis et al., Experimental results and direct Simulation Monte Carlo modeling of a high-performance large-scale cryopump, AVS Sympoisum, Tampa, FL, US, Oct. 2012.

Acknowledgement

This work, supported by the European Communities under the contract of Association between EURATOM and Karlsruhe Institute of Technology, was carried out within the framework of the European Fusion Development Agreement. The views and opinions expressed herein do not necessarily reflect those of the European Commission.

Investigation of Candidate Vacuum Pumping Systems for DEMO (WP12-DAS-05-T01 and -T02)

Background and objectives

In 2011, in a task by the EFDA Power Plant Physics & Technology department, the fuel cycle requirements and different vacuum pumping systems for DEMO have been assessed [1]. It was found that a simple up-scaling of the cryopump technology used at ITER to the DEMO throughput is critical, as it would lead to a very large tritium inventory in the whole pumping system and following from the batchwise operation mode of these pumps to a high cryogenic demand in a most complex operation mode. Instead of the discontinuous working solution adopted at ITER, a continuously working and non-cryogenic three stage pumping train was proposed. It consists of a vapour diffusion pump as primary pump, backed up by a liquid ring pump. Both pumps are hermetically sealed and apply a liquid metal (mercury as optional candidate) as working fluid to make them tritium compatible. Additional to these non-cryogenic pumps, a primary pump was proposed that provides a separating function for the pumped gas: The unburnt fuel (pure deuterium and tritium) is separated from other impurities (including helium) sharply and recycled directly to the machine [2, 3]. In consequence, only a small gas flow that is enriched with helium and other impurities must then be processed in the tritium plant, which could be appropriately downsized. This new concept has been introduced as an option for DEMO as Direct Internal Recycling (DIR) [4]. Depending on the results of the proof-of-principle tests that are needed to confirm this new concept, the metal foil pump may take over the pumping job during burn and the diffusion pump may only be needed when really high vacuum is required, for example between the pulses or for conditioning of the vacuum vessel.

If this strategy proves not to work, one would need to reconsider a fallback solution. For timing reasons this should be chosen in a conservative way, namely start from cryogenic pumps for primary pumping and from classical mechanical pumps for rough pumping.

In consequence, WP2012 did include two tasks. The first one was dedicated to start proof-of-principle testing of the novel pump concepts (to be completed in a 2 years time frame for all three technologies), whereas the second one (performed in collaboration between KIT and CCFE) was devoted to a numerical study on an advanced three-staged cryopump concept that has the potential to provide a separation function as well.

The THESEUS test facility

For testing all three pumps and for later demonstration of the DIR concept in a fusion relevant scale, a test facility is needed. At KIT, this facility is currently being set up, named THESEUS (Test facility for helium separating units, Fig. 1). It consists of a gas dosing dome to which all pumps can be connected. By a dosing system, gas can be introduced at a known flow rate. The dome pressure can be measured between 10^{-8} and 10^{5} Pa and the pumping speed at a given inlet pressure can be calculated. In 2012, all main components have been procured and set up. The THESEUS facility has become fully operational for testing of small scale pumps and has been employed to perform the proof-of-principle tests of a mercury vapour diffusion pump. It is now being extended (new dosing dome with an extended gas dosing system) for the experimental investigation of the mercury liquid ring pump with all corresponding infrastructure (gas clean-up column, liquid metal circuit). The liquid ring pump will be tested in 2013. As unique feature, tests of both, primary pumps and backing pumps can be done with various gases including hydrogen and deuterium. These gases, in combination with mercury as liquid metal working fluid for the pumps, ask for high safety precautions in the facility and a full remote control of all components from the control room. The set-up of the facility has been supported by the VACU-TEC Goal oriented training programme (see activity WP10-GOT-VACU-TEC elsewhere in this report).

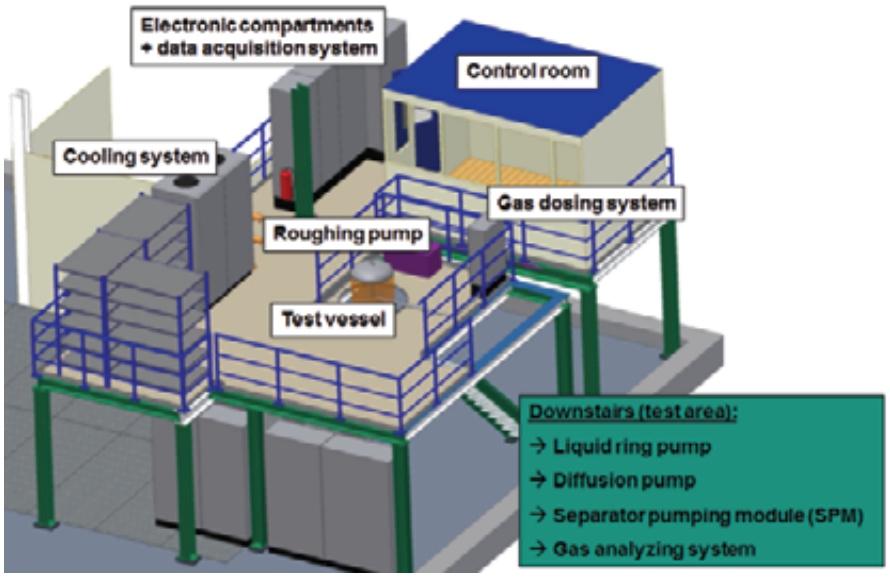

Fig. 1: The THESEUS facility.

Proof-of-principle testing of novel pump concepts

A suitable pumping system for a fusion power plant not only has to be fully tritium-compatible in order to work reliably over the whole lifetime, but also safety events have to be considered as well as different operation modes (burn and dwell) and harsh ambient conditions (especially dust and magnetic fields). The pumping speed that has to be provided by the pumping system during burn is in the order of several 100 m³/s for the primary pumps and several 1000 m³/h for the backing pumps.

The liquid metal vapour diffusion pump

As cryopumps, vapour diffusion pumps can provide very large pumping speeds at high vacuum conditions. A vapour diffusion pump has no movable parts and is practically maintenance-free which makes it perfectly suitable for fusion reactors. It is fully tritium-compatible, if chosen a suitable working fluid (e.g. mercury). Today, modern oil diffusion pumps are available in very large sizes (> 50 m³/s per pump) but liquid metal diffusion pumps are practically not used anymore in industry, although it is known from the vacuum history that mercury diffusion pumps work extremely well. To gain experience in the operation of such a pump and to investigate its performance, a small mercury diffusion pump (which had been used over a few decades but was taken out of operation 20 years ago) was tested in the THESEUS facility, see Fig. 2.

Fig. 2: Experimental set-up of a diffusion pump for proof-of-principle testing. The small dosing dome with the mass flow controller can be seen on top; the liquid nitrogen baffle and the diffusion pump are located below.

It must be noted that the way how the diffusion pump would be used during fusion burn at the moderate vacua and very high gas throughputs is not in line with normal operation conditions for such a high vacuum pump, hence a test was absolutely vital. It was found that such a diffusion

pump with internal jet stage (diffusion ejector pump) is applicable over the full pressure range expected in fusion reactors for primary pumps (~10 Pa during burn, ~ 10^{-4} Pa during dwell, ~ 10^{-5} Pa ultimate pressure). It was also demonstrated that the jet stage is able to provide a sufficiently high outlet pressure, an important issue as it is the most important interface between primary and roughing pump [5]. Pumping speed curves and foreline resistance data were measured for this pump for different gases and over the whole DEMO relevant throughput range.

The liquid metal ring pump

The primary pumps need backing pumps that have to cope with high throughputs and work well until an ultimate pressure below 100 Pa. This can be reached by liquid ring pumps which are very robust and industrially well established (using water as working fluid). For tritium compatibility reasons, one would use a full stainless steel pump with the same liquid metal as already used in the diffusion pump. This leads to a new pump design that would be required to handle the high forces due to the 15 times higher density of mercury compared with water and that is optimised in inventory and tightness (hermetically sealed). In WP2012, the design for a mercury ring pump was developed in cooperation with an industrial company, starting from an already existing water pump design. The procurement was brought on the way, the pump was completely manufactured and finally delivered in early November 2012, see Fig. 3. It will be prepared for an experimental campaign in the THESEUS facility. For safety reasons, extra control measures have to be taken to make sure that the liquid metal is kept inside the pump: a liquid nitrogen cooled gas clean-up column was designed and already manufactured at the KIT workshop. In this column, filled with stainless steel packaging, mercury vapour is first condensed and later frozen out in a three stage cooling process until a target mercury content in the exhaust gas of less than 0.1 ppb is reached.

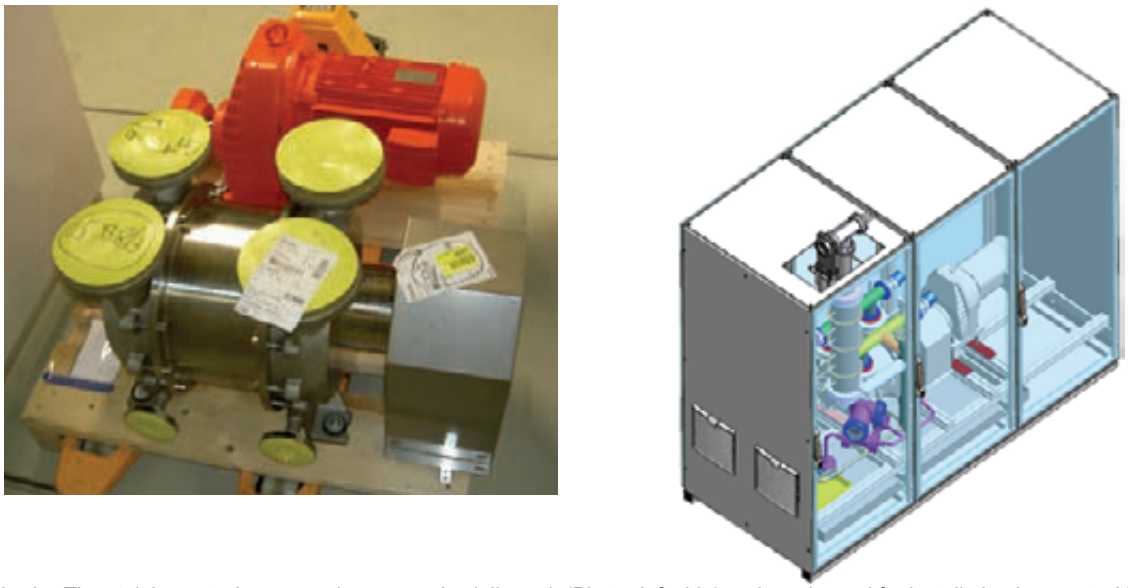

Fig. 3: The stainless steel mercury ring pump. As delivered (Photo, left side) and as planned for installation in a control box.

The metal foil pump

As central part of the DIR concept, a separator pumping module is under development for pumping and gas separation, based on a metal foil pump that is basically a vanadium foil exposed to monoatomic hydrogen isotopes. These atomic hydrogen isotopes can be created by hot rods at high temperatures (atomizer concept) or by plasma; for safety and reliability reasons, the plasma concept will be developed further. As a first step towards manufacturing a pump module for the proof-of-principle tests, a test module was manufactured (test volume with a vanadium foil welded to stainless steel) and installed in a plasma chamber at CRPP in Lausanne (see the report WP10-GOT-VACU-TEC). Welding, leak-testing and heating of the

metal foil was successful. Unfortunately the foil broke after a short time of operation. Nevertheless, first experiments have been performed and a lot of lessons could be learned that will be considered in the design of an optimized module to be tested in 2013.

Vacuum pump modelling

It was decided to initiate modelling efforts in parallel to the experimental work so as to have a design tool to validate with the experiments and good to minimize experimental work afterwards.

The pumping principle of diffusion pumps is given by the momentum transfer from the liquid jet onto the particles being pumped. Due to this working principle a molecular simulation approach was chosen. The KIT in-house Monte Carlo code ProVac3D, which is based on the accumulated time-of-flight method, was updated to be able to simulate diffusion pumps by properly implementing the interaction of gas with a background gas of different kind. For this task, a code parallelization was needed to take the advantages of the supercomputers of HPC-FF (Jülich) and Helios (Japan). The code development to simulate the diffusion pump advanced very well in 2012, cf the report HPC-FF-SIMVAC elsewhere in this annual report. Further tests and cross checks are needed before it will be used to study a well-documented literature case, namely a linear mercury diffusion pump from the 1950s. Such linear pumps can be scaled to the desired pumping speed by its length, which gives this pump type a high relevance for this work.

For the liquid ring pump, a set of lumped parameter equations was developed and needs now to be benchmarked which will become possible only after the testing of the liquid ring pump in mid-2013.

In case of the metal foil pump, as a first step, the physical principle was investigated theoretically and a self-consistent predictive calculation procedure was developed from a very comprehensive literature study so that also the performance calculation of a metal foil pump becomes now possible. Also here, benchmarking against experiments can only be done after manufacturing and testing a metal foil module (planned for 2013).

Theoretical examination of a three stage cryopump

As fallback solution, a cryopump with three cryogenic pump stages was proposed. Due to different temperature levels, it is expected to generate a pre-separation effect of the species being pumped given by helium being absorbed on a 4.5 K charcoal-coated surface, while deuterium and tritium are absorbed at 15-22 K on a second charcoal-coated surface, and all heavier species being condensed at the inlet thermal shield at 80 K. The helium would be released by rising the first surface to ~30 K; in a separate regeneration step, deuterium and tritium would be released at ~110 K. In this way the helium can be pre-separated.

A case study of this concept was conducted by CCFE with support of KIT. In the simplest design, all three stages are in the same vessel, with a single valve to close the pump off from the tokamak during regeneration. In an alternative design, the three stages are in separate vessels, connected by valves which can all be closed simultaneously, allowing the stages to regenerate without interfering with each other. It could be shown that the 15 K panels do not greatly reduce the overall pumping speed, depending on the sticking coefficient of the particles at that pumping surface. In order to clarify this point, an open panel experiment will be performed in 2013 to derive experimental values for this sticking coefficient.

Furthermore, it was found that, especially when the gas entering the pump is at very high density, the flow into the pump will be choked. Then, enlarging the aperture is the only way to increase the pumping speed.

Conclusions and outlook

The work done in 2012 progressed very well. This holds for the experimental work as well as for the theoretical work. No show-stoppers in view of the feasibility of the DIR concept have been found. The proof-of-principle testing will be continued in the area of the liquid ring pump and the metal foil pump. All experimental data will be used to validate the modelling tools that have been developed in parallel so far.

Staff:

Chr. Day
Th. Giegerich
Th. Johann
X. Luo
P. Pfeil
H. Stump
St. Varoutis
J. Weinhold

Literature:

[1] Chr. Day, Th. Giegerich, D. Valougeorgis, Assessment of the pumping systems for DEMO,EFDA WP11-DAS-HCD-FP final report, Dec. 2011.

[2] Chr. Day et al., Technology gaps for the fuel cycle of a fusion power plant, 24th Fusion Energy Conf., San Diego, CA, US, Oct 2012.

[3] Th. Giegerich, Chr. Day, Fusionskraftwerke - Anforderungen und gegenwärtige technische Entwicklungen der Vakuumpumpsysteme, DPG Spring meeting, Berlin, Germany, Mar 2012.

[4] Chr. Day, The direct internal recycling concept to simplify the fuel cycle of a fusion power plant, SOFT 2012, Liege, Belgium, Sept. 2012.

[5] Th. Giegerich, Chr. Day, Conceptuation of a continuously working vacuum pump train for fusion power plants, SOFT 2012, Liege, Belgium, September 2012.

Acknowledgement

This work, supported by the European Communities under the contract of Association between EURATOM and Karlsruhe Institute of Technology, was carried out within the framework of the European Fusion Development Agreement. The views and opinions expressed herein do not necessarily reflect those of the European Commission.

Goal Oriented Training Programme on Negative Ion Physics and Engineering Expertise (WP08-GOT-NIPEE (FU07-CT-2008-00043))

Background and objectives

The NIPEE programme is supporting the development of the PRIMA/MITICA neutral beam test facility which is currently being built at Consorzio RFX, Padova, Italy. This facility features a full 1:1 scale testing environment of the complete ITER Heating Neutral Beam (HNB). To provide training and experience in the design, specification and construction of high power Neutral Beam Injection systems and their integration with the test facility, six engineers receive expert training in the relevant aspects. The goal oriented training programme is co-ordinated by Consorzio RFX. KIT is hosting one trainee who specifically contributes to the final design of the large cryopumping system of MITICA [1-3]. The conceptual and detailed design of the NBI cryopumps has been developed by KIT over the last years jointly with IO/F4E and Consorzio RFX. Thus, most of the NIPEE work conducted in 2012 was supporting the finalisation of the detailed design work [4].

Numerical optimization of the cryopanel geometry

The cryopanel surfaces are passively cooled (i.e. cooled by heat conduction) via a central pipe which is supplied with cryogenic supercritical helium at 4.5 K and 0.4 MPa. To assure its maximum performance, the cryopanels, under thermal and electron radiation loads, should stay below a maximum operation temperature of 8 K at all locations at their surface. This limit was chosen based on the experience with the pumping behaviour of the used charcoal.

A schematic representation of the cryopump interior arrangement is shown in Fig. 1. It consists of two types of static components: thermal radiation shields (v-structured elements) and cryopanels with fins (straight elements) which are passively cooled by thermal conduction.

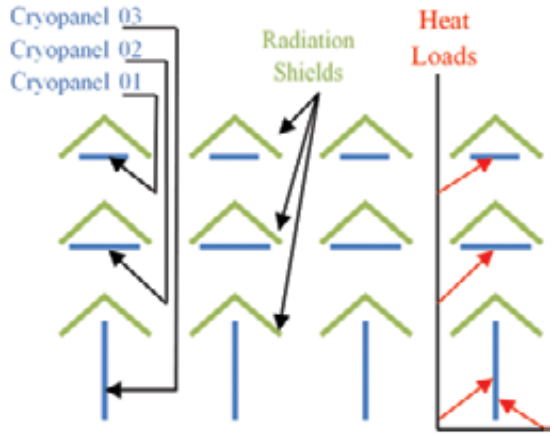

Fig. 1: Schematic representation of the cryopanel arrangement in the cryopump.

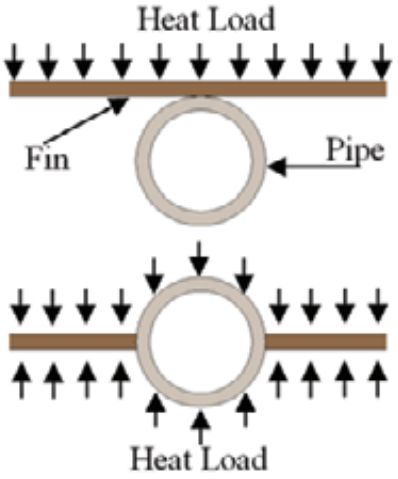

Fig. 2: Geometry of cryopanel: on the top 01 and 02, on the bottom 03 (not scaled).

A schematic illustration of the two basic types of cryopanels is presented in Fig. 2, where cryopanel 01 and 02 have the same shape but different fin length. The inlet and outlet helium temperatures for the cryopanels are 4.5 K and 6.5 K, respectively. The heat load major contribution on the cryopanels is thermal radiation but on the cryopump upstream end an additional high electron heat load from the beam source has to be considered. The calculated maximal total heat load (thermal radiation, conduction and upper limit of electron load), on the first upstream 1.5 m of the HNB cryopump, is 48 W/m^2 of charcoal coated area. For cryopanel 01 and 02 the heat load is applied on one side and for cryopanel 03 on both sides (see Figs. 1 and 2).

The cryopanel thermal capability is mainly influenced by its shape (pipe thickness, fin thickness, fin to pipe angle), material (thermal conductivity, heat capacity), composition (uniform or with an additional coating for improved heat conduction), and the joining process (welding, adhesive, diffusion, mechanical). The inner diameter (13.6 mm) of the pipe was already selected and frozen in previous stages of the design due to safety considerations and pressure losses. An optimum solution for the cryopanel geometry is obtained when the temperature rise and heat capacity are minimized simultaneously. A low heat capacity is essential to minimize the energy consumption in the regeneration phases. Manufacturability is also an important parameter, therefore it is recommended to use standard parts wherever possible to guarantee a reliable operation and to save costs.

The physics case considered here is a 2D steady-state heat transfer model of a solid. The mesh consists of about 50000 nodes with quadrilateral elements. Effects of thermal radiation are included in the boundary condition of a constant amount of heat flux of 48 W/m^2 and a constant temperature on the inner wall of 6 K. As mentioned before, there are two types of cryopanels and for each one several geometry configurations with different materials were analysed. As the configurations will be intercompared, the calculation of the heat capacities was based on the constant value at 300 K. Due to the longer fins, cryopanel 02 absorbs a higher heat load than cryopanel 01, thus, the optimized cryopanel 02 configuration will be used for cryopanel 01 as well. For cryopanel 02 we investigated five geometries (from “a” to “e”), and three for cryopanel 03 (from “f” to “h”). This can be seen in Fig. 3. Among these we always included cases with additional copper coatings on stainless steel (SS) surfaces, which became necessary in view of the poor thermal conductivity of SS.

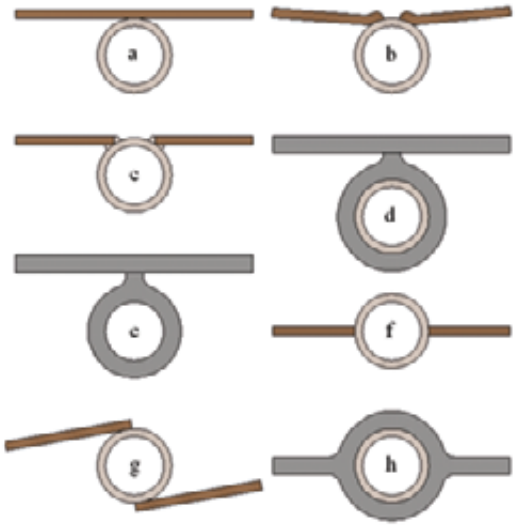

Fig. 3: Different geometries for Cryopanel 01, 02 (from “a” to “e”) and 03 (from “f” to “h”) - (fin length not scaled).

Table 1 describes all investigated panel configurations (in terms of materials for fin, pipe and coating) and lists the calculated maximum temperatures and the linear heat capacity values. It can be seen that adding a material with high conductivity on the cryopanel increases the thermal capability significantly.

From the calculations, the following main conclusions can be drawn:

- The lowest linear heat capacities at fully acceptable temperatures for cryopanel 02 and 03 are given by options “7” and “12”, respectively.
- The minimal copper coating thickness, necessary for cryopanel 02 and 03 to achieve a minimal temperature rise is 25 µm and 50 µm, respectively.
- The use of a good thermal conductor material only for the fins is not a solution in order to ensure the temperature requirements.

Table 1: Results for the studied material combinations for the cryopanels: Option 1-8 refer to cryopanel type 01/02, whereas options 9 to 14 refer to cryopanel type 03.

Option	Material			Geometry	Package Design	Maximal Temp [K]	Linear Heat Capac [J/kg/K]
	Fin	Pipe	Coat	Fig. 3			
1	316L	316L	-	A	4 mm SS-fin	15.9	1527
2	OFHC Cu	316L	-	A	4 mm Cu-fin	7.85	1375
3	316L	316L	OFHC Cu	A	500 µm Cu-coat only on radiated surface/2 mm SS-fin	10.8	1064
4	316L	316L	OFHC Cu	A	25 µm Cu-coat sur-round the cryopanel/2 mm SS-fin	7.28	953
5	316L	316L	OFHC Cu	B	25 µm Cu-coat only on radiated surface/2 mm SS-fin	7.95	919
6	316L	316L	OFHC Cu	C	25 µm Cu-coat only on radiated surface/2 mm SS-fin	7.80	890
7	Al	316L	-	D	0.5 mm Al-fin/SS-pipe	7.40	502
8	Al	Al	-	E	0.5 mm Al-fin/Al-pipe	7.05	641
9	316L	316L	-	F	4 mm SS-fin	26.8	1973
10	OFHC Cu	316L	-	F	4 mm Cu-fin	8.42	1763
11	316L	316L	OFHC Cu	F	50 µm Cu-coat sur-round the cryopanel /2 mm SS-fin	7.95	1202
12	Al	Al	-	F	1 mm Al-fin/Al-pipe	7.45	795
13	316L	316L	OFHC Cu	G	100 µm Cu-coat sur-round the cryopanel /2 mm SS-fin	7.71	1600
14	Al	316L	-	H	2 mm Al-fin/SS-pipe	7.55	1444

In deciding the final design, considerations for simple designs with easy manufacturing and sufficient thermal performance have to be weighed against complicated designs (such as in cryopanel 02 option “7” or cryopanel 03 option “14”) and best thermal performance but potentially more difficult manufacturing, potential stress issues due to different expansion coefficients and formation of virtual leaks. Finally, the options “6” and “11” were selected for the design of cryopanels 01/02 and 03, respectively.

Manufacturability studies

To protect the cryopanel manifolds from any direct thermal radiation, especially from the warm surfaces of the mounting structure on top, passively cooled shielding plates are employed as well. Contrary to the cryopanels, these plates are manufactured of copper to guarantee an excellent thermal conductivity and are attached to the shielding main supply pipes by welded contacts. Although the welding between components of SS and Cu is well known there were worries about the manufacturability of the manifold shield system and the reliability of the Cu/SS welding, especially in view of the thermal cycling requirements given by the regeneration of the cryopump. To demonstrate the feasibility and find a manufacturing path, sample parts were manufactured (Fig. 4), subjected to thermal cycling (10 times dipping into liquid nitrogen), and the welds investigated.

Due to space limitations, the welding during the assembly of the pump has to be done by hand. At KIT several prototypes were produced, by that optimizing the welding procedure and its preparation. Some prototypes were treated afterwards by a temperature cycling to demonstrate a sufficient strength under real conditions. This was additionally verified by micro-sectioning and investigations of the metal micro structure near the joint. The weld analysis showed the following results:

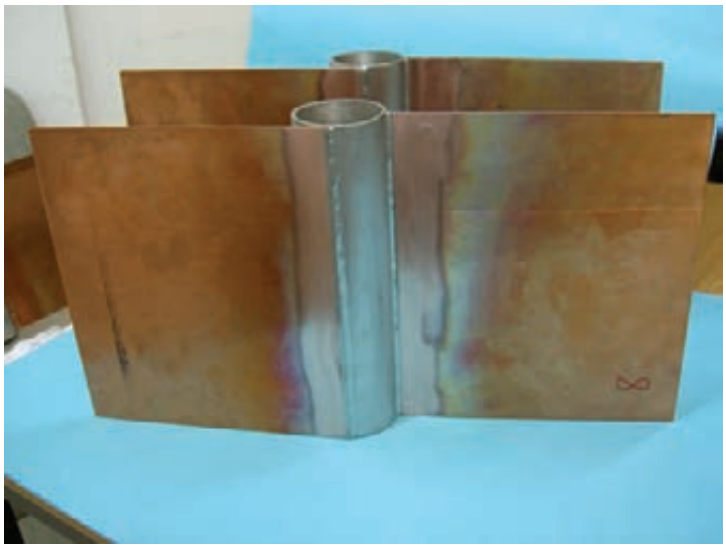

Fig. 4: Prototypes of tested and optimized manifold shielding system. The shielding Cu plates are welded by hand to the SS supply pipes under the use of an interface material which was previously electron beam welded.

- The penetration depth of the welding into the pipe wall is with ~ 1/3 (< 1 mm) far from being critical regarding the remaining non-affected wall thickness.
- Some distortions of the plates and the pipe occurred during welding but only on a minor and manageable level.
- The microscopy showed no heat affected zone of the welding.
- No cracks, voids or other defects have been found by these inspections, independently if the sample was thermally cycled or not.

Consequently, it was concluded that the manufacturing process is feasible.

Conclusions and future work

The ongoing design work of the NBI cryopump has seen a real benefit by this support provided under the EFDA GOT programme so that this scheme will be continued in the next

year. The trainee also had the opportunity to present his work in two talks at scientific Conferences [5, 6].

Staff:

A. Demsoreanu
St. Hanke (mentor)
S. Ochoa (trainee)

Literature:

[1] A. Masiello et al., EU development of the ITER neutral beam injector and test facility, Proc. 24th IAEA Fusion Energy Conf., San Diego, CA, US, Oct. 2012.

[2] P. Sonato et al., Design of the MITICA neutral beam injector: From physics analysis to engineering design, Proc. 24th IAEA Fusion Energy Conf., San Diego, CA, US, Oct. 2012.

[3] St. Hanke, Chr. Day, M. Dremel, F. Fellin, X. Luo, M. Scannapiego, P. Wikus, P. Zaccaria, Development of a large NBI cryopump, TOFE 2012, Nashville, TN, USA, Aug. 2012.

[4] S. Ochoa, St. Hanke, Chr. Day, Heat transfer enhancement of NBI vacuum pump cryopanels, SOFT 2012, Liege, Belgium, Sept. 2012, accepted for publication in FED.

[5] S. Ochoa, St. Hanke, Chr. Day, Vacuum system design of the MITICA test facility – challenges for the cryopump, German Physics Society spring meeting, Berlin, Germany, March 2012.

[6] S. Ochoa, Vacuum systems of fusion power plants, Escuela Superior Politecnico del Litoral, Guayaquil, Ecuador, Dec. 2012.

Acknowledgement

This work, supported by the European Communities under the contract of Association between EURATOM and Karlsruhe Institute of Technology, was carried out within the framework of the European Fusion Development Agreement. The views and opinions expressed herein do not necessarily reflect those of the European Commission.

Goal Oriented Training Programme on Vacuum Technologies and Pumping (WP10-GOT-VACU-TEC (FU07-CT-2010-00065))

Background and objectives

The aim of the VACU-TEC training programme is to prepare five scientists for activities to support the ITER project and the long-term fusion programme in Europe in the area of vacuum technologies and pumping.

The European procurement for ITER in the area of vacuum technologies and pumping systems covers activities for the supply of cryopumps for torus, cryostat, heating and diagnostics neutral beam systems as well as the supply of cold valve boxes, instrumentation and the R&D needed to finalize the design of these components. All these requested areas are fully covered in the VACU-TEC goal oriented training programme (GOT) and each area is reflected by an individual work package (WP 1 to 5):

- *Cryogenic Engineering:* Cold turbo pump development (WP1 by CEA Grenoble)
- *Instrumentation:* Identification of total and high resolution partial pressure as well as outgassing measurements for ITER leak detection (WP2 by KIT)
- *Leak Localization:* Development of remote devices for ITER in-vessel leak localization (WP3 by CEA Cadarache)
- *Mechanical Vacuum Engineering:* Mechanical design of large scale cryopumps for ITER and mechanical pumps (WP4 by KIT)
- *Physics:* Vacuum gas dynamics and flow modelling (WP5 by the Hellenic Association, Volos)

The training programme for all trainees follows the same generic scheme with four main elements:

1. *General education* by participation in introductory as well as specialized courses, lectures and seminars all along the first year of the project
2. *Practical education* by being involved in the group activities related to the corresponding training topic
3. *Secondments* to other partners of the training programme at various stages of the project as project introduction, improvement or conclusive training
4. *Participation in conferences, workshops* and *meetings*

KIT is co-ordinating this network which started in 2011. So, the reporting year was the first full running year with all trainees.

VACU-TEC Work Package 2 (Instrumentation)

The main objective for Work Package 2 is to develop and characterize vacuum pressure instrumentation and to improve the ITER leak detection system as well as to study the outgassing behaviour of materials which will be employed in the ITER vacuum systems.

<u>Outgassing Measurement Apparatus (OMA)</u>

A test facility for measuring outgassing rates was set up since outgassing plays an important role, especially if ultra-high vacuum conditions shall be reached and/or if the surface area involved is very high, like for ITER with a surface area of about 20.000 m^2.

The main work in 2012 was to build up the Outgassing Measurement Apparatus (OMA) [1], which was conceptualized already in 2011, and perform first measurements, which then were

presented at the SOFT conference [2]. In the beginning of the year, the laboratory equipment was completed and last modifications on the design of OMA were implemented. When the last components arrived, the apparatus was set up mechanically and electrically in summer. After completion, the whole test rig was leak-checked and heating and insulation were installed.

The Outgassing Measurement Apparatus uses the difference method. With this method the outgassing of the vacuum chamber can be subtracted and also very low outgassing rates can be measured.

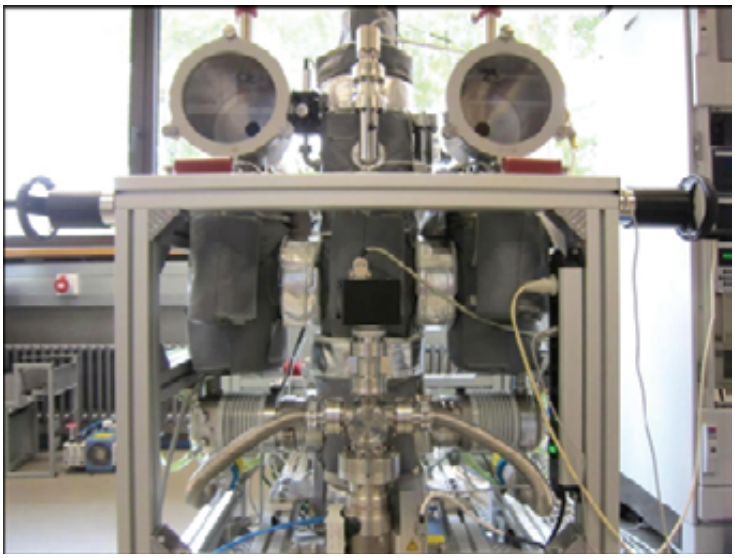

Fig. 1: Picture of the Outgassing Measurement Apparatus (OMA)

In parallel to the set-up of OMA, the literature research on outgassing rates was continue and a list of literature outgassing rates of different materials was compiled, including stainless steels, metals and alloys, polymers, ceramics and glasses.

As initial measurements at OMA, some blank measurements were carried out to see which pressure can be achieved and how much gas is inserted by transferring the sample holder into the vacuum chamber, combined with different bake-outs to decrease the base pressure. First sample measurements were performed for Viton® (fluoroelastomer) and Vespel® (polyimide). For these measurements the sample plates were only wiped with ethanol before measurement. The samples were inserted in the lock chamber and pumped down for 2 hours, so that a pressure in the range of 10^{-4} Pa was reached. After that, the sample holders, one containing the sample and the other acting as a reference, were transferred into the vacuum chambers and the pressures were measured for about 48 h. The outgassing rate per unit area of the sample is then calculated using the pressure differences, the known conductances of about 0.5 l/s and the surface area.

The results of the first measurements at OMA were compared to the literature and to the requirements mentioned in the ITER Vacuum Handbook where, according to different Vacuum Quality Classes (VQC), maximum steady state outgassing rates at a given temperature are stated.

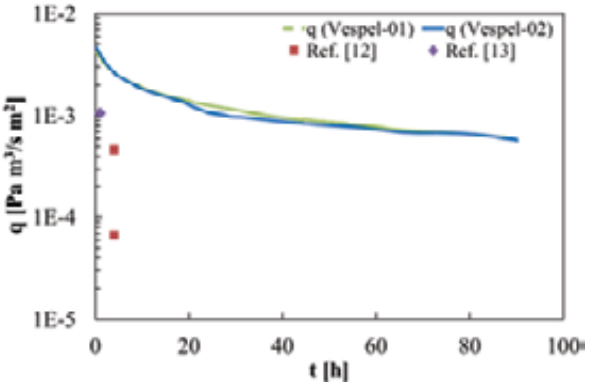

Fig. 2: Measured and literature outgassing rates of Vespel®.

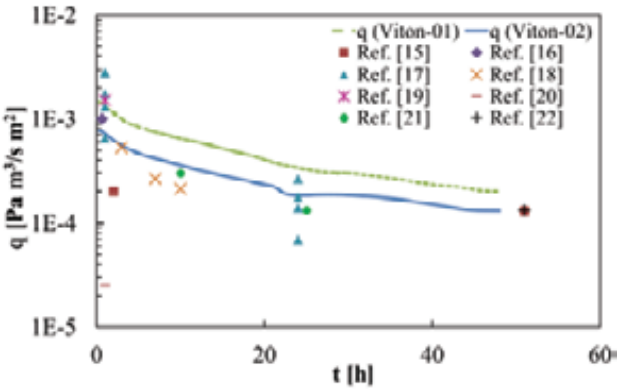

Fig. 3: Measured and literature outgassing rates of Viton® (01= plate, 02 = vacuum baked o-ring).

As shown in Figs. 2 and 3, Viton® and Vespel® both showed relatively high outgassing rates, so that they definitely need to be baked out before using them in a fusion high vacuum environment.

Partial pressure measurement for leak detection

Another topic of the work package is leak detection, for which mainly mass spectrometers are used. Thus, first measurements had already been performed with the high-resolution quadrupole mass spectrometer (GAM 400).

As a new device the auto-resonant ion trap mass spectrometer (ART-MS, Brooks 835 VQM) was bought, to check if it could be used instead of a quadrupole mass spectrometer in fusion applications. After some software issues had been solved, measurements of residual gases and a special gas for calibration were performed. First measurements with the ART-MS in comparison to a QMS (Pfeiffer Prisma) showed that the very fast scan time of the ART-MS leads to a decrease in accuracy.

VACU-TEC Work Package 4 (Pumps)

The research activities in 2012 under the VACU-TEC work package 4 focused mainly on the proof-of-principle testing of the new vacuum pumps proposed for the DIR (Direct Internal Recycling) concept at DEMO (reported elsewhere in this report, WP12-DAS-05 and WP12-SYS-01) [3, 4].

The cryo-based torus exhaust pumping system developed for ITER is considered to be a good solution for an experimental device such as ITER, but for DEMO, requirements are completely different due to the long-pulse operation, the higher flow rates involved and the requirement to be economically attractive. For this reason, a generic assessment of various pump types was performed (see WP11-DAS-HCD-FP) which identified a novel, promising pumping train concept that consists of a vapour diffusion pump as high vacuum pump [5] and a liquid ring pump as roughing pump, both with a tritium-compatible liquid metal as working fluid. For further reduction of the tritium inventories at DEMO, it is suggested to implement a metal foil pump, which is able to separate in a continuous process the hydrogenic species of the exhaust gas from the remaining components. The former fraction can then be recycled directly into the reactor and thus, it is called Direct Internal Recycling (DIR) concept.

Experimental manufacturability study of a Separator Pumping Module

Fig. 4: Photograph of the hydrogen plasma test of a metal foil module (left) and the set-up of the test module itself.

As preparation step for the development of a separator pumping module, a manufacturability study of a metal foil was performed: A thin vanadium metal foil was welded on a stainless steel tube and exposed to a hydrogen plasma in a special plasma chamber at CRPP Lausanne, to simulate the conditions in a ‘real’ DEMO separator pumping module. Welding,

leak-testing and heating of the metal foil was successful. Unfortunately the foil broke after a short time of operation. Nevertheless, valuable lessons have been learned and a new and optimized module will now be designed and manufactured for proof-of-principle testing in 2013. Figure 4 shows the test module built and tested in 2012.

Set-up of the THESEUS facility for testing the proposed solution/components

A test facility is needed that allows the proof-of-principle testing of all pumping components in a technical scale as well as the testing of the full DIR concept. This test facility is called THESEUS. The simulation of the fuel cycle pumping situation is a complex task with high demands on safety (hydrogen and deuterium handling), control and data acquisition. In 2012, the liquid ring pump was procured including all components necessary for the infrastructure. A dosing dome was built as central part of the facility. Also the old gas storage was completely updated and a safety system (for limiting the hydrogen inventory) was set up. Another safety system that was installed in THESEUS was the hydrogen survey system, that gives an alarm in case of a hydrogen leakage inside the facility, see Fig. 5.

In preparation of next year's work, the installation of a mercury content monitoring system is planned. This quality control system will be used for the measurement of the performance of the pump exhaust gas clean-up column and also to monitor the liquid ring pump housing against a mercury leakage.

In conclusion, the set-up of THESEUS is going on very well, the facility is on a good way to be ready for testing the coming fuel cycle components (liquid ring pump) in summer 2013.

Fig. 5: The hydrogen interlock system with the intermediate storage (left) and the safety relevant control system (right).

Conclusions

The EFDA GOT VACU-TEC training programme was continued in 2012, see Figure 6. It was demonstrated to be an excellent framework for young researchers to get a thorough education in fusion and be able to deliver own and self standing work for fusion research.

Staff:

K. Battes (trainee for WP2)
Chr. Day (for co-ordination)
A. Edinger
Th. Giegerich (trainee for WP4)
V. Hauer (mentor)
Th. Johann
P. Pfeil
H. Stump
J. Weinhold

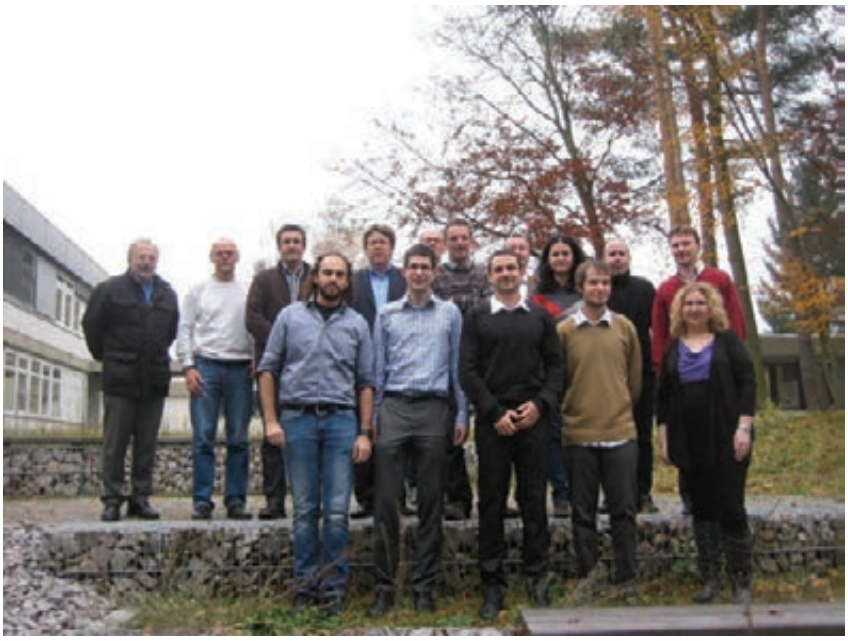

Fig. 6: 2nd network meeting of VACU-TEC, held in November 2012 at KIT. The front row features the five trainees.

Literature:

[1] K. Battes, V. Hauer, Outgassing rate measurement by using the difference method, DPG Spring Meeting, Berlin, Germany, Mar 2012.

[2] K. Battes, Chr. Day, V. Hauer, Outgassing measurement of fusion relevant materials, SOFT 2012, Liège, Belgium, Sept 2012.

[3] Chr. Day, The direct internal recycling concept to simplify the fuel cycle of a fusion power plant, SOFT 2012, Liege, Belgium, Sept. 2012.

[4] Th. Giegerich, Chr. Day, Fusionskraftwerke - Anforderungen und gegenwärtige technische Entwicklungen der Vakuumpumpsysteme, DPG Spring meeting, Berlin, Germany, Mar 2012.

[5] Th. Giegerich, Chr. Day, Conceptuation of a continuously working vacuum pump train for fusion power plants, SOFT 2012, Liege, Belgium, Sept. 2012

Acknowledgement

This work, supported by the European Communities under the contract of Association between EURATOM and Karlsruhe Institute of Technology, was carried out within the framework of the European Fusion Development Agreement. The views and opinions expressed herein do not necessarily reflect those of the European Commission.

Fuel Cycle –
Tritium Processing

R&D for Breeder Blanket and Tritium Technology (TLK contribution)

The work performed by the breeder blanket and tritium technology group of TLK in 2012 covered a wide range of activities tackling major tritium related issues for ITER and DEMO, such as highly tritiated water processing, and tritium permeation in the breeder blanket. In addition, management duties and coordination activities in the frame of the TBM Consortium of Associates were conducted. Advanced technology (membrane and membranes reactor) for tritium recovery from the helium-cooled blanket were also further developed.

Tritium Permeation Study in DEMO (WP12-DAS-02-T15-02)

Scope and objectives

Tritium related studies for DEMO have been re-launched by EFDA, focusing at first on the major and well known issue of tritium migration from the breeder blanket (BB) to the coolant, and the consecutive tritium losses into the environment. The generally accepted tritium losses from the BB to the environment shall be as low as 0.6 g/y (2 mg/d), which is more than 5 orders of magnitude lower than the tritium amount produced in the BB (360 g/d). However, both the BB and the steam generator comprise large surface areas with very thin walls operated at high temperatures that raise tritium permeation. An effective mitigation strategy has to be implemented, taking into account and balancing the size / efficiency of tritium extraction systems, and the feasibility / efficiency of anti-permeation barriers made of coatings or based on chemically controlled oxide layers.

Many studies were performed in the past and comprehensive literature exists. However, it is still very difficult to get a coherent and global understanding of the permeation issue, since all the previous studies focused on a single blanket concept. In this task, the objectives are i) to clarify the state of the art on key technologies (tritium process, anti-permeation barriers production), ii) to update materials database, iii) to consolidate operating parameters of the main loops, and iv) to produce a simulation tool enabling the direct comparison of different blanket concepts.

Achievements in 2012

A unique and generic simulation tool called FUS-TPC has been developed in collaboration with the Institute for neutron physics and reactor technology (INR). It is based on the SFR-TPC (Sodium cooled Fast Reactor - Tritium Permeation Code) developed in Italy that has been customised for fusion reactors. It encompasses the full tritium migration path, and computes tritium losses (permeation and leaks) considering the operating conditions of the three loops and the geometry/conditions of two interfaces (Fig. 1). Three slightly different variations of the code have been produced to reflect the particularity of the different blankets presently considered as serious options for the European DEMO: HCPB (helium cooled pebbles bed), HCLL (helium cooled lithium lead), and WCLL (water cooled lithium lead).

In parallel, a comprehensive literature review has been performed, to assess the maturity of tritium processes in helium / water / PbLi, and to consolidate input data concerning permeation in structural materials and efficiency of anti-permeation barriers. It has been firstly highlighted that most of the previous tritium migration studies are very difficult to compare (single blanket, different input data, different assumptions, different simplifications, many inconsistencies and error propagation via cross-references). For materials, the solubility measurements in PbLi are far to be conclusive (more than 2 orders of magnitude discrepancy exists between different authors), and anti-permeation barriers have not shown significant permeation reduction factor under relevant conditions. For tritium processes, it came out that tritium extraction from large water throughputs already exists (CANDU technology) but is energy

demanding and the technology from He cooled fission could be relevant for fusion tritium processes. On the other hand, the tritium extraction from PbLi suffer from a lack of maturity.

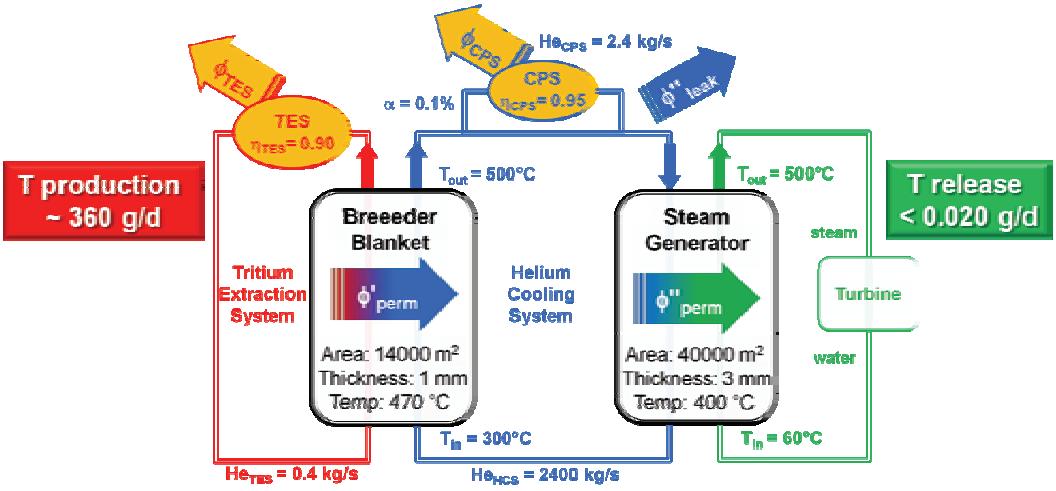

Fig. 1: Schematic view of tritium migration path from the breeder blanket to the environment (numbers are indicative and refer to HCPB DEMO concept).

Conclusion and perspectives

The work shall continue next year with some improvements of the numerical tool, taking into consideration gradients for temperatures and tritium generation rates, and advanced chemistry control (H_2 – H_2O addition) in the loops. These refinements will significantly impact the predicted tritium losses. A detailed assessment of the requirements for tritium processes and anti-permeation barriers shall follow, with the main objective to get a clear strategy for tritium migration mitigation (likely specific to blanket concepts) and a detailed road map for future R&D on materials and processes, for which more efforts will be needed.

Acknowledgement

This work, supported by the European Communities under the contract of Association between EURATOM and Karlsruhe Institute of Technology, was carried out within the framework of the European Fusion Development Agreement. The views and opinions expressed herein do not necessarily reflect those of the European Commission.

Experiments and Design of the Ancillary Systems of the EU Test Blanket Modules (F4E-OMF-331-Lot 2, F4E-FPA-372, and F4E-FPA-380-Action1)

Scope and objectives

Important milestones related to the European ITER test blanket modules (TBM) and their associated ancillary systems are forthcoming. The conceptual design and preliminary design reviews (CDR and PDR) are scheduled by ITER for end of 2013 and mid 2015, respectively. F4E launched in 2012 several framework contracts, strongly interconnected, and running in parallel over a 3-4 years period (Figure 2). The central activity is the design and engineering work under OMF-331, with Lot-2 focusing on the seven ancillary systems, stressing on integration in ITER buildings. In parallel, experimental campaigns under Framework Partnership Agreements (FPA-372, FPA-380) shall be performed to consolidate the technological choices, to demonstrate performances and size the different equipments.

Previous results

The present baseline for the ancillary systems is the outcome of the comprehensive technical review recently performed along F4E-GRT-09, and the first design of the tritium accountancy system (TAS) produced under F4E-GRT-254-Action2.

Achievements in 2012

Significant work has been invested to prepare the answers to the F4E calls, with very positive outcomes since all the contracts shown on Figure 2 have been awarded to the TBM Consortium of Associates (TBM-CA). Among the KIT project management responsibilities, TLK is acting as project leader for the full FPA-372 and for FPA-380-Action1, covering all the technologies of the ancillary systems: helium cooling, coolant purification (CPS), tritium extraction (TES) from solid breeder, PbLi loop, and tritium extraction & recovery from HCLL.

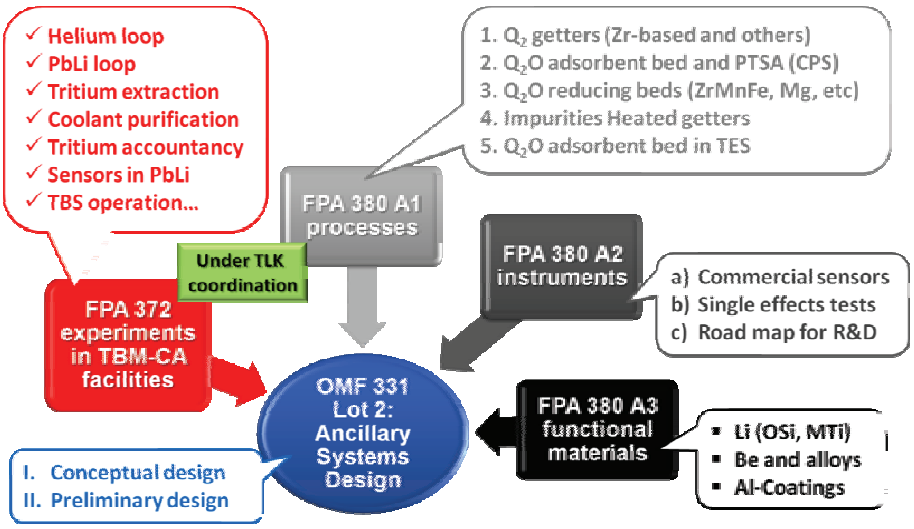

Fig. 2: Group of contracts awarded by F4E to the TBM Consortium of Associates in 2012 with TLK as project manager for the FPA-372 and FPA-380-A1 executions.

The FPA-372 is a F4E contract exclusive for utilising the unique features of the TBM-CA experimental facilities. In total, 17 facilities at KIT, CIEMAT, ENEA and CVR have been identified and 22 services (experimental campaigns) have been detailed. For KIT, the experimental campaigns will cover helium and cooling technology (in Flex, Gricaman, and Heloka), liquid metal flows (in Mekka) and tritium process and analytics (in TLK). At TLK, experiments have been defined on i) PERMCAT process included as baseline in CPS and TES, ii) dynamic tritium measurement using ionisation chambers as proposed for TAS, and also iii) tritium permeation through structural materials.

The FPA-380 was an open call but also awarded to TBM-CA. The Action 1 as proposed shall include experiments and modelling work on key technologies not covered by FPA-372. TLK will coordinate the whole contract, and dedicated experiments will focus on key tritium technology like metal getters and molecular sieves, respectively used to extract molecular tritium and tritiated water vapour from He, as it is foreseen in the baseline for TES and CPS.

Conclusion and perspectives

The contracts awarded in 2012 are important but only cover the frame and the conditions to implement the R&D work over the next three years. For experiments at TLK, it was agreed to perform in 2013 tests on the last technical scale PERMCAT reactor. The other proposed activities and services will be launched case by case in agreement with F4E.

PERMCAT Reactors Development towards Tritium Process in the Breeder Blanket (CoA)

Scope and objectives

Taking advantage of the simultaneous catalysed isotope exchange and permeation through a Pd-based membrane, the PERMCAT technology has proven to be efficient to process a large variety of tritiated streams. Originally developed and fully demonstrated for the tokamak exhaust processing, PERMCAT has been more recently proposed for tritium processing in the blanket, where it will have to deal with much higher total flow rates and very large helium dilution. To consolidate this choice, dedicated experiments are required and a reliable simulation tool is needed to size the PERMCAT reactors at the TBM and DEMO scales.

Previous results

A 1st technical scale multi-tube reactor based on a new design (Figure 3, left) produced with the KIT main workshop (TID) was especially constructed to study some geometrical effects on the performances. The optimum geometry has been afterwards duplicated to produce a 2nd reactor with increased processing capacity with two PERMCAT units (Fig. 3, middle).

Achievements in 2012

The latest tests have been carried out using these reactors. Firstly, each unit has been characterised separately, showing some discrepancies although they are identical from the design and manufacture point of view. Afterwards, working with 1, 2 or 3 units in series allowed measuring the increase in the decontamination factor when increasing the length of the reactor. The beneficial effect of increasing the temperature has also been quantified. Finally, increasing the helium inlet flow, a TES relevant feed stream has been tested (Figure 3, right) showing that the recovery rate drops dramatically at high flow rate. It is assumed that the kinetic of isotope exchange is the limiting step at high gas velocities.

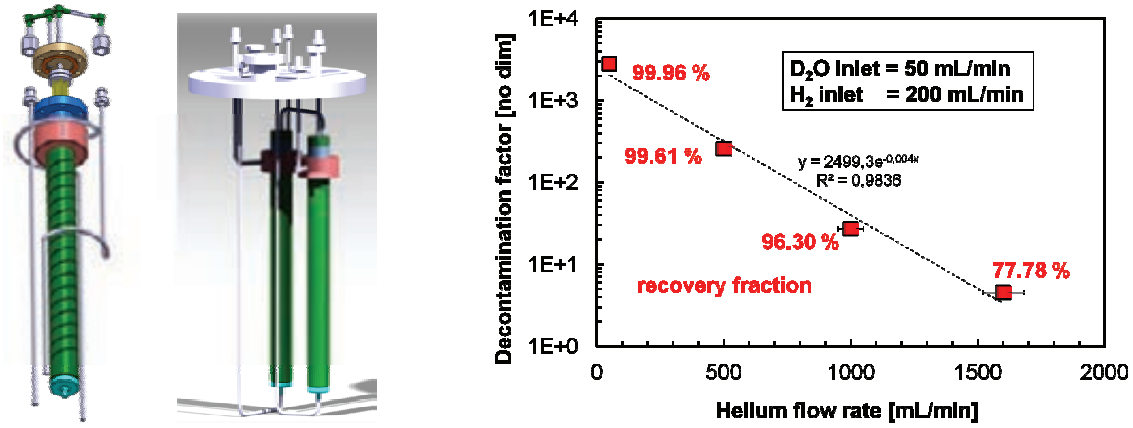

Fig. 3: CATIA view of the 3 PERMCAT units operated in series (left) and process performances up to high helium dilution as expected in the breeder blanket (right).

Conclusion and perspectives

These experimental results are the first important ones to consolidate the PERMCAT option for the TBM ancillary systems, and will also be very useful for benchmarking the PERMCAT simulation tool that is under finalisation in collaboration with the Akita University in Japan.

Zeolite Membranes as Front-end Process in Tritium Extraction System (CoA)

Scope and objectives

An improved DEMO fuel cycle should take benefit of advanced processes minimising tritium inventory and processing time. Newly developed zeolite (inorganic tritium compatible material) membranes appear attractive as front-end process when handling highly diluted tritium streams as encountered in the breeder blanket. A PhD work has been launched in collaboration with the Institute of thermal process engineering (TVT) to substantiate the use of zeolite membranes for tritium processing. Due to the rather limited selectivity anticipated for such membranes, a multi-stage process might be required to achieve high separations.

Previous results

For the first tests, a zeolite hollow fibre membrane provided by Ircelyon (France) is used. It is produced via plugging a porous asymmetric ceramic fibre with zeolite crystals so as to end up with a very thin (< 1 µm) defect free layer; the fibre is fixed in a membrane holder accommodated inside a permeation module (Figure 4, left). The permeability and selectivity measurements are performed in the new dedicated ZIMT facility (Zeolite Membrane for Tritium). ZIMT I was devoted to single gas tests. The first results highlighted very high H_2 permeability but a rather limited H_2/He ideal selectivity below 2.5 at 50°C (Figure 4, right).

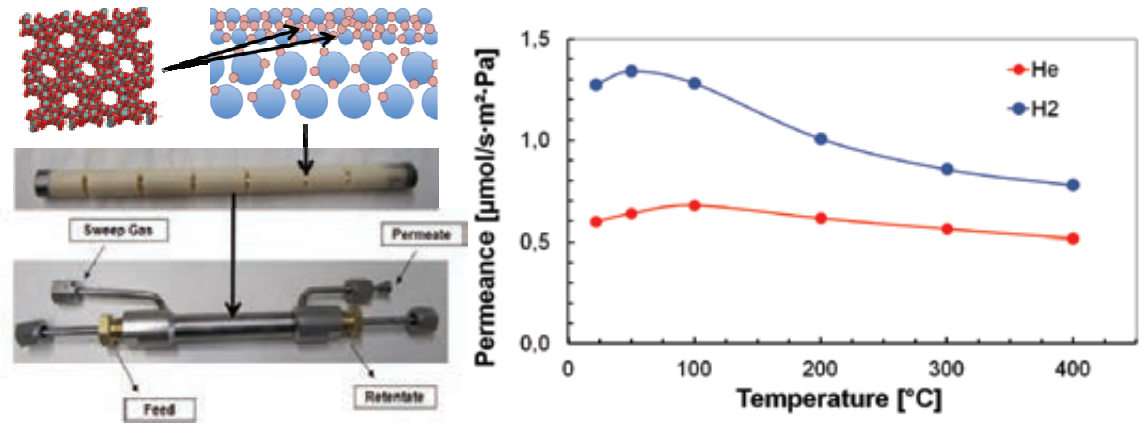

Fig: 4: Zeolite crystals inside the porous substrate (top left), membrane holder and permeation module (bottom left), and experimental results with single gases (right).

Achievements in 2012

The experimental rig has been improved (ZIMT II) to perform tests on binary mixtures of He and H_2. Higher H_2 permeation rates and higher selectivity (more than doubling compared to single gas tests) were observed when decreasing the H_2 concentration down to 20%. The experimental set-up has been further upgraded (ZIMT III – final stage) to characterise membranes under more relevant operating conditions, i.e. with the possibility to perform tests on ternary mixtures of He / H_2 / H_2O, with H_2 and H_2O concentrations down to traces, as encountered in tritium extraction from the solid breeder blanket.

In parallel, a numerical tool under Matlab simulating a multi-stage permeation cascade process has been completed (Figure 5). It allows calculating from the feed composition and the membrane selectivity the number of stages required to achieve a given enrichment factor. The total flow rate to be processed and the permeability values determine the necessary membrane surface and pressures of the process.

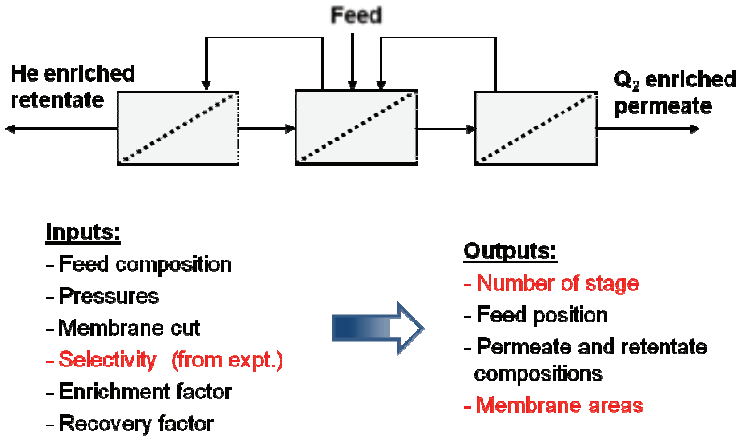

Fig. 5: Membrane cascade model (top) and inputs / outputs of the numerical simulation.

Conclusion and perspectives

The next experiments in ZIMT III will consider totally blanket relevant feed streams. It is anticipated higher selectivity for water vapour and for hydrogen, when it is present as traces. The experimental data gathered along the measurement phase will be finally implemented in the numerical toll to design such membrane cascade process for DEMO.

Staff:

O. Borisevich
D. Demange
E. Fanghänel
N. Gramlich
H. Moosmann
T.L. Le
K.H. Simon
M. Schwarz
R. Wagner
S. Welte

Literature:

[1] D. Demange, C.G. Alecu, N. Bekris, O. Borisevich, B. Bornschein, S. Fischer, N. Gramlich, Z. Köllö, T.L Le, R. Michling, F. Priester, M. Röllig, M. Schlösser, S. Stämmler, M. Sturm, R. Wagner, S. Welte " Overview of R&D at TLK for process and analytical issues on tritium management in breeder blankets of ITER and DEMO" Fusion Engineering and Design 87 (2012) 1206

[2] A. Ciampichetti, F.S. Nitti, A. Aiello, I. Ricapito, K. Liger, D. Demange, L. Sedano, C. Moreno, M. Succi "Conceptual design of tritium extraction system for the European HCPB test blanket module" Fusion Engineering and Design 87 (2012) 620

[3] S. Welte, D. Demange, R. Wagner, N. Gramlich "Development of a technical scale PERMCAT reactor for processing of highly tritiated water" Fusion Engineering and Design 87 (2012) 1045

[4] A.I.R.T. Parracho, D. Demange, S. Knipe, L.T. Le, K.H. Simon, S. Welte "Process of highly tritiated water desorbed from molecular sieve bed using PERMCAT" Fusion Engineering and Design 87 (2012) 1277

[5] A. Santucci, D. Demange, O. Goerke, T.L. Le, P. Pfeifer, S. Welte "Inactive commissioning of a micro channel catalytic reactor for highly tritiated water production in the CAPER facility of TLK" Fusion Engineering and Design 87 (2012) 547

[6] L.V. Boccaccini, U. Fischer, D. Demange “Blanket development for Fusion Power Plants” Poster at 2nd European Energy Conference, 17-20 April 2012, Maastricht, Netherlands.

[7] X. Lefebvre, D. Demange, O. Borisevich, M. Kind “Simulation of the performance of membrane cascade processes for gaseous separation using zeolite membranes” Poster at 12th International Conference on Inorganic Membranes, 9-13 July 2012, Enschede, Netherlands.

[8] D. Demange, O. Borisevich, B. Bornschein, M. Grasina*, T.L. Le, X. Lefebvre, R. Wagner, S. Welte “Membranes and catalytic membrane reactors as key components in the deuterium-tritium fuel cycle of future fusion machines” Poster at 12th International Conference on Inorganic Membranes, 9-13 July 2012, Enschede, Netherlands.

[9] O. Borisevich, D. Demange, M. Simplício, M. Pera-Titus, C.-H. Nicolas “Experimental study of binary mixture permeation of hydrogen and helium in nanocomposite MFI-alumina membrane for tritium processes” Poster at 9th Euromembrane, 23-27 September 2012, London, United Kingdom.

[10] D. Demange, O. Borisevich, N. Gramlich, R. Wagner, S. Welte “Zeolite membranes and palladium membrane reactor for tritium extraction from the breeder blankets of ITER and DEMO” Poster at 27th Symposium on Fusion Technology, 24-28 September, Liege, Belgium.

[11] B. Bornschein, C. Day, D. Demange, T. Pinna “Tritium management and safety issues in ITER and DEMO breeding blankets” Invited talk at 27th S Symposium on Fusion Technology, 24-28 September, Liege, Belgium.

[12] I. Ricapito, L.V. Boccaccini, P. Calderoni, A. Ciampichetti, D. Demange, Y. Poitevin “Tritium management in the European test blanket systems and extrapolation to Demo” Poster at 24th IAEA Fusion Energy Conference, 8-13 October 2012, San Diego, USA.

[13] C. Day, B. Bornschein, D. Demange, T. Giegerich, M. Kovari, B. Weyssow, R. Wolf “Technology Gaps for the Fuel Cycle of a Fusion Power Plant” Poster at 24th IAEA Fusion Energy Conference, 8-13 October 2012, San Diego, USA.

[14] M. Grasina M. Afonso, O. Borisevich, D. Demange, X. Lefebvre “Permeation of single gases and binary mixtures of hydrogen and helium through a MFI zeolite membrane for future application in nuclear fusion” submitted to Journal of Membrane Science.

Goal Oriented Training Programme "Tritium Technologies for the Fusion Fuel Cycle" (WP08-GOT-TRI-TOFFY (FU07-CT-2008-00047))

Background

The overall objective of the project is to support EU activities in the Deuterium-Tritium Fuel Cycle area for ITER by the training of six Early-Stage Researchers. The training programme is developed along existing projects in the framework of the European procurement package for the ITER Fuel Cycle with the main focus on water detritiation (WDS) and isotope separation (ISS) systems, detritiation processes, gas analytics and tritium measurements (see overview table: List of Work Packages). The participating Associations are: KIT, CEA, ENEA, HAS/MTA ATOMKI, MEdC/ICIT and CCFE.

No.	Title	Partners involved
1	Combined operation of WDS and ISS	KIT (ICIT, CCFE)
2	Detritiation of waste	CEA (KIT, CCFE)
3	Technologies for tritium recovery and trapping	ENEA (KIT, CCFE)
4	Calorimeter with large sample volume	MTA ATOMKI (KIT, CCFE)
5	Experimental Pilot Plant for Tritium and Deuterium Separation	ICIT (KIT, CCFE)
6	Participation in JET operation	CCFE (KIT)

The project was started in late 2008.

Status of project

The trainees from KIT, CEA, ENEA and CCFE finished their traineeship in 2012. The trainee from CEA and CCFE are now working at JET as scientists and thereby applying the skills they obtained during the TRI-TOFFY programme. The trainee from ENEA also remained in fusion science and is still doing research in the fusion programme at ENEA. The KIT trainee left the fusion field and is now working at a German company.

Having now 4 of the 5 trainees, who finished their traineeship, still working in the field of tritium fuel cycle is a great success of the programme.

Outlook

The Hungarian trainee will finish his traineeship in spring 2013. Until then he will submit at least one additional paper to an ISI reviewed journal. Whether he will stay in fusion will be decided in the near future.

Programme Coordinator:

B. Bornschein

Acknowledgement

This work, supported by the European Communities under the contract of Association between EURATOM and Karlsruhe Institute of Technology, was carried out within the framework of the European Fusion Development Agreement. The views and opinions expressed herein do not necessarily reflect those of the European Commission.

Safety

In-Vessel Dust Management: Development of In-Vessel Dust Measurement Techniques - Task 3 - Hot Dust Measurement (HDM) (F4E-2010-GRT-050 Task 3 (ES-AC))

The aim of the work is to investigate the feasibility of a recently proposed method to detect and measure the amount of beryllium dusts on hot surfaces of ITER. The method is to inject into ITER vacuum vessel some amount of hot steam, when the vessel is out of operation but still under high vacuum and high temperature. As typical, pressures under 10^{-6} mbar and temperature in the range of 300-400 °C have been indicated. There must be a hydrogen release due to reaction of Be dust and steam $Be+H_2O=BeO+H2$. Monitoring the amount of released hydrogen and the release dynamics, it is hoped to conclude on the amount of hot Be dust inside. Indicative hydrogen partial pressure range was 1-10 Pa.

The investigation had to be done with a Be-substitute, not with pure Be, because of safety reasons, while Be dust is toxic and requires special equipment to deal with. As a substitute, Al dust was chosen. In addition to chemical and physical similarity, aluminum has the same type of oxide film covering its metal surface, like beryllium. For both metals their oxide films protect free metal surface from further oxidation. The protection occurs up to 600-700 C. At higher temperatures the films crack and let the oxide molecules reaching metal surfaces. It means that in case the dust is oxidized, the proposed method won't work. However, the Be dust is produced in ITER under high vacuum and high temperature conditions and is kept then in oxygen-free atmosphere. So it is possible that metal dust in ITER vacuum volume is not oxidized, and can react with steam producing hydrogen. The question is if the hydrogen generation rate is high enough to make the released hydrogen detectable. Supposing that any collision of H_2O molecule with bare Be surface immediately produces H_2 molecule, one can calculate the hydrogen partial pressure rise rate under given conditions. With 10 kg of 10 μm Be powder and 10 Pa steam pressure, one obtains 0.2 Pa/s hydrogen generation rate which is quite detectable by modern mass-spectrometers.

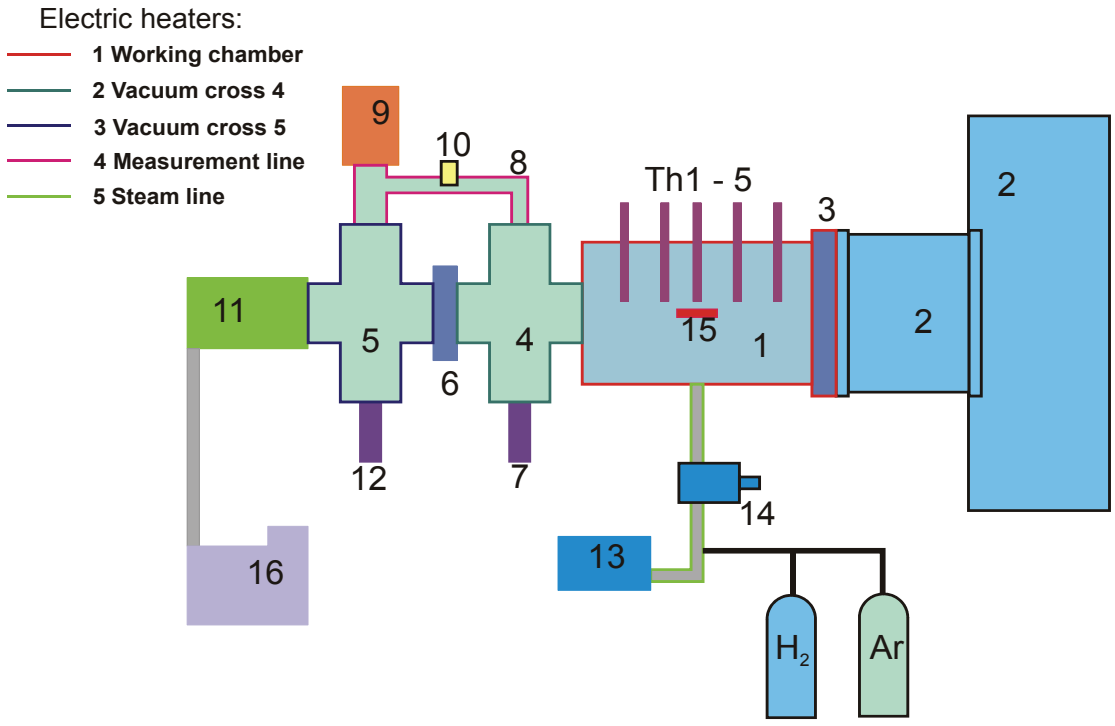

Fig. 1: Layout of the test facility. 1 – test chamber; 2 – glove box with oxygen-free atmosphere; 3 – sliding gate; 4 and 5 – vacuum connectors; 6 – sliding gate; 7 and 12 – precise pressure transducers; 8 – measuring line connecting the test chamber with mass-spectrometer head 9; 10 – dosing valve; 11 – turbomolecular pump; 13 – steam generator; 14 – steam injection valve; 15 – substrate to place the test dust sample; Th1-5 – thermocouples.

To investigate the feasibility of the proposed method, a test facility was designed and built up. Its scheme is shown in Fig. 1. Here 1 is test chamber where a dust sample is placed after its preparation in Ar-filled glove box 2 through the sliding gate 3. The test chamber is connected with a turbomolecular vacuum pump 11 through connectors 4 and 5 and sliding gate 6. Mass-spectrometer head 9 is connected with the test chamber through a measuring line 8 with a dosing valve 10. The temperature inside the chamber is controlled by an array of thermocouples 1-5. Testing was proceeded as follows. A dust sample was prepared in the glove box under oxygen-free atmosphere (high-purity Ar was used). The test chamber and all the vacuum parts were evacuated to about 10-7 mbar, then filled up with pure Ar to 1 bar pressure. After that the chamber was connected to the glove box and the sliding gate 3 opened. The prepared dust sample was put into the chamber, the gate was closed, and the facility was evacuated again to 10-7 mbar. The pressure inside the vacuum parts was controlled by two high-precision pressure sensors 7 and 12. Then the test chamber, vacuum connectors, and measuring line were heated electrically to the test temperature (200 to 400 C). After the pressure inside the test chamber was stabilized at some units of 10-7 mbar, the sliding gate 6 was closed, dosing valve 10 was opened, and necessary amount of steam prepared in the steam generator 13 was injected inside the test chamber through the steam injection valve 14. The content of the atmosphere in the test chamber was monitored by the quadrupole mass-spectrometer.

Several Al dusts were tested. First of all, commercially available dusts with dust particle size ranging from 1.5 to 44 μm were tested at 200 to 400 °C and steam pressure of 1-10 Pa. There was no hydrogen generation observed during all the observation period of about 30 min. Second, several Al dusts with reduced oxygen content were tested. The de-oxidation was made by milling a coarse 44 μm Al dust in a ball-mill with zirconium oxide jar and ball mills. The ball mill was placed inside the glove box and was operated in Ar atmosphere. The dust was immersed in pure ethanol and wet-milled 1, 5, and 10 hours, giving the resulting finesses of 20, 10, and 5 μm dusts, respectively.

Fig. 2: Coarse Al dust after wet milling in ethanol during 1 hour. Final fineness is about 20 μm.

All these dusts were tested at 370 °C under steam pressure ranging from 1 to 100 Pa. Exposure time was varied from 30 min to 80 hours. No hydrogen generation was observed.

Conclusions

The performed experiments have given negative results in a wide range of steam pressure in the temperature range of 300-400 °C. No hydrogen generation was observed for different Al dusts differing in their particle size and preparation methods.

These results can be consequence of either low reaction rate of Al surface oxidation by steam or insufficient de-oxidation of the tested dusts under preparation.

Final conclusion on the feasibility of the proposed method to detect/measure the amount of Be dust on hot surfaces by deliberate steam injection and measuring the hydrogen release dynamics cannot be made on the basis of the performed tests.

Outlook

Further modification of the facility can be proposed to test the both mechanisms:

1. Place the dust production/de-oxidation into the measuring chamber and make it at low pressures. This can exclude all 'parasitic' oxidation mechanisms and imitate a dust production under ITER conditions.
2. Extend the indicative pressures and temperatures to establish their detectable limits.

The dust can be produced inside the measuring chamber by exploding of thin wires, or arcing pure Al electrodes, or dispersing Al using hole cathode method. To provide it, only slight modifications are required: Sliding gate 3 must be replaced by a solid flange with one high-temperature port for wire exploding/arcing/hole cathode electrode. Additional tests must be performed to find out proper production conditions (wire length-diameter, explosion energy, arcing voltage-electrode geometry, hole cathode design and necessary VA-characteristic, etc). Another problem is the characterization of the produced dust (its particle size, how it is dispersed inside the chamber, etc.).

Staff:

A. Denkevits
B. Oechsler

Acknowledgement

This work was supported by Fusion for Energy under the grant contract No. F4E-2010-GRT-050 (ES-SF). The views and opinions expressed herein reflect only the author's views. Fusion for Energy is not liable for any use that may be made of the information contained therein.

Identification of a Beryllium Substitute-small/medium Scale Experiments - Physics Models Validation (F4E-GRT-371)

The aim of the work is to continue study of hydrogen/dust explosion hazard in case of severe accident in ITER. Previous studies concerned graphite and tungsten dusts as candidates for the material of the ITER first wall. The studies have shown that both dusts could be exploded, however the necessary ignition energy was irrelevantly high for ITER accidental conditions. Another ignition source was shown to be more realistic in this case, namely, a local hydrogen explosion event, which could be triggered by a weak ignition source like electric spark, can, in turn, initiate dust cloud explosion.

The presented work was aimed at further developing of a computer code DET3D capable to model pressure and temperature loads of hydrogen/dust explosions under ITER-relevant conditions. The code has demonstrated very good results at modelling graphite and tungsten dust explosions in hydrogen-containing air atmospheres. The code was validated against experimental results obtained in small- and medium-scale conditions. Now the concerned material is beryllium. Like previously, a series of experiments is planned to measure fundamental physical properties of the flames propagating in dust/hydrogen/air mixtures, which are used in phenomenological part of the code (dust/gas mixtures reactivity). Another experimental goal is to continue building up the experimental data base to validate the code. Beryllium dust is known to be toxic; dealing with Be dust requires special laboratory and equipment. It is hardly ever possible to test beryllium in medium-scale installations and looks unrealistic as far as large-scale tests are concerned. That is why for the study of the explosion properties of Be dust a proper Be substitute has been considered. For this, aluminum was selected. It is very similar to Be chemically and physically, mimicking Be not only in combustion but also in dispersion process, which is of great importance to determine spatial dust distribution and, hence, regimes of flame propagation.

Two series of experiments have been planned. Local explosion parameters like explosion indices (explosion pressure and pressure rise rate, limiting dust concentrations, limiting oxygen concentrations, ignition energy) were to be measured in a standard 20-l sphere of Siwek type (DUSTEX facility, small scale). Three Al dusts differing in dust particle size have been tested (1, 5, and 10 micron). Measurements of the dusts explosion indices must be complemented with tests of corresponding hybrid mixtures of the dusts and hydrogen.

The other experiments have been performed in two combustion tubes (PROFLAM facility) differing in their diameter, 15 and 35 cm, medium scale. Here only the most dangerous mixtures were to be tested, i.e. the finest dust. Flame propagation velocities were to be measured in PROFLAM I facility (15 cm id) in open geometry. Flame propagation regimes including flame acceleration were to be studied in PROFLAM II facility in closed geometry.

The tests were started with a coarse Al dust of 44 μm corn size. The dust was tested in DUSTEX facility both in pure air and in hydrogen-containing atmospheres. It was shown that the aluminum dust is much more reactive as C or W dust. As distinct from these dusts, Al dust belongs to the most explosive ST3 class. It generates about 10 bar explosion pressure and 1500 bar/s pressure rise rate. As distinct from both C and W dusts, its ignition energy is much lower, of the order of several joules. Next was tested 1 mm Al dust. It is even more explosive as compared to the coarse dust: explosion overpressure reaches 11 bar and pressure rise rate – 2500 bar/s. The test results are presented in Figs. 1 and 2.

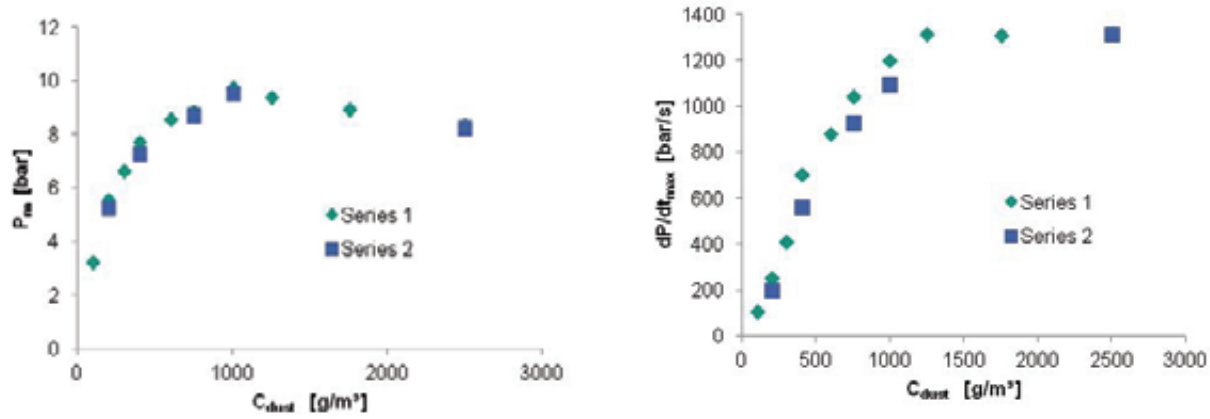

Fig. 1: Explosion indices (left – explosion pressure, right – explosion pressure rise rate) of 44 μm Al dust. Ignition energy 10 kJ.

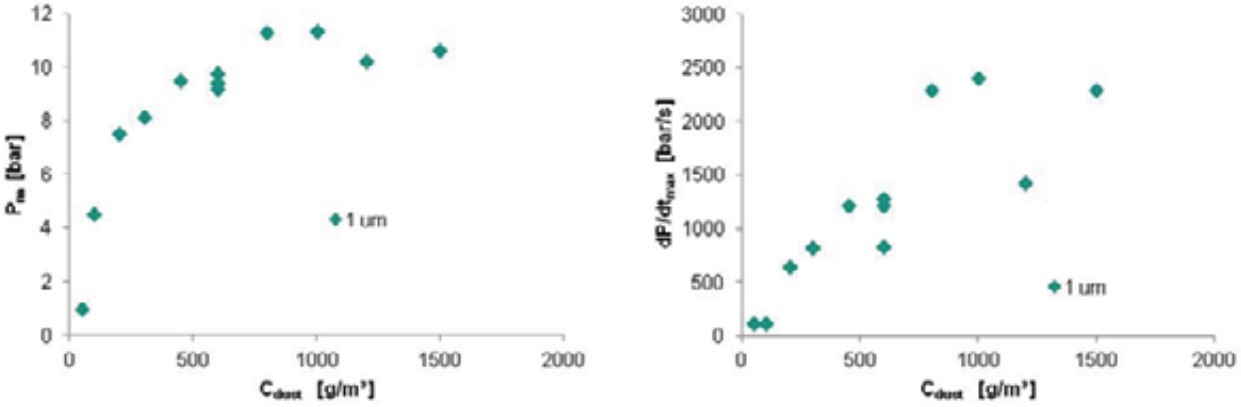

Fig. 2: Explosion indices (left – explosion pressure, right – explosion pressure rise rate) of 1 μm Al dust. Ignition energy 10 kJ.

Hybrid tests with the coarse Al dust have shown some similarities with the C and W dust hybrid mixtures. Al dust mixed with hydrogen can explode in two stages (Fig. 3), first stage, comparably fast, is hydrogen explosion, followed by a slower dust explosion stage. It illustrates the statement that Al dust can be ignited by a local hydrogen explosion. The two-stage regime occurs at lower dust/hydrogen concentrations. At higher fuel concentrations the explosions proceed in one stage which is much more severe than either hydrogen or pure dust explosion.

The tests on flame propagation velocity measurements were started in PROFLAM I facility. The tested dust was 1 μm corn size. The following concentration combinations have been tested:

C_{dust}=100 g/m^3 with H_2=8; 10; 12; 14; 16; 18; 20 vol. %;

C_{dust}=400 g/m^3 with H_2=8; 10; 12; 14; 16 vol. %;

C_{dust}=800 g/m^3 with H_2=8; 10; 12; 14 vol. %;

C_{dust}=1000 g/m^3 with H_2=8; 10; 12 vol. %

The tests have shown that the flame propagates in the hybrid mixtures faster than in corresponding hydrogen mixtures. It is the principal distinction from C and W hybrid mixtures. In case of tungsten the addition of the dust resulted in lower flame propagation; i.e. acted as a mitigation agent. In the tests with Al dust the flame propagated in accelerating regime producing local explosions. These events restricted us to lowering hydrogen concentrations in

testing with higher dust concentrations (see the list). The tests have been stopped to modify the facility to withstand with the explosion propagation regimes.

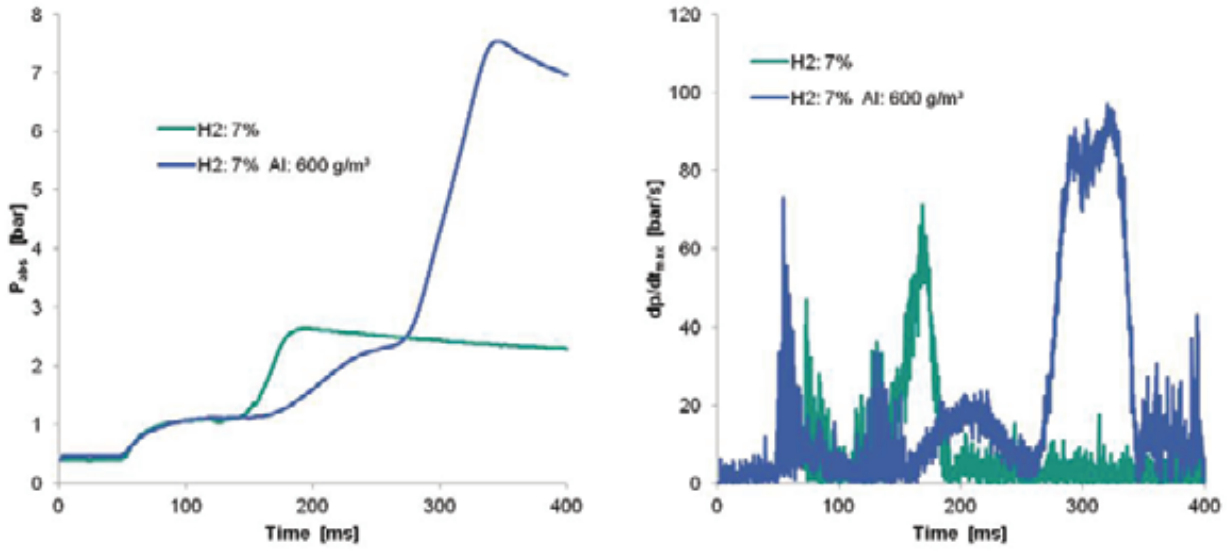

Fig. 3: Pressure evolution of pure hydrogen (blue lines) and hybrid H_2/Al dust (green lines) explosions in 20-l sphere. Hydrogen concentration is 7 vol. %; dust concentration is 600 g/m^3. On the right the corresponding pressure rise rates illustrating two-stage character of hybrid explosions.

Modelling of the performed experiments has been started proceeding in parallel with the tests. Now a new model of open geometry in combustion tube is being implemented in the code.

Conclusions

The measurements of explosion properties of Be-substituting Al dust in mixture with hydrogen have been started. First results have shown that hybrid Al/H_2 mixtures can propagate the flames in open geometries in flame accelerating regimes indicating that Be/H_2 hybrid mixture can be much more dangerous than C or W/H_2 mixtures resulting even in deflagration/detonation regimes.

Outlook

Modify PROFLAM facility to withstand explosive propagation regimes. Proceed with tests in PROFLAM II (closed geometry). Finalize small-scale tests in 20-l sphere.

Staff:

A. Denkevits
R. Redlinger
B. Hoess
F. Prestel
A. Veser (Pro-Science GmbH)

Acknowledgement

This work was supported by Fusion for Energy under the grant contract No. F4E-GRT-371. The views and opinions expressed herein reflect only the author's views. Fusion for Energy is not liable for any use that may be made of the information contained therein.

Supply of Documentation on Busbar Arcs Model Validation and Supporting Experiments (F4E-GRT-273)

Introduction

Experiences with tokamaks in operation indicate that electric arc accidents are not purely hypothetical [1]. Experience and calculations with the code system MAGS proved that damages due to shorts and arcs inside coils are basically restricted to the coils themselves. Here no safety relevant consequences are expected; nevertheless the replacement of a damaged coil typically means a considerable effort. Things are less clear for the coil current leads (busbars). In case the protection systems fail, mobile electric arcs at the busbars of the large fusion magnets may be able to penetrate the cryostat wall and threaten other safety relevant components in their neighbourhood. For ITER licensing this obviously requires an investigation of possible consequences of arcing. As full scale busbar arc experiments would be difficult, expensive and also of questionable significance due to the statistical behaviour of arcs, a numerical approach is advantageous. However, the real busbar arc behaviour is unknown and available models basing on plasma equations ask for unknown input parameters, therefore, experimental investigation seemed crucial for the development and later validation of a successful, realistic model. Experimental practice could also be helpful if full scale experiments cannot be avoided.

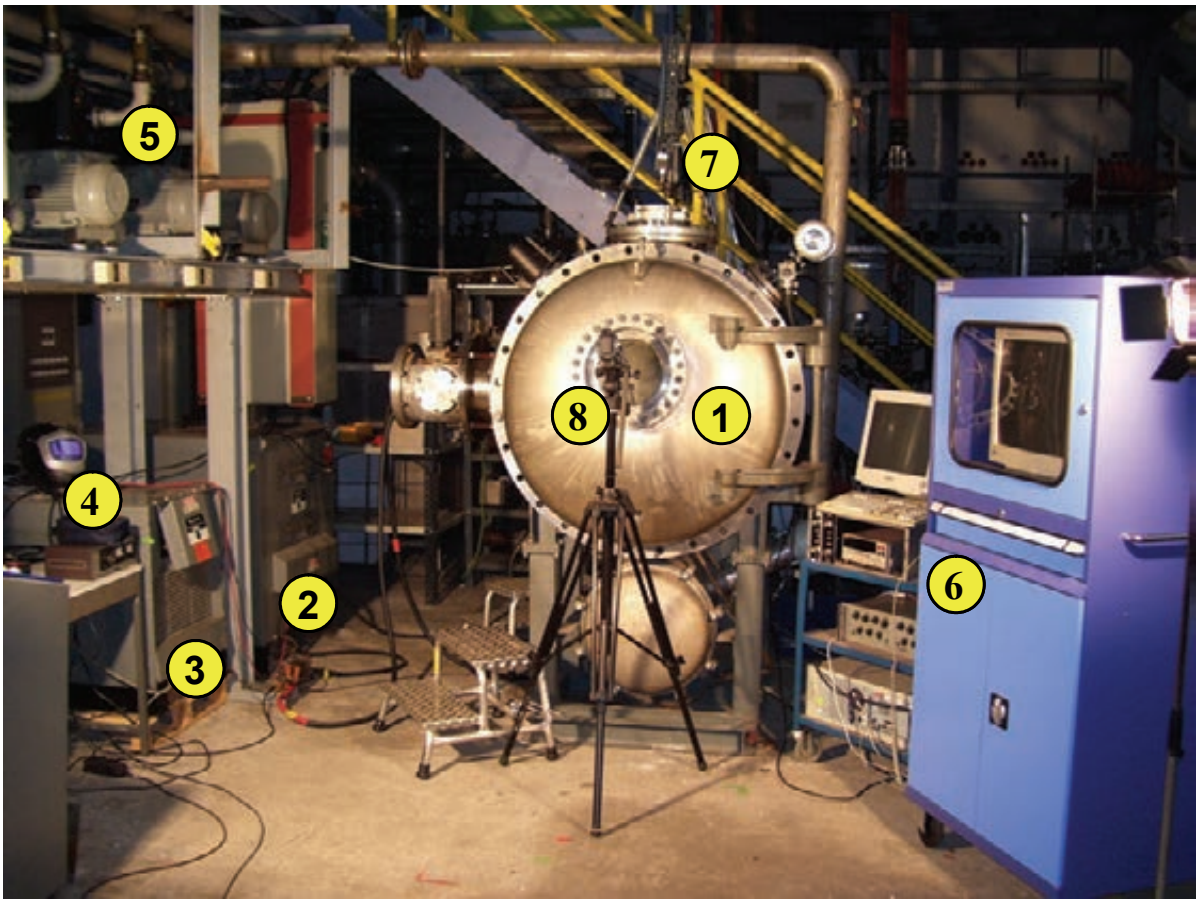

Fig. 1: VACARC device. 1) Vacuum vessel/arc chamber 2) large power converter 3) small power converter 4) Remote control for both power converters 5) Vacuum pumps 6) Data acquisition system 7) High speed camera 8) Canon camcorder.

The work in the frame of the task is basically documentation of the work that has been done previously. For subtask 1, the results of the VACARC experiments (2006-2011) were summarized and documented. The task of these small scale model experiments was to clarify

basic destruction and propagation behaviour of busbar arcs. A very simplified setup was used to investigate the impact of different parameters as polarity, insulation thickness, conductor scale and pressure. Then the setup was successively brought more similar to a real ITER busbar feeder line. The most important finding with regard to ITER is that long arcs tend to split spontaneously in the presence of conducting structures into two arcs in series while the current is carried by the structure in between. This will exclude extreme busbar arcs with lengths of several meters and powers of up to hundreds of megawatts in ITER. Another finding is that the ITER insulation is robust enough against arcing to avoid very fast arc propagation by cutting the insulation. The arc propagation speed is restricted to the burn down speed of the complete busbar metal and insulation cross section. It went also already clear that the inner ITER busbar feeder tube will not withstand a busbar arc. Moreover, these experiments were performed to provide a database for the development and later validation of a numerical model which is subject of subtask 2.

In subtask 2, the present status of the BUSARC development was summarized. BUSARC is a numerical model to simulate propagating arcs at VACARC model conductors. Instead of developing a new code from scratch, BUSARC was developed based on the proven MAGS code system formalisms and physical models. This way the work concentrates on the arc description only. As available arc simulation codes typically suffer from unproven assumptions and unknown input parameters, BUSARC is developed as a phenomenological model following the results of the accompanying VACARC experiments. So far only the model conductor side is modelled, the structure side is only formally implemented. Present BUSARC results agreement with data is good within the experimental spread, although still several experiments cannot be described accurately. The experimental background for positive polarity of the model conductor is still weak and needs to be improved for a realistic assessment of the code results for this case. The present status of BUSARC development will be documented in the frame of F4E-GRT-273. As next steps BUSARC is to be completed and validated using own model experiment results at different scales and afterwards to be extrapolated to full ITER scale.

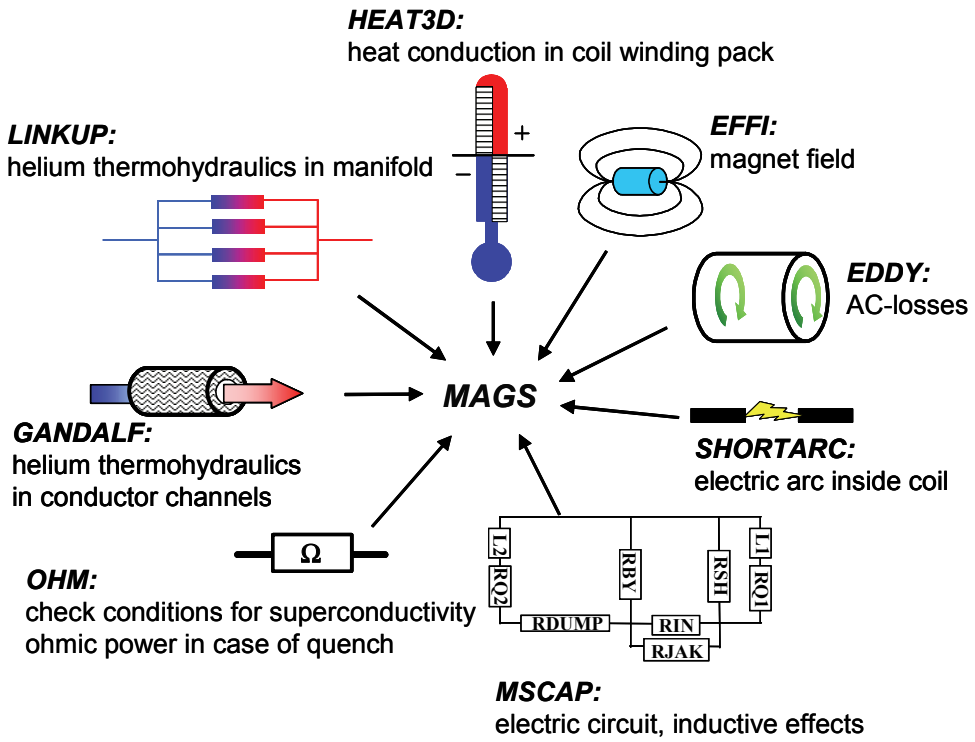

Fig. 2: Scheme of MAGS: main modules and capabilities.

Subtask 3 contains the advanced documentation of MAGS. While the MAGS code system is complete and works, the documentation still needs an upgrade to fulfil QA requirements that would allow using MAGS in ITER licensing. In order to achieve this goal, the MAGS documentation is to be revised using the INTRA documentation as a template. It will consist of the three volumes: (1) physical models, (2) user manual and (3) validation manual. These volumes are part of the deliverables of F4E-GRT-273. Volume 1 is completed; volumes 2+3 are expected to be completed in the frame of the foreseen time schedule of F4E-GRT-273 during 2013.

Staff:

V. Pasler
D. Klimenko

Literature:

[1] D. Bruce Montgomery (MIT), review of fusion system magnet problems, proc. of 13th IEEE symp. on fus. eng., Knoxville, TN, USA,Oct. 1989.

Acknowledgement

This work was supported by Fusion for Energy under the grant contract No. F4E-GRT-273. The views and opinions expressed herein reflect only the author's views. Fusion for Energy is not liable for any use that may be made of the information contained therein.

Appendix I: KIT Departments Contributing to the Fusion Programme

KIT Department	KIT Institut/Abteilung	Director	Ext.
Institute for Applied Materials - Applied Materials Physics	Institut für Angewandte Materialien – Angewandte Werkstoffphysik (IAM-AWP)	Prof. Dr. H.J. Seifert Dr. A. Möslang (Acting Head)	23895 24029
Institute for Applied Materials - Materials and Biomechanics	Institut für Angewandte Materialien - Werkstoff- und Biomechanik (IAM-WBM)	Prof. Dr. O. Kraft	24815
Institute for Applied Materials - Material Processing Technology	Institut für Angewandte Materialien - Werkstoffprozesstechnik (IAM-WPT)	Dr. R. Knitter (Acting Head)	22518
Institute for Pulsed Power and Microwave Technology	Institut für Hochleistungsimpuls- und Mikrowellentechnik (IHM)	Prof. Dr. J. Jelonnek	22440
Institute for Nuclear and Energy Technology	Institut für Kern- und Energietechnik (IKET)	Prof. Dr. T. Schulenberg	23450
Institute for Neutron Physics and Reactor Technology	Institut für Neutronenphysik und Reaktortechnik (INR)	Dr. R. Stieglitz	22550
Institute for Technical Physics	Institut für Technische Physik (ITeP)	Prof. Dr. M. Noe	23500
- Tritium Laboratory Karlsruhe	- Tritiumlabor Karlsruhe (TLK)	Dr. B. Bornschein	23239
Institute for Data Processing and Electronics	Institut für Prozessdatenverarbeitung und Elektronik (IPE)	Prof. Dr. M. Weber	25612

Appendix II: Fusion Programme Management Staff

Head of the Research Unit	Dr. K. Hesch	ext. 25460 e-mail: klaus.hesch@kit.edu
Secretariat:	Mrs. M. Spies	ext. 25461 e-mail: michelle.spies@kit.edu
Program Budget, Administration, Reports, EU-Affairs	BW. M. Henn	ext. 25547 e-mail: michael.henn@kit.edu
	Mrs. I. Pleli	ext. 28292 e-mail: ingrid.pleli@kit.edu
Blanket and Divertor Development, HELOKA, IFMIF, Structural Materials, CAD-Office ,Public Relations	Dr. D. Radloff	ext. 28750 e-mail: dirk.radloff@kit.edu
Fuel Cycle, Superconducting Magnets	Dr. M. Ionescu-Bujor	ext. 28325 e-mail: mihaela.ionescu-bujor@kit.edu
Plasma Heating Technology, Safety Studies, Neutronics, Physics	Dr. K. Hesch	ext. 25460 e-mail: klaus.hesch@kit.edu
Quality Management, Resource Loaded Planning, Document Management	Dr. J. Gafert	ext. 22923 e-mail: juergen.gafert@kit.edu
	Dr. I. Ignatiadis	ext. 85465 e-mail: Ioannis.ignatiadis@kit.edu
	Mrs. DI. Ch. Schweier	ext. 28325 e-mail: christine.schweier@kit.edu

Address: **Karlsruhe Institute of Technology**
Nuclear Fusion Programme Management

Post Office Box 3640, D - 76021 Karlsruhe / Germany

Telephone No: **0721-608-Extensions .....**

Telefax No: **0721-608-25467**

world wide web: **http://www.fusion.kit.edu/**

Appendix III: Publications

Plasma Wall Interaction

[1] Bazylev, B.; Arnoux, G.; Brezinsek, S.; Igitkhanov, Yu.; Lehnen, M.; Riccardo, V.
Modeling of the Impact of runaway electrons on the ILW in JET.
20th Internat.Conf.on Plasma Surface Interactions (PSI-20), Aachen, May 21-25, 2012

[2] Bazylev, B.; Coenen, J.W.; Pitts, R.A.; Philipps, V.
Modeling of tungsten armour damage under ITER-like transient heat loads.
15th Internat.Symp.on Flow Visualization, Minsk, Belarus, June 25-28, 2012; Proc.on CD-ROM

[3] Bazylev, B.; Landman, I.; Pestchanyi, S.; Igitkhanov, Y..; Pitts, R.A.; Putvinski, S.; Arnoux, G.; Brezinsek, S.; Lehnen, M.; Coenen, J. W.; Saibene, G.; Garkusha, I.; Makhlay, W.; Stangeby, P.; JET EFDA Contributors
Modelling of material damage and high energy impacts on Tokamak PFCs during transient loads.
24th IAEA Fusion Energy Conf., San Diego, Calif., October 8-13, 2012

[4] Bazylev, B.; Landman, I.; Pestchanyi, S.; Igitkhanov, Yu.; Pitts, R.A.; Putvinski, S.; Brezinsek, S.; Lehnen, M.; Coenen, J.W.; Philipps, V.
Modelling of material damage and high energy impacts on TOKAMAK PFCs during transient loads.
Alushta-2012 Internat.Conf.-School on Plasma Physics and Controlled Fusion and Adjoint Workshop 'Nano- and Micro-sized Structures in Plasmas', Alushta, UA,
September 17-22, 2012: Book of Abstracts S.3

[5] Bazylev, B.; Landman, I.; Pestchanyi, S.; Igitkhanov, Y..; Pitts, R.A.; Putvinski, S.; Arnoux, G.; Brezinsek, S.; Lehnen, M.; Coenen, J. W.; Saibene, G.; Garkusha, I.; Makhlay, W.; Stangeby, P.; JET EFDA Contributors
Modelling of material damage and high energy impacts on Tokamak PFCs during transient loads.
Compilation of the EFDA-JET Papers Presented at the 24th IAEA Fusion Energy Conf., San Diego, Calif., October 8-13, 2012; CD-ROM Paper ITR/P1-39

[6] Betz, M.; Caspers, F.; Gasior, M.; Thumm, M.
Status report and first results of the microwave LSW experiment at CERN.
8th Patras Workshop on Axions, WIMPs and WISPs, Chicago, Ill., July 18-22, 2012

[7] Borie, E.
Lamb shift in light muonic atoms - revisited.
Annals of Physics, 327(2012) S.733-763; DOI:10.1016/j.aop.2011.11.017

[8] Garkusha, L.; Aksenov, N.; Bazylev, B.; Chuvilo, A.; Chebotarev, V.; Landman, I.; Sadowski, M.; Makhlai, V.; Pestchanyi, S.; Skladnik-Sadowska, E.; Morgal, Y.
Analysis of tungsten dust generation under powerful plasma impacts simulating ITER ELMs and disruptions.
24th IAEA Fusion Energy Conf., San Diego, Calif., October 8-13, 2012; Abstracts on USB-Stick S.585

[9] Igitkhanov, Y.; Bazylev, B.; Landman, I.
Modelling of PFC life-time in tokamak fusion reactor.
KIT Scientific Reports, KIT-SR 7612 (Mai 2012)

[10] Igitkhanov, Yu.; Bazylev, B.; Boccaccini, L.
Analysis of W/Eurofer blanket lifetime in DEMO reactor.
20th Internat.Conf.on Plasma Surface Interactions (PSI-20), Aachen, May 21-25, 2012

[11] Igitkhanov, Yu.; Bazylev, B.; Landman, I.
CFC and W monoblock first wall concepts for fusion reactor.
Fusion Science and Technology, 62(2012) S.34-38

[12] Igitkhanov, Yu.; Bazylev, B.; Pestchanyi, S.; Boccaccini, L.
Plasma facing materials lifetime in fusion reactor.
27th Symp.on Fusion Technology (SOFT 2012), Liege, B, September 24-28, 2012

[13] Igitkhanov, Yu.; Bazylev, B.; Landman, I.
Plasma facing materials lifetime in fusion rector.
20th Topical Meeting on the Technology of Fusion Energy (TOFE 2012), Nashville, Tenn., August 27-31, 2012

[14] Igitkhanov, Yu.L.
The effect of non-Coulomb scattering of relativistic electrons on the generation of runaways in multicomponent plasma.
17th Joint EU-US Transport Task Froce Meeting, Padova, I, September 3-6, 2012

[15] Igitkhanov, Yu.L.
The effect of non-Coulomb scattering of relativistic electrons on the generation of runaways in multicomponent plasma.
Contributions to Plasma Physics, 52(2012) S.460-464; DOI:10.1002/ctpp.201210034

[16] Landman, I.; Bazylev, B.; Pitts, R.; Saibene, G.; Pestchanyi, S.; Putvinski, S.; Sugihara, M.
Radiation loads on the ITER first wall during massive gas injection.
27th Symp.on Fusion Technology (SOFT 2012), Liege, B, September 24-28, 2012

[17] Landman, I.S.; Pestchanyi, S.E.; Igitkhanov, Y.; Pitts, R.
Modelling of massive gas injection with tokamak code TOKES for mitigation of ITER disruptions.
20th Internat.Conf.on Plasma Surface Interactions (PSI-20), Aachen, May 21-25, 2012

[18] Makhlaj, V.A.; Garkusha, I.E.; Aksenov, N.N.; Byrka, O.V.; Chuvilo, A.A.; Landman, I.; Lebedev, S.I.; Shevchuk, P.B.
Plasma-surface interaction and mechanisms of dust production in ITER ELM simulation experiments with QSPA Kh-50.
Alushta-2012 Internat.Conf.-School on Plasma Physics and Controlled Fusion and Adjoint Workshop 'Nano- and Micro-sized Structures in Plasmas', Alushta, UA, September 17-22, 2012
Book of Abstracts S.67

[19] Pestchanyi, S.; Lehnen, M.; Huber, A.; Gerasimov, S.; Igitkhanov, Yu.; Landman, I.; JET EFDA Contributers
Analysis of energy cross-transport during MGI: JET experiments and TOKES simulations.
27th Symp.on Fusion Technology (SOFT 2012), Liege, B, September 24-28, 2012

[20] Pestchanyi, S.; Arkhipov, N.; Landman, I.; Poznyak, I.; Safronov, V.; Toporkov, D.
Simulation of tungsten plasma transport along magnetic field under ELM-like heat loads.
20th Internat.Conf.on Plasma Surface Interactions (PSI-20), Aachen, May 21-25, 2012

[21] Pestchanyi, S.; Lehnen, M.; Huber, A.; Landman, I. ; JET EFDA Contributors
Verification of TOKES simulations against the MGI experiments in JET.
Fusion Engineering and Design, 87(2012) S.1195-1200; DOI:10.1016/j.fusengdes.2012.02.107

[22] Polosatkin, S.; Astrelin, V.; Bazylev, B.; Beklemishev, S.; Burdakov, A.; Gavrilenko, D.; Huber, A.; Ivanov, A.; Ivanov, I.; Kalinin, P.; Kandaurov, I.; Kreter, A.; Landman, I.; Postupaev, V.; Sinitsky, S.; Shoshin, A.; Trunev, Yu.; Thumm, M.; Unterberg, B.
GDMT-T: Superconducting linear device for PMI studies.
Joint Conference on Open Magnetic Systems for Plasma Confinement (OS) and the International Workshop on Plasma Material Interaction Facilities for Fusion (PMIF), Tsukuba, J, August 27-31, 2012

[23] Zoletnik, S.; Buday, C.; Dunai, D.; Kalvin, S.; Krämer-Flecken, A.; Liang, Y.; Petravich, G.; Soldatov, S.; Pearson, J.; Refy, D.; TEXTOR Team
Dynamics of the electron density profile and plasma turbulence during the L-H transition and ELMs in TEXTOR.
39th European Physical Society Conf.on Plasma Physics, 16th International Congress on Plasma Physics, Stockholm, S, July 2-6, 2012

Physics: Heating and Current Drive – ECRH

[1] Erckmann, V.; Kasparek, W.; Plaum, B.; Lechte, C.; Petelin, M.I.; Braune, H.; Gantenbein, G.; Laqua, H.P.; Lubiako, L.; Marushchenko, N.B.; Michel, G.; Turkin, Y.; Weissgerber, M. ; W7-X ECRH-Teams at IPP Greifswald, IPF Stuttgart and KIT
Large scale CW ECRH systems: some considerations.
17th Joint Workshop on Electron Cyclotron Emission and Electron Cyclotron Resonance Heating (EC-17), Deurne, NL, May 7-10. 2012; Book of Abstracts S.70

[2] Erckmann, V.; Kasparek, W.; Plaum, B.; Lechte, C.; Petelin, M.I.; Braune, H.; Gantenbein, G.; Laqua, H.P.; Lubiako, L.; Marushchenko, N.B.; Michel, G.; Turkin, Y.; Weissgerber, M. ; W7-X ECRH-Teams at IPP Greifswald, IPF Stuttgart and KIT
Large scale CW ECRH systems: some considerations.
EPJ Web of Conferences, 32(2012) S.04006/1-6; DOI:10.1051/epjconf/20123204006

[3] Jelonnek, J.; Braune, H.; Dammertz, G.; Erckmann, V.; Flamm, J.; Gantenbein, G.; Hollmann, F.; Jonitz, L.; Kasparek, W.; Kern, S.; Laqua, H.P.; Lechte, C.; Legrand, F.; Leonhardt, W.; Litaer, G.; Michel, G.; Noke, F.; Purps, F.; Samartsev, A.; Schlaich, A.; Schmid, M.; Thumm, M.; Uhren, P.
Progress on 140 GHz, 1 MW, CW series gyrotrons for W7-X.
37th Internat.Conf.on Infrared, Millimeter and Terahertz waves (IRMMW-THz 2012), Wollongong, AUS, September 23-28, 2012; Proc.on USB-Stick

[4] Jelonnek, J.; Roy Choudhury, A.; Dammertz, G.; Flamm, J.; Gantenbein, G.; Illy, S.; Jin, J.; Kern, S.; Malygin, A.; Pagonakis, I.; Piosczyk, B.; Rzesnicki, T.; Samartsev, A.; Schlaich, A.; Schmid, M.; Thumm, M.
Status and prospects of gyrotron development at KIT.
3rd ITG Internat.Vacuum Electronics Workshop, Bad Honnef, August 20-21, 2012

[5] Laqua, H.P.; Braune, H.; Erckmann, V.; Gantenbein, G.; Jelonnek, J.; Michel, G.; Kasparek, W.; Kern, S.; Klinger, T.; Plaum, B.; Lechte, C.; Schmid, M.; Sunn Pederson, T.; Wolf, R.
Status of the Wendelstein 7-X project and the ECRH-system.
24th Joint Russian-German Meeting on ECRH and Gyrotrons, Nizhny Novgorod, Russia, June 11-15, 2012

[6] Wolf, R.C.; Baldzuhn, J.; Beidler, C.D..; Bluhm, T.; Braune, H.; Cardella, A.; Endler, M.; Erckmann, V.; Gantenbein, G.; Hathiramani, D.; Heimann, P.; Hennig, C.; Hirsch, M.; Jelonnek, K.; Kasparek, W.; König, R.; Kornejew, P.; Kroiss, H.; Krom, J.G.; Kühner, G.; Laqua, H.; Laqua, H.P.; Lechte, C.; Lewerentz, M.; Maier, J.; Michel, G.; Schacht, J.; Sunn Pedersen, T.; Thumm, M.; Turkin, Y.; Werner, A.; Zhang, D.; Zilker, M. ; Wendelstein 7-X Team
Preparation of steady-state operation of the Wendelstein 7-X stellarator.
24th IAEA Fusion Energy Conf., San Diego, Calif., October 8-13, 2012

[7] Drotzinger, S.; Fietz, W.H.; Heiduk, M.; Heller, R.; Hollik, M.; Lange, C.; Lietzow, R.; Richter, T.
Overview of results from Wendelstein 7-X HTS current lead testing.
27th Symp.on Fusion Technology (SOFT 2012), Liege, B, September 24-28, 2012

[8] Heller, R.; Drotzinger, S.; Fietz, W.H.; Kienzler, A.; Lietzow, R.; Richter, T.; Weiß, E.; Buscher, K.P.; Mönnich, T.; Rummel, T.
Status of series production and test of the HTS current leads for Wendelstein 7-X.
27th Symp.on Fusion Technology (SOFT 2012), Liege, B, September 24-28, 2012

[9] Rizzo, E.; Heller, R.; Savoldi Richard, L.; Zanino, R.
Analysis and performance assessment for a 68 kA HTS current lead heat exchanger.
IEEE Transactions on Applied Superconductivity, 22(2012) S.4801104/1-4
DOI:10.1109/TASC.2012.2182979

[10] Rummel, T.; Rißе, K.; Ehrke, G.; Rummel, K.; John, A.; Mönnich, T.; Buscher, K.P.; Fietz, W.H.; Heller, R.; Neubauer, O.; Panin, A.
The superconducting magnet system of the stellarator Wendelstein 7-X.
IEEE Transactions on Plasma Science, 40(2012) S.769-776; DOI:10.1109/TPS.2012.2184774

[11] Aloisio, M.; Van't Klooster, K.; Petelin, M.; Thumm, M.
Opportunities of phase controlled gyrotrons and quasi-optics for plasma fusion and space communication.
24th Joint Russian-German Meeting on ECRH and Gyrotrons, Nizhny Novgorod, Russia, June 11-15, 2012

[12] Arkhipov, A.; Louksha, O.; Sominski, G.G.; Kern, S.; Rzesnicki, T.
Development of X-ray diagnostics for determination of energy spectrum of electrons bombarding the collector.
24th Joint Russian-German Meeting on ECRH and Gyrotrons, Nizhny Novgorod, Russia, June 11-15, 2012

[13] Arkhipov, A.; Dvoretskaya, N.; Kern, S.; Louksha, O.; Rzesnicki, T.; Sominski, G.
Reconstruction of energy distributions in electron beams on the bases of Bremsstrahlung X-ray spectra.
4th Euro-Asian Pulsed Power Conf. (EAPPC 2012), 19th Internat.Conf.on High-Power Particle Beams (BEAMS 2012), Karlsruhe, September 30 - October 4, 2012; Book of Abstracts S.147; Proc.on CD-ROM

[14] Avramides, K.A.; Pagonakis, I.G.; Iatrou, C.T.; Vomvoridis, J.L.
EURIDICE: A code-package for gyrotron interaction simulations and cavity design.
17th Joint Workshop on Electron Cyclotron Emission and Electron Cyclotron Resonance Heating (EC-17), Deurne, NL, May 7-10. 2012; Abstract on USB-Stick

[15] Avramides, K.A.; Pagonakis, I.G.; Iatrou, C.T.; Vomvoridis, J.L.
EURIDICE: A code-package for gyrotron interaction simulations and cavity design.
EPJ Web of Conferences, 32(2012) S.04016/1-6; DOI:10.1051/epjconf/20123204016

[16] Avramides, K.A.; Ram, A.K.; Dumbrajs, O.; Alberti, S.; Tran, T.M.; Kern, S.
On the numerical scheme employed in gyrotron interaction simulations.
17th Joint Workshop on Electron Cyclotron Emission and Electron Cyclotron Resonance Heating (EC-17), Deurne, NL, May 7-10. 2012; Book of Abstracts S.80

[17] Avramides, K.A.; Ram, A.K.; Dumbrajs, O.; Alberti, S.; Tran, T.M.; Kern, S.
On the numerical scheme employed in gyrotron interaction simulations.
EPJ Web os Conferences, 32(2012) S.04017/1-6; DOI:10.1051/epjconf/20123204017

[18] Damyanova, M.; Balabanova, E.; Kern, S.; Illy, S.; Sabchevski, S.; Thumm, M.; Vasileva, E.; Zhelyazkov, I.
Simulation tools for computer aided design and numerical investigations of high-Power gyrotrons.
Journal of Physics: Conference Series, 356(2012) S.012044/1-4; DOI:10.1088/1742-6596/356/1/012044

[19] Flamm, J.; Jin, J.; Thumm, M.
New algorithm for field calculation in tapered gyrotron launchers with adaptive surface perturbation.
Internat.Vacuum Electronics and Vacuum Electron Sources Conf., Monterey, Calif., April 24-26, 2012; Proc.on USB-Stick; Piscataway, N.J. : IEEE, 2012 S.419-420
ISBN 978-1-4673-0187-9

[20] Flamm, J.H.
Diffraction and scattering in launchers of quasi-optical mode converters for gyrotrons.
Dissertation, Karlsruher Institut für Technologie 2012, Karlsruhe : KIT Scientific Publ., 2012 (Karlsruher Forschungsberichte aus dem Institut für Hochleistungsimpuls- und Mikrowellentechnik ; Bd.2); ISBN 978-3-86644-822-3

[21] Illy, S.; Kern, S.; Pagonakis, I.; Vaccaro, A.
Collector loading of the 2 MW, 170 GHz gyrotron for ITER in the case of power modulation.
4th Euro-Asian Pulsed Power Conf. (EAPPC 2012), 19th Internat.Conf.on High-Power Particle Beams (BEAMS 2012), Karlsruhe, September 30 - October 4, 2012; Book of Abstracts S.129; Proc. On CD-ROM

[22] Illy, S.; Kern, S.; Pagonakis, I.; Thumm, M.; Vaccaro, A.
Impact of gyrotron power modulation on the collector of the 2 MW, 170 GHz gyrotron for ITER.
39th IEEE Internat.Conf.on Plasma Science (ICOPS 2012), Edinburgh, GB, July 8-12, 2012
Abstract on USB-Stick

[23] Ioannidis, Z.C.; Tigelis, I.G.; Pagonakis, I.Gr.; Illy, S.; Schmid, M.
The eddy current effect on the transversal sweeping system of a gyrotron collector.
39th IEEE International Conference on Plasma Science (ICOPS 2012), Edinburgh, GB, July 8-13, 2012

[24] Jelonnek, J.; Alberti, S.; Erckmann, V.; Gantenbein, G.; Hogge, J.P.; Illy, S.; Jin, J.; Kern, S.; Pagonakis, I.; Piosczyk, B.; Rzesniki, T.; Thumm, M. ; W7-X Teams and EGYC Teams at KIT, EPFL-CRPP, HELLAS, IPF Stuttgart, IPF-CNR and IPP Greifswald
Development of advanced gyrotron.
20th Topical Meeting on the Technology of Fusion Energy (TOFE 2012), Nashville, Tenn., August 27-31, 2012

[25] Jelonnek, J.; Alberti, S.; Avramidis, K.; Braune, H.; Erckmann, V.; Gantenbein, G.; Hogge, J.P.; Illy, S.; Jin, J.; Kern, S.; Noke, F.; Pagonakis, I.; Piosczyk, B.; Purps, F.; Rzesnicki, T.; Samartsev, A.; Schlaich, A.; Schmid, M.; Thumm, M.
High power gyrotron development at KIT for ECH&CD of fusion plasmas.
Internat.Vacuum Electronics and Vacuum Electron Sources Conf., Monterey, Calif., April 24-26, 2012; Proc.on USB-Stick; Piscataway, N.J. : IEEE, 2012 S.111-112
ISBN 978-1-4673-0187-9

[26] Jelonnek, J.; Choudhury, A.R.; Dammertz, G.; Flamm, J.; Gantenbein, G.; Illy, S. ; Jin, J.; Kern, S.; Losert, M.; Malygin, A.; Pagonakis, I.; Piosczyk, B.; Rzesnicki, T.; Samartsev, A.; Schlaich, A.; Schmid, M.; Thumm, M.
Summary on gyrotron development at KIT.
24th Joint Russian-German Meeting on ECRH and Gyrotrons, Nizhny Novgorod, Russia, June 11-15, 2012

[27] Jin, J.; Flamm, J.; Jelonnek, J.; Kern, S.; Pagonakis, I.; Rzesnicki, T.; Thumm, M.
Synthesis of quasi-optical mode converter for $TE_{32,9}$ mode, 1 MW gyrotron.
4th Euro-Asian Pulsed Power Conf. (EAPPC 2012), 19th Internat.Conf.on High-Power Particle Beams (BEAMS 2012), Karlsruhe, September 30 - October 4, 2012, Book of Abstracts S.225; Proc.on CD-ROM

[28] Kern, S.; Gantenbein, G.; Illy, S.; Jelonnek, J.; Jin, J.; Pagonakis, I.; Piosczyk, B.; Rzesnicki, T.; Thumm, M.; Hogge, J.P.; Alberti, S.; Li, F.; Tran, M.Q.
EU gyrotron development for ITER: recent achievements and experimental results of the coaxial 2 MW gyrotron.
39th IEEE Internat.Conf.on Plasma Science (ICOPS 2012), Edinburgh, GB, July 8-12, 2012
Abstract on USB-Stick

[29] Kern, S.; Hogge, J.P.; Alberti, S.; Avramides, K.; Gantenbein, G.; Illy, S.; Jelonnek, J.; Jin, J.; Li, F.; Pagonakis, I.Gr.; Piosczyk, B.; Rzesnicki, T.; Thumm, M.K.; Tigelis, I.; Tran, M.Q. ; EU Home Team at EGYC
Experimental results and recent developments on the EU 2 MW 170 GHz coaxial cavity gyrotron for ITER.
17th Joint Workshop on Electron Cyclotron Emission and Electron Cyclotron Resonance Heating (EC-17), Deurne, NL, May 7-10. 2012; Book of Abstracts S.68

[30] Kern, S.; Hogge, J.P.; Alberti, S.; Avramides, K.; Gantenbein, G.; Illy, S.; Jelonnek, J.; Jin, J.; Li, F.; Pagonakis, I.Gr.; Piosczyk, B.; Rzesnicki, T.; Thumm, M.K.; Tigelis, I.; Tran, M.Q. ; EU Home Team at EGYC
Experimental results and recent developments on the EU 2 MW 170 GHz coaxial cavity gyrotron for ITER.
EPJ Web of Conferences, 32(2012) S.02011/1-8; DOI:10.1051/epjconf/20123204009

[31] Neudorfer, J.; Stock, A.; Flamm, J.; Hindenlang, F.; Gassner, G.; Munz, C.D.; Schneider, R.; Roller, S.
Numerical investigation of high-order gyrotron mode propagation in launchers at 170 GHz.
IEEE Transactions on Plasma Science, 40(2012) S.1512-1521; DOI:10.1109/TPS.2012.2191575

[32] Neudorfer, J.; Stock, A.; Munz, C.D.; Schneider, R.
Parallelization of a 3D high-order particle-in-cell method and numerical simulations of a 170 GHz resonator and launcher.
39th IEEE Internat.Conf.on Plasma Science (ICOPS 2012), Edinburgh, GB, July 8-12, 2012
Abstract on USB-Stick

[33] Pagonakis, I.G.; Illy, S.; Piosczyk, B.; Kern, S.; Jelonnek, J.; Avramides, K.A.; Hogge, J.P.
Numerical study of the effects of the magnetic axis misalignment in the Eu coaxial cavity gyrotron for ITER.
39th IEEE Internat.Conf.on Plasma Science (ICOPS 2012), Edinburgh, GB, July 8-12, 2012
Abstract on USB-Stick

[34] Roy Choudhury, A.; Kern, S.; D'Andrea, D.; Thumm, M.; Jelonnek, J.
Feasibility study of a 240 GHz 2.02.5 MW coaxial cavity gyrotron.
4th Euro-Asian Pulsed Power Conf. (EAPPC 2012), 19th Internat.Conf.on High-Power Particle Beams (BEAMS 2012), Karlsruhe, September 30 - October 4, 2012; Book of Abstracts S.120

[35] Roy Choudhury, A.; Kern, S.; D'Andrea, D.; Thumm, M.
Numerical investigations of parasitic oscillations in gyrotrons.
39th IEEE Internat.Conf.on Plasma Science (ICOPS 2012), Edinburgh, GB, July 8-12, 2012
Abstract on USB-Stick

[36] Rzesnicki, T.; Piosczyk, B.; Gantenbein, G.; Illy, S.; Jelonnek, J.; Jin, J.; Kern, S.; Pagonakis, I.; Schlaich, A.; Thumm, M.
2 MW coaxial-cavity pre-prototype gyrotron for ITER - recent experiments with the modified gyrotron setup.
37th Internat.Conf.on Infrared, Millimeter and Terahertz waves (IRMMW-THz 2012), Wollongong, AUS, September 23-28, 2012; Proc.on USB-Stick

[37] Schlaich, A.; Gantenbein, G.; Kern, S.; Thumm, M.
Dynamic spectral measurements on high-power oscillators in the millimeter-wave domain.
7th German Microwave Conf. (GeMiC 2012), Ilmenau, March 12-14, 2012
Conf.Proc.on USB-Stick; Ratingen : IMA e.V, 2012; ISBN 978-3-981668-5-6

[38] Schlaich, A.; Gantenbein, G.; Kern, S.; Thumm, M.
Systematic observation of time-dependent phenomena in the RF output spectrum of high power gyrotrons.
17th Joint Workshop on Electron Cyclotron Emission and Electron Cyclotron Resonance Heating (EC-17), Deurne, NL, May 7-10. 2012, Book of Abstracts S.67

[39] Schlaich, A.; Gantenbein, G.; Kern, S.; Thumm, M.
Systematic observation of time-dependent phenomena in the RF output spectrum of high power gyrotrons.
EPJ Web of Conferences, 32(2012) S.02011/1-8; DOI:10.1051/epjconf/20123204002

[40] Schmid, M.; Erckmann, V.; Gantenbein, G.; Illy, S.; Jelonnek, J.; Kern, S.; Legrand, F.; Samartsev, A.; Schlaich, A.; Rzesnicki, T.; Thumm, M.
Recent achievements on tests of series gyrotrons for W7-X and planned extensions at the KIT gyrotron test facility.
27th Symp.on Fusion Technology (SOFT 2012), Liege, B, September 24-28, 2012

[41] Stock, A.; Neudorfer, J.; Pfeiffer, M.; Schneider, R.; Fasoulas, S.; Munz, C.D.
A high-order discontinuous Galerkin-approach-based particle-in-cell method for the simulation of large scale plasma devices.
Scientific Computing in Electrical Engineering (SCEE 2012), Zürich, CH,
September 11-14, 2012

[42] Stock, A.; Neudorfer, J.; Munz, C.D.; Schneider, R.
Numerical simulation of a 30 GHz gyrotron resonator with a 3D high-order discontinuous Galerkin approach based particle-in-cell method.
39th IEEE Internat.Conf.on Plasma Science (ICOPS 2012), Edinburgh, GB, July 8-12, 2012
Abstract on USB-Stick

[43] Stock, A.; Neudorfer, J.; Schlaich, A.; Kern, S.; Schneider, R.; Munz, C.D.
Simulation of the W7-X 140 GHz gyrotron resonator with an explicit 3D discontinuous Galerkin method based particle-in-cell scheme.
39th European Physical Society Conf.on Plasma Physics, 16th International Congress on Plasma Physics, Stockholm, S, July 2-6, 2012

[44] Stock, A.; Neudorfer, J.; Riedlinger, M.; Pirrung, G.; Gassner, G.; Schneider, R.; Roller, S.; Munz, C.D.
Three-dimensional numerical simulation of a 30-GHz gyrotron resonator with an explicit high-order discontinuous-Galerkin-based parallel particle-in-cell method.
IEEE Transactions on Plasma Science, 40(2012) S.1860-1870; DOI:10.1109/TPS.2012.2195509

[45] Thumm, M.K.A.
Millimeter-wave RADAR systems with gyro-amplifiers.
Plasma Seminar, Budker Institute of Nuclear Physics (BINP), Novosibirsk, Russia,
6.November 2012

[46] Zohm, H.; Angioni, C.; Fable, E.; Federici, G.; Gantenbein, G.; Hartmann, T.; Lackner, K.; Poli, E.; Porte, L.; Sauter, O.; Tardini, G.; Ward, D.; Wischmeier, M.
On the physics guide lines for a Tokamak DEMO.
24th IAEA Fusion Energy Conf., San Diego, Calif., October 8-13, 2012

[47] Scherer, T.; Aiello, G.; Grossetti, G.; Meier, A.; Schreck, S.; Spaeh, P.; Strauss, D.; Vaccaro, A.; Siegel, M.; Meckbach, J.M.; Scheuring, A.
Reduction of surface losses of CVD diamond by passivation methods.
37th Internat.Conf.on Infrared, Millimeter and Terahertz waves (IRMMW-THz 2012),
Wollongong, AUS, September 23-28, 2012

[48] Aiello, G.; Grossetti, G.; Meier, A.; Scherer, T.; Schreck, S.; Spaeh, P.; Strauss, D.; Vaccaro, A.
CVD diamond Brewster window: feasibility study by FEM analysis.
17th Joint Workshop on Electron Cyclotron Emission and Electron Cyclotron Resonance Heating (EC-17), Deurne, NL, May 7-10. 2012

[49] Aiello, G.; Grossetti, G.; Meier, A.; Scherer, T.; Schreck, S.; Spaeh, P.; Strauss, D.; Vaccaro, A.
CVD diamond Brewster window: feasibility study by FEM analysis.
EPJ Web of Conferences, 32(2012) S.04014/1-6, DOI:10.1051/epjconf/20123204014

[50] Aiello, G.; Grossetti, G.; Meier, A.; Scherer, T.; Schreck, S.; Spaeh, P.; Strauss, D.; Vaccaro, A.
FEM analyses of a CVD diamond Brewster window.
37th Internat.Conf.on Infrared, Millimeter and Terahertz waves (IRMMW-THz 2012),
Wollongong, AUS, September 23-28, 2012

[51] Bagryansky, P.A.; Demin, S.P.; Gospodchikov, E.D.; Kovalenko, Yu.V.; Malygin, V.I.; Murakhtin, S.V.; Savkin, V.Ya.; Shalashov, A.G.; Smolyakova, O.B.; Solomakhin, A.L.; Thumm, M.; Yakovlev, D.V.
ECR heating system for the gas dynamic trap.
Joint Conference on Open Magnetic Systems for Plasma Confinement (OS) and the International Workshop on Plasma Material Interaction Facilities for Fusion (PMIF), Tsukuba, J, August 27-31, 2012

[52] Gantenbein, G.; Samartsev, A.; Dammertz, G.; Jelonnek, J.; Losert, M.; Schlaich, A.; Scherer, T.; Strauss, D.; Thumm, M.; Wagner, D.
Experimental investigations on a step-frequency tunable gyrotron with a diamond Brewster angle output window.
Workshop on Physics and Technology of RF Heating of Fusion Plasmas, Nara, J, December 11-13, 2012

[53] Gessner, R.; Aiello, G.; Grossetti, G.; Meier, A.; Ronden, D.; Spach, P.; Scherer, T.; Schreck, S.; Strauss, D.; Vaccaro, A.
The ITER EC H&CD upper launcher: design, analysis and testing of a bolted joint for the blanket shield module.
27th Symp.on Fusion Technology (SOFT 2012), Liege, B, September 24-28, 2012

[54] Henderson, M.A.; Darbos, C.; Albajar, F.; Alberti, S.; deBaar, M.; Baruah, U.; Becket, B.; Bigelow, T.; Bonicelli, T.; Bruschi, A.; caughman, J.; Chavan, R.; denisov, G.; Farina, D.; Fasel, D.; Gandini, F.; Gassman, T.; Goodman, T.P.; Hogge, J.P.; Jean, O.; Kajiwara, K.; Kasparek, W.; Kern, S.; Kobayashi, N.; Moro, A.; Nazare, C.; Oda, Y.; Omori, T.; Purohit, D.; Ramponi, G.; Rao, S.L.; Rasmussen, D.; Ronden, D.; Saibene, G.; Sakamoto, K.; Sauter, O.; Shapiro, M.; Scherer, T.; Singh, N.P.; Strauss, D.; Takahashi, K.; Temkin, R.; Zohm, H.
Progress in the ITER electron cyclotron system development.
17th Joint Workshop on Electron Cyclotron Emission and Electron Cyclotron Resonance Heating (EC-17), Deurne, NL, May 7-10. 2012

[55] Kasparek, W.; Holzhauer, E.; Kumric, H.; Plaum, B.; Wacker, R.; Zeitler, A.; Gantenbein, G.
Three-mirror resonator reflectivity measurement of plane and grooved surfaces: setup, options, results.
6th European Conf.on Antennas and Propagation (EUCAP 2012), Praha, CZ, March 26-30, 2012

[56] Omori, T.; Henderson, M.; Albajar, F.; Alberti, S.; deBaar, M.R.; Baruah, U.; Beckett, B.; Bigelow, T.; Bonicelli, T.; Bruschi, A.; Caughman, J.; Chavan, R.; Darbos, C.; Denisov, G.; Fasel, D.; Farina, D.; Gandini, F.; Gassman, T.; Goodman, T.P.; Hanson, G.; Hogge, J.P.; Jean, O.; Kajiwara, K.; Kasparek, W.; Kern, S.; Kobayashi, N.; Moro, A.; Nazare, C.; Oda, Y.; Paganakis, I.; Piosczyk, B.; Platania, P.; Plaum, B.; Poli, E.; Purohit, D.; Rampini, G.; Rao, S.L.; Rasmussen, D.; Ronden, D.M.S.; Saibene, G.; Sakamoto, K.; Scherer, T.; Shapiro, M.; Singh, N.P.; Strauss, D.; Sauter, O.; Takahashi, K.; Temkin, R.J.; Zohm, H.
Updates on ITER EC system design.
Workshop on Physics and Technology of RF Heating of Fusion Plasmas, Nara, J, December 11-13, 2012

[57] Scherer, T.; Aiello, G.; Grossetti, G.; Meier, A.; Schreck, S.; Spaeh, P.; Strauss, D.; Vaccaro, A.; Siegel, M.; Meckbach, J.M.; Scheuring, A.
Reduction of surface losses of CVD diamond by passivation methods.
37th Internat.Conf.on Infrared, Millimeter and Terahertz waves (IRMMW-THz 2012), Wollongong, AUS, September 23-28, 2012; Proc.on USB-Stick

[58] Scherer, T.A.; Meier, A.; Landmann, A.
Dielectric properties of natural grown Tourmaline at 100 GHz.
Proc.of 36th Internat.Conf.on Infrared, Millimeter and Terahertz Waves (IRMMW-THz 2011), Houston, Tex., October 2-7, 2011; Piscataway, N.J. : IEEE, 2011 S.213-214
ISBN 978-1-4577-0510-6; DOI:10.1109/irmmw-THz.2011.6104883

[59] Scherer, T.A.; Meier, A.; Strauss, D.; Schreck, S.; Takahashi, K.; Kajiwara, K.; Oda, Y.; Sakamoto, K.; Saibene, G.
Experimental analysis of the inserted waveguide CVD diamond window prototype for the ITER ECRH upper launcher.
Proc.of 36th Internat.Conf.on Infrared, Millimeter and Terahertz Waves (IRMMW-THz 2011), Houston, Tex., October 2-7, 2011; Piscataway, N.J. : IEEE, 2011 S.40-41
ISBN 978-1-4577-0510-6; DOI:10.1109/irmmw-THz.2011.6104800

[60] Scherer, T.A.; Strauss, D.; Vaccaro, A.; Aiello, G.; Schreck, S.; Meier, A.; Späh, K.; Takahashi, K.; Kajiwara, K.; Oda, Y.; Sakamoto, K.
ITER ECRH diamond window technology status.
Workshop on Physics and Technology of RF Heating of Fusion Plasmas, Nara, J, December 11-13, 2012

[61] Scherer, T.A.; Strauss, D.; Meier, A.; Nebel, C.
Microwave radiation losses in surface modified CVD diamond.
New Diamond and Nanocarbons Conf. (NDNC), San Juan, Costa Rica, May 20-24, 2012
Book of Abstracts

[62] Scherer, T.A.; Strauss, D.
The transmission of high-power microwaves via dielectric diamond windows: Design, qualification and first steps towards a broadband diamond window in the range of 30GHz to several THz for actual and future fusion devices.
76. Jahrestagung der DPG und DPG-Frühjahrstagung, Fachverband Dielektrische Festkörper, Berlin, D, 25.-30. März 2012
Verhandlungen der Deutschen Physikalischen Gesellschaft, R.6, B.47(2012), DF 17.7

[63] Schreck, S.; Aiello, G.; Meier, A.; Scherer, T.A.; Spaeh, P.; Strauss, D.; Vaccaro, A.
The ITEREC H&CD upper launcher: design develoments twards final design.
Workshop on Physics and Technology of RF Heating of Fusion Plasmas, Nara, J, December 11-13, 2012

[64] Shalashov, A.G.; Gospodchikov, E.D.; Smolyakova, O.B.; Bagryansky, P.A.; Malygin, V.I.; Thumm, M.
Auxiliary ECR heating system for the gas dynamic trap.
Physics of Plasmas, 19(2012), 052503; DOI:10.1063/1.4717757

[65] Shalashov, A.G.; Gospodchikov, E.D.; Smolyakova, O.B.; Bagryansky, P.A.; Malygin, V.I.; Thumm, M.
Auxiliary ECR heating system for the gas dynamic trap.
Problems of Atomic Science and Technology / Voprosy Atomnoj Nauki i Techniki, 82(2012) Nr.6, S.49-51

[66] Späh, P.; Aiello, G.; Goldmann, A.; Kleefeldt, K.; Kroiss, A.; Meier, A.; Obermeier, C.; Scherer, T.; Schreck, S.; Serikov, A.; Strauss, D.; Vaccaro, A.
Manufacturing studies of double wall components for the ITER EC H&CD upper launcher.
Fusion Engineering and Design, 87(2012) S.956-960; DOI:10.1016/j.fusengdes.2012.02.046

[67] Spaeh, P.; Aiello, G.; Gessner, R.; Grossetti, G.; Meier, A.; Scherer, T.; Schreck, S.; Serikov, A.; Strauss, D.; Vaccaro, A.; Weinhorst, B.
The ITER EC H&CD upper launcher: structural system.
27th Symp.on Fusion Technology (SOFT 2012), Liege, B, September 24-28, 2012

[68] Stober, J.; Reich, M.; Sommer, F.; Wagner, D.; Angioni, C.; Bock, A.; Giannone, L.; Herrmann, A.; Leuterer, F.; Maraschek, M.; Mlynek, A.; Monaco, F.; Müller, S.; Münich, M.; Poli, E.; Schubert, M.; Schütz, H.; Treutterer, W.; Zohm, H.; Meier, A.; Scherer, T.; Strauß, D.; Vaccaro, A.; Flamm, J.; Thumm, M.; Höhnle, H.; Kasparek, W.; Stroth, U.; Litvak, A.; Denisov, G.G.; Chirkov, A.V.; Tai, E.M.; Popov, L.G.; Nichiporenko, V.O.; Myasnikov, V.E.; Soluyanova, A.; Malygin, S.A.
ECRH on ASDEX upgrade. System status, feed-back control, plasma physics results.
17th Joint Workshop on Electron Cyclotron Emission and Electron Cyclotron Resonance Heating (EC-17), Deurne, NL, May 7-10. 2012; Book of Abstracts S.31

[69] Stober, J.; Bock, A.; Höhnle, H.; Reich, M.; Sommer, F.; Treutterer, W.; Wagner, D.; Giannone, L.; Herrmann, A.; Leuterer, F.; Monaco, F.; Maraschek, M.; Mlynek, A.; Müller, S.; Münich, M.; Poli, E.; Schubert, M.; Schütz, H.; Zohm, H. ; Kasparek, W.; Stroth, U.; Meier, A.; Scherer, T.; Strauß, D.; Vaccaro, A.; Flamm, J.; Thumm, M.; Litvak, A.; Denisov, G.G.; Chirkov, A.V.; Tai, E.M.; Popov, L.G.; Nichiporenko, V.O.; Myasnikov, V.E.; Soluyanova, A.; Malygin, S.A.; ASDEX Upgrade Team
ECRH on ASDEX upgrade. System status, feed-back control, plasma physics results.
EPJ Web of Conferences, 32(2012) S.02011/1-8; DOI:10.1051/epjconf/20123202011

[70] Strauss, D.; Aiello, G.; Chavan, R.; Cirant, S.; deBaar, M.; Farina, D.; Gantenbein, G.; Goodman, T.; Henderson, M.A.; Kasparek, W.; Kleefeldt, K.; Landis, J.D.; Meier, A.; Moro, A.; Platania, P.; Plaum, B.; Poli, E.; Ramponi, G.; Ronden, D.; Saibene, G.; Sanchez, F.; Sautter, O.; Scherer, T.; Schreck, S.; Serikov, A.; Sozzi, C.; Spaeh, P.; Vaccaro, A.; Zohm, H.
Preliminary design of the ITER ECH upper launcher.
27th Symp.on Fusion Technology (SOFT 2012), Liege, B, September 24-28, 2012

[71] Strauss, D.; Aiello, G.; Brusci, A.; Chavan, R.; Farina, D.; Figini, L.; Goodman, T.; Heemskerk, C.; Henderson, M.; Kasparek, W.; Koning, J.; Landis, J.D.; Meier, A.; Moro, A.; Platania, P.; Plaum, B.; Poli, E.; Ramponi, G.; Ronden, D.; Saibene, G.; Sanchez, F.; Sauter, O.; Scherer, T.; Schreck, S.; Serikov, A.; Sozzi, C.; Spaeh, P.; Vaccaro, A.; Zohm, H.
Progress of the ITER ECRH upper launcher development.
17th Joint Workshop on Electron Cyclotron Emission and Electron Cyclotron Resonance Heating (EC-17), Deurne, NL, May 7-10. 2012

[72] Strauss, D.; Scherer, T.A.
The transmission of high-power microwaves via diamond window: design, qualification and first steps towards a broadband diamond window in the range of 30 GHz to several THz.
New Diamond and Nanocarbons Conf. (NDNC), San Juan, Costa Rica, May 20-24, 2012
Book of Abstracts

[73] Thumm, M.
Mode conversion in overmoded waveguides and HE_{11} balanced hybrid mode.
Seminar Series on HE_{11} Waveguide Transmission, No.1, Budker Institute of Nuclear Physics (BINP), Novosibirsk, Russia, April 20, 2012

[74] Vaccaro, A.; Aiello, G.; Meier, A.; Scherer, T.; Schreck, S.; Späh, P.; Strauss, D.; Stober, J.; Wagner, D.; de Wit, H.G.M.
Grooved CVD diamond windows: grooves' profiles and structural simulations.
Proc.of 36th Internat.Conf.on Infrared, Millimeter and Terahertz Waves (IRMMW-THz 2011), Houston, Tex., October 2-7, 2011; Piscataway, N.J. : IEEE, 2011 S.383-384
ISBN 978-1-4577-0510-6; DOI:10.1109/irmmw-THz.2011.6105093

[75] Vaccaro, A.; Aiello, G.; Grossetti, G.; Meier, A.; Scherer, T.; Schreck, S.; Späh, P.; Strauß, D.; Saibene, G.; Cavinato, M.
The ITER EC H&CD upper launcher: EM disruption analysis.
27th Symp.on Fusion Technology (SOFT 2012), Liege, B, September 24-28, 2012

[76] Arzhannikov, A.V.; Burdakov, A.V.; Vyacheslavov, L.N.; Ivanov, I.A.; Ivantsivsky, M.V.; Kasatov, A.A.; Kuznetsov, S.A.; Makarov, M.A.; Mekler, K.I.; Polosatkin, S.V.; Postupaev, V.V.; Popov, S.S.; Sinitsky, S.L.; Sklyarov, V.F.; Thumm, M.K.A.
Diagnostic system for studying generation of subterahertz radiation during beam-plasma interaction in the GOL-3 facility.
Plasma Physics Reports, 38(2012) S.450-459; DOI:10.1134/S1063780X12050017

[77] D'Andrea, D.; Malygin, A.; Jelonnek, J.; Kern, S.; Schneider, R.; Stock, A.; Neudorfer, J.; Munz, C.D.
Start-up and parasitic modes analysis in TE_{31} cavity resonator.
39th European Physical Society Conf.on Plasma Physics, 16th International Congress on Plasma Physics, Stockholm, S, July 2-6, 2012

[78] Faillon, G.; Kornfeld, G.; Bosch, E.; Thumm, M.K.
High frequency electron tubes.
Handbook of Vacuum Electronics : Components and Devices
Moskva : Technosfera, 2011 S.17-95 (in russ.Sprache)

[79] Ginzburg, N.S.; Peskov, N.Yu.; Sergeev, A.S.; Zaslavsky, V.Yu.; Arzhannikov, A.V.; Kalinin, P.V.; Sinitsky, S.L.; Thumm, M.
Generation of powerful spatial coherent radiation in masers and lasers with two-dimensional distributed feedback.
37th Internat.Conf.on Infrared, Millimeter and Terahertz waves (IRMMW-THz 2012), Wollongong, AUS, September 23-28, 2012; Proc.on USB-Stick

[80] Ginzburg, N.S.; Peskov, N.Yu.; Sergeev, A.S.; Zaslavsky, V.Yu.; Arzhannikov, A.V.; Kalinin, P.V.; Sinitsky, S.L.; Thumm, M.
High selective two-dimensional Bragg resonators of planar geometry: Theoretical, computational, and experimental study.
Journal of Applied Physics, 112(2012) S.114504/1-12; DOI:10.1063/1.4766392

[81] Kalaria, P.C.; Kartikeyan, V.M.; Thumm, M.K.
Output system design for 170 GHz, 0.5 MW gyrotron for ECRH application.
Internat.Vacuum Electronics and Vacuum Electron Sources Conf., Monterey, Calif., April 24-26, 2012; Proc.on USB-Stick; Piscataway, N.J. : IEEE, 2012 S.501-502
ISBN 978-1-4673-0187-9

[82] Kartikeyan, M.V.; Thumm, M.
Feasibility studies of a 1.0 MW, 204 GHz CW, conventional cavity gyrotron for future thermonuclear fusion reactors.
37th Internat.Conf.on Infrared, Millimeter and Terahertz waves (IRMMW-THz 2012), Wollongong, AUS, September 23-28, 2012; Proc.on USB-Stick

[83] Kartikeyan, M.V.; Kalaria, P.C.; Thumm, M.
Studies on a 0.5 MW, 42 GHz CW, conventional cavity gyrotron.
37th Internat.Conf.on Infrared, Millimeter and Terahertz waves (IRMMW-THz 2012), Wollongong, AUS, September 23-28, 2012; Proc.on USB-Stick

[84] Malygin, A.; Illy, S.; Pagonakis, I.; Piosczyk, B.; Kern, S.; Weggen, J.; Thumm, M.; Jelonnek, J.; Avramides, K.; Ives, L.; Marsden, D.
Design and 3D simulations of a 10kW/28GHz gyrotron with a segmented emitter based on controlled-porosity reservoir cathodes.
4th Euro-Asian Pulsed Power Conf. (EAPPC 2012), 19th Internat.Conf.on High-Power Particle Beams (BEAMS 2012), Karlsruhe, September 30 - October 4, 2012
Book of Abstracts S.130; Proc. On CD-ROM

[85] Malygin, A.; Illy, S.; Pagonakis, I.; Piosczyk, B.; Kern, S.; Weggen, J.; Thumm, M.; Avramides, K.; Ives, L.; Marsden, D.
Design of a 10kW/28GHz gyrotron with a segmented emitter using controlled-porosity resevoir cathodes.
Internat.Vacuum Electronics and Vacuum Electron Sources Conf., Monterey, Calif., April 24-26, 2012; Proc.on USB-Stick
Piscataway, N.J. : IEEE, 2012 S.331-332; ISBN 978-1-4673-0187-9

[86] Malygin, A.; Illy, S.; Pagonakis, I.; Piosczyk, B.; Kern, S.; Weggen, J.; Thumm, M.; Avramides, K.; Ives, L.; Marsden, D.
Design of a 10kW/28GHz gyrotron with a segmented emitter using controlled-porosity resevoir cathodes.
3rd ITG Internat.Vacuum Electronics Workshop, Bad Honnef, August 20-21, 2012

[87] Malygin, A.; Illy, S.; Pagonakis, I.; Piosczyk, B.; Kern, S.; Weggen, J.; Thumm, M.; Avramides, K.; Ives, L.; Marsden, D.
Investigations towards a segmented emitter based on controlled-porosity reservoir cathodes for gyrotrons.
24th Joint Russian-German Meeting on ECRH and Gyrotrons, Nizhny Novgorod, Russia, June 11-15, 2012

[88] Ortwein, P.; Stock, A.; Neudorfer, J.; Kern, S.; Illy, S.; Schneider, R.; Jelonnek, J.; Munz, C.D.
High-accurate numerical full-wave simulation of an auto-modulation phenomenon for a 30 GHz gyrotron resonator.
4th Euro-Asian Pulsed Power Conf. (EAPPC 2012), 19th Internat.Conf.on High-Power Particle Beams (BEAMS 2012), Karlsruhe, September 30 - October 4, 2012; Proc.on CD-ROM
Karlsruhe : Karlsruhe Institute of Technology, 2012

[89] Petelin, M.; Bongers, W.; Bruschi, A.; Erckmann, V.; Kasparek, W.; Olstad, R.; Sakamoto, K.; Thumm, M.
Problems of high-power millimeter wave beam control.
4th Internat.Workshop on Far-Infrared Technologies (IW-FIRT 2012), Fukui, J, March 7-9, 2012
Proc.on CD-ROM Paper 7a-4; University of Fukui, 2012

[90] Samartsev, A.; Gantenbein, G.; Jelonnek, J.; Malygin, A.; Thumm, M.
Multimode numerical code for simulation of gyrotron interaction with inclusion of particle-in-cell method.
4th Euro-Asian Pulsed Power Conf. (EAPPC 2012), 19th Internat.Conf.on High-Power Particle Beams (BEAMS 2012), Karlsruhe, September 30 - October 4, 2012; Proc.on CD-ROM
Karlsruhe : Karlsruhe Institute of Technology, 2012

[91] Schlaich, A.; Gantenbein, G.; Kern, S.; Thumm, M.
Recent improvements in time-variant gyrotron RF output spectrum monitoring.
39th IEEE Internat.Conf.on Plasma Science (ICOPS 2012), Edinburgh, GB, July 8-12, 2012

[92] Stock, A.; Neudorfer, J.; Schneider, R.; Roller, S.; Munz, C.D.
A full-wave 3D high-order discontinuous-Galerkin-method-based particle-in-cell code for the simulation of high-power gyrotron resonators.
4th Euro-Asian Pulsed Power Conf. (EAPPC 2012), 19th Internat.Conf.on High-Power Particle Beams (BEAMS 2012), Karlsruhe, September 30 - October 4, 2012; Book of Abstracts S.238; Proc.on CD-ROM; Karlsruhe : Karlsruhe Institute of Technology, 2012

[93] Thumm, M.
Development and applications of THz gyrotrons.
Plasma Seminar, Budker Institute of Nuclear Physics (BINP), Novosibirsk, Russia, 13.März 2012

[94] Thumm, M.
Laboratory of advanced research on millimeter and terahertz radiation.
Wissenstransfer - die neue Kernaufgabe von Hochschulen, Deutsch-russisches Symp., Kassel, 24.-25.April 2012

[95] Thumm, M.
Results of laboratory of advanced research on millimeter and terahertz radiation.
Plasma Seminar, Budker Institute of Nuclear Physics, Novosibirsk, Russia, December 11, 2012

[96] Thumm, M.
State-of-the-art of high power gyro-devices and free electron masers: update 2011.
KIT Scientific Reports, KIT-SR 7606 (April 2012)

[97] Wagner, D.; Stober, J.; Leuterer, F.; Monaco, F.; Müller, S.; Münich, M.; Schubert, M.; Schütz, H.; Zohm, H.; Thumm, M.; Scherer, T.; Meier, A.; Strauss, D.; Gantenbein, G.; Flamm, J.; Kasparek, W.; Höhnle, H.; Lechte, C.; Litvak, A.G.; Denisov, G.G.; Chirkov, A.; Popov, L.G.; Nichiporenko, V.O.; Myasnikov, V.E.; Tai, E.M.; Solyanova, E.A.; Malygin, S.A. ; ASDEX Upgrade Team
Operation of the multifrequency ECRH system at ASDEX upgrade.
Proc.of 36th Internat.Conf.on Infrared, Millimeter and Terahertz Waves (IRMMW-THz 2011), Houston, Tex., October 2-7, 2011; Piscataway, N.J. : IEEE, 2011 S.468-470
ISBN 978-1-4577-0510-6; DOI:10.1109/irmmw-THz.2011.6105142

[98] Wagner, D.; Stober, J.; Honecker, F.; Leuterer, F.; Monaco, F.; Müller, S.; Münich, M.; Reich, M.; Schubert, M.; Schütz, H.; Treutterer, W.; Zohm, H.; Thumm, M.; Scherer, T.; Meier, A.; Gantenbein, G.; Jelonnek, J.; Kasparek, W.; Plaum, B.; Höhnle, H.; Lechte, C.; Litvak, A.G.; Denisov, G.G.; Chirkov, A.; Popov, G.; Nichiporenko, V.O.; Myasnikov, V.E.; Tai, E.M.; Solyanova, E.A.; Malygin, S.A. ; ASDEX Upgrade Team
The broadband multi-megawatt ECRH system at ASDEX upgrade.
37th Internat.Conf.on Infrared, Millimeter and Terahertz waves (IRMMW-THz 2012), Wollongong, AUS, September 23-28, 2012

[99] Wagner, D.; Stober, J.; Honecker, F.; Leuterer, F.; Monaco, F.; Müller, S.; Münich, M.; Reich, M.; Schubert, M.; Schütz, H.; Treutterer, W.; Zohm, H.; Thumm, M.; Scherer, T.; Meier, A.; Gantenbein, G.; Jelonnek, J.; Kasparek, W.; Plaum, B.; Höhnle, H.; Lechte, C.; Litvak, A.G.; Denisov, G.G.; Chirkov, A.; Popov, G.; Nichiporenko, V.O.; Myasnikov, V.E.; Tai, E.M.; Solyanova, E.A.; Malygin, S.A. ; ASDEX Upgrade Team
The broadband multi-megawatt ECRH system at ASDEX upgrade.
37th Internat.Conf.on Infrared, Millimeter and Terahertz waves (IRMMW-THz 2012), Wollongong, AUS, September 23-28, 201; Proc.on USB-Stick

Magnets and Affiliated Components

[1] Savoldi Richard, L.; Bonifetto, R.; Heller, R.; Zanino, R. Thermal-hydraulic simulation of 80 kA safety discharge in the ITER toroidal field model coil (TFMC) using the 4C code.
IEEE Transactions on Plasma Science, 40(2012) S.782-787; DOI:10.1109/TPS.2012.2184839

[2] Rizzo, E.; Bauer, R.; Heller, R.; Savoldi Richard, L.; Zanino, R.
1-D thermal-electrical analysis of the HTS current leads for the magnet system nof ITER.
27th Symp.on Fusion Technology (SOFT 2012), Liege, B, September 24-28, 2012

[3] Bagrets, N.; Weiss, E.; Westenfelder, S.; Weiss, K.P.
Cryogenic test facility CryoMaK.
IEEE Transactions on Applied Superconductivity, 22(2012) S.9501204/1-4
DOI:10.1109/TASC.2011.2176902

[4] Bagrets, N.; Schwarz, M.; Barth, C.; Weiss, K.P.
Thermal conductivity of materials used for preparation of the hybrid layered conductors based on high temperature conductors based on high temperature superconductors.
Cryogenic Engineering Conf.and Internat.Cryogenic Materials Conf. (CEC-ICMC), Spokane, Wash., June 13-17, 2011

[5] Bagrets, N.; Schwarz, M.; Barth, C.; Weiss, K.P.
Thermal conductivity of materials used for preparation of the hybrid layered conductors based on high temperature conductors based on high temperature superconductors.
Balachandran, U. [Hrsg.]; Advances in Cryogenic Engineering : Transactions of the Internat.Cryogenic
Materials Conf., Spokane, Wash., June 13-17, 2011; Melville, N.Y. : AIP, 2012 S.281-285
(AIP Conference Proceedings ; 1435); (Advances in Cryogenic Engineering ; 58)
ISBN 978-0-7354-1022-0

[6] Bagrets, N.; Goldacker, W.; Jung, A.; Weiss, K.P.
Thermal properties of REBCO copper stabilized superconducting tapes.
Applied Superconductivity Conf. (ASC 2012), Portland, Oreg., October 7-12, 2012

[7] Barth, C.; van der Laan, J.; Weiss, K.P.; Goldacker, W.
Measurements of HTS cables in a temperature range of 4.5 K to 80 K and background fields up to 12 T.
Applied Superconductivity Conf. (ASC 2012), Portland, Oreg., October 7-12, 2012

[8] Bayer, C.; Barth, C.; Weiss, K.P.; Goldacker, W.
Angular dependency of critical currents in HTS under the influence of agnetic fields at different temperatures.
Applied Superconductivity Conf. (ASC 2012), Portland, Oreg., October 7-12, 2012

[9] Bayer, Ch.; Weiss, K.-P.; Barth, Ch.; Bagrets, N.; Goldacker, W.
High temperature superconducting current leads: An essential component of efficient superconducting applications.
Deutsche Kälte-Klima-Tagung, Würzburg, 21.-23. November 2012

[10] Cheggour, N.; Nijhuis, A.; Tsui, Y.; Mondonico, G.; Awaji, S.; Nishijima, G.; Sugano, M.; Park, S.; Weiss, K.; Osamura, K.; Krooshoop, H.; Oh, S.; Hamshire, D.; Senatore, C.; Goodrich, L.; Devred, A.
Generalized benchnarking of strain-measured facilities available in the U.S.A., Europe, Japan, and Korea: First assessment at fixed temperature and magnetic field.
Applied Superconductivity Conf. (ASC 2012), Portland, Oreg., October 7-12, 2012

[11] Fietz, W.H.; Fink, S.; Kraft, G.; Scheller, H.; Weiss, E.; Zwecker, V.
High voltage testing of ITER prototype axial breaks.
Applied Superconductivity Conf. (ASC 2012), Portland, Oreg., October 7-12, 2012

[12] Fietz, W.H.; Fink, S.; Lange, C.; Noe, M.; Winkler, A.
Internal transient over-voltages in large fusion coils.
IEEE Transactions on Applied Superconductivity, 22(2012) S.4704405/1-4
DOI:10.1109/TASC.2012.2186551

[13] Fietz, W.H.; Drotziger, S.; Goldacker, W.; Heller, R.; Weiss, K.P.; Barth, C.
Prospects of high temperature superconductors for fusion magnets and power applications.
27th Symp.on Fusion Technology (SOFT 2012), Liege, B, September 24-28, 2012

[14] Fink, S.; Fietz, W.H.; Kraft, G.; Müller, R.; Scheller, H.; Urbach, E.; Zwecker, V.
Paschen testing of ITER prototype cryogenic axial breaks.
27th Symp.on Fusion Technology (SOFT 2012), Liege, B, September 24-28, 2012

[15] Heiduk, M.; Bagrets, N.; Weiss, K.P.
Data acquisition of a tensile test stand for cryogenic environment.
IEEE Transactions on Applied Superconductivity, 22(2012) S.9000604/1-4
DOI:10.1109/TASC.2011.2176897

[16] Heiduk, M.
Sensor measurement fully insulated from earth.
27th Symp.on Fusion Technology (SOFT 2012), Liege, B, September 24-28, 2012

[17] Hollik, M.; Fietz, W.H.; Fink, S.; Gehrlein, M.; Lange, C.; Möhring, T.
Design of electronic measurement and quench detection equipment for CuLTKa.
27th Symp.on Fusion Technology (SOFT 2012), Liege, B, September 24-28, 2012

[18] Lange, C.; Fietz, W.H.; Gröner, F.
Influence of contact material and surface quality on the contact resistance of high current connections.
27th Symp.on Fusion Technology (SOFT 2012), Liege, B, September 24-28, 2012

[19] Lange, C.; Baldzuhn, J.; Fink, S.; Heller, R.; Hollik, M.; Fietz, W.H.
Paschen problems in large coil systems.
IEEE Transactions on Applied Superconductivity, 22(2012) S.9501504/1-4
DOI:10.1109/TASC.2011.2179393

[20] Neumann, H.
Cryogenics. (eingeladen)
6th Karlsruhe Internat.School on Fusion Technologies, Karlsruhe, September 3-14, 2012

[21] Nyilas, A.; Weiss, K.P.; Sgobba, S.; Scheubel, M.; Libeyre, P.
Fatigue crack growth rate and fracture toughness of ITER central solenoid jacket materials at 7 K.
Balachandran, U. [Hrsg.]; Advances in Cryogenic Engineering : Transactions of the Internat.Cryogenic
Materials Conf., Spokane, Wash., June 13-17, 2011; Melville, N.Y. : AIP, 2012 S.47-54
(AIP Conference Proceedings ; 1435); (Advances in Cryogenic Engineering ; 58)
ISBN 978-0-7354-1022-0

[22] Pong, I.; Vostner, A.; Sgobba, S.; Jung, A.; Weiss, K.P.; Liu, S.; Wu, Y.; Boutbul, T.; Hamada, K.; Park, S.H.; Tronza, V.; Martovetsky, N.; Jewell, M.; Bessette, D.; Devred, A.
Jacket material mechanical properties benchmark tests for ITER CICC.
Applied Superconductivity Conf. (ASC 2012), Portland, Oreg., October 7-12, 2012

[23] Qin, J.; Weiss, K.P.; Wu, Y.; Wu, Z.; Li, L. ; Liu, Sh.
Fatigue tests on the ITER PF jacket.
Cryogenics, 52(2012) S.486-490; DOI:10.1016/j.cryogenics.2012.05.018

[24] Rizzo, E.; Heller, R.; Savoldi Richard, L.; Zanino, R.
Parametric analysis of pressure drop and heat transfer in th e meander-flow heat exchanger of HTS current leads for fusion applications.
CHATS on Applied Superconductivity (CHATS-AS), Geneve, CH, October 12-14, 2012

[25] Rizzo, E.; Drotzinger, S.; Grilli, f.; Heller, R.; Savoldi Richard, L.; Zanino, R.
Thermal-electrical modelling of a superconductive module for HTS current leads.
Applied Superconductivity Conf. (ASC 2012), Portland, Oreg., October 7-12, 2012

[26] Torre, A.; Bajas, H.; Ciazynski, D.; Durville, D.; Weiss, K.
Mechanical-electrical modeling of stretching experiment n 45 Nb_3Sn strands CICCs.
IEEE Transactions on Applied Superconductivity, 21(2011) S.2042-2045
DOI:10.1109/TASC.2010.2091385

[27] Weiß, E.; Bagrets, N.; Weiss, K.P.
Implementation of a quality management system at the PHOENIX facility (CryoMaK).
27th Symp.on Fusion Technology (SOFT 2012), Liege, B, September 24-28, 2012

[28] Weiss, K.-P.
CryoMak - an overview.
Vortrag: Chinese Academy of Science, Institute of Plasma Physics, Hefei, China, August 24, 2012

[29] Weiss, K.P.; Westenfelder, S.; Jung, A.; Bagrets, N.; Fietz, W.H.
Determination of mechanical and thermal properties of electrical insulation material at 4.2 K.
Balachandran, U. [Hrsg.]; Advances in Cryogenic Engineering : Transactions of the Internat.Cryogenic
Materials Conf., Spokane, Wash., June 13-17, 2011; Melville, N.Y. : AIP, 2012 S.148-155
(AIP Conference Proceedings ; 1435); (Advances in Cryogenic Engineering ; 58)
ISBN 978-0-7354-1022-0

[30] Weiss, K.-P.; Westenfelder, S.; Urbach, E.; Boyer, C.; Foussat, A.; Knaster, J.
Mechanical fatigue testing of TF-He-inlet prototypes at cryogenic temperature.
Applied Superconductivity Conference (ASC), Portland, Or., October 7-12, 2012

[31] Weiss, K.-P.; Urbach, E.; Kraft, G.; Scheller, H.
Cryogenic mechanical testing of ITER prototype axial breaks.
27th Symposium on Fusion Technology (SOFT 2012), Liege, B, September 24-28, 2012

[32] Winkler, A.; Fietz, W.H.; Fink, S.; Noe, M.
Transient electrical voltages within ITER poloidal field coils.
IEEE Transactions on Applied Superconductivity, 22(2012) S.9501304/1-4
DOI:10.1109/TASC.2011.2180277

[33] Drotziger, S.; Barth, C.; Fietz, W.H.; Gehrlein, M.; Goldacker, W.; Heiduk, M.; Heller, R.; Lange, C.; Lietzow, R.; Nast, E.; Rizzo, E.
Investigation of quench behavior in ReBCO coated conductors with different stabilizers.
Conference on Coated Conductors for Applications, Heidelberg, November 14-16, 2012

[34] Richter, T.; Kuffner, B.; Lietzow, R.
A test bench for cryogenic process control valves.
24th Internat.Cryogenic Engineering Conf., Internat.Cryogenic Materials Conference 2012, Fukuoka, J, May 14-18, 2012

[35] Drotzinger, S.; Barth, C.; Fietz, W.H.; Goldacker, W.; Heiduk, M.; Heller, R.; Lange, C.; Lietzow, R.; Nast, R.; Rizzo, E.
Investigation of quench behavior in ReBCO coated conductors with different stabilizers.
Applied Superconductivity Conf. (ASC 2012), Portland, Oreg., October 7-12, 2012

Blanket Breeding

[1] Aiello, A.; Ciampichetti, A.; Cismondi, F.; Ghidersa, B.E.; Ilkei, T.; Kosek, L.; Salavy, J.F.
European testing blanket modules auxiliaries design.
Fusion Engineering and Design, 86(2011) S.602-606, DOI:10.1016/j.fusengdes.2011.02.094

[2] Aiello, G.; Aktaa, J.; Cismondi, F.; Rampal, G.; Salavy, J.F.; Tavassoli, F.
Assessment of design limits and criteria requirements for Eurofer structures in TBM components.
Journal of Nuclear Materials, 414(2011) S.53-68, DOI:10.1016/j.jnucmat.2011.05.005

[3] Boccaccini, L.V.
Progresses in the European test blanket module systems for ITER.
10th Internat.Symp.on Fusion Nuclear Technology (ISFNT 2011), Portland, Oreg.
September 11-16, 2011

[4] Boccaccini, L.V.
Recent activities in KIT supporting the design and R&D of the HCPB Test Blanket Modules Systems in ITER.
27th Symp.on Fusion Technology (SOFT 2012), Liege, B, September 24-28, 2012

[5] Ciampichetti, A.; Nitti, F.S.; Aiello, A.; Ricapito, I.; Liger, K.; Demange, D.; Sedano, L.; Moreno, C.; Succi, M.
Conceptual design of tritium extraction system for the european HCPB test blanket module.
Fusion Enigeering and Design, 87(2012) S.620-624; DOI:10.1016/j.fusengdes.2012.01.047

[6] Commin, L.; Madeleine, S.; Dechelle, C.; Patterlini, J.C.; Doceul, L.; Rampal, G.; Cismondi, F.; Bede, O.
Test blanket module pipe forest integration in ITER equatorial port.
Fusion Engineering and Design, 86(2011) S.2143-2147; DOI:10.1016/j.fusengdes.2011.04.019

[7] Demange, D.; Stämmler, S.; Kind, M.
A new combination of membranes and membrane reactors for improved tritium management in breeder blanket of fusion machines.
Fusion Engineering and Design, 86(2011) S.2312-2316; DOI:10.1016/j.fusengdes.2010.12.083

[8] Hernandez, F.; Cismondi, F.; Kiss, B.
Fluid dynamic and thermal analyses of a HCPB TBM breeder unit mock-up.
Fusion Engineering and Design, 86(2011) S.2278-2281; DOI:10.1016/j.fusengdes.2011.04.053

[9] Hernandez, F.; Kolb, M.
Set-up of a pre-test mock-up experiment in preparation for the HCPB breeder unit mock-up experimental campaign.
27th Symp.on Fusion Technology (SOFT 2012), Liege, B, September 24-28, 2012

[10] Hernandez, F.; Cismondi, F.; Kiss, B.
Thermo-mechanical analyses and assessment with respect to the design codes and standards of the HCPB-TBM breeder unit.
Fusion Engineering and Design, 87(2012) S.1111-1117; DOI:10.1016/j.fusengdes.2012.02.088

[11] Kecskes, Sz.; Porempovics, G.; Ghidersa, B.E.
Experimental layout and thermo-mechanical studies on a thermomechanical cycle mock up (TCM) plate.
27th Symp.on Fusion Technology (SOFT 2012), Liege, B, September 24-28, 2012

[12] Poitevin, Y.; Aubert, P.; Diegele, E.; de Dinechin, G.; Rey, J.; Rieth, M.; Rigal, E.; von der Weth, A.; Boutard, J.L.; Tavassoli, F.
Development of welding technologies for the manufacturing of European tritium breeder blanket modules.
Journal of Nuclear Materials, 417(2011) S.36-42; DOI:10.1016/j.jnucmat.2010.12.259

[13] Von der Weth, A.
Two different medium scale first wall fabrication experiments for ITER helium cooled pebble bed test blanket module.
Fusion Science and Technology, 62(2012) S.116-121

[14] Zeile, C.; Neuberger, H.
A revised design approach of the attachment system for the ITER-EU-HCPB-TBM based on a central cylindrical connection element.
Fusion Engineering and Design, 87(2012) S.859-863; DOI:10.1016/j.fusengdes.2012.02.036

[15] Annabattula, R.K.; Gan, Y.; Zhao, S.; Kamlah, M.
Mechanics of a crushable pebble assembly using discrete element method.
Journal of Nuclear Materials, 430(2012) S.90-95; DOI:10.1016/j.jnucmat.2012.06.043

[16] Annabattula, R.K.; Gan, Y.; Kamlah, M.
Mechanics of a crushable pebble assembly using discrete element method.
8th European Solid Mechanics Conference, Graz, A, July 9-13, 2012

[17] Annabattula, R.K.; Gan, Y.; Kamlah, M.
Mechanics of binary and polydisperse spherical pebble assembly.
Fusion Engineering and Design, 87(2012) S.853-858; DOI:10.1016/j.fusengdes.2012.02.033

[18] Boccaccini, L.V.; Kallenbach, A.
An integrated view on plasma power exhaust and in-vessel components.
Internat.Workshop MFE Roadmapping in the ITER Era, Princeton, N.J., September 7- 10, 2011

[19] Boccaccini, L.V.
Blanket design.
10th Workshop on DEMO R&D in the BA Activities, Tokyo, J, February 1-3, 2012

[20] Boccaccini, L.V.; Norajitra, P.; Cismondi, F.
Breeding blankets and divertor design solutions for DEMO.
Meeting with Industry and Associations on Selected Engineering Topics for the Activities of the EFDA Power Plant Physics and Technology WP2011, Garching, May 10-11, 2011

[21] Boccaccini, L.V.
Progress in EU blanket technology.
20th Topical Meeting on the Technology of Fusion Energy (TOFE 2012), Nashville, Tenn., August 27-31, 2012

[22] Bühler, L.; Mistrangelo, C.
Influence of a spatially varying magnetic field on liquid metal flows in the European concept for a fusion test blanket.
Magnetohydrodynamics, 48(2012) S.169-176

[23] Bühler, L.; Mistrangelo, C.
Influence of strong non-uniform magnetic fields on the liquid metal flow in the European fusion test blanket module for ITER.
European GDR Dynamo & MHD Days, Nice, F, October 1-4, 2012

[24] Bühler, L.; Mistrangelo, C.; Koehly, C.
Layout of an experimental liquid-metal circuit based on MHD considerations.
IEEE Transactions on Plasma Science, 40(2012) S.590-595; DOI:10.1109/TPS.2011.2177864

[25] Chakin, V.; Reimann, J.; Moeslang, A.; Latypov, R.; Obukhov, A.
Thermal conductivity of highly neutron-irradiated beryllium in nuclear fusion reactors.
Progress in Nuclear Energy, 57(2012) S.2-7; DOI:10.1016/j.pnucene.2011.11.011

[26] Franza, F.; Boccaccini, L.; Ciampichetti, A.; Zucchetti, M.
Tritium transport analysis in HCPB DEMO blanket with the FUS-TPC code.
27th Symp.on Fusion Technology (SOFT 2012), Liege, B, September 24-28, 2012

[27] Gan, Y.; Annabattula, R.; Kamlah, M.; Einav, I.
The micromechanics of heat flow in compressed granular media.
22nd Australasian Conference on the Mechanics of Structures and Materials, Sydney, AUS, December 11-14, 2012

[28] Hayashi, K.; Nakajima, N.; Clement, S.; Baluc, N.; Nishitani, T.; Yamanishi, T.; Morono, A.; Hernandez, T.; Moriani, A.; Tosti, S.; Nozawa, T.; Lindau, R.; Spätig, P.; Ramesh, M.; Tanigawa, H.; Chakin, V.; Kurinskiy, P.; Nakamichi, M.; Knitter, R.; Hoshino, T.
EU and JA collaboration activities in DEMO R&D of the BA-IFERC project.
9th Joint Conf.on Fusion Energy, Kobe, J, June 28-29, 2012

[29] Jin, X.; Merrill, B.; Boccaccini, L.V.
Ex-vessel LOCA for the European HCPB TBM system using the pedigreed MELCOR182 for fusion.
4th Meeting of the European MELCOR User Group, Köln, April 16-17, 2012

[30] Jin, X.Z.; Merrill, B.J.; Boccaccini, L.V.
Preliminary safety analysis of ex-vessel LOCA for the European HCPB TBM system.
10th Internat.Symp.on Fusion Nuclear Technology (ISFNT 2011), Portland, Oreg., September 11-16, 2011

[31] Jin, X.Z.; Merrill, B.J.; Boccaccini, L.V.
Preliminary safety analysis of ex-vessel LOCA for the European HCPB TBM system.
Fusion Engineering and Design, 87(2012) S.454-460; DOI:10.1016/j.fusengdes.2011.12.007

[32] Knitter, R.
Recent activities in EU Task 5 (Advanced Tritium Breeders).
IFERC Newsletter, (2012) Nr.6

[33] Knitter, R.; Kolb, M.H.H.; Odemer, C.
Synthesis of tritium breeder ceramics from metallic lithium.
Journal of Nuclear Materials, 420(2012) S.268-272; DOI:10.1016/j.jnucmat.2011.10.008

[34] Kolb, M.H.H.; Leys, O.; Knitter, R.
Characterization of advanced tritium breeder ceramics.
Junior Euromat 2012, Lausanne, CH, July 23-27, 2012

[35] Kolb, M.H.H.; Annabattula, R.K.; Knitter, R.; Kamlah, M.
Determination of friction coefficients of tritium breeders and their influence on pebble bed mechanics.
27th Symp.on Fusion Technology (SOFT 2012), Liege, B, September 24-28, 2012

[36] Kolb, M.H.H.; Leys, O.; Knitter, R.
Lithium-Keramik als Treibstoff für die Fusion.
Chancen der Energiewende : 1.Jahrestagung des KIT-Zentrums Energie, Karlsruhe, 19.Juni 2012

[37] Kolb, M.H.H.; Bruns, M.; Knitter, R.; van Til, S.
Lithium orthosilicate surfaces: Characterization and effect on tritium release.
Journal of Nuclear Materials, 427(2012) S.126-132; DOI:10.1016/j.jnucmat.2012.04.024

[38] Kurinskiy, P.E.
Raspukhanie, termodesorbcionnye i mekhaniceskie svojstva berillida titana pri vysokodoznom nejtronnom obluchenii.
Das Schwellen sowie Thermodesorptions- und mechanische Eigenschaften von Titanberyllid bei hoher Neutronenstrahldosis.
Dissertation, Staatliche Universität Uljanowsk 2012

[39] Leys, O.; Kolb, M.; Knitter, R.
Fabrication of advanced ceramic tritium breeders.
Junior Euromat 2012, Lausanne, CH, July 23-27, 2012

[40] Leys, O.; Kolb, M.; Goraieb, A.; Knitter, R.
Melt-based breeder pebbles: effect of cooling and analysis of droplet formation.
27th Symp.on Fusion Technology (SOFT 2012), Liege, B, September 24-28, 2012

[41] Maione, I.A.; Marracci, M.; Tellini, B.
Experimental study on remanent magnetization of Fe-9Cr steel and its effect on in-vessel remote handling for future fusion reactors.
27th Symp.on Fusion Technology (SOFT 2012), Liege, B, September 24-28, 2012

[42] Mistrangelo, C.; Bühler, L.
Buoyancy-driven MHD flows in electrically and thermally coupled ducts.
European GDR Dynamo & MHD Days, Nice, F, October 1-4, 2012

[43] Mistrangelo, C.; Bühler, L.; Stieglitz, R.
Magnetohydrodynamic issues for liquid metal plasma facing components.
20th European Fusion Physics Workshop, Ericeira, P, December 3-5, 2012

[44] Mistrangelo, C.; Bühler, L.
Numerical study of fundamental magnetoconvection phenomena in electrically conducting ducts.
IEEE Transactions on Plasma Science, 40(2012) S.584-589; DOI:10.1109/TPS.2011.2175753

[45] Mukai, K.; Kolb, M.; Knitter, R.; Hoshino, T.; Suzuki, A.; Terai, T.
Investigation of crush load and microstructure on Li2+TiO3+y pebbles after annealing in a reducing atmosphere.
27th Symp.on Fusion Technology (SOFT 2012), Liege, B, September 24-28, 2012

[46] Pieritz, R.; Spino, J.; Vladimirov, P.; Ferrero, C.
Morpho-topological volume analysis of porous materials for nuclear applications.
International Journal of Materials Research, 103(2012) S.250-257; DOI:10.3139/146.110670

[47] Reimann, J.; Benesch, A.; Colle, J.Y.; Dorn, C.; Harsch, H.; Kurinskiy, P.
First measurements of beryllium vapor pressures.
10th IEA Internat.Workshop on Beryllium Technology, Karlsruhe, September 19-21,2012

[48] Reimann, J.; Abou-Sena, A.; Nippen, R.; Tafforeau, P.
Pebble bed packaging in prismatic containers.
27th Symp.on Fusion Technology (SOFT 2012), Liege, B, September 24-28, 2012

[49] Suhonen, H.; Xu, F.; Helfen, L.; Ferrero, C.; Vladimirov, P.; Cloetens, P.
X-ray phase contrast and fluorescence nanotomography for material studies.
International Journal of Materials Research, 103(2012) S.179-183; DOI:10.3139/146.110664

[50] Ying, A.; Reimann, J.; Boccaccini, L.; Enoeda, M.; Kamlah, M.; Knitter, R.; Gan, Y.; Van der Laan, J.; Magielsen, L.; Di Maio, P.A.; Dell'Orco, G.; Annabattula, R.K.; Van Lew, J.T.; Tanigawa, H.; Van Til, S.
Status of ceramic breeder pebble bed thermo-mechanics R&D and impact on breeder material mechanical strength.
Fusion Engineering and Design, 87(2012) S.1130-1137; DOI:10.1016/j.fusengdes.2012.02.090

[51] Zarins, A.; Supe, A.; Kizane, G.; Knitter, R.; Baumane, L.
Accumulation of radiation defects and products of radiolysis in lithium orthosilicate pebbles with silicon dioxide additions under action of high absorbed doses and high temperature in air and inert atmosphere.
Journal of Nuclear Materials, 429(2012) S.34-39; DOI:10.1016/j.jnucmat.2012.05.028

[52] Zhao, S.; Gan, Y.; Kamlah, M.
Pherical ceramic pebbles subjected to multiple non-concentrated surface loads.
International Journal of Solids and Structures, 49(2012) S.658-671
DOI:10.1016/j.ijsolstr.2011.11.009

[53] Jin, X.Z.; Ghidersa, B.E.
Thermal hydraulic system study of a high pressure, high temperature helium loopusing RELAP5-3D code.
Nuclear Engineering and Design, 249(2012) S.57-62; DOI:10.1016/j.nucengdes.2011.07.035

[54] Kunze, A.; von der Weth, A.; Nacke, B.; Nikanorov, A.
Conceptual design of an induction heating system for high heat flux testing of plasma facing components.
27th Symp.on Fusion Technology (SOFT 2012), Liege, B, September 24-28, 2012

Divertor

[1] Koncar, B.; Kosmrlj, S.; Norajitra, P.
On the accuracy of CFD modeling of cyclic high heat flux divertor experiment.
Fusion Engineering and Design, 87(2012) S.1621-1627; 10.1016/j.fusengdes.2012.06.005

[2] Norajitra, P.; Antusch, S.; Giniyatulin, R.; Mazul, I.; Ritz, G.; Ritzhaupt-Kleissl, H.J.; Spatafora, L.
Current state-of-the-art manufacturing technology for He-cooled divertor finger.
Journal of Nuclear Materials, 417(2011) S.468-471; DOI:10.1016/j.jnucmat.2010.12.113

[3] Norajitra, P.
Divertor development for a future fusion power plant.
Dissertation, Karlsruher Institut für Technologie 2011 Karlsruhe : KIT Scientific Publishing, 2011
(Schriftenreihe des Instituts für Angewandte Materialien Karlsruher Institut für Technologie ; 1)
ISBN 978-3-86644-738-7

[4] Norajitra, P.; Antusch, S.; Boccaccini, L.V.; Kuzmic, M.; Maione, I.; Spatafora, L.
He-cooled demo divertor: Design verification testing against mechanical impact loads.
Fusion Engineering and Design, 87(2012) S.932-934; DOI:10.1016/j.fusengdes.2012.02.049

[5] Norajitra, P.; Antusch, S.; Giniyatulin, R.; Kuznetsov, V.; Mazul, I.; Ritzhaupt-Kleissl, H.J.; Spatafora, L.
Progress of He-cooled divertor development for DEMO.
Fusion Engineering and Design, 86(2011) S.1656-1659; DOI:10.1016/j.fusengdes.2010.12.005

[6] Norajitra, P.; Richou, M.; Spatafora, L.
Technological study on manufacturing of multifinger module of He-cooled DEMO divertor and investigation of NDE method.
Fusion Science annd Technology, 62(2012) S.134-138

[7] Hesch, K.; Aktaa, J.; Antusch, S.; Boccaccini, L.V.; Day, C.; Demange, D.; Fietz, W.; Gantenbein, G.; Möslang, A.; Norajitra, P.; Rieth, M.
Technology developments at KIT towards a magnetic confinement fusion power plant.
Transactions of Fusion Science and Technology, 61(2012) S.64-69

[8] Simonovski, I.; Koncar, B.; Norajitra, P.
Thermal stress prediction in divertor cooling finger using the local heat transfer distribution.
Fusion Engineering and Design, 86(2011) S.1620-1624; DOI:10.1016/j.fusengdes.2010.12.018

Structural Materials

[1] Aktaa, J.
Impact of pulsed operation on lifetime of blanket module.
Final Report for EFDA-PPP&T WP11-DAS-PLS-P08-01/KIT (February 2012)

[2] Aktaa, J.; Konys, J.; Igitkhanov, J.; Pintsuk, G.; Linke, J.; You, J.H.
T2: Structural and functional materials.
German DEMO Working Group Meeting, Jülich, November 17-18, 2011

[3] Aktaa, J.; Gaganidze, E.; Konys, J.; Knitter, R.; Linke, J.; You, J.H.
T2: Structural and functional materials.
German DEMO Working Group Meeting, Karlsruhe, April 26-27, 2012

[4] Aktaa, J.
WP11-DAS-PLS-P08-01/KIT. Impact of pulsed operation on lifetime of blanket module.
EFDA-PPP&T Kick-off-Meeting of WP11-DAS-PLS, Garching, October 4, 2012

[5] Aktaa, J.
WP11-DAS-PLS-P08-01/KIT. Impact of pulsed operation on lifetime of blanket module.
EFDA-PPP&T Final Reports Meeting of WP11-DAS-PLS, Garching, January 18, 2012

[6] Albinski, B.; Sacksteder, I.; Schneider, H.C.
Ein fernhantierter Hochtemperatur-Indenter zur Untersuchung von Materialien für den Fusionsreaktor.
InnoMateria, Köln, 14.-15.Mai 2012

[7] Albinski, B.; Schneider, H.C.; Kraft, O.
Entwicklung und Aufbau einer Hochtemperatur-Indentationsanlage zur Charakterisierung bestrahlter Werkstoffe.
Workshop 'Kompetenzerhaltung in der Kerntechnik', Jahrestagung Kerntechnik 2012, Stuttgart, 22.-24.Mai 2012

[8] Albinski, B.; Schneider, H.C.; Kraft, O.
Entwicklung und Aufbau einer Hochtemperatur-Indentationsanlage zur Charakterisierung bestrahlter Werkstoffe.
Jahrestagung Kerntechnik 2012, Stuttgart, 22.-24.Mai 2012; Berlin : INFORUM GmbH, 2012

[9] Albinski, B.
High temperature characterisation of irradiated materials by indentation experiments.
Vortr.: University of Knoxville, Tenn., 25.Oktober 2011

[10] Albinski, B.; Sacksteder, I.; Schneider, H.-Ch.; Kraft, O.
High-temperature indentation experiments on fusion-related materials.
27th Symposium on Fusion Technology (SOFT 2012), Liege, B, September 24-28, 2012

[11] Antusch, S.; Commin, L.; Heneka, J.; Piotter, V.; Plewa, K.; Walter, H.
A new fully automatic PIM tool to replicate two component tungsten DEMO divertor parts.
27th Symp.on Fusion Technology (SOFT 2012), Liege, B, September 24-28, 2012

[12] Antusch, S.; Piotter, V.
KIT investigates the mass production and joining of divertor parts for nuclear fusion power plants via multicomponent tungsten PIM.
Powder Injection Moulding International, 6(2012) Nr.1, S.22-23

[13] Antusch, S.; Norajitra, P.; Piotter, V.; Ritzhaupt-Kleissl, H.J.; Spatafora, L.
Powder injection molding - an innovative manufacturing method for He-cooled DEMO divertor components.
Fusion Engineering and Design, 86(2011) S.1575-1578; DOI:10.1016/j.fusengdes.2011.01.009

[14] Antusch, S.; Commin, L.; Müller, M.; Piotter, V.; Rieth, M.; Walter, H.; Weingärtner, T.
Powder injection molding (PIM) a multi-purpose process for armor part fabrication and materials development.
Vortr.: Universität Oxford, GB, 30.Mai 2012

[15] Antusch, S.; Piotter, V.
Tungsten powder injection molding, tungsten armor, mockup fabrication.
Challenges to Developing W-Based Materials for Fusion Applications, Santa Barbara, Calif., February 13-15, 2012

[16] Antusch, S.; Müller, M.; Norajitra, P.; Pintsuk, G.; Piotter, V.; Ritzhaupt-Kleissl, H.J.; Weingärtner, T.
Two component tungsten powder injection molding for mass production of the He- cooled DEMO divertor parts.
Fusion Science and Technology, 62(2012) S.110-115

[17] Basuki, W.W.; Aktaa, J.
Diffusion bonding between W and EUROFER97 using V interlayer.
Journal of Nuclear Materials, 429(2012) S.335-340; DOI:10.1016/j.jnucmat.2012.05.049

[18] Basuki, W.W.; Aktaa, J.
Diffusion bonding between EUROFER97 and tungsten using V interlayer.
EFDA W&W Alloys Monitoring Meeting, Garching, February 7-9, 2012

[19] Choudhury, A.; Reuther, K.; Wesner, E.; August, A.; Nestler, B.; Rettenmayr, M.
Comparison of phase-field and cellular automaton models for dendritic solidification in Al-Cu alloy.
Computational Materials Science, 55(2012) S.263-268; DOI:10.1016/j.commatsci.2011.12.019

[20] Commin, L.; Rieth, M.; Widak, V.; Dafferner, B.; Heger, S.; Zimmermann, H.; Materna-Morris, E.; Lindau, R.
Characterization of ODS-Eurofer/Eurofer dissimilar electron beam welds.
15th Internat.Conf.on Fusion Reactor Materials, Charleston, S.C., October 16-22, 2011

[21] Commin, L.; Rieth, M.; Dafferner, B.; Zimmermann, H.; Bölich, D.; Baumgärtner, S.; Ziegler, R.; Dichiser, S.; Fabry, T.; Fischer, S.; Hildebrand, H.; Palussek, O.; Ritz, H.; Sponda, A.
Fail safe and cost effective fabrication of a first wall by diffusion welding.
2nd Joint IAEA - EC Topical Meeting on Development of New Structural Materials for Advanced Fission and Fusion Reactor Systems, Ispra, I, April 16-20, 2012

[22] Commin, L.; Dumont, M.; Rotinat, R.; Pierron, F.; Masse, J.E.; Barrallier, L.
Influence of the microstructural changes and induced residual stresses on tensile properties of wrought magnesium alloy friction stir welds.
Materials Science and Engineering A, 551(2012) S.188-292; DOI:10.1016/j.msea.2012.05.021

[23] Commin, L.; Antusch, S.; Goldacker, W.; Lukits, P.; Rieth, M.; Bolich, D.; Hoffmann, M.
Material development for the waer-cooled divertor concept of the DEMO European fusion reactor.
Nuclear Materials Conf. (NuMat 2012), Osaka, J, October 22-25, 2012

[24] Commin, L.; Dumont, M.; Rotinat, R.; Pierron, F.; Masse, J.E.; Barraillier, L.
Texture evolution in Nd:YAG-laser welds of AZ31 magnesium alloy hot rolled sheets and its influence on mechanical properties.
Materials Science and Engineering A, 528(2011) S.2049-2055; DOI:10.1016/j.msea.2010.11.061

[25] Commin, L.
Work package No.1: Irradiation damage - advanced characterization and modelling.
FabriCharMe GOT Program Progress Meeting, Karlsruhe, November 14, 2011

[26] Commin, L.
Work package No.1: Irradiation damage - advanced characterization and modelling.
FabriCharMe GOT Program Progress Meeting, Saclay, F, November 12, 2012

[27] Dethloff, C.
High dose irradiation damage of RAFM steels.
HGF-Workshop '20 Tage Deutschland in der Reion Uljanowsk', Uljanowsk, Russia, 5.September 2012

[28] Dethloff, C.
Modeling of helium bubble nucleation and growth in neutron irradiated RAFM steels.
Vortr.: Uljanowsk State University, Uljanowsk, Russia, 6.September 2012

[29] Dethloff, C.
Modeling of helium bubble nucleation and growth in neutron irradiated RAFM steels.
Dissertation, Karlsruher Institut für Technologie 2012
Karlsruhe : KIT Scientific Publishing, 2012
(Schriftenreihe des Instituts für Angewandte Materialien Karlsruher Institut für Technologie ; 6)
ISBN 978-3-86644-901-5

[30] Dethloff, Ch.; Gaganidze, E.
Quantitative TEM investigation of neutron irradiated EUROFER97 from WTZ and ARBOR1.
EFDA WP12-MAT-01-IREMEV-04-01 Monitoring Meeting, Garching, December 3-5, 2012

[31] Eiselt, Ch.Ch.; Klimenkov, M.; Lindau, R.; Möslang, A.
Characterization of microstructural and mechanical properties of a reduced activation ferritic oxide dispersion strengthened steel.
Journal of Nuclear Materials, 416(2012) S.30-34; DOI:10.1016/j.jnucmat.2011.03.017

[32] Eiselt, Ch.Ch.; Klimenkov, M.; Lindau, R.; Möslang, A.; Odette, G.R.; Yamamoto, T.; Gragg, D.
Tensile and fracture toughness properties of the nanostructured oxide dispersion strengthened ferritic alloy 13Cr-1W-0.3Ti-0.3Y_2O_3.
Journal of Nuclear Materials, 417(2012) S.193-196; DOI:10.1016/j.jnucmat.2010.12.066

[33] Gaganidze, E.; Aktaa, J.
Compilation and assessment of mechanical properties of neutron irradiated RAFM steels. Issues related to radiation on blanket and divertor.
Monitoring Meeting on Material Database Status and Needs for DEMO Conceptual Design Activities, Garching, April 11-12, 2012

[34] Gaganidze, E.; Walter, M.; Bürkle, U.; Klotz, M.
Fracture-mechanical and microstructural characterization of W-alloys.
EFDA W&W Alloys Monitoring Meeting, Garching, February 7-9, 2012

[35] Gaganidze, E.
Fracture-mechanical and microstructural characterization of W-alloys.
MAT-HHFM Monitoring Meeting, Ljubljana, SLO, June 13-15, 2012

[36] Gaganidze, E.
Issues related to radiation on blanket and divertor materials.
Monitoring Meeting on Material Database Status and Needs for DEMO Conceptual Design Activities, Garching, November 8-9, 2012

[37] Gaganidze, E.; Dethloff, C.
Quantitative TEM investigation of neutron irradiated EUROFER97 from WTZ and ARBOR1.
WP12-MAT-01-IREMEV Monitoring Meeting, Ljubljana, SLO, June 13-15, 2012

[38] Gludovatz, B.; Wurster, S.; Weingärtner, T.; Hoffmann, A.; Pippan, R.
Influence of impurities on the fracture behavior of tungsten.
Philosophical Magazine, 91(2011) S.3006-3020; DOI:10.1080/14786435.2011.558861

[39] Graivoronska, K.O.; Klimenkov, M.; Solonin, Yu.M.; Nepijko, S.A.; Schönhense, G.
Detailed study of defects in thin fullerite films.
Crystal Research and Technology, 47(2012) S.1255-1268; DOI:10.1002/crat.201200304

[40] Grossetti, G.; Aiello, G.; Heemskerk, C.; Elzendoorn, B.; Geßner, R.; Koning, J.; Meier, A.; Ronden, D.; Späh, P.; Scherer, T.; Schreck, S.; Strauß, D.; Vaccaro, A.
The ITER EC H&CD upper launcher: vertical remote handling applied to the BSM maintenance.
27th Symp.on Fusion Technology (SOFT 2012), Liege, B, September 24-28, 2012

[41] He, P.; Klimenkov, M.; Lindau, R.; Möslang, A.
Characterization of precipitates in nano structured 14% Cr ODS alloys for fusion application.
Journal of Nuclear Materials, 428(2012) S.131-138; DOI:10.1016/j.jnucmat.2011.08.026

[42] He, P.; Liu, T.; Möslang, A.; Lindau, R.; Ziegler, R.; Hoffmann, J.; Kurinskiy, P.; Commin, L.; Vladimirov, P.; Nikitenko, S.; Silveir, M.
XAFS and TEM studies of the structural evolution of yttrium-enriched oxides in nanostructured ferritic alloys fabricated by a powder metallurgy process.
Materials Chemistry and Physics, 136(2012) S.990-998; DOI:10.1016/j.matchemphys.2012.08.038

[43] Heintze, C.; Bergner, F.; Ulbricht, A.; Hernandez-Mayoral, M.; Keiderling, U.; Lindau, R.; Weissgärber, T.
Microstructure of oxide dispersion strengthened Eurofer and iron-chromium alloys investigated by means of small-angle neutron scattering and transmission electron microscopy.
Journal of Nuclear Materials, 416(2011) S.35-39; DOI:10.1016/j.jnucmat.2010.11.102

[44] Huang, Q.; Baluc, N.; Dai, Y.; Jitsukawa, S.; Kimura, A.; Kurtz, R.J.; Lindau, R.; Muroga, T.; Odette, G.R.; Raj, B.; Stoller, R.E.; Tan, L.; Tanigawa, H.; Tavassoli, A.F.; Wan, F.; Wu, Y.
Recent progress of R&D activities on reduced activation ferritic/martensitic steels.
15th Internat.Conf.on Fusion Reactor Materials, Charleston, S.C., October 16-22, 2011

[45] Ilchuk, N.; Commin, L.; Spätig, P.; Odette, G.R.
Effect of warm pre-stressing on fracture toughness of Eurofer97 steel.
27th Symp.on Fusion Technology (SOFT 2012), Liege, B, September 24-28, 2012

[46] Jäntsch, U.; Klimenkov, M.; Rieth, M.; Scherer, T.
Applications of dual beam SEM/FIB for microstructure analysis of refractory materials.
7.FIB-Workshop, Dresden, 25.-27.Juni 2012

[47] Jäntsch, U.; Klimenkov, M.; Rieth, M.
Mikrostrukturelle Untersuchungen am Transmissions-Elektronen-Mikroskop.
46. Metallographie-Tagung der Deutschen Gesellschaft für Materialkunde. Rostock, 19.-21.September 2012

[48] Klimenkov, M.; Materna-Morris, E.; Möslang, A.
Role of lithium in the formation of He bubbles in boron-alloyed steel after neutron irradiation.
15th European Microscopy Congress (EMC 2012), Manchester, GB, September 16-21,2012; Proc.publ.in the web

[49] Klimenkov, M.; Lindau, R.; Materna-Morris, E.; Möslang, A.
TEM characterization of precipitates in EUROFER 97.
Progress in Nuclear Energy, 57(2012) S.8-13; DOI:10.1016/j.pnucene.2011.10.006

[50] Klimenkov, M.; Materna-Morris, E.; Möslang, A.; Jäntsch, U.
TEM study of boron effect on the microstructure of 9CrWTaVB martensitic steel.
15th European Microscopy Congress (EMC 2012), Manchester, GB, September 16-21, 2012
Proc.publ in the web

[51] Konys, J.; Krauss, W.; Holstein, N.; Lorenz, J.; Wulf, S.; Bhanumurthy, K.
Impact of heat treatment on surface chemistry of Al-coated Eurofer for application as Anti-corrosion and T-permeation barriers in a flowing Pb-15.7Li.
Fusion Engineering and Design, 87(2012) S.1483-1486; DOI:10.1016/j.fusengdes.2012.03.042

[52] Kraft, O.
Plastizität und Bruch in kleinen Dimensionen: von Mikropfosten zu Nanodrähten.
Vortr.: Technische Universität Dresden, 17.Januar 2012

[53] Krauss, W.; Holstein, N.; Lorenz, J.; Konys, J.
Development of functional scales for joining of divertor components based on electrochemical plating technology.
Fusion Science and Technology, 62(2012) S.129-133

[54] Krauss, W.; Konys, J.; Holstein, N.; Lorenz, J.
Electro-chemical processing for tungsten fabrication and joining by layer deposition.
Challenges to Developing W-Based Materials for Fusion Applications, Santa Barbara, Calif., February 13-15, 2012

[55] Krauss, W.; Lorenz, J.; Konys, J.
Performance of electroplated and joined components for divertor applications.
27th Symp.on Fusion Technology (SOFT 2012), Liege, B, September 24-28, 2012

[56] Krauss, W.; Konys, J.; Li-Puma, A.
TBM testing in ITER: requirements for the development of predictive tools to describe Corrosion-related phenomena in HCLL blankets towards DEMO.
Fusion Engineering and Design, 87(2012) S.403-406; DOI:10.1016/j.fusengdes.2011.11.009

[57] Lemberg, J.A.; Middlemas, M.R.; Weingärtner, T.; Gludovatz, B.; Cochran, J.K.; Ritchie, R.O.
On the fracture toughness of fine-grained Mo-3Si-1B (wt. %) alloys at ambient to elevated (1300^0C) temperatures.
Intermetallics, 20(2012) S.141-154; DOI:10.1016/j.intermet.2011.09.003

[58] Linsmeier, Ch.; Fu, C.C.; Kaprolat, A.; Nielsen, S.F.; Mergia, K.; Schäublin, R.; Lindau, R.; Bolt, H. ; FEMaS Partners
Advanced materials characterization and modeling using synchrotron, neutron, TEM, and novel micro-mechanical techniques. A European effort to accelerate fusion materials development.
15th Internat.Conf.on Fusion Reactor Materials, Charleston, S.C., October 16-22, 2011

[59] Lindau, R.; Möslang, A.
Nano-scaled materials for fusion power plants.
5th German-Japanese Symp.on Nanostructures, 5th Internat.Symp.on Nanostructures OZ-12, Wenden-Olpe, March 4-6, 2012

[60] Malitckii, E.; Yagodzinskyy, Y.; Gnchenkova, M.; Binyukova, S.; Hänninenn, H.; Lindau, R.; Vladimirov, P.; Möslang, A.
Comparative study of hydrogen uptake and diffusion in ODS steels.
27th Symp.on Fusion Technology (SOFT 2012), Liege, B, September 24-28, 2012

[61] Möslang, A.; Diegele, E.; Dudarev, S.; Rieth, M.; Gonzalez de Vicente, S.M.
High temperature applications: the EU integrated fusion materials programme.
2nd European Energy Conference (E2C), Maastricht, NL, April 17-20, 2012

[62] Möslang, A.; Klimenkov, M.; Lindau, R.; Materna-Morris, E.; Rieth, M.
Overview on fatigue results after neutron irradiation of EUROFER steel.
6th International Conference on Creep, Fatigue and Creep-Fatigue Interaction (CF-6), Mamallapuram, IND, January 22-25, 2012

[63] Möslang, A.
The european fusion materials science programme.
German/Japan Seminar on Energy Materials, Institute of Advanced Energy, Kyoto, J, February 2-3, 2012

[64] Molnar, D.; Mukherjee, R.; Choudhury, A.; Mora, A.; Binkele, P.; Selzer, M.; Nestler, B.; Schmauder, S.
Multiscale simulations on the coarsening of Cu-rich precipitates in □-Fe using kinetic Monte Carlo, molecular dynamics and phase-field simulations.
Acta Materialia, 60(2012) S.6961-6971; DOI:10.1016/j.actamat.2012.08.051

[65] Pascal, R.; Beloglazov, S.; Bonagiri, S.; Commin, L.; Cortes, P.; Giancarli, L.M.; Gliss, C.; Iseli, M.; Lanza, R.; Levesy, B.; Martins, J.P.; Neviere, J.C.; Patisson, L.; Plutino, D.; Shu, W.; Swami, H.L.
Progress in the integration of test blanket system in ITER equatorial port cells and in the interfaces definition.
Fusion Engineering and Design, 87(2012) S.1347-1351; DOI:10.1016/j.fusengdes.2012.03.010

[66] Pascal, R.; Beloglazov, S.; Bonagiri, S.; Commin, L.; Cortes, P.; Giancarli L.M.; Gliss, C.; Iseli, M.; Lanza, R.; Levesy, B.; Martins, J.P.; Neviere, J.C.; Patisson, L.; Plutino, D.; Shu, W.; Swami, H.L.
Progress in the integration of test blanket systems in ITER equatorial port cells and in the interfaces definition.
10th Internat.Symp.on Fusion Nuclear Technology (ISFNT 2011), Portland, Oreg., September 11-16, 2011

[67] Reiser, J.; Rieth, M.; Dafferner, B.; Hoffmann, A.
Basic divertor design studies.
KIT-CCFE Divertor Technology Workshop, Culham, GB, May 29, 2012

[68] Reiser, J.; Rieth, M.; Dafferner, B.; Hoffmann, A.
Brazing / mockup fabrication / deep drawing.
Challenges to Developing W-Based Materials for Fusion Applications, Santa Barbara, Calif., February 13-15, 2012

[69] Reiser, J.; Rieth, M.; Dafferner, B.; Baumgärtner, S.; Ziegler, R.; Hoffmann, A.
Deep drawing of tungsten plates for structural divertor applications in future fusion devices.
Fusion Engineering and Design, 86(2011) S.2049-2953; DOI:10.1016/j.fusengdes.2011.07.011

[70] Reiser, J.; Rieth, M.; Dafferner, B.; Hoffmann, A.
Divertor from the technology perspective.
1st IAEA DEMO Programme Workshop (DPW-2012), Los Angeles, Calif., October 15-18, 2012

[71] Reiser, J.; Rieth, M.; Dafferner, B.; Hoffmann, A.
Divertor mockup testing - KIT plans for 2012-2013.
KIT-CCFE Divertor Technology Workshop, Culham, GB, May 29, 2012

[72] Reiser, J.; Rieth, M.; Dafferner, B.; Commin, L.; Hoffmann, A.
Ductile tungsten (W) pipes for divertor applications.
27th Symp.on Fusion Technology (SOFT 2012), Liege, B, September 24-28, 2012

[73] Reiser, J.; Rieth, M.; Möslang, A.; dafferner, B.; Hoffmann, A.; Schulmeyer, W.
Ductile tungsten (W) pipes for structural applications.
Managing Intellectual Property, Dispute Prevention and Technology Transfer in Fusion, Barcelona, E, November 28-29, 2011

[74] Reiser, J.; Rieth, M.; Dafferner, B.; Hoffmann, A.
Ductilisation of tungsten: tungsten laminate.
Ajou-KIT-Kyoto University Joint International Symp., Kyoto, J, January 31 - February 1, 2012

[75] Reiser, J.
Duktilisierung von Wolfram. Synthese, Analyse und Charakterisierung von Wolframlaminaten aus Wolframfolie.
Dissertation, Karlsruher Institut für Technologie 2012
Karlsruhe : KIT Scientific Publishing, 2012
(Schriftenreihe des Instituts für Angewandte Materialien Karlsruher Institut für Technologie ; 7)
ISBN 978-3-86644-902-2

[76] Reiser, J.; Rieth, M.; Dafferner, B.
Metallische Hochtemperaturwerkstoffe und deren mechanisch-technologische Prüfung.
Metall Symp., Ulm, 22.Mai 2012

[77] Reiser, J.; Rieth, M.
Optimization and limitation of known DEMO divertor concepts.
Fusion Engineering and Design, 87(2012) S.718-721; DOI:10.1016/j.fusengdes.2012.02.010

[78] Reiser, J.; Rieth, M.; Dafferner, B.; Widak, V.; Hoffmann, A.
Refraktär-Laminate für die Energiewende.
Chancen der Energiewende: 1.Jahrestagung des KIT-Zentrums Energie, Karlsruhe, 19.Juni 2012

[79] Reiser, J.; Rieth, M.; Dafferner, B.; Hoffmann, A.
Selected divertor studies and experiments.
20th European Fusion Physics Workshop, Ericeira, P, December 3-5, 2012

[80] Reiser, J.; Rieth, M.; Dafferner, B.; Hoffmann, A.
Tungsten foils laminate for structural divertor applications - basics and outlook.
Journal of Nuclear Materials, 423(2012) S.1-8; DOI:10.1016/j.jnucmat.2012.01.010

[81] Reiser, J.; Rieth, M.; Dafferner, B.; Hoffmann, A.; Yi, X.; Armstrong, D.E.J.
Tungsten foil laminate for structural divertor applications - analyses and characterisation of tungsten foil.
Journal of Nuclear Materials, 424(2012) S.197-203; DOI:10.1016/j.jnucmat.2012.02.030

[82] Reiser, J.; Rieth, M.; Dafferner, B.; Hoffmann, A.
W laminate.
Challenges to Developing W-Based Materials for Fusion Applications, Santa Barbara, Calif., February 13-15, 2012

[83] Reiser, J.; Rieth, M.; Dafferner, B.; Hoffmann, A.
W laminates and their possible use in divertor technology.
KIT-CCFE Divertor Technology Workshop, Culham, GB, May 29, 2012

[84] Reiser, J.; Rieth, M.; Dafferner, B.; Hoffmann, A.
W/Mo-Laminatrohre für Hochtemperaturanwendungen.
DFG-Nachwuchsakademie Materialwissenschaft und Werkstofftechnik, Attendorn, 29.- 31.Oktober 2012

[85] Rieth, M.
Divertor design and materials.
Vortr.: Universität Oxford, GB, 6.November 2012

[86] Rieth, M.; Reiser, J.; Dafferner, B.; Baumgärtner, S.
The impact of refractory material properties on the helium cooled divertor design.
Transactions of Fusion Science and Technology, 61(2012) S.381-384

[87] Rieth, M.
Tungsten - an overview of general properties and possible structural applications in fusion power plants.
Challenges to Developing W-Based Materials for Fusion Applications, Santa Barbara, Calif., February 13-15, 2012

[88] Rogozhkin, S.V.; Aleev, A.A.; Zaluzhnyi, A.G.; Iskanderov, N.A.; Nikitin, A.A.; Vladimirov, P.; Lindau, R.; Möslang, A.
Atom probe tomography of nanoscaled features of oxide-dispersion-strengthened ODS Eurofer steel in the initial state and after neutron irradiation.
Physics of Metals and Metallography, 113(2012) S:98-105; DOI:10.1134/S0031918X12010103

[89] Ryazanov, A.I.; Chugonov, O.K.; Latushkin, S.T.; Lindau, R.; Möslang, A.; Prikhodko, KE.; Semenov, E.V.; Unezhev, V.N.; Vladimirov, P.
Investigations of high concentration of helium atoms effects on microstructure and mechanical property changes in EUROFER ODS materials.
15th Internat.Conf.on Fusion Reactor Materials, Charleston, S.C., October 16-22, 2011

[90] Sacksteder, I.; Hostettler, S.; Charbonneau, G.; Albinski, B.; Schneider, H.C.
An evaluation of requirements for investigating the temperature-dependent fracture behavior of irradiated materials by indentation.
27th Symp.on Fusion Technology (SOFT 2012), Liege, B, September 24-28, 2012

[91] Sacksteder, I.; Albinski, B.
Characterization of RAFM steels up to 650^0C by means of the indentation technique.
WP12-MAT-01-IREMEV Monitoring Meeting, Ljubljana, SLO, June 13-15, 2012

[92] Sacksteder, I.; Albinski, B.; Schneider, H.-C.
Characterization of RAFM steels up to 650^0C by means of the intendation technique.
EFDA WP12-MAT-01-IREMEV Monitoring Meeting, Garching, Dezember 3-5, 2012

[93] Sacksteder, I.
Characterization of tungsten from room temperature up to 1000^0C by means of the indentation technique.
WP12-MAT-01-IREMEV Monitoring Meeting, Ljubljana, SLO, June 13-15, 2012

[94] Sacksteder, I.; Albinski, B.; Bernstein, I.; Schneider, H.C.; Kraft, O.
Une utilisation de l'indentation instrumentee a haute temperature pour tester des echantillons irradies.
Indentation 2012, Lyon, F, 29-31 Octobre 2012

[95] Sandim, H.R.Z.; Renzetti, R.A.; Padilha, A.F.; Möslang, A.; Lindau, R.; Raabe, D.
Annealing behaviour of rafm ods-eurofear steel.
Fusion Science and Technology, 61(2012) S.136-140

[96] Saoutic, B.; Abiteboul, J.; Allegretti, L.; Allfrey, S.; Ane, J.M.; Aniel, T.; Argouarch, A.; Artaud, J.F.; Aumenier, M.H.; Balme, S.; Basiuk, V.; Baulaigue, O.; Bayetti, P.; Becoulet, A.; Becoulet, M.; Benkadda, MS.; Benoit, F.; Berger- by, G.; Bernard, J.M.; Bertrand, B.; Beyer, P.; Bigand, A.; Blum, J.; Boilson, S.; Bonhomme, G.; Bottollier-Curtet, H.; Bouchand, C.; Bouquey, F.; ourdelle, C.; Bourmaud, S.; Brault, C.; Bremond, S.; Brosset, C.; Bucalossi, J.; Buravand, Y.; Cara, P.; Catherine-Dumont, V.; Casati, A.; Chantant, M.; Chatelier, M.; Chevet, G.; Ciazynski, D.; Ciraolo, G.; Clairet, F.; Coatanea-Gouchet, M.; Colas, L.; Commin, L.; Corbel, E.; Corre, Y.; Courtois, X.; Dachicourt, R.; Dapena Febrer, M.; Davi Joanny, M.; Daviot, R.; De Esch, H.; Decker, J.; ecool, P.; Delaporte, P.; Delchambre, E.; Delmas, E.; Delpech, L.; Desgranges, C.; Devynck, P.; ittmar, T.; Doceul, L.; Douai, D.; Dougnac, H.; Duchateau, J.L.; Dugue, B.; Dumas, N.; Dumont, R.; Durocher, A.; Duthoit, F.X.; Ekedahl, A.; Elbeze, D.; El Khaldi, M.; Escourbiac, F.; Faisse, F.; Falchetto, G.; Farge, M.; Farjon, J.L.; Faury, M.; Fedorczak, N.; Fenzi-Bonizec, C.; Firdaouss, M.; Frauel, Y.; Garbet, X.; Garcia, J.; Gardarein, J.L.; Gargiulo, L.; Garibaldi, P. ; Gauthier, E.; Gaye, O.; Geraud, A.; Geynet, M.; Ghendrih, P.; Giacalone, I.; Gibert, S.; Gil, C.; Giruzzi, G.; Goniche, M.; Grandgirard, V.; Grisolia, C.; Gros, G.; Grosman, A.; Guigon, R.; Guilhem, D.; Guillerminet, B.; Guirlet, R.; Gunn, J.; Gurcan, O.; Hacquin, S.; Hatchressian, J.C.; Hennequin, P.; Hernandez, C.; Hertout, P.; Heuraux, S.; Hillairet, J.; Hoang, G.T.; Honore, C.; Houry, M. ; Hutter, T.; Huynh, P.; Huysmans, G.; Imbeaux, F.; Joffrin, E.; Johner, J.; Jourd'heuil, L.; Katharria, Y.S.; Keller, D.; Kim, S.H.; Kocan, M.; Kubic, M.; Lacroix, B.; Lamaison, V.; Latu, G.; Lausenaz, Y.; Laviron, C.; Leroux, F.; Letellier, L.; Lipa, M.; Litaudon, X.; Loarer, T.; Lotte, P.; Madeleine, S.; Magaud, P.; Maget, P.; Magne, R.; Manenc, L.; Marandet, Y.; Marbach, G.; Marechal, J.L.; Marfisi, L.; Martin, C.; Martin, G.; Martin, V.; Martinez, A.; Martins, J.P.; Masset, R.; Mazon, D.; Mellet, N.; Mercadier, L.; Merle, A.; Meshcheriakov, D.; Meyer, O.; Million, L.; Missirlian, M.; Mollard, P.; Moncada, V.; Monier-Garbet, P.; Moreau, D.; Moreau, P.; Morini, L.; Nannini, M.; Naiim Habib, M.; Nardon, E.; Nehme, H.; Nguyen, C.; Nicollet, S.; Nouilletas, R.; Ohsako, T.; Ottaviani, M.; Pamela, S.; Parrat, H.; Pastor, P.; Pecquet, A.L.; Pegourie, B.; Peysson, Y.; Porchy, I.; Portafaix, C.; Preynas, M.; Prou, M.; Raharijaona, J.M.; Ravenel, N.; Reux, C.; Reynaud, P.; Richou, M.; Roche, H.; Roubin, P.; Sabot, R.; Saint-Laurent, F.; Salasca, S.; Samaille, F.; Santagiustina, A.; Sarazin, Y.; Semerok, A.; Schlosser, J.; Schneider, M.; Schubert, M.; Schwander, F.; Segui, J.L.; Selig, G.; Sharma, P.; Signoret, J.; Simonin, A.; Song, S.; Sonnendruker, E.; Sourbier, F.; Spuig, P.; Tamain, P.; Tena, M.; Theis, J.M.; Thouvenin, D.; Torre, A.; Travere, J.M.; Tsitrone, E.; Vallet, J.C.; Van der Plas, E.; Vatry, A.; Verger, J.M.; Vermare, L.; Villecroze, F.; Villegas, D.; Volpe, R.; Vulliez, K.; Wagrez, J.; Wauters, T.; Zani, L.; Zarzoso, D.; Zou, X.L.
Contribution of Tore Supra in preparation of ITER.
Nuclear Fusion, 51(2011) S.090104/1-12; DOI:10.1088/0029-5515/51/9/094014

[97] Scherwitz, M.; Walter, M.; Aktaa, J.; Schneider, H.C.
Low cycle fatigue behaviour of Eurofer97 welding joints.
27th Symp.on Fusion Technology (SOFT 2012), Liege, B, September 24-28, 2012

[98] Vondrous, A.; Nestler, B.; August, A.; Wesner, E.; Choudhury, A.; Hötzer, J.
Metallic foam structures, dendrites and implementation optimizations for phase- field modeling.
Nagel, W. [Hrsg.]
High Performance Computing in Science and Engineering '11 : Transactions of the
High Performance Computing Center, Stuttgart (HLRS) 2011
Berlin [u.a.] : Springer, 2012 S.595-606; ISBN 978-3-642-23868-0; e-ISBN 978-3-642-23869-7
DOI:10.1007/978-3-642-23869-7_43

[99] Wang, F.; Choudhury, A.; Selzer, M.; Mukherjee, R.; Nestler, B.
Effect of solutal Marangoni convection on motion, coarsening, and coalescence of droplets in a monotectic system.
Physical Review E, 86(2012) S.066318/1-13; DOI:10.1103/PhysRevE.86.066318

[100] Weiß, O.J.; Gaganidze, E.; Aktaa, J.
Quantitative characterization of microstructural defects in up to 32 dpa neutron irradiated EUROFER97.
Journal of Nuclear Materials, 426(2012) S.52-58; DOI:10.1016/j.jnucmat.2012.03.027

[101] Weiß, O.J.; Gaganidze, E.; Aktaa, J.
Quantitative microstructural investigation of neutron-irradiated RAFM steel for nuclear fusion applications.
Böllinghaus, T. [Hrsg.]
Materials Challenges and Testing Supply of Energy and Resources
Berlin [u.a.] : Springer, 2012 Part 1, S.13-22; ISBN 978-3-642-23347-0

[102] Wesner, E.; Choudhury, A.; August, A.; Berghoff, M.; Nestler, B.
A phase-field study of large-scale dendrite fragmentation in Al-Cu.
Journal of Crystal Growth, 359(2012) S.107-121; DOI:10.1016/j.jcrysgro.2012.08.036

[103] Wulf, S.E.; Holstein, N.; Krauss, W.; Konys, J.
Influence of deposition conditions on the microstructure of Al-based coatings for applications as corrosion and anti-permeation barrier.
27th Symp.on Fusion Technology (SOFT 2012), Liege, B, September 24-28, 2012

Nuclear Data

[1] Fischer, U.; Leichtle, D.; Serikov, A.; Pereslavtsev, P.
Monte Carlo based approaches to shielding analyses of ITER ports.
20th Topical Meeting on the Technology of Fusion Energy (TOFE 2012), Nashville, Tenn., August 27-31, 2012

[2] Serikov, A.; Fischer, U.; Leichtle, D.; Pitcher, C.S.; Suarez, A.
Local modeling approach for Monte Carlo parametric neutronic analysis in ITER.
Jahrestagung Kerntechnik 2012, Stuttgart, 22.-24.Mai 2012; Berlin : INFORUM GmbH, 2012

[3] Serikov, A.; Fischer, U.; Henderson, M.; Leichtle, D.; Pitcher, C.S.; Spaeh, P.; Strauss, D.; Suarez, A.; Weinhorst, B.
Mitigation of radiation streaming inside the ITER ports.
12th Internat.Conf.on Radiation Shielding (ICRS-12), 17th Topical Meeting of the Radiation Protection and Shielding Division of the American Nuclear Society (RPSD-2012), Nara, J, September 2-7, 2012

[4] Serikov, A.; Fischer, U.; Leichtle, D.; Pitcher, C.S.
Monte Carlo radiation shielding and activation analyses for the diagnostic equatorial port plug in ITER.
Fusion Engineering and Design, 87(2012) S.690-694; DOI:10.1016/j.fusengdes.2012.02.003

[5] Serikov, A.; Fischer, U.; Grosse, D.; Schreck, S.; Spaeh, P.; Strauss, D.
Neutronic analyses for the upper ports in the neutral beam cell of ITER.
19th Topical Meeting on the Technology of Fusion Energy (TOFE), Las Vegas, Nev., November 7-11, 2010

[6] Serikov, A.; Fischer, U.; Henderson, M.; Leichtle, D.; Pitcher, C.S.; Spaeh, P.; Strauss, D.; Suarez, A.; Weinhorst, B.
Neutronics for equatorial and upper ports in ITER.
27th Symp.on Fusion Technology (SOFT 2012), Liege, B, September 24-28, 2012

[7] Serikov, A.; Fischer, U.; Leichtle, D.; Pitcher, C.S.; Suarez, A.
Verification of the local Monte Carlo modeling approach for fusion neutronics applications in ITER.
Annual Meeting of the American Nuclear Society, Chicago, Ill., June 24-28, 2012

[8] Serikov, A.; Fischer, U.; Leichtle, D.; Pitcher, C.S.; Suarez, A.
Verification of the local Monte Carlo modeling approach for fusion neutronics applications in ITER.
Transactions of the American Nuclear Society, 106(2012) S.641-644

[9] Pereslavtsev, P.; Fischer, U.; Grosse, D.; Leichtle, D.; Majerle, M.
Shutdown dose rate analysis for the European TBM system ITER.
Fusion Engineering and Design, 87(2012) S.493-497; DOI:10.1016/j.fusengdes.2012.01.006

[10] Cabellos, O.; Klix, A.; Fischer, U.; Garcia-Herranz, N.; Sanz, J.; Simakov, S.
Impact of activation cross-section uncertainties on the tritium production in the HFTM specimen cells.
Journal of Nuclear Materials, 417(2011) S.1307-1310; DOI:10.1016/j.jnucmat.2010.12.269

[11] Fischer, U.; Große, D.; Kondo, K.; Leichtler, D.; Majerle, M.; Pereslavtsev, P.; Serikov, A.; Simakov, S.P.
KIT fusion neutronics R&D activities and related design.
24th IAEA Fusion Energy Conf., San Diego, Calif., October 8-13, 2012
Proc.publ.online Paper FTP/P7-19

[12] Fischer, U.; Simakov, S.P.; Kondo, K.; Pereslavtsev, P.
Status of the McDeLicious Approach for the D-Li Neutron Source Term Modeling in IFMIF Neutronics Calculations.
Fusion Science and Technology, 62(2012) S.233-239

[13] Grosse, D.; Fischer, U.; Kondo, K.; Leichtle, D.; Pereslavtsev, P.; Serikov, A.
The McCad geometry conversion tool and related visualisation capabilities for 3D fusion neutronics calculations.
27th Symp.on Fusion Technology (SOFT 2012), Liege, B, September 24-28, 2012

[14] Klix, A.; Adelhelm, Ch.; Fischer, U.; Gehre, D.; Kaiser, T.
Determination of the ^{6}Li content in the liPb of a neutronics mock-up of the European HCLL TBM.
15th Internat.Conf.on Fusion Reactor Materials, Charleston, S.C., October 16-22, 2011

[15] Klix, A.; Adelhelm, Ch.; Fischer, U.; Gehre, D.; Kaiser, T.
Determination of the ^{6}Li content in the liPb of a neutronics mock-up of the European HCLL TBM.
Fusion Science and Technology, 62(2012) S.196-203

[16] Klix, A.; Domula, A.; Fischer, U.; Gehre, D.; Kleizer, G.; Rovni, I.
Experimental test of activation foil materials with short half-lives for the ITER TBM.
20th Topical Meeting on the Technology of Fusion Energy (TOFE 2012), Nashville, Tenn., August 27-31, 2012

[17] Klix, A.; Fischer, U.; Förster, D.; Gehre, D.
Measurement of neutron flux spectra with a proton recoil counter in a neutronics mock-up of the HCLL TBM.
27th Symp.on Fusion Technology (SOFT 2012), Liege, B, September 24-28, 2012

[18] Klix, A.; Domula, A.; Fischer, U.; Gehre, D.; Pereslavtsev, P.; Rovni, I.
Neutronic diagnostics for European ITER TBMs: activation foil spectrometer for short measurement cycles.
Fusion Engineering and Design, 87(2012) S.1301-1306; DOI:10.1016/j.fusengdes.2012.02.129

[19] Klix, A.; Batistoni, P.; Gehre, D.; Pohorecky, W.
Neutronics experiments for the European ITER test blanket modules.
American Nuclear Society 2012 Winter Meeting, San Diego, Calif., November 11-15, 2012

[20] Klix, A.; Batistoni, P.; Gehre, D.; Pohorecky, W.
Neutronics experiments for the European ITER test blanket modules.
Transactions of the American Nuclear Society, 107(2012) Nr.1, S.377-378

[21] Klix, A.; Angelone, M.; Domula, A.; Eid, M.; Fischer, U.; Gehre, D.; Kleizer, G. ; Rovni, I.; Szalkai, D.
Neutronics experiments in support of the European fusion development program.
Vortr.: Colorado School of Mines, Golden, Colo., 6.September 2012

[22] Kondo, K.; Fischer, U.; Pereslavtsev, P.; Serikov, A.
Analyses of fusion relevant shielding benchmark experiments using the FENDL-3 nuclear data library.
12th Internat.Conf.on Radiation Shielding (ICRS-12), 17th Topical Meeting of the Radiation Protection and Shielding Division of the American Nuclear Society (RPSD-2012), Nara, J, September 2-7, 2012

[23] Kondo, K.; Fischer, U.; Heinzel, V.; Klix, A.; Serikov, A.
Dose rate analyses for the high energy beam transport section of IFMIF.
Fusion Science and Technology, 62(2012) S.226-232

[24] Kondo, K.; Arbeiter, F.; Fischer, U.; Große, D.; Heinzel, V.; Klix, A.; Serikov, A.; Tian, K.; Weber, V.
Neutronic analysis for the IFMIF target and test cell using a new CAD-based geometry model.
Fusion Engineering and Design 87(2012) S.983-988; DOI:10.1016/j.fusengdes.2012.02.060

[25] Kondo, K.; Arbeiter, F.; Fischer, U.; Große, D.; Heinzel, V.; Klix, A.; Serikov, A.; Tian, K.; Weber, V.
Re-evaluation of the irradiation cnditions in the IFMIF test cell based on the EVEDA phase design.
27th Symp.on Fusion Technology (SOFT 2012), Liege, B, September 24-28, 2012

[26] Kondo, K.; Fischer, U.; Serikov, A.; Pereslavtsev, P.
Shielding analysis for the IFMIF test facility.
Jahrestagung Kerntechnik 2012, Stuttgart, 22.-24.Mai 2012; Berlin : INFORUM GmbH, 2012

[27] Kondo, K.; Arbeiter, F.; Fischer, U.; Grosse, D.; Heinzel, V.; Leichtle, D.; Le Tonqueze, Y.; Mittwollen, M.; Serikov, A.; Tian, K.; Weber, V.
Shutdown dose calculations for the IFMIF test facility and the high flux test module.
12th Internat.Conf.on Radiation Shielding (ICRS-12), 17th Topical Meeting of the Radiation Protection and Shielding Division of the American Nuclear Society (RPSD-2012), Nara, J, September 2-7, 2012

[28] Konobeyev, A.Yu.; Fischer, U.; Pereslavtsev, P.
Comparison of TALYS-1.2 and TALYS-1.4 using (p,x) data and other problems.
NEA Nuclear Data Week, Issy-les-Moulineaux, F, April 23-27, 2012

[29] Konobeyev, A.Yu.; Fischer, U.; Pereslavtsev, P.
Evaluation of activation data for p+W reactions.
NEA Nuclear Data Week, Issy-les-Moulineaux, F, April 23-27, 2012

[30] Leichtle, D.; Fischer, U.; Serikov, A.
Neutronic analysis for the IFMIF target and test cell using a new CAD-based geometry model.
Fusion Engineering and Design, 87(2012) S.1030-1034; DOI:10.1016/j.fusengdes.2012.02.068

[31] Majerle, M.; Leichtle, D.; Fischer, U.; Serikov, A.
Verification and validation of the R2Smesh approach for the calculation of high resolution shut-down dose rate distribution.
Fusion Engineering and Design, 87(2012) S.443-447; DOI:10.1016/j.fusengdes.2011.12.010

[32] Pereslavtsev, P.; Fischer, U.; Leichtle, D.; Villari, R.
Novel approach for efficient mesh based Monte Carlo shutdown dose rate calculations.
27th Symp.on Fusion Technology (SOFT 2012), Liege, B, September 24-28, 2012

[33] Simakov, S.P.; Fischer, U.
Displacement damage induced in iron by gammas and neutrons under irradiation in the IFMIF test cell.
Journal of Nuclear Materials, 417(2011) S.1321-1324; DOI:10.1016/j.jnucmat.2010.12.175

International Fusion Materials Irradiation Facility (IFMIF)

[1] Abou-Sena, A.; Arbeiter, F.
Development of the IFMIF tritium release test module in the EVEDA phase.
27th Symp.on Fusion Technology (SOFT 2012), Liege, B, September 24-28, 2012

[2] Chen, Y.; Arbeiter, F.; Schlindwein, G.
A comparative study of turbulence models for conjugate heat transfer to gas flow in a heated mini-channel.
Numerical Heat Transfer A, 61(2012) S.38-60; DOI:10.1080/10407782.2012.638524

[3] Chen, Y.; Arbeiter, F.
Flow and heat transfer characteristics of helium cooled IFMIF high flux test module.
Fusion Engineering and Design, 87(2012) S.530-534; DOI:10.1016/j.fusengdes.2012.01.011

[4] Chen, Y.; Arbeiter, F.
Numerical simulation on gas-cooled closely-packed solid specimens.
Internat.Conf.of Numerical Analysis and Applied Mathematics (ICNAAM 2012), Kos, GR, September 19-25, 2012

[5] Chen, Y.; Arbeiter, F.
Numerical simulation on gas-cooled closely-packed solid specimens.
Simos, T.E. [Hrsg.]
Numerical Analysis and Applied Mathematics ICNAAM 2012 : Proc.of the Internat.Conf., Kos, GR, September 19-25, 2012
Melville, N.Y. : American Inst.of Physics, 2012; Vol.A S.78-81 (
AIP Conference Proceedings ; 1479) ISBN 978-0-7354-1088-6

[6] Chen, Y.; Arbeiter, F.; Heinzel, V.; Schlindwein, G.
Transient conjugated heat transfer within IFMIF high flux test module.
Nuclear Engineering and Design, 249(2012) S.172-179; DOI:10.1016/j.nucengdes.2011.07.051

[7] Draksler, V.
Auslegung eines Sensors zur Messung eines Referenz-Fluoreszenzsignals von Aceton-Tracer in Gasatmosphären.
Bachelorthesis, Hochschule Karlsruhe - Technik und Wirtschaft 2012

[8] Klein, C.; Arbeiter, F.; Martin, T.; Taubmann, P.
Hydraulic and thermal testing of different helium cooled irradiation rig models for the IFMIF high flux test module.
27th Symp.on Fusion Technology (SOFT 2012), Liege, B, September 24-28, 2012

[9] Klein, C.; Arbeiter, F.; Jackowski, T.; Martin, T.; Schlindwein, G.
Hydraulic testing of helium cooled irradiation rigs of the IFMIF high flux test module.
Fusion Engineering and Design, 87(2012) S.1414-1419; DOI:10.1016/j.fusengdes.2012.03.019

[10] Mittwollen, M.; Madzharov, V.; Kubaschewski, M.; Eilert, D.; Tian, K.
IFMIF-cells: Layout, arrangement, improvement.
Jahrestagung Kerntechnik 2012, Stuttgart, 22.-24.Mai 2012; Berlin : INFORUM GmbH, 2012

[11] Schlindwein, G.; Arbeiter, F.; Freund, J.
Start-up phase of the HELOKA-LP low pressure helium test facility for IFMIF irradiation modules.
Fusion Engineering and Design, 87(2012) S.737-741; DOI:10.1016/j.fusengdes.2012.02.020

[12] Tian, K.
Introduction on IFMIF, IFMIF test facility, and IFMIF test cell design.
Vortr.: Southwest Institute of Physics, Chengdu, China, 11.September 2012

[13] Tian, K.; Arbeiter, F.; Eilert, D.; Heinzel, V.; Heupel, T.; Madzharov, V.; Mittwollen, M.
Pipes, cables, and their connections under high neutron and gamma irradiation in the IFMIF test cell.
Jahrestagung Kerntechnik 2012, Stuttgart, 22.-24.Mai 2012
Berlin : INFORUM GmbH, 2012

[14] Vladimirov, P.; Borodin, V.
Role of Him in swelling of neutron irradiated beryllium.
10th IEA Internat.Workshop on Beryllium Technology, Karlsruhe, September 19-21, 2012

Fuel Cycle – Vacuum Pumping

[1] Scannapiego, M.; Day, C.; Hanke, S.; Hauer, V.; Ochoa Guaman, S.
Pressure loss and convective heat transfer coefficneints for ITER cryopumps hydroformed components.
24th Internat.Cryogenic Engineering Conf., Internat.Cryogenic Materials Conference 2012, Fukuoka, J, May 14-18, 2012

[2] Battes, K.; Day, Chr.; Hauer, V.
Outgassing measurement of fusion relevant materials.
27th Symp.on Fusion Technology (SOFT 2012), Liege, B, September 24-28, 2012

[3] Battes, K.; Hauer, V.
Outgassing rate measurement by using the difference method.
76.Jahrestagung der DPG und DPG-Frühjahrstagung, Fachverband Vakuumphysik und Vakuumtechnik, Berlin, 25.-30.März 2012
Verhandlungen der Deutschen Physikalischen Gesellschaft, R.6, B.47(2012), VA 2.1

[4] Day, C.; Giegerich, T.; Hauer, V.
A network modelling approach for complex vacuum systems in a wide range of the Knudsen number.
27th Symp.on Fusion Technology (SOFT 2012), Liege, B, September 24-28, 2012

[5] Day, Chr.; Giegerich, T.; Hauer, V.; Luo, X.; Varoutis, S.
The use of flow network tools for geometrically complex vacuum gas dynamics problems. (eingeladen)
6th European Congress on Computational Methods in Applied Sciences and Engineering (ECCOMAS 2012), Wien, A, September 10-14, 2012

[6] Day, Chr.
What large vacuum systems can learn from micro gas flows - and vice versa. (eingeladen)
1st European Conf.on Gas Micro Flows, Skiathos, GR, June 6-8, 2012

[7] Dremel, M.; Pearce, R.; Strobel, H.; Hauer, V.; Day, C.; Papastergiou, S.
The new build to print design of the ITER torus cryopump.
27th Symp.on Fusion Technology (SOFT 2012), Liege, B, September 24-28, 2012

[8] Haas, H.; Day, Chr.; Herzog, F.
TIMO-2 - a cryogenic test bed for the ITER cryosorption pumps.
Weisend, J.G. [Hrsg.]
Advances in Cryogenic Engineering : Transactions of the Cryogenic Engineering Conf., Spokane, Wash., June 13-17, 2011
Melville, N.Y. : AIP, 2012 S.1699-1705 (AIP Conference Proceedings ; 1434)
(Advances in Cryogenic Engineering ; 57A); ISBN 978-0-7354-1020-6

[9] Hanke, S.; Scannapiego, M.; Luo, X.; Day, Chr.; Fellin, F.; Zaccaria, P.; Wikus, P.; Dremel, M.
Development of a large customized NBI cryopump system.
20th Topical Meeting on the Technology of Fusion Energy (TOFE 2012), Nashville, Tenn., August 27-31, 2012

[10] Hanke, S.; Scannapiego, M.; Luo, X.; Day, Chr.; Fellin, F.; Zaccaria, P.
The development of the unique and large cryopump system for the heating neutral beam injection of ITER.
Internat.Symp.on Vacuum Science and Technology and its Application for Accelerators (IVS 2012), Kolkata, IND, February 15-17, 2012

[11] Hauer, V.; Day, Chr.; Dremel, M.; Haas, H.; Hanke, S.; Fellin, F.; Luo, X.; Lässer, R.; Papastergiou, St.; Pearce, R.; Scannapiego, M.; Simon, R.; Strobel, H.; Wikus, P.
Large cryopumps for fusion.
14th Joint Vacuum Conf.(JVC-14), 12th European Vacuum Conf.(EVC-12), 11th Annual Meeting of the German Vacuum Society (AMDVG-11), 19th Croatian-Slovenian Vacuum Meeting (CroSloVM-19), Dubrovnik, HR, June 4-8, 2012

[12] Luo, X.; Hauer, V.; Day, C.
Monte Carlo calculation of the thermal radiation heat load of the ITER preproduction cryopump.
Fusion Engineering and Design, 87(2012) S.603-607; DOI:10.1016/j.fusengdes.2012.01.036

[13] Luo, X.; Hauer, V.; Ochoa, S.; Day, Chr.
Simulation of the thermal radiation heat load of a large-scale customized cryopump with the Monte Carlo ray trace method.
24th Internat.Cryogenic Engineering Conf., Internat.Cryogenic Materials Conference 2012, Fukuoka, J, May 14-18, 2012

[14] Luo, X.; Giegerich, T.; Day, C.
Transient gas flow studied by test particle Monte Carlo approach with ProVac3D.
28th Internat.Symp.on Rarefied Gas Dynamics (RDG 28), Zaragoza, E, July 9-13, 2012

[15] Masiello, A.; Agarici, G.; Bonicelli, T.; Fantini, F.; Gagliardi, M.; Paolucci, F.; Simon, M.; Wikus, P.; Batchford, P.; Boilson, D.; Dalla Palma, M.; Day, C.; Dremel, M.; Decamp, H.; Franzen, P.; Graceffa, J.; Heinemann, B.; Hanke, S.; Hemsworth, R.; Kuriyama, M.; Luchetta, A.; Marcuzzi, D.; Pearce, R.; Rigato, W.; Schunke, B.; Svensson, L.; Toigo, V.; Zaccaria, P.; Sonato, P.
EU development of the ITER neutral beam injector and test facility.
24th IAEA Fusion Energy Conf., San Diego, Calif., October 8-13, 2012

[16] Ochoa, S.; Hanke, S.; Day, C.
Heat transfer enhancement of NBI vacuum pump cryopanels.
27th Symp.on Fusion Technology (SOFT 2012), Liege, B, September 24-28, 2012

[17] Ochoa, S.; Day, C.; Hanke, S.
Vacuum system design of the MITICA Test Facility - Challenges for the cryopump.
76. Jahrestagung der DPG und DPG-Frühjahrstagung, Fachverband Vakuumphysik und Vakuumtechnik, Berlin, D, 25.-30. März 2012
Verhandlungen der Deutschen Physikalischen Gesellschaft, R.6, B.47(2012), VA 3.2

[18] Ochoa, S.; Day, Chr.
Vacuum systems on fusion power plants.
Vortr.: Escuela Superior Politecnica del Litoral, Guayaquil, EC, 20.Dezember 2012

[19] Sonato, P.; Boilson, D.; Bonicelli, T.; Chakraborty, A.K.; Day, C.; Franzen, P.; Gorini, G.; Inoue, T.; Milnes, J.; Minea, T.
Design of the MITICA neutral beam injector: from physics analysis to engineering design.
24th Fusion Energy Conf., San Diego, Calif., October 8-13, 2012

[20] Valente, M.; Fellin, F.; Haas, H.; Hanke, S.; Scannapiego, M.; Zaccaria, P.
Design proposal for MITICA cryogenic plant.
Cryogenics : 12th IIR Internat.Conf., Dresden, September 11-14, 2012

[21] Varoutis, S.; Day, C.; Luo, X.; Haas, H.; Shapirov, F.
Experimental results and direct simulation Monte Carlo modelling of a high- performance large-scale cryopump.
American Vacuum Society 59th Internat.Symp.and Exhibition, Tampa, Fla., October 28 - November 2, 2012

[22] Varoutis, S.; Day, C.
Numerical modeling of an ITER type cryopump.
Fusion Engineering and Design, 87(2012) S.1395-1398; DOI:10.1016/j.fusengdes.2012.03.023

[23] Varoutis, S.; Day, C.; Sharipov, F.
Rarefied gas flow through channels of finite length at various pressure ratios.
Vacuum, 86(2012) S.1952-1959; DOI:10.1016/j.vacuum.2012.04.032

[24] Varoutis, S.; Giegerich, T.; Hauer, V.; Day, Chr.
TRANSFLOW: an experimental facility for vacuum gas flows.
1st European Conf.on Gas Micro Flows, Skiathos, GR, June 6-8, 2012

[25] Varoutis, S.; Giegerich, T.; Hauer, V.; Day, Chr.
TRANSFLOW: an experimental facility for vacuum gas flows.
DOI:10.1088/1742-6596/362/1/012027

[26] Yang, Y.; Marujama, S.; Kiss, G.; Ciattaglia, S.; Putvinski, S.; Yoshino, R.; Li, W.; Jiang, T.; Li, B.; Varoutis, S.; Day, C.
Concepts desing of fusion power shutdown system for ITER.
27th Symp.on Fusion Technology (SOFT 2012), Liege, B, September 24-28, 2012

[27] Day, C.
The direct internal recycling concept to simplify the fuel cycle of a fusion power plant.
27th Symp.on Fusion Technology (SOFT 2012), Liege, B, September 24-28, 2012

[28] Day, Chr.; Bornschein, B.; Demange, D.; Giegerich, Th.; Kovari, M.; Weyssow, B.; Wolf, R.
Technology gaps for the fuel cycle of a fusion power plant.
24th Fusion Energy Conf., San Diego, Calif., October 8-13, 2012

[29] Giegerich, T.; Day, C.
Conceptuation of a continuosly working vacuum pump train for fusion power plants.
27th Symp.on Fusion Technology (SOFT 2012), Liege, B, September 24-28, 2012

[30] Giegerich, T.; Day, C.
Fusionskraftwerke - Anforderungen und gegenwärtige technische Entwicklungen der Vakuumpumpsysteme.
76. Jahrestagung der DPG und DPG-Frühjahrstagung, Fachverband Vakuumphysik und Vakuumtechnik, Berlin, D, 25.-30. März 2012
Verhandlungen der Deutschen Physikalischen Gesellschaft, R.6, B.47(2012), VA 1.2

Fuel Cycle – Tritium Processing

[1] Alecu, C.G.; Besserer, U.; Bornschein, B.; Kloppe, B.; Köllö, Z.; Wendel, J.
Reachable accuracy and precision for tritium measurements by calorimetry at TLK.
Fusion Science and Technology, 60(2011) S.937-940

[2] Bekris, N.; Sirch, M.
On the mechanism of disproportionation of ZrCo hydrides.
Fusion Science and Technology, 62(2012) S.50-55

[3] Borisevich, O.; Demange, D.; Parracho, T.; Pera-Titus, M.; Nicolas, C.H.
Permeance and selectivity of helium and hydrogen in nanocomposite MFI-alumina hollow fibre for tritium processes.
Blasco, T. [Hrsg.]
5th Internat.FEZA Conf., Valencia, E, July 3-7, 2011; Extended Abstracts publ.online
Valencia : Universitat Politecnica de Valencia, 2011 S.1054-1055; ISBN 978-84-8363-722-7

[4] Bornschein, B.
Between fusion and cosmology - the future of the Tritium Laboratory Karlsruhe.
Fusion Science and Technology, 60(2011) S.1088-1091

[5] Demange, D.; Fanghänel, E.; Kloppe, B.; Le, T.L.; Scheel, F.; Simon, K.H.; Wagner, R.; Welte, S.
CAPER modifications and first experimental results on highly tritiated water processing with PERMCAT at the Tritium Laboratory Karlsruhe.
Fusion Science and Technology, 60(2011) S.1317-1322

[6] Demange, D.; Bekris, N.; Besserer, U.; Le, L.T.; Kramer, F.; Parracho, A.; Wagner, R.
Overview of processes using zeolite at the Tritium Laboratory Karlsruhe.
Blasco, T. [Hrsg.]
5th Internat.FEZA Conf., Valencia, E, July 3-7, 2011; Extended Abstracts publ.online
Valencia : Universitat Politecnica de Valencia, 2011 S.1060-1061; ISBN 978-84-8363-722-7

[7] Munakata, K.; Demange, D.
Development of numerical simulation code of membrane reactor for detritiation.
Fusion Engineering and Design, 86(2011) S.2334-2337; DOI:10.1016/j.fusengdes.2011.03.028

[8] Neuberger, H.; Rey, J.; von der Weth, A.; Freiner, P.
Progress in the KIT approach for development of the HCPB TBM stiffening plate feasibility mock up fabrication.
27th Symp.on Fusion Technology (SOFT 2012), Liege, B, September 24-28, 2012

[9] Parracho, A.I.; Demange, D.; Knipe, S.; Le, L.T.; Simon, K.H.; Welte, S.
Processing highly tritiated water desorbed from molecular sieve bed using PERMCAT.
Fusion Engineering and Design, 87(2012) S.1277-1281; DOI:10.1016/j.fusengdes.2012.02.118

[10] Plusczyk, C.; Bekris, N.; Cristescu, I.; Lohr, N.; Michling, R.; Moosmann, H.; Welte, S.
Experimental assessment of a catalytic hydrogen oxidation system for the off- gas processing of the ITER WDS.
27th Symp.on Fusion Technology (SOFT 2012), Liege, B, September 24-28, 2012

[11] Plusczyk, C.; Brad, S.
Numerical investigation of design influences on a material test setup at cryogenic temperatures.
Low Temperature Physics (ICYS LTP 2012) : 3rd Internat.Conf.for Young Scientists, Kharkov, UA, May 14-18, 2012

[12] Santucci, A.; Demange, D.; Goerke, O.; Le, L.T.; Pfeifer, P.; Welte, S.
Inactive commissioning of a micro channel catalytic reactor for highly tritiated water production in the CAPER facility of TLK.
Fusion Engineering and Design, 87(2012) S.547-550; DOI:10.1016/j.fusengdes.2012.01.021

[13] Welte, S.; Demange, D.; Wagner, R.; Gramlich, N.
Development of a technical scale PERMCAT reactor for processing of highly tritiated water.
Fusion Engineering and Design, 87(2012) S.1045-1049; DOI:10.1016/j.fusengdes.2012.02.100

[14] Bornschein, B.; Day, Chr.; Demange, D.; Pinna, T.
Tritium management and safety issues in ITER and DEMO breeding blankets.
27th Symp.on Fusion Technology (SOFT 2012), Liege, B, September 24-28, 2012

[15] Demange, D.; Borisevich, O.; Bornschein, B.; Grasina, M.; Le, T.L.; Lefebvre, X. ; Wagner, R.; Welte, S.
Membranes and catalytic membrane reactors as key components in the deuterium-tritium fuel cycle of future fusion machines.
12th Internat.Conf.on Inorganic Membranes, Enschede, NL, July 9-13, 2012

[16] Demange, D.; Alecu, C.G.; Bekris, N.; Borisevich, O.; Bornschein, B.; Fischer, S.; Gramlich, N.; Köllö, Z.; Le, T.L.; Michling, R.; Priester, F.; Röllig, M.; Schlösser, M.; Stämmler, S.; Sturm, M.; Wagner, R.; Welte, S.
Overview of R&D at TLK for process and analytical issues on tritium management in breeder blankets of ITER and DEMO.
Fusion Engineering and Design, 87(2012) S.1206-1213; DOI:10.1016/j.fusengdes.2012.02.105

[17] Demange, D.; Borisevich, O.; Lefebvre, X.; Wagner, R.; Welte, S.
Zeolite membranes and palladium membrane reactor for tritium extraction from the breeder blankets of ITER and DEMO.
27th Symp.on Fusion Technology (SOFT 2012), Liege, B, September 24-28, 2012

[18] Lefebvre, X.; Demange, D.; Borisevich, O.; Kind, M.
Simulation of the performance of membrane cascade processes for gaseous separation using zeolite membranes.
12th Internat.Conf.on Inorganic Membranes, Enschede, NL, July 9-13, 2012

[19] Ricapito, I.; Boccaccini, L.V.; Calderoni, P.; Ciampichetti, A.; Demange, D.; Poitevin, Y.
Tritium management in the European test blanket systems and extrapolation to DEMO.
24th IAEA Fusion Energy Conf., San Diego, Calif., October 8-13, 2012

Safety

[1] Klimenko, D.; Pasler, V.
Safety of fusion magnets: model experiments to high current arcs at ITER bushbars and feeder lines.
Fusion Engineering and Design, 87(2012) S.675-679; DOI:10.1016/j.fusengdes.2012.02.005

Appendix IV: Glossary

2C-PIM	2Componenten Power Injection Moulding
AC	Alternating Current
ALICE/ASH	The Code for the calculation of nuclear reaction cross-sections and secondary particle distributions using geometry dependent hybrid model
APD	Avalance Photo Diode
ARIES	Advanced Reactor Innovation and Evaluation Study
ART-MS	Auto-Resonant ion Trap Mass Spectrometer
ASTM	American Society for Testing and Materials
BA	Broader Approach
BA DEMO	Broader Approach DEMO
BB	Breading Blanket
BCA	Binary Collision Approximation
BDT	Brittle-to-Ductile Transition
BEKED	Nuclear Data Evaluation Code System developed by KIT
BGK	Bhatnagar–Gross–Krook kinetic model
BSM	Blanket Shield Module
BtP	Build-to-print
BTR	Beam Transport Room
BU	Breeder Unit
BUSARC	Subroutine of MAGS for the simulation of mobile arcs at coil external current leads (busbars)
CAD	Computer Aided Design
CCFE	Culham Centre for Fusion Energy, UK
CEA	Commissariat à l'Énergie Atomique, Saclay (France)
CFD	Computational Fluid Dynamics
CfT	Call for Tender
CHF	Critical Heat Flux
CIEMAT	Centro de Investigaciones Energeticas Medioambientales y Tecnologicas
CNR	Consiglio Nazionale delle Ricerche, Milano, Italy
COD	Crack Opening Displacement
Consorzia RFX	Italien Fusion Association Padova
CP	Cooling Plate
CP	Cryopanel System
CPU	Central Processing Unit

CQ	Current Quench
C-R	Circumferential Orientation
CRPP-EPFL	Centre de Recherces en Physique des Plasmas, - École polytechnique fédérale de Lausanne, Switzerland
CS	Compact Stellarator Power Plant
CTS	Collective Thomson Scattering
Cu	Copper
CuLTKa	Current Lead Test Facility Karlsruhe
CVD	Chemical Vapor Deposition
CW	Continuous Wave
cw	cold worked
D1S	Direct 1-Step, method for calculating shut-down dose rates based on Monte Carlo particle transport calculation for neutrons and decay photons in one run.
DAMC	Direct Simulation Monte Carlo
DBTT	Ductile-to-Brittle Transition Temperature
DCLL	Dual Coolant Lithium Lead
DEMO	DEMOnstration Fusion Reactor
DFW	First Wall of the Diagnostics Port Plug in ITER
DIFFER	Dutch Institute for Fundamental Energy Research, Netherland
DIR	Direct Internal Recycling Concept
dpa	displacements per atom
DSM	Shielding Module of the Diagnostics Port Plug in ITER
DSMC	Direct Simulation Monte Carlo
DTL	Drift Tube Linac
EAF	European Activation File
EASY	European Activation System
EB	Electron Beam Welding
EBSD	Electron Back Scatter Diffraction
ECCD	Electron Cyclotron Current Drive
ECH	Electron Cyclotron Heating launcher in the ITER port
ECH & CD	Electron Cyclotron Heating and Current Drive
ECRH	Electron Cyclotron Resonance Heating
EDM	Electrical Discharge Machining
EDX	Energy Dispersive X-ray Spectroscopy
EELS	Electron Energy Loss Spectroscopy
EFDA	European Fusion Development Agreement
EFF	Nuclear Data Evaluation Code System developed by KIT

EFREMOV	Scientific Research Institute, Saint Petersburg, Russia
EFTEM	Energy Filtered Transmission Electron Microscopy
EGYC	European Gyrotron Consortium
ELM	Edge Localised Mode
EM	Electromagnetic
ENDF	Evaluated Nuclear Data File (USA)
ENEA	Italian National Agency for New Technologies, Energy and Sustainable Economy Development
EPP	Diagnostic Generic Equatorial Port Plug in ITER
EU	European
EUROFER	European reduced activation ferritic-martensitic steel
EVEDA	Engineering Validation and Engineering Design Activities
EXFOR	Exchange Format for experimental data
F4E	Fusion for Energy
FCI	Flow channel insert
FDS	Fusion Design Study / Fusion Digital Simulation (Hefei, China)
FEG-SEM	Field Emission Gun Scanning Electron Microscope
FEM	Finite Element Method
FIB	Focused Ion Beam Microscope
FISPACT	Nuclear Inventory and Activation Code
FLUKA	Particle physics Monte Carlo simulation code system
FM	Fracture-Mechanical
FML	Fusion Materials Laboratory (KIT, Germany)
FMU	Feasibility Mock Up
FNG	Frascati Neutron Generator
FPD	Full Power Days
FPY	Full Power Year
FRS	Floor Response Spectrum
FSSS	Fisher Sub-Sieve Size
FT	Fracture Toughness
FW	First Wall
FWP	First Wall Panel
FZ	Fusion Zone
FZJ	Forschungszentrum Jülich
GB	Grain Boundary

GDH	Geometry Dependent Hybrid nuclear model
GDS	Glow Discharge Cleaning Unit in the ITER Port
GEANT	Toolkit for the Monte Carlo particle transport simulation
GOT	Goal Oriented Training Programme
GS2	Lithium Glass Scintallator
H2	Hydrogen
HAADF	High Angle Annular Dark Field
HAS	Hungarian Academy of Sciences
HAZ	Heat Affected Zone
HCLL	Helium Cooled Lithium Lead
HCPB	Helium Cooled Pebble Bed
He	Helium
HELIOS	Supercomputer at International Fusion Energy Research Centre (IFERC) – Computational Simulation Centre (CSC) in Rokkasho, Japan
HELLAS	A synonym for the collaborating Greek Institutions National Technical University of Athens, Greece and the National and Kapodistrian University of Athens, Greece
HELOKA	Helium Loop Karlsruhe
HFR	High Flux Reactor (Petten)
HHF	High Heat Flux
HHFM	High Heat Flux Materials
HIDOBE	HIgh DOse BEryllium (name of the irradiation campaign)
HIP	Hot Isostatic Pressing
HNB	Heating Neutral Beam Injector in ITER
HPC-FF	High Performance Computer for Fusion, Jülich
HR	Hot-Rolling
HTS	High Temperature Superconductor
IAEA	International Atomic Energy Agency
IAM-AWP	Institute for Applied Materials - Applied Materials Physics
IAM-WBM	Institute for Applied Materials– Materials and Biomechanics
ICIT	National Institute of Research and Development for Cryogenics and Isotope Technology, Rm. Valcea, Romania
IFMIF	International Fusion Material Irradiation Facility
IG	Impact Ground Vacuum Cast
IGES	CAD Data Format
INTRA	In-Vessel Transient Analysis Code by Studsvik
IPF	Institut für Plasmaforschung, Universität Stuttgart, Germany
IPP	Max Planck Institut für Plasmaphysik, Garching,/Greifswald, Germany
IPPLM-WUT	Institute of Plasma Physics and Laser Microfusion – Warsaw University of Technology, PL

ISS	Isotope Separation System
ISSP	Institute of Solid State Physics, Riga, Latvia
ITEP	Institute for Technical Physics
ITER	International Thermonuclear Experimental Reactor
ITERVAC	KIT simulation code for gas flow networks
ITN	Instituto Technologico e Nuclear, Lisbon, Portugal
IVVS	In-Vessel Viewing System
JAEA	Japan Atomic Energy Agency
JEFF	Joint Evaluated Fission and Fusion File (EU nuclear data library)
JENDL	Japanese Evaluated Nuclear Data Library
JET	Joint European Torus
J_{IC}	Critical value of J-integral at the onset of stable crack growth
JSC	Jülich Supercomputing Centre
JSC “SSC RIAR”	Joint Stock Company “State Scientific Centre Research Institute of Atomic Reactors”
JSI	Johan Stefan Institute, Ljubljana
JT-60	Japan Torus with D-shape Cross Section
JUROPA/HPC-FF	High Performance Computing for Fusion cluster at Juelich Supercomputing Centre at Forschungszentrum Juelich, Germany
KALOS	Karlsruhe Lithium Orthosilicate
K_{IC}	Critical Stress Intensity Factor for Model I Loading
KIT	Karlsruhe Institute of Technology
LCF	Low Cycle Fatigue
LHD	Helical Stellarator
LOM	Light Optical Microscope / Microscopy
L-S	Longitudinal – Short Transverse
MA	Mechanical Alloying
MAGS	KIT Magnet Safety Code System (MAGnet System)
MAXED	Unfolding Code
MC	Monte Carlo
MCAM	Software tool for CAD to MC geometry conversion (by FDS team, Hefei, China)
McCAD	Software tool for CAD to MC geometry conversion (by KIT)
MCNP	Monte Carlo code for neutron and photon transport simulations
MCNPX	Monte Carlo Code for Multi Particle Transport Simulations
MC-R2S	Rigorous 2-Step, method for calculating shut-down dose rates based on coupled Monte Carlo particle transport and inventory calculations.
MCSEN	Monte Carlo sensitivity code based on MCNP

MD	Major Disruptions
MD	Molecular Dynamics
MEMOS	Name of Code
mfr	Mass flow rate (kg/s)
MGI	Massive Gas Injection
MHD	Magnetohydrodynamic
MITICA	Neutral Beam Test Bed in Padova, Italy
MPI	Message Passing Interface
NBI	Neutral Beam Injector
NDE	Non-destructive experiment
NE213	Liquid scintillator with capability to discriminate between gamma-ray and neutron interaction
N_f	Fatigue lifetime up to specimen failure
NGK	NGK Insulators Ltd., Japan
Ni	Nickel
NJOY	Nuclear Data processing code (LANL, USA)
NRG	Nuclear Research and Consultancy Group, National Nuclear Research Institute of the Netherlands, located in Petten
NWL	Neutron Wall Loading
OB	Outboard
ODS	Oxygen Dispersion Strengthened
OM	Optical Microscopy
OMA	Outgassing Measurement Apparatus
OMP	Optical Model Potential
$P_{He, in}$	Helium pressure (MPa)
P/R	Ratio of Power over the Major Radius
PbLi	Lead-Lithium alloy
Pd	Palladium
pF/WPS	preliminary Fabrication/Welding Procedure Specifications
PFC	Plasma Facing Components
PIA	Post Irradiation Annealing
PIE	Post Irradiation Examination
PIM	Powder Injection Moulding
PLT	Princeton Large Tokamak
PM	Powder Metallurgy
PMT	Photo Multiplier Tube

PPCS	Power Plant Conceptual Study
PPPT	Power Plant Physics and Technology
PRIMA	Neutral Beam Test Facility in Padova, Italy
PROCESS	Code for system analyses (by CCFE, Culham)
ProVac3D	KIT Code for Vacuum Flow Calculations
PWHT	Post Weld Heat Treatment
q_{max}	Maximal surface power density (MW/m2)
QMS	Quadrupole Mass Spectrometer
R2Smesh	Rigorous 2-Step mesh method for shutdown-dose rate calculations
RAFM	Reduced Activation Ferritic Martensitic (Steel)
RASS	Reduced Activation Stainless Steel
RCT	Recrystallization Temperature (0C)
RD	Rolling Direction
RE	Runaway Electron
REM	Rotaiting Electrode Method
REMUX	Pre-Test Mock-up Experiment
RF	Radio Frequency, within this report above 100 GHz
RH	Remote Handling
RIR	Radiation Isolation Room
RMR	Remote Maintenance Rating
RT	Room Temperature
S/U	Sensitivity/Uncertainty
SA2	Safety scenario of irradiation in ITER for activation calculations
SATIR	Station d'Acquisition et de Traitement InfraRouge
SCK-CEN	Studiecentrum Voor Kernenergie – Centre d'Etude de L'Energie Nucleare
SDDR	Shut-Down Dose Rate
SDR	Shutdown Dose Rate
SEM	Scanning Electron Microscopy
SERPENT	Monte Carlo reactor physics burn-up code (by VTT, Finland)
SF	Snow-flake Configuration of Magnetic Field
SIC_f / SIC	Silicon carbide composite
SOL	Scrape-off Layer
SPND	Self-Power Neutron Detector
SRSS	Square Root of Sum of Squares

SS	Stainless Steel
ST	Spherical Torus
STEM	Scanning Transmission Electron Microscopy
STEP	CAD data format
SUSD3D	3D deterministic S/U code system
t	Time (s)
T	Temperature (°C)
T_{br}	Brazing temperature
$T_{He, in}$	Helium inlet temperature (°C)
T-111	Tantalum-base alloy (Ta-8%W-2%Hf)
TALYS	Nuclear model code (NRG)
TBM	Test Blanket Module
TC	Thermocouple
TC	Test Cell
TCP	Torus Cryopump
TD	Theoretical Density
TED	Thales Electron Devices at Velizy, France
TEKES	Finnish Funding Agency for Technology and Innovation
TEM	Transmission Electron Microscope / Microscopy
TENDL	TALYS based Evaluated Nuclear Data Library
TF	Toroidal Field
THESEUS	Test Facility for DEMO Vacuum Pumps
Ti	Titanium
TIG	Tungsten Inert Gas Welding
TIMO	Test Facility for ITER Model Pump
TIR	Target Interface Room
Tm	Melting point (°C)
TOKES	Name of Code
TORE SUPRA	Tokamak
TOSKA	Torusspulen Testanordnung Karlsruhe
TP	Target plate
TPMC	Test Particle Monte Carlo
TPR	Tritium Production Rate
TQ/CQ	Thermal/Current Quench

TRANSFLOW	Test Facility for Vacuum Flows at KIT
TRIPOLI	Monte Carlo particle transport code (by CEA, France)
TRS	Thermal Radiation Shield System
T-S	Transverse – Short Transverse
TUD-NG	Technical University of Dresden Neutron Generator
UL	University of Latvia, Riga, Latvia
UL	Upper Launcher
UNED	Universidad de Educación a Distancia, Madrid, Spain
US	United States
USE	Upper Shelf Energy
UTS	Ultimate Tensile Strength
VACARC	Experimental device for small scale model arc experiments /VACuum ARC)
VDE	Vertical Displacement Event
W	Tungsten
W7-X	The Wendelstein 7-X Stellarator Project in Greifswald, Germany
WDS	Water Detritiation System
WL10	Tungsten with 10 % of La2O3
WP	Work Package

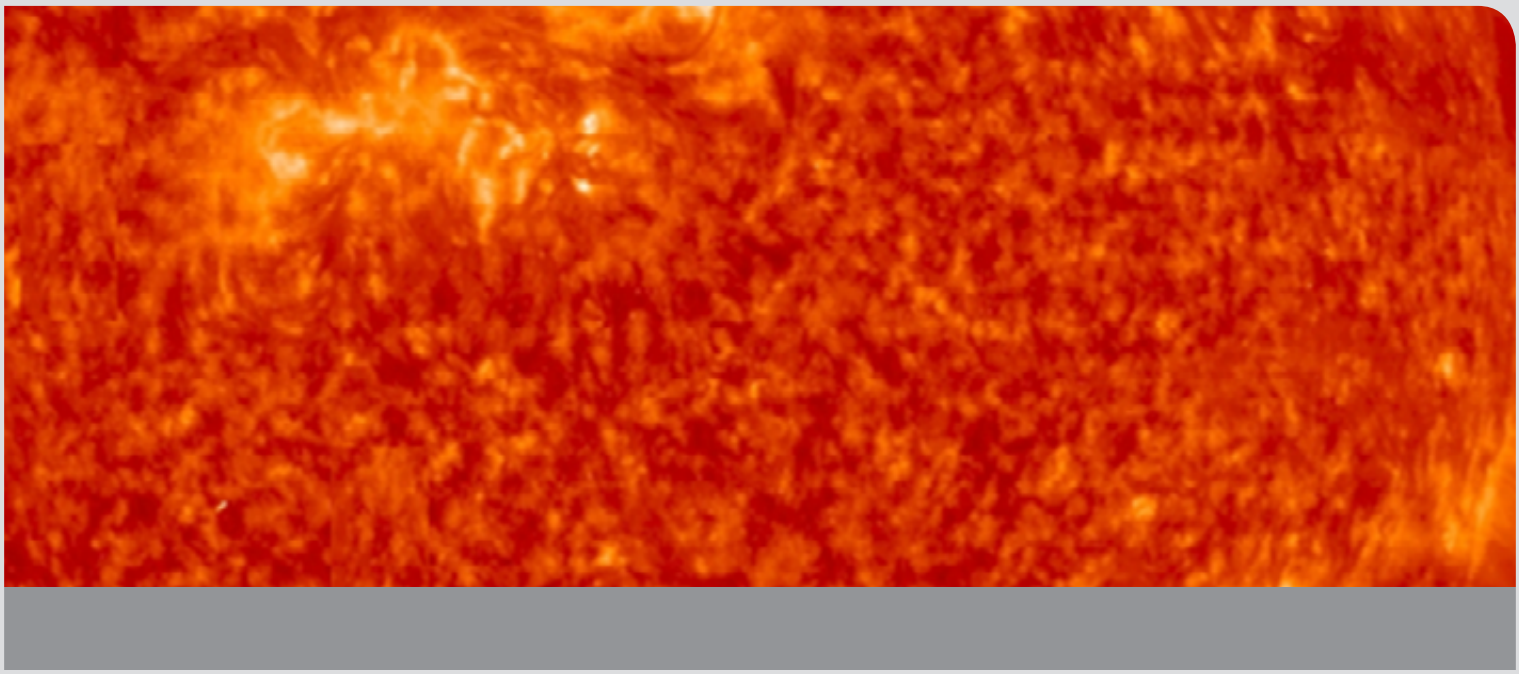

ISSN 1869-9669